Lecture Notes in Networks and Systems 329

Sanyog Rawat
Arvind Kumar
Pramod Kumar
Jaume Anguera *Editors*

Proceedings of First International Conference on Computational Electronics for Wireless Communications

ICCWC 2021

Springer

Lecture Notes in Networks and Systems

Volume 329

The series “Lecture Notes in Networks and Systems” publishes the latest developments in Networks and Systems—quickly, informally and with high quality. Original research reported in proceedings and post-proceedings represents the core of LNNS.

Volumes published in LNNS embrace all aspects and subfields of, as well as new challenges in, Networks and Systems.

The series contains proceedings and edited volumes in systems and networks, spanning the areas of Cyber-Physical Systems, Autonomous Systems, Sensor Networks, Control Systems, Energy Systems, Automotive Systems, Biological Systems, Vehicular Networking and Connected Vehicles, Aerospace Systems, Automation, Manufacturing, Smart Grids, Nonlinear Systems, Power Systems, Robotics, Social Systems, Economic Systems and other. Of particular value to both the contributors and the readership are the short publication timeframe and the world-wide distribution and exposure which enable both a wide and rapid dissemination of research output.

The series covers the theory, applications, and perspectives on the state of the art and future developments relevant to systems and networks, decision making, control, complex processes and related areas, as embedded in the fields of interdisciplinary and applied sciences, engineering, computer science, physics, economics, social, and life sciences, as well as the paradigms and methodologies behind them.

Indexed by SCOPUS, INSPEC, WTI Frankfurt eG, zbMATH, SCImago.

All books published in the series are submitted for consideration in Web of Science.

More information about this series at https://link.springer.com/bookseries/15179

Sanyog Rawat · Arvind Kumar · Pramod Kumar · Jaume Anguera
Editors

Proceedings of First International Conference on Computational Electronics for Wireless Communications

ICCWC 2021

Springer

Editors
Sanyog Rawat
Department of Electronics
and Communication Engineering
Manipal University Jaipur
Jaipur, Rajasthan, India

Pramod Kumar
Department of Electronics
and Communication Engineering
Manipal Institute of Technology, Manipal
Academy of Higher Education
Manipal, Karnataka, India

Arvind Kumar
Department of Electronics
and Communication Engineering
National Institute of Technology
Kurukshetra
Kurukshetra, Haryana, India

Jaume Anguera
Telecommunication Engineering
Ramon Llull University
Barcelona, Spain

ISSN 2367-3370 ISSN 2367-3389 (electronic)
Lecture Notes in Networks and Systems
ISBN 978-981-16-6245-4 ISBN 978-981-16-6246-1 (eBook)
https://doi.org/10.1007/978-981-16-6246-1

This Springer imprint is published by the registered company Springer Nature Singapore Pte Ltd.
The registered company address is: 152 Beach Road, #21-01/04 Gateway East, Singapore 189721, Singapore

Preface

It's a matter of great pleasure to bring out the volume containing the papers from the International Conference on Computational Electronics for Wireless Communications, ICCWC-2021, held at National Institute of Technology, Kurukshetra, India, during 11–12 June 2021. The conference was attended by faculty members, students and researchers from leading Institutes and universities along with industry professionals. The papers presented in the conference focused on the recent developments in the field of computational electronics and wireless communication. Out of nearly 200 research papers received, about 60 quality research papers were selected for presentation in the conference. The deliberations covered many upcoming technologies such as mm-Wave communications, massive MIMO, optical wireless communications technologies for 5G/6G, etc. that hold great promise in achieving the objective of performance enhancement of future networks. Technical program was rich and varied with keynote speeches, invited talks and multiple technical sessions. It provided a good platform for the scholars to enhance their knowledge by holding interaction with the experts and scholars.

The conference started with opening addresses by Dr. Vrinda Gupta, Head of Electronics and Communication Engineering Dept. NIT Kurukshetra, Prof. S. S. Pattnaik, Director of National Institute of Technical Teachers Training and Research (NITTTR), Chandigarh, India, Dr. Binoy Kumar Das, Director, IRDE Dehradun, India, and Dr. Satish Kumar, Dirctor, NIT Kurukshetra. The keynote addresses were delivered on the topics of "Fundamentals of ultraviolet wireless", "High Resolution RADAR for Atmospheric Probing", "Antenna Booster Technology: from Fundamentals to Applications", "Radio Frequency (RF) system for particle accelerators: History and Technology Developments", and "Intel compute & wireless technologies" by Prof. Yeon Ho Chung, Pukyong National University, Korea, Prof. K. P. Ray, Director, School of Radar Technology, Defence Institute of Advanced Technology (DIAT), DRDO, Pune, India, Prof. Jaume Anguera, Universitat Ramon Llull Barcelona, Spain, Dr. Hemendra Kumar Pandey Scientific Officer-G, Dept. of Atomic Energy (DAE), Kolkata, India and Mr. Sushil Mishra, Director of Software Engineering, Intel Bangalore, India, respectively. There were six technical sessions,

spread over two days, to facilitate paper presentations. With a wide range of quality papers, this volume will be of interest to researchers in both Industry and Academia.

We express our gratitude to the invited speakers for enriching this conference through their outstanding presentations. It is our pleasure to acknowledge the help we received in finalizing the technical contents of this conference. We wish to thank all reviewers and program committee members who helped us in completing the review process in a timely manner. We thank all the authors and participants for their contributions in the conference. We also gratefully acknowledge the guidance and support from the Advisory and Program Committee members of ICCWC-2021.

We hope this volume will be a valuable addition to the literature on Computational Electronics and Wireless Communication.

Jaipur, India — Sanyog Rawat
Kurukshetra, India — Arvind Kumar
Manipal, India — Pramod Kumar
Barcelona, Spain — Jaume Anguera

Contents

Design of DGS Compact UWB Antenna for C-, X-, Ku-, and Ka-Band Applications Using ANN and ANFIS Optimization Techniques 1
Rakesh K. Maurya, Binod Kumar Kannaujia, Ajay K. Maurya, and Ravi Prakash

Design and Analysis of MIMO Antenna to Reduce the Mutual Coupling Between the Circular Patches at 3.5 GHz 13
G. Naga Jyothi Sree and Suman Nelaturi

Comparative Analysis of Dipole and Bowtie Antenna on 2.4 GHz 21
Pravin Dalvadi and Amrut Patel

Gain Enhancement of Dual-Layer Patch Antenna for WLAN Applications 37
Ambavaram Pratap Reddy and Pachiyaannan Muthusamy

Dual-Band Microstrip Patch Antenna for Wireless Communication 47
Ritwik Shirbhate, Dattaji Diliprao Dhumal, and Avinash Keskar

Dual-Band RFID Tag Antenna Design for UHF Band Applications with High Read Range Performance 59
Aarti Bansal, Rajesh Khanna, and Surbhi Sharma

Impact of Packet Retransmission on VoWiFi Cell Capacity Using Fifth-Generation WLAN 75
Ayes Chinmay and Hemanta Kumar Pati

Efficient Channel Estimation in mm Wave Massive MIMO Using Hybrid Beamforming 87
Neha, Naresh Kumar, and Aarti Kochhar

Efficient Techniques for FIR Filter Designing 97
Rajni and Sanjeev Kumar Dhull

Design and Analysis of Two-Stage Operational Amplifier for Biomedical Applications 115
Pabba Sowmya, Mamatha Samson, Mohd Javeed Mehdi, and Shaik Afifa Farman

CMOS CDBA-Based Low-Voltage Low-Power Universal Filter 127
Komal, Ramnish Kumar, and K. L. Pushkar

A Case Study and Review on Current Trends in Solar Energy: Path to a Greener Environment 139
Aisha Joshna and Ravishankar Dudhe

Design and Simulation of Serial Peripheral Interface Protocol Using Pulsed Latches 155
Pujitha Karamalaputti and Arvind Kumar

Low-Power High-Performance Hybrid Scalable 161
Aishita Verma, Anum Khan, and Subodh Wairya

A Novel Controlled Positive Feedback Class AB OTA 173
Annu Dabas, Richa Yadav, and Maneesha Gupta

Low-Power and High-Speed Design of FinFET-Based MCML Delay Element 185
Pragya Srivastava, Richa Yadav, and Richa Srivastava

Design and Performance Analysis of 20 nm Si-Based DG-MOSFET 195
K. Jai Surya and Sobhit Saxena

Design and Implementation of Smart Healthcare Monitoring System Using FPGA 205
Prem Kumar Badiganti, Sumanth Peddirsi, Alla Tirumala Jagannadha Rupesh, and Suman Lata Tripathi

Performance Evaluation Using Machine Learning: Detecting Non-technical Losses in Smart Grid 215
P. Abhinayaa, R. Ezhilarasie, and A. Umamakeswari

The Study of Blockchain Technology to Enhance the Organizational Performance: Theoretical Perception 227
Swati Mathur and Lokesh Vijayvargy

Case Study on Server–Client Protocols of Industrial Controllers 241
H. Ramesh, S. Arockia Edwin Xavier, R. Pradheep Kumar, and S. Julius Fusic

Comparative Analysis on Diverse Heuristic-Based Joint Probabilistic Data Association for Multi-target Tracking in a Cluttered Environment 259
T. L. Purushottama and Pathipati Srihari

Developing a Cost Model for a Multi-Controller Software-Defined Network Using M/M/c/K Queue with Retention of Reneged Flows 271
G. Uma Maheswari and K. Vasudevan

Multi-wave Effect Estimate of Pandemic on Population: A Prediction Model and IoT-Based Alerting 281
Ratnala Vinay, M. P. R. Prasad, and T. S. V. S. Vijaya Kumar

Latency and Power Improvement of Hardware Sequences Using Collapse and Evolve Approach: Nature-Inspired Methodology 291
Ratnala Vinay and M. P. R. Prasad

Home Shanti (An Edge Computing-Based IoT System for Complete Home Security and Safety) 303
Atharv Tendolkar, Amit Choraria, K. S. Adithya, and Pramod Kumar

Review of V2g System Considering the Grid Impact and Cost Benefit 319
Umme Kulsum, Ahmed Wasim, and Ravishankar Dudhe

Energy-Efficient Cluster Head Rotation Using Fuzzy Logic 327
Jyoti Kumari, Amit Bhola, and Prabhat Kumar

Different Techniques in Neural Style Transfer-A Review 337
Kumarapu Jayaram, Malhaar Telang, Ravula Bharath Chandra Reddy, Yada Arun Kumar, Kore Shivanagendra Babu, Pooja Rana, Priyanka Chawla, and Usha Mittal

An Efficient Anonymous Authentication Scheme to Improve Security and Privacy in Large-Scale SDN-Based MANET 351
Suneel Miriyala and M. Satya Sai ram

Drowsy Alarm System Based on Face Landmarks Detection Using MediaPipe FaceMesh 363
Aman and A. L. Sangal

Siamese Network and Facial Ratios for Deformed Facial Matching 377
Ananya Sharma, Srikanth Prabhu, Aryamaan Yadav, P. Prithviraj, Vikas Venkat Sigatapu, and Pramod Kumar

Design of Novel Hamming Encoding and Decoding Circuits with Double Error Detection 391
Thanneru Chandrasekhar, M. P. R. Prasad, and Venkata Harish Babu Bhavanigari

Performance Evaluation of Iterative SRP-PHAT Techniques for Acoustic Source Localization 403
Ritu Boora and Sanjeev Kumar Dhull

Software Test Automation Using Selenium and Machine Learning 419
Nisha Jha, Rashmi Popli, Sudeshna Chakraborty, and Pramod Kumar

Project Curative Collaborative and Sponsoring Platform 431
Rishabh Sharma, Ashreeya Pant, Sudeshna Chakraborty, C. M. Shahadat, Shahid Shabir Dar, and Vivek Kumar Singh

Home Automation Using Internet of Things: An Extensive Review 441
Ruchi Yadav, Nitin Yadav, Kartik Gupta, Rashmi Priyadarshini, Sudeshna Chakraborty, and Pramod Kumar

Clustering Protocol Based on Game Theory in Heterogeneous Wireless Sensor Networks 451
Mansi Gupta, Navneet Singh Aulakh, and Inderdeep Kaur Aulakh

Data Variance-Based Distributed Outlier Detection in Wireless Sensor Networks 465
Yogita and Vipin Pal

Single-Image Super-Resolution Using Rational Fractal Interpolation and Adaptive Wiener Filtering 477
Ruchika Dhawan and Umesh Ghanekar

High-Performance Wallace Tree Multiplier Design Using Novel 8-4 Compressor Implementation for Image Processing 487
Saher Jawaid Ansari, Priyanka Verma, and Surya Deo Choudhary

Vital Signs Monitoring Using FMCW Radar for Different Body Orientations in the Presence of Random Body Movement 501
G. N. Rathna and Deepchand Meshineni

A Comparative Approach for Opinion Spam Detection Using Sentiment Analysis 511
Ashish Singh and Kakali Chatterjee

Image Dehazing Based on Colour Ellipsoid Prior and Low-Light Image Enhancement 523
Balla Pavan Kumar, Arvind Kumar, and Rajoo Pandey

A Fuzzy AHP Approach for Prioritizing Fog Computing Security Parameters 535
Jasleen Kaur, Alka Agrawal, and Raees Ahmad Khan

A Review on Local Binary Pattern Variants 545
Aditya Singh, Ramesh K. Sunkaria, and Anterpreet Kaur

Auto-luminance-Based Face Image Recognition System 553
Anurag Verulkar and Kishor Bhurchandi

A Novel Approach of Mutual Authentication in Fog Computing 567
Sameer Farooq and Priyanka Chawla

A Robust Massive MIMO Detection Based on Conjugate Gradient Approach 583
Mitesh Solanki and Shilpi Gupta

Performance Analysis of LAS Algorithm in Massive MIMO with Imperfect CSI 593
Mitesh Solanki and Shilpi Gupta

An Efficient Deep Neural Networks-Based Channel Estimation and Signal Detection in OFDM Systems 603
A. Krishnama Raju, Shilpi Gupta, and Akriti Jaiswal

Optimization of Channel Capacity of MmWave Massive MIMO Using Hybrid Precoding 615
A. Mounika Durga and Shaik Jakeer Hussain

A WDM-Based Optical Wireless Converged Architecture for Traffic Balancing 627
Abhishek Gaur and Vibhakar Shrimali

Key Pre-distribution Scheme for Wireless Sensor Networks Using Combinatorial Design 635
Lakshmi Jayant Kittur and Alwyn Roshan Pais

Performance of Kalman-Based Precoding in Millimeter-Wave Communication 645
Divya Singh

Congestion Estimation and Mitigation Using Fuzzy System in Wireless Sensor Network 655
Hemanth Kumar, S. M. Dilip Kumar, and E. Nagarjun

Refractive Index-based Ethanol Sensor using Hollow Core Photonic Crystal Fiber in THz region 669
Kajal Choudhary, Pankaj Verma, and Amit Kumar

Improving the Lifetime of Wireless Rechargeable Sensors Using Mobile Charger in On-Demand Charging Environment Based on Energy Consumption Rate Prediction 679
Anil Kumar Dudyala and Lalan Kumar Ram

Author Index 689

Editors and Contributors

About the Editors

Dr. Sanyog Rawat is presently associated with the Department Electronics and Communication Engineering, Manipal University Jaipur. He has been into teaching and research for more than seventeen years. He graduated with Bachelor of Engineering (B.E.) in Electronics and Communication, Master of Technology (M.Tech.) in Microwave Engineering and Ph.D. in the field of Planar Antennas. He has published more than 80 research papers in peer-reviewed international journals, book series and IEEE/Springer conferences. He has supervised nearly 30 M.Tech. Dissertations and 03 Ph.Ds. He has also edited the books on Proceedings of the International conference on Soft Computing Theories and Applications (SoCTA-2016, 2017), Proceedings of International Conference on Smart Systems, Innovations and Computing (SSIC-2017) and International Conference on Engineering Vibrations, Communication and Information Processing (ICoEVCI, 2018) for Springer publication. His current research interests include reconfigurable RF printed circuits, passive and active microwave integrated circuits. He is also an active member of professional bodies, i.e., Fellow IETE and Member IE.

Dr. Arvind Kumar did his B.Tech. in Electronics & Telecommunication from J. K. Institute of Applied Physics, University of Allahabad (1996), M.E. in Instrumentation & Control, MNNIT Allahabad (1999), Ph.D. from NIT Kurukshetra (2014). He also did his B.Sc. (Maths) in 1992 from Rohilkhand University, Bareilly (U.P.). Presently, he is serving as Associate Professor in the Department of Electronics & Communication Engineering, NIT Kurukshetra. He has more than 22 years of teaching experience. He has supervised one Ph.D. and more than 30 M.Tech. scholars. He has more than 50 research papers in journals and conferences in his credit. His research interests include wireless communications, OFDM/MIMO-OFDM, massive MIMO systems, Digital and image processing, optical communication, antenna and wave propagation.

Dr. Pramod Kumar received his B.E. degree in Electronics and Communication Engineering from Visvesvaraya Technological University in 2002 and M.Tech. degree in Microwave Engineering from Madhav Institute of Technology & Science; Gwalior, India, in 2007. He obtained Ph.D. from National Institute of Technology Karnataka, Mangalore, India. Currently, he is working as Associate Professor-Senior Scale in the Department of Electronics & Communication Engineering at Manipal Institute of Technology, Manipal, India. He has published more than 50 papers in reputed peer-reviewed international journals and conferences. His current areas of research are wireless sensor networks, design of antennas and microwave components for wireless communications. He is on the board of reviewers of journals like the IEEE Transactions on Antennas and Propagation, IET Networks, AEU International Journal of Electronics and Communications, Wireless Personal Communication (WPC), International Journal of Microwave and Wireless Technologies. International journal of Communications, etc.

Dr. Jaume Anguera IEEE Fellow, is the co-founder and CTO of the technology company Fractus Antennas (Barcelona). He is Associate Professor at Ramon LLull University and a member of the GRITS research group. He is Inventor of more than 130 patents, most of them licensed to telecommunication companies. He is the inventor of Virtual Antenna™ technology, which enables full functional multi-band wireless connectivity to wireless devices through miniature and off-the-shelf antenna boosters. He is Author of more than 250 scientific widely cited papers and international conferences (h-index 49) and author of 7 books. He has participated in more than 21 competitive research projects financed by the Spanish Ministry, by CDTI, CIDEM (Generalitat de Catalunya) and the European Commission for an amount exceeding €6M being principal researcher in most of them. He has taught more than 20 antenna courses around the world (USA, China, Korea, India, UK, France, Poland, Czech Republic, Tunisia, Spain). With over 21 years of R&D experience, he has developed part of his professional experience with Fractus in South Korea in the design of miniature antennas for large Korean companies such as Samsung and LG. He has received several national and international awards (ex. 2004 Best Ph.D. Thesis, two prizes, one given by Telefónica Mobile, 2004 IEEE New Faces of Engineering, 2014 Finalist European Patent Award). He has directed the master/doctorate thesis to more than 110 students; many of them have received awards for their thesis (COIT, COITT, Ministry of Education). His biography appears in Who'sWho in the World and Who'sWho in Science and Engineering. He is the associate editor of the IEEE Open Journal on Antennas and Propagation, Electronics Letters, International Journal of Electronics and Communications and reviewer in several IEEE and other scientific journals. He is Vice-chair of the working group "Software and Modeling" at EurAAP.

Contributors

P. Abhinayaa SASTRA Deemed University, Thanjavur, TN, India

K. S. Adithya Department of Electronics and Communication Engineering, Manipal Institute of Technology, Manipal, India

Alka Agrawal Department of Information Technology, Babasaheb Bhimrao Ambedkar University (A Central University), Lucknow, India

Aman Dr. B R Ambedkar National Institute of Technology, Jalandhar, India

Saher Jawaid Ansari Department of Electronics & Communication Engineering, Noida Institute of Engineering and Technology, Greater Noida, India

Inderdeep Kaur Aulakh University Institute of Engineering & Technology, Panjab University, Chandigarh, India

Navneet Singh Aulakh CSIO Analytical Facilities, CSIR-Central Scientific Instruments Organization (CSIR-CSIO), Academy of Scientific and Innovative Research (AcSIR-CSIO), Chandigarh, India

Kore Shivanagendra Babu School of Computer Science and Engineering, Lovely Professional University, Phagwara, Punjab, India

Prem Kumar Badiganti School of Electronics and Electrical Engineering, Lovely Professional University, Punjab, India

Aarti Bansal Thapar Institute of Engineering and Technology, Patiala, India

Venkata Harish Babu Bhavanigari NIT Kurukshetra, Kurukshetra, India

Amit Bhola National Institute of Technology Patna, Bihar, India

Kishor Bhurchandi Visvesvaraya National Institute of Technology (VNIT), Nagpur, Nagpur, India

Ritu Boora Department of ECE, GJUS&T, Hisar, Haryana, India

Sudeshna Chakraborty Sharda University, Greater Noida, India;
Department of CSE, SET Sharda University, Greater Noida, UP, India

Thanneru Chandrasekhar NIT Kurukshetra, Kurukshetra, India

Kakali Chatterjee Department of Computer Science and Engineering, National Institute of Technology, Patna, Bihar, India

Priyanka Chawla School of Computer Science and Engineering, Lovely Professional University, Phagwara, Punjab, India

Ayes Chinmay Department of Computer Science and Engineering, International Institute of Information Technology Bhubaneswar, Bhubaneswar, Odisha, India

Amit Choraria Department of Electronics and Communication Engineering, Manipal Institute of Technology, Manipal, India

Kajal Choudhary National Institute of Technology, Kurukshetra, Haryana, India

Surya Deo Choudhary Department of Electronics & Communication Engineering, Noida Institute of Engineering and Technology, Greater Noida, India

Annu Dabas Department of Electronics and Communication Engineering, Bharati Vidyapeeth's College of Engineering, New Delhi, India;
Department of Electronics and Communication Engineering, Indira Gandhi Delhi Technical University for Women, New Delhi, India

Pravin Dalvadi Electronics & Communication Department, Government Polytechnic Gandhinagar, Ganpat University, Mehsana, Gujarat, India

Shahid Shabir Dar Department of CSE, SET Sharda University, Greater Noida, UP, India

Ruchika Dhawan Department of Electronics and Communication, National Institute of Technology, Kurukshetra, Kurukshetra, Haryana, India

Sanjeev Kumar Dhull Department of ECE, GJUS&T, Hisar, Haryana, India

Dattaji Diliprao Dhumal Visvesvaraya National Institute of Technology, Nagpur, India

Ravishankar Dudhe Manipal Academy of Higher Education, Dubai, UAE

Anil Kumar Dudyala National Institute of Technology Patna, Patna, India

A. Mounika Durga Department of ECE, VFSTR, Guntur, Vadlamudi Andhra Pradesh, India

R. Ezhilarasie SASTRA Deemed University, Thanjavur, TN, India

Shaik Afifa Farman GRIET, Hyderabad, India

Sameer Farooq Lovely Professional University, Phagwara, Jalandhar, Punjab, India

S. Julius Fusic Thiagarajar College of Engineering, Madurai, India

Abhishek Gaur USICT, GuruGobindSinghIndraprasthaUniversity, Delhi, India

Umesh Ghanekar Department of Electronics and Communication, National Institute of Technology, Kurukshetra, Kurukshetra, Haryana, India

Kartik Gupta Sharda University, Greater Noida, India

Maneesha Gupta Department of Electronics and Communication Engineering, Netaji Subhas University of Technology, New Delhi, India

Mansi Gupta CSIO Analytical Facilities, CSIR-Central Scientific Instruments Organization (CSIR-CSIO), Academy of Scientific and Innovative Research (AcSIR-CSIO), Chandigarh, India

Shilpi Gupta Sardar Vallabhbhai National Institute of Technology, Surat, India

Shaik Jakeer Hussain Department of ECE, VFSTR, Guntur, Vadlamudi Andhra Pradesh, India

Akriti Jaiswal Sardar Vallabhbhai National Institute of Technology, Surat, India

Kumarapu Jayaram School of Computer Science and Engineering, Lovely Professional University, Phagwara, Punjab, India

Nisha Jha J.C. Bose University of Science and Technology, YMCA, Faridabad, India

Aisha Joshna Manipal Academy of Higher Education, Dubai, UAE

Binod Kumar Kannaujia School of Computation and Integrative Sciences, JNU, New Delhi, India

Pujitha Karamalaputti School of VLSI and Embedded Systems Design, National Institute of Technology, Kurukshetra, Haryana, India

Anterpreet Kaur Dr. B. R. Ambedkar National Institute of Technology, Jalandhar, India

Jasleen Kaur Department of Information Technology, Babasaheb Bhimrao Ambedkar University (A Central University), Lucknow, India

Avinash Keskar Visvesvaraya National Institute of Technology, Nagpur, India

Anum Khan Department of Electronics and Communication Engineering, Institute of Engineering and Technology, Lucknow, India

Raees Ahmad Khan Department of Information Technology, Babasaheb Bhimrao Ambedkar University (A Central University), Lucknow, India

Rajesh Khanna Thapar Institute of Engineering and Technology, Patiala, India

Lakshmi Jayant Kittur Information Security Research Lab, Department of Computer Science and Engineering, National Institute of Technology Karnataka, Mangalore, Karnataka, India

Aarti Kochhar University Institute of Engineering & Technology (UIET), Panjab University, Chandigarh, India;
Punjab Remote Sensing Centre, Ludhiana, India

Komal Department of Electronics and Communication Engineering, Guru Jambheswar University of Science and Technology, Hisar, Haryana, India

A. Krishnama Raju Sardar Vallabhbhai National Institute of Technology, Surat, India

Umme Kulsum Manipal Academy of Higher Education, Dubai, United Arab Emirates

Amit Kumar National Institute of Technology, Kurukshetra, Haryana, India

Arvind Kumar Department of ECE, National Institute of Technology, Kurukshetra, India

Balla Pavan Kumar NIT, Kurukshetra, Kurukshetra, India

Hemanth Kumar Department of MCA, J N N College of Engineering, Shivamogga, India

Naresh Kumar University Institute of Engineering & Technology (UIET), Panjab University, Chandigarh, India

Prabhat Kumar National Institute of Technology Patna, Bihar, India

Pramod Kumar Department of Electronics and Communication Engineering, Manipal Institute of Technology, Manipal, India

R. Pradheep Kumar Thiagarajar College of Engineering, Madurai, India

Ramnish Kumar Department of Electronics and Communication Engineering, Guru Jambheswar University of Science and Technology, Hisar, Haryana, India

S. M. Dilip Kumar Department of Computer Science and Engineering, University Visvesvaraya College of Engineering (UVCE), Bengaluru, India

Yada Arun Kumar School of Computer Science and Engineering, Lovely Professional University, Phagwara, Punjab, India

Jyoti Kumari National Institute of Technology Patna, Bihar, India

Swati Mathur Jaipuria Institute of Management, Jaipur, India

Ajay K. Maurya Departmet of Electronics Engineering, UNS, IET, VVS Purvanchal University, Jaunpur, India

Rakesh K. Maurya Department of Electronics and Instrumentation Engineering, Faculty of Engineering and Technology, MJP Rohilkhand University, Bareilly, U.P., India

Mohd Javeed Mehdi GRIET, Hyderabad, India

Deepchand Meshineni Department of Electrical Engineering, IISc, Bengaluru, India

Suneel Miriyala College of Engineering and Technology, Acharya Nagarjuna University, Guntur, AP, India

Usha Mittal School of Computer Science and Engineering, Lovely Professional University, Phagwara, Punjab, India

Pachiyaannan Muthusamy Department of Electronics and Communication Engineering, Advanced RF Microwave and Wireless Communication Lab, Vignan's Foundation for Science, Technology & Research (Deemed To Be University), Andhra Pradesh, India

E. Nagarjun Department of Computer Science and Engineering, University Visvesvaraya College of Engineering (UVCE), Bengaluru, India

Neha University Institute of Engineering & Technology (UIET), Panjab University, Chandigarh, India

Suman Nelaturi Department of ECE, VFSTR, Guntur, A.P, India

Alwyn Roshan Pais Information Security Research Lab, Dept. of Computer Science and Engineering, National Institute of Technology Karnataka, Mangalore, Karnataka, India

Vipin Pal National Institute of Technology Meghalaya, Shillong, India

Rajoo Pandey NIT, Kurukshetra, Kurukshetra, India

Ashreeya Pant Department of CSE, SET Sharda University, Greater Noida, UP, India

Amrut Patel Electronics & Communication Department, U.V. Patel College of Engineering, Ganpat University, Mehsana, Gujarat, India

Hemanta Kumar Pati Department of Computer Science and Engineering, International Institute of Information Technology Bhubaneswar, Bhubaneswar, Odisha, India

Sumanth Peddirsi School of Electronics and Electrical Engineering, Lovely Professional University, Punjab, India

Rashmi Popli J.C. Bose University of Science and Technology, YMCA, Faridabad, India

Srikanth Prabhu Department of Computer Science & Engineering, Manipal Institute of Technology, Manipal, India

Ravi Prakash Departmet of Electronics Engineering, UNS, IET, VVS Purvanchal University, Jaunpur, India

M. P. R. Prasad NIT Kurukshetra, Kurukshetra, India

P. Prithviraj Department of Electronics & Communication Engineering, Manipal Institute of Technology, Manipal, India

Rashmi Priyadarshini Sharda University, Greater Noida, India

T. L. Purushottama National Institute of Technology Karnataka, Surathkal, India

K. L. Pushkar Department of Electronics and Communication Engineering, Greater Noida Institute of Technology (Affiliated to GGSIP University, Delhi), Greater Noida, Uttar Pradesh, India

Rajni ECE Department, GJUS&T, Hisar, Haryana, India

Lalan Kumar Ram National Institute of Technology Patna, Patna, India

H. Ramesh Thiagarajar College of Engineering, Madurai, India

Pooja Rana School of Computer Science and Engineering, Lovely Professional University, Phagwara, Punjab, India

G. N. Rathna Department of Electrical Engineering, IISc, Bengaluru, India

Ambavaram Pratap Reddy Department of Electronics and Communication Engineering, Advanced RF Microwave and Wireless Communication Lab, Vignan's Foundation for Science, Technology & Research (Deemed To Be University), Andhra Pradesh, India

Ravula Bharath Chandra Reddy School of Computer Science and Engineering, Lovely Professional University, Phagwara, Punjab, India

Alla Tirumala Jagannadha Rupesh School of Electronics and Electrical Engineering, Lovely Professional University, Punjab, India

M. Satya Sai ram ECE Department, RVR & JC College of Engineering, Guntur, AP, India

Mamatha Samson GRIET, Hyderabad, India

A. L. Sangal Dr. B R Ambedkar National Institute of Technology, Jalandhar, India

Sobhit Saxena School of Electronics and Electrical Engineering, Lovely Professional University, Punjab, India

C. M. Shahadat Department of CSE, SET Sharda University, Greater Noida, UP, India

Ananya Sharma Department of Computer Science & Engineering, Manipal Institute of Technology, Manipal, India

Rishabh Sharma Department of CSE, SET Sharda University, Greater Noida, UP, India

Surbhi Sharma Thapar Institute of Engineering and Technology, Patiala, India

Ritwik Shirbhate Visvesvaraya National Institute of Technology, Nagpur, India

Vibhakar Shrimali GB Pant Government Engineering College, Delhi, India

Vikas Venkat Sigatapu Department of Electronics & Communication Engineering, Manipal Institute of Technology, Manipal, India

Aditya Singh Dr. B. R. Ambedkar National Institute of Technology, Jalandhar, India

Ashish Singh School of Computer Engineering, KIIT Deemed To Be University, Bhubaneswar, Odisha, India

Divya Singh Department of Electronics and Communication, GLA University, Mathura, India

Vivek Kumar Singh Department of CSE, SET Sharda University, Greater Noida, UP, India

Mitesh Solanki Sardar Vallabhbhai National Institute of Technology, Surat, India

Pabba Sowmya GRIET, Hyderabad, India

G. Naga Jyothi Sree Department of ECE, VFSTR, Guntur, A.P, India

Pathipati Srihari National Institute of Technology Karnataka, Surathkal, India

Pragya Srivastava ECE Department, IGDTUW, New Delhi, India

Richa Srivastava KIET Group of Institutions, Delhi-NCR, Ghaziabad, India

Ramesh K. Sunkaria Dr. B. R. Ambedkar National Institute of Technology, Jalandhar, India

K. Jai Surya School of Electronics and Electrical Engineering, Lovely Professional University, Punjab, India

Malhaar Telang School of Computer Science and Engineering, Lovely Professional University, Phagwara, Punjab, India

Atharv Tendolkar Department of Electronics and Communication Engineering, Manipal Institute of Technology, Manipal, India

Suman Lata Tripathi School of Electronics and Electrical Engineering, Lovely Professional University, Punjab, India

G. Uma Maheswari Thiagarajar College of Engineering, Madurai, India

A. Umamakeswari SASTRA Deemed University, Thanjavur, TN, India

K. Vasudevan Thiagarajar College of Engineering, Madurai, India

Aishita Verma Department of Electronics and Communication Engineering, Institute of Engineering and Technology, Lucknow, India

Pankaj Verma National Institute of Technology, Kurukshetra, Haryana, India

Priyanka Verma Department of Electronics & Communication Engineering, Noida Institute of Engineering and Technology, Greater Noida, India

Anurag Verulkar Visvesvaraya National Institute of Technology (VNIT), Nagpur, Nagpur, India

T. S. V. S. Vijaya Kumar NIT Kurukshetra, Kurukshetra, India

Lokesh Vijayvargy Jaipuria Institute of Management, Jaipur, India

Ratnala Vinay NIT Kurukshetra, Kurukshetra, India

Subodh Wairya Department of Electronics and Communication Engineering, Institute of Engineering and Technology, Lucknow, India

Ahmed Wasim Manipal Academy of Higher Education, Dubai, United Arab Emirates

S. Arockia Edwin Xavier Thiagarajar College of Engineering, Madurai, India

Aryamaan Yadav Department of Electronics & Communication Engineering, Manipal Institute of Technology, Manipal, India

Nitin Yadav Sharda University, Greater Noida, India

Richa Yadav Department of Electronics and Communication Engineering, Indira Gandhi Delhi Technical University for Women, New Delhi, India

Ruchi Yadav Sharda University, Greater Noida, India

Yogita National Institute of Technology Meghalaya, Shillong, India

Design of DGS Compact UWB Antenna for C-, X-, Ku-, and Ka-Band Applications Using ANN and ANFIS Optimization Techniques

Rakesh K. Maurya, Binod Kumar Kannaujia, Ajay K. Maurya, and Ravi Prakash

Abstract A novel tapered and slot loaded compact circular microstrip patch antenna (TSCCMPA) with DGS for ultra-wideband (UWB) applications is proposed. For designing of UWB TSCCMPA, a move toward optimizing the physical stricture, two vigorous techniques, namely, artificial neural network (ANN) and adaptive neuro-fuzzy inference system (ANFIS) are used. Commercially available Ansoft HFSS v.13 is utilized to extract the 144 datasets of TSCCMPAs having different sensitive parameters related to antenna dimensions and substrate materials. Apart from 144 simulated datasets, 129 were used for training and remaining 15 were utilized for testing of models. The average percentage errors (APE) for resonant frequencies of return loss are calculated regarding performance of tested datasets of ANN and ANFIS model. The APE in ANN and ANFIS model found in testing of resonant frequencies f_1 and f_2 are 0.8731%, 0.0699%, and 0.7698%, 0.0607%, respectively. The very low APE indicates that the models can be successfully applied for optimization of physical parameter of UWB TSCCMPA for computer-aided design (CAD) applications. The trained models can be used effectively for antenna parameter estimation, instead of running HFSS repetitively or other optimization techniques, which consume more time. Successful implementation of TSCCMPA shows broader impedance bandwidth of 2.6–53.5 GHz as 180% at 26.00 GHz of center frequency. The average gain of proposed antenna is found as 4.14 dBi. Due to very wideband the anticipated antenna can be effectively used in many applications.

Keywords Compact UWB microstrip antenna · Tapered and slotted circular microstrip patch · Artificial neural network · Adaptive neuro-fuzzy interface system · Computer-aided design

R. K. Maurya (✉)
Department of Electronics and Instrumentation Engineering, Faculty of Engineering and Technology, MJP Rohilkhand University, Bareilly, U.P. 243006, India
e-mail: rakesh_maurya@mjpru.ac.in

B. K. Kannaujia
School of Computation and Integrative Sciences, JNU, New Delhi 110067, India

A. K. Maurya · R. Prakash
Departmet of Electronics Engineering, UNS, IET, VVS Purvanchal University, Jaunpur, India

S. Rawat et al. (eds.), *Proceedings of First International Conference on Computational Electronics for Wireless Communications*, Lecture Notes in Networks and Systems 329,
https://doi.org/10.1007/978-981-16-6246-1_1

1 Introduction

Need of miniaturization and bandwidth enhancement of microstrip patch antenna (MPA) is today's challenge of researcher's due to portability and uniqueness features of MPA which covers maximum bands of communication applications. In this stare, many researchers used substrate material with high dielectric constant in traditional MPA, and have achieved miniaturization but the bandwidth and efficiency decreased [1–3]. Most of them have tried to overcome this problem by applying slit/slot loading in MPAs [4–9], sorting pins [10–12], sorting walls [13], and slot loaded patch [14–16] in traditional MPA and somehow succeeded to reduce the size but not even more for bandwidth enhancement. For bandwidth enhancement, the DGS MPA has been recently investigated [17–20] and the bandwidth enhancement up to 90% has been achieved.

To achieve compactness and bandwidth enhancement in the designing of traditional MPA, the analysis techniques such as cavity model [21] and transmission line model [22] were implemented. But the complicated shapes of MPA can't be analyzed with these traditional techniques. Hence, some other powerful techniques such as method of moment [23] and finite difference time domain method [24] are used. But again these techniques involve rigorous mathematical formulation with extensive numerical procedure, hence more time-consuming. In many of previous efforts, some of them tried to intend UWB MPA by these parametric analyses, and they have altered the parameters accordingly and achieved UWB characteristics [25–29]. Nowadays, most powerful software such as IE3D, HFSS, and CST Studio are widely used for analysis of any type of antenna and other microwave structure with trial-and-error basis [5, 10, 17–20]. Hence, again more time-consuming and has no guaranteed to attain an enviable goal even after numerous trial.

Recently, ANN, ANFIS, support vector machine (SVM), etc. techniques have been used efficiently for analysis of any types of MPA without any rigorous calculation and time consumption. Because once a model of ANN, ANFIS, and/or SVM has been designed for a MPA then it can be used many times at no time cost. Most of the researchers [30–37] have successfully used the ANN, ANFIS, and SVM to analyze the various parameters of MPAs and design the model.

In this paper, a novel tapered and slot loaded compact circular MPA with dimension of $20 \times 20\,\text{mm}^2$, significantly smaller than the antenna reported in above discussion, is proposed for UWB application like C, X, Ku, Ka, etc. The proposed work is followed by parametric analysis with the help of ANN and ANFIS model. The basic design procedure of ANN and ANFIS model for proposed MPA is shown in Fig. 1. ANN and ANFIS model is designed to compute the accurate resonant frequencies of proposed UWB TSCCMPA.

To design the ANN and ANFIS model, 144 datasets were collected with the help of commercially available Ansoft HFSS v.13. Apart from 144 simulated datasets, 129 were used for training the models and remaining 15 were utilized for testing the accuracy of models.

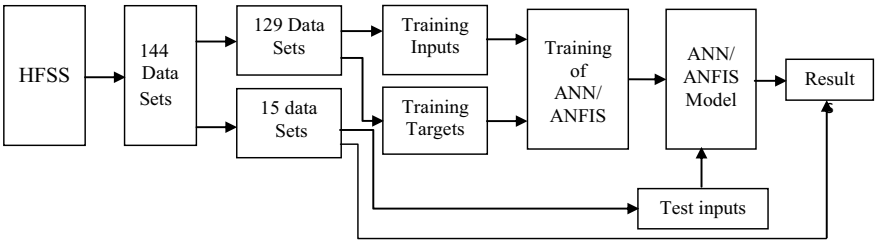

Fig. 1 Basic design procedure of ANN and ANFIS model of proposed UWB TSCCMPA

The proposed work is divided mainly into three parts (i) antenna structure and collection of input output datasets by using HFSS v.13, (ii) design of ANN and ANFIS model for computing resonant frequencies using simulated datasets, and (iii) results and discussion.

2 Antenna Structure and Simulation

Figure 2 exhibits the geometry of compact ($W = 20$ mm, $L = 20$ mm) UWB microstrip feed TSCCMPA. The MPA consists of a circular patch of radius r tapered with angle

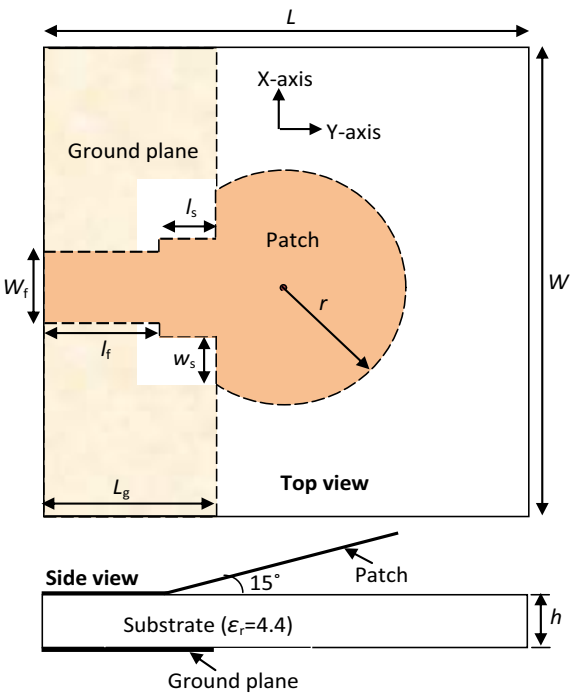

Fig. 2 Geometry of proposed UWB TSCCMPA

Table 1 Physical and electrical parametric sets of 144 simulated UWB TSCCMPAs

Number of simulation sets	Physical and electrical parameters					
	r (mm)	l_s (mm)	w_s (mm)	ϕ (degree)	h (mm)	ε_r
36	4.5	1.5 1.8	1.3 1.6	10, 15, 20	0.8, 1.6	2.2, 2.33, 4.4
36	5.0	1.8 2.0	2.0 2.0	15, 20, 25	0.8, 2.5	2.33, 4.4, 6.15
36	5.5	2.1 2.4	1.9 2.2	10, 15, 25	1.6, 3.2	2.2, 4.4, 6.15
36	6.0	2.4 2.7	2.2 2.5	20, 25, 30	3.2, 2.5	2.33, 4.4, 6.15

ϕ with two symmetrical slot of $w_s \times l_s$ at feed side, engraved into a dielectric substrate (20 mm $\times$ 20 mm) of thickness h, loss tangent of tan δ, and relative permittivity of ε_r. An open-ended microstrip line (50-Ω) feed of width $w_f \times l_f$ is placed on opposite side of the ground plane. The ground is defected, i.e., reduced rectangular size of 6 mm $\times$ 20 mm is taken at the opposite of feed as shown in Fig. 2. In proposed MPA, we have applied three techniques to achieve UWB antenna, i.e., two symmetrical slots on circular patch, tapering the patch and a partial ground plane.

In order to conclude the values of f_1 and f_2 of UWB for ANN and ANFIS model, the simulation is performed by HFSS v.13. The 144 TSCCMPAs having various sets of sensitive parameters of antenna proportions and substrate material are listed in Table 1. These sets of UWB TSCCMPA operate in band width of 2.3–53.5 to 3.4–54.6 GHz corresponding in C-, X-, Ku-, and Ka-bands. The 129 randomly selected input–output datasets of UWB TSCCMPA were used for training the ANN and ANFIS for designing the model, and rest 15 were utilized to test the accuracy of model.

3 Design of ANN and ANFIS Models

3.1 Design Procedure of ANN Model

ANN is one of the most intelligent, fast, and flexible tools to model nonlinear relation, simulation, and optimization of antenna [38]. The ANN, CAD models are very much popular nowadays, due to accuracy in results, learning ability and adaptability, very less information obligation, fast real-time retort, and easy execution attribute. For better model of a particular problem, many of basic parameters of ANN are settled on trial-and-error basis. Once an accurate model is ready then it can be used number of times without any time cost. The basic parameters of ANN are: network architecture, hidden layers, neurons in hidden layer, learning algorithm, activation functions, etc. Two special classes of ANN architecture, Multi-layer Perceptrons (MLPs) [39] and Radial-basis Function Networks (RBFNs) [40] have been widely used to analyze

this type of problem. In this paper, MLP network architecture is used. MLP has three types of layers: input layer, output layer, and one or more hidden layers. Results of MLPs for a meticulous problem depend on using suitable learning algorithm. After several trials for proposed work, the Levenberg–Marquardt (LM) algorithm is found suitable. The accurate ANN synthesis model needed a suitable number of neurons in hidden layers. For proper configuration of hidden layers of proposed model, many trials were carried out by changing the epoch, neurons, and activation functions in layers. High precision is achieved using MLP with two hidden layer networks. Finally, the ANN model has total four layers (two hidden layers, one input layer, and one output layer). Finally, the appropriate network configuration was found $6 \times 28 \times 12 \times 2$, which means that number of neurons are 6, 28, 12, and 2 in input layer, first, second hidden layers, and output layer, respectively. The activation function which is found suitable in both input and output layers was linear and tangent sigmoid activation function is found suitable for hidden layers. Initial weights of ANN model are set up arbitrarily. The weights adoption used mean square error (MSE) between target and output of ANN. The training epoch was found 543 for accurate model. Finally, the ANN model for proposed UWB TSCCMPA is shown in Fig. 3.

The accurateness of ANN-based analysis model depends on datasets used during training. Collections of more sets of data give more accurate result. The training and test datasets were generated from HFSS v.13 shown in previous section. Now the collected datasets were arranged in six-row input matrix (r, l_s, w_s, ϕ, h, and ε_r) and two-row target matrix (f_1 and f_2). Before training, the datasets were scaled in $[-1, +1]$ to each row of input as well as output matrix for easier learning process. Training process curtails the training error between ANN output and target output. The training error is checked by mean square error (MSE) performance graph. In

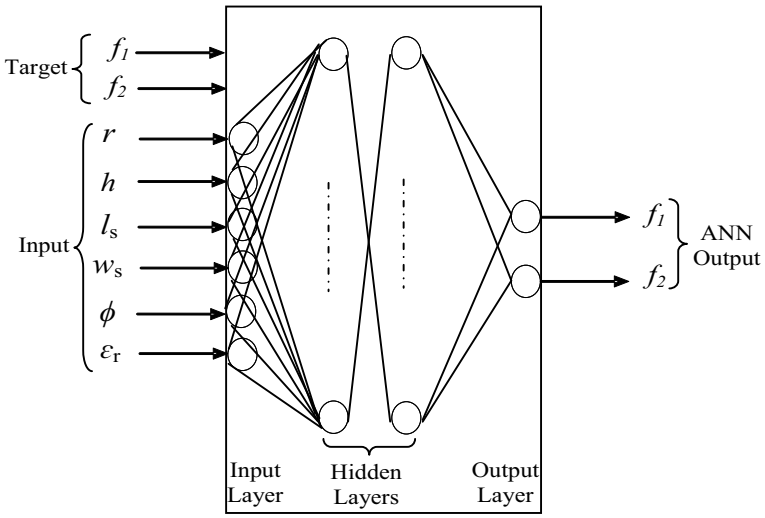

Fig. 3 ANN model of proposed UWB TSCCMPA

Table 2 The comparative results of HFSS (simulation), ANN, and ANFIS of proposed UWB TSCCMPA

Test patches	Input dimensions (mm)						Results (GHz)					
	r	l_s	w_s	Φ	h	ε_r	HFSS		ANN		ANFIS	
							f_1	f_2	f_1	f_2	f_1	f_2
1	4.5	1.5	1.3	15	0.8	4.4	4.582	46.552	4.540	46.577	4.555	46.578
2	4.5	1.8	1.6	10	0.8	2.33	4.625	46.992	4.657	46.967	4.651	46.971
3	4.5	1.8	1.6	20	1.6	2.2	5.071	47.417	5.112	47.389	5.109	47.392
4	5.0	1.8	2.0	15	0.8	2.33	4.937	46.148	4.965	46.179	4.961	46.175
5	5.0	2.0	2.0	15	0.8	4.4	4.900	46.660	4.677	46.598	4.674	46.591
6	5.0	1.8	2.0	20	2.5	2.33	6.884	48.588	6.851	48.551	6.855	48.557
7	5.0	2.0	2.0	20	0.8	6.15	6.422	48.225	6.449	48.258	6.446	48.252
8	5.0	2.0	2.0	25	2.5	6.15	5.871	47.844	5.845	47.877	5.850	47.869
9	5.5	2.1	1.9	10	1.6	4.4	6.461	48.692	6.497	48.728	6.490	48.722
10	5.5	2.1	1.9	25	3.2	2.2	5.818	47.567	5.839	47.592	5.836	47.588
11	5.5	2.4	2.2	15	1.6	6.15	3.229	45.094	3.253	45.125	3.251	45.119
12	5.5	2.4	2.2	15	3.2	2.2	3.466	45.347	3.497	45.312	3.492	45.323
13	6.0	2.4	2.2	20	2.5	4.4	4.893	47.495	4.862	47.471	4.873	47.473
14	6.0	2.7	2.5	30	2.5	4.4	6.056	48.884	6.089	48.850	6.081	48.857
15	6.0	2.7	2.5	25	3.2	6.15	5.990	47.503	5.961	47.539	5.967	47.533
Average Percentage Error (APE)									0.8731	0.0699	0.7698	0.0607

the training, when MSE is found near to zero, then training process stopped and the model is ready. The trained model is then validated by test inputs of 15 remaining input datasets, which is already extracted by HFSS v.13. Then APE of test output of model is calculated and shown in Table 2. The formula for the calculation of APE [30] is

$$\text{APE} = \frac{\sum \left| \left(f_{\text{FHSS}} - f_{\text{ANN/ANFIS}} \right) / f_{\text{HFSS}} \right|}{\text{number of antenna}} \times 100 \tag{1}$$

3.2 Design Procedure of ANFIS Model

ANFIS is a universal estimator [41], it combines the benefits of ANN and fuzzy inference system (FIS) in a single sculpt. FIS is an estimating tool, which is based on fuzzy set theory, fuzzy if then rules, and fuzzy reckoning. The neuro-adaptive learning methods for the membership function (MF) parameters of fuzzy system are similar to those used in neural network training. Hence, ANFIS is FIS execution in the scaffold of an adaptive fuzzy neural network, which is a very influential approach

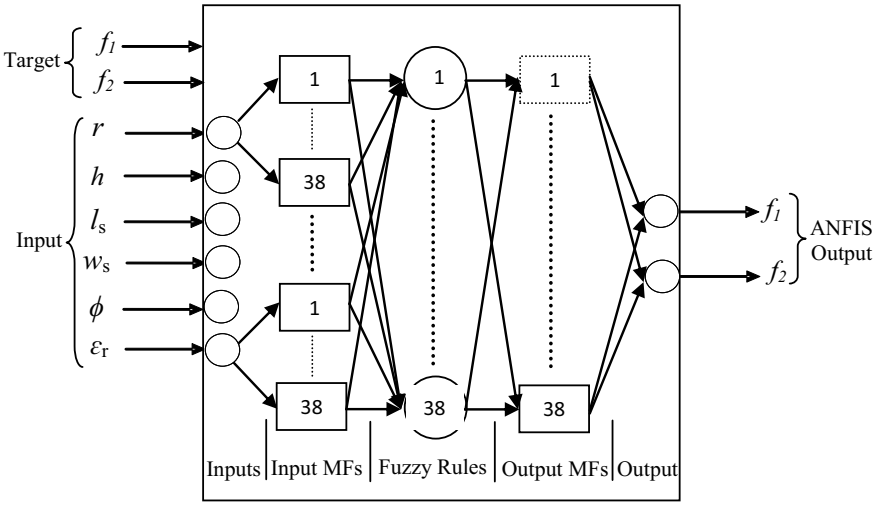

Fig. 4 ANFIS model of proposed UWB TSCCMPA

for analyzing nonlinear and complex association of input and output sets of data. The ANFIS architecture of proposed MPA is shown in Fig.4, which consists of five steps: inputs, membership functions of input, fuzzy rules, membership functions of output, and outputs.

For the best model for a particular problem, many of basic parameters of ANFIS are settled on trial-and-error basis. Once an accurate model is ready, then it can be used number of times without any time cost. After many trials in training of 129 input–output datasets (same datasets used in training of ANN), the following parameter of ANFIS model is found suitable for proposed MPA. These suitable ANFIS parameters are ANFIS model type-Sugeno, input/output MF type- Gaussian/linear, number of MFs-38, number of fuzzy rules-38, and training epochs-122. Again as in ANN, after designing the model remaining 15 input sets of data were used for testing of the model. Then APE of tested output of 15 datasets of ANFIS model is calculated and shown in Table 2.

4 Result and Discussion

The return loss characteristics, radiation pattern, and antenna gain of proposed UWB TSCCMPA are shown in Figs. 5, 6, and 7, respectively. In Fig. 5, it can be seen as a UWB performance of 51 GHz (2.6–53.5 GHz) impedance BW below 10 dB of return loss. Figure 6a and b shows the radiation pattern at resonant frequencies f_1 and f_2 for the proposed UWB TSCCMPA. The radiation patterns are almost stable across the entire operating frequency band. Variation of gain (dBi) w.r.t. frequency

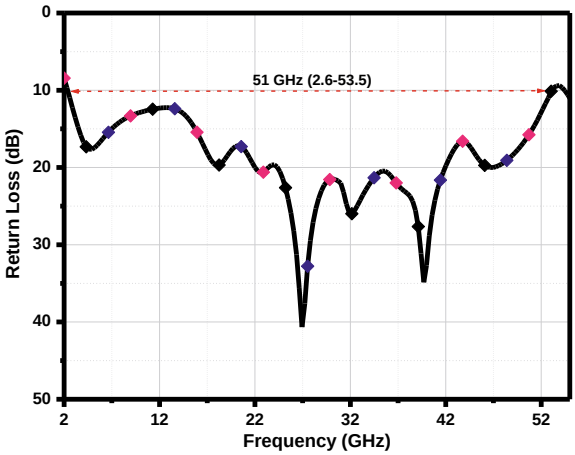

Fig. 5 Simulated return loss of proposed UWB TSCCMPA

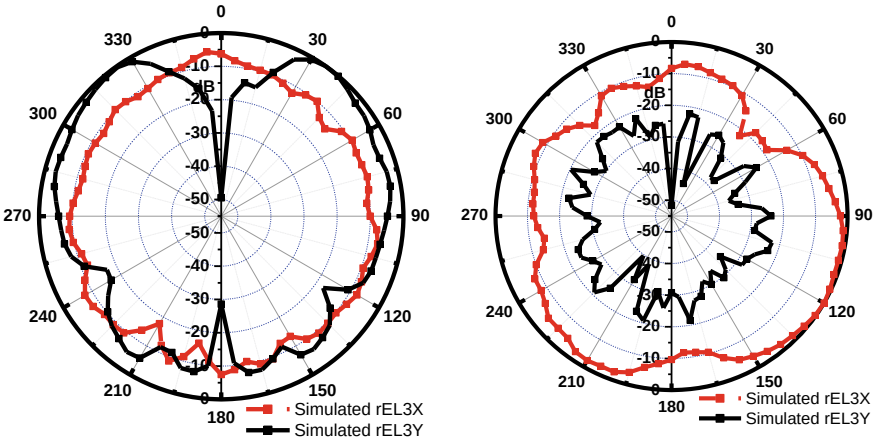

Fig. 6 Simulated radiation pattern for center frequency (f_1 = 27 GHz) of proposed UWB TSCCMPA

of the proposed antenna is shown in Fig. 7. The average gain of proposed antenna is found as 4.14 dBi.

The optimized ANN and ANFIS model has been fruitfully introduced for the analysis of UWB TSCCMPA. The HFSS simulation results and ANN, ANFIS tested results are shown in Table 2. These results are in very good agreement, which agreed the validity of ANN and ANFIS model. The results shown in Table 2 are enough to verify the proposed ANN and ANFIS model. The better results may be obtained

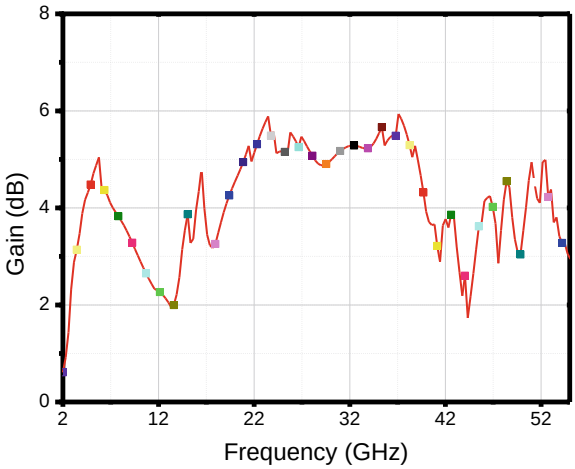

Fig. 7 Simulated gain of proposed UWB TSCCMPA

by wishing other training and test datasets from the ones used in this paper, or by collecting more dataset values for training and testing.

References

1. R. Garg, P. Bhartia, I. Bahl, A. Ittipihoon, *Microstrip Antenna Design Handbook* (Artech House, London, 2001)
2. N. Kumar, P. Kumar, M. Sharma, Reconfigurable antenna and performance optimization approach. Wireless Pers. Commun. **112**, 2187–2212 (2020). https://doi.org/10.1007/s11277-020-07145-0
3. G. Kumar, K.P. Ray, *Broadband Microstrip Antennas* (Artech House, USA, 2003)
4. A.A. Deshmukh, G. Kumar, Formulation of resonant frequency for compact rectangular microstrip antennas. Microw. Opt. Technol. Lett. **49**(2), 498–502 (2007)
5. A.K. Gautam, B.K. Kanaujia, A novel dual band asymmetric slit with defected ground structure for circular polarization operation. Microw. Opt. Technol. Lett. **55**, 1198–1202 (2013)
6. B.L. Ooi, Q. Shen, A novel E-shaped broadband microstrip patch antenna. Microw. Opt. Technol. Lett. **27**(5), 348–353 (2000)
7. A.F. Sheta, A. Mohra, S.F. Mahmoud, Multi-band operation of a compact H-shaped microstrip antenna. Microw. Opt. Technol. Lett. **35**, 363–368 (1982)
8. W. Chew, A broad-band annular-ring microstrip antenna. IEEE Trans. Antennas Propag. **30**(5), 918–923 (1982)
9. K.L. Wong, S.C. Pan, Compact triangular microstrip antenna. Electron. Lett. **33**, 433–435 (1997)
10. M.K. Khandelwal, B.K. Kanaujia, S. Dwari, S. Kumar, A.K. Gautam, Analysis and design of wide band microstrip-line-fed antenna with defected ground structure for Ku band application. Int. J. Electron. Commun. (AEU) **68**, 951–958 (2014)
11. N.P. Gupta, M. Kumar, Development of a reconfigurable and miniaturized CPW antenna for selective and wideband communication. Wireless Pers. Commun. **95**, 2599–2608 (2017). https://doi.org/10.1007/s11277-017-3942-8
12. S.C. Pan, K.L. Wong, Dual-frequency triangular microstrip antenna with a shorting pin. IEEE Trans. Antennas Propagat. **45**, 1889–1892 (1997)

13. Y.X. Guo, K.M. Luk, K.F. Lee, L-probe proximity-fed short-circuited patch antenna. Electron. Lett. **35**, 2069–2071 (1999)
14. K.L. Wong, K.P. Yang, Compact dual-frequency microstrip antenna with a pair of bent slots. Electron. Lett. **34**, 225–227 (1998)
15. W.S. Chen, C.K. Wu, K.L. Wong, Compact circularly polarized microstrip antenna with bent slots. Electron. Lett. **34**, 1278–1280 (1998)
16. S. Saxena, B.K. Kanaujia, S. Dwari, S. Kumar, R. Tiwari, A Compact microstrip fed dual polarized multiband antenna for IEEE 802.11 a/b/g/n/ac/ax applications. Int. J. Electron. Commun. (AEU) **72**, 95–103 (2017)
17. A.K. Gautam, S. Yadav, B.K. Kanaujia, A CPW-Fed compact UWB Microstrip antenna. IEEE Antenna Wireless Propag. Lett. **12**, 151–157 (2013)
18. K.H. Chiang, K.W. Tam, Microstrip monopole antenna with enhanced bandwidth using defected ground structure. IEEE Antennas Wireless Propag. Lett. **7**, 532–536 (2008)
19. R.K. Maurya, B.K. Kanaujia, A.K. Gautam, S. Chatterji, A.K. Singh, Circularly polarized hexagonal ring microstrip patch antenna with asymmetrical feed and DGS. Microwave Opt. Technol. Lett. 1–7 (2019)
20. N. Kishore, A. Prakash, V.S. Tripathi, A reconfigurable ultra-wide with defected ground structure for ITS application. Int. J. Electron. Commun. (AEU) **72**, 210–216 (2017)
21. W.F. Richards, Y.T. Lo, D.D. Hirrisson, An improved theory for microstrip antenna application. IEEE Trans. Antennas Propag. **29**, 84–87 (1981)
22. K. Bhattacharya, R. Garg, A generalized transmission line model for microstrip patches. IEE Proc. Microwave Antenna Propag. **132**, 93–99 (1985)
23. R.F. Harrington, *Field Computation by Moment Method* (IEEE Press, Piscataway NJ, 1993)
24. A. Taflove, *Computational Electrodynamics. The Finite Difference Time Domain* (Artech House, Baston, 1995)
25. J.X. Liang, C.C. Chiau, X.D. Chen, C.G. Parini, Study of a printed circular disc monopole antenna for UWB systems. IEEE Trans. Antennas Propag. **53**(11), 3500–3505 (2005)
26. M. John, M.J. Ammann, Optimization of impedance bandwidth for the printed rectangular monopole antenna. Microw. Opt. Technol. Lett. **47**(2), 153–155 (2005)
27. A.A. Eldek, Numerical analyses of a small ultra wideband microstrip-fed tap monopole antenna. Progress Electromagn. Res. **65**, 59–69 (2006)
28. R. Fallahi, A.A. Kalteh, M.G. Roozbahani, A novel UWB elliptical slot antenna with band-notched characteristics. Progress Electromagn. Res. **82**, 127–137 (2008)
29. M. Sadat, M. Houshmand, M. Roshandel, Design of a microstrip square-ring slot antenna filled by an H-shaped slot for UWB applications. Progress Electromagn. Res. **70**, 191–199 (2007)
30. A. Akdagli, A. Toktas, A. Kayabasi, I. Develi, An application of artificial neural network to compute the resonant frequency of E-shaped compact microstrip antennas. J. Electr. Eng. Elektrotechnicky Casopis **64**(5), 317–323 (2013)
31. T. Khan, A. De, A generalized ANN model for analyzing and synthesizing rectangular, circular, and triangular microstrip antennas. Hindawi Publishing Corp. Chin. J. Eng. **647191**, 1–9 (2013)
32. U. Chourasia, S. Silakari, Adaptive neuro fuzzy interference and PNN memory based grey wolf optimization algorithm for optimal load balancing. Wireless Pers. Commun. (2021). https://doi.org/10.1007/s11277-021-08400-8
33. R.K. Maurya, M.S. Vijay, N. Chaudhary, D. Kumar, Model for calculation of patch radius of circular microstrip antenna using artificial neural network. IEEE Int. Conf. **39**, 167–174 (2013). https://doi.org/10.1109/ICMIRA
34. H.J. Song, C.Y. Miao, Z.Q. Shen, W. Roel, D.H. Maja, C. Francky, Design of fuzzy cognitive maps using neural networks for predicting chaotic time series. Neural Netw. **23**(10), 264–275 (2010)
35. Z.B. Wang, S.J. Fang, Q. Wang, H.M. Liu, An ANN based synthesis model for the single-feed circularly-polarized square microstrip antenna with truncated corners. IEEE Trans. Antennas Propag. **60**, 5989–5993 (2012)
36. T.W.L. Wang, C. Quek, P. Cheng, GenSo-EWS: a novel neural-fuzzy based early warning system for predicting bank failures. Neural Netw. AEU **17**(4), 567–587 (2004)

37. A. Kayabasi, A. Akdagli, Predicting the resonant frequency of E-shaped compact microstrip antennas by using ANFIS and SVM. Wireless Pers. Commun. **82**, 1893–1906 (2015)
38. Q.J. Zhang, K.C. Gupta, *Neural Network for RF and Microwave Design* (Artech House: Norwood, Mass, USA, 2000)
39. E.D. Ubeyli, I. Guler, Multilayer perceptron neural network to compute quasistatic parameter of asymmetric coplanar waveguides. Neurocomputing **62**, 349–365 (2004)
40. R.K. Mishra, A. Patnaik, Neural network based CAD model for the design of square patch antennas. IEEE Trans. Antenna Propag. **46**, 1890–1892 (1998)
41. J.S.R. Jang, C.T. Sun, E. Mizutani, *Neuro-Fuzzy and Soft Computing* (Prentice Hall, 1997), pp. 335–368

Design and Analysis of MIMO Antenna to Reduce the Mutual Coupling Between the Circular Patches at 3.5 GHz

G. Naga Jyothi Sree and Suman Nelaturi

Abstract A compactness MIMO ultra-wideband MIMO radiator is presented in this paper. A novel technique of circular split ring resonator (SRR) is inserted in a circular patch, loaded stubs are added at the bottom of the patch and DGS placed in the ground plane. By considering this novel structure miniaturized antenna structure greatly improves the isolation between the patches which is obtained at 3.5 GHz. Due to the use of monopole ground plane structure, bandwidth impedance of the design is broadened. A very great broadband impedance bandwidth is achieved as a result from 3.0 to 10.0 GHz of the proposed structure. Moreover, the MIMO structure obtains the stable radiation patterns, low ECC around less than 0.02, and an efficiency around 93%. The current design has electrically compact size of $35 \times 53 \times 1.6$ mm^3. The proposed system with a configuration of low profile especially is a better candidate for wireless performance communication of MIMO system.

Keywords Group delay · Defected ground structures · Ultra-wideband · Mutual coupling

1 Introduction

In the current wireless communication system field, the development of WLAN which conform well the omni-directivity and achieves the higher amount of throughput to standards of 802.11a and 802.11b, the demand of high reliability and higher data rates is extremely urgent in MIMO technology. A Federal Communication Commission in 2002, officially mentioned as the unlicensed band of 3.3–10.6 GHz spectrum [1]. The band notch characteristics of slot antenna with 5.5 GHz are explained in [2]. Neutralization technique, metamaterial loading for gain enhancement, and UC-EBG superstrate for reduction of mutual coupling [3, 4]. In order to

G. N. J. Sree (✉) · S. Nelaturi
Department of ECE, VFSTR, Guntur, A.P, India

S. Rawat et al. (eds.), *Proceedings of First International Conference on Computational Electronics for Wireless Communications*, Lecture Notes in Networks and Systems 329,
https://doi.org/10.1007/978-981-16-6246-1_2

Table 1 Literature work with current design

References	Size (mm^2)	Frequency (GHz)	Element–Element distance	20 dB isolation bandwidth (%)	Efficiency (%)
[1]	5400	3.8	0.04 λ_0	1.7	75
[3]	5600	5.4	0.02 λ_0	4	73
[5]	4908	2.6	0.05 λ_0	1	82
[6]	4200	2.45	0.03 λ_0	9.2	81
[7]	4800	1.8	0.11 λ_0	3.3	84
[9]	4200	2.45	0.04 λ_0	11.1	74
[10]	6300	3.75	0.30 λ_0	26.7	78
MIMO antenna	1855	3.5	0.06 λ_0	23.7	74
		5.2	0.06 λ_0	25.8	82

obtain the enhanced band isolation, notched mushroom and EBG structure is introduced in [5]. New slots and EBG structures are introduced for bandwidth enhancement and also tree-like structure for wide band isolation enhancement is used in [6, 7]. UWB antenna is used for high isolation in [8], for dual-band characteristics rejection a slotted-edge substrate is used in [9]. Koch fractal MIMO antenna with better ECC is used in [10]. For the arrangement of very close design, a significant problem arises in envelope correlation coefficient and mutual coupling in between the radiating elements, which destroys the performance of the entire MIMO system. The mutual coupling and arrangement of space between the elements are always inversely proportional to each other. Without disturbing the size of the current MIMO design, minimizing the space between the inter-element raises a problems for usage of practical designs (Table 1).

2 Antenna Geometry and Their Performance

See Fig. 1 and Table 2.

3 Results and Discussion

The S-parameters of proposed MIMO system are depicted in Fig. 2. Figure 5 MIMO antenna shows the superior UBB response which confirms the frequencies from 3.1 GHz to −10 GHz have—10 dB value of reference for any antenna system with an isolation better than −40 dB. For the efficient performance of MIMO system, the 3.5 GHz region with VSWR $\leq$ 2 is demonstrated which is depicted in Fig. 3.

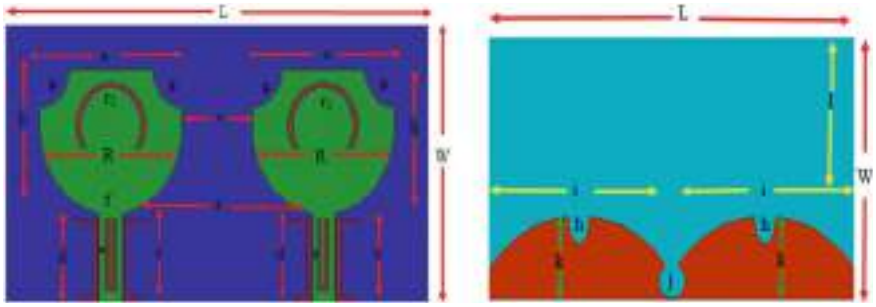

(a) Design Front-view (b) Design Back-view

Fig. 1 MIMO designs

Table 2 MIMO dimensions

Parameter	L	W	r_1	a	b	c	d	e	f
Dimensions (mm)	50	30	0.6	20	20	10	9	7	3
Parameter	g	h	i	j	k	l	s	t	R
Dimensions (mm)	2.5	1.5	21	1.5	8	22	2.5	18	9.5

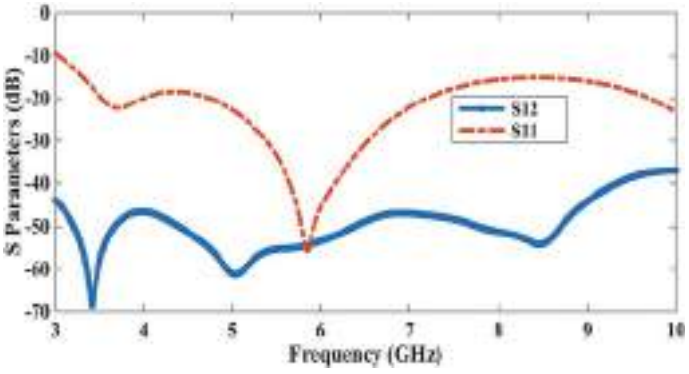

Fig. 2 S-parameters of the current design

Figure 4 shows the variation of input impedance for both real and imaginary parts. The representation of resonant frequency (f_r) at 5.2 GHz is clearly noticed. The real and imaginary values of MIMO design input impedances at the resonant frequency (f_r) are 50.2 and 0 Ω, respectively. From Fig. 3, it has been observed that quite clear at the resonant frequency the MIMO system acts like series resonant circuit which consists of inductance (L), resistor (R), and capacitance (C) connected in series fashion.

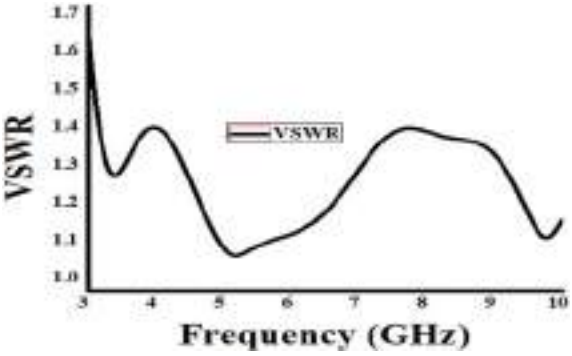

Fig. 3 VSWR of the current design

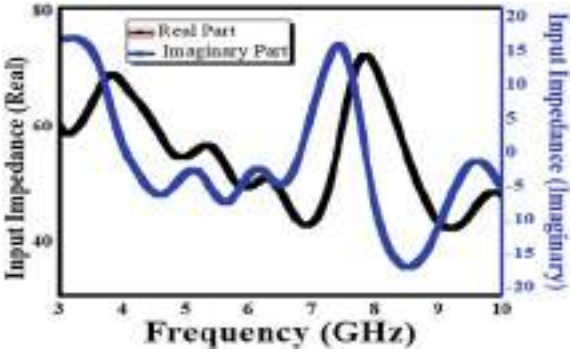

Fig. 4 Impedance of the current design

To understand the isolation and improved impedance matching, simultaneously another parameter distribution of surface current is plotted on the ground plane at 3.5 GHz with port # 1 which is excited as well as port # 2 which is matched terminated by 5.8 GHz port # 2 which is excited as well as port # 1 which is matched terminated as depicted in Fig. 5. From Fig. 5a, it is identified that the current is more concentrated on microstrip feed line and right side "C" shape rectangular stub lines and back side of ground plane stubs at arc shapes. Some amount of the current is also passed through the patch. Similarly, Fig. 5b identified that more current is flowing on microstrip feed line and "C"-shaped rectangular stub patches and some amount of current on the ground plane arcs. Due to this type of current distribution, high isolation and impedance matching between the two elements resulted.

Figure 6 represents the simulated radiation patterns about the MIMO antenna in xz-plane and yz-plane (principal planes) at 3.5 GHz as well as 5.2 GHz. When element-1 of the arrangement is excited, similarly the element-2 of the arrangement is matched terminated. The co-to-cross polarization couplings are observed at 3.5 GHz and 5.2 GHz which are approximately in omni-directional patterns.

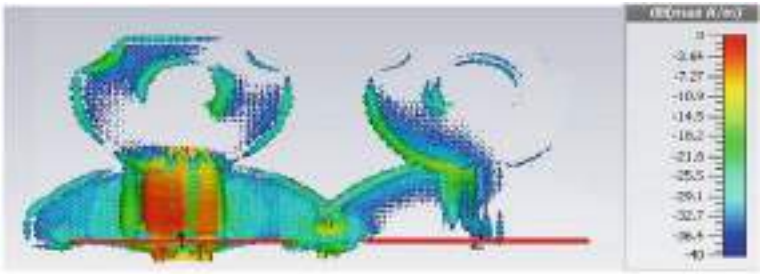

(a) Port 1 excited at 3.5 GHz

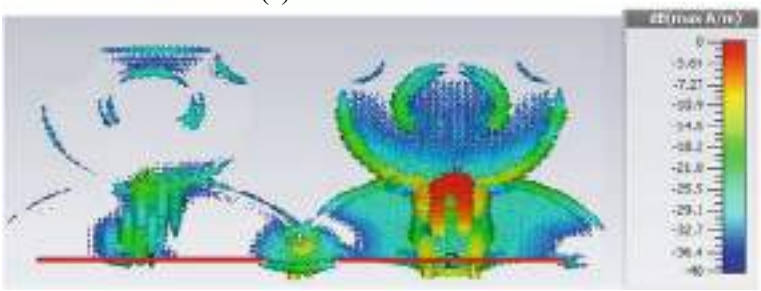

(b) Port 2 excited at 5.2 GHz

Fig. 5 Surface current distribution of the current design

$$ECC = \frac{\left| \iint\limits_{4\pi} [E_1(\theta, \phi) * E_2(\theta, \phi)] d\Omega \right|^2}{\iint\limits_{4\pi} |E_1(\theta, \phi)|^2 d\Omega \iint\limits_{4\pi} |E_2(\theta, \phi)|^2 d\Omega} \tag{1}$$

where $E_i(\theta, \phi)$ indicates complex 3-D far-field radiated pattern.

The expression using S-parameters is

$$ECC = \left| \frac{\iint\limits_{4\pi} \left| S_{11}^* S_{21} + S_{21}^* S_{22} \right|}{\left[(1 - (|S_{11}|^2 + |S_{21}|^2))(1 - (|S_{22}|^2 + |S_{12}|^2)) \right]^{1/2}} \right| \tag{2}$$

Figure 7 shows the frequency versus efficiency and peak gain of lower sub-6 GHz MIMO system. To find out the reliability of diversity gain MIMO system, first we have to evaluate the parameter of ECC using 3-D far-field and S-parameters using Eqs. (1) and (2) which are taken from [5]. From Fig. 8, it has been noticed that ECC of MIMO structure is less than 0.002 which satisfies the MIMO/diversity performance within the acceptable region. The parameter of DG evaluated with the mathematical formulae is [2]

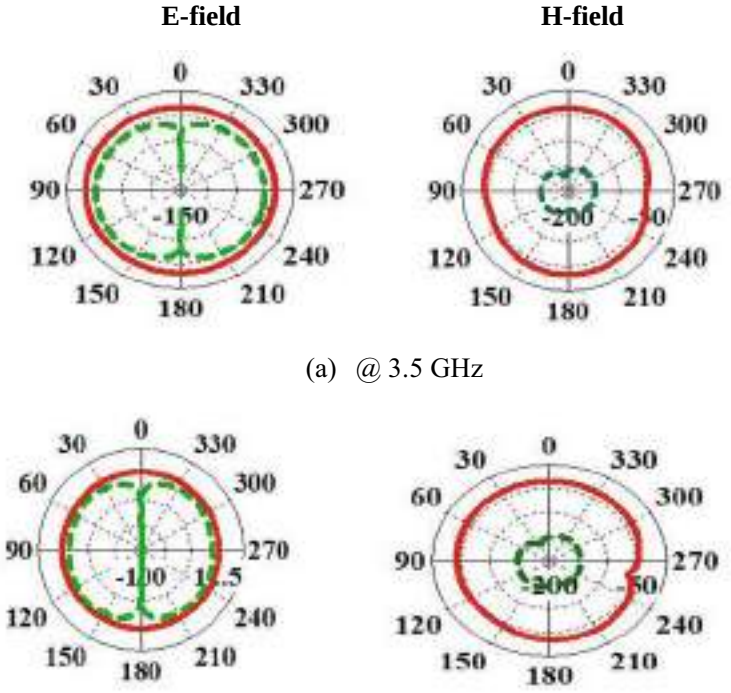

Fig. 6 Patterns of radiation **a** 3.5 GHz, **b** 5.2 GHz MIMO design

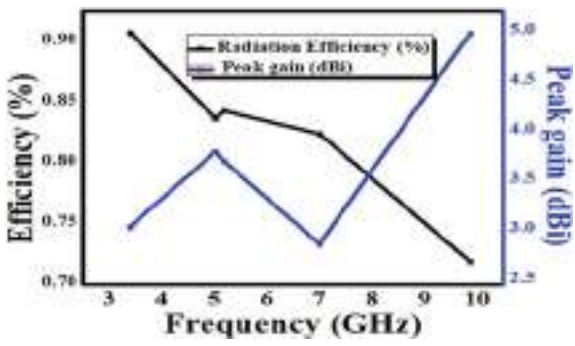

Fig. 7 Frequency vs. ECC and peak gain

$$DG = \sqrt{1 - |\rho_e|^2} = \sqrt{1 - |ECC|^2} \tag{3}$$

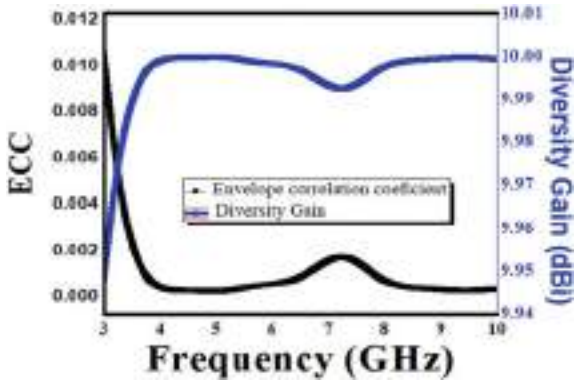

Fig. 8 Frequency vs. ECC and DG

where $E_1(\theta, \varphi)$ and $E_2(\theta, \varphi)$ indicated the 3-D complex field pattern representation of two elements in the MIMO system. The simulated DG and ECC results are evaluated using 3-D complex field pattern equation and S-parameters. The DG of lower sub-6 GHz MIMO system is nearly equal to 9.998 dB throughout the region, respectively. Figure 8 shows the frequency versus ECC as well as DG of lower sub-6 GHz MIMO system.

4 Conclusions

In this work, a compactness MIMO system has been investigated. The current MIMO radiator is designed with circular split ring resonator (SRR) slot to obtain optimum performance. A small portion of notch ground plane is considered in a monopole ground plane to explain the 3.5 GHz response, which indicates a bandwidth of impedance (IBW) of 3.0–10.0 GHz. Lower sub-6 GHz MIMO system with SRR, rectangular stubs and DGS reduces the isolation and hence the optimum performance of diversity is obtained. The MIMO model shows diversity gain of almost 10 dBi, peak gain around 4 dBi, and ECC less than around 0.02. Furthermore, good radiation characteristic is obtained with the MIMO system. The MIMO system performance is simulated and the proposed system is used for high performance for future generation wireless communication systems.

References

1. Washington, D. C., *First Report and Order Revision of Part 15 of the Commission's Rule Regarding Ultra-Wideband Transmission System FCC 02–48* (Federal Communications Commission, 2002)
2. P. Gao et al.,Compact printed UWB diversity slot antenna with 5.5-GHz band-notched characteristics. IEEE Antennas Wireless Propag. Lett. **13**, 376–379 (2014)

3. S. Luo et al.,A low mutual coupling antenna array with gain enhancement using metamaterial loading and neutralization line structure. Appl. Comput. Electromagn. Soc. J. **34**(3), (2019)
4. H.S. Farahani et al.,Mutual coupling reduction in patch antenna arrays using a UC-EBG superstrate. IEEE Antennas Wireless Propag. Lett. **9**, 57–59 (2010)
5. N. Jaglan et al.,Triple band notched mushroom and uniplanar EBG structures based UWB MIMO/Diversity antenna with enhanced wide band isolation. AEU-Int. J. Electron. Commun. **90**, 36–44 (2018)
6. Z. Guo et al.,Bandwidth enhancement of monopole UWB antenna with new slots and EBG structures. IEEE Antennas Wireless Propag. Lett. **12**, 1550–1553 (2013)
7. S. Zhang et al.,Ultrawideband MIMO/diversity antennas with a tree-like structure to enhance wideband isolation. IEEE Antennas Wireless Propag. Lett. **8**, 1279–1282 (2009)
8. J.-Y. Deng, L.-X. Guo, X.-L. Liu, An ultrawideband MIMO antenna with a high isolation. IEEE Antennas Wireless Propag. Lett. **15**, 182–185 (2015)
9. D.K. Raheja, B.K. Kanaujia, S. Kumar,Compact four-port MIMO antenna on slotted-edge substrate with dual-band rejection characteristics. Int. J. RF Microw. Comput. Aided Eng. **29**(7), e21756 (2019)
10. S. Tripathi, A. Mohan, S. Yadav, A compact Koch fractal UWB MIMO antenna with WLAN band-rejection. IEEE Antennas Wireless Propag. Lett. **14**, 1565–1568 (2015)

Comparative Analysis of Dipole and Bowtie Antenna on 2.4 GHz

Pravin Dalvadi and Amrut Patel

Abstract A comparative analysis of dipole and bowtie antenna with and without tapered balun feeding technique operating at 2.4 GHz is presented in this paper. The glass epoxy FR-4 substrate of thickness of 1.6 mm and dielectric constant of 4.4 is used in the proposed antennas. For S_{11} <−10 dB, the bandwidths obtained for dipole antenna with and without tapered balun are 24% and 16%, respectively. For S_{11} <−10 dB, the bandwidths obtained for bowtie antenna with and without tapered balun are 44% and 20%, respectively. The proposed antennas achieve more than 2 dB gain for the entire bandwidth. The antenna parameters such as radiation pattern, return loss (reflection coefficient S_{11} <−10 dB), bandwidth, gain, and Smith chart have been simulated and analyzed using Ansys HFSS. The proposed antennas find application in Industrial, Scientific, and Medical (ISM band-2.4 GHz) system.

Keywords Dipole antenna · Bowtie antenna · Tapered balun · Bandwidth · Gain and ISM band

1 Introduction

At present, the wireless communication applications have a huge demand of wideband, lightweight, compact size, low-profile antenna having simpler fabrication and easier integration method with other radio frequency components, especially in radio communication, mobile communication, radar, satellite communication, etc. Earlier, dipole antenna was designed using iron rod as radiating element. Due to this, dipole antenna becomes heavier and bulkier. To reduce its weight and size, nowadays antennas are fabricated on printed circuit board which consequently finds its applications in wireless communication system like IEEE 802.11 wireless local area

P. Dalvadi (✉)
Electronics & Communication Department, Government Polytechnic Gandhinagar, Ganpat University, Mehsana, Gujarat, India

A. Patel
Electronics & Communication Department, U.V. Patel College of Engineering, Ganpat University, Mehsana, Gujarat, India

S. Rawat et al. (eds.), *Proceedings of First International Conference on Computational Electronics for Wireless Communications*, Lecture Notes in Networks and Systems 329,
https://doi.org/10.1007/978-981-16-6246-1_3

network, radio communication, Bluetooth, Wi-Fi, WiMAX, ZigBee, ISM Band, etc. In aforementioned applications, antennas are widely operated in the 2.4 GHz ISM band [1]. Dipole antenna can be designed in different shapes like rectangular, cylindrical, square, triangular, bi-conical, bowtie, and I-shape using different feeding methods [2].

The dipole antenna consists of two radiating elements on the same axis which is fed at the center. In some dipole antenna designs, each arm is fabricated on same plane of the substrate [2, 6] while in some other designs both arms are fabricated on both sides of the dielectric substrate [3–5]. Feeding is the most important part in the antenna design, which provides impedance matching between source and antenna. It also facilitates maximum power transfer from the feeder/transmission line into the antenna itself. Microstrip feed line [2, 3, 10, 12], tapered balun [4, 5, 7, 11, 13–18], integrated balun [6], coplanar waveguide feed [2, 18], and many more feeding methods can be used for feeding dipole and bowtie antennas.

The dipole antenna designed using microstrip line feeding method provides limited bandwidth with approximately 2.4–2.58 dBi gain [3]. To enhance the bandwidth, low-profile printed dipole antenna is designed using tapered balun which achieves 19% bandwidth [4]. In [5], double-sided dipole antenna is presented which achieves 58% bandwidth. It is fed at center by using tapered balun with parallel microstrip line. The arms of the designed dipole antenna are printed on both sides of substrate having $\varepsilon r = 2.21$ and thickness of 1.58 mm using thin microwave laminate (Taconic TLY5) which increases bandwidth but at the price of increased size of antenna. In [6], the dipole with adjusted integrated balun using RO4230 substrate is presented which achieves 38% bandwidth.

Based on structure of antenna, bowtie antenna offers wider bandwidth as compared to dipole antenna [8–14]. As the angle of bowtie antenna is increased, bandwidth is improved with decrease in resonance frequency [7]. Printed dipole antenna (bowtie shape) with balun and impedance-matching network (tapered balun) is presented which obtained large band of 100 MHz to 2200 MHz with gain varying from -15 to 4dB [11]. To achieve high gain, bowtie antenna is designed on the top of the substrate using microstrip transmission line feeding method. It is specially designed for indoor radio-communications applications. It achieves 8.7dB gain with limited bandwidth of around 2% [12]. In [13], double side printed Bowtie antenna is presented for the FCC UWB band application. To feed the antenna, MS to tapered ground plane structure is designed, which provides impedance matching between SMA connector and antenna. The antenna achieves 3.1 GHz to 10.6 GHz frequency band for less -10dB.

In this paper, dipole and bowtie antennas are presented using two different feeding methods: microstrip line and tapered balun. The antennas are designed on glass epoxy FR-4 substrate with εr of 4.4, thickness (H) of 1.6mm, and loss tangent (δ) of 0.02. The comparative study of designed antennas is presented by considering antenna performance parameters such as return loss (reflection coefficient S11 <-10dB), gain, bandwidth, Smith chart, and radiation pattern. In addition, different bowtie antennas with tapered balun are also designed based on parametric study on various angles with and without changing the antenna length.

2 Dipole Antenna

Dipole comprises two radiating arms and fed at the center. Figure 1 shows dipole antenna for 2.4 GHz, where dipole is fed at the center by microstrip feed line and its arms are designed on both sides of substrate. Printed dipole antenna can be designed from the following formula:

$$L + W = 0.48(\phi) \tag{1}$$

where L, W, and λ are length, width, and wavelength of dipole, respectively. To match the 50 Ω input impedance, L and W of microstrip feed line are considered to be 21.5 mm (shorter than $\frac{\lambda}{4}$) and 3 mm, respectively. The antenna design parameters shown in Table 1 are chosen to get optimum results.

Figures 2 and 3 present reflection coefficient (S_{11}) and gain for dipole antenna, respectively. From the result, it is found that the antenna obtained 16% bandwidth (2.23 to 2.62 GHz) for S_{11} <−10 dB. The gains in 0° and 180° directions are 2.30 dB and 2.27 dB, respectively. It gives figure eight radiation pattern in E plane while it gives omni-direction radiation pattern in H-plane.

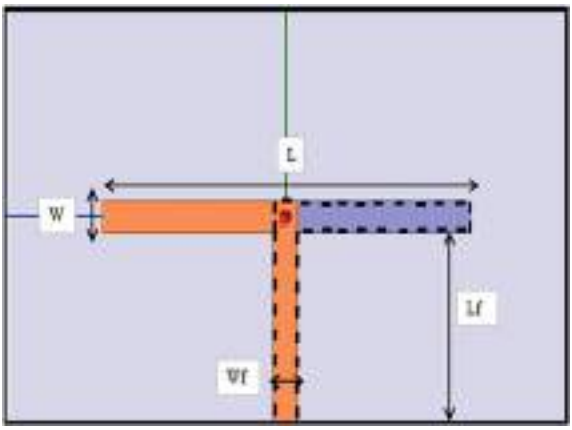

Fig. 1 Dipole antenna (Design 1)

Table 1 Design parameters for dipole antenna

Parameter	Value (mm)
Length of dipole (L)	49
Width of dipole (W)	3
Microstrip feed line length (Lf)	21.5
Microstrip feed line width (Wf)	3
Substrate thickness (H)	1.6

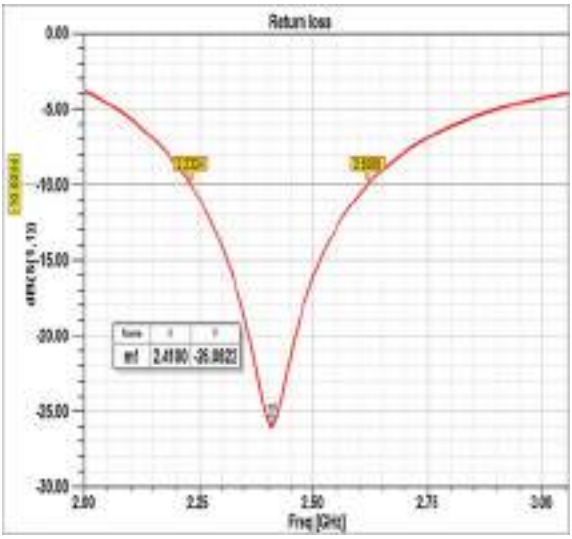

Fig. 2 Reflection coefficient (S_{11}) of dipole antenna

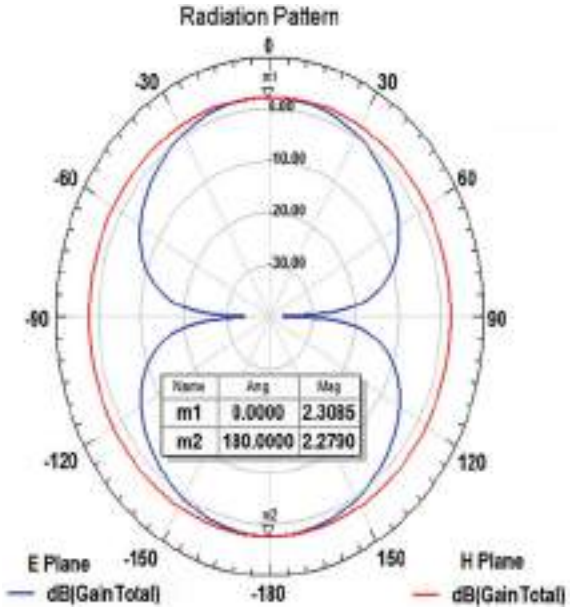

Fig. 3 Gain of dipole antenna

3 Bowtie Antenna

The bandwidth of dipole antenna can be improved by using bowtie shape or tapered shape instead of rectangle shape. A bowtie antenna consists of bi-triangular sheet of conductor instead of rectangular sheet and the feed at the vertex [8, 9]. For bowtie

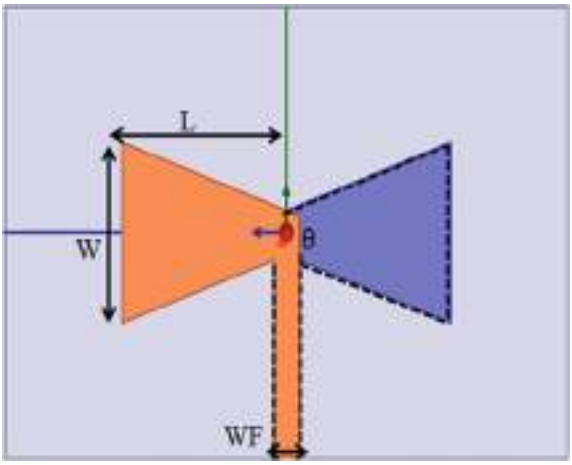

Fig. 4 Bowtie antenna (Design 2)

Table 2 Design parameters for bowtie antenna

Parameter	Value (mm)
Length of bowtie arm (L)	22
Width of bowtie arm (W)	16
Microstrip feed line length (Lf)	21.5
Microstrip feed line width (Wf)	3
Substrate thickness (H)	1.6
Bowtie antenna angle (θ)	40

antenna, the length determines the resonance bandwidth and angle determines its impedance [14]. The bowtie antenna is designed on both sides of the substrate and its design is completely defined by its length L and angle θ. The bowtie antenna fed by microstrip feed line is shown in Fig. 4 and its design parameters are mentioned in Table 2.

Figures 5 and 6 present reflection coefficient (S_{11}) and gain for bowtie antenna, respectively. From the result, it is found that the antenna obtained 20% bandwidth (2.20 to 2.69 GHz) for $S_{11} < -10$ dB. It achieves higher bandwidth compared to dipole antenna. The gains in 0° and 180° directions are 2.48 dB and 2.36 dB, respectively.

4 Dipole Antenna with Tapered Balun

The feeding technique plays an important role for antenna by impedance matching which will lead to maximum power transmission. The dipole antenna is a balanced structure having 73 Ω impedance (practically 68 Ω). The design of balun is required when coaxial feed is used as input source as coaxial fees is unbalanced structure with

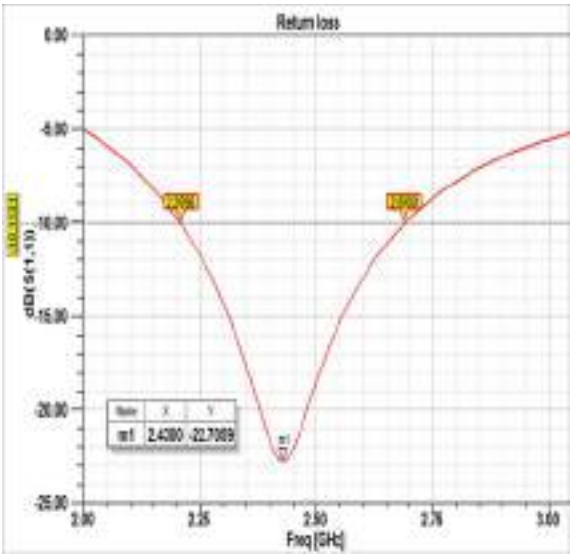

Fig. 5 Reflection coefficient (S_{11}) of bowtie antenna

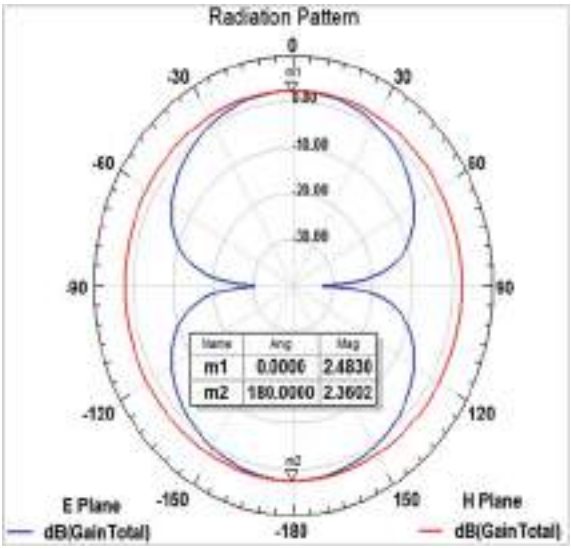

Fig. 6 Gain of bowtie antenna

50 Ω impedance. A balun is a passive device which acts a transformer, matching an unbalanced transmission line to a balanced line and vice versa. A tapered balun is formed like a slowly peeled coaxial cable and reshaped until it is a balanced transmission line [1, 11, 13–18]. Inline tapered balun and Marchand balun are the two types of tapered balun techniques. In inline tapered balun, gradual tapering is required at top and bottom of the conductor to develop the potential at the conductor

ends. While in Marchand balun, tapering is required only at bottom conductor to develop the potential at the middle of the ground plane of the MS circuit [15].

The tapered balun is designed which transforms unbalanced coaxial input to balanced output as shown in Fig. 7, where gradual tapering is required at top and bottom of the conductor. The characteristic impedance (Z) of transmission line gradually varies with respect to length (Lf) from unbalanced input point Z1 to balanced output point Z2 [4, 15–18]. Width of bottom plane (Wb1) is much wider than top plane (Wt1) in tapered balun. In the proposed tapered balun design, a ratio of Wb1/Wt1 = 5 is considered. The dipole antenna with tapered balun and its design parameters are shown in Fig. 8 and Table 3, respectively.

Figure 9 shows reflection coefficient (S_{11}) for dipole antenna with tapered balun. From the result, it is found that the antenna obtained 24% bandwidth (2.21 to 2.81

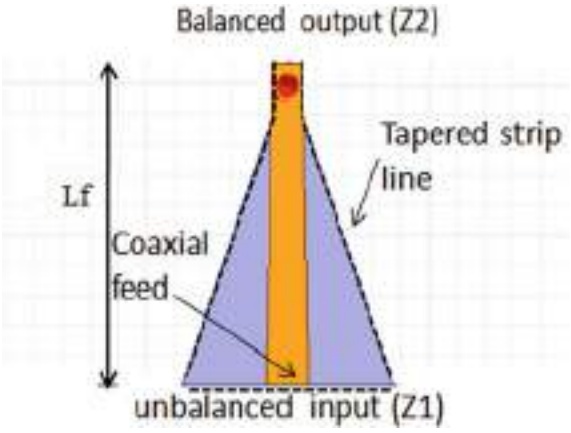

Fig. 7 Tapered balun (orange color is top side and blue color with dotted lines is on bottom side of substrate)

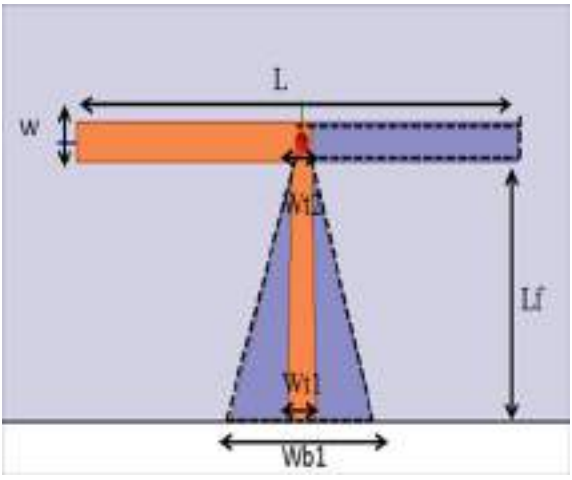

Fig. 8 Dipole antenna with tapered balun (Design 3)

Table 3 Design parameters for dipole antenna with tapered balun

Parameter	Value (mm)	Description
L	47	Length of dipole
W	3	Width of dipole
Lf	21.5	Microstrip feed line length
Wt1	3	Tapered balun top width at point 1
Wb1	15	Tapered balun bottom width at point 1
Wt2 and wb2	2	Tapered balun top/bottom width at point 2
H	1.6	Thickness of substrate

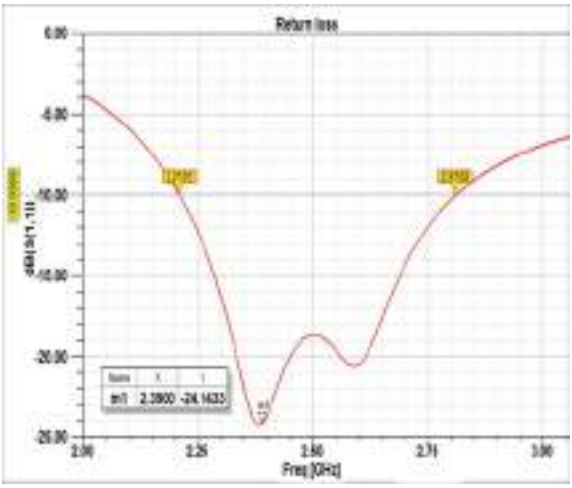

Fig. 9 Reflection coefficient (S_{11}) of dipole antenna with tapered balun

GHz) for $S_{11}<-10$ dB. It is better than dipole antenna with microstip feed line. Figure 10 shows gain of dipole antenna with tapered balun. The gains in 0° and 180° direction are 2.14 dB and 2.26 dB, respectively.

5 Bowtie Antenna with Tapered Balun

To improve the performance of aforementioned antennas, bowtie antenna with tapered balun is designed. Figure 11 shows bowtie antenna with tapered balun where designed parameters are chosen in such a way that it gives optimum results and it is mentioned in Table 4.

Figures 12 and 13 present reflection coefficient (S_{11}) and gain for bowtie antenna with tapered balun, respectively.

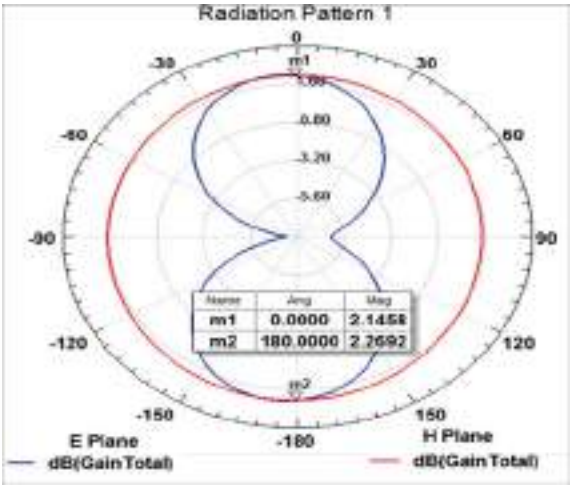

Fig. 10 Gain of dipole antenna with tapered balun

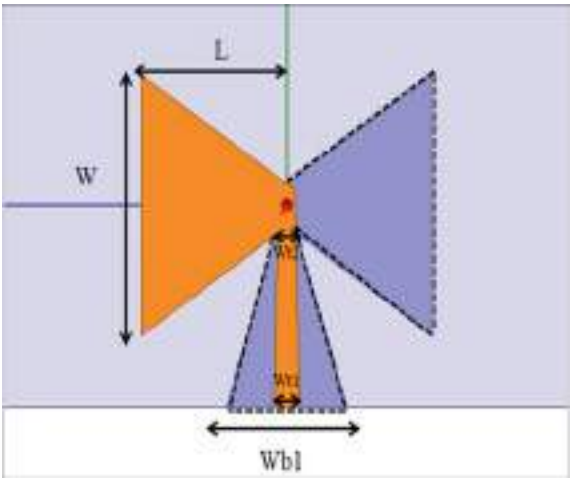

Fig. 11 Bowtie antenna with tapered balun (Design 4)

Table 4 Design parameters for bowtie antenna with tapered balun

Parameter	Value (mm)
Length of bowtie arm (L)	19
Width of bowtie arm (W)	26
Microstrip feed line length (Lf)	21.5
Tapered balun top width at point 1 (Wt1)	3
Tapered balun bottom width at point 1 (Wb1)	15
Tapered balun top/bottom width at point 2 (Wt2 and wb2)	2
Thickness of substrate (H)	1.6
Bowtie antenna angle (θ)	68

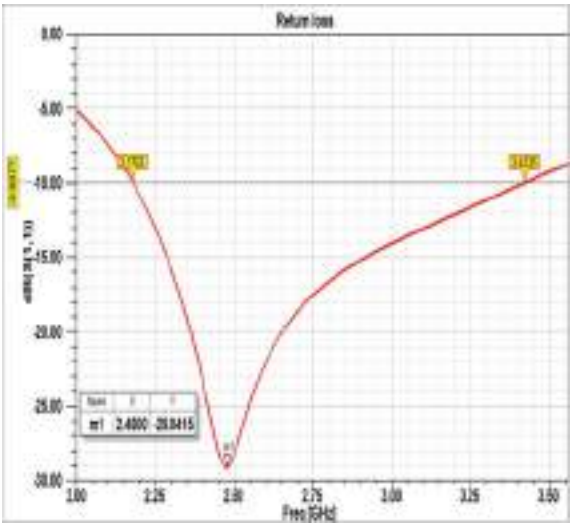

Fig. 12 Reflection coefficient (S_{11}) of bowtie antenna with tapered balun

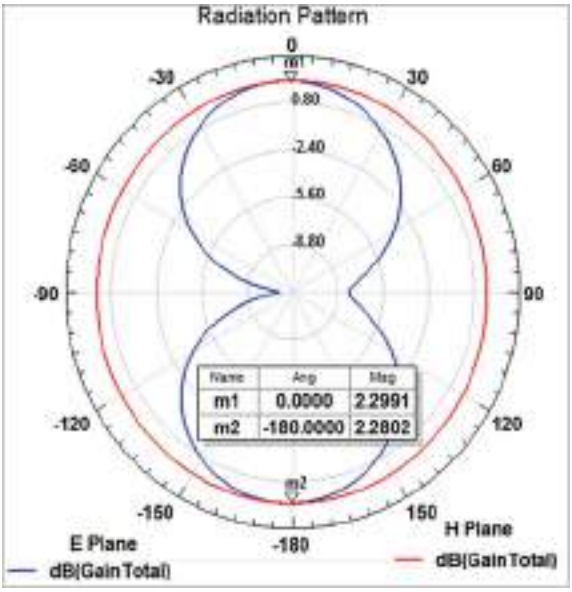

Fig. 13 Gain of bowtie antenna with tapered balun

From the results, it is found that the bowtie antenna with tapered balun obtained 44% bandwidth (2.17 to 3.42 GHz) for $S_{11}<-10$ dB. It is better than designed antennas in above sections. This antenna obtained broad bandwidth with almost same gain as achieved in antennas mentioned in above sections. The gains in 0° and 180° direction are 2.29 dB and 2.28 dB, respectively. This antenna design is more suitable for broadband applications in ISM band.

To achieve above result, the parametric study for reflection coefficient of bowtie antennas with tapered balun on different angles with constant length is carried out as shown in Figure 14. The designed parameters and obtained results of the antenna are mentioned in Table 5.

From the results, it is found that as the angle of bowtie antenna is increased, it gives broader bandwidth as the resonance frequency is decreased. Hence, the length of bowtie antenna has to be increased/decreased as per application. To resonate the bowtie antennas with tapered balun at 2.4 GHz, antennas are designed on different angles with various lengths as mentioned in Table 6 and their reflection coefficient (S_{11}) is shown in Fig. 15.

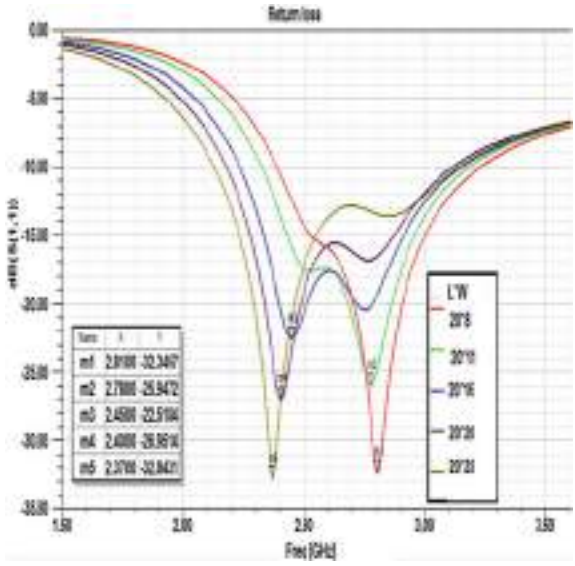

Fig. 14 Reflection coefficient (S_{11}) of bowtie antennas with tapered balun for different angles with constant length

Table 5 Bowtie antennas with tapered balun for different angles with constant length

Sr	L * W	Antenna angle	Bandwidth	Bandwidth range	Frequency
	(mm)	θ	%	GHz	GHz
1	20 * 8	23	30	2.38–3.23	2.81
2	20 * 11	31	31	2.32–3.18	2.78
3	20 * 16	44	35	2.23–3.16	2.45
4	20 * 20	53	36	2.17–3.12	2.41
5	20 * 25	64	37	2.13–3.10	2.37

Table 6 Bowtie antennas with tapered balun for different angles with change in length

Sr	L * W (mm)	Antenna angle θ	Bandwidth %	Bandwidth range GHz	Frequency GHz
1	22 * 8	21	30	2.20–2.98	2.40
2	21 * 12	32	32	2.21–3.02	2.41
3	20.5 * 16	43	34	2.19–3.08	2.40
4	20 * 20	53	36	2.17–3.12	2.40
5	19.5 * 22	59	37	2.22–3.22	2.45
6	19 * 26	68	44	2.17–3.42	2.47

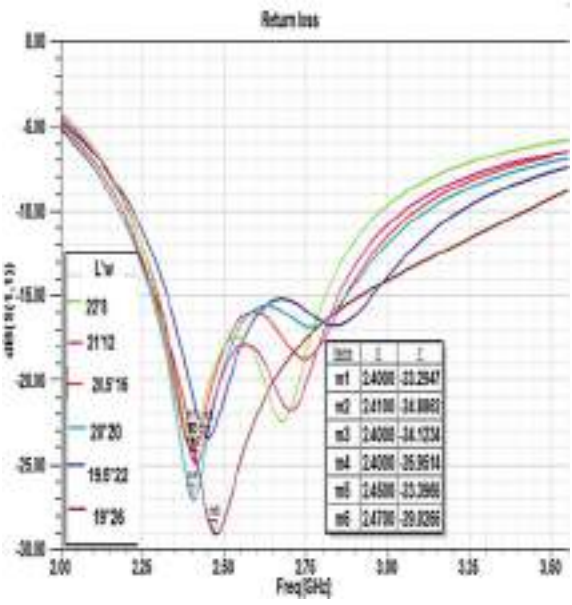

Fig. 15 Reflection coefficient (S_{11}) of bowtie antennas with tapered balun for different angles with change in length

6 Comparison Between Designed Antennas with Reported Work

A comparative analysis of reflection coefficient (S11) of designed antenna is shown in Fig. 16. Bowtie antenna with tapered balun provides broader bandwidth as compared to all designed antenna with the same gain. The dipole antenna with tapered balun has more bandwidth compared to that of dipole antenna with microstrip feed line. Figure 17 shows Smith chart of dipole antenna and bowtie antenna with and without tapered balun which gives impedance location on different frequencies. By using tapered balun feeding method, antenna is operated on real axis and also made a loop on unity circle in Smith chart which indicates impedance matching for broad

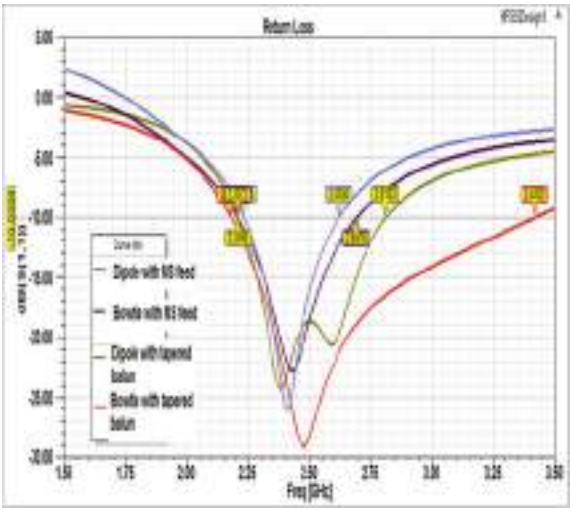

Fig. 16 Comparative reflection coefficient (S_{11} < 10) of designed antenna

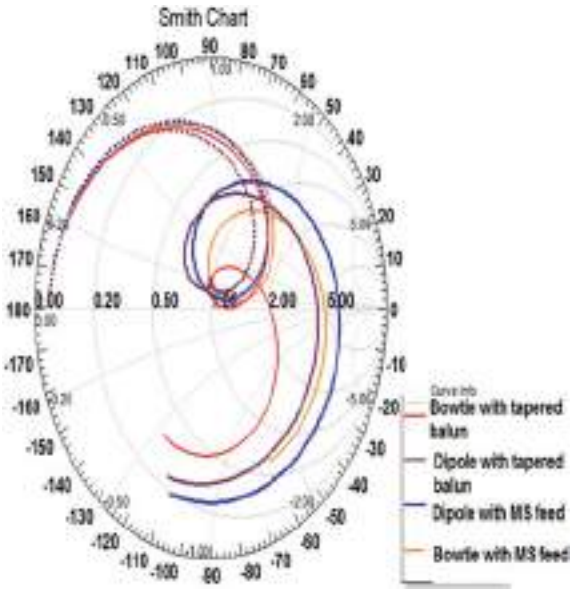

Fig. 17 Impedance variation on the Smith chart for designed antenna

bandwidth while in microstrip line feeding method antenna operated on real axis for particular frequency only so that impedance matching is done for that frequency only. A comparison between designed antennas with reported work available in literature is mentioned in Table 7. Proposed antenna design 4 achieves broad bandwidth using low-cost FR-4 Substrate. In [6, 7], designed antenna achieved broad bandwidth using costly dielectric substrate Taconic TLY5 and RO4230, respectively. In [11], antenna

Table 7 Comparison of design antenna with reported work

Reference paper		Frequency range (GHz)	% Bandwidth	Gain dB	Substrate, dielectric constant	Substrate thickness (mm)	Feeding technique	Antenna shape
*	1	2.23–2.62	16	2.30	FR-4, εr = 4.4	1.6	Microstrip line	Dipole
	2	2.20–2.69	20	2.48	FR-4, εr = 4.4	1.6	Microstrip line	Bowtie
	3	2.21–2.81	24	2.14	FR-4, εr = 4.4	1.6	Tapered balun	Dipole
	4	2.18–3.42	44	2.29	FR-4, εr = 4.4	1.6	Tapered balun	Bowtie
3		2.8 to 3.3	16	2.58	–	–	Microstrip line	Dipole
4		2.45	19	2.5	FR-4, εr = 4.4	1.6	Tapered balun	Dipole
5		2.19–3.97	58	2.9	Taconic TLY5, 2.21	1.58	Tapered balun	Dipole
6		1.7–2.5	38	–	RO4230, εr = 3	1	Adjusted integrated balun	Dipole
10		2.10–2.72	26	–	FR-4, εr = 4.4	–	Microstrip line	Bowtie
11		0.1–2.2	180	−15 to 4	FR-4, εr = 4.4	1.6	Tapered balun	Bowtie
12		2.05–2.1	2	8.6	FR-4, εr = 4.22	1.544	Microstrip line	Bowtie

*Proposed antenna design

obtained UBW bandwidth using tapered balun feeding method with gain varying from -15 dB to 4 dB over the bandwidth which is not desirable.

7 Conclusion

The design of dipole and bowtie antenna with and without tapered feeding technique operating at 2.4 GHz is explored. From this study, it is found that bowtie antenna with tapered balun obtained 44% bandwidth with more than 2 dB gain for entire frequency band which is almost double as compared to other designed antennas. The dipole antenna with tapered balun and microstrip line feeding obtained bandwidths of 24% and 16%, respectively, with the same gain. Tapered balun feeding method achieves broader bandwidth as compared to microstrip feeding method.

References

1. C.A. Balanis, *Antenna Theory Analysis and Design*, 3rd edn (Wiley-Interscience, 2005)
2. G. Kumar, K.P. Ray, *Broadband Microstrip Antennas* (Artech House, 2003)
3. J.M. Floc'h, F. Queudet, E. Fourn, *Design of printed dipole with reflector* (IEEE Xplore, 2007)
4. G.-Y. Chen, J.-S. Sun, A printed dipole antenna with microstrip tapereded balun. Microw. Opt. Technol. Lett. **40**, 344–346 (2004)
5. T.G. Vasiliadis, E.G. Vaitsopoulos, G.D. Sergiadis, A wideband printed dipole antenna with optimized tapered feeding balun for ISM and FWA Bands. Microw. Opt. Technol. Lett. **43**(5), (2004)
6. R. Li, T. Wu, B. Pan, K. Lim, J. Laskar, M.M. Tentzeri, Equivalent-circuit analysis of a broadband printed dipole with adjusted integrated balun and an array for base station applications. IEEE Trans. Antennas Propag. **57**(7), (2009)
7. H. Kumar, G. Kumar, Compact planar Yagi-Uda antenna with improved characteristics, in *2017 11th European Conference on Antennas and Propagation (EUCAP), 2008–2012* (Paris, 2017)
8. M.K.A. Rahim, M.Z.A. Abdul Aziz, C.S.Goh, *Bow-Tie Microstrip Antenna Design* 1-4244-0000-7/05/$20.00 02005 (IEEE)
9. Y. Tawk, K.Y. Kabalan, A. El-Hajj, S. Sadek, M. Al-Husseini, *A Modified Bowtie Antenna Design for Wi-Fi and WiMAX Applications* (IEEE, 2008), 978–1–4244–2202–9/08/$25.00
10. H Andre1, R Fernandez, Baharuddin, *Dipole planar bowtie printed antenna for ism application*, in *IOP Conf. Series: Materials Science and Engineering* (2009)
11. S.D. Ahirwar, D. Ramakrishna, V.M. Pandharipande, Design and development of a broadband planar dipole antenna, in *Proceedings of Asia-Pacific Microwave Conference* (2020)
12. H. Fraga-Rosales, M. Reyes-Ayala, G. Hernandez-Valdez, E.A. Andrade-Gonzalez, J.R. Miranda-Tello, F.A. Cruz-Perez, S.L. Castellanos-Lopez, *Design of a Microstrip Bowtie Antenna for Indoor Radio-Communications*, in *ITM Web of Conferences* 9, 03011 (2017)
13. Y. Tao, S. Kan, G. Wang, Ultra-wideband bow-tie antenna design, in *Proceedings of 2010 IEEE International Conference on Ultra-Wideband* (ICUWB, 2010)
14. D.A. Abd El-Aziz, T.G. Abouelnaga, E.A. Abdallah, M. El-Said, Y.S.E. Abdo, *Analysis and design of UHF bow-tie RFID Tag antenna input impedance*. Open J. Antennas Propag. **4**, 85–107.
15. K.V. Puglia, *Electromagnetic Simulation of Some Common Balun Structures* (IEEE Microwave Magazine, 2002)
16. M. Farran, S. Boscolo, A. Locatelli, A.-D. Capobianco, M. Midrio, V. Ferrari, D. Modotto, *Compact quasi-Yagi antenna with folded dipole fed by tapereded integrated balun*, ELECTRONICS LETTERS 12th May 2016, vol. 52, no. 10, pp. 789–790
17. D.M. Pozar, *Microwave Engineering*, 4th edn (Wiley & Sons, Inc.)
18. P. Dalvadi, A. Patel, A comprehensive review of different feeding techniques for quasi Yagi Antenna. Int. J. Emerg. Trends Eng. Res. **9**(3), (2021)

Gain Enhancement of Dual-Layer Patch Antenna for WLAN Applications

Ambavaram Pratap Reddy and Pachiyaannan Muthusamy

Abstract This paper presents a gain enhancement of dual-layer patch antenna for WLAN applications. With help of conventional rectangular patch and modified structure, the dual-layer patch antenna achieves the required frequency of 5.4 GHz. For dual layer, air was used for second layer with height of 1.6 mm mounted on the first FR-4 substrate layer with height of 1.6 mm with dielectric constant of 4.3. The total height is 3.2 mm and radiating element is mounted on top layer with thickness of 0.035 mm. The 50 Ω impedance transmission line is fed with radiating element. Single layer −10 dB return loss is −34 dB which is simulated, fabricated, and measured. The VSWR value is <2 and corresponding gain and directivity are 4.12 dB and 5.35 dB, respectively, and bandwidth is achieved from 5.35 to 5.43 GHz. For dual layer −10 dB return loss is −29 dB, VSWR is <2, bandwidth from 5.38 to 5.54 GHz, gain and directivity are 7.57 dB and 7.51 dB, respectively, which is simulated with the help of 3D CSTMW software. The measurement result of single layer achieved is 5.38 GHz and return loss is −34 dB which is 20 MHz shifting because of indoor measurement. By observation dual-layer micro-strip patch antenna gives good result compared to the single-layer antenna. In this work, overall gain, directivity, and bandwidth are compared with single-layer and dual-layer patch antenna. The proposed antenna S-parameter measurement using keysight E5053A (100 kHz–14 GHz) vector network analyzer and then prototype single-layer antenna was fabricated. The dual-layer patch antenna gain and bandwidth is improved. This result proved better performance which is more suitable for WLAN applications.

Keywords Dual layer · Gain enhancement · Patch antenna · WLAN

A. P. Reddy (✉) · P. Muthusamy
Department of Electronics and Communication Engineering, Advanced RF Microwave and Wireless Communication Lab, Vignan's Foundation for Science, Technology & Research (Deemed To Be University), Andhra Pradesh, India

S. Rawat et al. (eds.), *Proceedings of First International Conference on Computational Electronics for Wireless Communications*, Lecture Notes in Networks and Systems 329,
https://doi.org/10.1007/978-981-16-6246-1_4

1 Introduction

In present communication scenario, there is the demand for dual-layer micro-strip patch antenna to improve their performance of antenna parameters like gain, bandwidth, and directivity. In [1], author reported single-feed, dual-layer, dual-band linear polarization antenna. With help of E and U slot achieved dual-band operation. A triple-band dual-layer antenna with frequencies of 0.9, 1.798, and 2.402 GHz is reported in [2] and overall impedance bandwidth, gain is improved. In [3], author projected circular parasitic radiator patch on the upper layer and square parasitic radiator patch on the bottom layer. In [4], 2.396 and 2.543 GHz antenna is proposed with improvement of gain and bandwidth using two substrates. The high gain dual-layer corrugated plate antenna for X-band applications is reported in [5]. Another author [6] exhibited dual-band antenna with −10 dB impedance bandwidth enhancement. Two metallic layer printed in opposite side of single dielectric substrate array antenna is reported in [7]. In [8], stacked patch antenna is designed using edge feed techniques which achieved high gain and more bandwidth which is used for Bluetooth and wireless LAN application. The low-profile circularly polarized antenna with improved gain using quarter-mode substrate integrated waveguide cavities array is reported in [9]. The conformal array using ultra-thin layer dual layer with improved gain and bandwidth is reported in [10]. Another [11] discussed conventional single-layer antenna for WLAN applications. From the above literature, author motivated to design dual-layer patch antenna for WLAN application with gain improvement.

2 Single-Layer Patch Antenna Design Analysis

This section describes about the dimensions and structure details of the proposed antenna as shown in Fig. 1 and Table 1 shows the proposed single-layer radiating element design and design parameter details. To make the desired frequency, 4.6 mm × 1.2 mm slot is removed from the basic rectangular patch antenna. The single-layer proposed antenna using FR-4 substrate with dielectric constant 4.3 having 23 mm × 27.68 mm with height 1.6 mm, feed-line length, and width is 5.68 mm × 1.4 mm, respectively. Figures 2 and 3 show the simulated results of the single-layer proposed design S-parameter and VSWR values. The bandwidth of the proposed design 5.35–5.45 GHz, gain and bandwidths are 4.12 dB, 5.35 dB, respectively. Figure 4 shows simulated and measured S-parameters result, due to fabrication process the measured resonant frequency achieved at 5.38 GHz. Figures 5 and 6 depicted fabricated prototype single antenna structure and measured setup of the proposed antenna. Figure 7 shows the surface current distribution of the entire patch area at 5.4 GHz. Figure 8 shows the gain and directivity of the 3D radiation pattern of the proposed single-layer design. Figure 9 shows the radiation pattern of the proposed antenna which almost shows omni-directional radiation pattern.

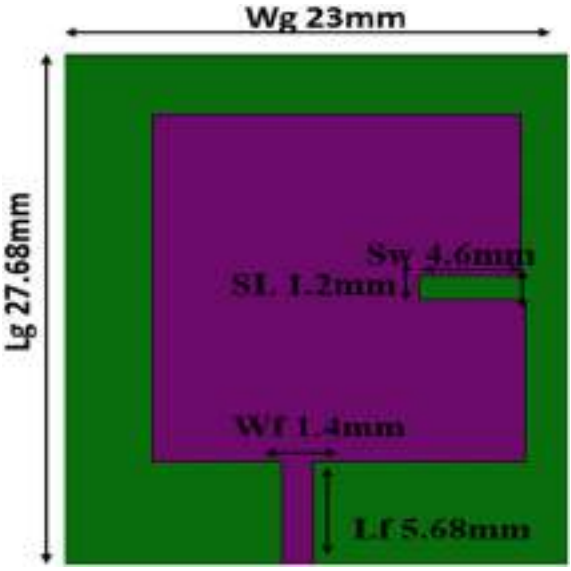

Fig. 1 Single-layer proposed design

Table 1 Single-layer antenna design parameters

Parameters	Dimensions in mm
Wg	23
Lg	27.68
Wf	1.4
Lf	5.68
Sw	4.6
SL	1.2

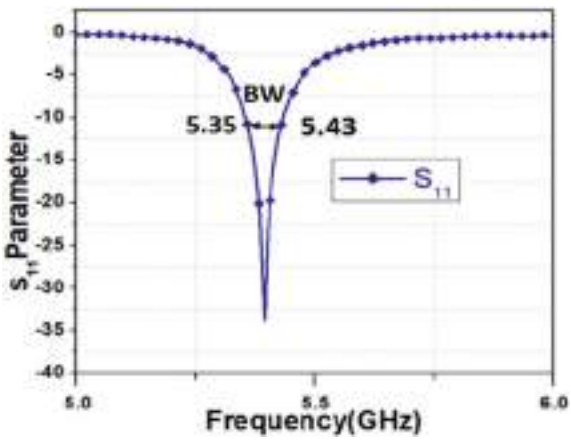

Fig. 2 S_{11}-parameter simulated result

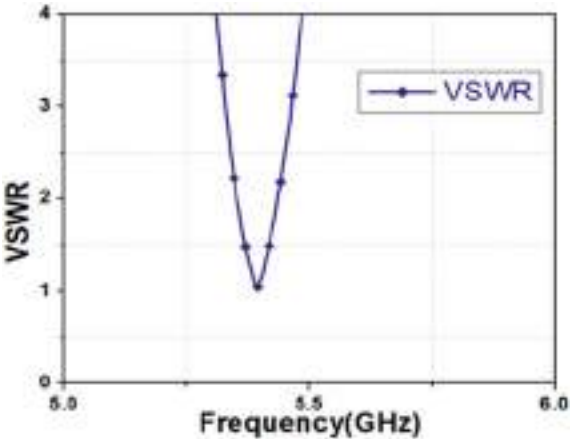

Fig. 3 VSWR simulated result

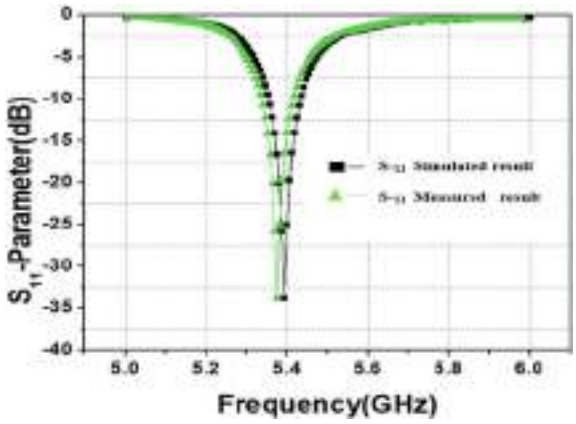

Fig. 4 Simulated and measured S_{-11} results

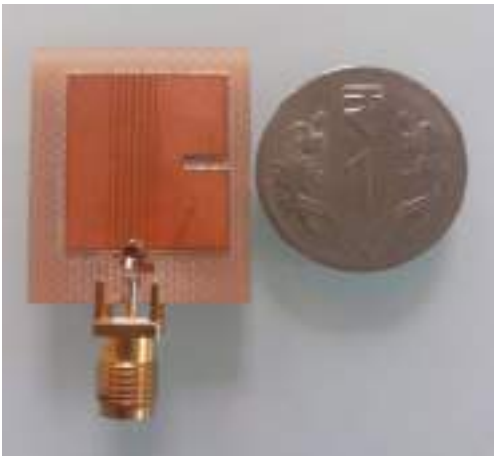

Fig. 5 Fabricated single-layer antenna structure

Fig. 6 Measured S_{11}-parameter plot displayed in network analyzer

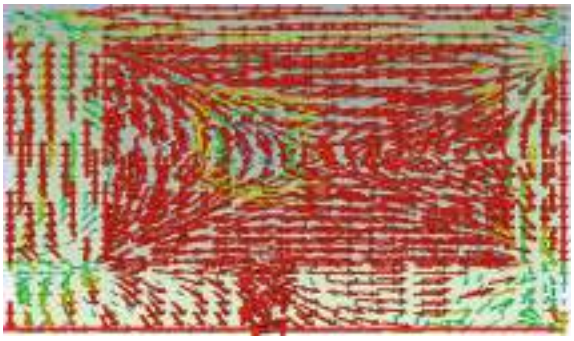

Fig. 7 Surface current distribution of the single-layer patch antenna

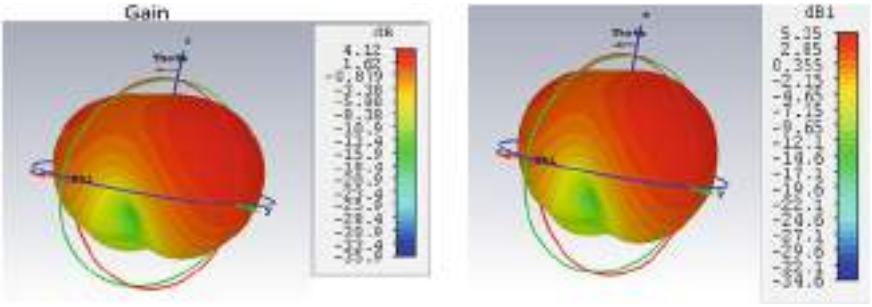

Fig. 8 3D radiation pattern **a** gain **b** directivity

3 Dual-Layer Patch Antenna Design Analysis

This section reports dual-layer patch antenna. Figure10 shows top and side view dual-layer micro-strip patch antenna with dimensions. To enhance the gain and directivity,

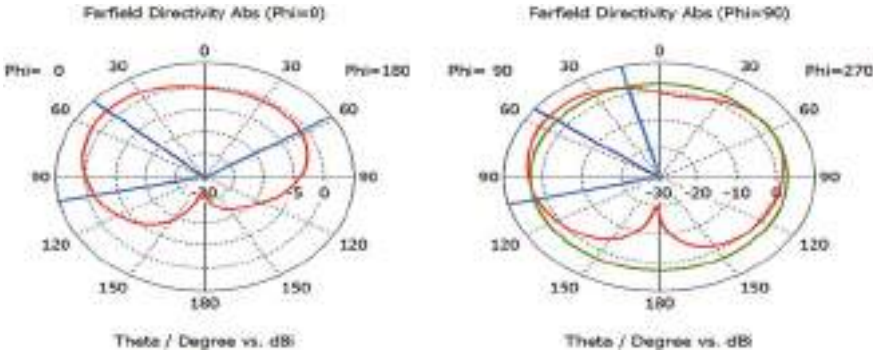

Fig. 9 Radiation pattern E-plane and H-plane

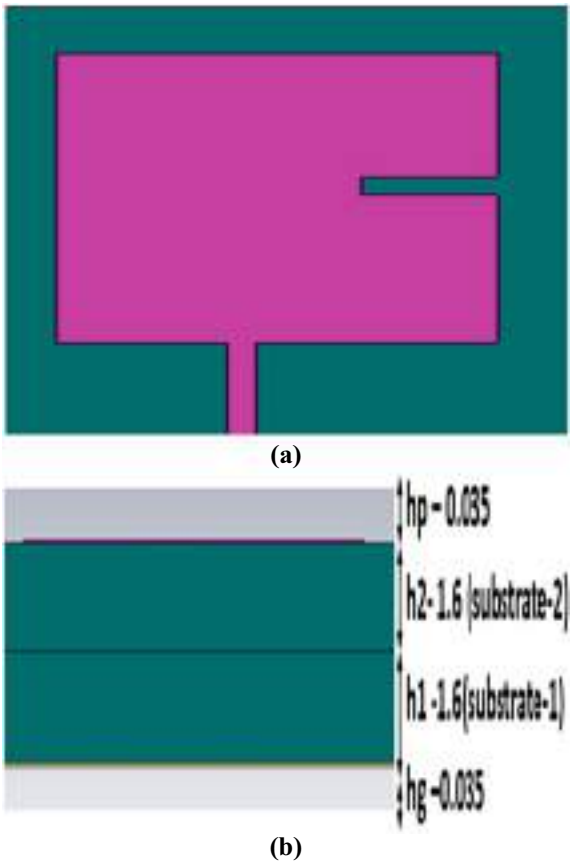

Fig. 10 Dual-layer micro-strip patch antenna design model **a** top view **b** side view

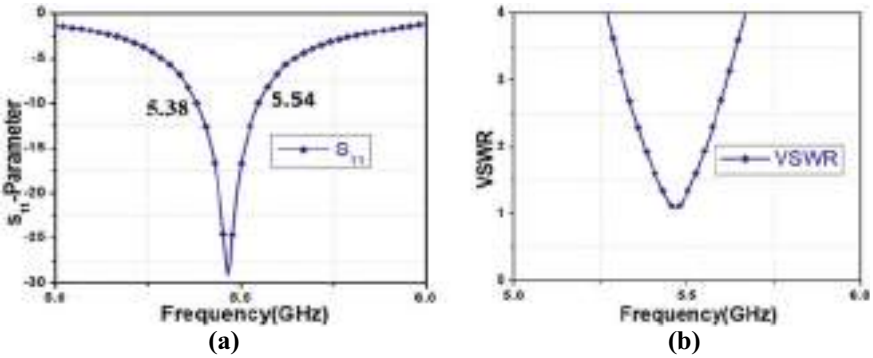

Fig. 11 **a** Simulated S_{11}-parameter **b** VSWR result

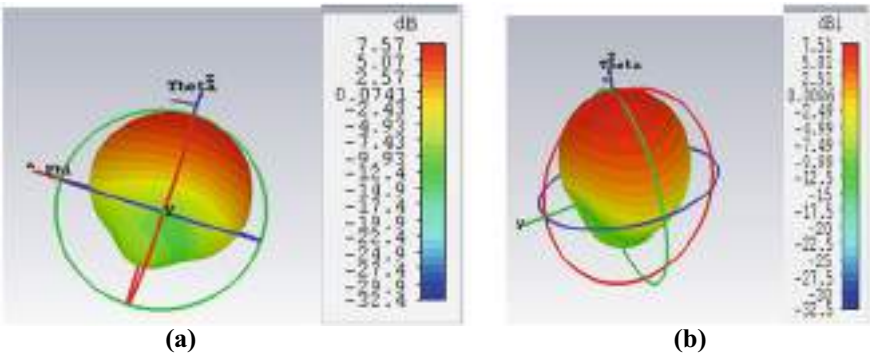

Fig. 12 **a** Simulated gain result **b** directivity result

the air substrate with dielectric constant of 1.00 was used. The radiating element is placed on the second substrate with height 0.035 mm. Figure11 shows s_{11} parameters and VSWR result shows the enhanced bandwidth results of the proposed dual-layer antenna, i.e., from 5.38–5.54 GHz. Figure 12 shows the radiation pattern of the gain and directivity 3D plots, respectively. By the observation compared to the single-layer radiating element, dual-layer micro-strip patch antenna achieved large bandwidth, increases the gain 3.45 dB, and directivity 2.16 dB. Table 2 reports a comparison of proposed antenna with existing antenna performance.

4 Conclusion

In this research work, the conventional single-layer micro-strip patch antenna was designed at resonant frequencies of 5.4 GHz. The dual-layer air was used for second layer with height of 1.6 mm mounted on the first FR-4 substrate layer height of 1.6

Table 2 Comparison of proposed antenna with previous antenna

Ref. no	Dual-layer antenna dimensions in mm	Dual-layer gain in dB	Band
[1]	150 × 150	8.05	WLAN (2.40–2.4835 GHz) and WiMAX (3.40–3.61 GHz) bands
[2]	60 × 50	5.6	0.9 GHz,1.798 GHz, 2.402 GHz (Bluetooth, Wi-Fi)
[11]	39 × 47 (single layer)	8.96	(WLAN) 2.4 GHz
Proposed work	27.68 × 23	7.67	WLAN (5.4 GHz)

mm with dielectric constant 4.3. The total height is 3.2 mm and radiating element is mounted on top layer with thickness of 0.035 mm. Single-layer −10dB return loss is −34 dB which is simulated, fabricated, and measured. The VSWR value is <2 and corresponding gain and directivity are 4.12 dB, 5.35 dB, and bandwidth is achieved from 5.35 to 5.43 GHz. For dual layer −10 dB return loss is −29 dB, VSWR is <2, bandwidth from 5.38 to 5.54 GHz, gain and directivity are 7.57 dB, 7.51 dB. By observation, dual-layer micro-strip patch antenna gives good result compared to the single-layer antenna. This proposed antenna gives good solution of gain enhancement of 5.4 GHz WLAN application.

References

1. S. Liu, W. Wu, D.G. Fang, Single-feed dual-layer dual-band E-shaped and U-slot patch antenna for wireless communication application. IEEE Antennas Wirel. Propag. Lett. **15**, 468–471 (2015)
2. G.M. Faisal, Dual-layer microstrip antenna design for wireless communications. Am. J. Electr. Electron. Eng. **6**(2), 66–71 (2018)
3. E. Sandi, A. Diamah, M.W. Iqbal, D.N. Fajriah, Double layer parasitic radiator for S-Band antennas to increase gain and bandwidth performances. In *Journal of Physics: Conference Series*, vol. 1402, no. 4 (IOP Publishing, 2019), p. 044030
4. H. Nornikman, B.H. Ahmad, M.Z.A. Abd Aziz, H.A. Bakar, Dual frequencies band and enhanced wideband effect of dual layer microstrip patch antenna with parasitic, in *Journal of Physics: Conference Series*, vol. 1049, no. 1 (IOP Publishing, 2018), p. 012012
5. S. Alkaraki, Y. Gao, C. Parini, Dual-layer corrugated plate antenna. IEEE Antennas Wirel. Propag. Lett. **16**, 2086–2089 (2017)
6. Z. Liang, J. Liu, Y. Li, Y. Long, A dual-frequency broadband design of coupled-fed stacked microstrip monopolar patch antenna for WLAN applications. IEEE Antennas Wirel. Propag. Lett. **15**, 1289–1292 (2015)
7. X. Zhang, F. Yang, S. Xu, A. Aziz, M. Li, Dual-layer transmit array antenna with high transmission efficiency. IEEE Trans. Antennas Propag. **68**(8), 6003–6012 (2020)
8. J.C. Rao, A.K. Chaitanya, Performance analysis of double layer stacked patch antenna with edge feed. Int. J. Energy, Inform. Commun. **4**(5), 15–24 (2013)

9. Z. Wang, C. Pang, Y. Li, X. Wang, A method for radiation pattern reconstruction of phased-array antenna. IEEE Antennas Wirel. Propag. Lett. **19**(1), 168–172 (2019)
10. L.Z. Song, P.Y. Qin, Y.J. Guo, A high-efficiency conformal transmit array antenna employing dual-layer ultra-thin Huygens element. IEEE Trans. Antennas Propag. (2020)
11. E. Aravindraj, K. Ayyappan, Design of slotted H-shaped patch antenna for 2.4 GHz WLAN applications, in *2017 International Conference on Computer Communication and Informatics (ICCCI)* (IEEE, 2017), pp. 1–5

Dual-Band Microstrip Patch Antenna for Wireless Communication

Ritwik Shirbhate, Dattaji Diliprao Dhumal, and Avinash Keskar

Abstract In this paper, a novel microstrip patch antenna (MPA) which is having dual-band characteristics is presented. The proposed MPA, with resonating frequencies of 2.43 GHz and 5.872 GHz, has applications in S-band and C-band (in license-free band, i.e., 2.4–2.4835 GHz and 5.825–5.875 GHz). It is designed on a substrate FR4 ($\varepsilon r = 4.3$ and $\tan\delta = 0.04$). In this, line feeding scheme is used to supply current to the antenna so as to excite it. The results of actual fabricated antenna are close to that of simulation one. The proposed antenna having dual-band resonance and comparatively better and high gain performance can be easily mounted into systems for wireless communications such as radar and satellite communications.

Keywords Microstrip patch antenna · Dual-band antenna · License-free frequency

1 Introduction

Since their first introduction to mankind, microstrip patch antennas (MPAs) have splendid of research work with constant and regular evolution, they have been widely integrated into many wireless applications. The size of antenna plays an important role in designing and characterizing the device in which it is going to operate, the microstrip patch antennas has a key role in applications such as satellite, radar, Bluetooth, simultaneous wireless information and power transfer (SWIPT), etc., as they are planar, smaller in size, lightweight, robust and hence inexpensive [1, 2]. However, narrow bandwidth, lower gain, etc. are some of the limitations of microstrip patch antennas [3]. To reduce the patch antenna size, different methodologies have been proposed which includes a square-shaped patch fed by a microstrip line, L-slots or cross and bent slots cut on microstrip antenna [4–6]. These methods provide alternate paths for the excited current so as to achieve accurate resonant frequencies at smaller size with higher gain [7]. The carving effect of notches [8, 9] and slots [10–12] plays an important role in pulse broadening and introducing side frequencies.

R. Shirbhate (✉) · D. D. Dhumal · A. Keskar
Visvesvaraya National Institute of Technology, Nagpur, India
e-mail: Shirbhateritwik47@students.vnit.ac.in

S. Rawat et al. (eds.), *Proceedings of First International Conference on Computational Electronics for Wireless Communications*, Lecture Notes in Networks and Systems 329,
https://doi.org/10.1007/978-981-16-6246-1_5

The basic form of patch antenna resembles to dielectric as a base material and a radiating conducting material itched on the upper side of substrate.

This paper contains a dual-band microstrip patch antenna with two different resonating frequencies 2.43 GHz and 5.872 GHz which are in license-free band with higher value of gain and reflection coefficient as compared to previous models. Also, most of the previous research in antenna concentrates mainly on licensed frequencies. But this model is different from those versions of microstrip antenna.

2 Antenna Design and Analysis

The most important factor while designing the antenna is the frequency of operation. Here, being a dual band antenna, we choose 2.43 GHz and 5.872 GHz as desired frequencies. The antenna structure in Fig. 1 was designed using the fundamental equations in [13].

The following equations can be used to calculate the dimensions of the patch:

$$W = \frac{c}{2f_0\sqrt{\frac{\phi_r+1}{2}}} \phi_{eff} = \frac{\phi_r+1}{2} + \frac{\phi_r-1}{2}\left[\frac{1}{\sqrt{1+12\left(\frac{h}{W}\right)}}\right]$$

$$L = \frac{c}{2f_0\leq\overline{\phi_{eff}}} - 0.824h\left(\frac{\left(\phi_{eff}+0.3\right)\left(\frac{W}{h}+0.264\right)}{\left(\phi_{eff}-0.258\right)\left(\frac{W}{h}+0.8\right)}\right)$$

where

$\frac{c}{2f_0\leq\overline{\phi_{eff}}} = L_{eff}$,

c = speed of light.

f_0 = resonating frequency.

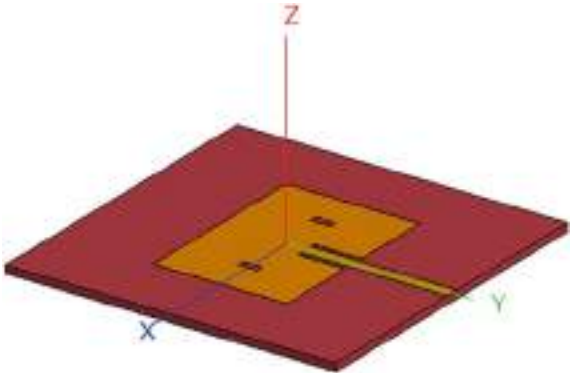

Fig. 1 Microstrip Patch Antenna (with slots) and actual model

ϕ_r = dielectric constant of the dielectric substrate (relative permittivity).

W = patch width.

L = patch length.

h = substrate thickness = 1.6 mm for FR4 material.

Here, 2.43 Ghz is considered as first resonating frequency of proposed MPA. So, from the above equations we obtained as length l_p * 40 mm and width w_p * 28.3 mm of the patch. Then, we will start with designing of ground layer of 70*70 mm^2. The subsequent stage is determining the type of substrate and its dimensions. The height and dielectric constant of substrate plays a key role in designing of antenna as dimensions of antenna are inversely proportional to dielectric constant of substrate. In this module, we are taking a substrate of 70*70 mm^2 with a relative permittivity of 4.4. On one side surface of the substrate, patch antenna is mounted while the ground plane is attached on the other surface. There are various types of current feeding techniques are used such as microstrip line feeding, capacitive feeding, coaxial feeding, etc. [14].

For the calculations for the width of the feeder, we can use the following equation [13]:

$$W_f = \frac{7.48h}{e^{\left(Z_0 \frac{\sqrt{\phi_r}+1.41}{87}\right)}} - 1.25t$$

where

ϕ_r = relative dielectric constant.

Z_0 = single ended impedance.

t = thickness of trace

h = dielectric thickness

W = width of the feeder which is * 3mm.

So, current is fed into patch using microstrip line of 3*20.85 mm^2. In some cases, full power is not transmitted when the feed line impedance is not perfectly matched with the radiation resistance of the patch, the output of antenna suffers [15]. As a result, a matching network on the feed line system must be introduced to reduce back scattering and thus improve the antenna's efficiency. In such situations, providing an inset feed is a popular solution [16]. The inset feed is measured in order to match the impedance of the antenna's feeding edge with transmission line's characteristic impedance. Line feed is a method where the feed is simply a broadening of the patch that connects to the substrate, making it simple to fit the impedance by changing the inset location. This can be accomplished by specifically changing the wire and line port location [17]. This method is thought to be the simplest because this allows for easy impedance matching, fabrication as well as modeling [18, 19].

Also, the slot cutting is performed in surfaces of antenna which can be the one with the feed or the ground and it can be any geometrical shape. Figure 1 shows the patch of the antenna with the slots. The dimensions of the slot are w_c and l_c, i.e., width and length of the slot cut, respectively (Fig. 2). The approximate dimensions of slot can be calculated with the complex equations [11] and the upper bound of the length is given as

$$L_{slot} = \frac{0.45c}{f\sqrt{\phi_{eff\_slot}}}$$

where $\phi_{eff\_slot} = \frac{\phi_r+1}{2}$

From Fig. 3, we can observe that the square patch proposed here is a planar patch without any slots or cuts on it. Figure 4 displays the reflection coefficient of the microstrip patch antenna without slots at frequencies 2.43453 GHz and 5.89452 GHz.

Fig. 2 Size comparison of fabricated MPA

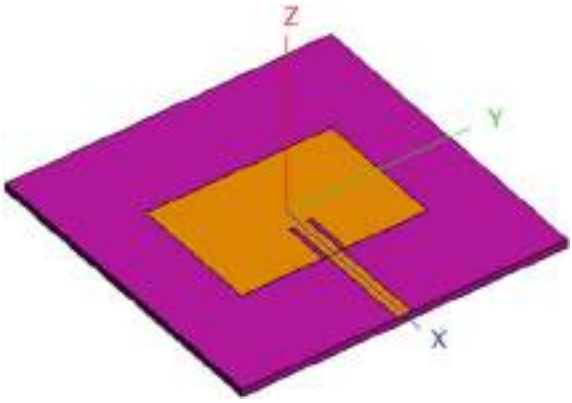

Fig. 3 Microstrip patch antenna (without slots)

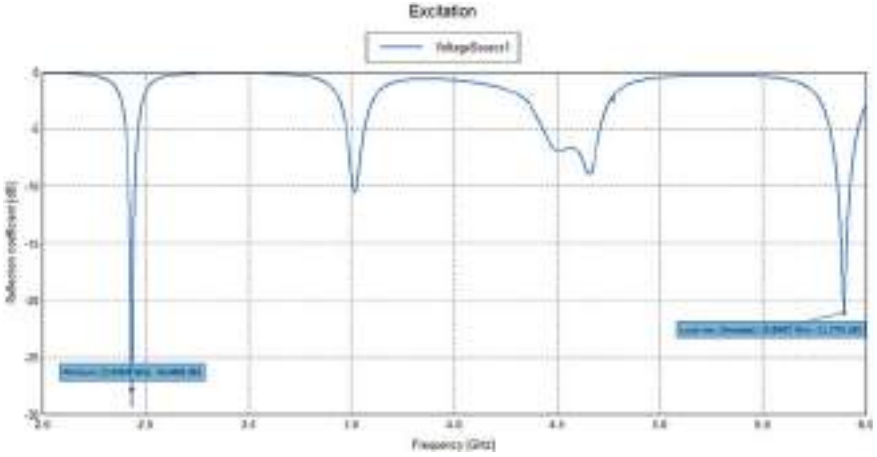

Fig. 4 Reflection coefficient (without slots)

So, when compared to the other antenna, both the frequencies and the magnitude of reflection coefficient at them varied with introduction of slots in antenna in Fig. 1. And the change here is positive, i.e., in the favor of the desired result. From Fig. 6, the reflection coefficient at both frequencies increased with respect to the without slot version of antenna. The frequency at 5.89452 GHz is reduced to 5.87243 GHz which is desired. The magnitude of reflection coefficient on frequency 2.429 GHz is increased by 12.9841%, i.e., from 38.4856 dB to 43.4826 dB and at 5.87243 GHz it is increased by 67.2294%, i.e., from 21.2755 dB to 35.5789 db (Table 1).

Considering all these, the simulation model will look like as shown in Fig. 1.

Table 1 Lists the values of all the parameters required while designing the antenna in Fig. 1

Sr. nno	Parameters	Symbols	Value (mm)
1	Length of substrate	ls	70
2	Length of patch	lp	40
3	Width of substrate	ws	70
4	Width of patch	wp	28.3
5	Substrate thickness	t	1.6
6	Patch and base thickness	tp	0.035
7	Microstrip length	lf	20.85
8	Microstrip width	wf	3
9	Slot lengths (cut)	lc	4
10	Slot widths (cut)	wc	1.5

3 Results and Discussion

The simulation of the proposed patch antenna is done with the help of CADFEKO software. The reflection coefficient gives an idea about the impedance matching of the devices. Usually, a value of S_{11} less than −10 dB is acceptable for minimum insertion loss. From Fig. 5, reflection coefficient was achieved to be −43.4826 dB for 2.429 GHz and −35.5789 dB for 5.872 GHz. The VSWR is another figure of merit for the antenna designing. Figure 10 shows the graph with VSWR. The VSWR is having maxima of 0.1163 dB at 2.429 GHz and 0.289 dB at 5.872 GHz frequencies. Efficiency of the antenna is characterized from its gain. Gain is the capacity of the antenna to transform input power into output radiations. Figure 6 shows the directional gain of antenna which is found to be 5 dB (Fig. 7).

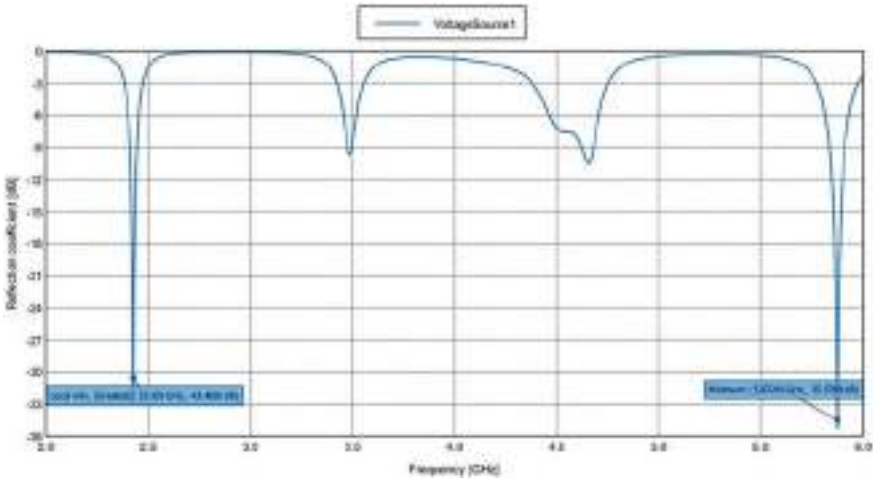

Fig. 5 Reflection coefficient (with slots)

Fig. 6 Radiation pattern and gain of antenna

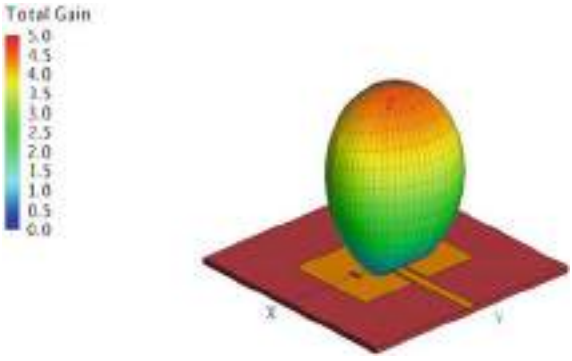

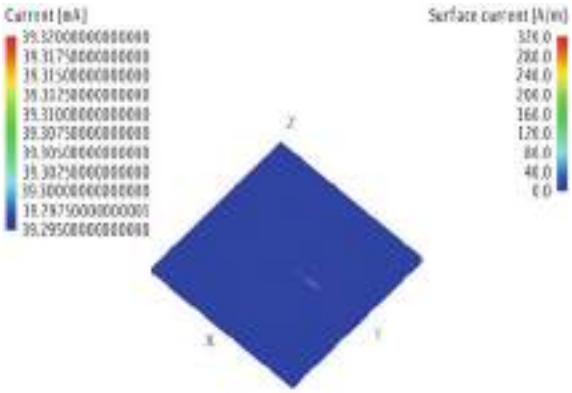

Fig. 7 Surface current distribution

Impedance matching for the slot is also obtained which can be observed from the Smith chart in Figs. 8 and 9 (Fig. 10). Also, Fig. 11 shows the closeness between reflection coefficient for the simulated and practical results. Figure 7 provides the behavior of surface current in our proposed model (Table 2).

The proposed model concentrates on license-free frequencies as they are available at free of cost. Also, no legal permission is needed to access them from any government or private authority. So, the proposed antenna will play an important role in wireless communication applications that are designed on license-free band such as license-free walkie-talkie. However, network traffic and limited bandwidth

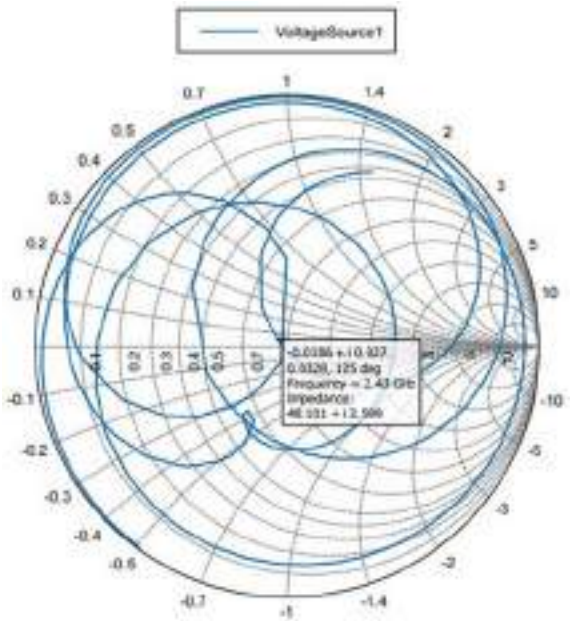

Fig. 8 Smith chart for 2.43 GHz

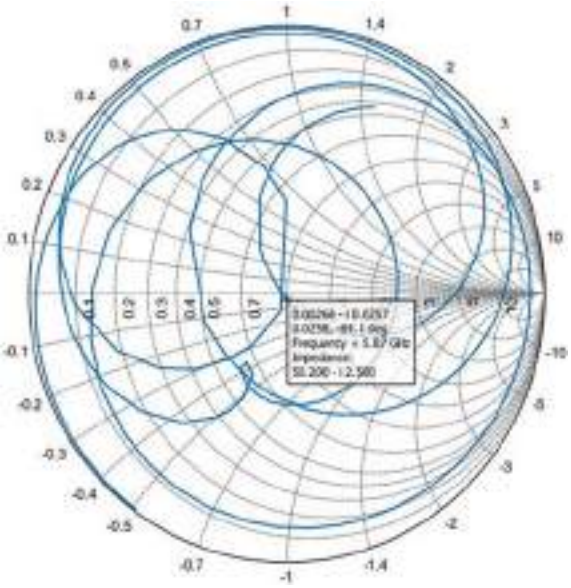

Fig. 9 Smith chart for 5.872 GHz

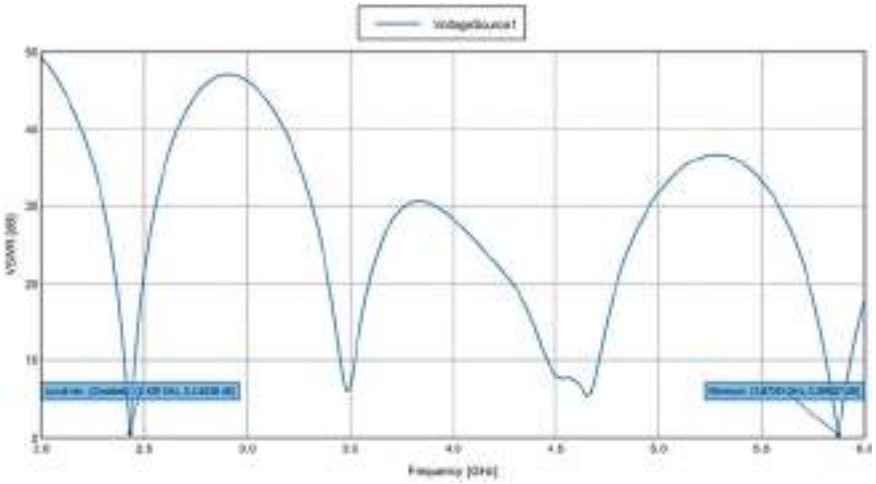

Fig. 10 VSWR

are some drawbacks of license-free band. Also, as everyone has free access to the band, it is difficult to maintain data privacy and security in communication. But still in case of license-free applications, the proposed antenna suits well.

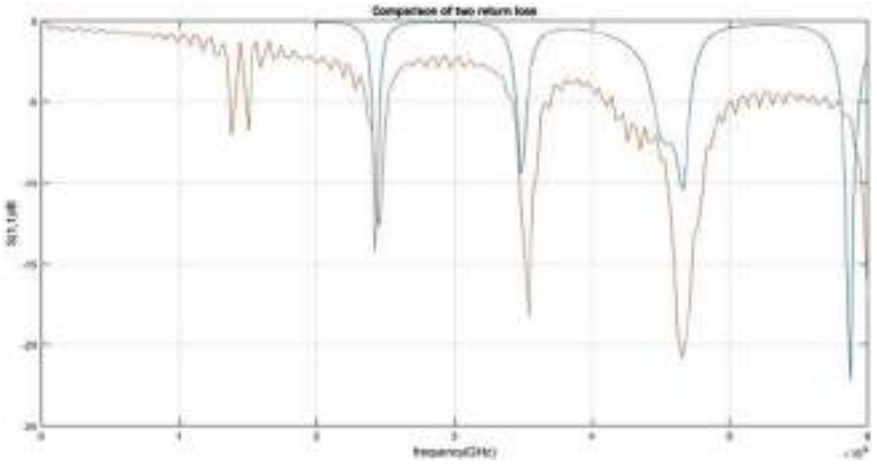

Fig. 11 Comparison between simulated and practical output

Table 2 Comparison table

	Parameters			
	Resonant frequencies (GHz)	Reflection coefficient (dB)	VSWR (dB)	Is the frequency license free?
Proposed antenna	2.43	−43.4826	0.1163	Yes
	5.872	−35.5789	0.289	Yes
Antenna in [20]	2.4	−30	–	No
	5.5	−41	–	No
Antenna in [21]	6.53	−18.69	1.014	No
	8.62	−24.31	0.526	No
Antenna in [22]	2.44	−28	–	Yes
	5.775	−16	–	No
Antenna in [23]	1.8	−16	–	No
	2.4	−34	–	No

$$\text{Percentage Matching} = \left(1 - \frac{vnafreq - simfreq}{simfreq}\right) * 100\%$$

From Fig. 3,
Percentage matching = 98.7% (first resonant frequency).
vnafreq = 2.461 GHz and simfreq = 2.43 GHz.
= 97.8% (second resonant frequency).
vnafreq = 6 GHz and simfreq = 5.872 GHz.

4 Conclusion

In this work, microstrip patch antenna in license-free band is fabricated. The resonant frequencies are 2.43 and 5.872 GHz. Multiband microstrip antennas cover a wide area in the field of wireless communication. The reflection coefficient at the resonant frequencies is also found to meet the requirement (<−10 dB) in simulated as well as practical model. Gain of the antenna is also much better than previous models for the above frequencies. However, VSWR is also found to be less than 2 which is acceptable. Also, the percentage of frequency matching is 98.7% for 2.43 GHz and 97.8% for 5.872 GHz which is quite good. This antenna can be used in simultaneous wireless information and power transfer (SWIPT) walkie-talkie.

References

1. S. Dwivedi, S.G. Yadav, A.K. Singh, Annular ring embedded L-slot rectangular microstrip patch antenna, in *IEEE Student Technology Symposium* (2014), pp. 372–375
2. R. Garg, P. Bhartia, I. Bahl, A. Ittipiboon, *Microstrip Antenna Design Handbook* (Artech House, 2001)
3. R. Mishra, An overview of microstrip antenna. HCTL Open Int. J. Technol. Innov. Res. (IJTIR) **21**, 2–4 (2016)
4. C.Y. Huang, J.Y. Wu, K.L. Wong, Cross-slot-coupled micro-strip antenna and dielectric resonator antenna for circular polarization. IEEE Trans. Antennas Propag. **47**(4), 605–609 (1999)
5. H. Iwasaki, A circularly polarized small-size microstrip antenna with a cross slot. IEEE Trans. Antennas Propag. **44**(10), 1399–1401 (1996)
6. J.S. Row, C.Y. Ai, Compact design of single-feed circularly polarised microstrip antenna. Electron. Lett. **40**(18), 1093–1094 (2004)
7. Bao X.L., Ammann M.J., Compact annular-ring embedded circular patch antenna with cross-slot ground plane for circular polarization. Electron. Lett. **42**(4) 2006
8. R.S. Kushwaha, D.K. Srivastava, J.P. Saini, S. Dhupkariya, Bandwidth enhancement for microstrip patch antenna with microstrip line feed. Comput. Commun. Technol. (ICCCT) 183–185 (2012)
9. S.W. Su, K.L. Wong, C.L. Tang, Band-notched ultra-wideband planar monopole antenna. Microw. Opt. Technol. Lett. **44**, 217–219 (2005)
10. R.K. Chaurasia, V. Mathur, Enhancement of bandwidth for square of micro strip antenna by partial ground and feedline technique. Asia Pac. J. Eng. Sci. Technol. **3**(1, 49–53
11. R. Mishra, R.G. Mishra, P. Kuchhal, Analytical study on the effect of dimension and position of slot for the designing of ultra-wide band (UWB) microstrip antenna, in *5th IEEE International Conference on Advances in Computing, Communications and Informatics (ICACCI)*, 978–1–5090–2028–7 (2016)
12. K.F. Lee, K.M. Luk, K.F. Tong, S.M. Shum, T. Huyn, R.Q. Lee, Experimental and simulation studies of the coaxially fed U–slot rectangular patch. IEEE Proc. Microw. Antenna Propag. **144**(5), 354–358 (1997)
13. C.A. Balanis, *Antenna Theory: Analysis and Design* (Wiley, 2005)
14. A. Kumar, J. Kaur, R. Singh, Performance analysis of different feeding techniques. Int. J. Emerg. Technol. Adv. Eng. **3**(3), 884–890 (2013)
15. K.F. Lee, K.M. Luk, H.W. Lai, *Microstrip Patch Antennas* (World Scientific, 2017)
16. T. Ghosh et al., Mutual coupling reduction between closely placed microstrip patch antenna using meander line resonator. Progress Electromagn. Res. **59**, 115–122 (2016)

17. R. Garg, P. Bhartia, I. Bahl, A. Ittipiboon, *Microstrip Antenna Design Handbook* (Artech House, 2001)
18. X. Zhang, L. Zhu, High-gain circularly polarized microstrip patch antenna with loading of shorting pins. IEEE Trans. Antennas Propag. **64**(6), 2172–2178 (2016)
19. B.P. Smyth, S. Barth, A.K. Iyer, Dual-band microstrip patch antenna using integrated uniplanar metamaterial-based EBGs. IEEE Trans. Antennas Propag. **64**(12), 5046–5053 (2016)
20. X. Guo, W. Liao, Q. Zhang, Y. Chen, A dual-band embedded inverted T-slot circular microstrip patch antenna, in *2016 IEEE 5th Asia-Pacific Conference on Antennas and Propagation (APCAP)*. https://doi.org/10.1109/APCAP.2016.7843143
21. G. Djengomemgoto, R. Altunok, C. Karabacak, Ş. Taha İmeci, T. Durak, Dual-band gemini-shaped microstrip patch antenna for C-band and X-band applications, in *2017 International Applied Computational Electromagnetics Society Symposium-Italy (ACES)*. https://doi.org/10.23919/ROPACES.2017.7916059
22. S.M. Kim, J.M. Son, H.J. Kim, W.G. Yang, Design and implementation of dual-band square patch antenna for wireless LAN of 2.4GHz and 5.7GHz, in *2005 Asia-Pacific Microwave Conference Proceedings* (Suzhou, China, 2005), p. 4. https://doi.org/10.1109/APMC.2005.1606963
23. H. Omidi, H. Oraizi, Enhanced properties of a novel dual band shorted square patch with E-shaped slot for GSM/WLAN bands, in *2016 IEEE Middle East Conference on Antennas and Propagation (MECAP)* (Beirut, Lebanon, 2016), pp. 1–4. https://doi.org/10.1109/MECAP.2016.7790117

Dual-Band RFID Tag Antenna Design for UHF Band Applications with High Read Range Performance

Aarti Bansal, Rajesh Khanna, and Surbhi Sharma

Abstract The tag antenna exhibiting operation in European and North American regions covering major UHF RFID bands resonating at 866 MHz and 915 MHz, respectively, has been designed in this paper. The tag antenna operating in single UHF RFID region is converted to operate in dual UHF RFID region band tag antenna by modifying its geometry and optimizing the final geometry to obtain resonance at the required resonant frequencies. The tag antenna proposed in this paper comprises a meandered line element with extended lower stub to obtain additional band at European Region. The designed tag employs Alien Higgs-4 RFID chip having capacitive reactance. The designed tag utilizes inductive spiral loop to obtain conjugate impedance to match the capacitive RFID IC. Further, the designed modified tag antenna is simulated and its performance is analyzed based on different parameters such as its resistance, reactance, radiation efficiency, realized gain, etc. Also, it has been seen that the designed dual band antenna shows bidirectional and omnidirectional radiation pattern in E-plane and H-plane, respectively.

Keywords Single-band and dual-band tag · Read range · Ultra-high frequency (UHF) · RFID (radio frequency identification) tag antenna

1 Introduction

RFID systems are observed to possess multifold potential in the field of tracking, identification, and data acquisition. These RFID-equipped objects need not lie in line of sight and can communicate wirelessly with the interrogator or reader. These

A. Bansal (✉) · R. Khanna · S. Sharma
Thapar Institute of Engineering and Technology, Patiala, India
e-mail: aarti.bansal@thapar.edu

R. Khanna
e-mail: rkhanna@thapar.edu

S. Sharma
e-mail: surbhi.sharma@thapar.edu

S. Rawat et al. (eds.), *Proceedings of First International Conference on Computational Electronics for Wireless Communications*, Lecture Notes in Networks and Systems 329,
https://doi.org/10.1007/978-981-16-6246-1_6

RFID systems find applications in logistics and supply chains, inventory control and management, health care, sensing, and IoT fields [1]. Various RFID bands are allocated for different frequency ranges such as low frequency, high frequency, and ultra-high frequency. Out of these, RFID systems at ultra-high frequency (UHF) band are mostly preferred owing to their higher read range, data rate, and lower antenna profile [1].

RFID systems comprises a RFID reader, tags, and a host computer to maintain the database. RFID tags further include two components, i.e., tag antenna and an RFID microchip. The microchip is used to store the information related to the tracking object. Each RFID microchip has its own reading power sensitivity. Passive RFID tags utilize electromagnetic power received from the interrogatory signal to power up the RFID IC/microchip. This RFID microchip further exhibits high capacitive reactance and low resistance. Thus, the tag antenna must be designed to possess high inductance to transfer maximum power to the employed microchip [2].

There are different impedance-matching techniques as single T-match/double T-match networks [3, 4], nested loop [5, 6], tuning impedance using slots or comb structure in patch [7–9], inductive coupling [10, 11], etc. Along with *conjugate matching* requirement in tag antenna design, there is a need to decrease the size of tag. This is required as the tag has to be affixed on the object to be tracked as in various logistics, supply chain, monitoring of health, safety of construction workers, etc. The size of the antenna can be miniaturized by incorporating high permittivity substrates [12], using planar inverted-F antenna structures and employing shorting vias or pins [13], and also meandering [14]. The antenna design using meandering increases its electrical length at UHF frequency range and thereby leads to miniaturization. It is also preferred as it is simple to fabricate. Hence, to summarize, the design of tag antenna must be planar, and of low profile to be easily affixed upon the tracking object in practical implementation scenario and also exhibit high read range.

RFID bands at UHF range are further distributed according to different regions such as 865–867 MHz in European, 902–928 MHz in North American, 908–914 MHz in Korean region, etc. Hence, tag design operating in a specific region has a limited utility and thus for achieving interoperable operations, tags must be designed to operate in two or more regions simultaneously [3, 15]. Multiband tag antennas for UHF range have better conjugate matching with respect to the microchip impedance and therefore higher reading range at two or more operating frequency regions. Hence, it is challenging to design tag antenna with multiband feature to fulfill the need of different inter-export commercial and industrial applications.

To track the objects, RFID tag needs to be affixed on them and hence tag antenna with low profile is preferred. The size of the tag is mainly dependent on the antenna size as microchip being extremely tiny. Most commonly, meandering is applied to obtain compact sized antenna structure [1, 2, 9, 13]. The radiation properties of the antenna such as efficiency along with realized gain of meandered antenna tend to decrease due to current crowding effect [9, 13]. This can be explained as cancellation of currents flowing in opposite directions in the adjacent line segments of meandered structure which results in poor radiations. Hence, meandering tends to miniaturize

the size but results in poor radiation. Therefore, the meandered length of the adjacent segments must be optimized to achieve compromise between the two factors.

The tag antenna proposed here employs highly inductive spiral loop to compensate the capacitive reactance of the attached RFID IC/microchip. Further, the single-band tag antenna structure designed in [9] is modified and optimized to obtain dual bands operating in European and North American UHF regions with UHF bands having frequency ranges of 865–867 MHz and 902–928 MHz, respectively. The designed tag also possesses high radiation efficiency and realized gain.

The contents of this paper are organized as: antenna configuration is explained in Sect. 2. Further, in Sect. 3, effect of varying tag antenna dimensions is illustrated through parametric analysis. Simulated performance of the proposed tag is presented in Sect. 4, far-field radiation patterns in Sect. 5, and thereafter conclusions are discussed.

2 Tag Antenna Design Configuration

The antenna configuration for the tag designed in [10] as shown in Fig. 1a is modified as shown in Fig. 1b to obtain dual-band performance. The initial meandered line element is extended downward by adding additional lower stub to the element. The S_{11} performance of the initial and the modified tag antenna structures is shown in Figs. 2 and 3 for comparison.

The meandered element is inductively coupled to the spiral loop feeding element to achieve matching to that of the attached Alien Higgs-4 microchip impedance [16]. The antenna is designed by etching using copper with thickness of 0.035 mm on RO

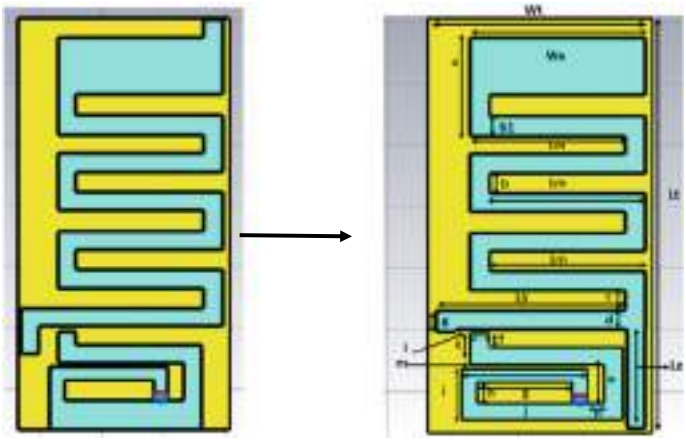

(a) (b)

Fig. 1 **a** Single-band and **b** modified dual-band tag antenna structure coupled to spiral loop

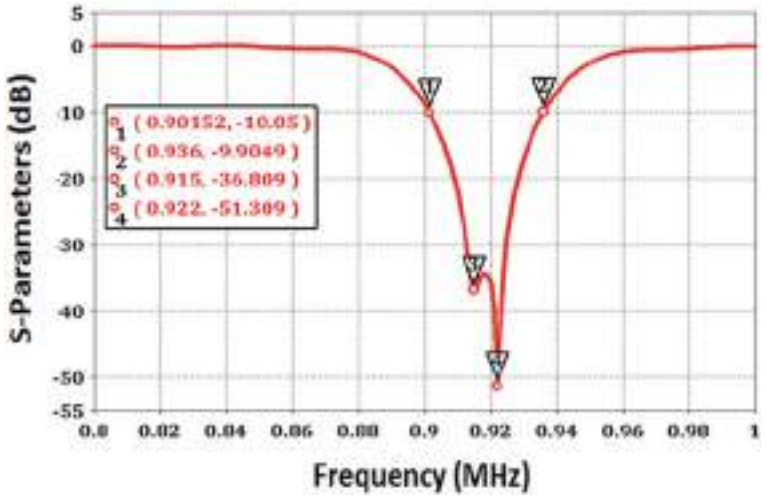

Fig. 2 S_{11} results of antenna designed in Fig. 1a

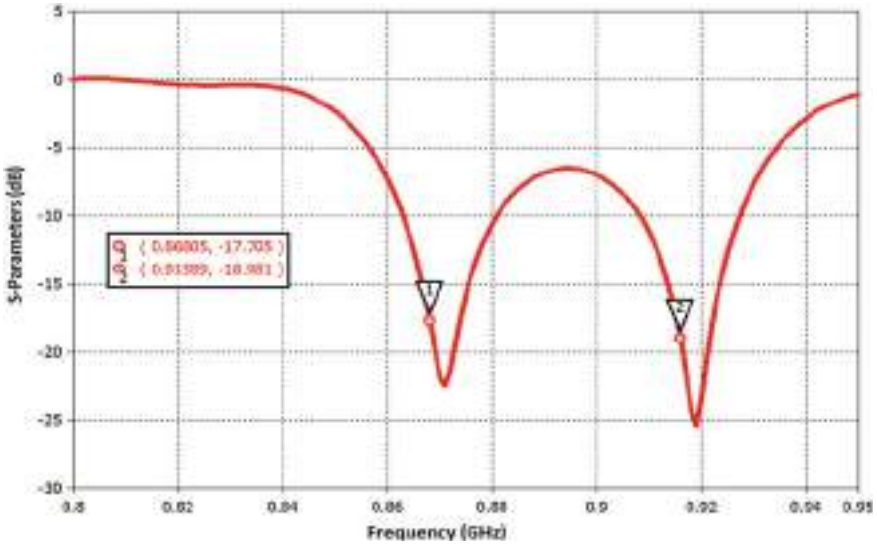

Fig. 3 S_{11} results of antenna designed in Fig. 1b

4350 B substrate with $\epsilon_r = 3.66$ and tan delta $= 0.004$. The design is designed and simulated in CST software v 2016. The employed chip Higgs-4 has a -18 dBm of power sensitivity (P_{ic}) and impedance of $20 - j\,181\ \Omega$ at 915 MHz (center frequency of North American band). The chip is integrated at the feeding port of the antenna. A narrow slit of 0.7 mm is kept for accommodating the chip. As observed in Fig. 2, the designed tag antenna exhibits resonance in North American band. Also, from Fig. 3,

Table 1 Geometrical parameters of optimized folded dipole integrated tag antenna

Parameters	a	c	e	g	i	k	m	L_h	W_t	Wa	L_m
Value (mm)	15.9	3.3	6.11	14.62	8.3	5.11	0.61	31.9	34.4	26.8	13.4
Parameters	b	d	f	h	j	l	n	L_e	L_t	b_1	
Value (mm)	3.3	3.15	2.11	3.3	19.46	0.65	2.5	15	67.12	3.3	

it has been seen that the modified tag resonates in European (866 MHz) and North American (915 MHz) UHF RFID regions.

It is important to note down that the additional lower stub is employed in such a way so that the available area of the antenna may be utilized and the size of the antenna does not increase. The optimized parameter values for the designed tag structure have been displayed in Table 1.

3 Parametric Analysis

The tag antenna's resonant frequency and its impedance have been tuned by optimizing spiral loop parameters, length of meandered element, and other antenna dimensions. The spiral loop being highly inductive and coupling it with the meandered line element compensates the capacitance of the employed chip. Also, any variations in the dimensions of spiral loop vary the enclosed loop area. This feature is highly beneficial in tuning the tag's impedance. The resistance is highly adjusted by optimizing the coupling gap amid the spiral loop and that of meandered radiating element [10]. Further, the dual-band operation at required resonant frequencies, the length "L_m", length "L_e", and length "L_h" have been tuned. The process of obtaing the optimized dimensions has been explained here by carrying out parametric analysis as given below.

3.1 Effect of Variation in the Length "L_m" of Meandered Line Element

The meandered element length is tuned from 13.3 to 13.6 mm. It is seen that optimum length "L_m" is found to be 13.4 mm at which both the resonant bands at required frequencies are obtained (Fig. 4).

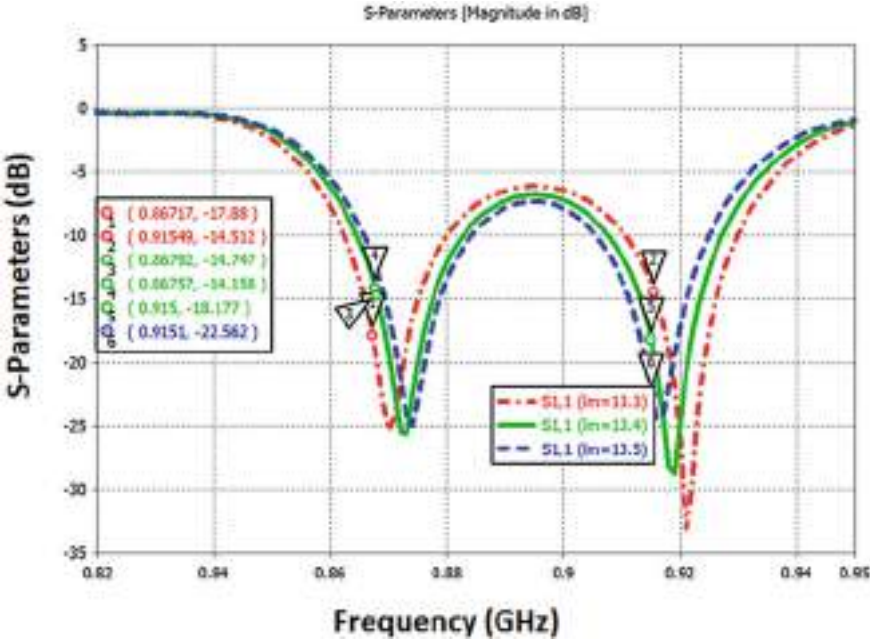

Fig. 4 S_{11} Results with respect to variation in "L_m"

3.2 *Effect of Variation in Length "L_e" of Additional Stub on the Dual-Band Resonance*

The lower stub length "L_e" of radiating element varied from 14 to 16 mm. It is seen from Fig. 5 that optimum length "L_m" is found to be 14 mm at which both the resonant bands are obtained (Fig. 5). The length "L_e" is responsible to optimize and tune the resonant frequency at the two resonant bands.

3.3 *Effect of Variation in Length "L_h" of Upper Coupling Arm on Resonant Frequency*

Further, by varying the length "L_h", it is observed that the lower band resonance is easily tuned and also impedance matching at upper band at 915 MHz is also affected. Finally, the optimum length of 31.9 mm is kept to achieve the best resonance at both the required bands (Fig. 6).

From the above discussion, it is concluded that the lower stub is responsible in obtaing the additional lower resonant band. Also, the upper stub with length L_h is mainly responsible in tuning the resonance frequency in the lower frequency range, i.e., 865–867 MHz (European UHF RFID bands (Fig. 6)).

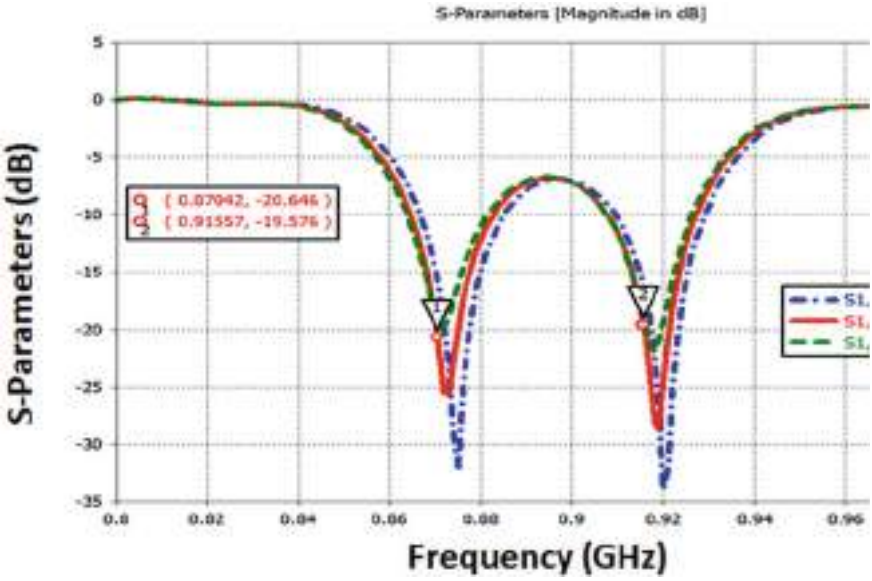

Fig. 5 S_{11} Results with respect to variation in "L_e"

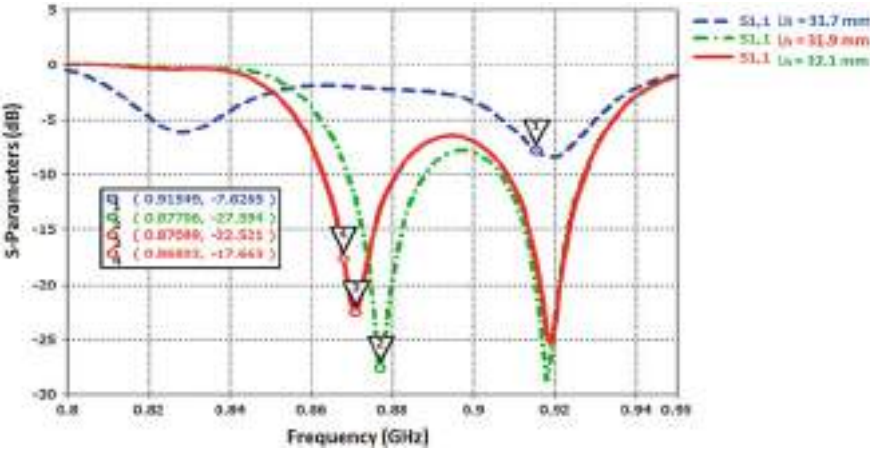

Fig. 6 S_{11} Results with respect to variation in "L_h"

4 Simulation Results

The simulated performance for the tag antenna proposed here is analyzed and its impedance, i.e., (resistance, reactance), radiation efficiency and realized gain results are discussed next.

4.1 Input Impedance

The power transfer coefficient (PTC) accounts the capability of the tag in transferring the power which is obtained from the reader to the RFID microchip [4] and is given as follows:

$$\mathrm{PTC} = 1 - |\Gamma|^2 = \frac{4 * Real\left(Z_{chip}\right) * Real(Z_{in})}{\left|Z_{chip} + Z_{in}\right|^2} \tag{1}$$

where Z_{in} = Rin + jXin and Z_{chip} = Rchip + jXchip are the input impedance and chip impedance at antenna's input feed terminal. For achieving the dual-band resonant tag antenna, it needs to exhibit conjugate impedance to that chip impedance in both the required resonant regions. The real (resistance) and imaginary (reactance) parts of impedance response of the designed tag antenna are plotted in Fig. 7a and b.

From the figure, it is observed that the impedances of 22.8 + j 186.5 Ω and 22.4 + j 173.97 Ω have been possessed by the designed tag compared to the impedance of chip, i.e., 21 − j 191 Ω and 20 − j 181 Ω at the 866 MHz and 915 MHz, respectively.

4.2 Radiation Characteristics

The performance of the tag designed here is also analyzed by plotting its radiation characteristics, i.e., efficiency and gain in Figs. 8 and 9, respectively. These parameters are significant in determining the read distance of tag. The efficiency of 91 and 95.3% are obtained at both the resonant bands. Also, the proposed tag possesses gain of 1.78 dB at 866 MHz (European UHF band) and 2.07 dB at 915 MHz (North American UHF RFID band), respectively.

4.3 Distribution of Surface Current

The surface current distribution is also studied to depict the designed tag antenna's radiation mechanism. It is observed from Figs. 10 and 11 that spiral loop has a significant role in exciting the radiating element at both the resonant frequencies. Further, the current is seen to be crowded on outer side of additional lower stub and hence significantly excited at lower frequency of 865 MHz. At 915 MHz, the current is strongly observed at the coupling area between loop and the inner side of the lower stub.

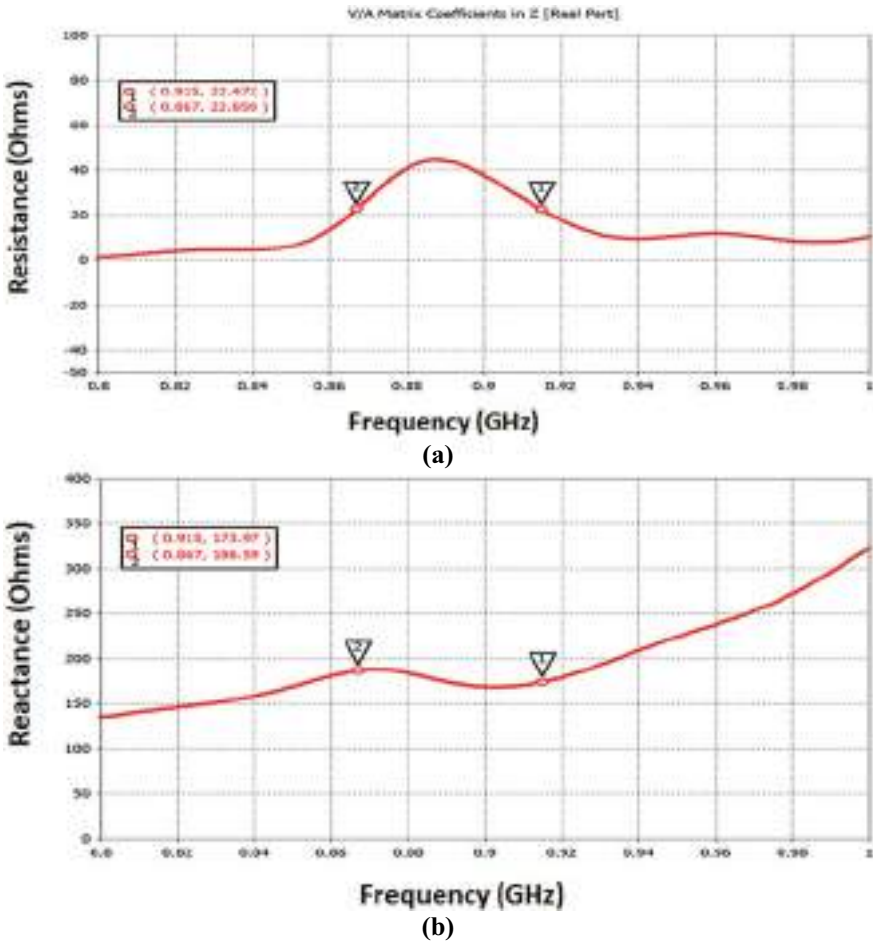

Fig. 7 Impedance response in terms of simulated **a** real and **b** imaginary parts of impedance of the designed tag antenna

4.4 Read Range Performance (Simulated and Measured)

The most significant parameter in accessing the performance of any RFID tag is analyzed by determining its read distance [4] expressed as

$$R_{max} = \frac{\lambda}{4\theta}\left(\frac{P_{EIRP}G_r\varphi}{P_{ic}}\right)^{1/2} = \frac{\lambda}{4\theta}\left(\frac{P_{EIRP}}{P_{tag}}\right)^{1/2} \quad (2)$$

The simulated measured read range at two required resonant bands is shown in Fig. 12 and is observed to be more than 18 m. The measurement setup to measure the

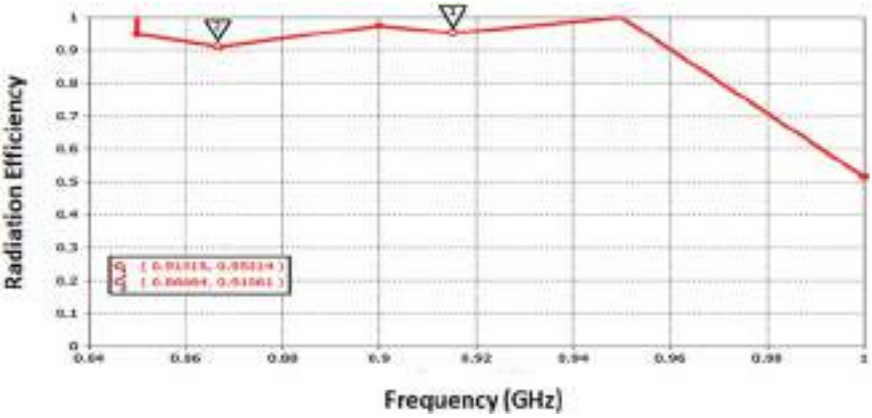

Fig. 8 Radiation efficiency performance

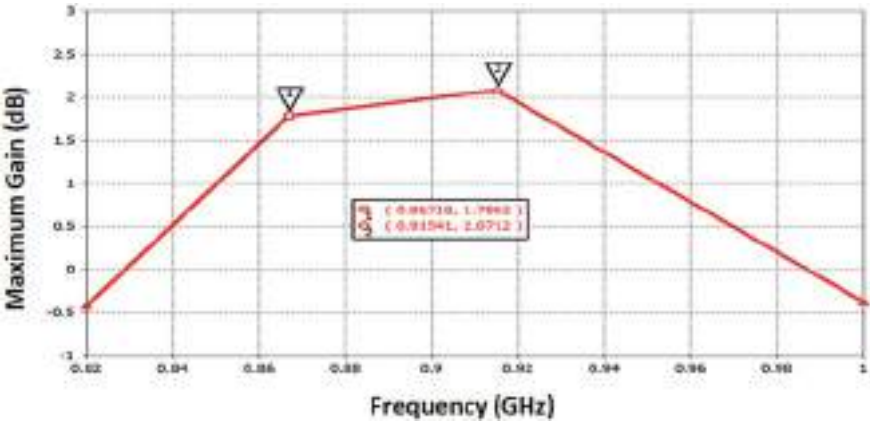

Fig. 9 Gain performance (dB)

read range comprises a Reader (Skytek Ltd.), Reader antenna (gain 9 dBi) and host computer. The read distance can be measured by moving the tag far from the reader till it is recognizable. The proposed tag is fabricated and the Higgs-4 chip is soldered at its feed terminals. The tag prototype is fabricated and is shown in Fig. 13. The measured read distance has been found to be 11.6 m (866 MHz) and 12.1 m (915 MHz) in free space. This deterioration of the read range is attributed to the propagation losses due to multipath propagation and different fabrication inaccuracies.

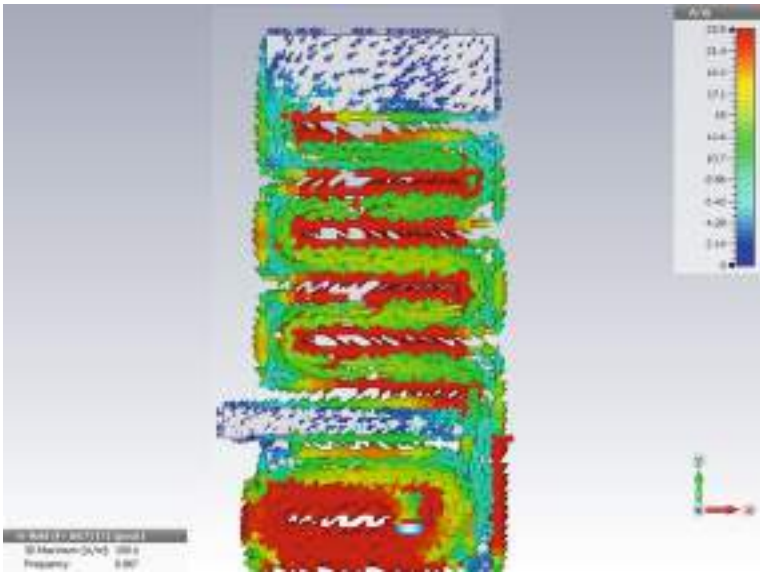

Fig. 10 Distribution of surface current at 866 MHz

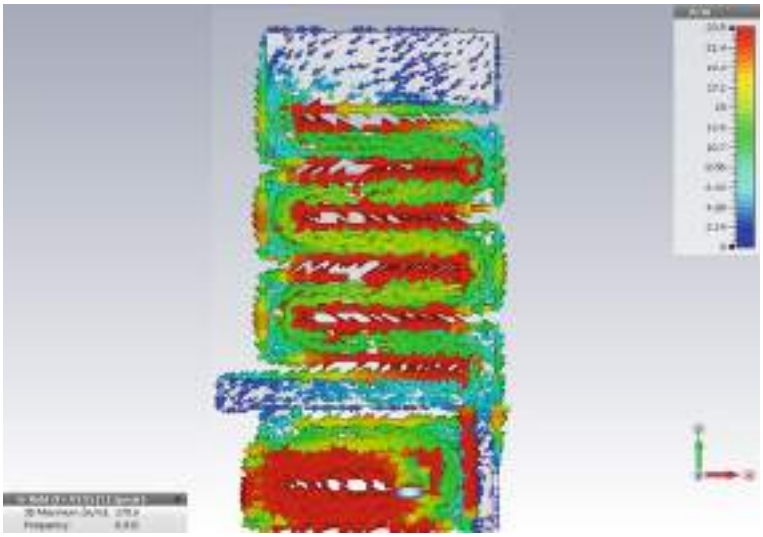

Fig. 11 Distribution of surface current at 915 MHz

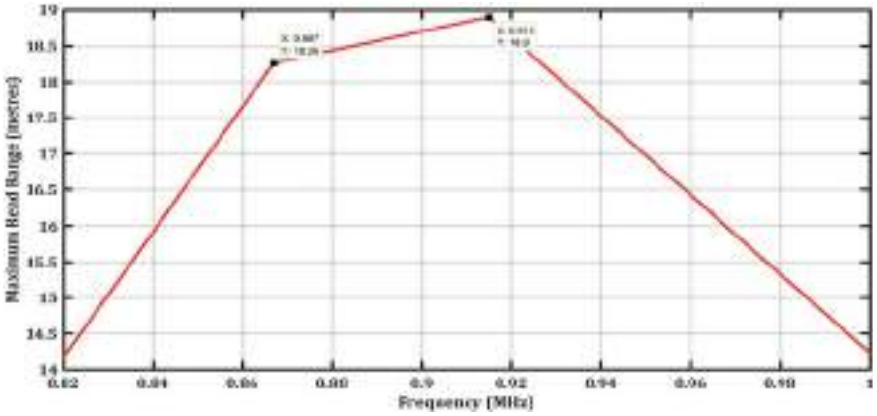

Fig. 12 Read range performance for the designed tag

Fig. 13 Prototype of the fabricated tag antenna (and soldered Higgs-4 chip)

5 Far-Field Radiation Patterns

The tag antenna's far-field radiation pattern plays important role in determining its orientation. The radiation patterns (2-D and 3-D) of the designed tag are shown in Fig. 14 corresponding to both the resonant frequencies of 866 MHz and 915 MHz, respectively.

From the figure, it has been seen that the proposed tag has bidirectional pattern (E-plane) and omnidirectional pattern (H-plane) at both the resonant frequencies, respectively.

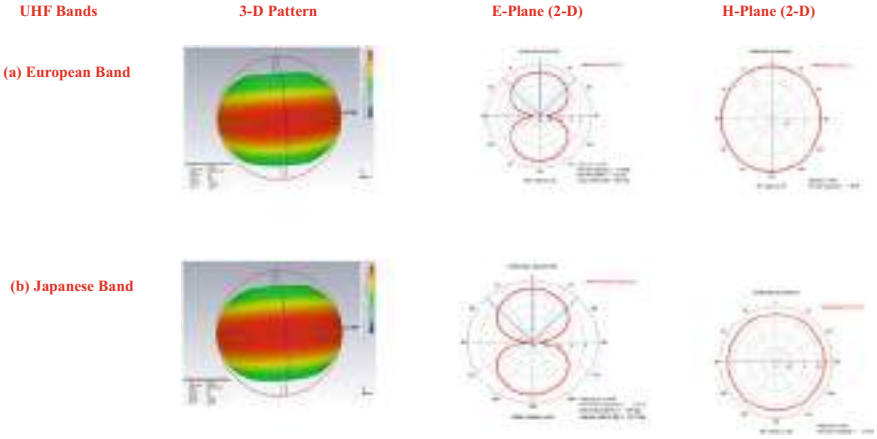

Fig. 14 Radiation patterns (2-D and 3-D) at **a** European **b** Japanese UHF bands for the designed tag

Table 2 compares the work reported here in this paper to that of other recently designed tags. As observed, the tags designed in [18, 19] exhibit dual band but have larger antenna size. Alternately, the designed dual-band tags proposed in [18, 19] also possess lower gain in comparison to the tag reported in this paper. Further, the gain of the tag reported in [20–23] is smaller. Also, the size of the tags proposed in [20, 22] is smaller but with a lower gain and single UHF operational band. Hence, considering these advantages, it has been deduced that the tag designed here is applicable to be

Table 2 Comparison table

S. no	Substrate thickness (mm)	Size of the tag (mm × mm)	Volumetric size (mm^3)	Gain (dB/dBi)	
				ETSI (European UHF band) (865–869 MHz)	FCC (North American UHF band) (902–928 MHz)
9	0.767	67 × 34.4	1736 mm^2	–	2.62 dBi
17	1.6	66 × 20	2112 mm^3	X	X
18	1.6	91 × 91	1,32,49 mm^3	−12 dB	−12.5 dB
19	1.6	128.3 × 50	10,240 mm^3	−7.4 dB	−1.09 dB
20	1.6	31 × 31	1537 mm^3	−11 dB	X
21	1.6	70 × 70	7840 mm^3	−9 dB	X
22	0.8	55 × 20	880 mm^3	X	−13 dB
23	3.2	58 × 26	4825 mm^3	−11 dBi	X
Proposed work	0.767	67 × 34.4	1736 mm^3	1.78 dB	2.07 dB

utilized for various applications such as supply chain, logistics, IoT-enabled network applications, biomonitoring applications, etc.

6 Conclusions

In this work, an RFID tag antenna with dual-band operation, i.e., operating in North American and European RFID bands is designed. The designed tag antenna possesses high radiation efficiency and high realized gain in both the resonating bands. Further, the tag antenna achieves a conjugate impedance matching by coupling the meandered line element to the inductive spiral loop. Also, the resonance at lower European band is achieved by adding a stub in the lower part of the meandered element. The radiation pattern is further analyzed to exhibit omnidirectional and bidirectional pattern in H-plane and E-plane, respectively. The designed tag in this paper is suitable to be employed in different tracking and monitoring applications such as in health monitoring, logistics, and IoT applications.

Acknowledgements The first author wants to thank the DST, Govt. of India for assisting her financially to carry out her research work under women Scientist Scheme (WOS-A) bearing reference no. (SR/WOS-A/ET-78/2018(G)).

References

1. K. Finkenzeller, RFID Handbook, 2003. *Fundamentals and Applications in Contactless Smart Cards and Identification*, 2nd ed (Wiley, Hoboken, NJ, 2003)
2. D.M. Dobkin, Introduction, in *The RF in RFID: UHF RFID in Practice*, 2nd edn (Elsevier, 2013)
3. A. Bansal, S. Sharma, R. Khanna, Linearly tapered meander line broadband monopole tag antenna with T-match for UHF-RFID applications. Int. J. RF Microw. Comput. Aided Eng. (2019)
4. A. Choudhary, D. Sood, C. C. Tripathi, Wideband long range, radiation efficient compact UHF RFID Tag. IEEE Antennas Wirel. Propag. Lett. 2–6 (2018)
5. A. Bansal, G. Sethi, S. Sharma, PSO optimized nested slot structure RFID tag antenna at 5.8 GHz for metallic applications, in *2018 2nd International Conference on Micro-Electronics and Telecommunication Engineering (ICMETE)*, Ghaziabad, India (2018) pp. 81–84
6. Morocco_Marrocco GPV, The art of UHF RFID antenna design: impedance matching and size-reduction techniques. Antennas Propag. Mag. **50**(1), 1–21 (2008)
7. R. Quiroz, T. Alves, B. Poussot, J.M. Laheurte, Combined RFID tag antenna for recipients containing liquids. IEEE Int. Conf. RFID-Technol. Appl. RFID-TA **49**(4), 101–106 (2012)
8. P.H. Yang, Y. Li, L. Jiang, W.C. Chew, T.T. Ye, Compact metallic RFID tag antennas with a loop-fed method. IEEE Trans. Antennas Propag. **59**(12), 4454–4462 (2011)
9. R. Quiroz, J.M. Laheurte, Metal mount RFID tag antenna excited by integrated loop/IC module. Electron. Lett. **49**(23), 1421–1423 (2013)
10. A. Bansal, S. Sharma, R. Khanna, Compact meandered RFID tag antenna with high read range for UHF band applications. Int. J. RF Microw. Comput. Eng. 1–12 (2018)

11. H. Son, C. Pyo, Design of RFID tag antennas using an inductively coupled feed. Electron. Lett. **41**(18), 3–4 (2005)
12. A.A. Babar, T. Björninen, V.A. Bhagavati, et al., Small and flexible metal mountable passive UHF RFID tag on high dielectric ceramic-polymer composite substrate. IEEE Antennas Wireless Propag. Lett. 1319–1323 (2012)
13. J.H. Lu, G.T. Zheng, Planar broadband tag antenna mounted on the metallic material for UHF RFID system. IEEE Antennas Wirel. Propag. Lett. **10**, 1405–1408 (2011)
14. H. Li, J. Zh, Y. Yu, Compact single-layer RFID tag antenna tolerant to background materials. IEEE Access. **5**, 21070–21079 (2017)
15. A. Bansal, S. Sharma, R. Khanna, Compact meandered folded-dipole RFID tag antenna for dual band operation in UHF range. Wireless Personal Commun. (2018)
16. Alien Technology, Higgs TM 4 IC datasheet. http://www.alientechnology.com/wpcontent/uploads/AlienTechnology-Higgs-4-ALC-360.pdf. (2014)
17. B. Barman, S. Bhaskar, A.K. Singh, Spiral resonator loaded S-shaped folded dipole dual band UHF RFID tag antenna. Microw. Opt. Technol. Lett. **61**(3), 720–726 (2019)
18. B. Barman, S. Bhaskar, A.K. Singh, Dual-band Uhf RFID tag antenna using two eccentric circular rings. Prog. Electromagn. Res. M. **71**, 127–136 (2018)
19. S. Bhaskar, A.K. Singh, A dual band dual antenna with read range enhancement for UHF RFID tags. Int. J. RF Microw. Comput. Eng. 1–8 (2019)
20. F.L. Bong, E.H. Lim, F.L. Lo, Compact folded dipole with embedded matching loop for universal tag applications. IEEE Trans. Antennas Propag. **65**(5), 2173–2181 (2017)
21. P. Kamalvand, G. Kumar Pandey, M. Kumar Meshram, A. Mallahzadeh, A single sided dual-antenna structure for UHF RFID tag applications. Int. J. RF Microw. Comput. Eng. **25**(7), 619–628 (2015)
22. Y.J. Zhang, D. Wang, M.S. Tong, An adjustable quarter-wavelength meandered dipole antenna with slotted ground for metallically and airily mounted RFID tag. IEEE Trans. Antennas Propag. **65**(6), 2890–2898 (2017)
23. J. Zhang, Y. Long, S. Member, Dual-layer broadband compact UHF RFID tag antenna for platform tolerant application. IEEE Trans. Antennas Propag. **61**(9), 4447–4455 (2013A)

Impact of Packet Retransmission on VoWiFi Cell Capacity Using Fifth-Generation WLAN

Ayes Chinmay and Hemanta Kumar Pati

Abstract The rapid increase in the deployment of Wireless Local Area Network (WLAN) particularly over the existing infrastructure is growing tremendously. Such an infrastructure-based WLAN, widely known as Wireless Fidelity (WiFi) network, needs to support voice service because, in general, it contributes a large portion of the traffic supporting personal communication. Voice over Internet Protocol (VoIP) over WiFi commonly known as VoWiFi can be used for providing voice services. In order to provide quality of service (QoS) to such voice calls, it is essential to establish a call admission control (CAC) policy. This policy requires VoWiFi cell capacity. In this paper, we have estimated the number of VoWiFi calls possible using the IEEE 802.11ac standard Access Point (AP). To estimate the cell capacity, we have used DCF Inter-frame Spacing (DIFS) to sense channel status before sending data and Short Inter-frame Spacing (SIFS) is used for acknowledgement, Request To Send (RTS), and Clear To Send (CTS) frames. We have estimated the VoWiFi cell capacity using different voice codecs like G.729 and G.723.1. We have used packet retransmission technique to avoid packet loss and Arbitration Inter-frame Space (AIFS) to enhance the VoWiFi cell capacity.

Keywords VoWiFi · DIFS · AIFS · Retransmission · Capacity analysis

1 Introduction

The use of cell phones is growing rapidly in recent years. This contributes to the demand for both WiFi and cellular networks. Although the availability of cell towers is enough for making voice calls, call drop (loss of calls) still occurs due to large buildings, trees etc. In many different places, such as basements of large buildings, medical offices, and showrooms, cellular networks are hard to get. In order to solve this problem, voice communication using WiFi AP or WLAN AP is going to be

A. Chinmay · H. K. Pati (✉)
Department of Computer Science and Engineering, International Institute of Information Technology Bhubaneswar, Bhubaneswar, Odisha 751003, India
e-mail: hemanta@iiit-bh.ac.in

S. Rawat et al. (eds.), *Proceedings of First International Conference on Computational Electronics for Wireless Communications*, Lecture Notes in Networks and Systems 329,
https://doi.org/10.1007/978-981-16-6246-1_7

introduced in the future. This can enhance the wireless coverage to support customers for communication. To satisfy these specifications over WiFi, IEEE 802.11 WLAN Working Group has released a standard called IEEE 802.11ac which is regarded as very high-throughput WiFi. Therefore, we have developed an analytical model to estimate how many voice call users would be feasible. The main contributions of this paper are given in the following.

- We derive an analytical model to estimate VoWiFi cell capacity using IEEE 802.11ac (i.e., fifth-generation WLAN) standard AP.
- To increase the number of voice calls, we have used the Compressed RTP (cRTP) in our derived model.
- We have used the retransmission technique in our derived model to prevent the loss of voice packet.
- Finally, we have compared the results using AIFS and DIFS.

The rest of this paper is organized as follows. Section 2 describes related work. Section 3 describes the model to estimate physical data rate of WLAN AP using IEEE 802.11ac standard. In Sect. 4, we propose the model to estimate the capacity for VoWiFi traffic. In Sect. 5, we present results using the IEEE 802.11ac standard. Finally, in Sect. 6, we conclude this paper.

2 Related Work

Capacity analysis focusing on throughput has been studied for WLAN. These estimates do not address delay, loss, and layer overhead requirements for the voice application. However, QoS provisioning to existing VoWiFi connections require user-based capacity estimation. We have done extensive research to find the existing analytical models estimating VoIP user capacity of IEEE 802.11a/b/g/n WLAN standards. The work reported in [1] presents an experimental study of VoIP user capacity in an IEEE 802.11b standard wireless AP. It concluded that the backoff delay and the inherent access fairness in IEEE 802.11b limit the voice capacity to less than 10 by the help of G.711 codec. In [2], considering IEEE 802.11a/b/g standards in infrastructure mode, it is found that voice capacity strongly depends on the codec packetization interval, channel bandwidth, the packet size used by data, and data traffic. Further, it is found that the capacity depends on the RTS-CTS and CTS-to-self- procedures, with the RTS-CTS procedure achieving lower capacity by considering the IEEE 802.11b standard. The upper bound on the voice capacity of IEEE 802.11b is found in [3] considering both the G.711 and G.729 voice encoding schemes. Further, the work reported in [4] considered IEEE 802.11a/b/g WLAN Medium Access Control (MAC) protocols to check the voice capacity in Constant Bit Rate (CBR) and Variable Bit Rate (VBR) traffics. The work reported in [5] prioritized an AP by reducing the contention window (CW) size and duration of DIFS to improve the capacity of an IEEE 802.11b standard AP. This work could increase the cell capacity to 12 stations instead of 10. In [6], the VoIP architecture over WLAN is investigated under

the limiting capacity of such systems when operating in the distributed coordination function (DCF) or enhanced distributed channel access function (EDCAF) mode as specified in the IEEE 802.11b/e standards. They have found that without any optimization techniques legacy IEEE 802.11b APs can handle approximately 13 cellular-quality voice calls. In [7], a mechanism is proposed by allowing the AP to use scheduling in the uplink and packet aggregation in the downlink to enhance the throughput. It achieved an improvement of 300% in VoIP capacity over the baseline model. The work reported in [8] proposed an enhancement to the legacy IEEE 802.11 MAC protocol that mitigates the AP bottleneck effect and boosts the VoIP transmission capacity. They found that the Voice Over WLAN (VoWLAN) capacity is increased by 20%. In [9], an analytical model is introduced to analyze the performance of AIFS and contention window in a WLAN with contention-based channel access. They found that the AIFS has a significantly stronger impact on WLAN voice capacity in the ad hoc mode in comparison to that of the infrastructure mode. In [10], a metamodel is proposed using formal empirical modeling technique to obtain the tighter bound on VoWiFi cell capacity. Through this model, it is revealed that 4 VoIP users is the upper bound to IEEE 802.11b standard AP with G.711 voice codec. In [11], some factors such as transmission rate control, preamble size, packet generation offset among VoIP sources, physical data rate of acknowledgement frames, scanning APs, network buffer size at the AP, and retry limit are identified that directly affect the VoIP over WLAN cell capacity while conducting experiments and simulations. They have found that the IEEE 802.11b standard AP can accommodate up to 15 calls for 64 kb/s CBR VoIP traffic with a 20 ms frame interval using G.711 voice codec. The work reported in [12] improves the capacity by 14.3% of VoWLANs in Full Duplex (FD) communications. In [13], by considering two commonly used voice codecs G.729 and G.711 over IEEE 802.11b standard AP causes less packet loss, less delay, and better quality that results in an enhancement in VoIP capacity. From this above-discussed literature, we found that the VoWiFi cell capacity is not thoroughly studied considering the newer voice codecs like G.729 and G.723.1, all the possible layer overheads, and header compression generally used in such communication. Therefore, in this paper, we have formulated an analytical model to estimate VoWiFi cell capacity for IEEE 802.11ac standard which is the fifth-generation WLAN AP. We have also enhanced the VoWiFi cell capacity by considering AIFS. Further, we have used packet retransmission to prevent the loss of voice. Our proposed analytical models are described in the following sections.

3 IEEE 802.11ac System Bandwidth Estimation

Wireless speed has three factors: channel bandwidth, constellation density, and number of spatial streams. It can be estimated using the following expression:

$$D_{\mathrm{PHY}} = \frac{N_{\mathrm{SC}} \times N_{\mathrm{SS}} \times D_{\mathrm{TCR}} \times N_{\mathrm{BPSCS}}}{T_{\mathrm{OSD}} + T_{GI}} \tag{1}$$

Table 1 Parameters used in IEEE 802.11ac [14]

Parameters	Value
Channel spacing (Φ)	80 MHz
Total subcarriers ($\leq$)	256
Number of data subcarriers (N_{SC})	234
Number of bits per subcarrier in a stream (N_{BPSCS})	8
Number of spatial streams (N_{SS})	1–8

where D_{PHY} is physical data rate (in bps), N_{SC} is the number of data subcarriers, N_{SS} is the number of spatial streams, D_{TCR} is the turbo code rate used with modulation, N_{BPSCS} is the bits per subcarrier in a stream, T_{OSD} is the time duration per OFDM symbol transmission, and T_{GI} is the guard interval. Now, we can get the value of T_{OSD} using the following expression:

$$T_{OSD} = \frac{1}{\Psi} \tag{2}$$

where Ψ denotes carrier spacing. It can be obtained using the following expression:

$$\Psi = \frac{\Phi}{\leq} \tag{3}$$

where Φ and $\leq$ denote channel bandwidth and total number of subcarriers, respectively. Using Table 1, we can calculate the data rate of IEEE 802.11ac by using the above equations. $\Psi = \frac{80}{256} = 0.3125\text{MHz} * 312.5\text{kHz}$. $T_{OSD} = \frac{1}{312.5\text{kHz}} = 3.2\mu\text{s}$. For example, the physical layer speed of IEEE 802.11ac with 80 MHz channel bandwidth using 256-QAM with four spatial streams and a short guard interval (i.e., 0.4 μs) is $\frac{234\times4\times\frac{5}{6}\times8}{3.2+0.4} = 1733.33\text{Mbps}$.

4 VoWiFi Cell Capacity Analysis

Initially, we found the VoWiFi cell capacity considering the basic Carrier Sense Multiple Access with Collision Avoidance (CSMA/CA). Subsequently, we have found the VoWiFi cell capacity considering the RTS/CTS extensions. Further, we have used the retransmission technique in our derived model to prevent the loss of voice packets.

4.1 VoWiFi Cell Capacity Considering Basic CSMA/CA

The time required to transmit a packet of any size denoted by (i.e., Time) utilizing the maximum bandwidth of IEEE 802.11 can be expressed as given below:

$$Time = \begin{cases} Size \times \frac{8}{D_{PHY}}, & Size\ in\ Bytes \\ Size \times \frac{1}{D_{PHY}}, & Size\ in\ bits \end{cases} \tag{4}$$

Now, we can find the time required to transmit the raw voice packet denoted by T_P using the following expression:

$$T_P = C^B \times C^{\mathrm{FI}} \times \frac{1}{D_{\mathrm{PHY}}} \tag{5}$$

where C^B is the voice codec bit rate in bps and C^{FI} is the codec frame interval. Similarly, we can find the time for transmission of the acknowledgement frame as given in the following expression:

$$T_{\mathrm{ACK}} = \frac{ACK^{\mathrm{Size}}}{D_{\mathrm{PHY}}} + T_{\mathrm{PHY}} \tag{6}$$

where T_{ACK} is the total time taken by the acknowledgement frame, $\mathrm{AC}K^{\mathrm{Size}}$ is the size of the acknowledgement frame in bits, and T_{PHY} is the time taken for the physical header. Now, the total time taken by the Arbitration Inter-frame Spacing (AIFS), DCF Inter-frame Space (DIFS), and Short Inter-frame Space (SIFS) denoted by T_{IFS} are given in the following expression:

$$T_{IFS} = \begin{cases} DIFS + SIFS, & DIFS\ is\ used \\ AIFS + SIFS, & AIFS\ is\ used \end{cases} \tag{7}$$

Further, the total time for all the headers denoted by T_L is given in the following expression:

$$T_L = \begin{cases} T_{RTP} + T_{UDP} + T_{IP} + T_{MAC} + T_{PHY}, & Uncompressed \\ T_{cRTP} + T_{MAC} + T_{PHY}, & Compressed \end{cases} \tag{8}$$

where T_{RTP} is the time taken for RTP header, T_{UDP} is the time for UDP header, T_{IP} is the time for IP header, T_{MAC} is the time for MAC frame header, and T_{cRTP} is the time for compressed header when cRTP is used. Now, time for a successful transmission denoted by T_{success} is given in the following expression:

$$T_{\text{success}} = T_P + T_L + T_{\text{ACK}} + T_{\text{IFS}} + \left(T_S \times \frac{CW_{\min}}{2} \right) \tag{9}$$

where T_S is slot time and $CW_{\min}$ is contention window size. Here, the contention window size is defined as the best effort contention window (i.e., CWmin = aCWmin) [14]. Now, we can find the total number of VoWiFi calls the WLAN AP simultaneously accommodates denoted by N_{CALL} using the following expression:

$$N_{\text{CALL}} = * \frac{C^{\text{FI}}}{2 \times T_{\text{success}}} \rfloor \tag{10}$$

Now, we can rewrite Eq. (10) by using the expressions for T_P and T_{success} from Eqs. (5) and (9), respectively, as given in the following:

$$N_{\text{CALL}} = \left\lfloor \frac{C^{FI}}{2 \times \left(\frac{C^B \times C^{\text{FI}}}{D_{\text{PHY}}} + T_L + T_{\text{ACK}} + T_{\text{IFS}} + T_S \times \frac{\text{CW}_{\min}}{2} \right)} \right\rfloor \tag{11}$$

4.2 VoWiFi Cell Capacity Considering Basic CSMA/CA with RTS/CTS Extensions

The time taken for successful packet transmission considering RTS and CTS packets can be obtained by using the following expression:

$$T_{\text{success(RC)}} = T_{\text{RTS}} + T_{\text{CTS}} + 2 \times \text{SIFS} + T_{\text{success}} \tag{12}$$

where $T_{\text{success(RC)}}$ is the time to transmit a packet successfully including RTS and CTS frames, T_{RTS} is the time required to transmit the RTS frame, and T_{CTS} is the time required to transmit the CTS frame. We can find the time required for transmission of the RTS frame by using the following expression:

$$T_{\text{RTS}} = \frac{\text{RTS}^{\text{Size}}}{D_{\text{PHY}}} + T_{\text{PHY}} \tag{13}$$

where RTS^{Size} is the size of the RTS frame in bits. Similarly, we can find the time required for transmission of the CTS frame by using the following expression:

$$T_{\text{CTS}} = \frac{\text{CTS}^{\text{Size}}}{D_{\text{PHY}}} + T_{\text{PHY}} \tag{14}$$

where CTS^{Size} is the size of the CTS frame in bits. Now, the number of VoWiFi calls the WLAN AP simultaneously accommodates considering the RTS and CTS frames denoted by $N_{\text{CALL}(RC)}$ can be found using the following expression:

$$N_{\text{CALL(RC)}} = *\frac{C^{\text{FI}}}{2 \times T_{\text{success(RC)}}}\rfloor \tag{15}$$

Now, we can rewrite Eq. (15) by using the expressions for T_P, T_{success} and $T_{\text{success(RC)}}$ from Eqs. (5), (9), and (12), respectively, as given in the following:

$$N_{\text{CALL(RC)}} = \left\lfloor \frac{C^{\text{FI}}}{2 \times \left(T_{\text{RTS}} + T_{\text{CTS}} + 2 \times \text{SIFS} + \frac{C^B \times C^{\text{FI}}}{D_{\text{PHY}}} + T_L + T_{\text{ACK}} + T_{\text{IFS}} + T_S \times \frac{CW_{\min}}{2} \right)} \right\rfloor \tag{16}$$

4.3 Effect of Packet Retransmission on VoWiFi Cell Capacity

The average contention window time is a more accurate representation of the real scenario. We have considered the average contention window time for VoWiFi cell capacity estimation. The VoWiFi cell capacity considering packet retransmission denoted as $N_{\text{CALL\_RT}}$ can be found using the following expression:

$$N_{\text{CALL\_RT}} = *\frac{C^{\text{FI}}}{2 \times \left((n+1) \times \Upsilon + \left(T_S \times \frac{\text{CW}_{\min}}{2}\right) \times \left(2^{n+1} - 1\right)\right)}\rfloor \tag{17}$$

where $\Upsilon = T_P + T_L + T_{\text{ACK}} + T_{\text{IFS}}$ and n is the number of retransmissions per packet. Now, the VoWiFi cell capacity by considering the RTS and CTS packets for CBR traffic allowing packet retransmission denoted as $N_{\text{CALL\_RT\_RC}}$ can be found using the following expression:

$$N_{\text{CALL\_RT\_RC}} = *\frac{C^{\text{FI}}}{2 \times \left((n+1) \times \Upsilon_{\text{RC}} + \left(T_S \times \frac{\text{CW}_{\min}}{2}\right) \times \left(2^{n+1} - 1\right)\right)}\rfloor \tag{18}$$

where $\Upsilon_{\text{RC}} = T_P + T_L + T_{\text{ACK}} + T_{\text{IFS}} + T_{\text{RTS}} + T_{\text{CTS}} + 2 \times SIFS$. Here, the time-out time for receiving the ACK or NACK is approximated with T_{ACK}.

Table 2 Parameters used

Parameters	Size	Time
D_{PHY}	1733.33 Mbps or 1.733 Gbps	–
T_{RTP}	12 Bytes	0.05538 μs
T_{UDP}	8 Bytes	0.03692 μs
T_{IP}	20 Bytes	0.09237 μs
T_{cRTP}	2 Bytes	0.00923 μs
T_{MAC}	40 Bytes	0.18461 μs
T_{PHY}	–	40 μs
T_{ACK}	14 Bytes	40.0646 μs
T_S	–	9 μs
SIFS	–	16 μs
AIFS	–	25 μs
DIFS	–	34 μs
CW_{min}	15	–
C^B	8 kbps (G.729)	–
T_P	10 Bytes (in 10 ms)	0.04615 μs
T_{RTS}	20 Bytes	40.0923 μs
T_{CTS}	14 Bytes	40.0646 μs

5 Numerical Results

The parameters of IEEE 802.11ac we have used to estimate the VoWiFi cell capacity are summarized in Table 2. Results obtained considering G.723.1 and G.729 voice codecs are presented in Fig. 1. It is observed that these two codecs are giving almost similar results. However, the MOS of G.729 is better in comparison to G.723.1 as given in Table 1 of [15]. So, we considered the G.729 voice codec with a frame interval of 20 ms to make VoWiFi cell capacity comparison among IEEE 802.11b/g/n/ac standard APs. In Fig. 2, we have shown the number of voice calls possible with and without RTS/CTS frames considering AIFS and DIFS in IEEE 802.11b/g/n/ac standard APs using G.729 voice codec. In Fig. 3, we have shown the effect of packet retransmission on VoWiFi cell capacity for IEEE 802.11ac.

6 Conclusion

In this paper, we have formulated an analytical model to estimate the VoWiFi cell capacity. Using our analytical model, we have found the results obtained for IEEE 802.11ac standard and compared it with some of the earlier WLAN standards like IEEE 802.11b/g/n. From the results presented using Fig. 2, we have observed that the number of VoWiFi calls in IEEE 802.11ac using AIFS is showing 4.76% gain

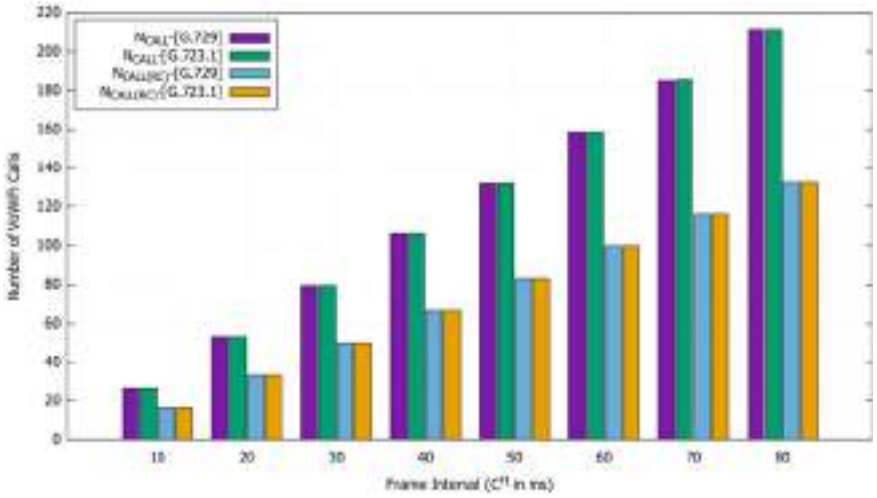

Fig. 1 VoWiFi cell capacity in IEEE 802.11ac

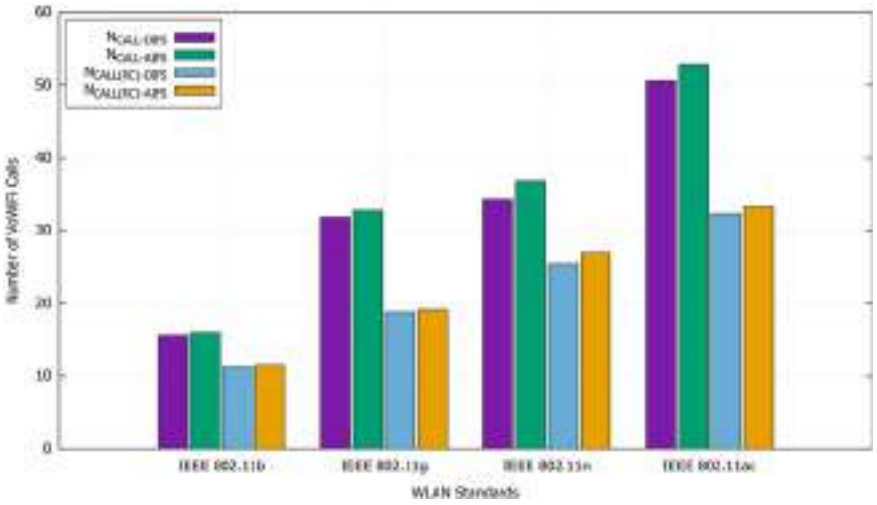

Fig. 2 VoWiFi cell capacity in IEEE 802.11b/g/n/ac using G.729 voice codec

compared to DIFS without considering RTS and CTS. Similarly, from Fig. 2, we have observed that using RTS and CTS with AIFS in IEEE 802.11ac is showing 2.98% gain w.r.t. DIFS. From the results presented in Fig. 2, considering the G.729 voice codec with a frame interval of 20 ms, we have observed that IEEE 802.11ac is showing 230.90% gain w.r.t. IEEE 802.11b, 61.71% gain w.r.t. IEEE 802.11g and 43.776% gain w.r.t. IEEE 802.11n without using RTS and CTS. Further, from Fig. 2, we found that IEEE 802.11ac is showing 186.25% gain w.r.t. IEEE 802.11b,

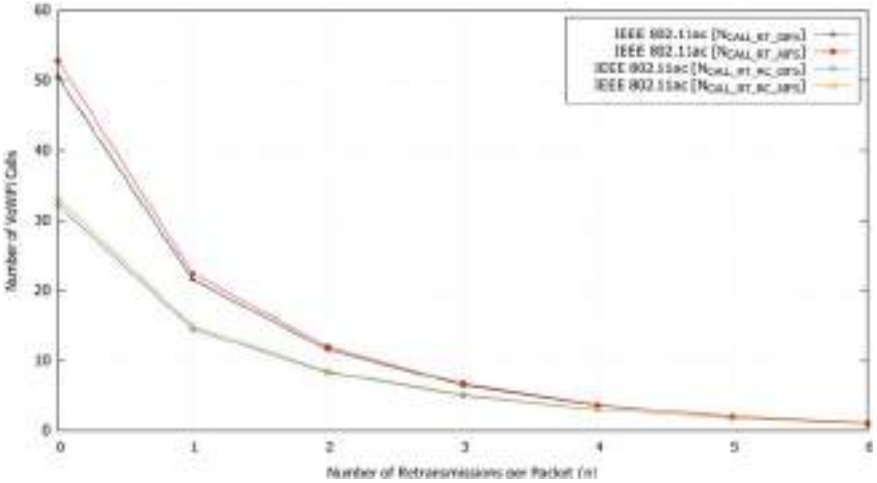

Fig. 3 VoWiFi cell capacity in IEEE 802.11ac using DIFS and AIFS under collision

73.56% gain w.r.t. IEEE 802.11g, and 23.58% gain w.r.t. IEEE 802.11n while using RTS and CTS. This indicates that the IEEE 802.11ac standard has the potential to support much higher VoWiFi cell capacity in comparison to other earlier WLAN standards. Further, from the results presented in Fig. 3 we have observed that IEEE 802.11ac without considering RTS and CTS using AIFS supports higher number of users allowing retransmission compared to DIFS. Similarly, from Fig. 3, we have observed that in IEEE 802.11ac considering RTS and CTS using AIFS supports higher number of users allowing retransmission compared to DIFS.

References

1. M. Elaoud, P. Agrawal, Voice capacity in IEEE 802.11 networks, in *IEEE International Symposium on Personal, Indoor and Mobile Radio Communications* (Barcelona, Spain, 2004) pp. 78–82
2. K. Medepalli, P. Gopalakrishnan, D. Famolari, T. Kodama, Voice capacity of IEEE 802.11b, 802.11a and 802.11g wireless LANs, in *IEEE Global Telecommunications Conference* (Dallas, TX, USA, 2004) pp.1549–1553
3. D.P. Hole, F.A. Tobagi, Capacity of an IEEE 802.11b wireless LAN supporting VoIP, in *IEEE International Conference on Communications* (Paris, France, 2004) pp. 196–201
4. W. Wang, S.C. Liew, V.O.K. Li, Solutions to performance problems in VoIP over a 802.11 wireless LAN. IEEE Trans. Vehicular Technol. **54**(1), 366–384 (2005)
5. D. Hashmi, P.V. Kiran, B. Lall, Access point priority based capacity enhancement scheme for VoIP over WLAN, in *IEEE India Conference* (New Delhi, India, 2006)
6. S. Abraham, P.M. Feder, M.C. Recchione, H. Zhang, The capacity of VoIP over 802.11. Bell Labs Tech. J. **11**(4), 253–271 (2007)
7. M. Chhawchharia, A. Guchhait, High capacity VoIP services in 802.11 networks, in *International Symposium on Wireless Pervasive Computing* (San Juan, PR, USA, 2007), pp. 321–326

8. Y. Lu, S. Zhu, X. Lin, Enhanced MAC protocol for voice communication in IEEE 802.11 WLAN, in *International Conference on Digital Telecommunications* (San Jose, CA, USA, 2007)
9. X. Ling, Y. Cheng, X. Shen, J.W. Mark, Voice capacity analysis of WLANs with channel access prioritizing mechanisms. IEEE Commun. Mag. **46**(1), 82–89 (2008)
10. J. Hui, M. Devetsikiotis, The use of metamodeling for VoIP over WiFi capacity evaluation. IEEE Trans. Wireless Commun. **7**(1), 1–5 (2008)
11. S. Shin, H. Schulzrinne, Measurement and Analysis of the VoIP Capacity in IEEE 802.11 WLAN. IEEE Trans. Mobile Comput.**8**(9), 1265–1279 (2009)
12. W. Kim, T. Song, T. Kim, H. Park, S. Pack, VoIP capacity analysis in full duplex WLANs. IEEE Trans. Veh. Technol. **66**(12), 11419–11424 (2017)
13. H. Kazemitabar, A.M. Said, Capacity analysis of G.711 and G.729 codec for VoIP over 802.11b WLANs. Commun. Comput. Inform. Sci. **253**, 519–529 (2011)
14. IEEE, Wireless LAN medium access control (MAC) and physical layer (PHY) specifications. IEEE Std. **802**(11–2016), 1–3532 (2016)
15. ITU, Application guide for objective quality measurement based on recommendations P.862, P.862.1 and P.862.2. *ITU-T Recommendation P.862.3* (2007), pp. 1–26.

Efficient Channel Estimation in mm Wave Massive MIMO Using Hybrid Beamforming

Neha, Naresh Kumar, and Aarti Kochhar

Abstract Beamforming with MIMO (Multiple-Input Multiple-Output) system is only solution to maximize high data rate and extended cell coverage with satisfying quality of Service (QoS) for fifth generation (5G) cellular networks. In hybrid millimeter-wave (mmWave) massive MIMO systems, estimation of information about Channel State is difficult due to the large channel and small number of RF chains. The present paper accomplishes millimeter-wave-based massive MIMO for hybrid beamforming based on Sparse Estimation. The proposed iterative hybrid algorithms accomplish the low rank and beamforming sparsity properties in massive MIMO to gain full data recovery with minimal error for small time duration. The proposed work model is an mmWave-based beamforming system with imperfect channel state information (CSI) to minimize channel estimation errors. Experimental section highlights the efficiency of our proposed method over traditional methods for the sake of simulation with accounting its improved temporal efficiency, fast convergence, and tolerance to abnormality channel information.

Keywords Beamforming · 5G · MIMO · Hybrid beamforming

1 Introduction

Frequency resource shortage problem in wireless communication can be unraveled using Millimeter wave communications. Wireless communication requires large bandwidth for 5G; thus, millimeter Wave waveband satisfy highly demanding data rate requirements for 5G and beyond, broadband wireless networks [1]. MIMO system with mmWave communications is fulfilling the goal of high-speed data communication with greater than 1 GB per user in urban areas also, hence mmWave-based MIMO system becomes milestone in the development of 5G wireless system.

Neha (✉) · N. Kumar · A. Kochhar
University Institute of Engineering & Technology (UIET), Panjab University, Chandigarh, India

A. Kochhar
Punjab Remote Sensing Centre, Ludhiana, India

S. Rawat et al. (eds.), *Proceedings of First International Conference on Computational Electronics for Wireless Communications*, Lecture Notes in Networks and Systems 329,
https://doi.org/10.1007/978-981-16-6246-1_8

Sufficient antenna array gain with MIMO will resolve the significant transmission losses of mm Wavesignal [2].

However, for large antenna array gain, the development of beamforming matrix uses mmWave radio frequency (RF) chains which is costly. Digital beamformer requires the use of an antenna part inside an RF chain which increases energy consumption and equipment costs, hence such type of traditional digital beamformer requires large implementation and maintenance cost. Recently, to fulfill the higher data rate requirements, the 5G New Radio technology [1] may help Composite Beam Forming [3] for a maximum of four spatial sources for wireless transmission. These innovations exploit digital as well as analog signal processing to empower an enormous number of radio wave components to be associated with a small number of RF chains. Thus, minimizing the total implementation and maintenance cost.

In mm Wave massive MIMO frameworks, CSI is required for improvement in Data rate. For all intents and purposes, it appears to be difficult due to high channel inconsistency and enormous numbers of transceiver antenna elements [4]. In most of the available literature, Channel State Information estimation is formulated as an issue having solution in compressive sensing [5], where the Orthogonal Matching Pursuit framework [6] is used to estimate transmitted Data with maximum likelihood. However, the efficiency with which these channel estimation strategies work is satisfactory practically. Large array antenna gains are needed at both uplink and downlink side to minimize the extreme isotropic path loss caused by mmWave frequencies. But mmWave frequencies require little carrier wavelength which make it feasible for large antenna arrays to exhibit in a little structure, with the end goal of beamforming providing a significant increase in antenna gain.Implementation of quick and precise mmWave steerable beamforming is not an easy approach. One major issue is that the Traditional digital transceiver architecture having antenna element equipped with one RF chain is troublesome due to implementation cost, power utilization and dissemination Analog-to-digital and digital-to-analog converters, up-down conversion mixers, filters, power amplifiers, with low-noise amplifiers are all part of an RF chain. The fundamental issue in mmWave transceiver architecture is to keep the number of RF chains much lower than the number of antenna array components. Consequently, hybrid digital (HD) beamforming model, the concatenation of digital and analog beamforming has been widely considered. The main purpose of HD beamforming would be to improve the multi-user system throughput while minimizing cost of hardware, complexity, including power performance.

2 Literature Review

Elbir et al. [7] studied Machine learning for hybrid beamforming using centralized machine learning (CML) techniques and presented a united learning-based structure for hybrid beamforming, where gathering the gradients from the users at BS model training is accomplished. Song et al. [8] investigate the performance of two common

designs that might be regarded as exceptional examples, namely, the totally associated and the one-stream-per-subarray structures. The method Song et al. [9] have proposed comprises a strong and highly adjustable artificial learning system that uses low-rank channel recuperation for an array-based massive MIMO framework. The system contains a standard feature extraction module as well as an adaptive recuperation module. Huang et al. [10] proposed an extraordinary learning machine system to mutually improve transmitting and receiving beamformers. This structure is fundamentally expanding the heartiness of beamformers.

To provide the telecommunications industry with an edge, Salh et al. [11] assess and work to increase the energy efficiency and to increase the unpredictability of hybrid-precoding algorithms to benefit the lowering of the number of radio frequency chains within the base station. It also incorporates high-resolution phase shifters specifically for the downlink multi-user mmwave architecture. Kaushik et al. [12] proposed novel design with a structure that progressively actuates the ideal number of radio frequency chains used to execute hybrid beamforming in a millimeter-wave MIMO framework. Chen et al. [13] explore the consolidated effects of quantized phase shifters, channel non-correspondence, and channel estimation errors on the spectral efficiency of a hybrid beamforming MIMO framework working in time-division duplex (TDD) mode.

There are two difficulties in acknowledging hybrid beamforming, and present potential arrangements can handle these difficulties.

(1) Low-Complexity Precoder and Combiner Designs:

The fundamental problem for analog beamformers originates from the low-resolution phase requirements. The ideal exhaustive search algorithm has exponential intricacy in the number of antenna element and is unquestionably illogical for practical implementation.

(2) Channel Estimation with Hybrid Beamforming:

The hybrid precoder and combiner configuration requires full information on channel state, which is hard to be gotten in mmWave MIMO frameworks since the channel is interlaced with analog beamformers and the baseband has no immediate access to the channel matrix. Because of the particular meager quality of mm Wave channels in the angle domain, compressed sensing-based methodologies are regularly utilized to execute productive channel estimation by investigating the channel sparsity in mmWave framework.

3 Methodology

Problem

The following are some insights from the discussion: Array were represented by lowercase characters and matrix using uppercase. The Hermitian, complex conjugate

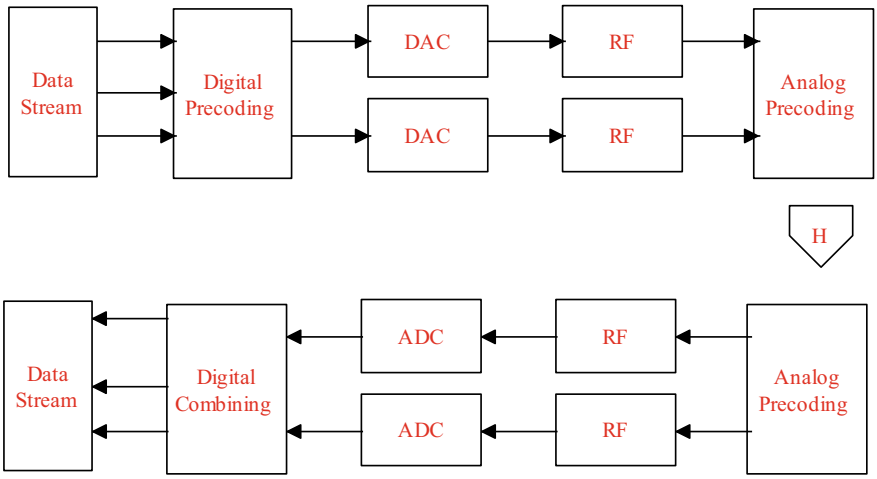

Fig. 1 Architecture of hybrid beamforming for mmWave multi-user massive MIMO system

form, and the matrix transpose, are noted by (•) H, (.)*, (•) T separately; N × N is Identity matrix indicated by N. Re, Im denote real and imaginary parts of the data.

However, MIMO frameworks with transmitting Antenna M and receiving antennas N and N > M is shown in Fig. 1. For discovery, Encoder ought to be known to receiver. Let us expect the channel to be quasi-static Rayleigh channel of order N × M complex channel framework indicated by H. Denoting the complex got information by Y. AWGN (Additive White Gaussian Noise) is introduced by C, having zero mean and one variance with some noise power. On the off chance that encoder produces nsb symbol and span of it is lns, at that point utilizing nsb symbol it makes block matrix of and this can be composed as [13].

$$B_d(S) = \sum_{k=1}^{n} (\mathrm{A}_k R_e(S_k) + A_{k+n} I_m(S_k)) \tag{1}$$

The following are the characteristics of energy regularization:

$$\delta = \mu \left[\left(\frac{B_d(s).B_d(s)'}{1_{ns}} \right) \right] \tag{2}$$

$$B(s) = \frac{B_d(s)}{\sqrt{\delta}} \tag{3}$$

The obtained frame function is given as follows by [14]

$$\mathbf{Y_i} = \mathbf{H}\mathrm{B(s)} + \mathbf{C_i} \tag{4}$$

Additive noise is indicated by term C. The objective is to make an approximation H from Yi. H would be modeled by [15]

$$H = \frac{1}{\sqrt{1_c}} * \mathrm{U} * V^{1/2} * W \tag{5}$$

Unitary matrix with full rank is indicated by W which have dimension of MXM.

Diagonal array has real values id indicated by v of dimension MXM. U is NXM matrix.

The significance of W must be defined in order to approximate the direction and retrieve the transmitted symbol. There is really no knowledge at the receiver's hand in a blindness sense. W could be evaluated through optimizing numerical autonomy by calculating its Kurtosis, defined by K [15].

$$\mathbf{w} = \left\{ \min \mathrm{J(W)} = \sum_{k=1}^{n} \mathrm{K} \left(\hat{S}_k^{(i)} \right) \right\} \ldots (6) \tag{6}$$

Subject to $\mathrm{WW^H} = \mathrm{I_{nt}}$. Cost function with real number is indicated by J(w). Gradient cost function J(w) is $M \times M$ matrix

$$\tau_{\mathrm{W}} = \frac{\mathrm{dJ(W)}}{\mathrm{dW^*}} \tag{7}$$

$$\frac{\mathrm{dJ(W)}}{\mathrm{dW^*}} = \left(\frac{\mathrm{dJ(W)}}{2\mathrm{dR_e(W)}} + \frac{\mathrm{dJ(W)}}{2\mathrm{dI_m(W)}} \right) \tag{8}$$

Now, model the descent gradient [15]

$$Z = -\tau_W \tag{9}$$

$$W_g = W + Z\mu \tag{10}$$

Where $\mu = 1$

$$W_{new} = Wg * \left(W_g^H * W_g \right)^{-\frac{1}{2}} \tag{11}$$

The recommended methodology combines a primal–dual interior point methodology with a unique preconditioned to provide nonzero sparse signal recovery using the l1-norm normalized least square estimate.

We'd want to restore a missing signal. From its linear observation [16].

$$b = Ax + n \in r^M \tag{12}$$

Exemplary least square technique requires abundant estimation

$$\mathrm{M} > N \, and \, A \, has \, full \, rank$$

$$x^* = (A^\tau A)^{-1} A^\tau b$$

Current compressive detection methods can reconstruct x from either a large number of less estimates because signal is sparse by exploiting the proceeding basis pursuits dimensionality reduction issue:

$$\min_{xe^N} \frac{1}{2} \|Ax - b\|^2 + \tau \|x\|_1$$

Algorithm Primal Dual Preconditioned PDP Framework

Inputs: choose $\left(x^0, s^0\right) > 0$ from Sect. 2.1, stop accuracy ϵ (e.g. 1e–6),

And maximum iteration number k_{max}.

for $k = 1, 2, \ldots.., k_{\max}$ do.

Perform Prediction Step: set $\sigma \leftarrow 0.001$
$(x^k, s^k, \alpha_p, \alpha_d) = UPDATE\ (x^{k-1}, s^{k-1}, \sigma)$
if $\mu_k \leq \epsilon h\left(x^k\right)$ and $\|r_d^k\|$ then.

Break.

Output:x^k

Function $UPDATE\left(x^{k-1}, s^{k-1}, \sigma\right)$

Compute Δx, Δs with σ, x^{k-1}, s^{k-1}
Compute α_p, α_d with x^{k-1}, s^{k-1}, Δx, Δs

4 Channel Estimation Problem

A difficulty with the channel computation is determining the maximum CSI H that can be obtained from low-rank data Y. There are two well-known frameworks; one of them is known as LS and the other is known as CS. The LS technology incorporates a set of L to obtain analog beamformers. The channel coherence interval is initiated with the introduction of W, which is used to gather the required predictions C, and then the complete CSI is retrieved [8]. By taking care of an optimization problem, the CS strategy will obtain low-rank observations from arbitrarily projected sparse signals and reconstruct the input signals precisely.

5 Experiment and Results

In this part, simulation model is undertaken to give more information and insights into sparse channel estimation, which proves the benefits and downsides of that method.

The proposed method is compared with the well-known state of the art of the methods in Table 1. First one is the hybrid beamforming using centralized machine learning (CML) techniques [7]. An alternative is a novel and successful convolutional neural network dependent low-rank channel recovery technology that is specifically built for an array-based massive MIMO framework, and integrates a conventional feature extraction mechanism as well as the adaptable recuperation module shown in Fig. 2 [9]. Third one used for comparison is an extraordinary learning machine system to mutually improve transmitting and receiving beamformers in Fig. 3 [10]. Last one is hybrid-precoding algorithm to empower the decrease of reduction of radio frequency chains inside the base station in Fig. 4 [11].

Table 1 Throughput comparison

SNR	Proposed	CML [7]	LRCR [9]	ELM [10]	HPA [11]
−5	0.88	0.86	0.82	0.76	0.71
0	0.88	0.87	0.83	0.78	0.73
5	0.89	0.88	0.85	0.80	0.76
10	0.90	0.89	0.86	0.82	0.79
15	0.91	0.90	0.88	0.85	0.83

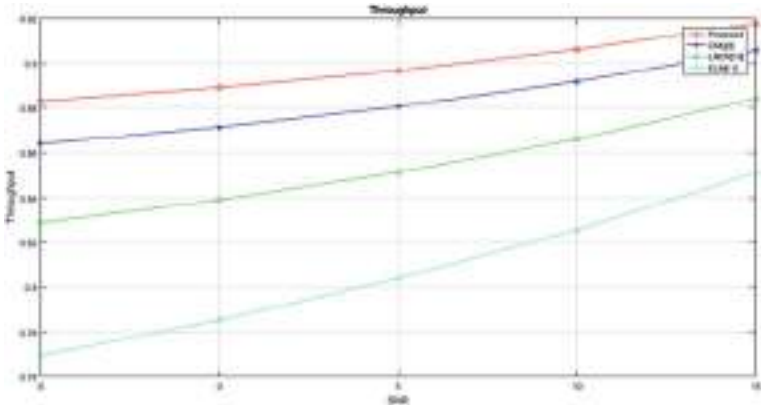

Fig. 2 Comparison of throughput between proposed and reference method

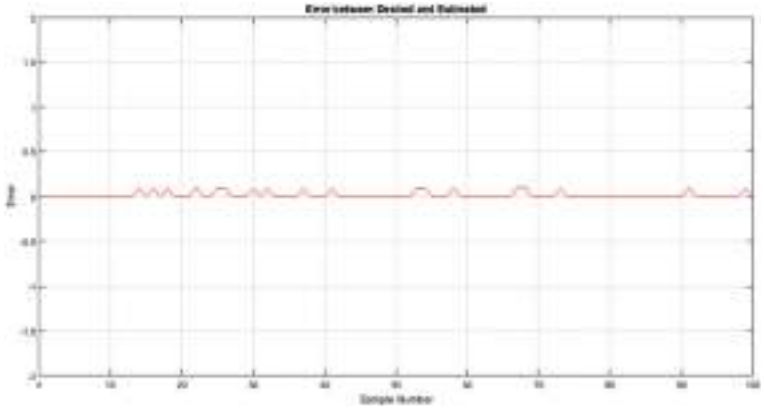

Fig. 3 Error between Tx and Rx signal

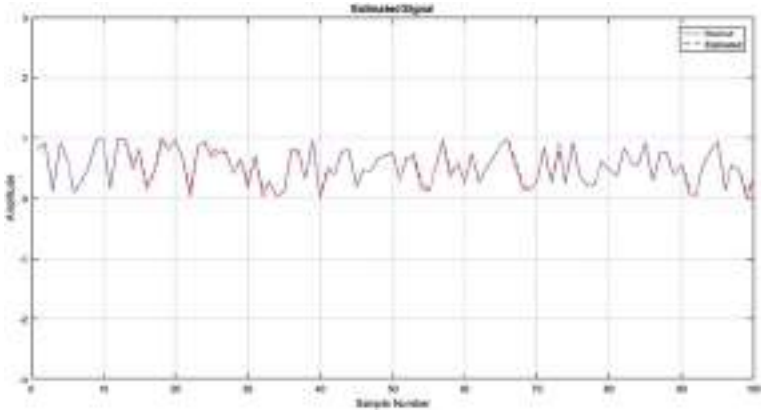

Fig. 4 Transmitted and estimates signal

6 Conclusion

Future mmWave MIMO communication systems may rely heavily on hybrid precoding as well as linking. For this mmwave hybrid beamforming framework, the suggested scheme overcomes design problems and explores approximated approaches of precoder/combiner design and channel approximation. In this paper, we provide an efficient and scalable Sparsed-based method to the low-rank channel recovery issue in mmWave large MIMO systems, where we use a hybrid array structure. Simulation results showed that the optimization model performs better in terms of MSE for channel estimation with shorter frame lengths [17].

References

1. T.S. Rappaport, S. Sun, R. Mayzus, H. Zhao, Y. Azar, K. Wang, G. Wong, J.K. Schulz, M. Samim, F. Gutierrez, Millimeter wave mobile communications for 5G cellular: it will work! IEEE Access **1**, 335–349 (2013)
2. Q. Wang, K. Feng, X. Li, S. Jin, PrecoderNet: hybrid beamforming for millimeter wave systems with deep reinforcement learning. IEEE Wirel. Commun. Lett.
3. A.F. Molisch, V.V. Ratnam, S. Han, Z. Li, S.L.H. Nguyen, L. Li, K. Haneda, Hybrid beamforming for massive MIMO: a survey. IEEE Commun. Mag. **55**(9), 134–141 (2017)
4. R.W. Heath, Jr., N. Gonz´alez-Prelcic, S. Rangan, W. Roh, A.M. Sayeed, An overview of signal processing techniques for millimeter wave MIMO systems. IEEE J.
5. D.L. Donoho, Compressed sensing. IEEE Trans. Inf. Theory **52**(4), 1289–1306 (2006)
6. T.T. Cai, L. Wang, Orthogonal matching pursuit for sparse signal recovery with noise. IEEE Trans. Inf. Theory **57**(7), 4680–4688 (Jul. 2011)
7. A.M. Elbir, S. Coleri, Federated learning for hybrid beamforming in mm-wave massive MIMO. IEEE Commun. Lett.
8. X. Song, T. Kühne, G. Caire, Fully-/partially-connected hybrid beamforming architectures for mm wave MU-MIMO. IEEE Trans. Wirel. Commun. **19**(3), 1754–1769 (March 2020)
9. N. Song, C. Ye, X. Hu, T. Yang, "Deep learning based low-rank channel recovery for hybrid beamforming in millimeter-wave massive MIMO,", , IEEE Wireless Communications and Networking Conference (WCNC), Seoul. Korea (South) **2020**, 1–6 (2020)
10. S. Huang, Y. Ye, M. Xiao, Hybrid beamforming for millimeter wave multi-user MIMO systems using learning machine. IEEE Wirel. Commun. Lett.
11. A. Salh, L. Audah, N.S.M. Shah, S.A. Hamzah, Energy-efficient power allocation with hybrid beamforming for millimetre-wave 5G massive MIMO system. Wirel. PersCommun. (2020)
12. A. Kaushik, J. Thompson, E. Vlachos, C. Tsinos, S. Chatzinotas, Dynamic RF chain selection for energy efficient and low complexity hybrid beamforming in millimeter wave MIMO systems. IEEE Trans. Green Commun. Netw. **3**(4), 886–900 (2019)
13. Y. Chen, X. Wen, Z. Lu, Achievable spectral efficiency of hybrid beamforming massive MIMO systems with quantized phase shifters, channel non-reciprocity and estimation errors. IEEE Access **8**, 71304–71317 (2020)
14. B. Gu, J. Liu, and Y. Yu, Orthogonal detection of beam space time block coding using ICA, in *IEEE Neural Netw. Brain*, vol. 2 (Beijing, China, Oct. 2005), pp. 836–840
15. V. Choqueuse, A. Mansour, G. Burel, Senior Member, IEEE, L. Collin, K. Yao, Blind channel estimation for STBC systems using higher-order statistics. IEEE Trans. Wirel. Commun. **10**(2) (2011)
16. X. Huang, K. He, S. Yoo, O. Cassairt, A. Katsaggelos, An interior point method for nonnegative sparse signal reconstruction. 25th IEEE International Conference on Image Processing (ICIP) (2018).
17. E. Vlachos, G.C. Alexandropoulos, J. Thompson, Wideband MIMO channel estimation for hybrid beamforming millimeter wave systems via random spatial sampling. IEEE J. Select. Top. Sig. Process. **13**(5), 1136–1150 (2019)

Efficient Techniques for FIR Filter Designing

Rajni and Sanjeev Kumar Dhull

Abstract In this paper, a review on some of the techniques of designing the FIR filter efficiently has been presented. Most of the Digital Signal Processing (DSP) devices use digital FIR filter due to its various advantages over IIR filter. In designing these filters, there are many performance parameters like area, power consumption, speed and complexity, which put challenges in front of a designer. In order to meet the desired performance, many techniques have been proposed. This paper is mainly focused on some of these techniques.

Keywords Adaptive filter · Digital Signal Processing (DSP) · Distributed Arithmetic (DA) · FIR filter · Reconfigurable

1 Introduction

In today's electronic world, digital signal processing (DSP) is an integral part of electronic devices. There are a large number of DSP applications which includes audio and speech processing, statistical signal processing, data compression, RADAR, SONAR and other sensor processing, video coding, audio coding, signal processing for telecommunication and many more [1].

Digital filters are essential and a very common part of any DSP application. These filters are somewhat expensive than their equivalent analog filters due to larger complexity, but by using these filters many designs can be possible which are not practical with analog filters. Digital filters are of two types, FIR and IIR. Mostly FIR digital filters are used due to their large number of advantages over IIR filters. In an FIR filter, the multipliers and the adders are the fundamental components. And by the performance of these components, the performance of FIR filter can be judged. Among these components, the multipliers are more complex to design and hence consume large area and power. A number of multiplier-less FIR filter architectures have been presented to improve the performance of FIR filter. These are divided into

Rajni (✉) · S. K. Dhull
ECE Department, GJUS&T, Hisar, Haryana, India

S. Rawat et al. (eds.), *Proceedings of First International Conference on Computational Electronics for Wireless Communications*, Lecture Notes in Networks and Systems 329,
https://doi.org/10.1007/978-981-16-6246-1_9

two categories—conversion-based designs [2, 3], and memory-based designs [4]. One of the multiplier-less architecture is Distributed Arithmetic-based architecture which is a memory-based design and an efficient method of designing FIR.

The multipliers are also used in Adaptive filters which is an important part of signal processing applications like echo cancellation [5]. There have been discussions about some other DA-based techniques [6]. Many researchers proposed DA-based adaptive filters which were either memory-less [7] or suitable for smaller order filters [8]. A large number of techniques have been proposed by researchers to make the filter efficient with regard to area, power, speed, complexity and reconfigurability in larger order FIR filters. They tried to reduce the number of computations and eliminate the need for multipliers. In [9], the multiply and accumulate (MAC) module along with a modified carry select adder and a Wallace tree has been utilized to attain area and power efficacy. A new algorithm that is the RAG-n algorithm is used in [10], which omits the multipliers and reduced the adders and hence the overall complexity. Chia-Yu et al. [11] presents a less complicated FIR filter in fixed configuration by reducing the number of adders in a practical method of designing FIR filter. Pramod and Yu [12] and [13] utilized very effective Multiple Constant Multiplication (MCM) technique for designing block FIR filter in transpose type configuration and for larger order filters also. A method using Computation Sharing Multipliers (CSHM) has been presented in [14]. They divided the larger constant multiplications into smaller multiplications and precompiled those values. This method is efficient for complexity in smaller order filters but is inefficient for larger order filters.

For getting a particular frequency response, there are many methods which are commonly used to design an FIR filter: (1) Frequency Sampling method, (2) Window-based method, (3) Least Mean Square (LMS) method and (4) Parks-McClellan method. There are many other methods which are derived from these methods or somewhere else.

In this paper, Sect. 2 explains the literature review on various currently used techniques of VLSI designing of FIR filter. Section 3 contains the discussion on the advantages and disadvantages of these surveyed techniques. We have concluded our review in Sect. 4. And Sect. 5 gives the future scope.

2 Literature Review

Various currently used techniques proposed by researchers have been studied and surveyed for their performance regarding area used, complexity, power consumption and reconfigurability.

2.1 Distributed Arithmetic Approach

P.V. Praveen Sunder et al. [15] proposed a new approach in which the decimation filter in the hearing aid has been replaced by a single Distributed Arithmetic (DA) unit as shown in Fig. 1 using multiplier-less architecture. Generally, the multipliers, adders and shift registers are used to design adaptive filters, and the multipliers are well known to occur in larger area and consume more power. To overcome this limitation, here in this design, a multiplier-less and memory-less DA architecture has been used. In the adaptive algorithm used, the outputs from filter alongside the error values are calculated for every cycle and are used to upgrade the filter coefficient.

Methodology: The multiplexers and compressor adder have been used to design the proposed enhanced DA (EDA) architecture as shown in Fig. 4. This EDA contains 2:1 multiplexer instead of ROM and 4:2 compressor in place of accumulator. The input to EDA is given by shift register and is given as one of the inputs to the 2:1 multiplexer and the other input signal for v is given as zero. The filter coefficients will act as selections for the 2:1 multiplexer and the multiplexer outputs are given to the 4:2 compressor which give final output.

Blocks: The presented architecture (of Fig. 3) consists of:

(1) Weight Increment Block (Fig. 2), which further consist of (a) Adder/Subtractor, (b) Delay unit and (c) Word parallel Bit serial converter.
(2) Memory-less Inner Product block (MLIP), which consist of multiplexers and the multiplexer's outputs are fed to compressor.
(3) Compressor Adder.

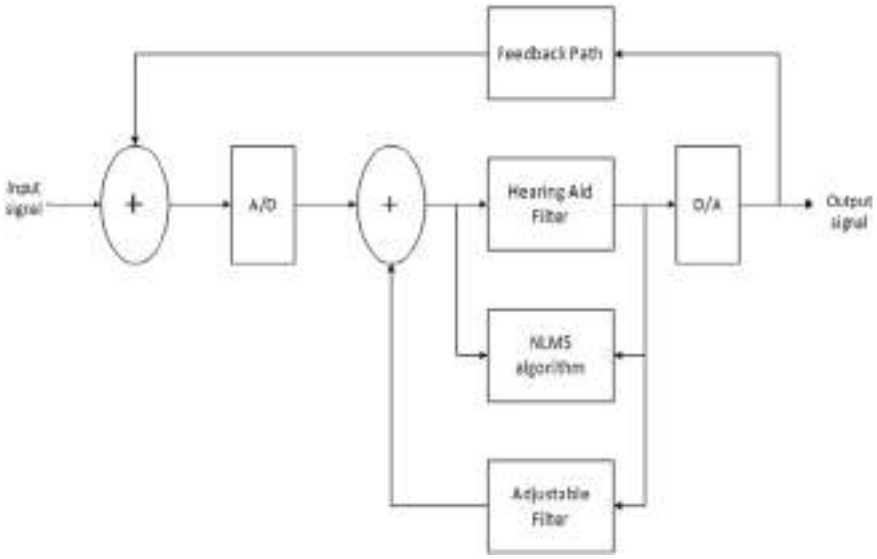

Fig. 1 Digital hearing aid with the use of proposed adaptive filter [15]

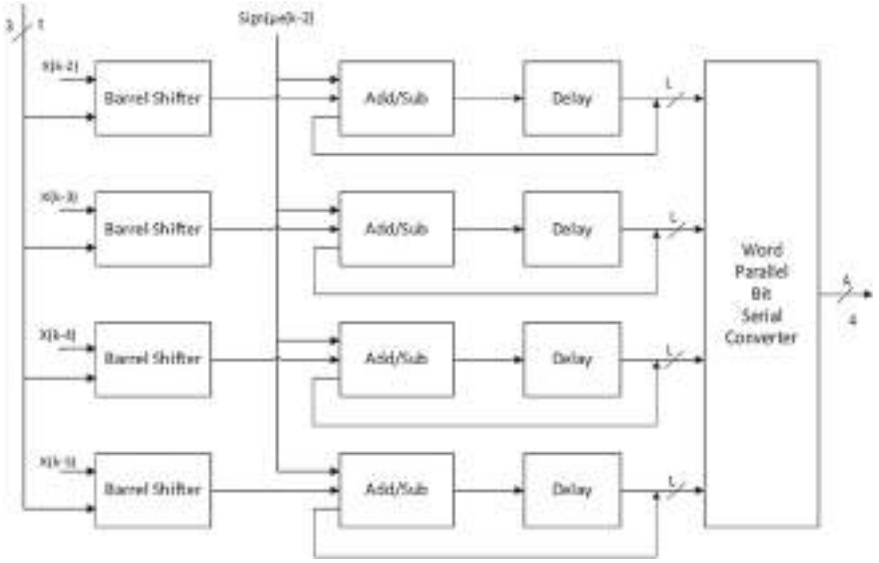

Fig. 2 Basic diagram of Weight Increment Block (WIB) [15]

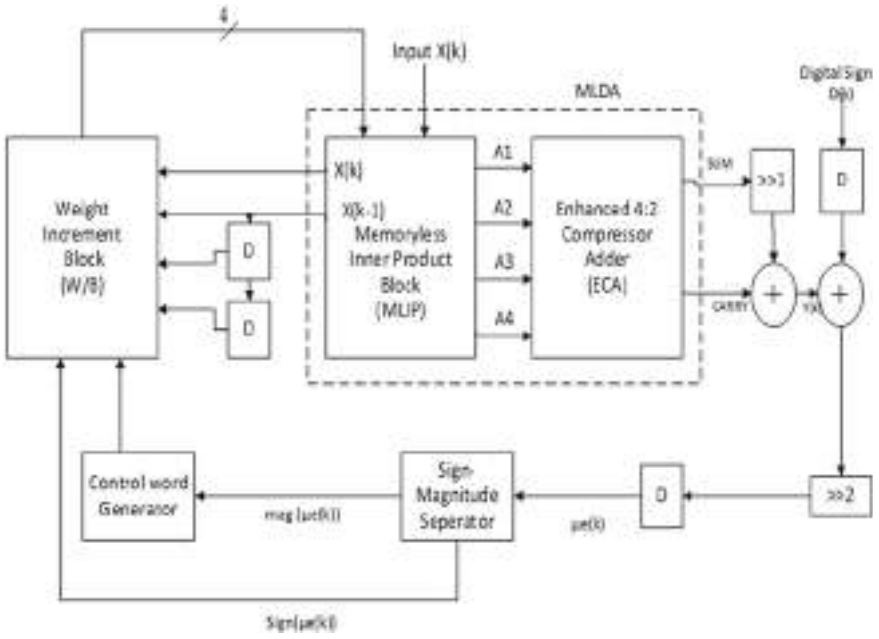

Fig. 3 Basic diagram of the proposed EDA architecture [15]

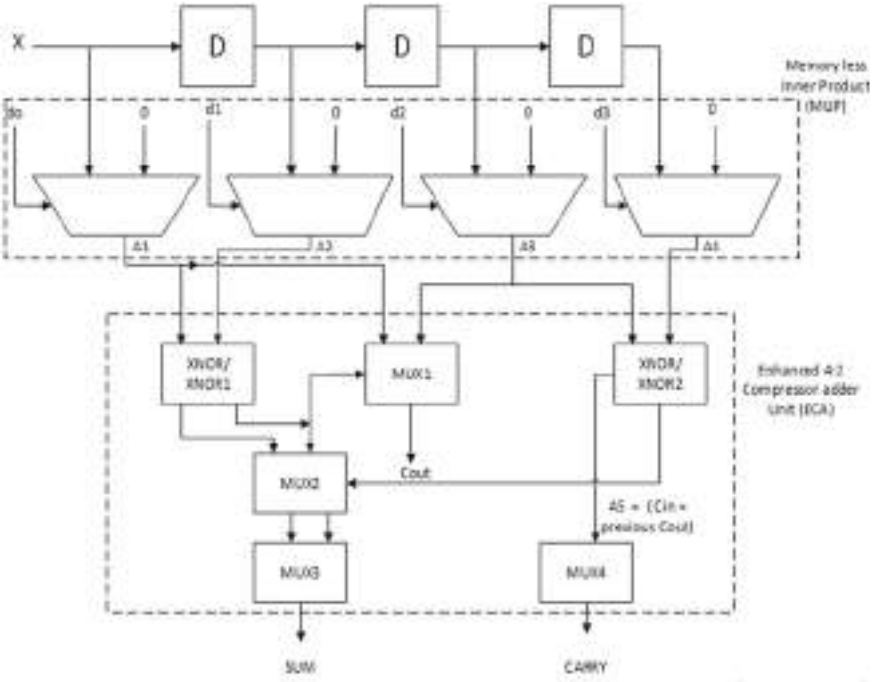

Fig. 4 Basic diagram of Enhanced Distributed Arithmetic (DA) architecture [15]

(4) Sign-Magnitude Separator.
(5) Control Word Generator.

2.2 Least-Squares Approach

Mansoor Khan et al. [16] presented the method of weighted least-squares optimization problem which is considered as a specific case of the category of peak-constrained least-squares optimization problems. The squared weighted error among the magnitude response of the ideal filter and actual filter has been minimized non-repeatedly by the solution of the scheme of linear equations in numerical designs. Solving these equations they get an impulse response which is true and symmetric. The proposed method of least squares FIR filter (Fig. 6) presents the frequency response which features a flat passband, almost proportional attenuation as Parks-McClellan method, with an equal order and a better stop band attenuation apart from the conventional window-formed FIR filter design.

In the VLSI architecture of this FIR filter, after the multiplication stage, to feature the results alongside with least delay, the "adder tree" (Fig. 5) has been used, which

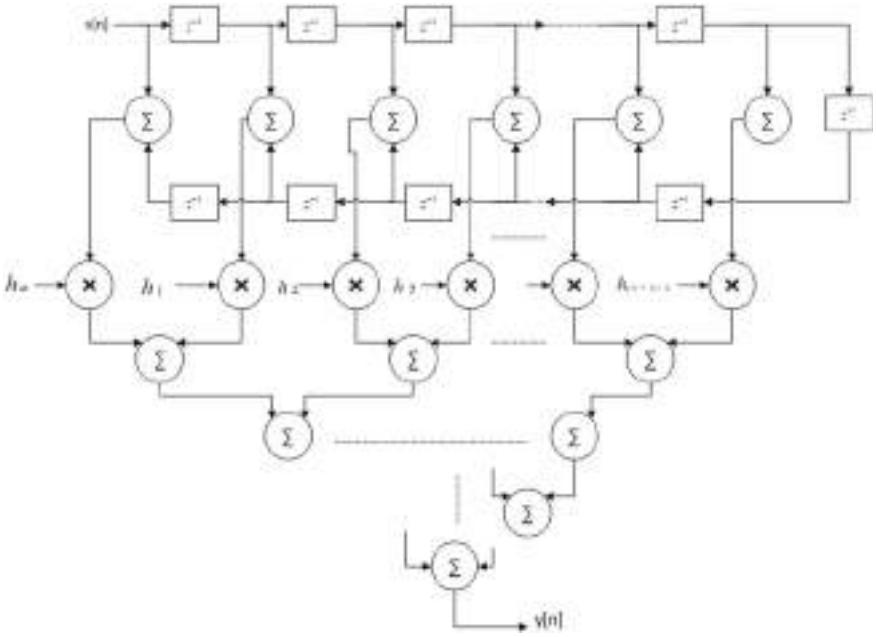

Fig. 5 VLSI architecture of FIR filter by using pipelined adder tree [16]

alongside pipeline levels at the output of every layer of every adder tree have considerably improved the outturn of this filter. Further, the throughput can be increased by pipelining the multiplier but the area and pipeline delay will be increased.

2.3 Residue Number System (RNS) DA-Based Approach:

Grande Naga Jyothi et al. [17] proposed a memory-less Distributed Arithmetic (DA)-based architecture of an efficient FIR filter (Fig. 8) using residual numeration system (RNS) for top speed Digital Signal Processing Systems. During this architecture, the DA block inputs are in residue number form, and to urge the outputs in binary form, Chinese Remainder Theorem has been used.

Blocks and Methodology used: This method of designing FIR filter (Fig. 7) consists of: (1) Forward Converter block (2) Memory-less Distributed Arithmetic (MLDA) block and (3) the Reverse Converter (RC) block.

As seen from Fig. 9, the input x(k) in block FC is divided into N residue set based on modular arithmetic. The values of moduli are set and are in $\{2^{n-1}, 2^n, 2^{n+1}\}$ manner. Using moduli, the signal from the input and the filter coefficients are transformed into residues. The output signal from the FC blocks is given to the 2:1 multiplexers of the MLDA block as selection line, and the residue filter coefficients are given to

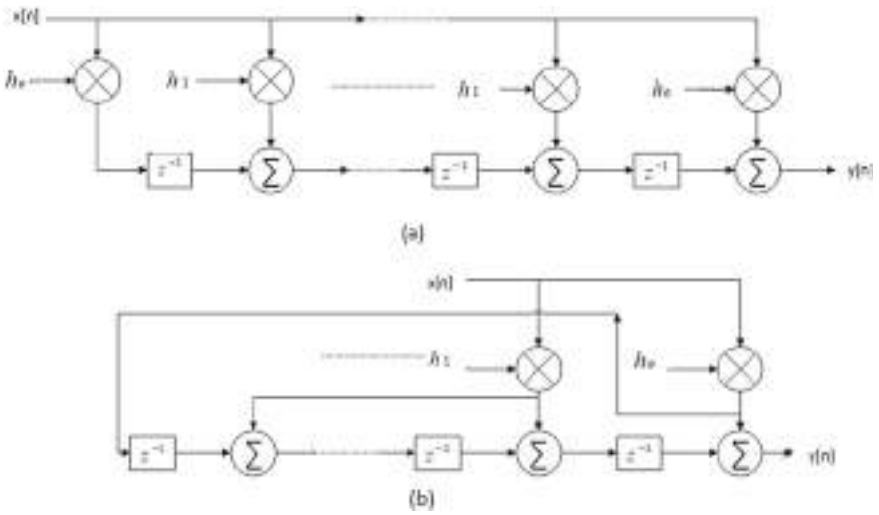

Fig. 6 Broadcasting VLSI architecture for FIR filter **a** architecture in the absence of multiplier reused, **b** architecture accompanying multiplier reused [16]

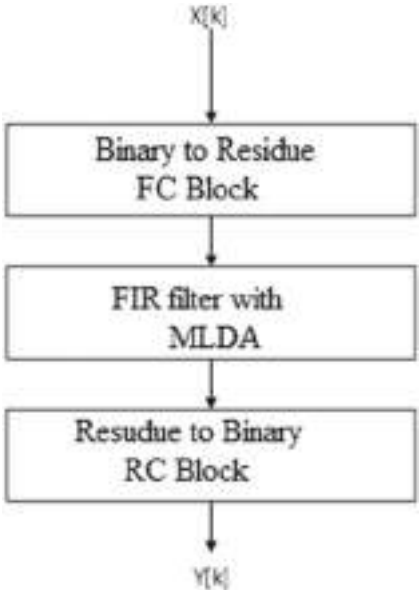

Fig. 7 Block diagram of residue number system (RNS)-based FIR filter [17]

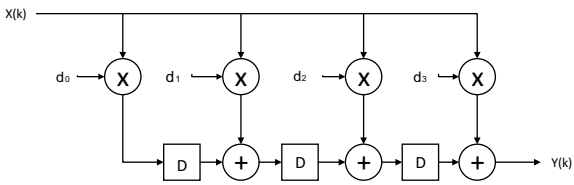

Fig. 8 RNS domain FIR filtering [17]

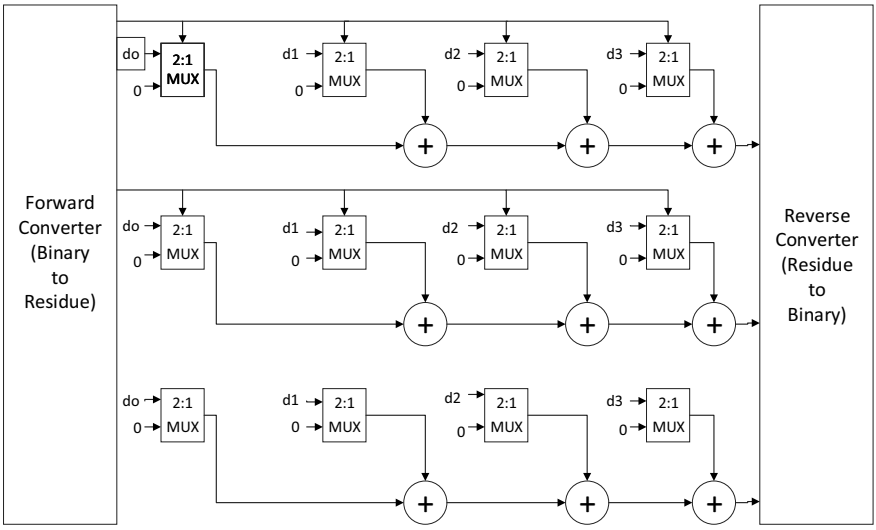

Fig. 9 RNS DA-based FIR filter [17]

2:1 mux as one input and ground or "0" is taken from the other input. The output is provided to the reverse converter from the mux. The residue number can be modified in the reverse converter to binary numbers using the Chinese Remainder Theorem.

The RNS is able to perform the computation very fast and parallel, therefore the design using RNS has gained higher speed than the existing one. But one of its drawback is that there is the need for converters in filter.

2.4 Distributed Arithmetic Approach with Transposed Form Block FIR Filter

Naushad Ali et al. [18] proposed "an energy efficient, multiplier less, transposed form block FIR filter (Fig. 10) architecture for reconfigurable applications" using Distributed Arithmetic technique. They utilized:

(1) Distributed Arithmetic Algorithm,
(2) Transpose form architecture which provides inherent pipelining that further decreases the calculation complexity and support higher operating frequency and
(3) Block processing of inputs which results in high and adaptable throughput by splitting the calculation into small multipliers operating in parallel.

Blocks and Methodology used: The presented design (Fig. 11) consists of:

(1) Register unit—to give a high and scalable throughput the input sample is processed in blocks.

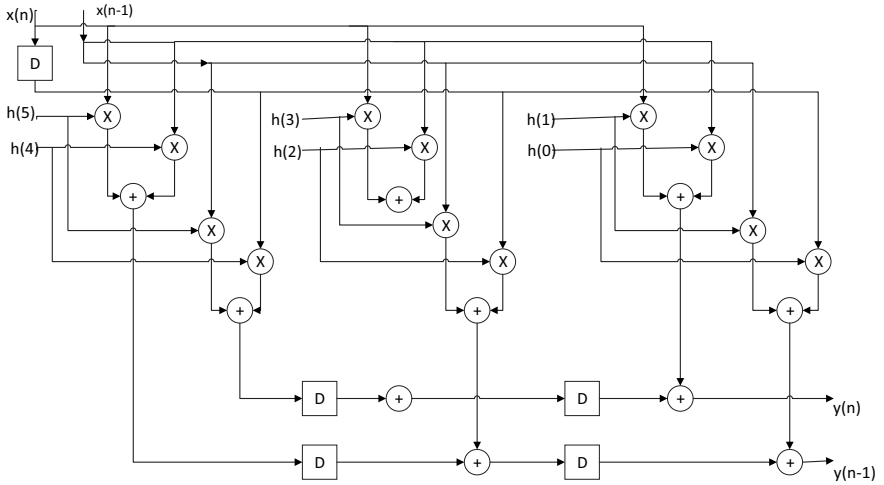

Fig. 10 Block realization in transpose form with block size 2 [18]

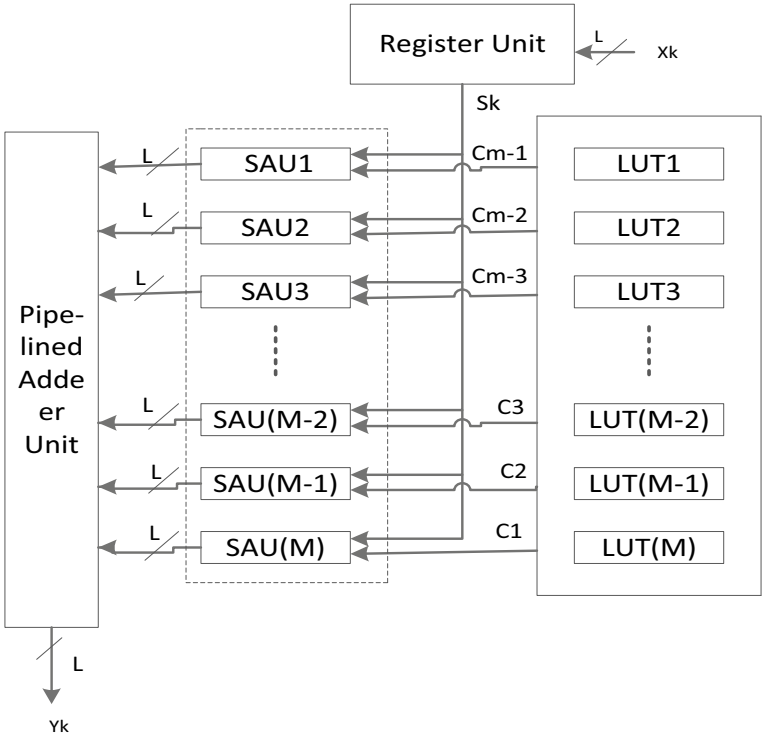

Fig. 11 Proposed Reconfigurable FIR filter [18]

(2) Storage unit—the filter coefficients are stored in ROM-based LUTs which requires less memory and less access time. This provides reconfigurability to the filter.
(3) Shift and add units (SAU)—It consists of shift and add product generators which generates partial products. These generators use shift and add algorithms instead of conventional multiplication to achieve larger multiplications which consumes very less power and area and complexity is reduced. Therefore, overall area of FIR filter has been reduced considerably.
(4) Pipelined adder unit—This unit receives partial results from SAU units and adds them using pipeline-connected ripple carry adders. For each n samples obtained from the register unit, this unit gives a block of n filter output. Thus improving the overall performance of the filter.

2.5 *Direct Form FIR Filter with Modified Booth Multiplier Based on Spanning Tree*

Greeshma Haridaas et al. [19] proposed an FIR filter (Fig. 12) with modified Booth Multiplier which was area efficient as well as consumed low power. Today, the major issues in designing an efficient FIR filter are area and speed and these constraints are usually conflicting. The proposed multiplier uses modified booth multiplier (Fig. 13)

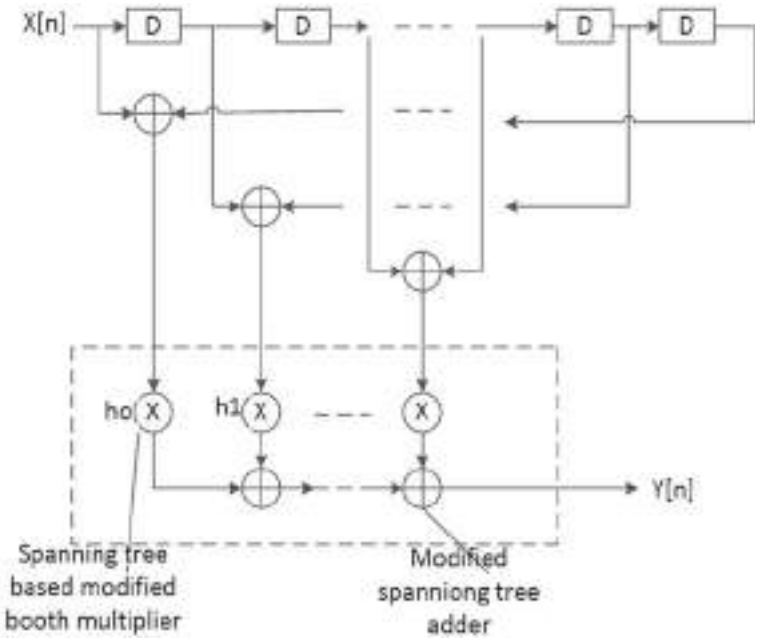

Fig. 12 Proposed FIR filter architecture [19]

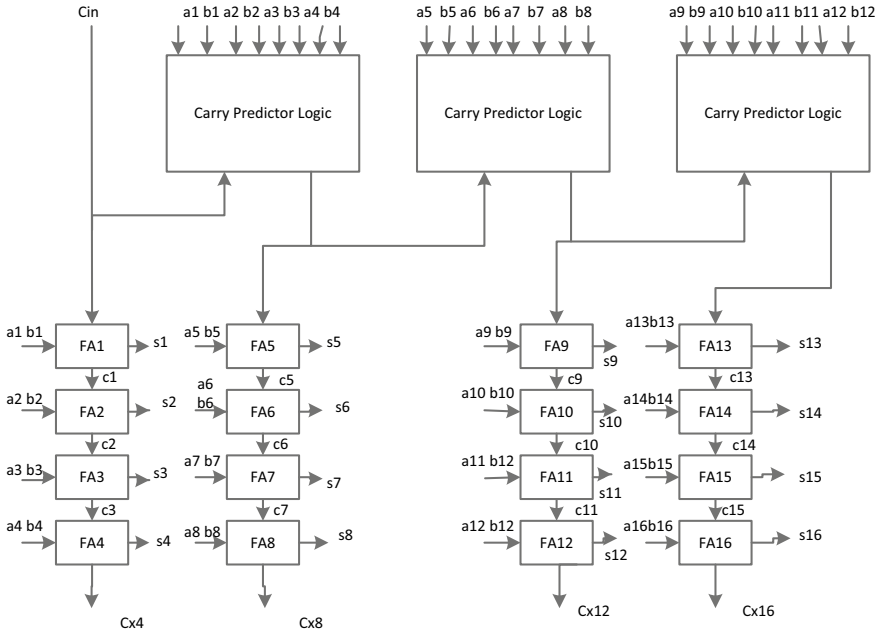

Fig. 13 Modified spanning tree adder [19]

based on spanning tree. After multiplication, modified spanning tree adders adds the results and for final addition, the spanning tree parallel prefix adder which was an area-efficient adder, was used for reducing the overall area of the multiplier.

Blocks and Methodology used: The main blocks of the proposed FIR filter structure and their working are as follows:

(1) Modified Spanning Tree Adder (Fig. 13)—It consists of 4-bit carry adder using carry predictor logic. Before the actual carry is generated from the previous ripple carry adders, the carry predictor logic predicts the carry input to the ripple carry adder, thereby reducing the overall delay. These ripple carry adders are operated in the circuit almost parallel and therefore the speed of the filter has been increased considerably.
(2) Modified Booth Multiplier based on Spanning tree—This comprises of (a) Booth encoder (BE) and (b) Partial Product Generator (PPG).
(3) Wallace Tree.
(4) Modified Spanning Tree-based Parallel Prefix Adder.

As shown in Fig. 14, the Booth encoder encodes the multiplier output bits. The second block, that is PPG, generates the partial products by operation on multiplicands which reduces the number of partial products. The next block Wallace tree adds the resulting partial products. And the final block, modified spanning tree parallel prefix adder adds the last sum and carry and, finally the adder gives the final concluded product.

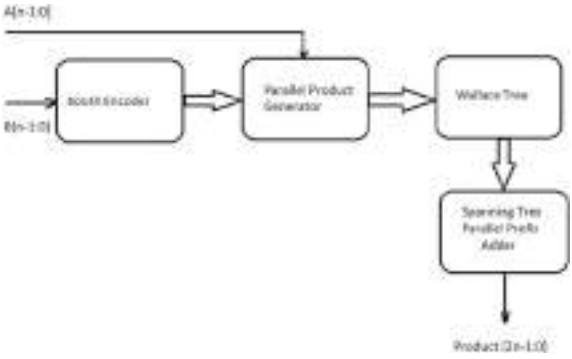

Fig. 14 Architecture of modified Booth multiplier [19]

The performance of this presented FIR filter with booth multiplier based on spanning tree was one step ahead of the subsisting FIR filter designs in concern of area, delay and power consumption. Delay calculated was 1.933 ns and power consumed was 0.032 watts.

2.6 MAC Unit with Booth Multiplier and Carry Look Ahead Adder

Deepika et al. [20] proposed an FIR filter that was constructed utilizing a reconfigurable booth multiplier with a carry look ahead adder (CLAA) which made the design faster. The booth multiplier is a very useful multiplier to reduce the complexity of the circuit by reducing the partial products. Here in this proposed work, with a booth multiplier (Fig. 15), that was built on existing algorithm, they used a finite state machine (FSM) in the basic programming of the design to make the calculations

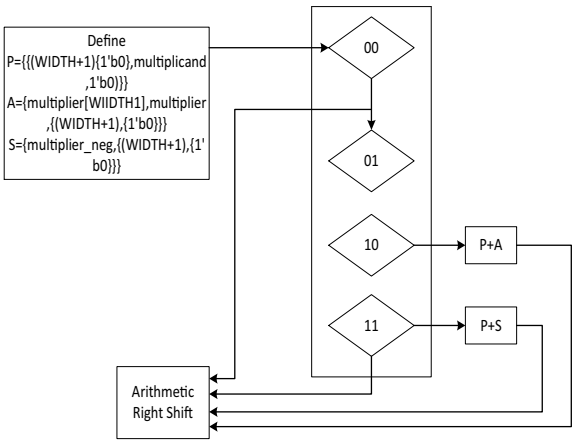

Fig. 15 Reconfigurable booth multiplier architecture [20]

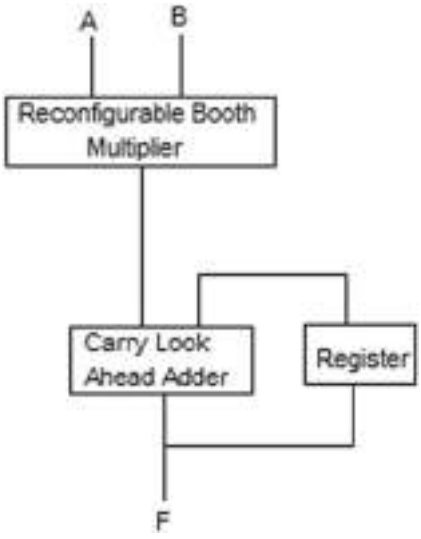

Fig. 16 Proposed multiplier accumulate (MAC) unit architecture [20]

easy. In the main module of the used booth multiplier, a configuration register, which is a special purpose 16-bit register, has been used.

From Fig. 16, initially, the Booth multiplier receives two inputs and multiplies them and gives the result to CLAA, which adds the previously stored results of the multiply accumulate block (MAC) and the multiplication result from the multiplier. A register was used to save the previous multiplication results.

The proposed FIR filter is a high speed filter by using the reconfigurable booth multiplier and a carry look ahead adder where a finite state machine was utilized with reconfigurable booth multiplier. The flow chart for proposed Booth multiplier is shown in Fig. 17. This resulted in lesser delay and higher maximum frequency as compared to previous FIR filter design. The proposed filter performed better. The delay calculated was 3.247 ns, maximum frequency achieved was 307.977 MHz and the power consumed was 0.424 watts.

2.7 Multiple Constant Multiplication (MCM) Technique for Large-Order FIR Filter in Transpose Form

Basant Kumar Mohanty et al. [21] proposed an inherently pipelined block FIR filter configured in transpose form which was possible to realize with larger order filters. This design was very efficient in area and delay, both for fixed and reconfigurable applications. This structure showed remarkably lesser ADP and lesser EPS than the previous designs. Main contribution of their proposed work is:

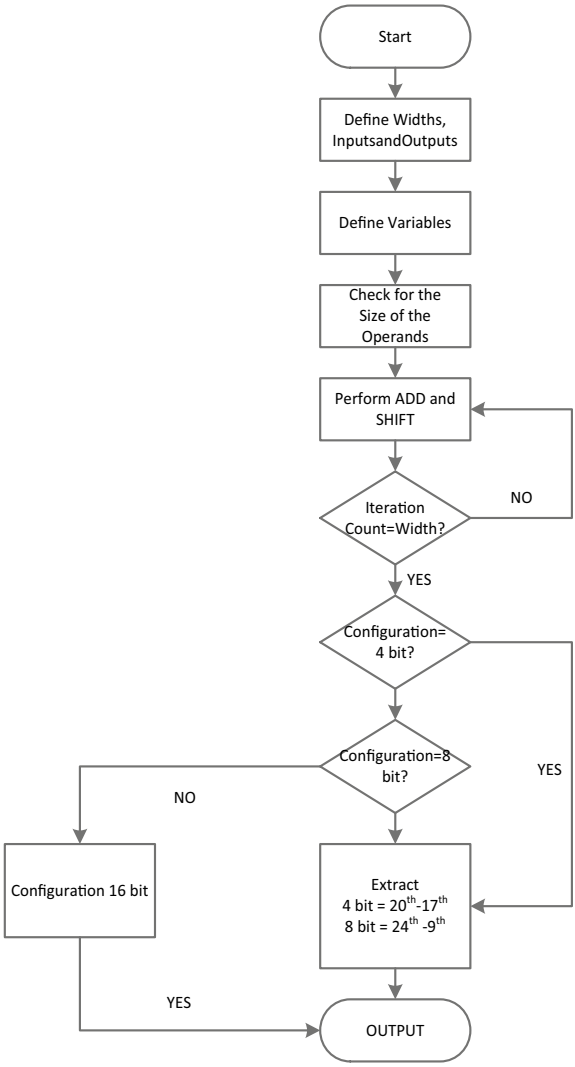

Fig. 17 Proposed booth multiplier flow chart [20]

(1) In this architecture, they utilized Multiple Constant Multiplication (MCM) technique to reduce computations and hence complexity. In the MCM technique, when a given input and a set of constants are multiplied together, common subexpression sharing has been used which reduced the number of additions used in the realizations of multiplications. Hence, this method reduced the computations and hence complexity in large-order FIR filter. But, this can only be used with the transposed configured FIR filter.

(2) The block processing is not directly favored by transpose form of FIR filter, but the direct form directly supports the block processing. In transpose type configuration, they investigated the possibility of block processing.
(3) And for reconfigurable filter, they inferred a general architecture based on the multiple constant multiplication (MCM) method for their transpose-form block FIR filter.

Blocks: This design (Fig. 18) consists of:

(1) A number of Inner Product Unit (IPU) (Fig. 19)
(2) A Coefficient Selection Unit (CSU)
(3) A Pipeline Adder Unit (PAU)
(4) A Register Unit (RU) (Fig. 20).

Methodology: The CSU reserves the coefficients for all the reconfigurable application filters. For implementing this unit, N-ROM LUTs have been used in such a way that in just one clock cycle, we get the filter coefficients of any specific channel filter. N is the length of the filter here. During the kth cycle, the RU (Fig. 20) receives input x_k and gives a parallel output of L rows of s_k. The M number of IPUs which

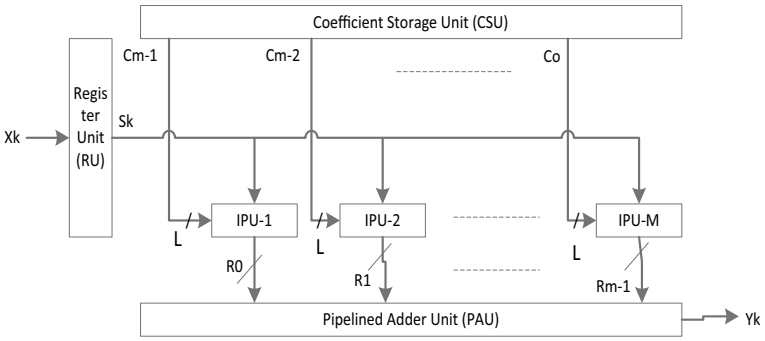

Fig. 18 Proposed Block FIR filter structure [21]

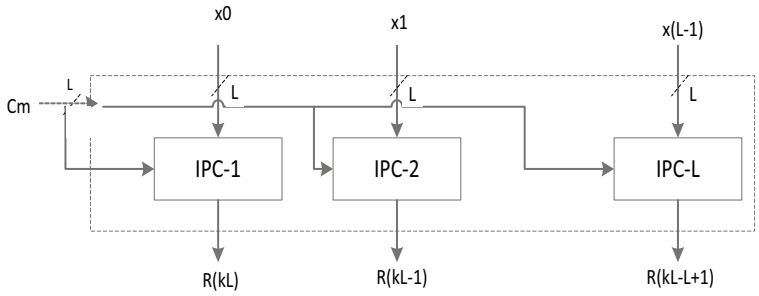

Fig. 19 Structure of $(M + 1)$th IPU [21]

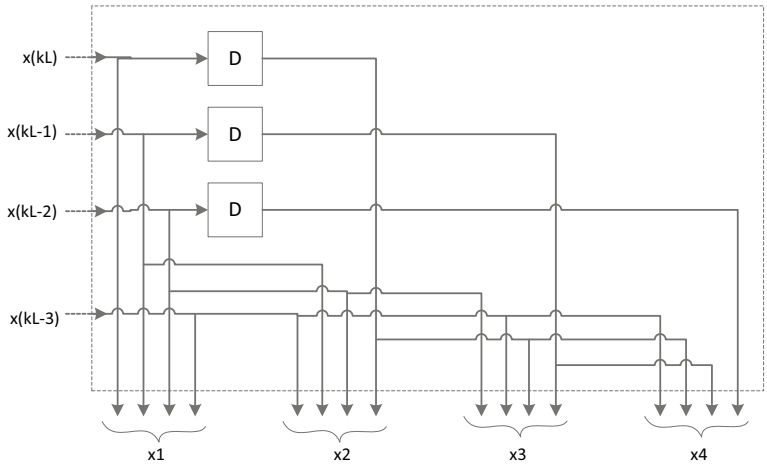

Fig. 20 Register Unit (RU) internal structure for block size 4 [21]

are proposed, receives the produced L rows of s_k. The M number of IPUs works in parallel and produce an M block result. In PAU, the partial products produced by IPUs are added and gives an L block output.

The performance of the proposed filter: for a block size of 4, a 16-bit filter showed minimum clock period (MCP) of 1.30 ns, power consumption of 59.3 mW and sampling rate of 3.07 GHz.

3 Brief Discussion

We have briefly discussed some of the currently explored methods of designing an FIR filter both for fixed and reconfigurable filters.

The DA-based adaptive filter technique offers a multiplier-less architecture with low complexity, lesser area and is cost effective. The FIR filter designed by the second technique discussed above, the least squares technique in which the equations are solved non-iteratively by minimizing the squared error, has the advantage that it has flat pass band and a higher attenuation in stopband for the same order filter.

The third discussed technique, design by RNS-based method, got the higher speed and lesser area than the existing filters. The next technique, the reconfigurable DA-based FIR filter using LUTs and pipelined adder unit, offers reconfigurability, high throughput and lesser area delay product ADP. The FIR filter designed with modified Booth multiplier based on spanning tree gives more area-efficient design and hence cost effective. The next technique discussed used multiply accumulate unit, which offered lesser delay and higher maximum frequency.

The last technique is a very effective technique, as the researchers of this technique have done very challenging tasks. First, they used the MCM technique for larger order

FIR filter in transpose form; secondly, they explored the possibility of realizing block processing in transpose form for the use of MCM technique; and most of all, they utilized pipelining for larger order FIR filter for both fixed and reconfigurable filters. This is the most advantageous technique among all the above discussed techniques.

4 Conclusion

A number of the latest suggested efficient design techniques for FIR filter have been reviewed. Each technique has its own opportunities and obstacles with regard to area, delay, power and complexity. Designing a low-power, low-complex, high performance and reconfigurable block FIR filter of large order is a very critical task. Conspicuous design efforts have been done to achieve these performance issues. Among the above discussed techniques, the Multiple Constant Multiplication (MCM) and the Distributed Algorithm (DA) methods are the most efficiently used methods. These provide area-efficient, low-power and high performance larger order reconfigurable FIR filter.

5 Future Scope

The above mentioned techniques can be implemented in various low power and high performance applications. It would be strenuous to test some of the above discussed techniques for higher number of bits and higher order filters. Using Least-squares method, the throughput can further be increased by pipelining the multiplier, but the area and pipeline delay will be increased. Using RNS DA-based approach for designing FIR filter, the speed of the filter can further be increased by using better converters.

References

1. G.P. John, G.M. Dimitris, Digital signal processing: principles, algorithms and applications, 4th edn. (Principles Pearson Education Inc., 2007)
2. H.I. Richard, Subexpression sharing in filters using canonic signed digit multipliers. IEEE Trans. Circ. Syst.-II Analog Digital Sig. Process. **43**(10), 677–688 (1996). https://doi.org/10.1109/82.539000
3. A.K. Kei–Yong, L.W. Alan, A programmable FIR digital filter using CSD coefficients. IEEE J. Solid-State Circ. **31**(6). https://doi.org/10.1109/4.509877
4. Y.P. Sang, K.M. Pramod, ASIC and FPGA realization of a DA based reconfigurable FIR digital filter. IEEE Trans. Circ. Syst. II: Express Briefs. https://doi.org/10.1109/TCSII.2014.2324418
5. Y.P. Sang, K.M. Pramod, Low-power, high-throughput and low-area adaptive FIR filter based on distributed arithmetic. IEEE Trans. Circ. Syst. II: Express Briefs **60**(6), 346–350 (2013). https://doi.org/10.1109/TCSII.2013.2251968

6. N.J. Grande, S. Sridevi, Distributed arithmetic architectures for FIR filters- a comparative review, in *IEEE International Conference on Wireless Communications, Signal Processing and Networking (WiSPNET)* (2017), pp. 2684–2690. https://doi.org/10.1109/WiSPNET.2017.8300250
7. N.J. Grande, S. Sridevi, ASIC implementation of low power, area efficient adaptive FIR filter using pipelined DA, in *Microelectronics, Electromagnetics and Telecommunications* (Springer, Berlin, 2019), pp. 385–394. https://doi.org/10.1007/978-981-13-1906-8_40
8. G. Rui, S.D. Linda, Two high-performance adaptive filter implementation schemes using distributed arithmetic. IEEE Trans. Circ Syst. II: Express Briefs **58**(9), 600–604 (2011). https://doi.org/10.1109/TCSII.2011.2161168
9. K.V. Nitish, R.N. Koteswara, G. Lakshminarayanan, Design of area and power efficient digital FIR filter using modified MAC unit, in *IEEE Sponsored 2nd International Conference on Electronics and Communication System CECS* (2015). https://doi.org/10.1109/ECS.2015.7125041
10. R. Sakthivel, M. Ishita, J. Vrushali, W. Asmita, A custom reconfigurable power efficient FIR filter, in *International Conference on Circuit, Power and Computing Technologies (ICCPCT-2016)* (IEEE, 2016). https://doi.org/10.1109/ICCPCT.2016.7530133
11. Y. Chia-Yu, H. Wei-Chun, H. Yung-Hsiang, Designing hardware-efficient fixed-point FIR filters in an expanding subexpression space. IEEE Trans. Circ. Syst. **61**(1) (2014). https://doi.org/10.1109/TCSI.2013.2268551
12. K.M. Pramod, P. Yu, MCM-based implementation of block FIR filter for high-speed and low-power applications, in *IEEE/IFIP 19th International Conference on VLSI and System-on-Chip* (2011), pp. 119–121. https://doi.org/10.1109/VLSISoC.2011.6081653
13. B.T. Manish, G.C. Purushottam, FIR filter implementation on FPGA using MCM design technique, in *Proceeding of second International Conference on Circuits, Controls and Communications* (2017), pp. 213–217. https://doi.org/10.1109/CCUBE.2017.8394140
14. P. Jongsung, R. Kaushik, Computation sharing programmable FIR filter for low-power and high performance applications. IEEE J. Solid State Circ. **39**(2), 348–357 (2004). https://doi.org/10.1109/JSSC.2003.821785
15. S.P.V. Praveen, D. Ranjith, T. Karthikeyan, K.V. Vinod, B. Jayakumar, Low power area efficient adaptive FIR filter for hearing aids using distributed arithmetic architecture. Int. J. Speech Technol. **23**, 287–296 (2020). https://doi.org/10.1007/s10772-020-09686-y
16. K. Mansoor, K. Shahrukh, Least squares linear phase FIR filter design and its VLSI implementation. Analog Integr. Circ. Sig. Process. **105**, 99–109 (2020).https://doi.org/10.1007/s10470-020-01688-9
17. N.J. Grande, S. Kishore, A. Vijaylaxmi, ASIC Implementation of distributed arithmetic based FIR filter using RNS for high speed DSP systems. Int. J. Speech Ttechnol **23**(259–264) (2020). https://doi.org/10.1007/s10772-020-09683-1
18. A. Naushad, G. Bharat, New energy efficient reconfigurable FIR filter architecture and its VLSI implementation, in *VLSI design and test* (2017), pp. 519–532. https://doi.org/10.1007/978-981-10-7470-7_51
19. H. Greeshma, S.G. David, Area efficient low power modified booth multiplier for FIR filter, in *International Conference on Emerging Trends in Engineering, Science and Technology (ICETEST-2015).* Proceedia Technology. DOI: https://doi.org/10.1016/j.protcy.2016.05.070
20. N.G. Deepika, Design of FIR filter using reconfigurable MAC unit, in *Third International Conference on Signal Processing and Integrated Networks (SPIN)* (IEEE, 2016), pp. 312–314. https://doi.org/10.1109/SPIN.2016.7566710.
21. K.M. Basant, K.M. Pramod, A high-performance FIR filter architecture for fixed and reconfigurable applications. IEEE Trans. Very Large Scale Integr. (VLSI) Syst. **24**(2), 444–452 (2016). https://doi.org/10.1109/TVLSI.2015.2412556

Design and Analysis of Two-Stage Operational Amplifier for Biomedical Applications

Pabba Sowmya, Mamatha Samson, Mohd Javeed Mehdi, and Shaik Afifa Farman

Abstract The key purpose of this paper is to implement an amplifier that retains less power and large gain which is appropriate for precise biomedical applications. The circuit design of a two-stage opamp is executed with the help of LTspice tools employing 180 nm technology files. Numerous analog systems, for example, filters, integrators, data converters like ADCs, and summing circuits are carried out with operational amplifiers as it is the most necessary building block for the above-mentioned circuits. It is essential to design an effective amplifier that enhances the performance of analog circuits. Present work largely focused on executing a two-stage opamp with maximum gain. Further, utilizing this two-stage opamp, an instrumentation amplifier is realized. Several performance parameters, for example, voltage gain, AC gain, slew-rate, average power consumption, and bandwidth are calculated and observed.

Keywords Voltage gain · Bandwidth · Average Power · Slew-rate

1 Introduction

Most of the biomedical signals are with the amplitude ranging between 10 microvolts and 10 millivolts, the amplitude of Electrocardiogram (ECG) signals is nearly 1 millivolt, the amplitude of Electroencephalogram (EEG) signals is nearly 100 microvolts, the amplitude of Electromyogram (EMG) signals is nearly 5 millivolts, including a large amount of common-mode interference and noise signals [1]. Operational amplifiers being the most fundamental building block for most of the biomedical applications for signal acquisition, it is necessary to design an opamp that offers huge gain. Opamp is the short form used to refer to an operational amplifier [2].

P. Sowmya (✉) · M. Samson · M. J. Mehdi · S. A. Farman
GRIET, Hyderabad, India

M. J. Mehdi
e-mail: javeed954@grietcollege.com

S. Rawat et al. (eds.), *Proceedings of First International Conference on Computational Electronics for Wireless Communications*, Lecture Notes in Networks and Systems 329,
https://doi.org/10.1007/978-981-16-6246-1_10

Numerous mathematical tasks, for example, integration, differentiation, addition, etc. Very large-scale integrated applications, for instance, active filters such as band-pass filters in addition to LPF, wave-shaping circuits say as table multivibrator, sinusoidal waveform generators, along with circuits like comparators require operational amplifier as it the most fundamental building block in all the above-stated applications [3].

An operational amplifier is a huge gain voltage amplifier, employed with direct coupled logic, that produces single-ended output from differential input. Opamp with negative feedback must provide compensation circuitry to achieve high gain and good phase margin with desirable cross-over frequency [4]. Most of the biomedical applications and other electronic applications tend to prefer devices that consume less power, less area, with high gain, long battery usage, and portable devices and prone to less noise. Most of these applications focus on performance characteristics such as area, speed, power, less noise, and high gain.

Based on the number of stages, operational amplifier is classified into two types, i.e., single-stage amplifier and multi-stage amplifier. A multi-stage operational amplifier is again classified into three types based on the topologies; they are telescopic opamp topology, folded cascode opamp topology, and lastly, there is additional amplifier topology consisting of two stages. The design of a single-stage opamp is much simple. It consumes less power and offers high speed. The single-stage amplifier provides a high-frequency response and the settling time of this circuit is faster. The main drawback of a single-stage operational amplifier is it has less open-loop voltage gain and does not resist high frequencies [5].

Two-stage operational amplifiers comprise of voltage to the current stage followed by a current to voltage stage. In the two-stage amplifier, first stage comprises the differential stage. It comprises inverting and non-inverting input terminals [6].

The applied differential input voltages are converted to currents with the help of a differential amplifier. At last, by employing the current mirror as load, we can transform differential voltages in such a way that we get differential currents. A strategy employing CMOS technology is demonstrated for designing an operational amplifier due to the fact that CMOS devices consume low static power, and high withstanding noise in these devices is reported [7].

Numerous operational amplifier performance characteristics as well as the effect of width to length ratio on two-stage opamp have been analyzed. They have proposed scaling techniques and its impact on various features such as feature size, number of transistors, power dissipation, and cost factor [8]. Various parameters are analyzed by reducing the width and observed a fact that as width decreases, the gain of the opamp also will decrease. Phase margin will increase and all other factors will decrease [9].

Biomedical signals have very low amplitudes and are often prone to interference and noise [10]. To obtain a signal without losing necessary information, we need to have an instrumentation amplifier that exhibits a large gain and high common-mode rejection ratio. In this paper, using various opamp topologies, instrumentation amplifier is designed and analyzed for biomedical applications.

1.1 Two-Stage Opamp Block Diagram

Figure 1a shows the two-stage opamp block diagram. A differential stage is incorporated with dual input that can be applied to both inverting as well as non-inverting input terminal which ultimately transforms differential inputs. The dissimilarity between the applied two input voltages is responsible for the production of voltage at the output end. As a result, single-ended is attained at output end.

Due to this single-ended output, we get a low output swing and less CMRR. Most of the opamp gain is due to differential stage gain that ultimately leads to the desired offset and noise performance. The gain provided by the differential stage is not enough. For further amplification, an additional stage is provided known as the common source stage [11].

If the single-ended output is not attained by the differential stage, the desired single-ended output can be made possible by the second stage. The output buffer stage ensures less output resistance and high output current. This stage is capable of driving huge load capacitances. The output buffer is unnecessary when capacitance loads are tiny. To drive higher capacitive loads, buffer stage is incorporated. The output buffer stage offers a large output swing.

Biasing ensures that all transistors are operated in a saturation region. To achieve high gain, various gain boosting techniques are adopted, but these techniques require schematics that are highly complex and consume high power. Output produced by the application of gain boosting techniques is bounded. If compensation is not inculcated, we cannot achieve opamp stability while employing opamp with closed-loop performance [12].

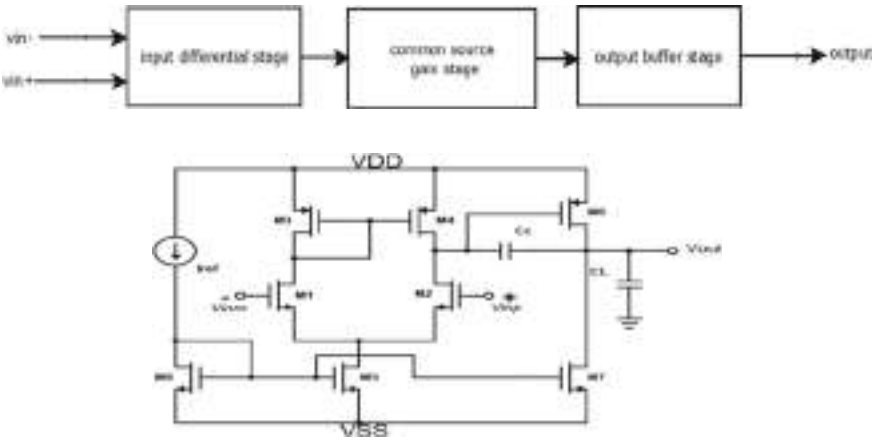

Fig. 1 **a** Figure shows the two-stage opamp block diagram. **b** Two-stage opamp schematic

1.2 Relationship Describing Operational Amplifier Performance

Step 1: Design procedure of opamp is started by choosing device length in an appropriate manner which is used in the entire circuit.

Step 2: To get a phase margin of sixty degrees (60º), compensation capacitor (C_C) must be 0.22 times greater than load capacitor (C_L).

Step 3: The value of tail current is measured with the help of slew-rate and compensation capacitor (C_C).

$$\text{Tail current (I)} = \text{compensation capacitor } (C_C) * \text{slew}-\text{rate}. \tag{1}$$

Step 4: Negative ICMR can be estimated using saturation voltage

$$\text{ICMR}(-) = [\sqrt{2I/\beta} + V_{t1}]_{\text{maximum}} + V_{\text{dsat}} \tag{2}$$

Step 5: Positive ICMR can be estimated as

$$\text{ICMR}(+) = [\text{VDD} + |V_{t3}|]_{\text{a minimim}} + V_{t1\ \text{minimum}} \tag{3}$$

Step 6: Saturation voltage V_{dsat} is calculated with the help of negative input common-mode rejection ratio

$$\text{Vdsat} = \text{ICMR}(-) - [\sqrt{2I/\beta} + V_{t1}]_{\text{maximum}}. \tag{4}$$

Step 7: The total amplifier gain can be calculated with the help of given specifications

$$\text{Differential stage gain } A_{V1} = -g_{m1}/g_{ds1} + g_{ds4}. \tag{5}$$

$$\text{Second stage gain } A_{V2} = -g_{m6}/g_{ds6} + g_{ds7}. \tag{6}$$

Step 8: The gain bandwidth of the product is given as

$$\text{Gain bandwidth (GB)} = g_{m1}/C_C \tag{7}$$

The above-mentioned steps are used to design a two-stage opamp. The designed opamp has the specifications as mentioned in Table 1. The corresponding aspect ratios of transistors are calculated using design specifications which are as shown in Table 2.

Table 1 Design specifications of Opamp

Opamp parameters	Specifications
Bandwidth	5 MHz
Load capacitance (CL)	10 pF
Slew-rate	10 V/μs
Maximum power dissipation	2 mW
Channel length	180 nm
Open loop gain	100 V/V = 40 dB
CMRR, PSRR	≥60 dB
Power supply	±1.8 V

Table 2 Designed opamp transistor ratio

Transistor	Aspect ratio
M1, M2	0.54/0.18
M3, M4	2.7/0.18
M5	0.81/0.18
M6	16.92/0.18
M7	2.52/0.18
M8	0.81/0.18

1.3 Conventional Two-Stage Operational Amplifier Schematic

Figure 1b depicts a schematic of a two-stage opamp. It encompasses two supply voltages and dual input terminals as well as an output terminal. M1 along with M2 are NMOS transistors, M3 accompanying M4 are PMOS transistors, these are availed to form the differential opamp stage. Depending upon the gain of the differential stage, the differential input signal applied across the gate terminals of transistors M1 (inverting input) and M2 (non-inverting input) gets amplified. The transistors M3 and M4 in the differential stage form current mirror circuit. The functionality of this circuit is it copies current from transistor M1 and gets deducted from transistor M2. Biasing is provided to transistors M8 along with M5 to guarantee transistors must function in the saturation region [13].

The majority gain of the opamp is contributed by the differential stage. To intensify the opamp gain further, it is supplemented with common source stage formed by transistors M6 and M7. The overall gain of opamp depends on output resistance of M3 and transconductance of transistors M1 and M3.

2 Different Two-Stage Opamp Topologies

2.1 Two-Stage Opamp with PMOS as Load in Common Source Stage

Figure 2a shows a two-stage opamp with PMOS load in the common source stage. In this topology, output of the first stage is given to NMOS transistor of the common source stage and PMOS transistor is considered as load. This topology offers less gain.

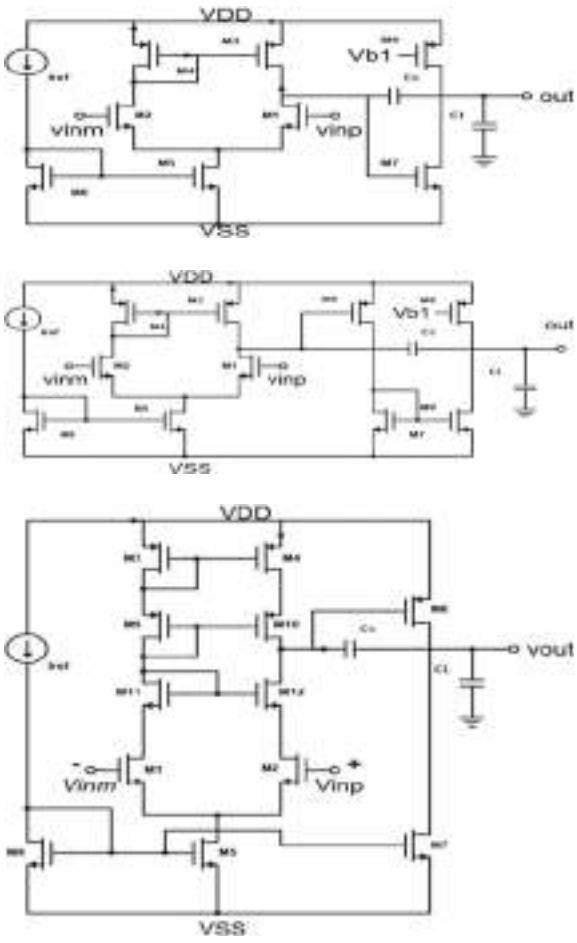

Fig. 2 **a** Two-stage opamp with PMOS load in common source stage **b** Two-stage opamp with active current mirror load in common source stage **c** Two-stage opamp with cascoded first stage

2.2 Two-Stage Opamp with Modified Second Stage

Figure 2b shows a two-stage opamp with active current mirror load in the common source stage. In this topology, common source stage is modified by incorporating active current mirror which is formed by the transistors M6, M7, M8, M9. This topology offers a high gain in comparison to other topologies.

2.3 Two-Stage Opamp with Cascoding First Stage

In this topology, amplifier gain can be increased by cascoding the first stage of the two-stage opamp formed by transistors M9, M10, M11, M12. The voltage gain of improved opamp is estimated by the product of the output resistance along with transconductance. The inverting input of the opamp is nothing but gate terminal of M1 transistor and non-inverting input is nothing but gate terminal of M2 transistor [14]. Two-stage opamp with cascoded first stage topology is shown in Fig. 2c. The voltage gain of modified opamp upto cascoded first stage is given as

$$A_{v1} = g_{m1}\left(g_{m2}r^2 d_{s2} || g_{m4}r^2 d_{s4}\right) \tag{8}$$

3 Instrumentation Amplifier Implementation Using Two-Stage Opamp

Instrumentation amplifiers are vital circuits in major VLSI applications. These circuits are utilized to eliminate common-mode interference and amplify low voltage level signals. In order to attain high accuracy, electronic applications need instrumentation amplifiers. Instrumentation amplifiers do not require input impedance matching, electronic equipment make use of this feature for testing and measurement. The term inamp is used as a short form for instrumentation amplifier [15].

Instrumentation amplifier mainly consists of three opamps. The instrumentation amplifier is made of an output terminal and two input terminals. The first two operational amplifier acts as the input stage, also called a buffer stage of instrumentation amplifier [16]. This stage mainly helps to increase input impedance and helps to avoid input impedance matching. This inamp is mainly classified into two stages, i.e., differential input stage which is formed by the first two operational amplifiers and difference stage formed by another operational amplifier [17].

Block diagram of the instrumentation amplifier is shown in Fig. 3a. Three opamps are typically used to form an instrumentation amplifier. To implement an instrumentation amplifier, an opamp has to be designed first. We generally use a two-stage opamp since a single-stage amplifier will have low gain. Presently, an instrumentation

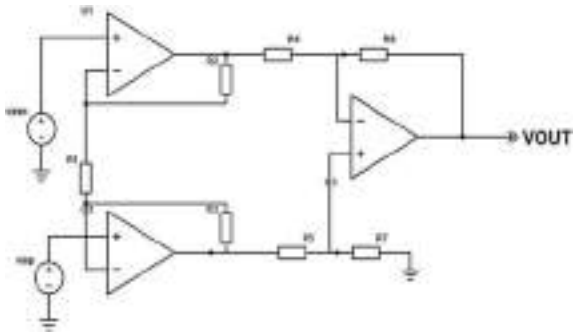

Fig. 3 **a** Block diagram of instrumentation amplifier

amplifier is presented incorporating 180 nm CMOS technology.

$$\text{Gain of instrumentation amplifier is given as } V_{output} = [(R_6/R_5) * (1 + 2R_2/R_{gain}) * (V_1 - V_2)]. \quad (9)$$

The values of resistors for instrumentation amplifier are chosen such that $R_{gain} = 1\ K\Omega$, R

$2 = R3 = 100\ K\Omega$, $R4 = R5 = 1\ K\Omega$, $R6 = R7 = 200\ K\Omega$.

Transient analysis: Transient analysis is executed for a two-stage opamp by applying differential inputs which is a sinusoidal signal having an amplitude 2 mV peak to peak and frequency of 40 Hz having a phase shift of 180 degrees, and between the two differential inputs, corresponding voltage gain is calculated.

$$\text{Differential mode voltage gain} = V_{output}/V_{input.}$$
$$\text{Gain in decibels} = 20 \log(V_{output}/V_{input})\ \text{dB} \quad (10)$$

AC analysis: AC analysis is performed by supplying input with the AC signal source. This analysis is used to analyze the frequency response of the designed schematic. Slew-rate is stated as the fraction of amount of variation in opamp output voltage for corresponding variation in time in input. Slew-rate units are expressed as V/μsec.

$$\text{Slew}-\text{rate} = (V2 - V1)/(T2 - T1)\text{V}/\mu\text{sec} \quad (11)$$

4 Results

4.1 Two-Stage Opamp and Implementation of Instrumentation Amplifier Results

Two-stage opamp is designed using LTspice tools employing 180 nm technology. Various performance parameters such as voltage gain, slew-rate, AC gain, and bandwidth calculations are done. Further, instrumentation amplifier is implemented using two-stage operational amplifier, and inamp gain and 3 dB frequency are calculated which is shown in Fig. 4a–f.

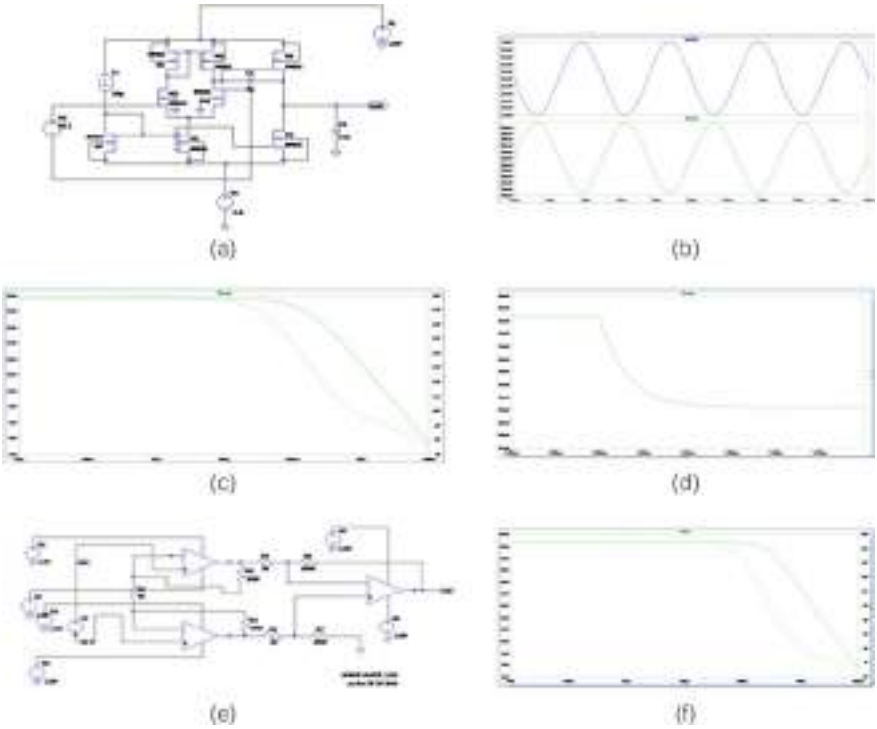

Fig. 4 **a** Figure shows two-stage opamp schematic, **b** Transient analysis, **c** AC analysis, **d** Slew-rate and bandwidth calculation, **e** Implementation of two-stage instrumentation amplifier using conventional two-stage opamp, **f** Gain and bandwidth calculation of inamp

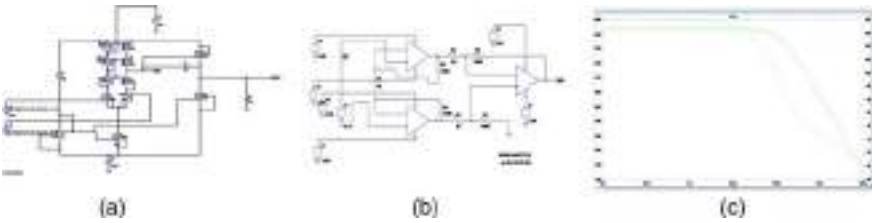

Fig. 5 **a** Two-stage opamp with cascoding first stage. **b** Inamp implementation. **c** AC analysis of inamp

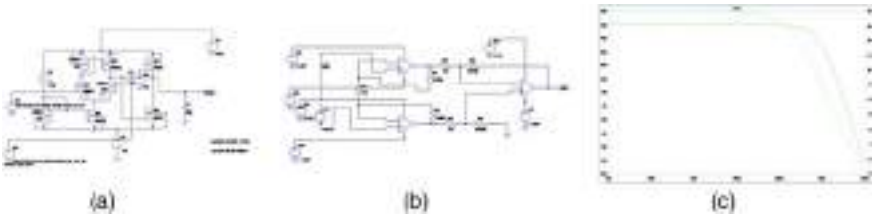

Fig. 6 **a** Two-stage opamp with PMOS as load in common source amplifier, **b** Inamp implementation, **c** AC analysis of inamp

4.2 Two-Stage Opamp with Cascoding First Stage and Implementation of Instrumentation Amplifier Results

4.3 Implementation of Instrumentation Amplifier with PMOS as Load in Common Source Amplifier

4.4 Implementation of Instrumentation Amplifier with Active Current Mirror Load in Common Source Amplifier

Two-stage opamp with various topologies and implementation of instrumentation amplifier using various opamp topologies are shown in Figs. 5, 6, and 7. Various performance parametrics are calculated and shown in Table 3.

5 Comparison of Performance Metrics

From the table, a two-stage opamp with cascoding first stage offers high voltage gain and AC gain compared to other topologies. 3 dB frequency is high for two-stage opamp with PMOS load in CS stage amplifier. Instrumentation amplifier parameters such as gain and 3 dB frequency are calculated, and it is large for two-stage opamp

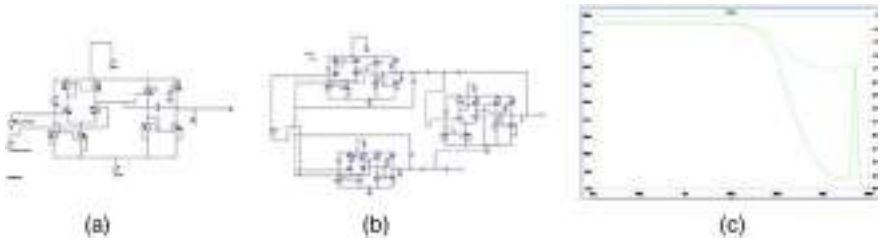

Fig. 7 **a** Two-stage opamp with active current mirror load in CS stage, **b** Inamp implementation, **c** AC analysis of inamp

Table 3 Comparison of various opamp topologies

Performance parameters	Conventional two-stage opamp	Two-Stage opamp with PMOS load in CS stage	Two-stage opamp with active current mirror load in CS stage	Two-stage opamp with cascoding first stage
Voltage gain (dB)	41.06	22	42.14	58.97
AC gain (dB)	34.88	20.8	36	53.39
3 dB frequency (KHz)	157.29	892.9	477.07	24.6
Slew-rate (V/μsec)	0.007	0.299	0.913	0.0194
Inamp gain (dB)	61.847	28	59.4	83.072
Inamp 3 dB Frequency (KHz)	236.977	593.86	10.4	83.24
Average power	6.3 nW	4.2 fW	1.08f W	7.291 nW

with cascoding the first stage. Other performance parameters such as slew-rate, average power consumption are calculated and compared.

6 Conclusion

In the present study, a two-stage operational amplifier using various topologies is designed and verified using LTspice tools in 180 nm technology. There has always been a tradeoff between the gain and bandwidth of the amplifier. Performance parameters of a two-stage operational amplifier such as slew-rate, voltage gain, AC gain, and bandwidth parameters were calculated. Further, using these different two-stage operational amplifier topologies, instrumentation amplifier is implemented. Among all these topologies, inamp implemented employing two-stage opamp with PMOS load in common source stage exhibits less gain which is undesirable. Inamp implemented using two-stage opamp with active current mirror load exhibits a gain 59.4 dB

and bandwidth 10 kHz. This inamp circuit can be used to amplify signals that possess much smaller amplitudes usually in biomedical signal acquisition systems. Inamp implemented using two-stage opamp with cascoding the first stage offers a high gain of 83.2 and 3 dB frequency 83 kHz. This high gain inamp can be used for the applications such as ECG (electrocardiogram) by adding filters to it.

References

1. B. Razavi, *Design of Analog CMOS Integrated Circuits* (Mcgraw-Hill, New York, 2000)
2. S. Saman, Two-stage CMOS operational amplifier: analysis and design. Int. J. Comput. Eng. Res. **3**(1) (2019)
3. S. Kothapalli, M. Samson, M. Sankararao, A novel approach for high gain instrumentation amplifier in $\Delta\Sigma$ ADC. Mater. Today: Proceed. (2020)
4. S. Kothapalli, M. Samson, S. Majji, T.R. Patnala, S.R. Karanam, C.S. Pasumarthi, Comparative experimental analysis of different op-amps using 180 nm CMOS technology, in *2020 International Conference on Emerging Trends in Information Technology and Engineering (ic-ETITE)* (Vellore, India, 2020)
5. S. Kundeal, S. Priyanka, A. Kundra, Low power folded cascode OTA. Int. J. VLSI Des. Commun. Syst. **3**(1) (2012)
6. S. Kumar, A. Sharma, Design of CMOS operational amplifier in 180 nm technology. Int. J. Innov. Res. Comput. Commun. Eng. **5**(4) (2017)
7. K. Yoshioka, T. Sugimoto, N. Waki, Digital amplifier: a power-efficient and process scaling amplifier for switched capacitor circuits. IEEE Trans. Very Large Scale Integr. Syst. **27**(11) (2019)
8. R. Rao, D. Nageshwarrao, Implementation and simulation of CMOS two stage operational amplifier. Int. J. Adv. Eng. Technol. (2013)
9. R.K. Baruah, Design of a low power low voltage CMOS opamp. Int. J. VLSI Des. Commun. Syst. (VLSICS) **1**(1) (2010)
10. P. Kora, ECG based myocardial infarction detection using hybrid firefly algorithm. Comput. Methods Programs Biomed. **152**, 141–148 (2017)
11. A.K. Pardeep, Design and performance analysis of two-stage opamp under impact of scaling. Int. J. Res. Appl. Sci. Eng. Technol. **5** (2017)
12. V. Goel, S.K. Surshetty, Design of an area efficient and high gain CMOS instrumentation amplifier for VLSI applications. Innov. Power Adv. Comput. Technol. (2019)
13. D.A. Johns, K. Martin, *Analog Integrated Circuit Design* (Wiley, New York, 1997)
14. D. Mukherjee, R. Chatterjee, Design of two-stage CMOS operational amplifier in 180 nm technology with low power and high CMRR. Int. J. Recent Trends Eng. Technol. **11** (2014)
15. M. Konar, R. Sahu, S. Kundu, *Improvement of the Gain Accuracy of the Instrumentation Amplifier Using a Very High Gain Operational Amplifier, 2019 Devices for Integrated Circuit (DevIC)* (Kalyani, India, 2019)
16. B.R.B. Jawanth, G.S. Santhosh, A comparative analysis of CMOS amplifiers for ECG signals. Int. Res. J. Eng. Technol. **6** (2019)
17. O.V. Krishna, Design and implementation of instrumentation amplifier for EEG in 180 nm CMOS technology. CVR J. Sci. Technol. **8** (2015)

CMOS CDBA-Based Low-Voltage Low-Power Universal Filter

Komal, Ramnish Kumar, and K. L. Pushkar

Abstract A new resistor-less current differencing buffered amplifier (CDBA)-based voltage-mode (VM) Multifunction filter is proposed with single CDBA, three NMOS transistors and two capacitors. The presented filter circuit implements all standard filter responses without altering the circuit properties. The study of non-idealities and parasitic effects of the CDBA and their effect on transfer function is also carried out. This circuit also proves to give adequate response even in the presence of non-idealities and process parameter variations. The presented circuit is having low ($\leq$0.5) sensitivity. The proposed circuit feasibility has been justified by using PSPICE 0.18 μm CMOS technology with supply voltage $\pm$0.6 V and power dissipation of 171 μW.

Keywords CDBA · Universal filter · Voltage-Mode (VM)

1 Introduction

In modern centuries, there are ample struggles to decay the voltage and the power consumption of the circuits. In the present era, in the field of circuit designing, analog active filters play an important role in research. Universal filters are the most useful analog building blocks with abundant applications in communication, control system and instrumentation system. CDBA, a CM device has been implemented by Acar and Ozoguz [1]. CDBA has various applications in signal processing and signal generation circuits. CDBA has the following properties: high SR, wide BW, unity gain voltage and current amplifier, so this CDBA is also used in mixed circuit applications. CDBA device is used in designing of square rooting circuits [2], quadrature oscillator circuits [3], poly phase filters [4], synthetic floating inductance circuits

Komal (✉) · R. Kumar
Department of Electronics and Communication Engineering, Guru Jambheswar University of Science and Technology, Hisar, Haryana, India

K. L. Pushkar
Department of Electronics and Communication Engineering, Greater Noida Institute of Technology (Affiliated to GGSIP University, Delhi), Greater Noida 201306, Uttar Pradesh, India

S. Rawat et al. (eds.), *Proceedings of First International Conference on Computational Electronics for Wireless Communications*, Lecture Notes in Networks and Systems 329,
https://doi.org/10.1007/978-981-16-6246-1_11

[5] and analog multiplier [6]. Some other multifunction filter containing CDBA as an active device was available in literature [7–11]. However, they used more than two CDBAs to realize multifunction filter responses. Sadri et al. (2002) present the current mode multifunction filter with single CDBA, 3 resistors and 2 capacitors. This circuit implements only three filter responses (LP, HP and BP) [7]. Ali Umit Keskin and Erhan Hancioglu (2005) present current mode universal filter with two CDBAs, 4 resistors and 4 capacitors [8]. Ozoguz et al. (1999) present a fully integrated multifunction filter using two CDBAs and 4 MOS resistors. The proposed circuit realizes LP, HP and BP responses only [9]. Worapong Tangsrirat et al. (2008) present universal filter using two CDBAs, 4R and 2C. The circuit realizes filter responses [10]. Jitender Pathak et al. (2013) present a VM universal filter using two CDBAs, 4R and 2C passive components. The proposed circuit realizes all five filter responses [11]. Cakir, Shahram Minaei and Oguzhan Cicekoglu (2010) present AP and NF responses using single CDBA and 3R and 2C [12]. Hence, the aim of this paper is to present a new low-voltage low-power-based single CDBA universal filter, which can realize filter responses. This CMOS CDBA structure has less number of transistors as previously used CDBA structures. The proposed circuit feasibility has been justified by using PSPICE 0.18 μm CMOS technology with supply voltage ±0.6 V and power dissipation of 171 μW. Table 2 shows the comparison with other presented multifunction filters by different analog building blocks.

2 The Presented Circuit Configuration

The block diagram of CDBA is presented in Fig. 1a, CDBA device having two input terminals P and N, two output terminals W and Z. The equivalent model of CDBA is presented in Fig. 1b. CDBA characteristic equation is given below (Fig. 2).

$$\begin{bmatrix} V_P \\ V_N \\ I_Z \\ V_W \end{bmatrix} = \begin{bmatrix} 0 & 0 & 0 & 0 \\ 0 & 0 & 0 & 0 \\ \beta_P & -\beta_N & 0 & 0 \\ 0 & 0 & \alpha & 0 \end{bmatrix} \begin{bmatrix} I_P \\ I_N \\ V_Z \\ I_W \end{bmatrix} \tag{1}$$

CDBA can be defined by Eq. (1), i.e., $I_Z = \beta_P I_P - \beta_N I_N V_W = \alpha V_Z$, $V_P = V_N = 0$. β_P and β_N are current gain and α is voltage gain. Ideally, the current and voltage gain is equal to unity. The current difference of terminals P and N are flows through Z-terminal. The voltage at W-terminal follows the voltage at Z-terminal, it is called output voltage. The output impedance at W-terminal is ideally zero.

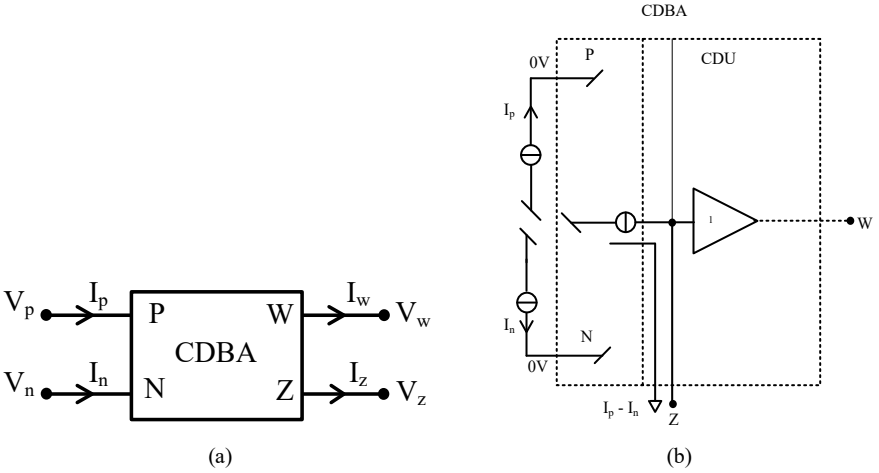

Fig. 1 **a** Block diagram **b** Equivalent model

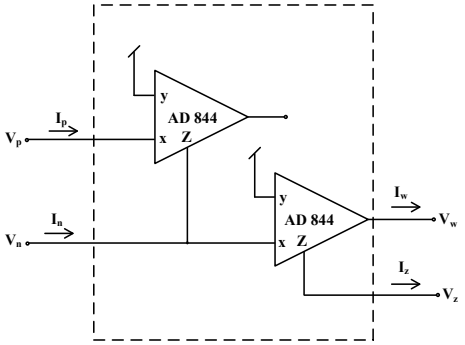

Fig. 2 Implementation of CDBA using AD844 (CFOAs)

2.1 MOS-Based Resistor Topology

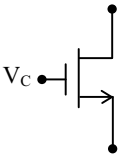

This MOS-based active resistor topology is used to design resistor-free circuit.

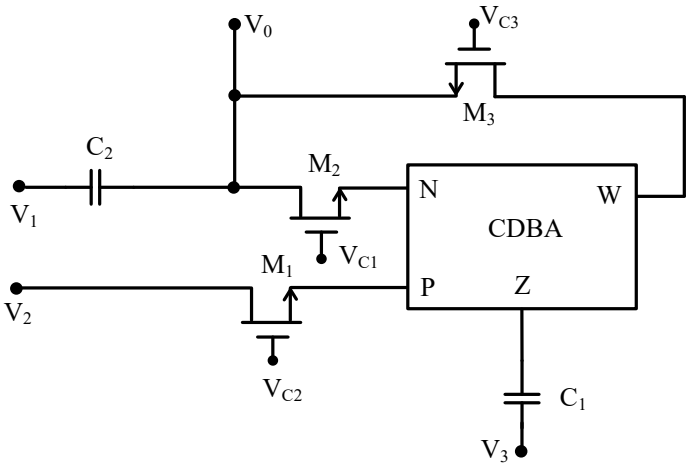

Fig. 3 Presented multifunction filter

$$R_{MOS} = \frac{1}{\mu_n C_{ox}\left(\frac{W}{L}\right)(V_C - V_{THn})} \tag{2}$$

where μ_n is the mobility of the free electron, C_{ox} is the gate-oxide capacitance per unit area, W and L are the effective channel width and length, V_{THn} is the threshold voltage of the NMOS and V_C is the DC voltage used for tuning of R_{MOS}. When we replace the resistor with *MOS*, then there must be area reduced. The proposed circuit of multifunction filter is shown in Fig. 3.

The study and analysis of Fig. 3 gives this transfer function.

$$V_0 = \frac{V_1 s^2 + V_3 s\left(\frac{1}{CR_{MOS}}\right) + V_2\left(\frac{1}{C^2R_{MOS}^2}\right)}{s^2 + s\left(\frac{2}{CR_{MOS}}\right) + \frac{1}{C^2R_{MOS}^2}} \tag{3}$$

$$R_{MOS1} = R_{MOS2} = R_{MOS3} = R_{MOS}$$
$$and \quad C_1 = C_2 = C$$

$$\omega_0 = \frac{1}{CR_{MOS}} \tag{4}$$

$$BW = \frac{2}{CR_{MOS}} \tag{5}$$

From calculation (3), different filter responses can be realized as:
$V_1 = V_3 = 0$ and $V_2 = V_{\text{in}}$, then realized as a Low pass filter (LPF).
$V_2 = V_3 = 0$ and $V_1 = V_{\text{in}}$, then realized as a High pass filter (HPF).
$V_1 = V_2 = 0$ and $V_3 = V_{\text{in}}$, then realized as a Band pass filter (BPF).

$V_3 = 0$ and $V_1 = V_2 = V_{\text{in}}$, then realized as a Band reject pass filter (BRF).
$V_1 = V_2 = V_{\text{in}}$ and $V_3 = -V_{\text{in}}$, then realized as an All pass filter (APF).

3 Non-ideal Analysis

The practical CDBA can be described by the Eq. (1), when we consider non-idealities then takes current and voltage tracking errors at P, N and Z terminals. These are less than unity.

Transfer function after including the non-idealities

$$V_0 = \frac{V_1\left[s^2 + s\left(\frac{1}{R_Z(C_1+C_Z)}\right)\right] + \frac{sC_1\alpha V_3}{C_2(C_1+C_Z)(R_{MOS3}+R_W)} + \frac{\alpha\beta_P V_2}{(R_{MOS2}+R_P)C_2(C_1+C_Z)(R_{MOS3}+R_W)}}{s^2 + s\left(\begin{array}{l}\frac{1}{C_2(R_{MOS3}+R_W)}+ \\ \frac{1}{C_2(R_{MOS1}+R_N)} \\ +\frac{1}{R_Z(C_1+C_Z)}\end{array}\right) + \left(\begin{array}{l}\frac{1}{C_2R_Z(C_1+C_Z)(R_{MOS1}+R_N)}+ \\ \frac{\alpha\beta_N}{(R_W+R_{MOS3})(C_1C_2+C_2C_Z)(R_{MOS1}+R_N)} \\ +\frac{1}{(C_1C_2+C_2C_Z)(R_W+R_{MOS3})R_Z}\end{array}\right)} \tag{6}$$

Natural frequency ($\dot{\varphi}0$)

$$\omega_0 = \sqrt{\frac{(R_W + R_{MOS3}) + \alpha\beta_N R_Z + (R_{MOS1} + R_N)}{C_2R_Z(C_1+C_Z)(R_{MOS1}+R_N)(R_W+R_{MOS3})}} \tag{7}$$

The impedances seen (Fig. 4) at terminals of CDBA are shown in Figs. 5, 6, 7 and 8.

Parasitic capacitances at N, P and W-terminals have negligible effect as shown in Figs. 5, 6, 7, but parasitic capacitance at Z-terminal is measured at high frequency as shown in Fig. 8.

$$Z_Z = \frac{R_Z}{1 + sC_ZR_Z}$$

$$|Z_Z| = \frac{R_Z}{\sqrt{1 + \omega^2C_Z^2R_Z^2}}$$

C_Z is measured at high frequency where the effect is predominant. Impedance seen through Z-terminal is very high (Rmos $< R_Z$ and $C1 = C2 > C_Z$).

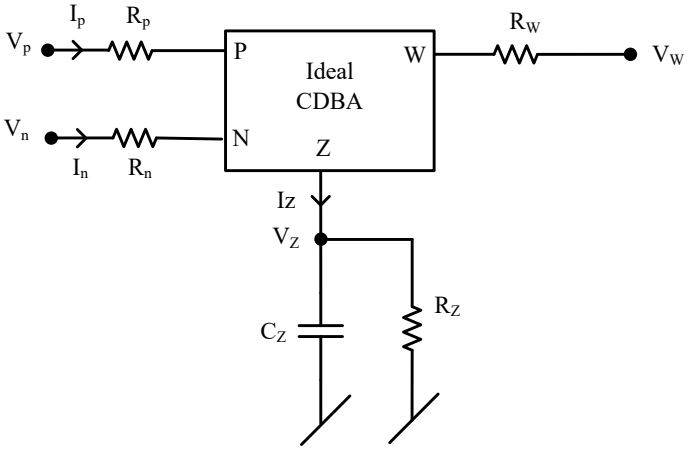

Fig. 4 Non-ideal CDBA

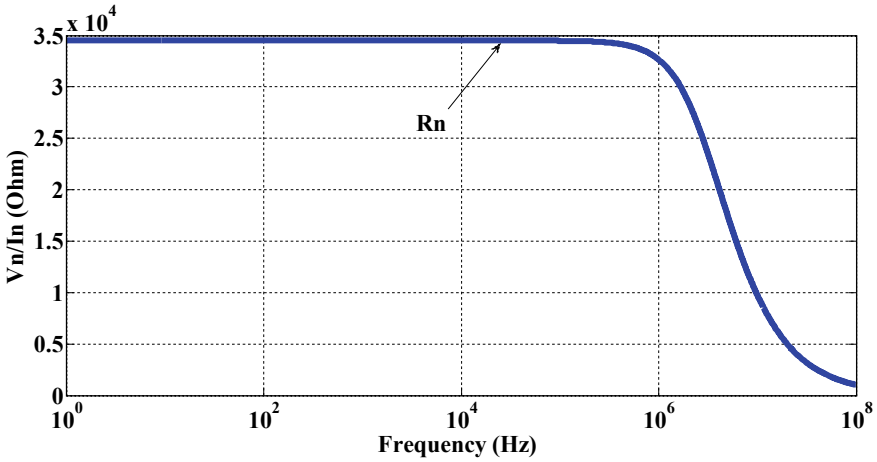

Fig. 5 Impedance at N-terminal

3.1 Sensitivity Analysis

Sensitivity is a significant parameter to define the circuit performance. The sensitivities of natural frequency with respect to different active and passive components are calculated as:

$$\omega_0 = \sqrt{\frac{A}{B}} \tag{8}$$

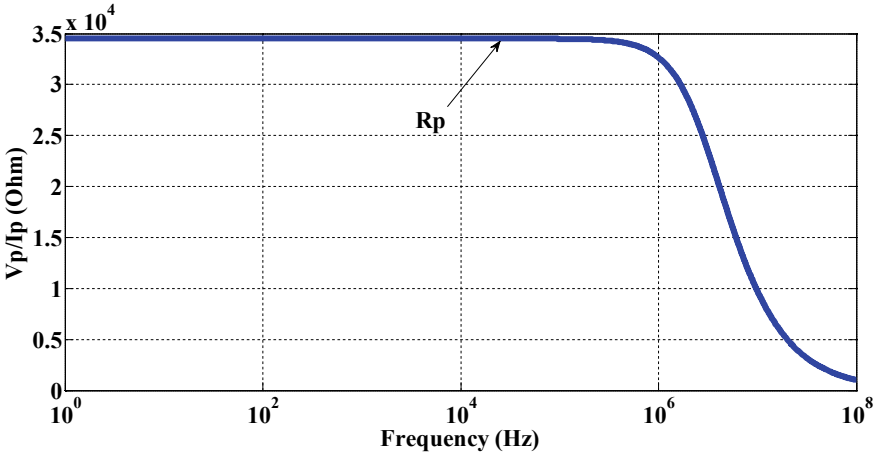

Fig. 6 Impedance at P-terminal

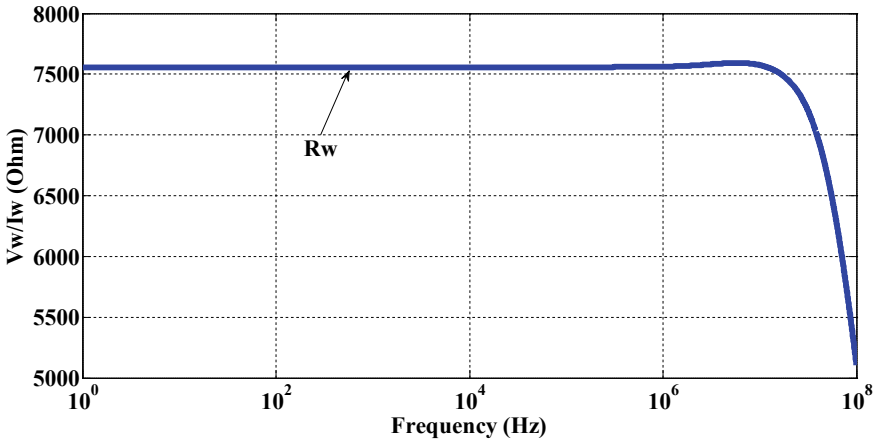

Fig. 7 Impedance at W-terminal

$A = (R_W + R_{MOS3}) + \alpha\beta_N R_Z + (R_{MOS1} + R_N).$
$B = C_2 R_Z (C_1 + C_Z)(R_{MOS1} + R_N)(R_W + R_{MOS3})$

$$S_{C_1}^{\omega_0} = -\frac{1}{2}\frac{C_1}{C_1 + C_Z} \tag{9}$$

$$S_{C_2}^{\omega_0} = -\frac{1}{2} \tag{10}$$

$$S_{C_Z}^{\omega_0} = -\frac{1}{2}\frac{C_Z}{C_1 + C_Z} \tag{11}$$

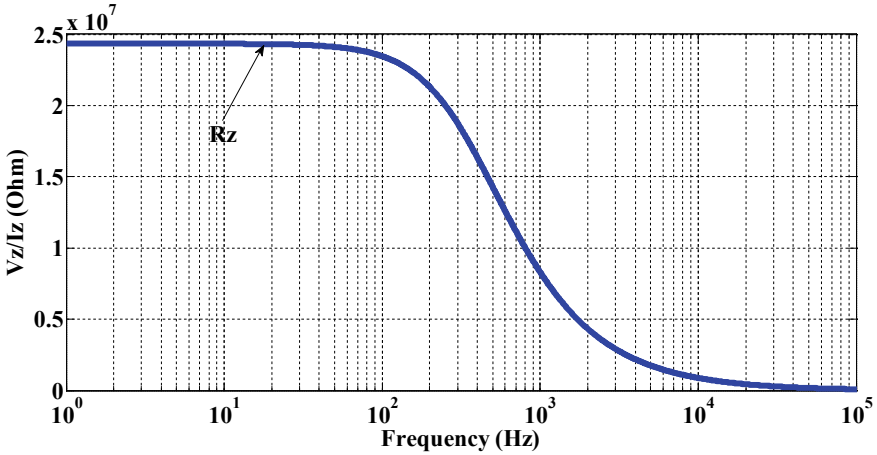

Fig. 8 Impedance at Z-terminal

$$S_{R_{MOS1}}^{\omega_0} = \frac{1}{2}\left(\frac{R_{MOS1}}{A} - \frac{R_{MOS1}}{R_{MOS1} + R_N}\right) \tag{12}$$

$$S_{R_{MOS3}}^{\omega_0} = \frac{1}{2}\left(\frac{R_{MOS3}}{A} - \frac{R_{MOS3}}{R_0 + R_{MOS3}}\right) \tag{13}$$

$$S_{R_W}^{\omega_0} = \frac{1}{2}\left(\frac{R_W}{A} - \frac{R_W}{R_W + R_{MOS3}}\right) \tag{14}$$

$$S_{R_N}^{\omega_0} = \frac{1}{2}\left(\frac{R_N}{A} - \frac{R_N}{R_{MOS1} + R_N}\right) \tag{15}$$

$$S_{R_Z}^{\omega_0} = \frac{1}{2}\left(\frac{\alpha\beta_N R_Z}{A} - 1\right) \tag{16}$$

$$S_{\alpha}^{\omega_0} = \frac{1}{2}\left(\frac{\alpha\beta_N R_Z}{A}\right) \tag{17}$$

$$S_{\beta_N}^{\omega_0} = \frac{1}{2}\left(\frac{\alpha\beta_N R_Z}{A}\right) \tag{18}$$

After considering the parasitic effects and using the values of parasitic impedances, the active and passive sensitivities are very low (<0.5).

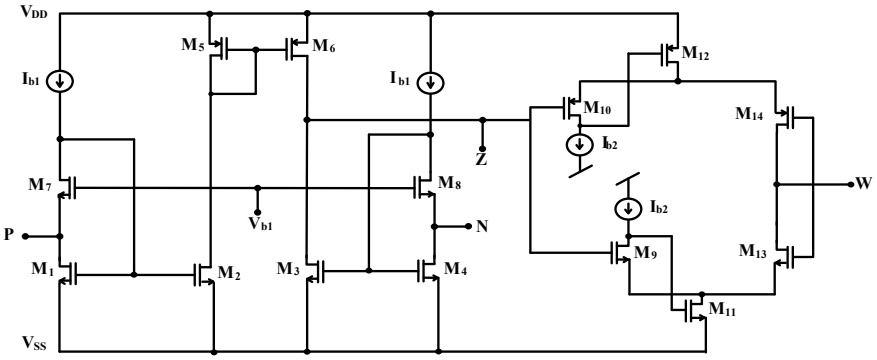

Fig. 9 CMOS Implementation of CDBA $V_{dd} = V_{ss} = 0.6$ V, $Ib1 = 56$ μA, $Ib2 = 84$ μA, $V_{b1} = 0.9$ V [12]

Table 1 *W/L* ratio of presented CMOS CDBA

Transistors	W (μm)	L (μm)
M_1–M_4	3.6	1.80
M_5–M_8	180	1.80
M_9	45	0.36
M_{10}, M_{12}, M_{14}	240	0.36
M_{11}, M_{13}	72	0.36

4 Simulation Results

The presented VM multifunction filter was verified by software simulations with the CMOS implementation of CDBA [12] as shown in Fig. 9. The design transistor is modeled by TSMC 0.18 μm. CMOS process parameters are $V_{THn} = 0.3725$ V, $\mu_n = 259.5304$ cm^2/(V.s), $T_{ox} = 4.1$ nm. Table 1 shows the W/L ratios of transistors. The values of passive components $C_1 = C_2 = 1$nf, and $R_{MOS1} = R_{MOS2} = R_{MOS3} = 1.45$ kΩ are obtained with the aspect ratio $W/L = 6.36/1.08$ μm and DC control voltage $V_C = 0.9$ V. The PSPICE simulated frequency response is shown in Fig. 10 (Table 2).

5 Conclusion

A new resistor-less CDBA-based VM universal filter is proposed using single CDBA, three NMOS transistors and two GCs (grounded capacitors). The presented filter circuit implements all filter responses without altering the circuit properties. The study of non-idealities and parasitic effects of the CDBA and their effect on transfer function is also carried out. This circuit also proves to give adequate response even

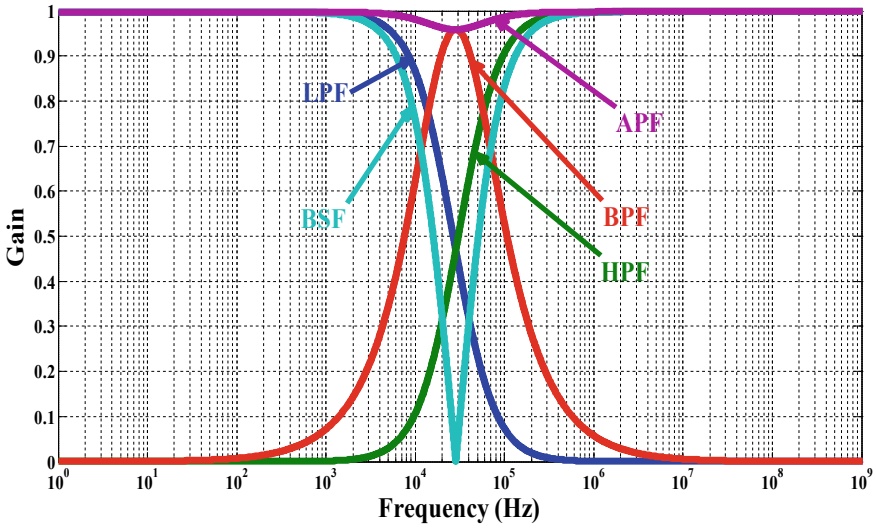

Fig. 10 Frequency response of proposed filter

in the presence of non-idealities and process parameter variations. The proposed circuit is easily verified using commercially available IC AD844 (CFOA) as shown in Fig. 2. The presented circuit is less sensitive because all the components have less than unity sensitivity. The presented circuit feasibility is justified using pspice 0.18 μm CMOS technology with supply voltage ±0.6 V and power dissipation of 171 μW.

Table 2 Comparison of previously presented filters

Refs.	No. of ABBs	C/R	No. of transistors used	Output mode	Filter responses	DC power supply (V)
[7]	1 CDBA	2/3	20	CM	LP, HP, BP	±10
[8]	2 CDBAs	3/4	40	CM	LP, HP, BP, BR, AP	±2.5
[9]	2 CDBAs	2/0	40	CM	LP, HP, BP	±10
[10]	2 CDBAs	2/4	40	VM	LP, HP, BP, BR, AP	±2.5
[11]	2 CDBAs	2/4	40	VM	LP, HP, BP, BR, AP	±1
[12]	1 CDBA	2/3	14	VM	AP, NF	±0.6
[13]	1 DVCCTA	2/3	24	VM	LP, HP, BP, BR, AP	±0.9
[14]	4 MO-OTAs	2/0	84	CM	LP, HP, BP, BR, AP	±2.5
[15]	3 MO-CCIIs	2/5	48	CM	LP, HP, BP, BR, AP	±1.25
[16]	1 CDTA	2/3	22	CM	LP, HP, BP, BR, AP	±1
[17]	1 VDIBA	2/1	6	VM	LP, HP, BP, BR, AP	±0.9
[18]	1 CDTA	2/3	23	VM	LP, HP, BP, BR, AP	±3
[19]	1 VD-DIBA	2/1	22	VM	LP, HP, BP, BR, AP	±2
[20]	1 UVC	2/2	40	VM	LP, HP, BP, BR, AP	±1.9
Proposed work	1 CDBA	2/0	14	VM	LP, HP, BP, BR, AP	±0.6

References

1. C. Acar, S. Ozoguz, A new versatile building block current differencing buffered amplifier suitable for analog signal processing filters. Microelectron. J. **30**, 157–160 (1999)
2. J.K. Pathak, A.K. Singh, R. Senani, New suaring and square-rooting circuits using CDBA. Am. J. Electr. Electron. Eng. **2**(6), 175–179 (2014)
3. A.U. Keskin, C. Aydin, E. Hancioglu, C. Acar, Quadrature oscillator using current differencing buffered amplifiers (CDBA). Frequenz **60**, 3–4 (2006)
4. M. Sagbas, Design of CDBA-based active polyphase filter for low-IF receiver applications. Turk. J. Elec. Eng. Comp. Sci. **19**(4), 565–574 (2011)
5. A.U. Keskin, E. Hancioglu, CDBA-based synthetic floating inductance circuits with electronic tuning properties. ETRI J. **27**(2), 239–242
6. A.U. Keskin, A four quadrant analog multiplier employing single CDBA. Analog Integr. Circ. Sig. Process. **40**, 99–101 (2004)

7. C. Acar, H. Kuntman, S. Ozoguz, Cascadable current mode multipurpose filters employing current differencing buffered amplifier (CDBA). Int. J. Eelectron. Commun. **56**(2), 67–72 (2002)
8. A.U. Keskin, E. Hancioglu, Current mode multifunction filters using two CDBAs. Int. J. Eelectron. Ccommun. **59**, 495–498 (2005)
9. S. Ozoguz, A. Toker, C. Acar, Current-mode continuous-time fully integrated universal filter using CDBAs. Electron. Lett. **35**(2), 97–98 (1999)
10. W. Tangsrirat, T. Pukkalanun, W. Surakampontorn, CDBA-based universal biquad filter and quadrature oscillator. Act. Passive Electron. Compon. **6**. Article ID 247171 (2008)
11. J.K. Pathak, A.K. Singh, R. Senani, New voltage mode universal filters using only two CDBAs. Active Passive Electron. Compon. **6** (2013). Article ID 987867
12. C. Cakir, S. Minaei, O. Cicekoglu, Low voltage low power CMOS current differencing buffered amplifier. Analog Integr. Circ. Sig. Process **62**, 237–244 (2010)
13. H.P. Chen, S.F. Wang, Voltage mode biquadratic filters using DDCCTA. Int. J. Eelectron. Ccommun. **70**, 491–499 (2016)
14. D.R. Bhaskar, A.K. Singh, R.K. Sharma, R. Senani, New OTA-C universal filter current mode/trans-admittance biquads. ICICE Electron. Express. **2**(1), 8–13 (2005)
15. J.W. Horng, Current-mode and transimpedance-mode universal biquadratic filter using multiple outputs CCIIs. Ind. J. Eng. Mater. Sci. **17**, 169–174 (2010)
16. D. Prasad, D.R. Bhaskar, A.K. Singh, Universal current-mode biquad filter using dual output current differencing transconductance amplifier. Int. J. Electron. Ccommun. **63**, 497–501 (2009)
17. K.L. Pushkar, D.R. Bhaskar, D. Prasad, Voltage-mode new universal biquad filter configuration using a single VDIBA. Circ. Syst. Sig. Process. **33**, 275–285 (2013)
18. D. Prasad, D.R. Bhaskar, A.K. Singh, Multi-function biquad using current differencing transconductance amplifier. Analog Integr. Circ. Sig. Process. **61**, 309–313 (2009)
19. K.L. Pushkar, D.R. Bhaskar, D. Prasad, Voltage-mode universal biquad filter employing single voltage differencing differential input buffered amplifier. Circ. Syst. **4**, 44–48 (2013)
20. K.L. Pushkar, K. Gupta, MISO-type voltage-mode universal biquadratic filter using single universal voltage conveyor. Circ. Syst. **8**, 227–236 (2017)

A Case Study and Review on Current Trends in Solar Energy: Path to a Greener Environment

Aisha Joshna and Ravishankar Dudhe

Abstract The way energy can be captured is by using photovoltaics. It will enable us to use the natural resources that are available around us rather than being dependent on fossil fuel and oils. We focus on the renewable source that is the light. A solar-powered house and the requirements to make the same has been familiarized and understood to design AC- and DC-based solar systems and compare the same. Materials used to create are silicon based, and now there are many emerging materials that can be used to capture light. The material that is effective and probably even more than silicon is called perovskite. Then, we look at the technologies that are making significant changes in the photovoltaics sector. Such technologies are 3D Printed Solar Panels that will help in cutting cost and create solar panels faster and 3D Printed Solar Trees that will mimic trees and help capture energy from all around its surroundings.

Keywords Inverter · Charge controller · Thin-film · Perovskite · 3D-Printing · Solar energy tree

1 Introduction

To provide a clean, sustainable, and reliable energy, we need to depend on natural resources. Companies are finding ways to harvest energy from the environment as all other resources are starting to reduce [1]. In order to run factories, charge appliances, we need electricity. The world as we know it today is depending on find alternatives that can help power appliances. The use of fossil fuels and oils will not last forever and soon can cause a lot of downfall [2]. That is why, when photovoltaics was introduced, this would convert the light from the sun to electricity. The light is an unlimited source of energy and is widely available free of cost. This method reduces the need of parts, reduces pollution, and increases the use of unlimited resources around us more effectively [3]. A case study on the DC and AC solar energy system has been performed to conclude that DC systems are more affordable than AC systems. This

A. Joshna · R. Dudhe (✉)
Manipal Academy of Higher Education, Dubai, UAE
e-mail: ravishankar.dudhe@manipaldubai.com

S. Rawat et al. (eds.), *Proceedings of First International Conference on Computational Electronics for Wireless Communications*, Lecture Notes in Networks and Systems 329,
https://doi.org/10.1007/978-981-16-6246-1_12

study is supported with the monthly and yearly electricity bill amount calculations, to further familiarize with the return of interest in both the cases, DC and AC solar systems. We look at the various technologies that can be implemented to harvest the sun energy. Before that, we can see that a vast number of materials have been wasted when it comes to creating the photovoltaic appliances. Passive systems use the energy from sunlight directly. Using a 3D printer can increase efficiency and can create the desired products faster and with minimum wastage of materials. The reason for this is to reduce the time taken to create it and prototypes can be created with ease. We have 3D printed solar energy trees. These leaves will be able to capture light, the wind, and heat temperature variations. This can change the way how energy can be harvested and thus can produce electricity in greater quantities.

2 A Case Study on the Effective Use of Solar Energy: Understanding the Dc and Ac Characteristics

The objectives of conducting this case study are to design a cost-effective solar power system for house/office/workplace, to design for low carbon emission environment friendly system, and to study cost effectiveness through DC power system and AC power system comparison. This case study is performed on a 3BHK apartment to design the ac solar system and dc solar system that can be incorporated.

The list of house-hold items included for the comparison study includes refrigerator, microwave oven, blender, tabletop water dispenser hot and cold, TV, washing machine, lighting fixtures, HVAC (FCU, CU, W/H), and laptop and mobile chargers.

2.1 Ac Solar System

The block diagram of an AC solar system comprises of the following components (see Fig. 1).

The following Table 1 shows the AC load calculations for all the appliances at home.

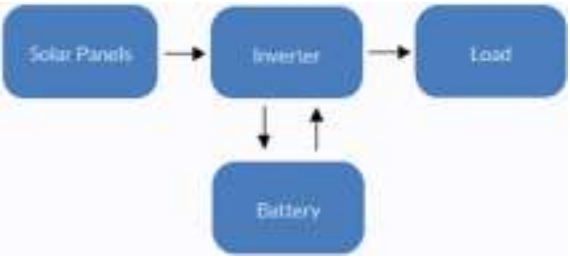

Fig. 1 AC solar system block diagram

Table 1 AC load calculations (power and energy usage)

Ac load calculations					
S. No	Name of appliance	Number of appliances	Power (wattage)	User per day (Hours)	Per day Wh uage
Kitchen					
1	Refrigerator	1	350	24	8400
2	Microwave oven	1	1500	1	1500
3	Blender	1	600	0.3333	199.98
4	Table top water dispenser hot and cold	1	630	5	3150
Total for Kitchen					13,249.98
Hall					
5	TV	1	200	8	1600
Washroom					
6	Washing machine	1	450	0.75	337.5
Lighting					
7	Lighting fixture with three bulbs (hall)	2	10 * 3 * 2 = 60	7	420
8	Lighting fixture (bath)	3	6 * 3 = 18	1	18
9	Tube light (bath)	3	10 * 3 = 30	0.5	15
10	Lighting fixture with three bulbs (bedroom)	3	10 * 3 * 3 = 90	6	540
11	60 cm x 60 cm LED panel light (kitchen)	1	60	2	120
12	LED light fixtures (Hallway)	4	6 * 4 = 24	3	72
Total for lighting					1185
HVAC					
13	Fan Coil Unit (FCU)	2	870 * 2 = 1740	5	8700
14	Coil Unit (CU)	2	4190 * 2 = 8380	5	41,900
15	Water Heater (W/H)	3	1200 * 3 = 3600	0.25	900
Total for HVAC					51,500
Other equipments					
17	Laptop charger	2	65	6	390

(continued)

Table 1 (continued)

Ac load calculations					
S. No	Name of appliance	Number of appliances	Power (wattage)	User per day (Hours)	Per day Wh uage
18	Mobile charger	4	6	2	12
Total for other qquipments					402
Total load in Wh					68,274.48
Total load in KWh					68.27448

AC solar system design (Calculation of power and energy):

$$Power\ or\ Wattage\ =\ Current\ \times\ Voltage$$

Electrical Energy = *Power* × *Total time the appliance is running* (*in hours*).
AC load calculations:

$$Power = 17.803\ \text{KW}$$

$$Energy = 68.274\ \text{KWh}$$

$$Solar\ radiance = 5.8\ \text{KWh/m}^2\ (daily)$$

Selection of inverter:

$$Since,\ Power\ = 17.803\ \text{KW}$$

$$So,\ inverter\ rating\ =\ 18\,\text{KW}\ or\ 18\,\text{KVA}$$

$$Loss\ in\ inverter\ =\ 20\%\ of\ \text{KWh}$$

$$Loss\ in\ inverter\ =\ (20/100) \times 68.274\ =\ 13.654$$

Selection and designing of batteries:
Battery supply = *Loss in inverter* + *Energy* = 13.654 + 68.274 = 81.928 KWh
Note: Stored energy in battery should be more than the battery supply, because of Depth of Discharge.

$$DoD\ (Lead\ Acid\ battery)\ =\ 0.5$$

$$Battery\ storage = \frac{Battery\ supply}{Depth\ of\ Discharge\ (DoD)} = \frac{81.928}{0.5} = 163.856\,KWh$$

Battery Sizing (Calculations):
Let us assume 12 V and 200 Ah battery is available.

$$So,\ each\ battery\ will\ provide\ 2.4\,\text{KWh}\ (12V \times 200\,\text{Ah} = 2.4\ \text{KWh}).$$

$$The\ total\ number\ of\ batteries\ required = \frac{\text{Battery storage}}{2.4} = \frac{163.856}{2.4} = 68.273$$

$$Hence,\ the\ total\ number\ of\ batteries\ required = 68\ batteries$$

$$\begin{aligned} Losses\ in\ lead\text{-}acid\ battery\ (15\%) &= Battery\ supply \times 0.15 \\ &= 81.928 \times 0.15 = 12.289 \end{aligned}$$

Design and selection of solar panels:
To find the energy to be supplied by the solar panel.

$$Energy\ supplied\ by\ the\ panel = Battery\ supply + Battery\ losses$$

$$Energy\ supplied\ by\ the\ panel = 81.928 + 12.289$$

$$Energy\ supplied\ by\ the\ panel = 94.217\ \text{KWh/day}$$

Transfer losses by panel is 4% losses.

$$Total\ energy\ supplied\ by\ the\ panel = loss + energy\ supplied\ by\ panel$$

$$Total\ energy\ supplied\ by\ the\ panel = 94.217 \times 0.04 + 94.217$$
$$Total\ energy\ supplied\ by\ the\ panel = 97.985\ \text{KWh/day}$$

Solar panel sizing (Calculations):
Solar panel losses are approximately 25%

$$Energy\ solar\ panel\ must\ generate = 97.985\ \text{KWh/day}$$
$$Losses\ with\ solar\ panel = 0.25 \times 97.985$$
$$Losses\ with\ solar\ panel = 24.496$$

$$Total\ energy\ solar\ panel\ must\ generate = Energy\ solar\ panel\ generates + losses$$
$$Total\ energy\ solar\ panel\ must\ generate = 97.985 + 24.496$$
$$Total\ energy\ solar\ panel\ must\ generate = 122.481\ \text{KWh}$$

$$Solar\ radiation\ unit\ =\ \mathrm{KWh/m^2/day}$$

$$Solar\ irradiation\ available\ at\ our\ location\ =\ 5.8\ \mathrm{KWh/m^2/day}$$

$$Hours\ of\ solar\ radiation\ =\ \frac{5.8\,\mathrm{KWh/m^2/day}}{1000\,\mathrm{W/m^2}}\ =\ 5.8\ \mathrm{hours/day}$$

$$Power\ of\ solar\ panel\ =\ \frac{Total\ solar\ panel\ energy}{5.8\,\mathrm{hours/day}}$$

$$=\ \frac{122.481}{5.8}\ =\ 21.117\ \mathrm{KW}$$

Suppose, we take 1 KW panel from market (This is the peak or max. power rating).

$$Number\ of\ solar\ panels\ required\ =\ \frac{\text{Power of solar panel}}{1\,\mathrm{KW}}\ =\ \frac{21.117}{1}$$

$$Number\ of\ solar\ panels\ required\ =\ 21\ solar\ panels$$

Cost estimation for AC system: the following Table 2 summarizes the cost estimate for the AC system.

DC solar system design (Calculation of power and energy):

$$Power\ =\ 11,531\ \mathrm{W}\ =\ 11.531\ \mathrm{KW}$$

$$Energy\ =\ 44.262\ \mathrm{KWh}$$

$$Solar\ radiance\ =\ 5.8\ \mathrm{KWh/m^2}\ (daily)$$

Table 2 Cost estimation for AC system

Pricing of solar system for AC appliances				
S. No	Component	Rating	Cost (Rs)	Total cost (Rs)
1	Solar panel	21.117 KW	25	527,925
2	Battery (lead acid)	163.856 KWh	8	1,310,848
3	Inverter	18 KVA	10	180,000
4	BoS	21.117 KW	10	211,170
Overall cost (Rs)				2,229,943

2.2 Dc Solar System

The block diagram of a DC solar system comprises of the following components (see Fig. 2).

Selection of charge controller:

$$Since,\ power\ =\ 11.531\ \text{KW}$$

$$Charge\ controller\ rating\ =\ 12\ \text{KW}\ or\ 12\,\text{KVA}$$

$$Loss\ in\ charge\ controller\ =\ 5\%\ of\ 12\ \text{KW}\ =\ 0.05\ \times\ 12\ =\ 0.6\ \text{KW}$$

Selection and designing of batteries

$$Battery\ supply\ =\ Energy\ +\ Loss\ in\ charge\ controller\ =\ 44.262\ +\ 0.6\ =\ 44.862$$

$$Battery\ storage = \frac{Battery\ supply}{DoD} = \frac{44.862}{0.5} = 89.724\ \text{KWh}$$

$$(DoD\ for\ lead-acid\ battery\ =\ 50\%\ =\ 0.05)$$

Battery sizing calculations:
Let us assume 12 V and 200Ah battery is available.

$$So,\ each\ battery\ will\ provide\ 2.4\ \text{KWh}\ (12\,\text{V}\ \times\ 200\,\text{Ah}\ =\ 2.4\ \text{KWh}).$$

$$The\ total\ number\ of\ batteries\ required\ = \frac{Battery\ storage}{DoD} = \frac{89.724}{0.5} = 180\ batteries$$

$$Losses\ in\ lead\text{-}acid\ battery\ (15\%)\ =\ 0.15\ \times\ Battery\ supply$$

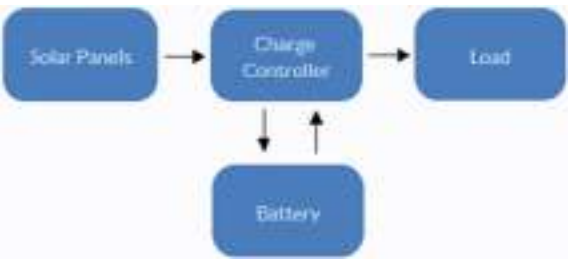

Fig. 2 DC solar system block diagram

$$= 0.15 \times 44.862 = 6.729$$

Design and selection of solar panels:
To find the energy to be supplied by the solar panel.

$$\begin{aligned} \textit{Energy supplied by the panel} &= \textit{Battery supply} + \textit{Battery losses} \\ &= 44.862 + 6.729 = 51.591 \text{ KWh/day} \end{aligned}$$

$$\textit{Transfer losses by panel is } 4\% \textit{ losses}.$$

$$\begin{aligned} \textit{Total energy supplied by the panel} &= \textit{loss} + \textit{energy supplied by panel} \\ &= 51.591 \times 0.04 + 51.59 \\ &= 53.654 \text{ KWh/day} \end{aligned}$$

Solar panel sizing (Calculations):
Solar panel losses are approx. 25%

$$\textit{Energy solar panel must generate} = 53.654 \text{ KWh/day}$$

$$\textit{Losses with solar panel} = 0.25 \times 53.654 = 13.413$$

$$\begin{aligned} &\textit{Total energy solar panel must generate} \\ &= \textit{Energy solar panel generates} + \textit{losses} \\ &= 53.654 + 13.413 = 67.067 \text{ KWh} \end{aligned}$$

$$\textit{Solar radiation unit} = \text{KWh/m}^2\text{/day}$$

$$\textit{Solar irradiation available at our location} = 5.8 \text{ KWh/m}^2\text{/day}$$

$$\textit{Hours of solar radiation} = \frac{5.8 \text{ KWh/m}^2\text{/day}}{1000 \text{ W/m}^2} = 5.8 \text{ hours/day}$$

$$\textit{Power of solar panel} = \frac{\text{Total solar panel energy}}{5.8 \text{ hours/day}} = \frac{67.067}{5.8} = 11.563 \text{ KW}$$

Suppose, we take 1 KW *panel from market* (*This is the peak or max. power rating*).

$$\textit{Number of solar panels required} = \frac{\text{Power of solar panel}}{1 \text{ KW}} = \frac{11.563}{1} = 12 \textit{ solar panels}$$

Cost estimation for DC system: the following Table 3 summarizes the cost estimate for the DC system.

Comparison of AC and DC solar system design: the following Table 4 compares both AC and DC solar system design, and it can be concluded that DC solar system is more economic-friendly.

Table 3 Cost estimation for DC system

Pricing of solar system for DC appliances				
S. No	Component	Rating	Cost (Rs)	Total cost (Rs)
1	Solar panel	11.563 KW	25	289,075
2	Battery (lead acid)	89.724 KWh	8	717,792
3	Charge controller	12 KVA	5	60,000
4	BoS	11.563 KW	12	138,756
Overall cost (Rs)				1,205,623

Table 4 Comparison of AC and DC solar system design

Comparison AC and DC				
Solar DC system		Component	Solar AC system	
Rating	Cost		Rating	Cost
11.563 KW	289,075	Solar panel	21.117 KW	527,925
89.724 KWh	717,792	Battery (lead acid)	163.856 KWh	1,310,848
12 KVA	60,000	Charge controller/inverter	18 KVA	180,000
11.563 KW	138,756	BoS	21.117 KW	211,170
1,205,623		Total cost (Rs)	2,229,943	
Difference in cost				1,024,320

The DC solar system and AC solar system total installation cost is calculated. Now, the electricity bill total amount per annum for the same apartment is calculated. Comparison study is performed to see which case has a better ROI (return of interest). The electricity bill from Sharjah Electricity and Water Authority is studied to find the total amount per month and also to find an average total per annum (See Fig. 3).

$$Per\ month\ electricity\ bill\ total\ amount\ = AED\ 800\ (approximate)$$

$$AED\ 800\ = Rs.16,000\ (Approximately\ as\ per\ the\ currency\ conversion\ rate)$$

$$Per\ annumelectricity\ bill\ total\ amount\ = AED\ 10,000\ (approximate)$$

$$AED\ 10,000\ = Rs.200,371$$
$$(Approximately\ Rs.2\ lakhs\ as\ per\ the\ currency\ conversion\ rate)$$

$$Overall\ installation\ cost\ for\ DC\ solar\ system\ = 12,05,623$$
$$= Rs.12\ lakhs\ (approximate)$$

هيئة كهرباء ومياه الشارقة
Sharjah Electricity & Water Authority

Personal ID	2873567301	معرف العضوية
Account number	2761941137	رقم الحساب
Customer class	RES NR	فئة المشتركين
Tax Invoice No	276194388561	رقم الفاتورة
Invoice Date	21/09/2020	تاريخ الفاتورة
Premise ID	3450614873	معرف العقار
Due Date	29/08/2020	تاريخ الاستحقاق
Billing Period	AUG 2020	الفترة
Billing Cycle	Bill Cycle 03	دورة الفاتورة
Last Receipt Date	23/07/2020	تاريخ آخر إيصال

Bill Summary — ملخص الفاتورة

Total Amount المبلغ الإجمالي	Adjustments التعديلات	Receipts المقبوضات	Other Chgs رسوم أخرى	Arrears المتأخرات	Current Amt المبلغ الحالي
817.35	0.00	684.10	0.00	684.10	817.35

Financial Details — تفاصيل الرسوم

Mun. Ser رسوم البلدية	Gas الغاز	Water المياه	Electricity الكهرباء	Serv. Seq الخدمات
10.00	32.55	76.65	564.90	Arrears المتأخرات
10.00	32.55	76.65	564.90	Receipts المقبوضات
12.00	9.00	70.00	553.75	Current Amount المبلغ الحالي
0.00	21.00	21.00	92.25	Service Charges رسوم خدمات
0.00	0.00	0.00	3.00	Other Charges رسوم أخرى
0.00	0.00	0.00	3.00	Adjustments تعديلات
0.00	30.00	91.00	646.00	Net Taxable Amount صافي الخاضع للضريبة
0.00	5.00	5.00	5.00	VAT Rate % معدل الضريبة %
0.00	1.50	4.55	32.30	VAT Amount القيمة الضريبية
12.00	31.50	95.55	678.30	Total including VAT المجموع
			817.35	Total Amount Due إجمالي

Fig. 3 The electricity bill from SEWA (Sharjah Electricity and Water Authority) for a month

$$Per\ annum electricity\ bill\ total\ amount\ =\ Rs.2\ lakhs$$

$$Hence\ Return\ of\ Interest\ =\ 12/2\ =\ 6\ years.$$

$$Overall\ installation\ cost\ for\ AC\ solar\ system\ =\ 22,29,943$$
$$=\ Rs.22\ lakhs\ (approximate)$$

$$Per\ annum electricity\ bill\ total\ amount\ =\ Rs.2\ lakhs$$

$$Hence,\ Return\ of\ Interest\ =\ 22/2\ =\ 11\ years.$$

The currency is converted to rupees, as the installation costs were calculated in INR (Indian Rupees). Here, it can be seen that the money invested is received back within a span of 6 years in the case of DC solar system compared to AC solar system where it takes 11 years. The return of interest in AC solar system is almost double the time span of DC solar system. Hence, the DC solar system is much more economical-friendly and return of interest is less comparatively as well.

The learning outcomes from this case study are that a cost-effective sustainable solar system design has been done, also through the design it was observed that the DC solar system is cost effective than the AC solar system. Now, with the implementation

of this locally, the environmental carbon emission can be reduced drastically. Also, to further this study, the total electricity bill amount per annum was calculated to find the ROI (return of interest) in both the cases and are compared.

3 Emerging Materials as an Alternative for Crystalline Silicon

3.1 Thin Film

Thin films are the second-generation solar cells. They are made from various materials such as: Cadmium Telluride, Gallium Arsenide, Copper Indium Gallium Selenide, and Amorphous Silicon. The wafer of these thin films, when compared to others, are more flexible. They can be placed on surfaces such as roofs or can be placed on frames [4–6].

3.2 Perovskite

Silicon is a commonly used material when it comes to creating solar panels, but companies are now looking to use perovskite as a new material for solar panels. The reason is, it is low-cost, has low temperature manufacturing, light, and flexible. So far as efficiency go by, it has not proven as much as the use of silicon [7].

In today's world, as the technologies advance, so does designing them. The perovskite cell design has been made to match or even exceed that of the typical silicon cell. The use of perovskite cells has brought a percentage increase of 20–22, but further improvement can be made. On the perovskite cell, a specially treated conductive layer of tin dioxide can be added, thus improving the path for the charge carriers. The modified perovskite, has an increased efficiency of 25.2%, when compared to current materials used, this eclipses their efficiency [7].

4 Emerging Technologies in the Field

4.1 Passive Systems

It is a simple and cost-efficient system. They do not use any mechanical devices such as blowers, fans, or pumps to distribute solar energy from the collector. It instead, takes advantage of the sun's natural energy as it is a free and renewable energy. To create a passive system, we need to plan for the location of the building,

the orientation, and the materials that will be needed [8]. The passive system uses materials that have large heat capacities such as water, stone, or concrete, these are also known as thermal masses. These passive systems can be placed in three types: Direct Gain: This will allow solar energy from the south-facing windowpanes. Indirect Gain: This allows the solar radiation to heat the wall of the house, then slowly will pass the wall, and enter inside the house. The Trombe Wall has openings in the wall. This will promote convection currents. Greenhouse Addition: It will have an attached sunspace and maybe a solar greenhouse heated by using the solar energy. Some of the energy will be used to heat the house and some to help the plants grow [9].

4.2 3D-Printing

This is a process used in making three-dimensional objects taken from a digital file. This uses an additive process; this will create layers until the product or object is created. This has become a major asset in the energy sector. This will help to combat the climate situations, use less fossils fuels, and try and use more green energies. When looking at it, 3D printing is still expensive and still has more space for improvement [8].

For example, this would be a great method in the solar industry. This would prove to be more effective than using ordinary solar panels and would also reduce the production cost by 50%, reason being the use of additive manufacturing [10].

This method has proven in fields such as medical, construction, and architecture, so why can it not help and prove a success in the energy sector. This manufacturing process can improve the quality of the products and help be cost effective at the same time. Here are some reasons why 3D technology should be considered: It improves development process. This is especially helpful when making prototype models. It would allow companies to create a project faster at low cost when it is compared to traditional methods which can be time consuming. Once the prototype model has been made, this will help in identifying if there are any problems and can easily be modified again and created until the perfect model is created. These 3D models can be created endlessly with the help of 3D modeling software until the perfect design is acquired. It helps in reducing the cost. This will for sure reduce the cost and only the amount of material used will be only for the project creation. Unlike traditional methods, where a mold has to made and take a long process to do each time you need to make a product even if it is just a prototype. Additive manufacturing control production and make the specified number of parts which has to be printed. This allows for a greater finish and a long-lasting product [10].

3D printed solar panels. A solar panel absorbs the sun's energy to create electricity. These solar panels are manufactured from solar cells that help achieve this process. The solar cells produce electricity by the help of physical and chemical phenomenon. The solar panels are made with crystalline silicon, this technology

is evolving quite rapidly, and newer materials are emerging such as thin-film technology. The high costs are a big factor when it comes to the development of renewable energy. They will be helpful, but at the current period it is expensive and not accessible by everyone [10].

When creating solar panels, the materials used are quite expensive because they need to be able to convert light to electricity. So, creating these panels can be a time-consuming process. When developing these models, there will be a lot of prototypes and testing going in the process. Here is where 3D printing could be the turning point. This will enable to create high quality prototypes and can be done repeatedly with high accuracy and producibility [10] (see Fig. 3).

Benefits of 3D printed solar panels: these will help in reducing the cost up to 50%. This cost will decrease due to additive manufacturing. Expensive materials like glass, polysilicon, and indium would not be required anymore. As an example, synthetic perovskite is a cheap material to use in building photovoltaic structures. Easy to implement in developing countries: Using 3D printed solar panels are much cheaper than using a traditional glass panel. These panels will be light in weight so thus make transporting easier and as a result could be more affordable to the population and places where electricity is not able to be accessed. It will improve effectiveness by 20%: Compared to traditional panels, these 3D printed panels would be more efficient as the designs would be better and the quality would be better [10].

These 3D printed solar panels are created: these solar panels are created: this technology is changing the way how renewable energy industry works. Below, we can see an example of a company that is using 3D printing to manufacture solar panels. The CSIRO (Commonwealth Scientific and Industrial Research Organization) use industrial 3D printers to create rolls of solar cells. They successfully created A3 sheets of solar cells that are functional and efficient. The larger solar cells are produced by using a flexible lightweight plastic. The process used are slot-die coating, gravure coating, and screen printing. Additive manufacturing has made it possible to create accurate solar panels [10].

3D Printed Solar Energy Trees. At VTT Technical Research Centre of Finland, there is a new prototype that has been developed and it is called the energy harvesting trees. The leaves can store and generate solar energy and can be used to power small number of devices. It can be used indoors as well as outdoors from the captured energy that is heat and wind that affect the surrounding environment [11].

Working: The flexible organic solar cells are the leaves of the solar energy tree. There is a power converter that is placed in all the leaves and thus creates a multi-converter system. It allows collecting energy from a range of sources such as wind, solar, and surrounding heat difference. So, if there are more leaves like this, more energy can be harvested. The tree trunks used in creating this are wood-based biocomposites. As a result, these can be mass produced and can be replicated infinitely. At the current size, it can power compact devices such as mobile phones, thermometers, humidifiers, and LED light bulbs [12].

The creation of 3D printed solar trees: These are made from an organic solar panel or from an OPV (organic photovoltaics). These OPV are very reactive to any interior lighting or sunlight and thus would be good to collect energy. The ultra-thin solar

panels measure 0.2 mm thick; they use polymer and electrode layers to provide a visual graphic appeal. They are printed in a leaf-shaped design and the surface area is of 0.0144 m^2 and this would include the wiring and the needed connections. So, if 200 OPV leaves were made, they could generate upto 3.2 amperes of electricity and 10.4 watts of power outdoors in a one square meter formation. They are light and flexible. They are produced by the roll-to-roll method and able to produce upto 100 m of layered film per minute. The leaves of the tree are attached to the trunks that are made up of a wood-based biomaterial. These are flexible and made to form an electronic system that conduct energy to a converter system [13].

Future of the 3D printed solar energy trees: At the current period, it only exists in small numbers. If VTT proves to be successful, a forest size printed trees will be created and thus will be able to power cities and so on. These trees would be scalable and would mimic real-life trees [12]. This could be a real asset for this industry. This would allow industry for mass production and can be customized-based according to the customers' needs. The materials used in 3D printing could easily revolutionize the solar industry. The low cost and efficient structures can be made easily without worry and can also be made available in remote areas.

5 Conclusion

It is very clear that photovoltaics can and bring a major change to the world. Using solar energy has become more popular as this brings an economic benefit. These will eventually help stop the use of fossil fuels, oils, and many more to power our appliances. Rather than using silicon material for photovoltaic, we can use perovskite because of its low cost, lightness, and flexibility to use. Using passive systems are simple and cost efficient because they utilize the energy from sun directly, without the need for any conversion. Use of 3D printing can effectively reduce cost, reduce waste materials, and produce results with high accuracy and which are repeatable. They include technologies such as 3D printed solar panels. Using this can help create a better environment, reduce the waste in order to create these solar panels, and mostly will be super-efficient to implement these in developing countries. Another technology used under this is 3D printed solar trees, these will not only use light, but even the wind and heat temperature variations. The leaves are made with organic

cells and the trees are made of wood-based biomaterial and these will help to create a cleaner and better environment. Using these new materials and technologies, we can help create a cleaner and greener environment.

References

1. J. Anderson, S. Bassi, E. Stantcheva, P. Brink, Innovation case study: photovoltaics (2006)
2. M.R.S. Shaikh, S.B. Waghmare, S.S. Labade, P.V. Fuke, A. Tekale, *A Review Paper on Electricity Generation from Solar Energy*, vol. 5, no. IX (2017)
3. M.A.G. de Brito, L.P. Sampaio, L.G. Junior, C.A. Canesin: research on photovoltaics: review, trends and perspectives (2011)
4. Energysage, https://www.energysage.com/solar/101/types-solar-panels/. Accessed 20 Feb 2021
5. 8MSOLAR, https://www.8msolar.com/types-of-solar-panels. Accessed 20 Feb 2021
6. SOLAR MAGAZINE, https://solarmagazine.com/solar-panels/. Accessed 23 Feb 2021
7. PRESCOUTER, https://www.prescouter.com/2020/09/current-and-upcoming-innovations-in-solar-cell-technologies/. Accessed 24 Feb 2021
8. EESI, https://www.eesi.org/topics/solar/description#:~:text=Solar%20energy%20systems%20use%20the%20sun%27s%20rays%20for%20electricity%20or%20thermal%20energy.&text=Passive%20systems%20are%20structures%20whose,as%20hot%20water%20or%20electricity. Accessed 22 Feb 2021
9. PennState College of Earth and Mineral Sciences, https://www.e-education.psu.edu/egee102/node/2098. Accessed 22 Feb 2021
10. The Green Optimistic, https://www.greenoptimistic.com/3d-printed-solar-cells/. Accessed 24 Feb 2021
11. P. Gangwar, N.M. Kumar, A.K. Singh, A. Jayakumar, M. Mathew, Solar photovoltaic tree and its end-of-life management using thermal and chemical treatments for material recovery (2019)
12. Sculpteo, https://www.sculpteo.com/blog/2018/01/24/3d-printed-solar-panels-meet-the-renewable-energy-revolution/. Aaccessed 24 Feb 2021
13. Drupa, https://blog.drupa.com/de/printed-trees/. Accessed 22 Feb 2021

Design and Simulation of Serial Peripheral Interface Protocol Using Pulsed Latches

Pujitha Karamalaputti and Arvind Kumar

Abstract Communication protocols are useful for transfer of data between devices. Even though we have many protocols, SPI is one of the most important bus protocol. SPI is used to connect microprocessor to the peripheral devices. It works on the principle of FIFO (Ring topology). Normally, Flipflops were used to synchronize the data between the Master and Slave but it consumes more power. In this paper, SPI is implemented using Pulsed Latches to reduce the power consumption. Pulsed latches consumes less power, and area occupied by the pulsed latches is less compared to Flipflops. The design is simulated using Verilog. The Integrated Development Environment (IDE) used is Xilinx-ISE, and ISE Simulator (ISIM) is used to verify the waveforms.

Keywords SPI · Protocol · Pulsed latches · Master · Slave

1 Introduction

1.1 SPI Protocol

SPI is the most widely used protocol to transfer data between the devices in a serial fashion using clock, and hence data is transferred in synchronism to the clock.

By using SPI, one can transfer the data without any interruption. The number of bits that can transferred are not restricted. With I2C and UART, information is sent in packets, restricted to a particular number of bits. Start and stop conditions characterize the start and end of every packet, so the information is interfered with during transmission.

P. Karamalaputti (✉)
School of VLSI and Embedded Systems Design, National Institute of Technology, Kurukshetra, Haryana, India

A. Kumar
Department of ECE, National Institute of Technology, Kurukshetra, India
e-mail: arvind_sharma@nitkkr.ac.in

S. Rawat et al. (eds.), *Proceedings of First International Conference on Computational Electronics for Wireless Communications*, Lecture Notes in Networks and Systems 329,
https://doi.org/10.1007/978-981-16-6246-1_13

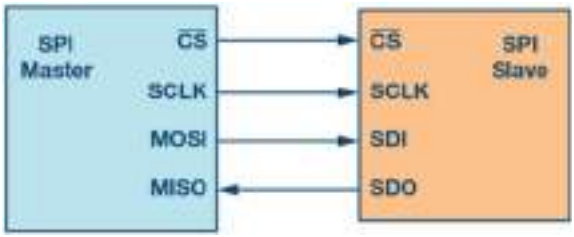

Fig. 1 Master and slave configuartion in SPI

SPI follows four logic signals and they are described below.

- Serial Clock which is described as SCLK in the following figure is used to synchronize the clock.
- Master Output Slave Input (MOSI) is used for transferring data from Master and receives data from Slave.
- Master Input Slave Output (MISO) is used for transferring data from Slave and receives data from Master.
- Slave Select (SS) is used to select particular slave.

Active Low: The slave is initiated just when it is given low logic level/"0" logic level (Fig. 1).

1.2 Pulsed Latch

The pulsed latch requires pulse generators that create pulse clock waveforms with a source clock. The pulse width is picked with the end goal that it encourages the progress. The accompanying graph speaks to a basic pulse generator and the related pulse waveform. In this methodology, the pulse generators are consequently inserted to fulfill a few principles during clock-tree amalgamation. Along with pulse generators, this methodology likewise utilizes various matching delay cells to take into account coordinate clock insertion delays with or without pulse generators (Fig. 2).

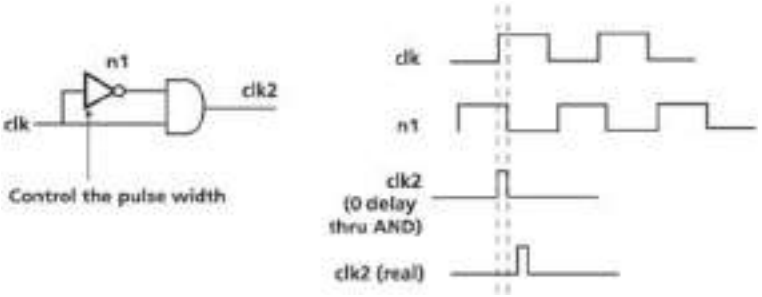

Fig. 2 Pulsed latch

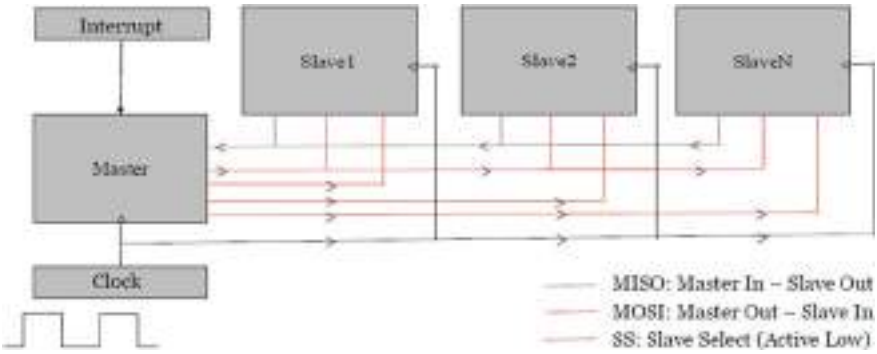

Fig. 3 SPI protocol functional block diagram

2 Design

2.1 SPI Master–Slave Interconnect

Master generates the clock signal. The clock generator synchronizes the data that is being transmitted between master and slave. The devices that use SPI support high clock frequencies when compared to the devices that use I^2C interfaces.

One Master is compulsory when working with SPI and the number of slaves can be one or more than one. Figure 3 shows how Master and Slaves are connected in SPI interface.

Slave is selected by using Chip Select signal. Chip Select is an active low signal, and whenever the slave wants to disconnect from the master, it will be set to high. Every slave will be provided with their individual Chip Select signals when working with multiple slaves.

2.2 Transmission of Data

To transer data through SPI, Master first impart the clock sign and by setting Chip Select (CS) to high, it selects the Slave. Generally, an active low signal is used for Chip Select (CS) signal. Hence, Master sends logic 0 to CS line to select that particular Slave. By using SPI, one can transfer data from Master to Slave and from Slave to Master simultaneously. Hence, SPI is a full duplex communication.

The pulsed clock synchronizes the shifting and sampling of the data.

2.3 Steps Followed to Transfer Data

From the data sheet available, with the frequency equal to or less than that of a slave, the Master configures the Slave. The Master sends active high signal to the Slave for which it wants to send the data.

During each clock cycle, a full duplex communication occurs as it was through Ring Topology as shown in Fig. 4.

With the help of MOSI line, the Master transfers a bit, which is read by Slaves and at the same time with the help of MISO line, Slave transfers a bit which is read by Master.

Data is shifted out at the Most Significant Bit (MSB) and taken through Left Most Bit (LSB).

Transmission of data can occur at any number of clock cycles. But, once the data is transmitted, the Master switches off the toggling. Then deselects the selected slave.

As shown in Fig. 5, the clocking is given using latched pulses.

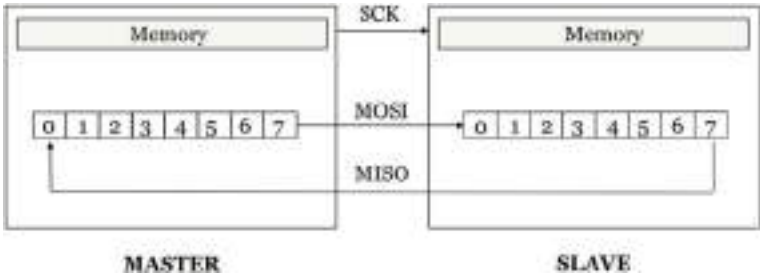

Fig. 4 Ring topology

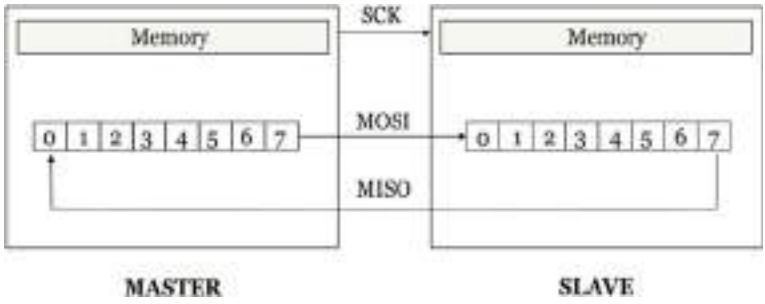

Fig. 5 Data transfer

3 Simulation Results

ISE Simulator (ISim) is used for testing the results.

We stored initially "8'b10101101" in master and "8'b01101011" in slave, and after eight clock cycles, we get "8'b01101011" in master and "8'b10101101" in master.

As shown in Figs. 6 and 7, the transfer of data is taking place successfully from Master to Slave and from Slave to Master at each clock pulse, and at the end of eighth clock pulse, one byte of data will be transferred.

Fig. 6 Simulation results

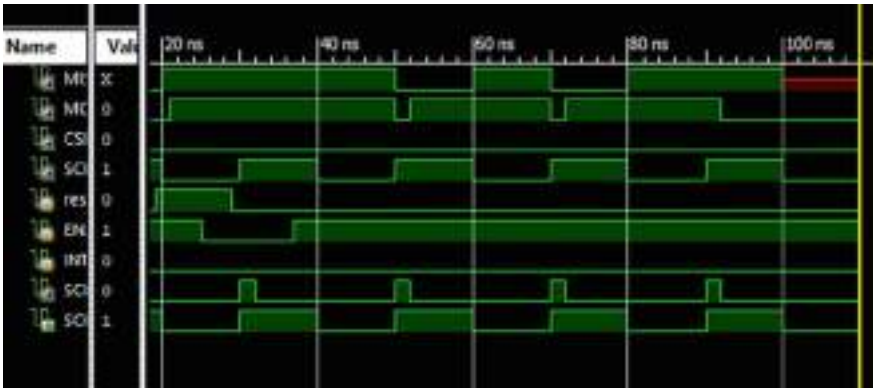

Fig. 7 Simulation results

3.1 The Simulation Result for the Above Data

4 Conclusions

Using pulsed latches, the Master and Slave of SPI protocol was implemented, and its data transfer functionality was verified through ISE Simulator. Here, we reduced the power consumption of the circuit to some extent because of pulsed latches instead of Flipflops.

5 Future Scope

In this design, we just reduced the power in clock, but there are techniques by making the power supply cut to the part of the circuit which is not in use with the help of state diagrams. We can implement this pulsed latch technology in that to reduce more power.

References

1. https://en.wikipedia.org/wiki/Serial_Peripheral_Interface
2. D.N. Oruganti, Design of power efficient SPI interface, in *2014 IEEE International Conference on Advanced Communications, Control and Computing Technologies* (IEEE, 2014)
3. J. Hennessy, N. Jouppi, F. Baskett, J. Gill, MIPS: a VLSI processor architecture, in *VLSI Systems and Computations* (Springer, Berlin, Heidelberg, 1981), pp. 337–346
4. Y.K. Kumar, S.S. Kiran, B. Sangeeth Kumar, Low power and area efficient shift register using pulsed latches. Int. J VLSI Syst. Des. Commun. Syst (2018)
5. K. Singh, O.A.R. Rosas, H. Jiao, J. Huisken, J.P. de Gyvez, Multi-bit pulsed-latch based low power synchronous circuit design (IEEE, 2018)

Low-Power High-Performance Hybrid Scalable

Aishita Verma, Anum Khan, and Subodh Wairya

Abstract In this paper, a hybrid 1-bit Full Adder (FA) using Pass Transistors, Transmission Gates, and conventional CMOS logic is designed and also extended for 4-bit and 64-bit. Less power, delay, and PDP are the foremost features of the proposed approach. Circuit parameters have been analyzed using Cadence Virtuoso 45 nm technology. Parameters such as power, delay, PDP, EDP were compared to extant designs. With the 1 V supply, the average power consumption (0.1379 μW) and delay (66.6878 ps) were found to be extremely low as compared with existing designs. For 4-bit, the power consumption is 1.95 μW with 285.6 ps and PDP 0.56 fJ with 0.8 V supply. To examine its scalability, the 64-bit ripple carry adder is designed. In this work, a low-power 4:2 Compressor is presented. The average power consumption of compressor is 542.7 nW, delay is 116.5 ps, PDP is 63.21 aJ, and EDP is 7.364 $\times$ 10^{-27} J with 1 V supply. Meticulous Monte Carlo simulation is performed in CADENCE SPECTRE at 45 nm CMOS technology. Simulation results conclude that proposed design signifies remarkable results in power consumption and delay which enunciated for low PDP. The proposed full adder cells attain a 44% power improvement metric in comparison with reported designs of full adder. In the field of digital technology specifically, the image and signal processing predicated applications that necessitate high speed, less power, and lessen delay, a proposed adder is suited, as adder unit, it is one of the primary blocks of FIR Filter.

Keywords Full adder · Power · Monte Carlo simulation · Corner analysis · Compressor

1 Introduction

Increased development of battery-regulated portable applications comprising of cellular phones, smart cards, PDAs needs lesser silicon area and foremost less power; hence, research work associated with low power designing of arithmetic

A. Verma (✉) · A. Khan · S. Wairya
Department of Electronics and Communication Engineering, Institute of Engineering and Technology, Lucknow, India

S. Rawat et al. (eds.), *Proceedings of First International Conference on Computational Electronics for Wireless Communications*, Lecture Notes in Networks and Systems 329,
https://doi.org/10.1007/978-981-16-6246-1_14

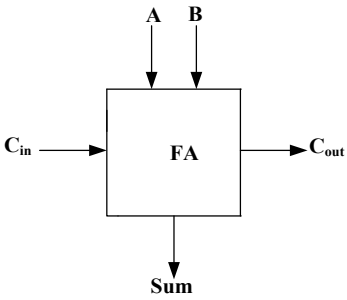

Fig. 1 Symbol of full adder

circuits has been of great concern. The processors utilized in DSP execute the operations, including video processing, filtering, and fast Fourier transforms and there is a broad timeline of addition, operation in these. The elementary operations are addition accomplished in arithmetic circuits. Intensifying upon the performance of the 1-bit adder will improve all-inclusive architecture, performance [1]. The main focus of designers in the VLSI industry in the context of digital circuits is to design the circuit which consumes lesser power and offers reliability; hence, design engineers mainly focus on designing the circuit consuming less power thereby providing fast operation [2]. Various methods of designing direct to assist one performance perspective contrary to existing ones. Several logic styles have been deliberated to ensure the prominent performance of full adder cells [3]. Figure 1 shows 1-bit full adder symbol. The designing of compressors is done with full adders and/or half adders for counting number of "logic-1's" in input. Several designs of compressors including 3–2, 4–2, 5–2, and 7–3 were presented by researchers in the last two decades. In this paper, 4:2 compressor is designed using the proposed adder and also the meticulous Monte Carlo simulation is done with parameters such as power, delay, PDP, and EDP.

In this paper, various adders have been considered and thereafter a novel FA design is proposed and explained in detail, exhibiting full output swing with the potentiality of operating even at low supply. The entire paper is systematized by respective sections. Section 2 comprises topology and a detailed operation of proposed full adder. A 4:2 Compressor design is presented in Sect. 3. Section 4 includes results obtained, followed by conclusion in Sect. 5.

2 Full Adder Circuit Topology

CMOS full adder is based on an elementary manner of designing [4]. FA circuits can be segmented into full-swing and non-full-swing category. CCMOS is Conventional Complementary Metal Oxide Semiconductor [5], TGA [6] transmission function [7], 14T in [8], 16T in [9], and hybrid logic [2, 10, 11]. FAs are one of the most major full-swing adders. 10T [12], 9T [1], and 8T [13] are non-full-swing adders. The desirability of conventional CMOS consisting of 28T is its simpleness contrary

to voltage scaling and size of the transistors [4], but there is large input capacitance and requires buffers which is a drawback of this logic. CPL offers better voltage swing restoration consisting of 32 transistors, but it is not relevant since it requires an increased number of transistors which will route to expand the chip area [14]. Hybrid adders are delineated by hybrid logic and termed hybrid adders [15, 16]. They are designed by a combination of logic styles [6] with the intent of upgrading the all-around performance of the system [17] with minimization of transistors and power dissipation [18]. The necessary intent of this paper is to focus on parameters, namely, power, delay, PDP, EDP in contrast to existing full adders.

2.1 Proposed Structure of Full Adder

Four important modules realize the operation of proposed full adder. The block diagram is shown in Fig. 2.

Full adders consist of sum and carry generation, which is carried by two separate modules for each of them. The schematic of the proposed adder structure is depicted in Fig. 3. A detailed explanation of modules is described as follows.

A. Module 1: AND-OR Module

The truth table of full adder shows that when input carry is 0, then AND operation is performed for output carry between A and B inputs, but when Cin = 1, in this case, there is OR operation of inputs for output carry. This module is designed to avail TG and CPL logic.

B. Module 2: TG based MUX

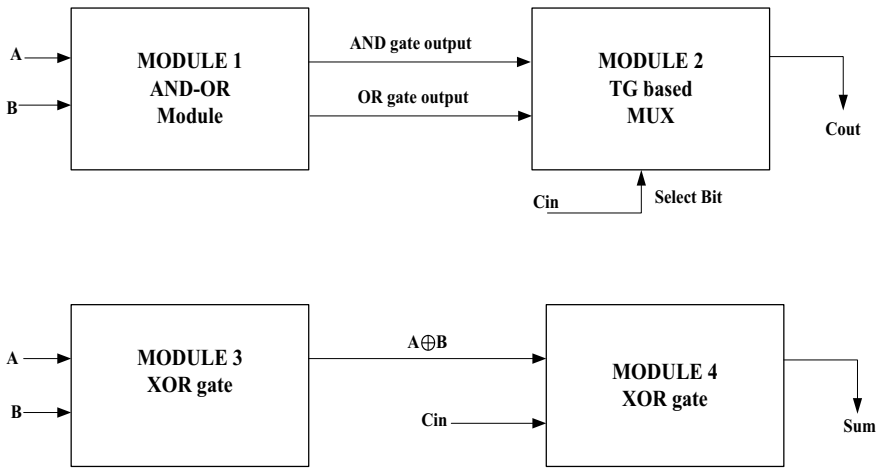

Fig.2 Block diagram of proposed adder

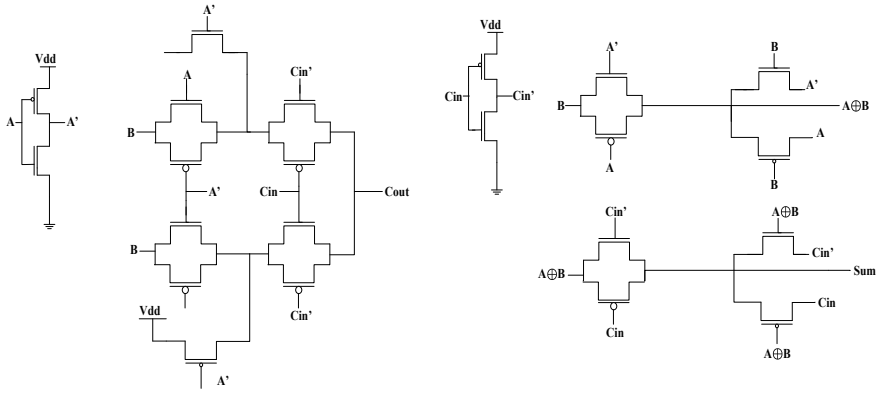

Fig. 3 Schematic of proposed FA

To obtain the output carry, module 2 consists of output from module 1 as input with Cin. 2:1 MUX with selection line select the carry-out signal from module 1.

C. Module 3 and 4: XOR gate module.

The two cascaded XOR modules are responsible for the output SUM of three inputs, this module is implemented with TGs, PTs. The condition of module 3 is that when A = 1, B = 0, the output is A, and when A = 1, B = 1, the output is $\overline{A}$. Module 4 has been designed with carrying input and XOR input (which is output from module 3) and when Cin = 0, output = A ≤ B whereas if Cin = 1 with A ≤ B = 0, the output is Cin, and for Cin = 1, A ≤ B = 1, the output = $\overline{Cin}$.

2.2 *Ripple Carry Adder*

To investigate the expandability, this design is extended for Ripple carry adder of 4-bits illustrated in Fig. 4. The buffers are not added in the design while extending the bits in the ripple carry adder, so this adder is compatible while designing. This design has the capability to operate on extending to 64-bits. As interpreted from

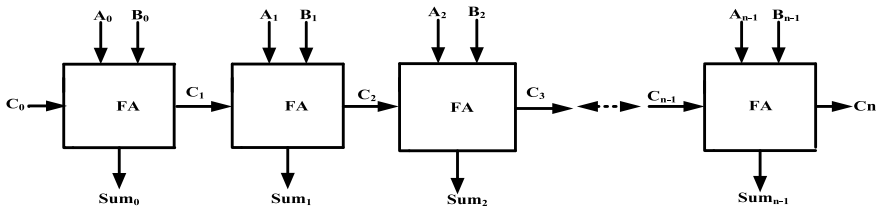

Fig. 4 Block of n-bit adders [18]

Fig. 1, there is a symbol of 1-bit adder with the inputs and output pins, in each stage input terms are added. The design in Fig. 3 shows that the carry input is used for controlling the gate of TG. The signals which are possible at the output node (COUT node) are B, V_{DD}, or gnd. If B is only considered (because gnd, V_{DD} are inputs which are provided in each stage), when n equals 0, at the output node which is a C1 output node, the B0 will arise, but when n equals 1, B1 will arise at output node which is C2 output node. This all represents that identical signal is not propagating from n = 0 to n = 63, so this design does not subject to degradation of voltage on extending to larger bits adder [19–21].

3 4:2 Compressor

A 4–2 compressor consists of five inputs Cin, X1, X2, X3, X4, and three outputs Cout, Carry, Sum, as shown in Fig. 5. The compressors are ideal candidates which can be used in reduction process of partial product [22], instead of the full adders. There is same binary weight of all of the input bits and output sum [23]. The operation of 4:2 compressor is represented by Boolean Eqs. (1–3).

$$\text{Sum} = X1 \leq X2 \leq X3 \leq X4 \leq \text{Cin} \tag{1}$$

$$\text{Cout} = (X1 \leq X2)X3 + \left(\overline{X1 \leq X2}\right)X1 \tag{2}$$

$$\text{Carry} = (X1 \leq X2 \leq X3 \leq X4)\,\text{Cin} + \left(\overline{X1 \leq X2 \leq X3 \leq X4}\right)X4 \tag{3}$$

Fig. 5 Compressor [23]

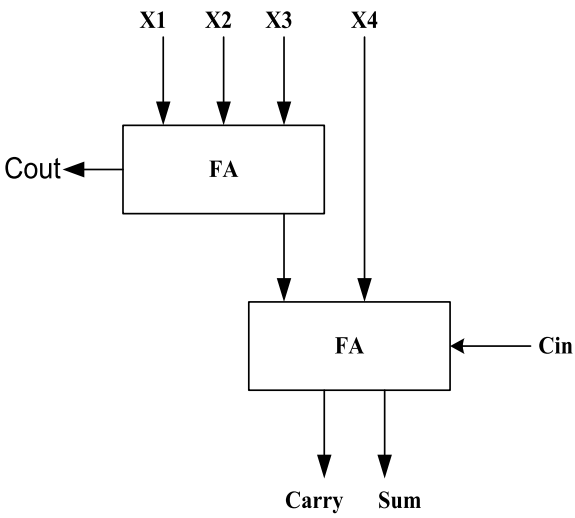

4 Results and Discussion

The simulation was executed utilizing 45-nm technology and the design was compared with existing adder designs on parameters including power, delay, PDP, and EDP. Table 1 depicts the results of simulation and comparison of proposed adder with existent designs [24]. The simulation was followed through varying supply voltages (0.8–1.2 V). The proposed hybrid design has been compared with the existent hybrid adder [2]. The hybrid adder comparison was simulated in Cadence 45-nm technology. EDP of proposed full adder is proportionally less. The Cadence Spectre GPDK 45-nm is utilized for schematic, simulation, of the 1-bit FA circuit, and the analysis is also done on the same. Transistor sizing is also considered while the parameters have been calculated. For comparison, FAs viz., TGA, Hybrid-1, CPL, SERF, GDI 1, GDI 2 have been considered [9], and the outcomes of performance aggregate of these FAs with proposed 1-bit FA are drafted in Table 1. Table 1 infers that the proposed adder in contrast with existing designs offers relatively less value of power, delay, PDP, and EDP, also proposed FA has lowest power consumption 0.137 μW at 1-V supply indiscriminate to all other FA [8].

4.1 Proposed Full Adder

With results of PDP in the table, it is confirmed that the proposed FA shows minimum PDP which is less as compared to the FA circuits altogether. Figure 6 shows simulation waveform for 1-bit FA at 1 V supply and Fig. 7 depicts the proposed full adder gives least power dissipation.

The proposed adder architecture is inclusive mainly by 22 transistors, as compared to designs in [5] that have a necessity of more than 22 transistors. The Simulation waveforms of proposed adder are depicted in Fig. 6 having the full-swing voltage level at 1.0 V supply. It shows that this proposed adder corresponds to an exemplary performance with low power, and can be used for high-speed applications.

The analysis is done for five corners SS-TT with appropriate model files. The other parameters are the same at all corners, but the delay alters from SS to TT corner. Table 2 shows the nominal value with minimum and maximum values.

4.2 Ripple Carry Adder (RCA)

To establish the Scalability of Hybrid adder implemented earlier, 1-bit hybrid scalable adder is extended to 4-bit and 64-bit RCA. Table 3 depicts simulation results of the implemented 1-bit hybrid adder and Ripple carry adders at 0.8 V supply.

Table 1 Results of simulation of full adders at different supply voltages

Design	No. of Trs	At 0.8 V supply voltage			At 1 V supply voltage			At 1.2 V supply voltage		
		Avg power (μW)	Delay (ps)	PDP (aJ)	Avg power (μW)	Delay (ps)	PDP (aJ)	Avg power (μW)	Delay (ps)	PDP (aJ)
CPL[5]	32	0.14	209.04	28.74	0.25	137.78	33.79	0.36	364.8	146.16
HYBRID [2]	16	0.048	150.26	7.329	0.060	459.58	27.81	0.129	138.82	17.951
PROPOSED	22	0.09	138.18	5.64	0.14	66.69	9.19	0.20	56.14	11.27

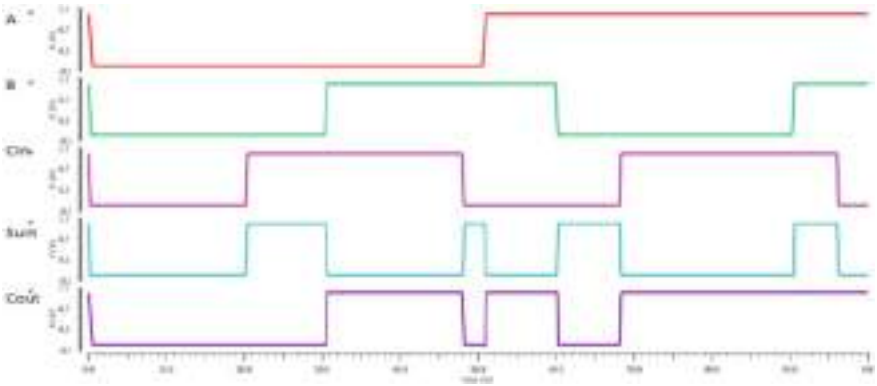

Fig. 6 Simulation waveform of full adder at 1 V supply

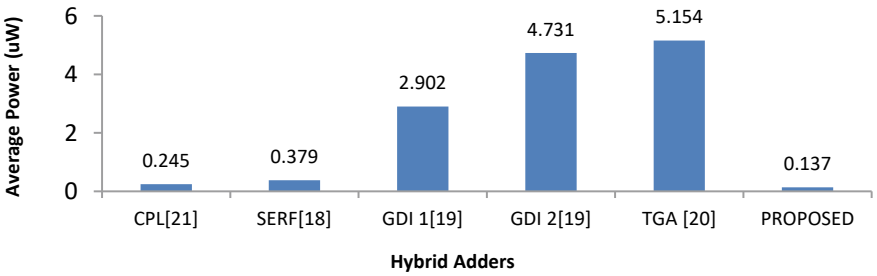

Fig. 7 Average power dissipation of hybrid full adders at a supply voltage of 1 V

Table 2 Analysis at different corners at 1.2 V supply voltage

Output	Nominal	Min	Max	SS	SF	FS	FF	TT
Delay (ns)	1.061	1.047	1.075	1.075	1.066	1.066	1.047	1.061
Total power (nW)	200.8	200.8	200.8	200.8	200.8	200.8	200.8	200.8
PDP (aJ)	11.27	11.27	11.27	11.27	11.27	11.27	11.27	11.27

Table 3 Simulation results of RCA at 0.8 V supply

Design	At 0.8 V supply voltage			
	average power (μW)	Delay (ps)	PDP (fJ)	EDP(10^{-24} J)
1-bit Adder	0.089	138.185	0.05	0.006
4-bit RCA	1.95	285.6	0.56	0.159
64-bit RCA	14.23	748.943	10.66	7.984

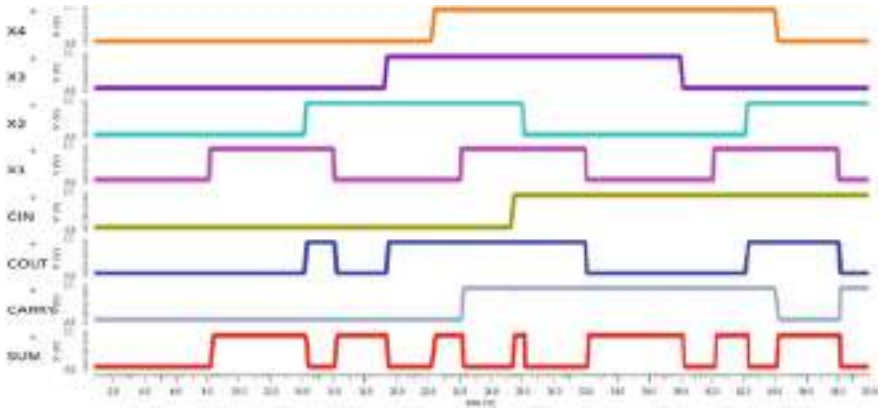

Fig. 8 Simulation waveform of 4:2 compressor

The extension of proposed adder in RCA gives satisfactory performance at 4-bit and 64-bit, respectively, and the performance comparison establishes the hybrid scalable adder as promising circuit for high-performance digital circuits.

4.3 4:2 Compressor

The operation of 4:2 compressor has been verified using the Eqs. 1–3, Fig. 8 shows simulation waveform of 4:2 compressor.

The standard deviation of delay of designed compressor is achieved to be 6.835 ps with Monte Carlo simulations for a run of 1000 samples as depicted in Fig. 9. Table 4 shows the max, min, mean, median, and std dev. of designed compressor.

5 Conclusion

In this paper, a new hybrid FA is presented which shows enhanced performance while maintaining full swing operation. The parameters of this proposed design have been compared from existent FAs. For comparison and analysis, Cadence Virtuoso 45-nm technology was used. The results of simulation depicts that proposed FA shows the supercilious performance of power and PDP when steered as one cell, and also when further extended to 64-bits. For 64-bits at 1 V supply, static power is 7.65489 μW and dynamic power is 6.57304 μW. This proposed FA has the potentiality for operating while not including buffers in intermediary stage, on extending. This design, in comparison with several designs like CPL, TGA, Hybrid 1, GDI 1, GDI 2, SERF, shows significantly lesser power consumption. The design shows 44% at 1 V and 35% power improvement at 0.8 V in comparison with other designs. The results of

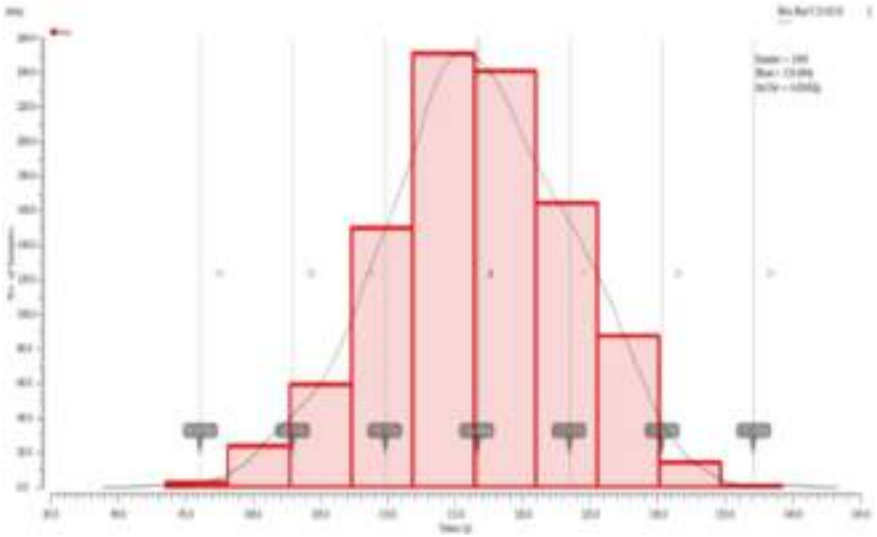

Fig. 9 Histogram diagram of Monte Carlo simulation for delay with 1000 samples

Table 4 Monte Carlo simulation results

Output	Min	Max	Mean	Median	Std. Dev
Total power (nW)	542.7	542.7	542.7	542.7W	0
Delay (ps)	93.54	139.2	116.6	116.5	6.835
PDP (aJ)	63.21	63.21	63.21	63.21	0
EDP (J)	7.364×10^{-27}	7.364×10^{-27}	7.364×10^{-27}	7.364×10^{-27}	0

simulation infer that this design offers the finest PDP as compared with others, which sums this design can be a righteous alternative at scaled technology. Finally, a 4:2 compressor implemented with this adder shows superior performance for the supply of 1 V with the power 542.7 nW, delay 116.5 ps, PDP 63.21 aJ, and EDP 7.364e-27 J. From the analysis, it is realized that this proposed adder manifests exemplary integrity of signal with propel proficiency in low voltage operation. It is notable that this design of full adder consumes low power and has higher speed. In future, this design can be used in FIR filters, processors with ALUs, and MAC units.

References

1. S. Usha, T. Ravi, Design of 4-BIT ripple carry adder using hybrid 9T full adder, in *2015 International Conference on Circuits, Power and Computing Technologies [ICCPCT-2015]* (2015), pp. 1–8. https://doi.org/10.1109/ICCPCT.2015.7159490
2. I. Hassoune, D. Flandre, I. O'Connor, J. Legat, ULPFA: a new efficient design of a power-aware full adder. IEEE Trans. Circ. Syst. I Regul. Pap. **57**(8), 2066–2074 (2010). https://doi.org/10.1109/TCSI.2008.2001367
3. I.C. Wey, C.H. Huang, H.C. Chow, A new low-voltage CMOS 1-bit full adder for high performance applications, in *Proceedings. IEEE Asia-Pacific Conference on ASIC* (Taipei, Taiwan, 2002), pp. 21–24. https://doi.org/10.1109/APASIC.2002.1031522
4. S. Goel, S. Gollamudi, A. Kumar, M.A. Bayoumi, On the design of low energy hybrid CMOS 1-bit full adder cells, in *Proceedings of 47th IEEE International Conference Midwest Symposium Circuits and System* (Hiroshima, Japan, 2004), pp. 209–212
5. S. Nagaraj, G.M.S. Reddy, S.A. Mastani, Analysis of different Adders using CMOS, CPL and DPL logic, in *14th IEEE India Council International Conference (INDICON).* (Roorkee, India, 2017), pp. 1–6. https://doi.org/10.1109/INDICON.2017.8487636
6. P. Lee, C. Hsu, Y. Hung, Novel 10-T full adders realized by GDI structure, in *International Symposium on Integrated Circuits* (Singapore, 2007), pp. 115–118. https://doi.org/10.1109/ISICIR.2007.4441810
7. V. Saraswat, A. Kumar, P.K. Pal, R.K. Nagaria, A survey on different modules of low-power high-speed hybrid full adder circuits, in *2017 4th IEEE Uttar Pradesh Section International Conference on Electrical, Computer and Electronics (UPCON)* (Mathura, India, 2017), pp. 323–328. https://doi.org/10.1109/UPCON.2017.8251068
8. R. Katragadda, Analysis of low power methods in 14T full adder, in *2015 2nd International Conference on Electronics and Communication Systems (ICECS)* (Coimbatore, India, 2015), pp. 1210–1215. https://doi.org/10.1109/ECS.2015.7124776
9. M. Gadekar, R. Chavan, N. Matkar, S. Jagushte, S. Joshi, Design of 16T full adder circuit using 6TXNOR gates, in *2017 International Conference on Advances in Computing, Communication and Control (ICAC3)* (Mumbai, India, 2017), pp. 1–4. https://doi.org/10.1109/ICAC3.2017.8318761
10. M. Amini-Valashani, M. Ayat, S. Mirzakuchaki, Design and analysis of a novel low-power and energy-efficient 18T hybrid full adder. Microelectron. J. **74**, 49–59 (2018). https://doi.org/10.1016/j.mejo.2018.01.018
11. N.A. Kamsani, V. Thangasamy, S.J. Hashim, Z. Yusoff, M.F. Bukhori, M.N. Hamidon, A low power multiplexer based pass transistor logic full adder, in *Regional Symposium Micro and Nanoelectronics (RSM)* (Kuala Terengganu, Malaysia, 2015), pp. 1–4. https://doi.org/10.1109/RSM.2015.7354994
12. S. Mishra, S.S. Tomar, S. Akashe, Design low power 10T full adder using process and circuit techniques, in *2013 7th International Conference on Intelligent Systems and Control (ISCO)* (2013), pp. 325–328. https://doi.org/10.1109/ISCO.2013.6481172
13. V. Nafeez, M.V. Nikitha, M.P. Sunil, A novel ultra-low power and PDP 8T full adder design using bias voltage, in *2nd International Conference for Convergence in Technology (I2CT)* (Mumbai, India, 2017), pp. 1069–1073. https://doi.org/10.1109/I2CT.2017.8226292
14. C. Venkatesan, S.M. Thabsera, M.G. Sumithra, M. Suriya, Analysis of 1- bit full adder using different techniques in Cadence 45 nm Technology, in *2019 5th International Conference on Advanced Computing & Communication Systems (ICACCS)* (2019), pp. 179–184. https://doi.org/10.1109/ICACCS.2019.8728449
15. P. Meher, K.K. Mahapatra, A high speed low noise CMOS dynamic full adder cell, in *International Conference on Circuits, Controls and Communications (CCUBE)* (Bengaluru, India, 2013), pp. 1–4. https://doi.org/10.1109/CCUBE.2013.6718575
16. M. Shoba, R. Nakkeeran, GDI based full adders for energy efficient arithmetic applications. Eng. Sci. Technol. Int. J. **19**(1), 485–496 (2016). https://doi.org/10.1016/j.jestch.2015.09.006

17. A. Neve, H. Schettler, T. Ludwig, D. Flandre, Power-delay product minimization in high-performance 64-bit carry-select adders, in *IEEE Transactions on Very Large Scale Integration (VLSI) Systems*, vol. 12, no. 3 (2004), pp. 235–244. https://doi.org/10.1109/TVLSI.2004.824305
18. K.A.K. Maurya, Y.R. Lakshmanna, K.B. Sindhuri, N.U. Kumar, Design and implementation of 32-bit adders using various full adders, in *2017 Innovations in Power and Advanced Computing Technologies (i-PACT)* (Vellore, India 2017), pp. 1–6. https://doi.org/10.1109/IPACT.2017.8245176
19. A.S. Vani, M.R. Lokesh, B.S. Devi, A.K.K.V.N.S. Kushal, A.P. Kumar, A novel low power multiplier and full adder using hybrid CMOS logic, in *International Conference of Electronics, Communication and Aerospace Technology (ICECA)* (Coimbatore, India, 2017), pp. 303–307. https://doi.org/10.1109/ICECA.2017.8203692
20. G. Manikannan, K. Mahendran, P. Prabakaran, Low power high speed full adder cell with XOR/XNOR logic gates in 90 nm technology, in *2017 International Conference on Technical Advancements in Computers and Communications (ICTACC)* (Melmaurvathur, 2017), pp. 61–65. https://doi.org/10.1109/ICTACC.2017.25
21. A.K. Yadav, B.P. Shrivatava, A.K. Dadoriya, Low power high speed 1-bit full adder circuit design at 45nm CMOS technology, in *2017 International Conference on Recent Innovations in Signal processing and Embedded Systems (RISE)* (Bhopal, India, 2017), pp. 427–432. https://doi.org/10.1109/RISE.2017.8378203
22. A. Khan, S. Wairya, High performance 3–2 compressor using efficient XOR-XNOR in nanotechnology, in *International Conference on VLSI & Microwave and Wireless Technologies, (ICVMWT)* (Gorakhpur, India, 2021)
23. H. Pei, X. Yi, H. Zhou, Y. He, Design of ultra-low power consumption approximate 4–2 compressors based on the compensation characteristic. IEEE Trans. Circuits Syst. II Express Briefs **68**(1), 461–465 (2021). https://doi.org/10.1109/TCSII.2020.3004929
24. P. Bhattacharyya, B. Kundu, S. Ghosh, V. Kumar, A. Dandapat, Performance analysis of a low-power high-speed hybrid 1-bit full adder circuit, in *IEEE Transactions on Very Large Scale Integration (VLSI) Systems*, vol. 23, no. 10 (2015), pp. 2001–2008. https://doi.org/10.1109/TVLSI.2014.2357057

A Novel Controlled Positive Feedback Class AB OTA

Annu Dabas, Richa Yadav, and Maneesha Gupta

Abstract This paper presents a novel controlled positive feedback RFC OTA. An extra current source is used in feedback to control and enhance the transconductance of RFC OTA. A flipped voltage follower is used to provide the biasing to the input differential pair, which performs the class AB operation. The simulation has been done using Mentor Graphics Eldo with the CMOS technology of 0.18 μm. The capacitive load of 15 pF and supply voltage of ±0.5 V has been used for the simulation. The proposed amplifier results in an improved gain, bandwidth, and phase margin of 73.29 dB, 4.37 MHz, and 69.8°, respectively. The power dissipated by the proposed OTA is 55.50 μW. The figures of merits validate the results of the proposed amplifier. The effects of PVT variations on the proposed amplifier are negligible, which verifies the stability of the circuit.

Keywords Positive feedback · Transconductance · Flipped voltage follower · Bandwidth · Slew rate

1 Introduction

In low-power analog circuits, it has become necessary to implement high-performance amplifiers. The operational transconductance amplifier (OTA) has become very famous in designing analog circuits due to the advancement in CMOS

A. Dabas
Department of Electronics and Communication Engineering, Bharati Vidyapeeth's College of Engineering, New Delhi, India
e-mail: annu.dabas@bharatividyapeeth.edu

A. Dabas · R. Yadav (✉)
Department of Electronics and Communication Engineering, Indira Gandhi Delhi Technical University for Women, New Delhi, India
e-mail: richayadav@igdtuw.ac.in

M. Gupta
Department of Electronics and Communication Engineering, Netaji Subhas University of Technology, New Delhi, India

S. Rawat et al. (eds.), *Proceedings of First International Conference on Computational Electronics for Wireless Communications*, Lecture Notes in Networks and Systems 329,
https://doi.org/10.1007/978-981-16-6246-1_15

technology. Folded Cascode (FC) OTA [1, 2] is generally used for fast and high gain operation at the cost of high power consumption. Now, FC OTA is replaced by Recycling Folded Cascode (RFC) OTA [3] because of its high gain and bandwidth at low power usage. The performance of RFC OTA is restricted by parameter k, which can degrade the phase margin of RFC OTA. Recently various methods like positive feedback [4, 5], local common-mode feedback [6, 7], multipath technique [8, 9], or shunting of current sources [10, 11] have been implemented to boost the performance of RFC OTA. The partial positive feedback technique [4] enhances the output resistance of the OTA, which results in the improved frequency response of the RFC OTA. A local common-mode feedback technique is used to improve the DC gain, unity-gain bandwidth, and also boost the slew rate [6]. The multipath technique [8] is utilized to separate the AC and DC current path of recycling current leads to the improvement in gain and bandwidth of RFC OTA [8]. The shunting of current sources [10] has been implemented to increase the transconductance in the Double Recycling Folded Cascode (DRFC) OTA, which recycles the current at output once again without any extra power [10]. A fully RFC OTA has been designed in [11], which is the enhancement in DRFC OTA [10]. The fully RFC OTA [11] further enhances the DC gain, unity-gain bandwidth, and slew rate without any extra power loss. To double the slew rate of conventional RFC OTA, shorting of two nodes has been implemented in [12]. A new DTMOS based RFC OTA is implemented in [13] to boost the transconductance and slew rate of the amplifier [13].

In this work, a novel Controlled Feedback Recycling Folded Cascode (CFRFC) OTA is introduced. The proposed circuit employs positive feedback that can be controlled by using an extra current source used in feedback to separate the AC and DC currents to boost the transconductance of the amplifier. The bias voltage source is replaced by a flipped voltage follower which provides the class AB operation to the proposed OTA.

This work is described as follows: The conventional FC OTA and RFC OTA are explained in Sect. 2. The concept and circuit of the proposed work are discussed in Sect. 3. The performance parameters of the proposed amplifier are explored in Sect. 4. Sections 5 and 6 contain the simulation results and conclusion, respectively.

2 The Conventional FC OTA and RFC OTA

Figure 1 represents the circuits of conventional FC and RFC OTA. The output current flowing through the folded node in FC OTA has been recycled in RFC OTA to boost the transconductance of the OTA. The output current is limited to factor 'k' in RFC OTA. If the value of 'k' is taken above 3, the phase margin of the OTA degrades severely.

The effective transconductances of both OTAs are given as

$$G_{mFC} = g_{m1} \tag{1}$$

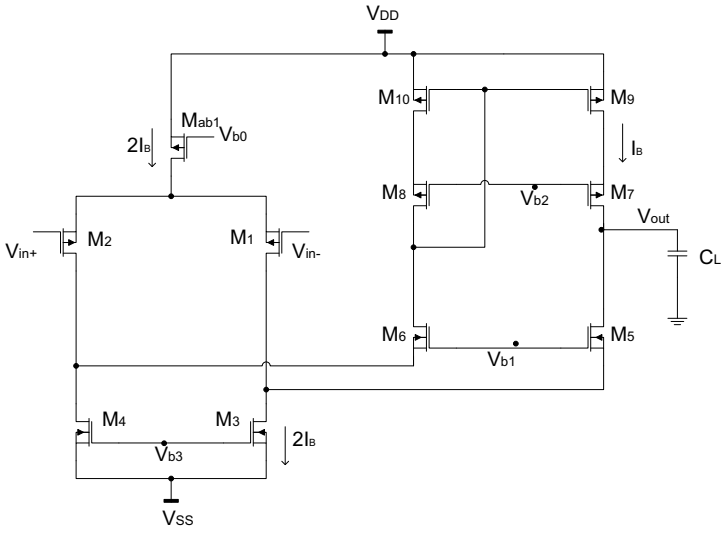

(a)

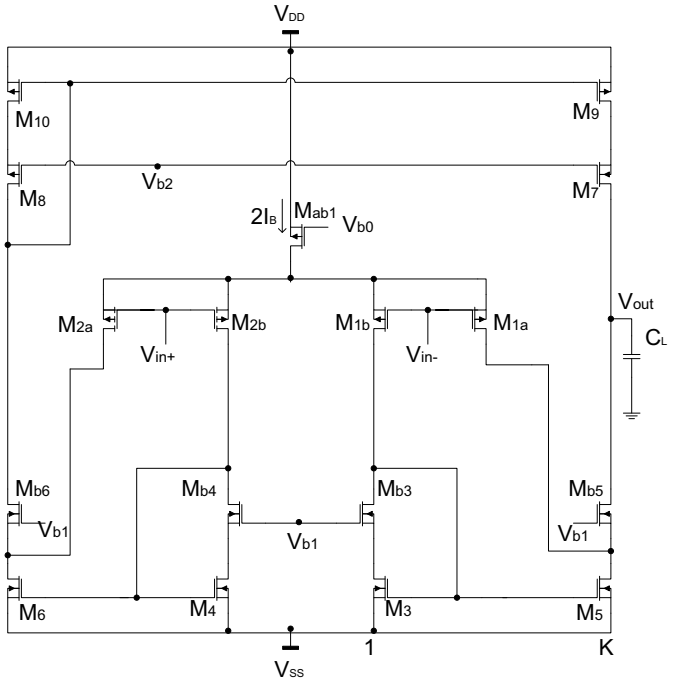

(b)

Fig. 1 **a** The conventional FC OTA [1] **b** The conventional RFC OTA [2]

$$G_{mRFC} = (K+1)g_{m1} \tag{2}$$

The expressions to calculate slew rate in FC and RFC OTAs are given as

$$SR_{FC} = \frac{2 \cdot I_B}{C_L} \tag{3}$$

$$SR_{RFC} = \frac{2 \cdot k \cdot I_B}{C_L} \tag{4}$$

3 The Proposed CFRFC OTA

3.1 Positive Feedback Concept

The block diagram of a positive feedback amplifier is represented in Fig. 2a. Assume that S_{out} is the output signal and S_{in} is the input signal put into the feedback amplifier. So, the closed-loop gain of the positive feedback amplifier can be given as

$$\text{Gain} = \frac{S_{\text{out}}}{S_{\text{in}}} = \frac{A}{(1 - A \cdot \Phi)} \tag{5}$$

Here, 'A' is the forward gain of the feedback amplifier and 'Φ' is the feedback gain for the feedback amplifier. The term '$A \cdot \Phi$' is known as loop gain. The gain of the feedback amplifier can be raised by a factor $\frac{1}{(1-A \cdot \Phi)}$ by precisely choosing the value of loop gain '$A \cdot \Phi$'. The loop gain should be such that $0 < A \cdot \Phi < 1$ provided it should not be either near to 0 or 1, which can lead to no improvement in gain or unstable system respectively [4]. Hence, the idea behind the proposed work is to design such a positive feedback at the load which can be controlled by adjusting the loop gain.

3.2 The Proposed Circuit

Figure 2b shows the proposed circuit. It comprises a split input differential pair made up of transistors M_{1a}:M_{1b} (M_{2a}:M_{2b}) and the cross-coupled current mirror load formed by transistors M_3:M_5 (M_4:M_6). The current flowing through the transistor M_3 (M_4) is recycled at the output by using split transistor M_{1b} (M_{2b}) at the load. The drain current flowing through the input stage transistors M_{1b} (M_{2b}) is portioned into two paths: AC current path which flows through transistor M_3 (M_4) and DC current path which flows through transistor M_7 (M_8). The positive feedback to the CFRFC

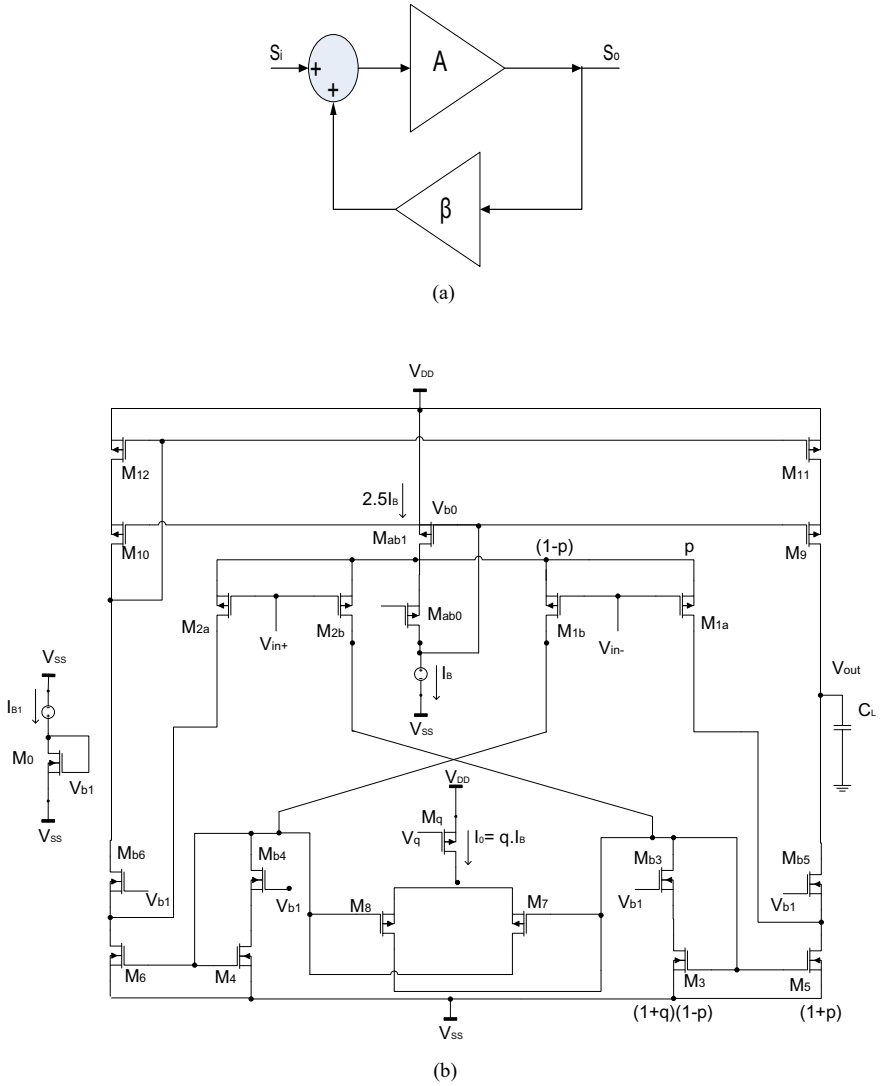

Fig. 2 **a** Block diagram of feedback amplifier [4] **b** The proposed CFRFC OTA circuit

OTA is provided by using PMOS transistors M_7 (M_8) and a DC current source, I_0 which controls the DC current in feedback. A PMOS transistor M_q with a bias voltage of V_q generates the DC current, I_0. The loop gain $A \cdot \beta$ of the proposed amplifier is dependent on device sizes of PMOS transistors M_7 (M_8) and is controlled by DC current I_0.

The biasing current to the input differential pair is provided by a flipped voltage follower formed by transistors M_{ab0} and M_{ab1}, which turn out in class AB operation.

The flipped voltage follower is also used to bias the transistors M_9 and M_{10}. The bias voltage V_{b1} is produced by using transistor M_0 and the current source I_{B1} as shown in Fig. 2b.

4 Performance Parameters of Proposed CFRFC OTA

4.1 Transconductance

The effective transconductance of the CFRFC OTA can be depicted as

$$G_{mCFRFC} = \left(g_{m1a} + \frac{g_{m1b}}{\left(1 - {g_{m7}}/{g_{m3}}\right)} g_{m5} \right) \tag{6}$$

In terms of current ratio, the effective transconductance can be given as

$$G_{mCFRFC} = g_{m1}\left(p + \frac{(1+p)}{(1+q)} \right) \tag{7}$$

By employing positive feedback, the gain of the proposed amplifier can be enhanced by a factor $\frac{1}{(1-A\cdot\Phi)}$. For the proposed circuit, the loop gain, $A \cdot \beta$, can be derived as

$$A \cdot \Phi = \frac{g_{m7}}{g_{m3}} \tag{8}$$

$$A \cdot \Phi = \sqrt{\left(\frac{K_p}{K_n}\right)\left(\frac{W_7/L_7}{W_3/L_3}\right)\left(\frac{I_0}{I_0 + I_B}\right)} \tag{9}$$

where 'K_p' and 'K_n' are the transconductance parameters of PMOS and NMOS transistors, respectively. Hence, the loop gain of the proposed OTA is dependent on the transistors sizes, transconductance parameters, and the biasing currents.

4.2 Gain Bandwidth Product

To design the RFC OTA, gain-bandwidth product is a very important figure. Since the OTA exhibits a trade-off between its gain and bandwidth, it is required to carefully design the OTA. The expression of the gain-bandwidth product of the proposed OTA is given as

$$GBW_{CFRFC} = \frac{\left(g_{m1a} + \frac{g_{m1b}}{\left(1-g_{m7}/g_{m3}\right)} g_{m5}\right)}{2\Psi C_L} \tag{10}$$

4.3 Slew Rate

Slew rate is also a very challenging parameter in designing OTA, which is described as the maximum rate of change of output voltage provided by the proposed circuit. When a small positive signal is put into the input V_{in+}, the transistors M_{2a} and M_{2b} turn off which drives the transistors M_3, M_5, and M_8 to turn off. It results in the rising of the drain voltage of M_5 and transistors M_{1a} and M_{b5} go into the deep triode region. Since transistors M_{1a} and M_{1b} turn on, the bias current flows through the transistor M_4, which is rectified by transistor M_6. The expression of CFRFC OTA can be calculated as

$$SR_{CFRFC} = \frac{(1+p)}{(1+q)} \frac{(I_B + I_0)}{C_L} \tag{11}$$

The total bias current increases due to the addition of extra current I_0, which further enhances the slew rate.

5 Simulation Results

The conventional FC, RFC, and the proposed CFRFC OTA have been simulated in Mentor Graphics Eldo with 180 nm CMOS technology and the supply voltage of ±0.5 V. The capacitive load of 15 pF and biasing current I_B of 8 μA are used in the circuit. The biasing current $I_0 = 0.1$ μA is generated by using a PMOS transistor M_q with biasing voltage V_q of −0.7 V. The transconductance of CFRFC OTA can be varied by varying the biasing current I_0. To confirm the working of all the transistors in the saturation region, the biasing voltage V_{b1} is set by the transistor M_0 and current source I_{B1} as shown in Fig. 2b and the biasing voltages V_{b2} and V_{b3} in FC and RFC OTA are taken as −0.6 and 0.4 V, respectively. The power dissipation for all three OTAs is the same as 55.50 μW. The size of all the transistors in the proposed CFRFC OTA is listed in Table 1.

Figure 3 shows the frequency response of all three OTAs. It depicts that the simulated FC, RFC, and the proposed CFRFC OTAs result in the DC gain of 56.44, 64.38, and 73.29 dB and unity-gain bandwidth of 0.7, 3.86, and 4.37 MHz at phase margin of 88.19°, 67.22°, and 69.80°, respectively. The simulated frequency response depicts that the DC gain of CFRFC OTA is improved by 1.3 and 1.1 times of FC and

Table 1 The size of the transistors of CFRFC OTA

S. No.	Transistors	W(μm)/L(μm)
1	M_{1a}, M_{1b}, M_{2a}, M_{2b}	20/1
2	M_3, M_4, M_{3b}, M_{4b}	5/1
3	M_5, M_6, M_{5b}, M_{6b}	50/1
4	M_7, M_8	1/1
5	M_9–M_{12}	140/1
6	M_{ab0}	80/1
7	M_{ab1}	14/1
8	M_p	1/1

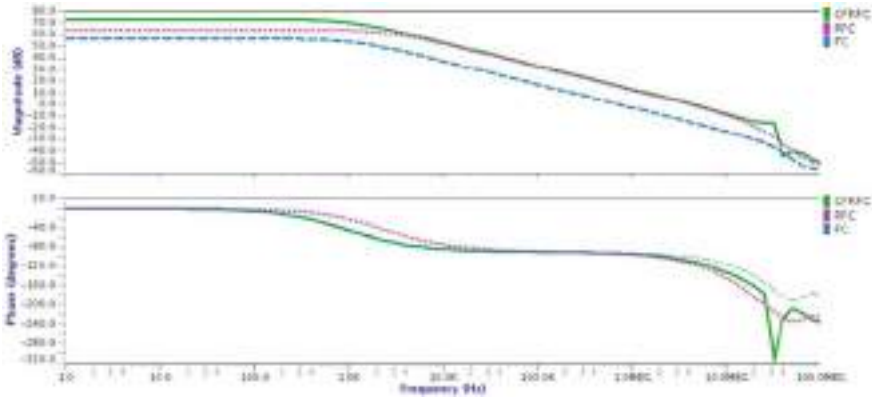

Fig. 3 Frequency response of the FC, RFC, and CFRFC OTAs

RFC OTA, respectively whereas the unity-gain bandwidth is 6.2 and 1.1 times of FC and RFC OTA, respectively.

Figure 4 shows the simulated results of the slew rate for all three OTAs. The slew rates of 0.54, 1.03, and 1.01 V/μs are achieved by FC, RFC, and CFRFC OTA, respectively. The slew rate of the CFRFC OTA is 1.8 times that of FC OTA and is almost equal to the RFC OTA.

Figure 5 depicts the noise performance of all the simulated OTAs. The PMOS input differential pair is used in the simulated circuits, which provide better noise performance and results in input noise of 73.49, 37.53 and 39.88 $^{nV^2}/_{\sqrt{\text{Hz}}}$ for FC, RFC, and CFRFC OTA, respectively.

Tables 2 and 3 depict that there is a negligible effect of the PVT variation on the frequency response of the proposed CFRFC OTA, which proves the stability of the circuits. In Table 2, the best case and worst case process variation results have been shown at temperatures −40 and 40 °C, whereas Table 3 shows the effects of ±5% variation in power supply on the frequency response of the proposed circuit. Table 4 compares the simulated results of FC, RFC, and CFRFC OTA. The figure of merits,

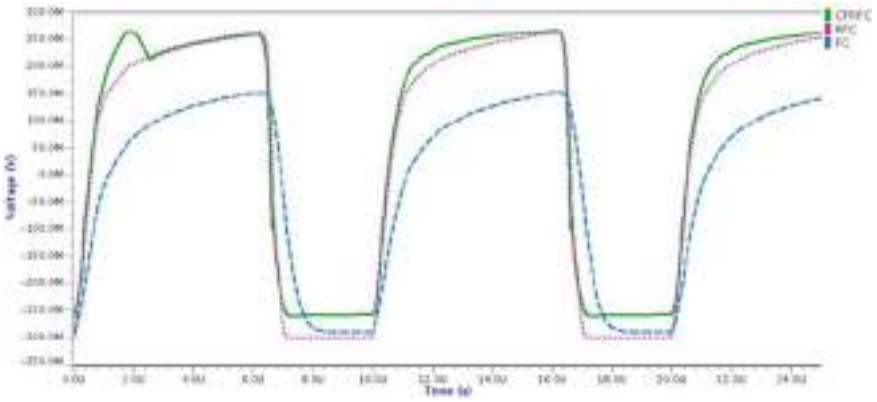

Fig. 4 Simulated results of FC, RFC, and CFRFC OTAs to measure the slew rate

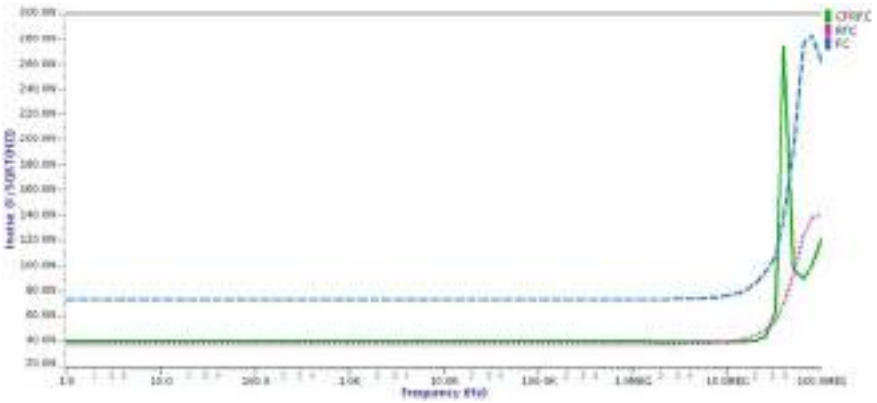

Fig. 5 Simulated results of input noise of FC, RFC, and CFRFC OTAs

Table 2 Process and temperature variation effects on the frequency response of the CFRFC OTA

	Temp = −40°		Temp = 40°	
	FF	SS	FF	SS
Gain (dB)	71.58	70.67	73.32	71.19
Unity gain bandwidth (MHz)	5.66	3.70	4.63	2.21
Phase margin (°)	69.69	77.07	68.03	79.53

Table 3 Effects of power supply variation for the frequency response of the proposed OTA

Voltage supply	±0.45	±0.55
Gain (dB)	70.75	73.83
Unity gain bandwidth (MHz)	2.79	4.76
Phase margin (°)	77.62	68.18

Table 4 Comparative analysis of the performance of FC, RFC, and CFRFC OTAs

	FC	RFC	CFRFC
Technology (nm)	180	180	180
Supply (V)	±0.5	±0.5	±0.5
Load (pF)	15	15	15
Gain (dB)	56.44	64.38	73.29
Unity gain bandwidth (MHz)	0.73	3.96	4.37
Phase margin (°)	88.19	67.22	69.8
CMRR (dB)	105.75	94.63	98.26
Average slew rate (V/μs)	0.54	1.03	1.01
Noise $\left(V^2/\sqrt{Hz}\right)$	73.49n	37.52n	39.68n
P_d (μW)	55.50	55.50	55.50
FOM1 (MHz · dB · pF)/μW	11.11	68.88	86.48
FOM2 (V/μs · dB · pF)/μW	8.18	17.89	19.93

FOM1 and FOM2, for all three OTAs demonstrate the remarkable enhancement in the performance of the proposed CFRFC OTA against the counterparts.

6 Conclusion

The FC, RFC, and CFRFC OTAs are simulated in this work. The DC gain of the simulated circuit is measured as 56.44, 64.34, and 73.29 dB for FC, RFC, and CFRFC OTA, respectively. The frequency response of FC, RFC, and CFRFC OTA also results in unity-gain bandwidth of 0.73, 3.96, and 4.37 MHz, respectively. The slew rate of the FC, RFC, and CFRFC OTA can be measured as 0.54, 1.03, and 1.01 V/μs, respectively. Hence, the proposed CFRFC OTA shows the remarkable improvement of 1.3, 6.2, and 1.8 times in DC gain, unity-gain bandwidth, and slew rate of FC OTA. The gain of the proposed circuit is also controllable just by controlling the current in the feedback of the amplifier.

References

1. P.R. Gray, R.G. Meyer, *Analysis and Design of Analog Integrated Circuits* (John Wiley & Sons Inc., 1990)
2. S. Banagozar, M. Yargholi, Ultra-low power two-stage class-AB recycling double folded cascode OTA. Int. J. Electron. Commun. (AEU) **110**, 152848 (2019). https://doi.org/10.1016/j.aeue.2019.152848
3. R.S. Assaad, J. Silva-Martinez, The recycling folded cascode: a general enhancement of the folded cascode amplier. IEEE J. Solid State Circuit **44**, 2535–2542 (2009). https://doi.org/10.

1109/JSSC.2009.2024819
4. R. Wang, R. Harjani, Partial positive feedback for gain enhancement of low power CMOS OTAs. Analog Integr. Circuits Signal Process. **8**(1), 21–35 (1995). https://doi.org/10.1007/BF01239377
5. A. Toktam, B. Sadegh, A. Golmakani, Gain boosting of recycling folded cascode OTA using positive feedback and introducing new input path. Analog Integr. Circuits Signal Process. **90**, 237–246 (2017). https://doi.org/10.1007/s10470-016-0874-2
6. X. Zhao, Q. Zhang, Y. Wang, M. Deng, Transconductance and slew rate improvement technique for current recycling folded cascode amplifier. J. Electron. Commun. (AEU) **70**, 326–330 (2016). https://doi.org/10.1016/j.aeue.2015.12.015
7. M.P. Garde, A.J. Lopez-Martin, R.G. Carvajal, J. Ramirez-Angulo, Super class AB RFC OTA with adaptive local common-mode feedback. Electron. Lett. **54**, 1272–1274 (2018). https://doi.org/10.1049/EL.2018.6362
8. Q. Zhang, X. Zhao, X. Zhang, Q. Zhang, X. Zhao, Multipath recycling method for transconductance enhancement of folded cascade amplifier. Int. J. Electron. Commun. (AEU) **72**, 1–7 (2016). https://doi.org/10.1016/j.aeue.2016.11.010
9. Y. Li, K.F. Han, X. Tan, N. Yan, H. Min, Transconductance enhancement method for operational transconductance amplifiers. Eletron. Lett. **46**(19), 1321–1323 (2010). https://doi.org/10.1049/el.2010.1575
10. Z. Yan, P. Mak, R.P. Martins, Double recycling technique for folded-cascode OTA. Analog Integr. Circuits Signal Process. **71**, 137–141 (2012). https://doi.org/10.1007/s10470-011-9762-y
11. M. Akbari, Single-stage fully recycling folded cascode OTA for switched-capacitor circuits. Electron. Lett. **51**(13), 977–979 (2015). https://doi.org/10.1049/el.2015.1053
12. S.V. Feizbakhsh, G. Yosef, An enhanced fast slew rate recycling folded cascode Op-Amp with general improvement in 180 nm CMOS process. Int. J. Electron. Commun. (AEU) **101**, 200–217 (2019). https://doi.org/10.1016/j.aeue.2019.01.021
13. A.S. Khade, S. Musale, R. Suryawanshi, V. Vyas, A DTMOS-based power efficient recycling folded cascode operational transconductance amplifier. Analog Integr. Circuits Signal Process. **107**, 227–238 (2020). https://doi.org/10.1007/s10470-021-01809-y

Low-Power and High-Speed Design of FinFET-Based MCML Delay Element

Pragya Srivastava, Richa Yadav, and Richa Srivastava

Abstract This paper carries a performance evaluation of delay elements based on propagation delay (t_p), power (PWR), Power-delay product (PDP), and Energy-delay product (EDP). The research article analyses a MOSFET-based CMOS delay element (M-CMOS DE) and a MOSFET-based MCML delay element (M-MCML DE). Simulation results establish the superior performance of M-MCML DE in terms of t_p, PWR, PDP and EDP. M-MCML DE exhibit improvement in t_p (58.98×), PWR (1.66 K×), PDP (98.07 K×), and EDP (5781.99 K×). Simulation outcomes validate that the MCML based design is a competent candidate to replace the traditional CMOS-based design. As an extension of work, M-MCML DE is implemented using an emerging device—FinFET. The proposed FinFET-based MCML delay element (FinFET MCML DE) emerges as ultra-fast and low power design of delay element. It offers improvement in t_p (1.1×), PWR (34.28×), PDP (37.71×), and EDP (41.29×). In this research article, we restrict our attention to design metrics such as t_p, PWR, PDP, and EDP. This monograph will rouse more research activities in the area of low power and robust design of digital circuits.

Keywords CMOS · MOS current mode logic (MCML) · Delay element · Propagation delay (t_p) · Power (PWR) · Power-delay product (PDP) · Energy-delay product (EDP) · FinFET · Delay element

P. Srivastava (✉) · R. Yadav
ECE Department, IGDTUW, New Delhi, India

R. Yadav
e-mail: richayadav@igdtuw.ac.in

R. Srivastava
KIET Group of Institutions, Delhi-NCR, Ghaziabad, India
e-mail: richa.srivastava@kiet.edu

S. Rawat et al. (eds.), *Proceedings of First International Conference on Computational Electronics for Wireless Communications*, Lecture Notes in Networks and Systems 329,
https://doi.org/10.1007/978-981-16-6246-1_16

1 Introduction

The delay element is an integral component of a circuit that introduces a predetermined amount of time delay. Similarly, delay lines also serve the same purpose in various electronic circuits. Delay elements serve numerous applications, one such application is time-to-digital converters [1]. A 4 bit digitally controlled, Differential Delay Element (DCDE) exhibiting high resolution has been presented in [2]. A unique design of a non-foster delay element that uses a distributed amplifier and is synthesized by adjusting transconductance has been demonstrated in [3]. A photonic time delay element has been realized in a lossy environment that is also voltage controlled [4]. A Delay-Locked Loop (DLL) using a data delay line is designed at a 45-nm technology node in [5] which only consumes 17 mW of power. A tunable and dispersion-less optical delay showing high speed has been realized in [6].

A delay element can be realized using 'n' number of inverters, connected back-to-back, where 'n' must be an even number. In this research article, a delay element is studied and analyzed for its CMOS- and MCML-based implementation. The above-mentioned study was carried out using MOSFETs for both variants of the delay element. Simulation work carried out in this treatise has been conducted at a 16-nm technology node using an HSPICE simulator. Also, the study of process parameters and their related simulations has been conducted using the Predictive Technology Model (PTM), by the Nanoscale Integration and Modeling (NIMO) Group at Arizona State University (ASU) [7].

The remaining of the paper is structured as follows:

- Section 2 conducts a comparative analysis of M-CMOS DE and M-MCML DE at 0.7 V VDD. An analysis is done for significant parameters such as t_p, PWR, PDP, and EDP.
- Section 3 implements the superior design of delay element (emerged in Sect. 1) with FinFET. In this section, the conventional MOSFETs are replaced with emerging device FinFETs. A novel design of FinFET based MCML delay element—FinFET MCML DE is proposed.
- Finally, the conclusion of the treatise appears in Sect. 4.

2 Analysis of Delay Element

2.1 M-CMOS DE

CMOS-based implementations are the most common extensively used in digital circuits for their efficient performance. Their tremendous noise immunity and reduced static power utilization is an add-on. In this research work, an M-CMOS DE is implemented as shown in Fig. 1.

Fig. 1 M-CMOS DE

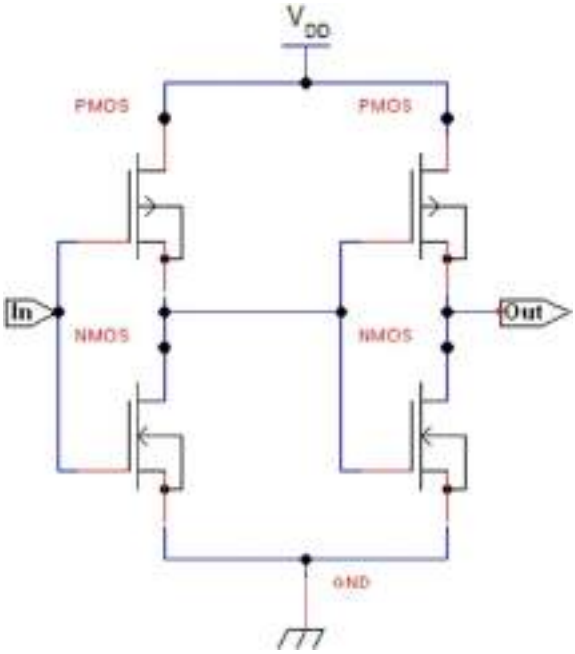

2.2 M-MCML DE

MCML topologies are low power and high-speed delivering implementations [8]. They also provide the complement of the output along with the output itself, in the same circuit [9]. This is achieved by its differential operation. As compared to CMOS based delay element, MCML-based design earns more importance because the latter can be realized using only a single stage. Whereas the former needs an additional second stage to process a buffer operation. An M-MCML DE is implemented using MCML topology as shown in Fig. 2.

M-CMOS DE and M-MCML DE are implemented at a 16-nm technology node at 0.7 V VDD. These circuits are further examined for important design metrics using the HSPICE simulator. The corresponding results are reported in the next subsection.

2.3 Simulation Results and Discussion

The above-described delay element circuits were successfully simulated. The corresponding simulation waveforms are shown in Fig. 3 (waveform of M-CMOS DE) and Fig. 4 (waveform of M-MCML DE). As the delay element is a buffer circuit that adds a time delay to the circuit, its related waveform shows the replica at the output.

Fig. 2 M-MCML DE

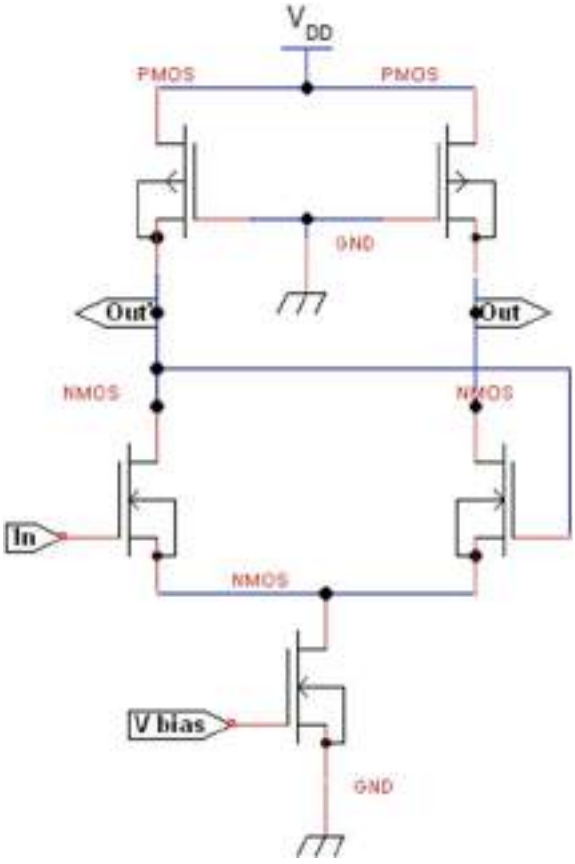

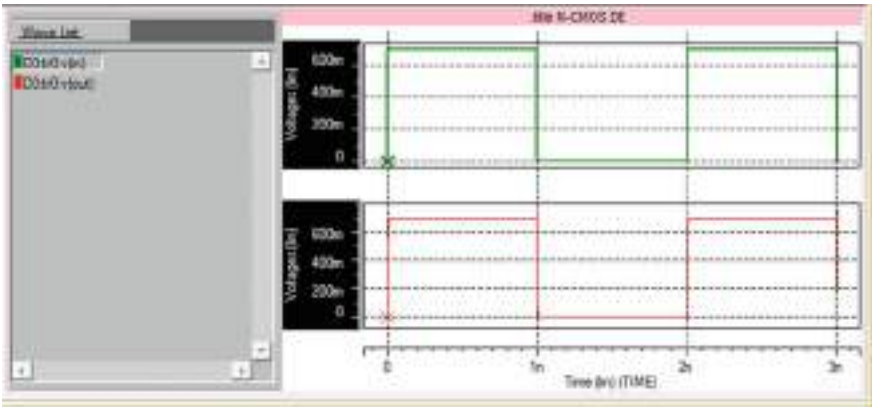

Fig. 3 Simulation waveform of M-CMOS DE

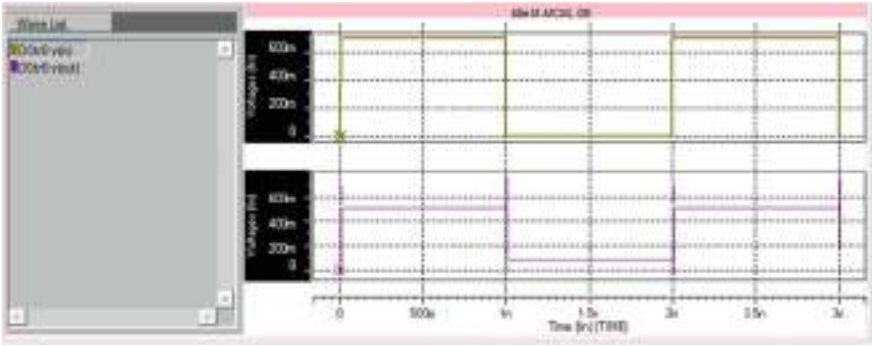

Fig. 4 Simulation waveform of M-MCML DE

Table 1 Design metrics of M-CMOS DE and M-MCML DE

Device parameter Supply = 0.7 V	M-CMOS DE	M-MCML DE
t_p (ns)	1.85	0.0313 (58.98)
PWR (μW)	3.59	0.00216 (1.66 K)
PDP (fJ)	6.62	0.0000675 (98.07 K)
EDP (fJ-ns)	12.2	0.00000211 (5781.99 K)

It can be seen that MCML based delay element is exhibiting a low voltage swing (Fig. 4) and hence the short delay.

The two variants of the delay element are also investigated for t_p, PWR, PDP, and EDP. The simulation outcomes are tabulated in Table 1 and also shown in Figs. 5 and 6 to visualize the comparison easily. Our simulation results validate high speed and low power characteristics of M-MCML DE as compared to CMOS-based M-CMOS DE. t_p and PWR comparison for both circuits are plotted using 3D stacked column

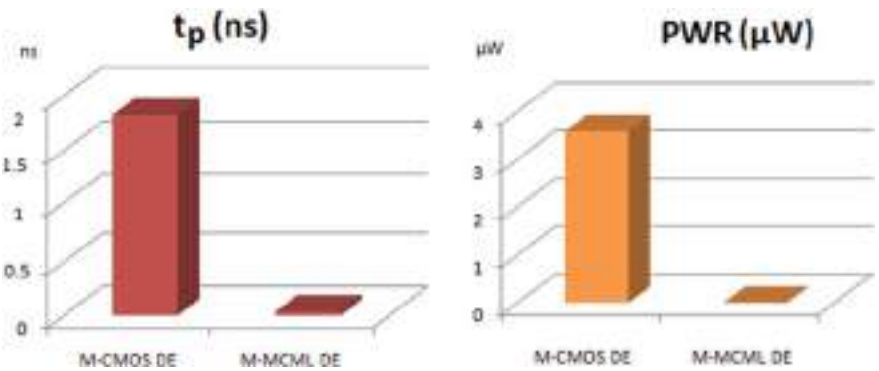

Fig. 5 t_p and PWR comparison of M-CMOS DE and M-MCML DE

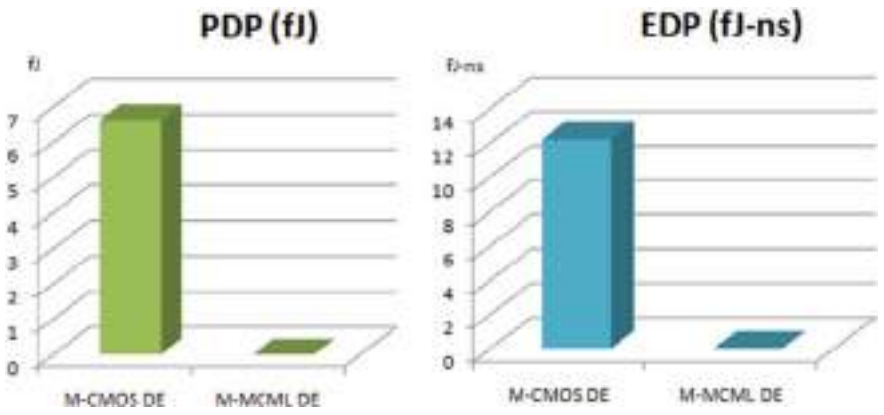

Fig. 6 PDP and EDP comparison of M-CMOS DE and M-MCML DE

in Fig. 5. M-MCML DE is faster (58.98×) and exhibits less PWR (1.66 K×) than M-CMOS DE.

PDP and EDP are essential to design metrics mathematically derived from t_p and PWR. PDP is the product of t_p and PWR. Similarly, EDP is the product of t_p and PDP. Therefore, a design engineer finds PDP and EDP as more effective evaluation parameters as they combine the properties of t_p and PWR. PDP and EDP comparisons for M-CMOS DE and M-MCML DE are plotted using a 3D stacked column in Fig. 6. M-MCML DE shows improvement in PDP (98.07 K×) and EDP (5781.99 K×) as compared to the CMOS counterpart.

Extensive simulation and its results establish M-MCML DE as a competent candidate to be considered for future research. As an extension to this work, a novel design of delay elements is proposed by replacing conventional MOSFETs with the most modish FinFETs in M-MCML DE. The novel design 'FinFET MCML DE' is implemented and discussed in the next section.

3 Emerging Device Technology

3.1 FinFET as an Emerging Device

FinFET-based designs have excellent electronic properties [10] and are more compatible with present technology. In this article, a FinFET-based delay element is implemented. FinFET is typically a multiple-gate transistor, wherein the gate terminal is located around the sides of the channel. In case of a double gate structure, either of the gate terminals is placed on the two sides of the channel. These terminals are called as front gate and back gate. Such a vertical double-gate structure also leads to reduced short-channel effects with improved scalability [11].

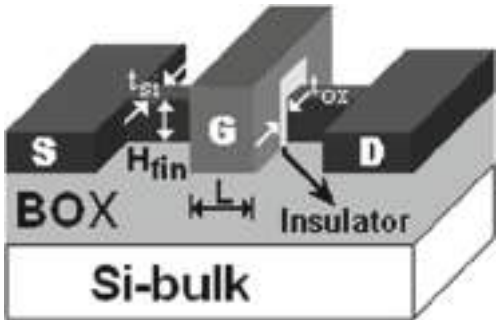

Fig. 7 A typical FinFET structure [11]

Table 2 FinFET device and technology parameters used to implement FinFET MCML DE

Parameter	L_{eff}	W_{fin}	H_{fin}	T_{ox}	V_{DD}
Value	20 nm	12 nm	16 nm	1.35 nm	0.7 V

FinFET has nonplanar geometry with its front gate (FG) and back gate (BG) hitched together. It is also called double gate MOSFET (DG-MOS). A symmetrical FinFET structure is shown in Fig. 7. 'Fin' like the structure of gate terminal gives the device its name—FinFET. The width of the Fin is notably smaller than the height of the Fin (H_{fin}). As a result, the width of the device is 2 H_{fin}. Similarly, the use of multiple Fins can provide a larger device width. Further, λ is the term used as scaling limit of FinFET, and $L_{min} * 1.5$ λ. λ is mathematically defined as $\lambda = W_{fin} + 2tox$, where W_{fin} is the silicon Fin width and tox is insulator thickness. L_{min} is the 'minimum channel length' of the FinFET which lies between 5 and 10 nm [12].

The corresponding FinFET device parameters utilized to implement the design, 'FinFET MCML DE', are reported in Table 2.

3.2 Proposed Design of Delay Element—FinFET MCML DE

Simulation and results discussed in Sect. 2 establish the superior performance of M-MCML DE over M-CMOS DE. Therefore, our proposed circuit is a design of MCML-based delay element implemented by using FinFETs instead of conventional MOSFETs. The proposed circuit is shown in Fig. 8 as 'FinFET MCML DE'. The proposed design is also examined for t_p, PWR, PDP, and EDP, and the corresponding results are tabulated in Table 3. Table 3 shows that FinFET-based realization offers shorter delay (1.1×), reduced PWR (34.28×), less PDP (37.71×), and even lesser EDP (41.29×). These improved design metrics are required for the faster response of circuits with efficient use of energy.

Fig. 8 FinFET MCML DE

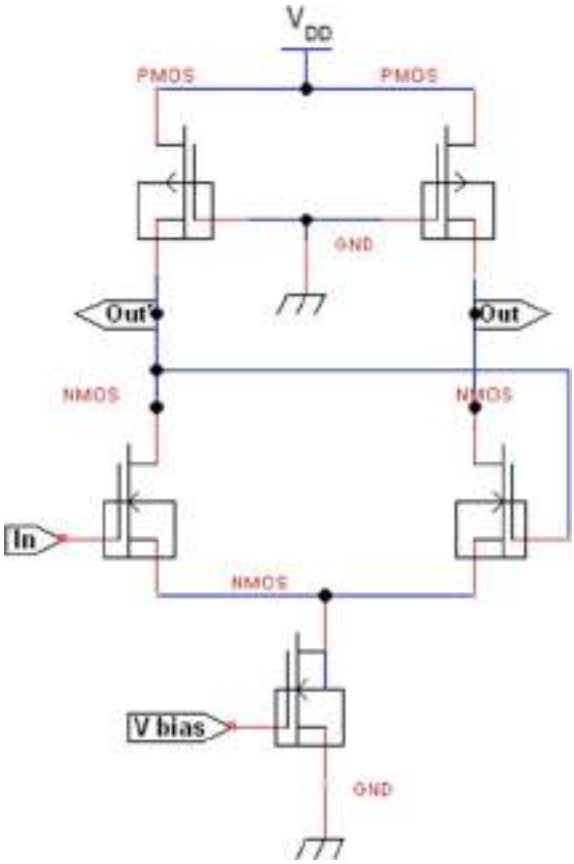

Table 3 Design metrics of FinFET MCML DE

Device parameter Supply = 0.7 V	M-MCML DE	FinFET MCML DE
t_p (ns)	0.0313	0.0284 (1.1)
PWR (μW)	0.00216	0.000063 (34.28)
PDP (fJ)	0.0000675	0.00000179 (37.71)
EDP (fJ-ns)	0.00000211	0.0000000511 (41.29)

Use undoped or lightly doped or depleted body (silicon film) in FinFET owe to higher mobility and hence the improved results in our proposed design 'FinFET MCML DE'.

4 Conclusion

This paper successfully investigates CMOS- and MCML-based designs of delay elements for important design metrics such as t_p, PWR, PDP, and EDP. M-MCML DE (Fig. 2) is observed to be superior to M-CMOS DE (Fig. 1) in this investigation. Further, this treatise also proposes FinFET implementation of the best delay element as 'FinFET MCML DE'. This proposed circuit emerges as a preferable circuit to its MOSFET counterpart. Specifically, it shows improvement in t_p (1.1×), PWR (34.28×), PDP (37.71×) and EDP (41.29×). This article gives a vast research horizon to optimize delay elements, such as its dynamic implementation [13, 14].

References

1. S.U. Rehman et al., A 16 mW 250 ps double-hit-resolution input sampled time-to-digital converter in 45-nm CMOS. IEEE Trans. Circuits Syst. II Exp. Briefs **65**(5), 562–566 (2018)
2. S.U. Rehman, M.M. Khafaji, C. Carta, F. Ellinger, A 10-Gb/s 20-ps delay-range digitally controlled differential delay element in 45-nm SOI CMOS. IEEE Trans. Very Large Scale Integr. (VLSI) Syst. **27**(5), 1233–1237 (2019). https://doi.org/10.1109/TVLSI.2019.2894736
3. T. Zhang, R. Xu, C.M. Wu, Unconditionally stable non-foster element using active transversal-filter-based negative group delay circuit. IEEE Microw. Wirel. Compon. Lett. **27**(10), 921–923 (2017). https://doi.org/10.1109/LMWC.2017.2745487
4. B.-J. Seo, H. Fetterman, True-time-delay element in lossy environment using EO waveguides. IEEE Photonics Technol. Lett. **18**(1), 10–12 (2006). https://doi.org/10.1109/LPT.2005.860043
5. S.U. Rehman, M.M. Khafaji, A. Ferschischi, C. Carta, F. Ellinger, A 0.2–1.3 ns range delay-control scheme for a 25 Gb/s data-receiver using a replica delay-line-based delay-locked-loop in 45-nm CMOS. IEEE Trans. Circuits Syst. II Express Briefs **67**(5), 806–810 (2020). https://doi.org/10.1109/TCSII.2020.2980813
6. Y. Wang et al., 44-ns continuously tunable dispersionless optical delay element using a PPLN waveguide with two-pump configuration, DCF, and a dispersion compensator. IEEE Photonics Technol. Lett. **19**(11), 861–863 (2007). https://doi.org/10.1109/LPT.2007.895900
7. Nanoscale Integration and Modeling (NIMO) Group, Arizona State University (ASU). [Online]. https://ptm.asu.edu/
8. P. Srivastava, R. Yadav, R. Srivastava, Ultra high speed and novel design of power-aware CNFET based MCML 3-bit parity checker. Analog Integr Circuits Signal Process (2020). https://doi.org/10.1007/s10470-020-01609-w
9. J. Musicer, An analysis of MOS current mode logic for low power and high performance digital logic. Ph.D. Dissertation, Department of Electrical Engineering & Computer Science, University of California Berkeley, Berkeley, CA, 2002
10. P. Srivastava, A.K. Dwivedi, A. Islam, Power- and variability-aware design of FinFET-based XOR circuit at nanoscale regime, in *2014 IEEE International Conference on Advanced Communications, Control and Computing Technologies* (Ramanathapuram, India, 2014), pp. 440–444. https://doi.org/10.1109/ICACCCT.2014.7019481
11. A. Islam, A. Imran, M. Hasan, Variability analysis and FinFET-based design of XOR and XNOR circuit, in *2011 2nd International Conference on Computer and Communication Technology (ICCCT-2011)* (Allahabad, India, 2011), pp. 239–245. https://doi.org/10.1109/ICCCT.2011.6075163
12. Y. Taur, T.H. Ning, *Fundamentals of Modern VLSI Devices* (Cambridge University Press, New York, 2009)

13. J. Praveen, K.N. Subhani, D.D. Peter, K. Jogi, D.N. Darshan, Design and implementation of low power dynamic buffer circuit for nanotechnology application. Mater. Today Proc. **35**(Part 3), 461–464 (2021). ISSN: 2214-7853. https://doi.org/10.1016/j.matpr.2020.03.002
14. S.R. Ghimiray, P. Meher, P.K. Dutta, An improved charge-sharing elimination pseudo-domino logic. Int. J. Circuit Theory Appl. **48**(issue 8). https://doi.org/10.1002/cta.2798

Design and Performance Analysis of 20 nm Si-Based DG-MOSFET

K. Jai Surya and Sobhit Saxena

Abstract The MOSFET has a wide range of usages like switching, amplification, sensing, and many more required in the modern world for industrial, biomedical, and environmental purposes. In this work, a DG-MOSFET (Double Gate Metal Oxide Semiconductor Field Effect Transistor) with optimized channel width is proposed. The DG-MOSFET is designed separately with Si and Ge wafers. The device is constructed on the silicon wafer with three different regions, namely source, channel and drain. The double gate concept introduced in the device increases the control over the channel region. Further, the simulation is done using Visual TCAD 2D analysis. This 20 nm gate length device shows very good electrical characteristics with I_{on}/I_{off} ratio (~10^{12}) and almost negligible DIBL. The performance of this device indicates that it is useful for amplification applications.

Keywords DG-MOSFET · Visual TCAD · Sub-threshold swing · I_{on}/I_{off} · DIBL

1 Introduction

In the past few decades, usage of the technology based on MOSFETs has grown exponentially. Moore's law states that for every 2 years the number of transistors inside the IC is doubled. The size of the devices has been reduced and the performance has increased off the charts. This was possible only because of the scaling down of the channel length of the MOSFETs [1]. The short channel effects (SCE) and the drain-induced barrier lowering DIBL [2] play a crucial role when the channel length reaches the nanoscale.

Many researchers designed different structures of MOSFET in order to achieve improvement in its performance and that led to the invention of the double-gate MOSFET where the gate is in contact with both sides of the channel [1]. The first DG-MOSFET was fabricated by Sekigawa and Hayashi in 1984 in which the

K. J. Surya · S. Saxena (✉)
School of Electronics and Electrical Engineering, Lovely Professional University, Punjab, India
e-mail: sobhit.23364@lpu.co.in

S. Rawat et al. (eds.), *Proceedings of First International Conference on Computational Electronics for Wireless Communications*, Lecture Notes in Networks and Systems 329,
https://doi.org/10.1007/978-981-16-6246-1_17

researchers demonstrated that an additional gate could reduce the short channel effect significantly [3, 4].

This type of contact is useful to control the semiconductor channel very efficiently and results in higher drain currents [5].

The best device for CMOS is DGMOSFET as it can suppress SCE under 50 nm technology [6].

The DMDG MOSFET with cavities acts as a biosensing device and the sensitivity is dependent on the dielectric used in making the device [7].

The AJ DG MOSFET [9] proposed by the author in their paper is junction less and asymmetrical [9]. DGJL-MOSFET [10] by Chebaki and the other JLDG-MOSFET by Roy are also junction less [10, 11].

2 Basic MOSFET Versus DG-MOSFET

A MOSFET is constructed like a sandwich structure where the channel is made with one type of doping and the source and drains with the other type of doping, this forms two junctions one in between source and channel and the other in between channel and drain. The conventional MOSFET has designing limitations like ultra-sharp when the device size is reduced further than 32 nm. So here the device with the channel length of 20 nm is implemented and simulations have been performed on it. The DG-MOSFET has two gates and they are placed above and below the channel region to control the channel region's conductivity by applying the voltage. The change in the gate voltage is reflected in the drain current (I_d). The doping concentrations of the source, channel, and Drain can be different. The oxide used in this device is silicon dioxide (SiO_2). The material used for making drain, source, and gate contacts in this device is Ag (Silver). The PMOS have the source and drain regions doped with P-type material and the channel is doped with N-type material and for NMOS the source and drain regions are doped with N-type material and the channel is doped with P-type material. The channel in PMOS only conducts the current if the applied voltage is greater than the threshold voltage (V_T), whereas in NMOS the channel stops conducting current if the applied voltage is greater than the threshold voltage. The I_{on}/I_{off} ratio for the conventional MOSFET must be greater than 10^9 and the sub-threshold swing (SS) must be less than 70 mV/dec.

The Junction-Less Double-Gate MOSFET (JL-DGMOSFET) is another type of MOSFET where the source, channel, and drain have the same doping profile unlike the conventional MOSFET where source and drain have the same doping profile and the channel have the different doping profile [8]. The name junction less is given as there are no junctions like source-to-channel and channel-to-drain.

Fig. 1 Structure of Si-based DGMOSFET

3 Proposed Device Structure

The proposed DGMOSFET has three regions in which the channel is a silicon wafer doped with P-type (Acceptor) material with the doping concentration of 1×10^{19} cm^{-3} and has the length $L_c = 20$ nm and thickness $T_c = 3$ nm. The source is a silicon wafer doped with N-type (Donor) material with the concentration of 1×10^{19} cm^{-3} and has the length $L_s = 5$ nm and thickness $T_s = 3$ nm. The drain is a silicon wafer doped with N-type (Donor) material with the concentration of 1×10^{19} cm^{-3} and has a length of $L_d = 5$ nm and thickness of $T_d = 3$ nm. The gates are made of Ag with thickness $T_g = 4$ nm, and length $L_g = 20$ nm. The oxide region is made of silicon dioxide (SiO_2) with length $L_{ox} = 20$ nm, thickness $T_{ox} = 2$ nm. The source and drain contacts are made of aluminum (Al) material with thickness of 4 nm and length of 20 nm.

The gate material chosen in the proposed device is Ag as its work function is 4.73 eV which is much higher than the work function of Al i.e. 4.3 eV. The dielectric used for oxide region is SiO_2 having a dielectric constant equal to 3.6. The proposed device is symmetrical and the arrangement of this device in arrays is easier than the non-symmetrical device (Figs. 1 and 2).

The below table represents the dimensions and the type of material used for the construction of this device (Table 1).

4 Electrostatic Characteristics of Device on Si Wafer

4.1 Potential

The potential at the channel is way below the potential at the drain and it is even below the source potential, due to this condition no current flows between the source and drain through the channel.

Fig. 2 Structure of Ge-based DGMOSFET

Table 1 Dimensions of DGMOSFET

Region	Length (nm)	Thickness (nm)	Material	Doping Conc.	Dopant type
Source	5	3	Silicon	1×10^{19}	Donor
Drain	5	3	Silicon	1×10^{19}	Donor
Channel	20	3	Silicon	1×10^{19}	Acceptor
Gate1/gate2	20	4	Silver	NA	NA
Oxide1/oxide2	20	2	SiO_2	NA	NA
Contacts	2	3	Aluminum	NA	NA

When the $V_{gs} = 3$ V, i.e., above the threshold voltage, the potential of the channel is increased to an extent that the flow of the current from source to drain is possible (Fig. 3).

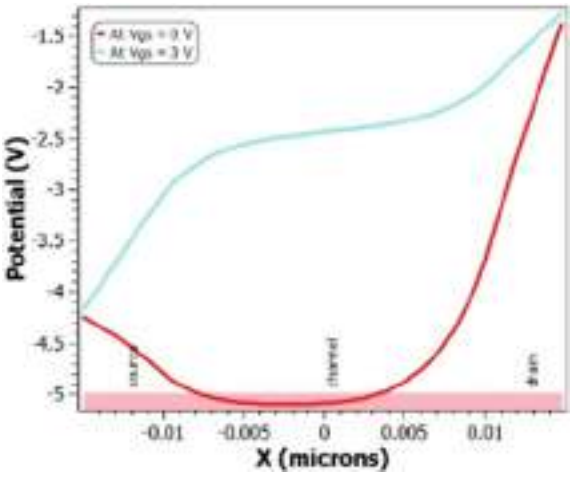

Fig. 3 Surface potential along the device

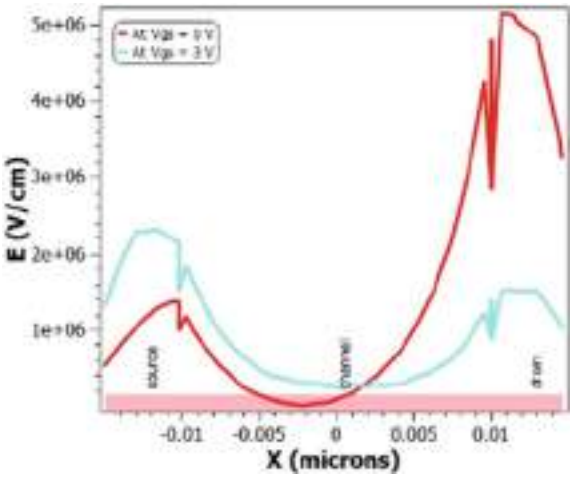

Fig. 4 Electric field along the device

4.2 Electric Field

The surface electric field at the source is higher in the OFF state, i.e., when $V_{gs} = 0$ V, and the electric field of the drain is higher when the device is in the ON state (Fig. 4).

4.3 Electron and Hole Density

The channel is doped with acceptor so the hole concentration at $V_{gs} = 0$ V is high. Similarly, the drain and source are doped with donor and the electron concentration at $V_{gs} = 0$ V is high. But when $V_{gs} = 3$ V the holes are attracted toward the gate and the electron concentration is increased in the channel region (Fig. 5).

4.4 Energy Band Diagram

The red lines in the energy band diagram show the conduction band and valence band at $V_{gs} = 0$ V. This does not allow the electron in the valence band of the source to move forward into the channel and further into the drain due to the step created by the channel. This step can be overcome by applying the voltage at gate. 3 V is applied at the gate due to which the electron can easily enter into the conduction band of the channel from the valence band of the source.

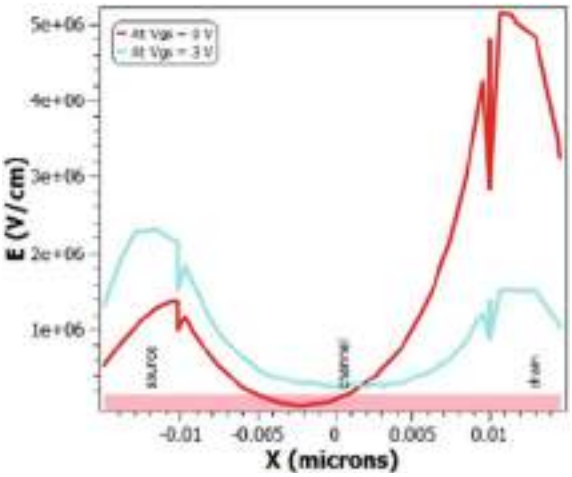

Fig. 5 Density of holes and electrons along the device

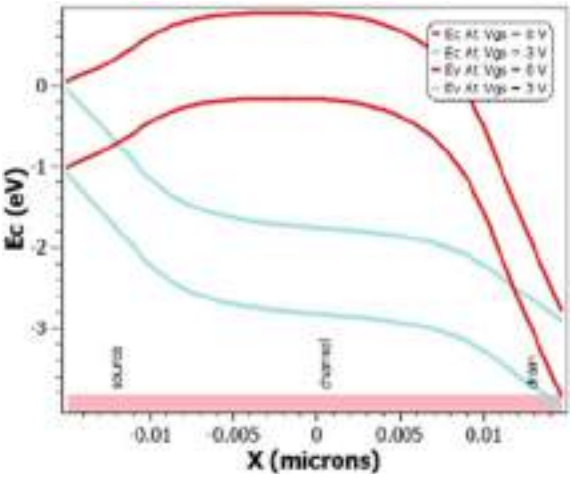

Fig. 6 E_c and E_v along the device

5 Results and Discussion

5.1 2D Simulation Results

In Fig. 7, the plotted graph shows the variation of drain current with respect to the applied gate voltage (0–3 V) for fixed drain voltage ($V_d = 3$ V) for DGMOSFETs designed with different materials, i.e., Si and Ge separately. The difference in the I_{off} value of both the devices can be clearly observed from the plotted curves.

The I_{off} of the Si-based DGMOSFET is in the range of ~10^{-16} A/μm, and the Ion is in the range of 0.0001 A/μm. Whereas I_{off} of the Ge-based DGMOSFET is in

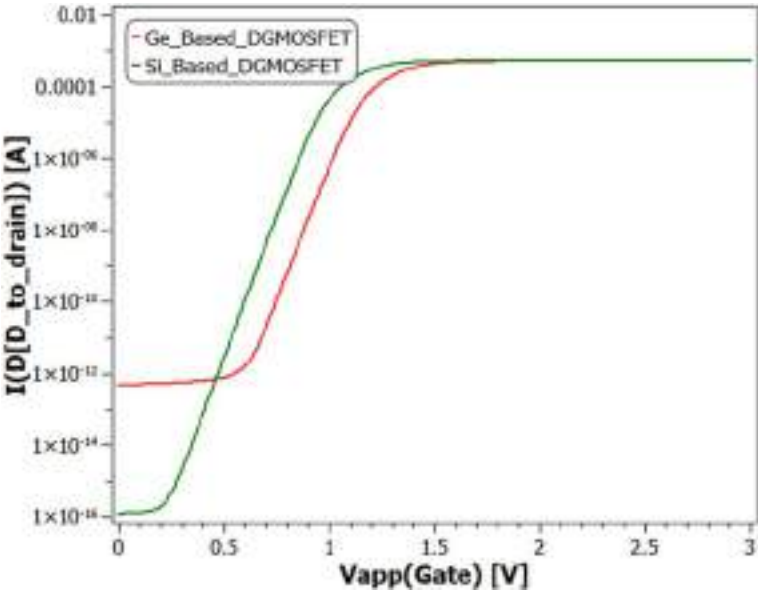

Fig. 7 Drain current versus gate voltage for DGMOSFET for Si based and Ge based

the range of ~10^{-12} A/μm, and I_{on} is similar to the Si-based device. This contributes I_{on}/I_{off} ratio and the current ratio of Si-based device (~10^{12}) is greater than the Ge-based device (~10^{8}).

5.2 Sub-threshold Swing Characteristics

The sub-threshold swing (SS) which is calculated in volt per decade describes the relationship between the logarithm of drain current and gate voltage. The SS can be calculated by the Eq. (1)

$$\mathrm{SS} = \frac{V_{gs2} - V_{gs1}}{\log(I_{d2}) - \log(I_{d1})} \tag{1}$$

The calculated value of SS for the designed structure is 63 mV/decade.

Figure 8. shows the plot of drain current versus gate voltage for Si-based DGMOSFET at different drain voltages (V_{ds}) to calculate the value of DIBL.

DIBL is the reduction of threshold voltage at higher drain voltages by lowering of potential barrier on the drain that affects the gate.

This can be calculated by the Eq. (2)

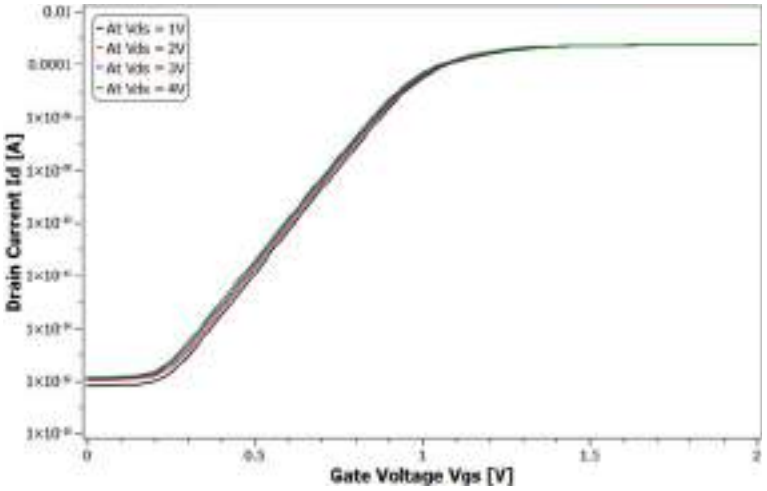

Fig. 8 Drain current versus gate voltage for DGMOSFET at different drain voltages

$$\text{DIBL} = \frac{V_{th} - V_{th}(\text{low})}{V_{dd} - V_{dd}(\text{low})} \tag{2}$$

For this device, DIBL is negligible and it says that the applied drain voltage does not affect the working of the device and the working of the device is completely dependent on the applied gate voltage.

The main factors responsible for the reduction of DIBL are the suppression of the electric field in and nearby the channel region and the width of the channel region (in this case 3 nm) (Table 2).

The AJ DG MOSFET [9] proposed by the author in their paper is junction less and asymmetrical [9].

DGJL-MOSFET [10] by Chebaki and the other JLDG-MOSFET by Roy are also junction less [10, 11].

Table 2 Performance comparison of device DG-MOSFET with other available MOSFETs

Device structure	I_{ON}/I_{OFF}	SS (mV/decade)	DIBL (mV/V)
AJ DG MOSFET [9]	~10^{13}	59	13.9
DGJL-MOSFET [10]	4.03×10^9	63.34	79.58
DGJL-MOSFET [11]	4.86×10^9	62.32	75.98
This work	~10^{12}	63	~20

6 Conclusion

In this work, the proposed DG-MOSFET not only has less leakage current (I_{off} = ~10^{-16} A/μm), but it also has a better I_{on}/I_{off} ratio. This is a very important feature for the devices like amplifiers and other uses like switching can also be performed by this device. The proposed DG-MOSFET has improved the value of I_{on}/I_{off} ratio (~10^{12}), DIBL (~20 mV/V), Sub-threshold Swing (~63 mV/Decade), and the device is symmetrical.

References

1. S.C. Neetu, B. Prasad, Simulation of double gate MOSFET at 32 nm technology node using visual TCAD TM tool. Adv. Res. Electr. Electron. Eng. **1**(4), 9–13 (2014)
2. H.S.P. Wong, Beyond the conventional transistor. Solid State Electron. **49**, 755–762 (2005)
3. T. Sekigawa, Solid State Electron. **27**, 827 (1984)
4. N. Mendiratta, S.L. Tripathi, S. Padmanaban, E. Hossain, Design and analysis of heavily doped n+ pocket asymmetrical junction-less double gate MOSFET for biomedical applications. Appl. Sci. MDPI **10**, 2499 (2020)
5. K. Suzuki, Scaling theory for double-gate SOI MOSFET's. IEEE Trans. Electron. Devices **40**, 2326–2329
6. DighHisamoto, IEEE Trans. Electron. Devices **47**(12) (2000), www.eecs.berkeley.edu/~hu/PUBLICATIONS/PAPERS/700
7. B. Buvaneswari, N.B. Balamurugan, 2D analytical modeling and simulation of dual material DG MOSFET for biosensing application. AEU Int. J. Electron. Commun. **99**, 193–200 (2019)
8. K.P. Londhe, Y.V. Chavan, Design of double gate junctionless MOSFET using Germanium for improvement of performance parameters, in *2016 International Conference on Automatic Control and Dynamic Optimization Techniques (ICACDOT)* (IEEE, 2020), pp. 855–858. https://doi.org/10.1007/s42341-020-00222-y
9. N. Mendiratta, S.L. Tripathi, S. Padmanaban, E. Hossain, Design and analysis of heavily doped n+ pocket asymmetrical junction-less gate MOSFET for biomedical applications. Appl. Sci. **10**, 2499 (2020)
10. E. Chebaki, F. Djeffal, H. Ferhati et al., Improved analog/RF performance of double gate junctionless MOSFET using both gate material engineering and drain/source extensions. Superlattices Microstruct. **92**, 80 (2016)
11. N.C. Roy, A. Gupta, S. Rai, Analytical surface potential modeling and simulation of junction-less double gate (JLDG) MOSFET for ultra-low power analog/RF circuits. Microelectron. J. **46**, 916 (2015)

Design and Implementation of Smart Healthcare Monitoring System Using FPGA

Prem Kumar Badiganti, Sumanth Peddirsi, Alla Tirumala Jagannadha Rupesh, and Suman Lata Tripathi

Abstract With growing health awareness and the increasing cost of medical care, there is an impetus to new and advanced technologies for disease prevention and early diagnosis and treatment. The weakest link exposed by the COVID-19 pandemic in India is health care. Investment in critical health Infrastructure aided by modern technology is the need of the hour. So, this project aims to develop a comprehensive healthcare monitoring system by blending IoT and VLSI. It can monitor a patient's basic health signs as well as the room condition where the patients are now in real time. We use Nexys4 Artix7 as a processor. In this system, six sensors are used to capture the data from the hospital environment named heartbeat sensor, body, and room temperature sensor, fall detection sensor, blood pressure sensor, air quality monitoring sensors, ECG sensor. The condition of the patients is conveyed via the ThingSpeak website and telephonic calls/SMS to relatives, medical staff.

Keywords FPGA · IoT · VLSI · Medical sensors · Wi-Fi · GSM · Ethernet · Thingspeak · Air quality monitoring

1 Introduction

The role of VLSI in healthcare monitoring cannot be ignored. The accessibility and availability of healthcare services in India particularly in rural areas are not well organized. Technologies like VLSI and IoT can make a big difference in transforming the rural healthcare system. Besides, this system can easily be employed in urban areas with the existing infrastructure [1]. India spends only 1.3% of its GDP on health care which is meager considering our population. India's burden of diseases is gradually increasing, and COVID-19 had further accelerated it. Early detection of any disease can help us to contain it in the best possible way [2]. For this early detection, we require the historical data of the patient to be collected, analyzed, and accessed by doctors. Heart rate, Temperature, Blood pressure, and ECG are

P. K. Badiganti · S. Peddirsi · A. T. J. Rupesh · S. L. Tripathi (✉)
School of Electronics and Electrical Engineering, Lovely Professional University, Punjab, India

S. Rawat et al. (eds.), *Proceedings of First International Conference on Computational Electronics for Wireless Communications*, Lecture Notes in Networks and Systems 329,
https://doi.org/10.1007/978-981-16-6246-1_18

health parameters considered. The data is measured from the patient using specialized medical sensors which are to be interfaced with an FPGA board [3]. The project uses Verilog HDL for programming FPGA boards. The proposed system aids healthcare workers in collecting and analyzing the patient's data in real time without their presence. This is being achieved using an open cloud server ThingSpeak. Doctors can get access to patient's data in Thingspeak [4]. If there exist any fluctuations in data, i.e., abnormal conditions then an emergency call and SMS will be sent to doctors, caretakers, and relatives to alert them for taking necessary action. The function of the proposed system can be achieved using the GSM module/or existing ethernet module in FPGA. The proposed system also considers the environmental aspects of health care, which is air quality monitoring. It measures the amount of particulate matter in its surroundings. With this, the patient can monitor the cleanliness of the air which he/she is breathing. If the particulate matter raises above safe level, then the system alerts the patient and his/her acquaintances. Also, the proposed system displays all values that it gets from sensors in onboard seven-segment display.

2 Proposed Work

The proposed work is summarized in Fig. 1.

The whole project is subdivided into 4 blocks.

- Sensors block

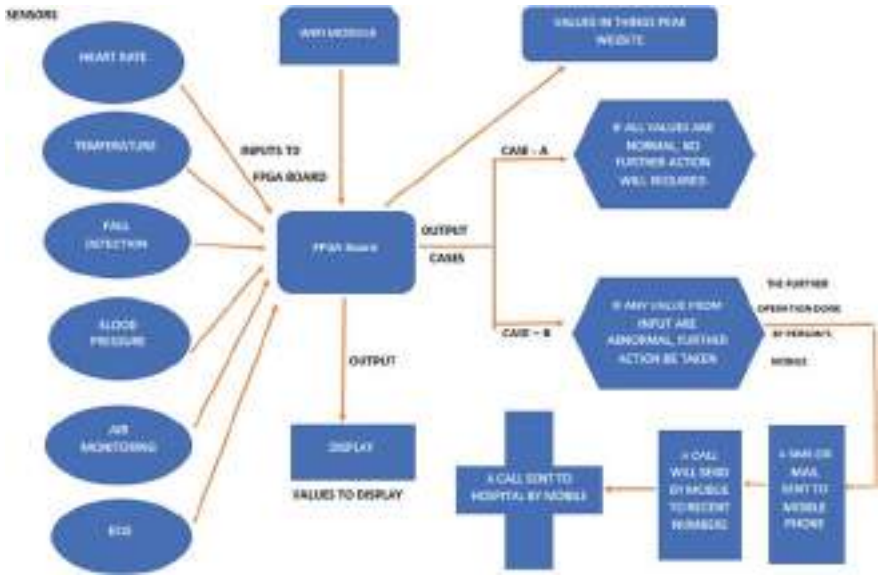

Fig. 1 Proposed work

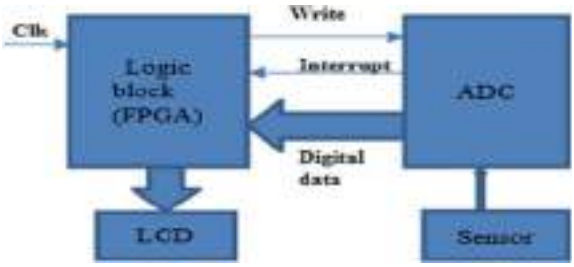

Fig. 2 Interfacing external ADC with FPGA

- Display block
- IoT block
- GSM block.

Sensors block:

Sensors in the project are to be interfaced with the FPGA board as shown in Fig. 2. As FPGA works only on digital data, interfacing analog sensors requires the use of Analog to Digital converters (ADC) [5]. Hence, interfacing external ADC to FPGA would be the first step to interface analog sensors [6]. Each sensor is interfaced with FPGA using an external ADC.

Display block:

In Nexys4, we use a seven-segment display to display the sensor data. Seven-segment is internally embedded in FPGA as shown in Fig. 3. Hence no need to interface it separately. ADC requires low to high pulse for its activation. Write pin supply low to high signal to ADC from FPGA [7] Analog sensor data is fed to ADC which converts it into digital and sends to FPGA which in turn displays the data in seven-segment

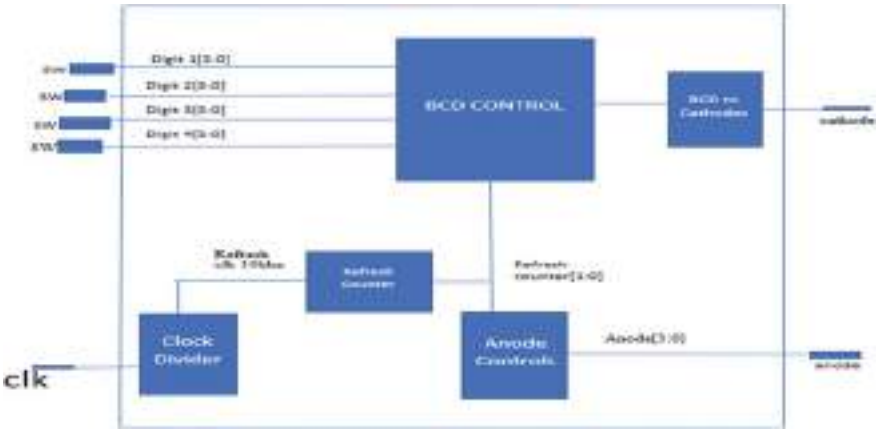

Fig. 3 Seven-segment display with refresh counter for FPGA

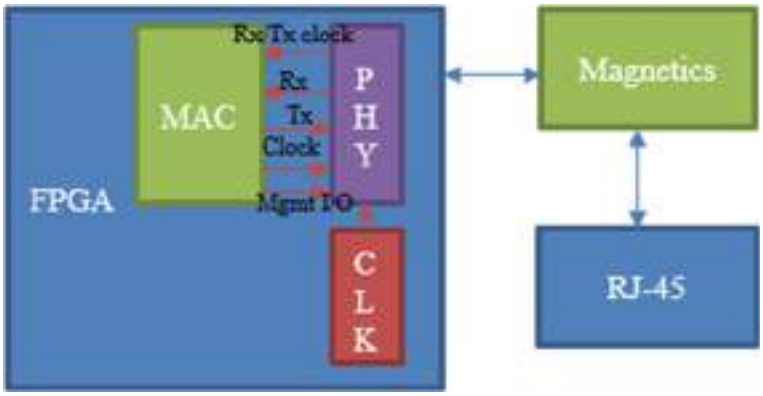

Fig. 4 Using onboard ethernet port

display. The refresh counter is used to create a counter that counts from 0 to 3 values that inputs to a BCD controller and analog controls which then choose which anode will be turned on. BCD controller is used to converting decimal numbers into binary as the seven-segment display works only on binary digits. The output from BCD will pass through BCD to the cathode module, which will turn the one-digit BCD value into a number on seven-segment display by turning on certain cathodes.

IoT block:

To connect the FPGA board with external devices, we can use an onboard ethernet port as connected in Fig. 4. Each sensor is interfaced with FPGA using an external ADC.

A clock divider is used to slow down the clock signal which is achieved through the counter clock divider divides the 100 MHz clock into a 10 kHz clock. This clock pulse is sensitive to our vision and can be able to sense switching among seven segments [8]. MII (media-independent interface) is a communication standard used to connect the MAC (media access control) block to the PHY (physical) layer for networking devices [9].

PHY: It is an IC embedded within FPGA that converts digital data from MAC and sends it along the networking interface as an analog signal. The IC also modulates the analog signal and acts as a trans receiver.

MAC functions as an interface between FPGA for data processing and communicating with the PHY. MII is not bidirectional, the number of signals required for PHY with MAC is quite large, and hence to reduce it we developed another standard called RMII. In RMII, the clock frequency used in the PHY runs continuously at 50 MHz for both 10 and 100 Mbps data rates. This doubling of the clock rate at 100 Mbps also allows the number of signals for communication between the PHY and MAC to be cut in half. In total, 9 signals are required for communication, of which up to 3 can be shared among multiple PHYs [10].

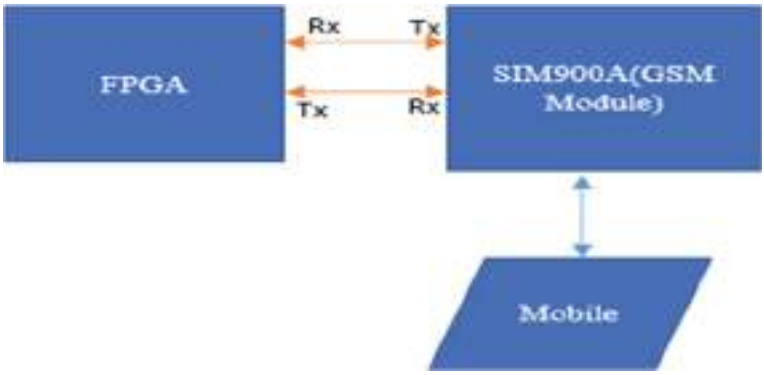

Fig. 5 GSM interfacing with FPGA

GSM block:

We can use a separate GSM module which is to be interfaced with FPGA to send SMS to mobile phone as shown in Fig. 5. Global System for Mobile Communication (GSM) is used to send and receive SMS. It works on a 4.5 V regulated supply. It sends messages to mobile numbers recorded in the program. GSM uses UART communication protocol to communicate with FPGA and is based on ad hoc topology [11].

UART Protocol:

In this protocol, two devices communicate with each other using transmitter and receiver. There is no master/slave in UART (Fig. 6). Data is sent byte by byte. It has a unique bit frame of communication which is an 11-bit frame [2]. When two devices are far away from each other noise in the surrounding can distort the original signal. Hence, to minimize noise, we use RS232 protocol which also requires multiple handshakes between the transmitter and receiver [12].

Fig. 6 UART

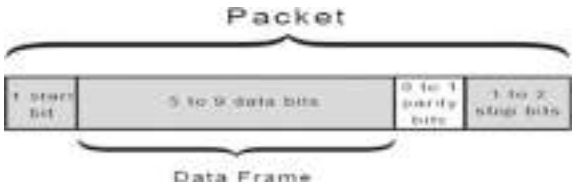

3 Simulation Results

This project uses Xilinx Vivado 2019.2 for simulation. Simulation is shown for interfacing external ADC, seven-segment display, and Ethernet schematic.

Figure 7 is depicting the schematic of the ADC block with an FPGA board.

Figure 8 represents the output waveform of external ADC interfaced with the FPGA board. When the interrupt pin of ADC is low, ADC sends digital data to FPGA.

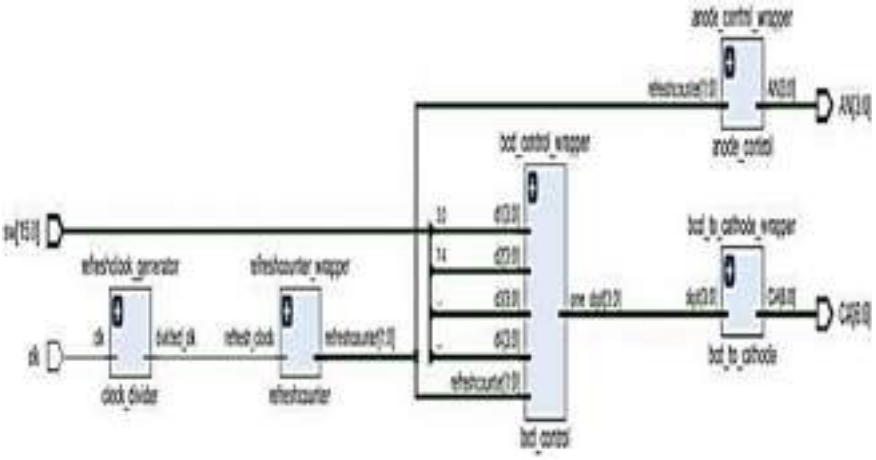

Fig. 7 Schematic of ADC interfacing with an FPGA

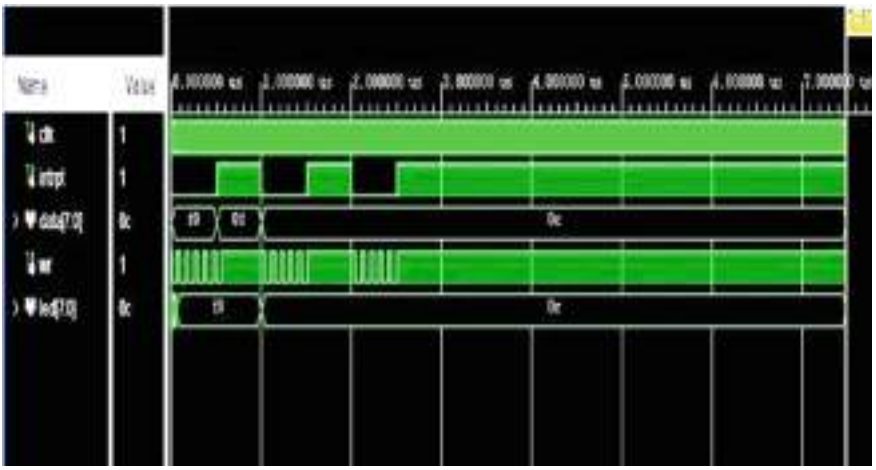

Fig. 8 Waveform of functioning of external ADC

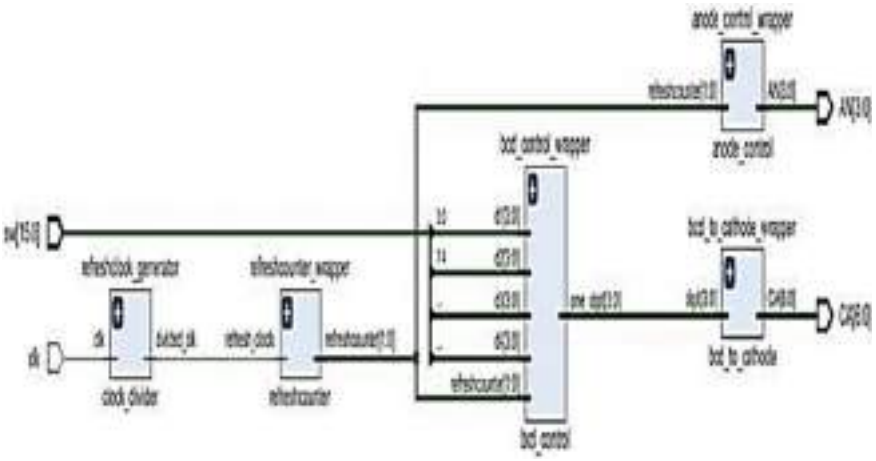

Fig. 9 Schematic representing the use of onboard seven-segment display

Figure 9 represents a schematic circuit diagram for using an onboard seven-segment display. It activates 4 seven-segment displays which display sensor data. Figure 10 shows the waveform on seven-segment display.

Figure 11 represents a schematic diagram showing the blocks used to activate the ethernet port present in the Nexys4 board. It requires the use of a micro-blaze block and Ethernet PHY block [13, 14]

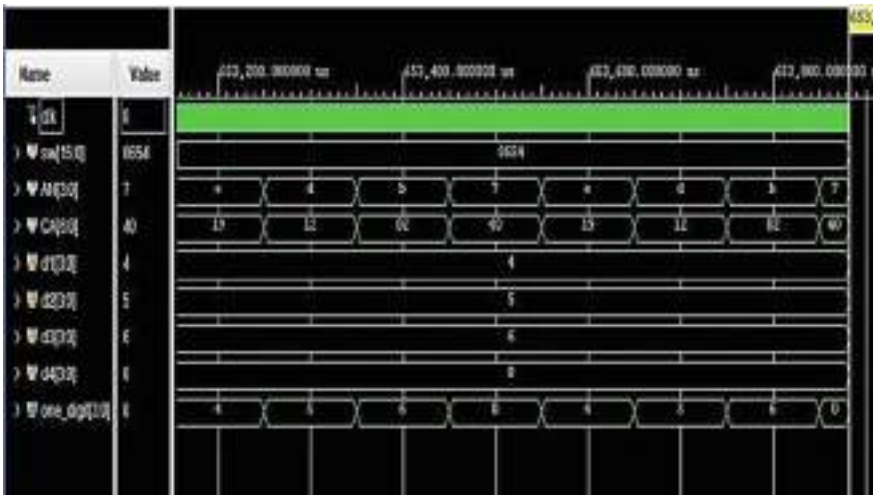

Fig. 10 Output waveform for seven-segment display

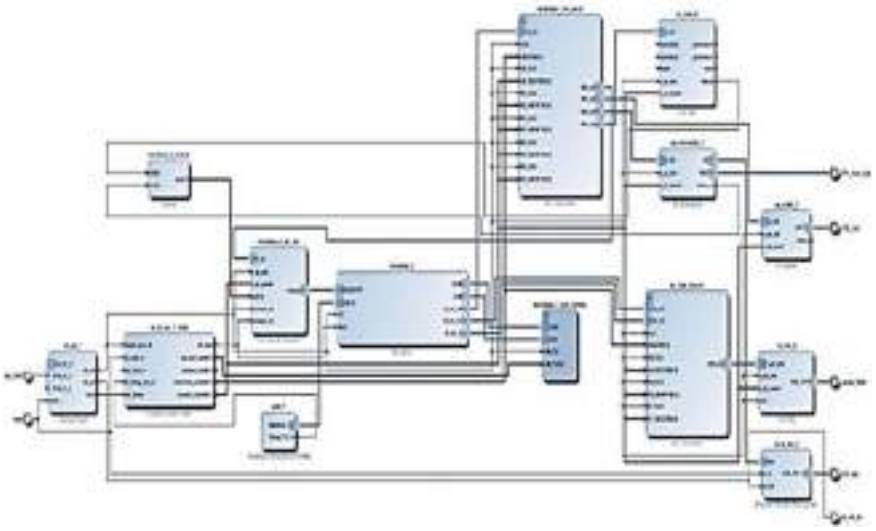

Fig. 11 Schematic showing usage of onboard ethernet port

4 Conclusion

In this paper, we introduced a smart healthcare monitoring system using FPGA. This system is suitable for real-time monitoring of patient's health parameters. Using FPGA as a microcontroller is a novelty as it gives us more performance and flexibility. We can update and modify the whole design by modifying code in FPGA. This design can be integrated into a small portable integrated circuit that can be used for commercial purposes. In this paper, we focused on designing a module of patient monitoring system using FPGA as a processor.

References

1. S.P. Dash, The impact of IoT in healthcare: global technological change & the roadmap to a networked architecture in India. J. Indian Inst. Sci. **100**, 773–785 (2020)
2. M. Awedh, A. Mueen, Design and FPGA implementation of UART using microprogrammed controller. Sch. J. Eng. Technol. **3**, 600–608 (2015)
3. A. Sanaullah, C. Yang, Y. Alexeev et al., Real-time data analysis for medical diagnosis using FPGA-accelerated neural networks. BMC Bioinform. **19**, 490 (2018)
4. F. Noorbasha, B. Kishore, K. Reddy, K. Srinivas, FPGA based health monitoring system. Int. J. Recent Technol. Eng. (IJRTE) **8**(5) (2020)
5. Y. Wang, S. Jang, A pulse sensor interface design for FPGA based multisensor health monitoring platform. Int. J. Biosens. Bioelectron. **5** (2019). https://doi.org/10.15406/ijbsbe.2019.05.00147
6. S. Abba, J.-A. Lee, FPGA-based design of an intelligent on-chip sensor network monitoring and control using dynamically reconfigurable autonomous and sensor agents. Hindawi Publishing Corporation. Int. J. Distrib. Sens. Netw. (2016)

7. C. Sisterna, M. Segura, M. Guzzo, G. Ensinck, C. Gil,FPGA implementation of an ultra-high speed ADC interface. (2011). https://doi.org/10.1109/SPL.2011.5782642
8. A. Abdulrahman, A. Emhemed, Implementation 7 segment display by educational board-software/hardware interfacing. Int. J. Eng. Res. Appl. **2**(3), 748–751 (2012)
9. S. Sangani, K. Vikram, S.R. Pankaj Kumar, Implementation of ethernet based data transfer using FPGA. Int. J. Electron. Commun. Eng. **8**(1), 75–80 (2015)
10. L80227 10BASE-T/100BASE-TX ethernet PHY technical manual. LSI Logic Corporation (2002)
11. SIM900A GSM module datasheet
12. B. Krishna, G. Chowdary, G. Vardhan, K. Ram, P. Kishore, G. Madhumati, H. Khan,FPGA based wireless electronic security system with sensor interface through GSM. **89**, 489–494 (2016)
13. M. Kucharczyk, G. Dziwoki, Simple communication with FPGA device over ethernet interface, in *Computer Networks. CN 2013. Communications in Computer and Information Science*, vol. 370 (2013)
14. J.-A. Mondol,Cloud security solutions using FPGA. (2011), pp.747–752

Performance Evaluation Using Machine Learning: Detecting Non-technical Losses in Smart Grid

P. Abhinayaa, R. Ezhilarasie, and A. Umamakeswari

Abstract In the generation and distribution of electricity in the power grid, there is a chance for the occurrence of non-technical loss while transmitting by various means. One of the most concern needed loss varieties is electricity theft. The theft occurrence may cause significant loss and harm to the power grid and also to the economy by leading to unprofitable accounts for the power supply companies. Regular inspection on irregular consumption of power is inefficient and very time consuming. Utilizing machine learning in this theft detection system helps to prevent huge losses. In this paper, various machine learning models are employed to state the better performing model for the given data. By employing the various techniques of machine learning, an effective model for theft detection can be obtained and the problem associated with non-technical loss especially theft detection can be monitored and controlled.

Keywords Electricity theft detection · Non-technical losses · Machine learning algorithms

1 Introduction

In the world of modern life, electricity has turned to be a very mandatory thing since without it every work to be done seems to be impossible. Such kind of mandated life element needs to be conserved and should use it efficiently. The effective usage of electricity is turned to be an unlearned art for both the electricity providers and consumers. On seeing from the side of electricity providers, the major thing that should be considered and regulate is electricity loss [1] occurring while generation and distribution of it. As in [2], the electricity losses can be said as the occurrence of technical loss and non-technical loss. The technical losses are due to machinery problems occurring during the generation of electricity. In the case of non-technical losses [3], loss occurs when there is a chance for incorrect meter reading, improper meter installation and theft [4]. Among them, theft is a very serious issue facing everywhere

P. Abhinayaa · R. Ezhilarasie (✉) · A. Umamakeswari
SASTRA Deemed University, Thanjavur, TN 613401, India

S. Rawat et al. (eds.), *Proceedings of First International Conference on Computational Electronics for Wireless Communications*, Lecture Notes in Networks and Systems 329,
https://doi.org/10.1007/978-981-16-6246-1_19

by the power-producing companies. The electricity theft makes the economy of the government to get degrade as the customer won't pay the bill that they have actually consumed, which causes the revenue loss that should return as a profit. The impact of loss is not limited to the degradation of power quality [5]. The theft causes load imbalance in the grid that makes the electricity provider not meet the demand needs of that region. The increase in the demand may result in voltage drop, transformer overload, etc., that affect the corresponding power line and in the worst situation, put the life of the public in danger. Hence, the theft in electricity should get detected and vanish.

The theft occurrence can be monitored by the conventional method that is in-person inspection and verification on the customer and their usage by the corresponding authorities but it is very time consuming and can be manipulated by the corrupted people. As an alternate method, the installation of smart meters [6, 7] and implementation of machine learning algorithms [8, 9] come into play.

Employing a machine learning algorithm for this process is a very useful and simple way to monitor and detect theft occurrence on power and pattern of consumption rates. Employing the machine learning techniques in the smart grid which comprises various power producing units and sectors is very useful to protect the grid connectivity from damage caused by any fluctuation due to load imbalances. With the implementation of this detection system, the grid can be assured for theft prone as it categorizes the anonymous activity from the usual behavior while reviewing the consumption pattern of the smart grid. Here various algorithms were discussed to obtain the optimized better performing model for the given data. The historical data were used to frame the various machine learning model. The dataset was released by the State Grid Corporation of China (SGCC) [10] from that 1035 days were taken into account for the process of framing the model of machine learning.

This paper proposes a comparative analysis of different machine learning model solutions for energy theft detection. In Sect. 2, it compares the works and theory related to proposing work that exists. Section 3 presents the stages that the model undergoes while performing the theft detection process. In Sect. 4, the obtained results are discussed and analyzed with various performance metrics. Section 5 concludes the result and presents the outcome of the proposed work.

2 Related Works

This section presents the existing works that are related to theft and fraud occurrence detection in power systems for both the traditional and smart grid networks.

Different approaches were implemented to realize the rate of energy production, monitoring and control and forecasting of energy production, distribution, energy loss either by means of technical loss or non-technical loss. However, the detection of theft occurrence in the smart grid plays a vital role in the reliability of the consumer. As the detection process needs accurate pointing of the fraudulent customer. Using smart meter data on the advanced metering infrastructure (AMI) in the smart grid is

helpful to detect the occurrence of electricity theft [11]. On the other hand, the AMI is prone to other techniques of theft attacks [12] especially by means of cyber-attacks and using digital tools. In order to solve these kinds of issues arising, many techniques were put forward to overcome the drawbacks resulted from various means. The state-based detection [13] model is based on the combination of distribution transformer and wireless sensors [14]. This model is dependent on the real-time data acquisitions of physically measured that are unattainable on some occasions and also opens a door to cyber-attacks on it where the data can be altered illegally. As in [15, 16] game-based detection model, support the process of theft detection by establishing a game between the power utility and the theft from which the normal and abnormal, that is, fraudulent and non-fraudulent characteristics can be obtained from the game equilibrium. Using a game-based detection model, it is possible to achieve a low cost and reasonable result of theft reduction but the establishment of utility function for all players is a challenging task.

From [17], it is agreeable that machine learning should be deployed to identify the possible occurrence of fraudulent behavior, however after that the physical inspection should take place. And also, it insisted on the necessity of thinking wider social, economic, and legal considerations should not be neglected as a way of reducing the loss. The non-technical loss also appears by means of cyber-attacks on the distribution network itself, using the preventive methods provided in [18] it can be detected. According to the survey of [19], most of the solutions of detection techniques of electricity theft lie in two wide circles as an expert system and machine learning model. The expert system seeks human experts to solve the problem by following the regulations with user-defined rules. However, such a system is very time consuming, and most importantly there is a chance of biases in judgments while the decision-making process. Machine learning solutions are emerging as a popular alternative [20] and they will perform effectively with the support of the availability of large quantities of data that are obtained from smart meters. For machine learning techniques, it is easier to learn defined patterns from historical data and it reduces the need for being explicitly programmed to it.

The algorithms that help for machine learning solutions can be segregated into clustering (unsupervised) and classification (supervised) models. [21] supports the theft detection solution by using the principal component analysis, [22] uses K-means clustering technique, [23] uses a C-fuzzy technique, but this method has a drawback in terms of accuracy though fuzzy gives good accuracy there are still the chances that the training set fuzzy clusters may not yield an accurate load details. Although clustering-based machine learning detection solutions are remarkable, their scaled performances were still not far enough to reach the real-time implementation. Hence classification techniques come into play. There are different algorithms involved, [24] details the theft detection solution based on the support vector machine technique where the desired detection hit rate of 60% was achieved and this rate is improved in [25] by 70%. Similarly, [26] supports the K-nearest neighbor. Algorithms based on supervised learning methodologies produce a good result for real-time needs comparatively.

3 Methodology Description

In this work, five different algorithms are taken into consideration to frame the solution to the electricity theft detection system. They are logistic regression (LR) [27], Support vector machine (SVM), Naive Bayes (NB) [28], Decision tree (DT) [29], and Random forest (RF) [30]. The data set is collected from the state grid corporation of china. The data consist of details of the electricity consumption value of 42,372 customer details for a period of 1035 days from 01 January 2014 to 09 September 2016. Using this dataset, the analysis of different algorithms is made. The theft detection solution undergoes the stages like data preprocessing, generation of train, test and validation set, building of machine learning algorithm, and performance analysis of the different techniques that were taken into consideration. The overall flow of the process is described in Fig. 1.

Data preprocessing. The data that are provided as an input to any machine learning model should be preprocessed and verified to avoid the confusion that occurs at the algorithm as it causes more generalization on the learning model. The dataset taken is primarily preprocessed by removing the noise/outliers present in the dataset. Then, the outlier-removed data set will get checked for presence for any null values. It can also be said as checking for missing values which is referred to as data imputation.

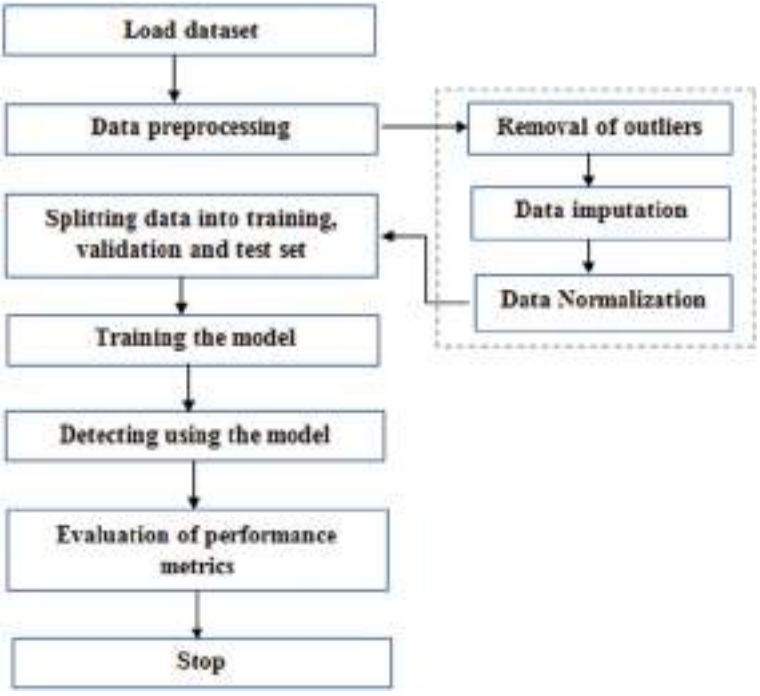

Fig. 1 Overall flow of the proposed work

Finally, after completing the aforesaid stages, the data present in the dataset will get normalized by min–max techniques for a range of (0, 1). The normalization should be done to avoid the suffering of a machine learning model with a diverse range of data.

Generation of train, test, and validation set. The dataset consists of details of the behavior of customer of 42,372 where the count of details of an honest user is more than the dishonest user. It causes the dataset to be imbalanced [31]. In order to overcome the imbalanced dataset, the oversampling technique, SMOTE is applied [32]. Hence, the minority count of fraudulent customer details got oversampled and increased the count equal to the non-fraudulent customer details. After applying the SMOTE algorithm, the dataset has to get split for the process of training, testing, and validation of the dataset.

Building machine learning models. Accordingly, the segregated set of data will be used for training the model. The different machine learning models will process the data given to yield results. Since the learning models use the hyper-parameters, the parameters got optimized and selected by using the grid search method [33]. The tuned parameter is given to the model. For example, the parameter like maximum depth, number of estimators for the random forest is selected based on the grid search method.

4 Result and Analysis

The implementation was done with the help of Python 3.6. Experiments are conducted with the support of Intel Core i3 with 4.0 GB of RAM on a standard PC in the virtual environment called Google Collaboratory.

Evaluation of the proposed work is an important criterion to be followed as it describes the nature of the model and how well the model achieves the objective of the work. However, it is not enough to fully judge the model but helps to understand the performance level of the model. The evaluation metrics include different types like classification accuracy, logarithmic loss, confusion matrix [34], area under curve, f1 score, mean absolute error, and mean squared error. Here, the mean squared error (MSE), mean absolute error (MAE) and root mean squared error (RMSE) are used to evaluate the model.

Different machine learning models are evaluated to find an accurate prediction scheme.

4.1 Logistic Regression (LR)

Logistic regression is used to predict values within a continuous range rather than trying to classify them into categories. In LR, parameter *C* is considered and given to

grid search to pick the value that yields higher accuracy when applied. For that, the value for C ranges from $1e{-}7$ to $1e0$. With the tuned parameter value, LR produces 0.72 as an accuracy value. Also, the MAE, MSE, and RMSE are computed as 0.27, 0.26, and 0.52, respectively, and can graphically view this in Fig. 5.

4.2 Decision Tree (DT)

In the decision tree, while calculating the target value of a model, the predictive model uses binary rules and in this model, each individual tree has branches, nodes, and leaves. Parameters like max_depth, min_sample_split and criterion are considered for grid search method with the values 1–8 for max_depth, 2–4 for min_sample_split and Gini and entropy for criterion. With those values, it had scored the accuracy value as 0.73 which is much near to the previously discussed model logistic regression. As shown in Fig. 5, the error calculated for this model is 0.26, 0.26, and 0.51 for MAE, MSE, and RMSE, respectively.

4.3 Random Forest (RF)

It is a specialized decision tree where multiple decision trees got integrated to achieve better performance. It helps to maintain the distinctive control of overfitting than implementing with a single decision tree. The RF classifier can handle data that are with high-dimensionality while maintaining computational efficiency higher. The parameters like max_depth, max_features, min_sample_leaf, min_sample_split, n_estimators are taken into consideration for the tuning process. It has produced the result when computed as 91.96% that is 0.92 as accuracy value with the MAE, MSE, and RMSE as 0.08, 0.08, and 0.2 which is shown in Table 1 and Fig. 5.

4.4 Naive Bayes (NB)

Mostly due to the NB's oversimplified assumptions, this classifier works in a much better way in many complex real-world situations. Here, the model is reported the 60% as accuracy with the error rate of 0.39 as MAE, 0.39 as MSE, and 0.63 as RMSE when the parameter var_smoothing is tuned. This can be visualized in Fig. 5.

Table 1 Experimental parameters used in the discussed algorithm

Algorithms	Parameters	Values
LR	Inverse regularization strength	1.0
	Penalty	l2
	n_jobs	−1
NB	vaar_smoothing	$1e{-}9$
DT	Criterion	entropy
	max_depth	8
	min_samples_split	3
RF	max_depth	100
	max_feature	3
	min_sample_leaf	3
	min_sample_split	12
	n_estimators	100
SVM	C	0.7
	gamma	0.1
	Kernel	rbf

4.5 Support Vector Machine (SVM)

With the help of hyper-parameters like C, gamma, and kernel the support vector model performs the desired work and yields the output with the accuracy of 71.9% along with the error of 0.28 in MAE and 0.52 in RMSE where the comparison between all the model's error value can be seen in Table 2 and Fig. 5.

Overall, it is found that the random forest algorithm outperformed the various kinds of machine learning algorithms. Also, the AUC value obtained from the ROC plot for the model random forest is 0.98, this can be seen in Fig. 2. The different values obtained during the evaluation of different algorithms are plotted in the graph as shown in Figs. 3 and 4 where the precision, recall, f1 score are taken into consideration as some of the performance metrics for both non-fraudulent (Class 0) and fraudulent customers (Class 1), respectively. From the before-mentioned Figs. 3 and 4, it is clearly interpretable that the model random forest outperformed the remaining model by means of the three performance metrics that are taken into account. Similarly, from the graph of Fig. 5, it is crystal clear that the loss occurring for the same model is comparatively low.

Table 2 Computed accuracy of different models in percentage

Accuracy for different models				
LR	DT	NB	RF	SVM
72.02	73.33	60.11	92	71.9

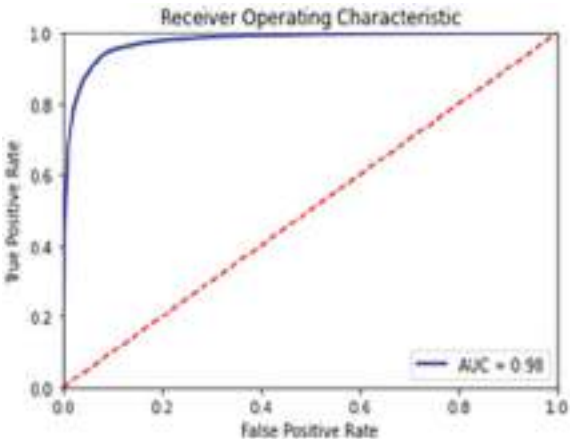

Fig. 2 ROC of random forest which performed better in the overall analysis

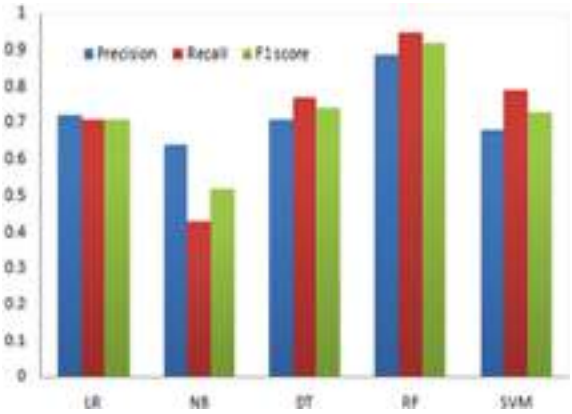

Fig. 3 Performance metrics for different algorithms for test data (non-fraudulent)

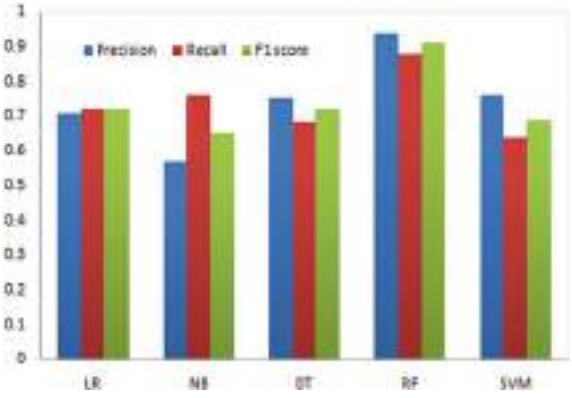

Fig. 4 Performance metrics for different algorithms for test data (fraudulent)

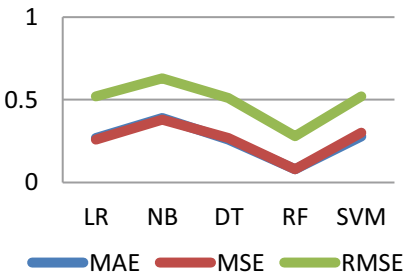

Fig. 5 Graph of error rate MAE, MSE, and RMSE obtained for the test

5 Conclusion

In the work described, different types of machine learning algorithms are proposed for the process of theft detection happening in the smart grid. Different conventional as well as modern methods of machine learning methods used for theft detection have been discussed and analyzed with their merits and demerits. These methods use historical power consumption data for detection. There are many types of evaluation criteria for checking the accuracy and error/loss of these models and the same has been identified and used to evaluate the test data in this paper. Based on the results obtained, random forest performed well, as it progresses based on bagging by considering the needed set of features rather than all the features and another advantage of RF is that little preprocessing and can be parallelizable.

Acknowledgements The authors wish to express their sincere thanks to the Department of Science & Technology, New Delhi, India (Project-ID: SR/FST/ETI-371/2014), SASTRA Deemed University, Thanjavur, India, for extending the infrastructural support to carry out this work.

References

1. L. Weijun et al., Research on transmission line power losses effected by harmonics, in *China International Conference on Electricity Distribution (CICED)*, Xi'an (2016), pp. 1–3
2. A. Al-Hinai, A. Al-Badi, E. Feilat, M. Albadi, H. Al-Nassri, A. Al-Busaidi, Energy losses in power system—practical case study (2012)
3. P. Chandel, T. Thakur, B.A. Sawle, R. Sharma, Power theft: major cause of non-technical losses in Indian distribution sector, in *IEEE 7th Power India International Conference (PIICON)*, Bikaner (2016), pp. 1–6
4. M. Golden, B. Min, Corruption and theft of electricity in an Indian state (2011)
5. L.G. Arango, E. Deccache, B.D. Bonatto, H. Arango, P.F. Ribeiro, P.M. Silveira, Impact of electricity theft on power quality, in *17th International Conference on Harmonics and Quality of Power (ICHQP)*, Belo Horizonte (2016), pp. 557–562
6. S. Sahoo, D. Nikovski, T. Muso, K. Tsuru, Electricity theft detection using smart meter data, in *IEEE Power & Energy Society Innovative Smart Grid Technologies Conference (ISGT)*, Washington, DC (2015), pp. 1–5
7. S.S.S.R. Depuru, L. Wang, V. Devabhaktuni, Electricity theft: overview, issues, prevention and a smart meter-based approach to control theft. Energy Policy 1007–1015 (2011)

8. J. Jeyaranjani, D. Devaraj, Machine learning algorithm for efficient power theft detection using smart meter data. Int. J. Eng. Technol. 900–904 (2018)
9. N. Dahringer, Electricity theft detection using machine learning (2017)
10. X. Yi-chong, The state grid corporation of China, in *The Political Economy of State-Owned Enterprises in China and India. International Political Economy Series*, ed. by X. Yi-chong (Palgrave Macmillan, London, 2012)
11. S.K. Singh, R. Bose, A. Joshi, Energy theft detection in advanced metering infrastructure, in *IEEE 4th World Forum on Internet of Things (WF-IoT)*, Singapore (2018), pp. 529–534
12. R. Jiang, R. Lu, Y. Wang, J. Luo, C. Shen, X. Shen, Energy-theft detection issues for advanced metering infrastructure in smart grid. Tsinghua Sci. Technol. 105–120 (2014)
13. S.-C. Huang, Y.-L. Lo, C.-N. Lu, Non-technical loss detection using state estimation and analysis of variance. IEEE Trans. Power Syst. **28**(3), 2959–2966 (2013)
14. I.F. Akyildiz, W. Su, Y. Sankarasubramaniam, E. Cayirci, Wireless sensor networks: a survey. Comput. Netw. **38**(4), 393–422 (2002)
15. S. Amin, G.A. Schwartz, A.A. Cardenas, S.S. Sastry, Game-theoretic models of electricity theft detection in smart utility networks: providing new capabilities with advanced Journal of Electrical and Computer Engineering metering infrastructure. IEEE Control Syst. Mag. **35**(1), 66–81 (2015)
16. D. Yao, M. Wen, X. Liang, Z. Fu, K. Zhang, B. Yang, Energy theft detection with energy privacy preservation in the smart grid. IEEE Internet Things J. **6**(5), 7659–7669 (2019)
17. V. Krishna, G.A. Weaver, W.H. Sanders, Non-technical losses in the 21st century: cause, economic effects, detection and perspectives. Technical Report (University of Luxembourg, 2018)
18. J. Leite, J. Mantovani, Detecting and locating non-technical losses in modern distribution networks. IEEE Trans. Smart Grid **9**(2), 1023–32 (2018)
19. P.O. Glauner, J.A. Meira, P. Valtchev, R. State, F. Bettinger, The challenge of nontechnical loss detection using artificial intelligence: a survey. Int. J. Comput. Intell. Syst. **10**, 760–775 (2017)
20. B. Yildiz, J. Bilbao, J. Dore, A. Sproul, Recent advances in the analysis of residential electricity consumption and applications of smart meter data. Appl. Energy **208**, 402–427 (2017)
21. S.K. Singh, R. Bose, A. Joshi, PCA based electricity theft detection in advanced metering infrastructure, in *7th International Conference on Power Systems (ICPS)*, Pune (2017), pp. 441–445
22. D. Dangar, S.K. Joshi, Normalization based K means clustering algorithm. IJREDR (2014)
23. E.W.S. dos Angelos, O.R. Saavedra, Detection and identification of abnormalities in customer consumptions in power distribution systems. IEEE Trans. Power Deliv. **26**(4) (2011)
24. J. Nagi, K. Yap, S. Tiong, S. Ahmed, M. Mohamed, Nontechnical loss detection for metered customers in power utility using support vector machines. IEEE Trans. Power Deliv. **25**(2), 1162–1171 (2010)
25. J. Nagi, K. Yap, S. Tiong, S. Ahmed, F. Nagi, Improving SVM-based nontechnical loss detection in power utility using the fuzzy inference system. IEEE Trans. Power Deliv. **26**(2), 1284–1285 (2011)
26. S. Aziz, S.Z. Hassan Naqvi, M.U. Khan, T. Aslam, Electricity theft detection using empirical mode decomposition and K-nearest neighbors, in *International Conference on Emerging Trends in Smart Technologies (ICETST)*, Karachi, Pakistan (2020), pp. 1–5
27. L. Connelly, Logistic regression. Medsurg Nurs. **29**(5), 353–354 (2020)
28. S. Chen, G.I. Webb, L. Liu, X. Ma, A novel selective naïve Bayes algorithm. Knowl. Based Syst. **192** (2020).
29. L. Li, S. Dai, Z. Cao et al., Using improved gradient-boosted decision tree algorithm based on Kalman filter (GBDT-KF) in time series prediction. J Supercomput **76**, 6887–6900 (2020)
30. M. Schonlau, R.Y. Zou, The random forest algorithm for statistical learning. Stata J. **20**(1), 3–29 (2020)
31. J. Pereira, F. Saraiva, A Comparative analysis of unbalanced data handling techniques for machine learning algorithms to electricity theft detection, in *IEEE Congress on Evolutionary Computation (CEC)*, Glasgow, United Kingdom (2020), pp. 1–8

32. Z. Qu, H. Li, Y. Wang, J. Zhang, A. Abu-Siada, Y. Yao, Detection of electricity theft behavior based on improved synthetic minority oversampling technique and random forest classifier. Energies **13**(8), 2039 (2020)
33. B.H. Shekar, G. Dagnew, Grid search-based hyperparameter tuning and classification of microarray cancer data (2019), pp. 1–8
34. P. Flach, Performance evaluation in machine learning: the good, the bad, the ugly, and the way forward. AAAI **33**(1), 9808–9814 (2019)

The Study of Blockchain Technology to Enhance the Organizational Performance: Theoretical Perception

Swati Mathur and Lokesh Vijayvargy

Abstract Blockchain Technology (BT) enables decentralized, distributed, encrypted, and immutable logging of digital transactions. Blockchain features a decentralized database and public registry which helps transactions across a peer-to-peer network secured through cryptography. The aim of this paper is to how BT could be useful in enhancing the business performances of an organization based on research in the past decade. The study will be based on theoretical aspects of blockchain implementations, their application in various processes of an organization. This study focused on the detailed description of blockchain technology and its various business application, showing its impact on the different business models. The study highlights various barriers, motivators, and tools for BT and its impact on different parts of an organization.

Keywords Blockchain technology (BT) · Implementations · Organizations · Performance · Barriers · Motivators

1 Introduction

In the past decade, blockchain is one of the most promising areas of modernization as it discourses the problem of data and trust by making the ledger public and decentralized. Blockchain is an innovative, distributive, and decentralized technology that keeps the transactions and data intact and unaltered [1]. "Blockchain will do for transactions what the Internet did for information" [2]. Blockchain is a decentralized, distributed ledger that simplifies the method of taping transactions and tracking resources in a corporate network. Transactions made for blockchain are resistant to alteration and corruption through hashing and distributed algorithms. Blockchain is

S. Mathur · L. Vijayvargy (✉)
Jaipuria Institute of Management, Jaipur, India
e-mail: Lokesh.vijayvargy@jaipuria.ac.in

S. Mathur
e-mail: swati.mathur.fpm20j@jaipuria.ac.in

S. Rawat et al. (eds.), *Proceedings of First International Conference on Computational Electronics for Wireless Communications*, Lecture Notes in Networks and Systems 329,
https://doi.org/10.1007/978-981-16-6246-1_20

an expanding list of linked records, known as blocks, which are related and locked through encryption algorithms [3]. It is very tough to alter any block after it has been added to the list, because of the links that are designed from one block to the next. Thus, the name "blockchain" is given as it is a chain of blocks of various forms of data.

Blockchain emerged as a concept in the early 2000s. The primary notion behind this concept was the availability of a source through which the reliability and accuracy of a set of records could be formed and validated when this series of records were distributed among the cluster of recipients. The technology was comparatively slow in getting that recognition as the advantages and application of blockchain technology were not identified at that time. Bitcoin is the first BC that came into existence in 2009 [4]. Primarily the literature of Bitcoin was controlled by three major facets; ethical, safety, and legal but now the recent literature has observed Bitcoin as the face of money. Bitcoin's design permits for irreparable transactions, a given path of money conception over time, and a public transaction record. The Bitcoin transactions are publicly verifiable transactions where all the transactions are readable to the users. Each discrete Bitcoin can be traced back through all the transactions in which it was used. The new transaction in the Bitcoin network is stored in a block of recent transactions. Block is used to store the transaction with the data. Thus, a chain of blocks is formed with every new transaction. This chain of blocks keeps the recorded data of all the transaction occurred in the past. With the help of this sort of data structure, a Bitcoin user can verify the authenticity of any transaction in the chain. A bitcoin transaction is finalized only when it has been added to the consensus blockchain (a general agreement between the participants of a blockchain). This validation process in the blockchain is referred to as mining [5]. The nodes which perform mining are known as miners which verify the transactions in the blockchain. The Bitcoin follows the Proof of work (PoW) mining challenge which is open to all. Miners compete to add the next block. PoW calculations are power incentives as nodes with more computational power win.

Bitcoin stepped Blockchain into the public eye with it. As a new technology, the acceptance of Blockchain was not that easy. Many questioned the security, usage, application, and outcome of this new technology. But some people believed in the potential of blockchain technology and started working on its implementation in various domains.

Blockchain-based technologies are alluring because of their distinguishing characteristics of keeping the transactions secure, trustworthy, and transparent as compared to the existing technologies in terms of reliability, transparency, and traceability [6, 7]. Records of various transactions and data once added in the blocks of blockchain cannot be altered without making any changes in the previous records and that too with the consent of the majority of people involved in that transaction. This makes the application of blockchain technology relatively safe and secure in business operations where all the operations are authorized by operators and are observable.

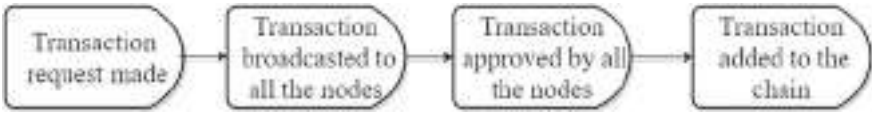

Fig. 1 The flow of transactions in the blockchain

The decentralized and traceable transaction ledger available for public addresses is the significant advantage of blockchain technology. In fiscal systems and enterprises, it enhances an extraordinary level of accountability. It helps in verifying the authenticity of traded assets with improved security and avoiding fraud in exchange-related businesses. In the pharma industries, it can be used to trace the Supply Chain (SC) from manufacturer to distributor.

Blockchain facilitates a decentralized platform for all the associates of the network without the need for dependable authorization for interactions among themselves. Hence, it eradicates the prerequisite of central power by authenticating and storing all the transactions. To execute blockchain with these characteristics, Fig. 1 depicts the flow of transactions using blockchain. In the first step, the transaction request is made. In the next step, this transaction data and the digital signature of that transaction are broadcasted to all the nodes. Each node then validates the transaction made which is further broadcasted to the miners in the network. When the transaction is approved by all the nodes it is added to the chain.

It has been reasoned for blockchain technology to be globally acclaimed it should merge with the other existing technologies, viz. IoT, cloud computing, and other decision-making systems [8]. The advent of practical blockchain implementation is providing pragmatic proof of how business organizations is gaining advantages from blockchain solutions [9, 10]. The resulting division offers an overview of BT and BT in organizational performance.

Blockchain technology is earning momentum with progressively numerous uses, along with growing amounts of elements involved in its implementation. This study plays a role in our opinion of the prospective uses of blockchain technology in an organization. Therefore, the objective of the study is to identify various barriers and motivators for the implementations of BT in an organization.

1.1 Introduction to Blockchain Technology

Blockchain technology was initially laid ahead by a group of researchers in 1991, but at that time, the idea was unused. The concept of a BC was again mentioned [4].

There are three most important virtues of blockchain, which are as follows:

- **Decentralized Structure**—There is no mediator or influential third party in the network. Decentralization can conserve the money given to the third-party bureaus and slash the consequent time cost.

- **Transparency**—The transaction process of the system is not dependent on the nodes to trust one another. The data exchange of the whole system and all data contents are accessible and translucent. Therefore, nodes are incompetent to cheat each other.
- **Reliability and Security**—The data stockpiled in a blockchain cannot be altered and is accessible for all the nodes in the network. It is also an essential property for recording transactions.

The structure of BC: BC is a distributed database or a public registry that is secured through cryptography, wherein the transaction across a Peer-to-Peer (P-2-P) network is done. This operation regulations history will be assembled and deposited as blocks of data. A group of people validates the transactions in a blockchain in an organization. The members of the group can only assess the previous transactions done, but they are not accessible to do any alteration or eliminate any of the previously recorded transactions. Blocks are linked together with cryptography. This makes blockchain maintain the immutable history of the events of the group's participants. This history is distributed among all or selected group representatives. This extends high levels of traceability of all recorded operations and transparency that permits everyone involved to view these transactions.

Data Structure of BC: Each block in a BC consists of the following:

(a) Data: Store up the data.
(b) Previous Hash: Stores the hash for the preceding block.
(c) Hash: Hash value for the existing block which can be utilized to describe this block.

Figure 2 showed the linkage between different blocks of the blockchain which are recognized with the help of a hash, the encrypted value of data in the block which is generated cryptographically. Hash helps in identifying data from the dataset and store them as hash values.

Data Distribution in BC

The Peer-to-Peer (P-2-P) distribution approach is followed in blockchain technology, where no central authority is there to regulate the data. The data is deposited in all the applicant nodes in the network. All the specific nodes will have the carbon copy

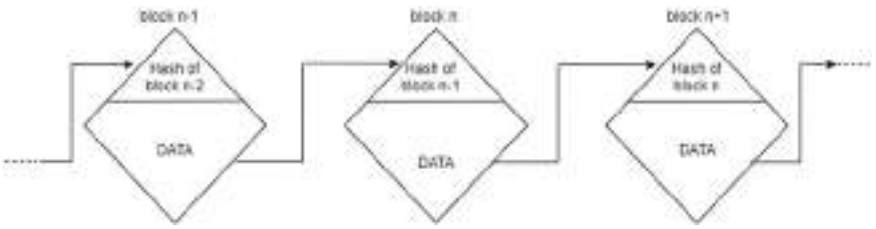

Fig. 2 Data structure of blockchain

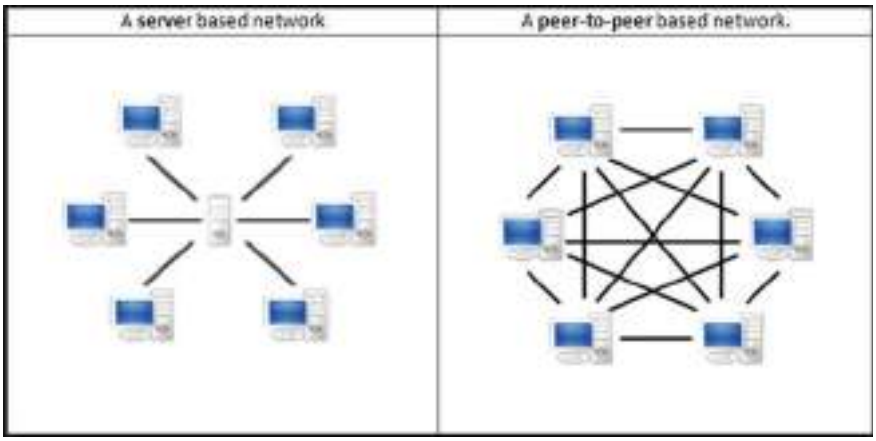

Fig. 3 Difference between control of data exchange in two different networks. *Source* [11]

of the complete "blocks", and any alteration in a certain block will be informed in all the nodes.

Figure 3 displayed the difference between the regulation of the data in a server-based network and a peer-to-peer-based network. In a server-based network, a central authority is there to regulate the data but in a peer-to-peer network, data is stored in all the participatory nodes of the network.

2 Methodology

Systematic Literature Review (SLRs) proposes the reader's all-inclusive acquaintance of the literature in an arena over a holistic and ordered sketch that observes typical protocols [12–15]. A valuable literature review is one that generates a firm foundation for proceeding information [16]. The purpose of this systematic review is to compare a varied range of sources to create a comprehensive and stable outline of blockchain adoption in the various divisions of an organization. SLRs support in explaining prevailing knowledge gaps and resultant documentation of paths for future research [17]. The SLR procedure is comprised of three main stages, namely planning, execution, and reporting integrated evidence.

Two databases—Scopus, and Shodhganga—were acknowledged by preceding studies as widespread sources of information for articles related to blockchain technology and its implementation in organizational performance. Notable exclusion and inclusion criteria of the database as mentioned above help in selecting the desired articles. The keyword combination used for the search was Blockchain OR Block

Chain AND Impact AND Business OR Organization. These keywords were strained from an evaluation of previous studies that used parallel keywords. Later, relevant articles were curtained according to precise standards for defining quality, relevance, and robustness [16].

3 Finding

This study highlights the implementation of BT in different sectors for enhancing organizational performance. The process involved the expansion of this prior research and filling the research gap identified. This detailed literature review helped in developing a research framework in this field to advance the work in academics. The results are presented in Table 1.

Innovation theory and technological organizational and environmental research framework were used for BT implementation which enhance the operational performance of processes [18]. Business model taxonomy and business model patterns model were also used to analyze the importance of blockchain technology in the financial and supply chain sectors of industry [19]. In the HR division, two models were used, Input Process Output Model and Blockchain Modeling Language Framework focusing on human resource management, employee skills shortage, and human resource information management, respectively [20].

3.1 Outcomes

BT has a vast potential to transform all the departments of an organization. The use of blockchain in data validation, transaction, and supply chain is appreciable, which leads efficiency [21]. Blockchain also expands an organization's operational proficiency by the smooth flow of information to everyone in the process [1]. Blockchain provides network participants to control their business and extensible business networks. Blockchain offers digital transformation and decentralized data storage, which helps to increase the authenticity and lessen fraud risks. Thus, integrating blockchain technology in an organization can boost its productivity level and enhance organizational goals. Refer to Table 1.

To summarize it, we can say that BT enhances the performance of an organization by:

- Increasing the effectiveness of the SC
- Helping HRM by providing relevant information at a given period
- Storing healthcare data in digital form to be readily available
- Strengthening the operational competencies.

Table 1 Various blockchain model and its outcomes and scope

Authors	Model	Outcomes	Scope
[1]	Literature review	This study explored the potential uses of BT in transforming SCs by increasing the operational efficiency of an organization through data collection, validation, and fulfilling the requirements of the organization	This study observed the prior research done in the BC application in the SC division
[18]	Innovation theory, TOE framework	The author suggested that BT when bundled with other technologies, enchanted business process transformational competencies that enabled the organization to modify their business model	The purpose of this paper is to provide the theoretical foundation of BC adoption and various technological considerations
[19]	Business model taxonomy and patterns	The author expounded various patterns of BC application like BC for business integration which systematizes shared database for a company; BC as a multi-sided platform putting back the need for unifying mediators, reveal that the BC-based corporation caters to a new value proposition increasing the effectiveness of the firm	The aim of this paper is to develop a classification of BC business models to reveal the influence of BT on business models
[20]	Input process output model	The study explained the application of AI and BC modified human resource management by saving time for the division and by creating the apt information about skills needed by an industry for a competent standard workforce	The objective of this research is to prosper a BC-based HR framework to meet the needs of an industry and workforce competencies

(continued)

3.2 Barriers

Over the past 5 years, blockchain technology enticed many researchers and practitioners' interest. A substantial concern for many organizations is the absence of

Table 1 (continued)

Authors	Model	Outcomes	Scope
[21]	Literature review	The outcome of this paper emphasizes on the application of BT on the supply chain of the organization in tracing a product's origin, which aids in the effectiveness of the logistic department and in an unaltered flow of information	The study intends to provide information on how BC helps in securing and managing the information system of an organization
[22]	Literature review	This study emphasized on the refinement of the healthcare sector after the implementation of BT which helped in the digitalization of health documents and making the claim and transaction procedures simpler and more efficient	This study focused on utilizing BT for ecosystem evolution in the healthcare industry
[23]	Technology assessment framework	The author suggested that BC technologies application in the food supply chain is unique because it keeps the information transparent, traceable, and trustworthy	This paper discussed the social and environmental connection of BC-based technologies in the food supply chain
[24]	Case study	The study traversed that BC offers the CFO of an organization to enhance many of his role-specific key performance indicators. It also promotes the digital transformation of the data and records	This case study explained the impact of BT on the CFO, to initiate the digitalization flow of information within the organization
[25]	SLR (3 stage process)	The outcome of the study explored the potential ideas and evaluation strategies for the BC adoption decision to develop and retain sustained leadership and market space	The aim of this research is to study the prior research done in the field of BC and how BC affects the decision-making characteristics of the organization

(continued)

Table 1 (continued)

Authors	Model	Outcomes	Scope
[26]	Business models	The author explained the principles of sustainable networks in BT as protecting competitive data and existing with the current system of keeping all the transactions and records. Thus, increasing the performance of the organization	The purpose of this paper on IBM BC is to display the benefits of BC for an enterprise

blockchain technology; business uses cases across industries. Due to this least familiarity with this technology, the organization doesn't trust integrating this technology [23]. The interoperability of the system is a barrier to adopting this new technology by many organizations [1, 21]. Some barriers are lack of clarity, governance and legal, security, and privacy concerns for the new technology, which block blockchain technology adoption in an organization [25]. The other noticeable barriers are the following:

- Compatibility issues in using the new technology
- Data collection and management
- Significant cost to the enterprise
- Lack of knowledge towards the new technology.

3.3 Enablers

Blockchain enables cost-effective business process management through blockchain-based technologies like transparency, traceability, authenticity, and trust [23]. The other enablers for implementing blockchain technology are the following:

- Data and process transparency
- Improved speed of the process
- Increased operational efficiency of an organization
- Smart contract management due to high speed
- Immutability
- Data security and management
- Cost and risk reduction
- Digital identity management.

Adopting blockchain technology by an organization depends upon many aspects. The organization should examine the technological consideration and the human resource involved in the implementation of the blockchain technology in the organization.

3.4 Challenges

Implementing blockchain technology in any organization requires efforts from all the organization departments; the complete understanding and knowledge of the technology are essential. Hence, various challenges are there in implementing blockchain technology, such as:

- Technical scalability of BT
- Transaction and integration speed of a blockchain process
- Decentralization process of an organization for BT
- Lack of awareness about BT capabilities
- Decentralized ecosystem for cloud storage for BT
- Energy consumption of decentralized networks
- Data storage and collections.

4 Impact of BT on Organizational Performance (OP)

Organizational performance (OP) represents the potential for accomplishing its objectives and stakeholders' prospects along with market persistence [27]. It can also be identified as the procedure of 'analyzing and assessing the organization's effect against its objectives and goals, which requires an analogy of actual results with preferred results [28, 29]. The organizational performance incorporates the real efficiency of the organization equated with the preferred result or goals.

In this Internet era, every organization is packed with significant volumes of data. The different departments of the organization have their own set of data to be stored for future reference. This massive amount of data helps the organization in many decision-making processes. Blockchain technology helps store this data in a decentralized manner with transparency, which can be used by the organization to improve their performance and create an enhanced business decision that aids an organization to achieve their goals and targets, thus leading to success. Let us discuss the impact of Blockchain technology in various areas of an organization.

4.1 Human Resources (HR)

Blockchain technology will bring a drastic change in the HR department and procurement. With the help of blockchain technology, the stored data of HR will be programmed to receive the applications and categorize them with the support of artificial intelligence [1, 8, 9]. Candidates can directly gain access to the system, get the login, and know their application's exact status. HR executives will efficiently appraise, employ, reimburse, and even lay off employees. Blockchain technology will help the HR staff to validate the candidates and existing staff in a much quicker

way. Thus, blockchain will diminish the lengthy and time taking process of hiring in the HR department [22, 25]. Job.com recently has implemented AI and blockchain to contest job seekers with a suitable company. The sign-up amount for the employers in job.com is only 7% instead of the standard 20% commission. The 5 of 7% is instantly transferred back to the employer as the signing reward. All these transactions are motorized by blockchain technology. Many other organizations like ETCH, eXo Platform, Gospel Technology, Lympo, and Peoplewave, etc., have also implemented blockchain technology to enhance organizational performance.

4.2 Marketing

Implementing BT in the marketing department will bring noticeable progress in the system. The department will spare a lot in the advertising budget as the money and time wasted in the fraudulent activities will be averted by blockchain [16, 19, 22, 24]. This will further help the organization get a better return on investment (ROI). Organizations can make use of the system to pursue and administer their budget spending. This diminishes the chance of being overpriced and guarantees superior execution in the long run [27, 28].

IBM's digital platform is guiding the network for media deals with Unilever, Pfizer, and Kellogg, for which the ledger will remove the "ad-tech tax." It will spread out to other larger companies soon.

4.3 Legal Affairs

Legal affairs play a critical role in an organization. The legal contracts of an organization are prepared on a paper. With smart contracts, managing an organization's legal affairs is way easy as smart contracts turn this paper contract into a code. Both parties need to agree on some conditions and sign the contract before the smart contract becomes operational [24, 28, 29]. Everything needs to be accomplished on a blockchain platform that stores all the information. Thus, the whole process of legal affairs is accomplished in a transparent and immutable manner with blockchain technology. Lantmateriet is Sweden's land registry agency which is now operating with banks and businesses for a blockchain pilot project. They believe that buying any property is a long and time-consuming process but using blockchain enables saving time and resources. To add, all the relevant documents would be in digital formats or smart contracts.

4.4 Accounting

Blockchain technology will facilitate handling the chores of the accounting department with utmost solace. The accountancy department is responsible for handling the operations on a large scale, controlling byzantine tax codes, and supervising diverse currencies. For any organization to be successful, this department mandates the most accuracy. This level of accuracy is met with the help of blockchain. It also extends confidentially and ambiguity in trading with specific transactions [18, 20, 26, 28, 29]. The financial service and technology company ABRA is BITCOIN based secure remittance application. The companies using blockchain technology in the banking and financial sectors are HSBC, Barclays, VISA, BBVA, etc.

4.5 IT Department

Cybersecurity is vital in the Internet era where all the organizations are in a menace of getting their confidential data leaked. Blockchain can help the organization store their trade secret transactions in a secure and immutable manner, offering transparency and protection to the organization [20, 25, 29]. The software behemoth, Microsoft offers blockchain as a service through it is cloud computing arm, Azure. More examples of the IT department using blockchain technology are IBM, Google, Accenture, etc.

4.6 Operations

Supply Chain Management has also apprehended the latent of blockchain technology [30]. Supply chain (SC) processes are often imprecise concepts from the viewpoint of a customer. To eradicate this, blockchain is applied to demand transparency and visibility to clients in SC. The implementation of blockchain technology can progress information flow between SC stakeholders. It results in diminishing supply and demand qualms to improve SC performances [23, 26–28]. The IBM Food Trust is a blockchain association assembled by the company and is aimed to move complex food supply chains to one distributed, shared ledger. Nestle launched a new brand "Chain of Origins" in Australia where the consumers can see the coffee's supply chain by employing blockchain technology.

4.7 Management

The management of an organization is the crucial link between all the departments of the organization. The management process must be quite dynamic and valuable

when dealing with the trade transactions of the organization. This can be done with the help of blockchain technology [19, 20, 28]. The data first needs to be stored in a digitalized manner, and then the blockchain platform is used to store it for future transactions. This stored data is immutable and distinctive with full transparency. Thus, the management of an organization gets enhanced after implementing blockchain technology.

5 Conclusion

The present study aims to understand the scope of blockchain technology in the various departments of an organization. An SLR was performed on digital databases following specific protocols to identify specific articles to be reviewed (Table 1). Various BT models, outcomes, barriers, challenges, and enablers for implementing BT are identified, leading to organizational performance. The paper also concluded the impact of BT on various fields of management. Future research is needed to investigate the long-term impact of implementing blockchain technology in enhancing organizational performance. Blockchain reduces the cost and increases an organization's efficiency by its shared ledger and smart contracts, but the absence of appropriate guidelines and affirmed benchmarks might instigate a counter effect. Thus, this new technology demands more research in its long-term influence in an organization.

References

1. P. Dutta, T.M. Choi, S. Somani, R. Butala, Blockchain technology in supply chain operations: applications, challenges and research opportunities. Transp. Res. Part E Logist. Transp. Rev. **142**, 102067 (2020)
2. S.S. Gupta, *Blockchain* (Wiley, 2017)
3. G. Zyskind, O. Nathan, Decentralizing privacy: using blockchain to protect personal data, in *2015 IEEE Security and Privacy Workshops* (IEEE, 2015), pp. 180–184
4. S. Nakamoto, Bitcoin: a peer-to-peer electronic cash system. (2008)
5. R. Bohme, N. Christin, B. Edelman, T. Moore, Bitcoin: economics, technology, and governance. J. Econ. Perspect. **29**(2), 213–238 (2015)
6. R.V. George, H.O. Harsh, P. Ray, A.K. Babu, Food quality traceability prototype for restaurants using blockchain and food quality data index. J. Clean. Prod. **240**, 118021 (2019)
7. Y. Liu, Y. Zhang, S. Ren, M. Yang, Y. Wang, D. Huisingh, How can smart technologies contribute to sustainable product lifecycle management? J. Clean. Prod. **249**, 119423 (2020)
8. T. Clohessy, S. Clohessy, What's in the box? Combating counterfeit medications in pharmaceutical supply chains with blockchain vigilant information systems, in *Blockchain and Distributed Ledger Technology Use Cases* (Springer, Cham, 2020), pp. 51–68
9. H. Treiblmaier, T. Clohessy, *Blockchain and Distributed Ledger Technology Use Cases* (Springer, 2020)
10. G.R. White, Future applications of blockchain in business and management: a Delphi study. Strat. Chang. **26**(5), 439–451 (2017)
11. GOOGLE, https://sites.google.com/site/cis3347cruzguzman014/module-2/client-server-and-peer-to-peer-networking/p2p-network-vs-server.jpg?attredirects=0

12. S. Afrooz, N.J. Navimipour, Memory designing using quantum-dot cellular automata: systematic literature review, classification and current trends. J. Circuits Syst. Comput. **26**(12), 1730004 (2017)
13. F. Aznoli, N.J. Navimipour, Cloud services recommendation: reviewing the recent advances and suggesting the future research directions. J. Netw. Comput. Appl. **77**, 73–86 (2017)
14. M.O. Ahmad, D. Dennehy, K. Conboy, M. Oivo, Kanban in software engineering: a systematic mapping study. J. Syst. Softw. **137**, 96–113 (2018)
15. N. Mehta, A. Pandit, Concurrence of big data analytics and healthcare: a systematic review. Int. J. Med. Inform. **114**, 57–65 (2018)
16. J. Webster, R.T. Watson, Analyzing the past to prepare for the future: writing a literature review. MIS Q. xiii–xxiii (2002)
17. S. Gopalakrishnan, P. Ganeshkumar, Systematic reviews and meta-analysis: understanding the best evidence in primary healthcare. J. Fam. Med. Prim. Care **2**(1), 9 (2013)
18. T. Clohessy, H. Treiblmaier, T. Acton, N. Rogers, Antecedents of blockchain adoption: an integrative framework. Strat. Chang. **29**(5), 501–515 (2020)
19. J. Weking, M. Mandalenakis, A. Hein, S. Hermes, M. Böhm, H. Krcmar, The impact of blockchain technology on business models—a taxonomy and archetypal patterns. Electron. Markets 1–21 (2019)
20. O. Fachrunnisa, F.K. Hussain, Blockchain-based human resource management practices for mitigating skills and competencies gap in workforce. Int. J. Eng. Bus. Manag. **12**, 1847979020966400 (2020)
21. D. Berdik, S. Otoum, N. Schmidt, D. Porter, Y. Jararweh, A survey on blockchain for information systems management and security. Inf. Process. Manag. **58**(1), 102397 (2012)
22. S.E. Chang, Y. Chen, Blockchain in health care innovation: literature review and case study from a business ecosystem perspective. J. Med. Internet Res. **22**(8), e19480 (2020)
23. S. Kohler, M. Pizzol, Technology assessment of blockchain-based technologies in the food supply chain. J. Clean. Prod. 122193 (2020)
24. P. Sandner, A. Lange, P. Schulden, The role of the CFO of an industrial company: an analysis of the impact of blockchain technology. Futur. Internet **12**(8), 128 (2020)
25. N. Upadhyay, Demystifying blockchain: a critical analysis of challenges, applications and opportunities. Int. J. Inf. Manag. **54**, 102120 (2020)
26. N. Gaur, Blockchain challenges in adoption. Manag. Financ. (2020)
27. J.M. Griffin, X. Ji, J.S. Martin, Momentum investing and business cycle risk: evidence from pole to pole. J. Financ. **58**(6), 2515–2547 (2003)
28. L.A. Ho, What affects organizational performance? Ind. Manag. Data Syst. (2008)
29. R.G. Chung, C.L. Lo, The relationship between leadership behavior and organizational performance in non-profit organizations, using social welfare charity foundations as an example. J. Am. Acad. Bus. **12**(1), 83–87 (2007)
30. S.A. Abeyratne, R.P. Monfared, Blockchain ready manufacturing supply chain using distributed ledger. Int. J. Res. Eng. Technol. **5**(9), 1–10 (2016)

Case Study on Server–Client Protocols of Industrial Controllers

H. Ramesh, S. Arockia Edwin Xavier, R. Pradheep Kumar, and S. Julius Fusic

Abstract Industry 4.0 is one of the rapidly growing technologies of present-day industries. The development of newer technologies such as cloud computing, internet of things and cyber-physical systems has brought a new revolution to the manufacturing industry. Interoperability among devices is one of the key goals of Industry 4.0. Modbus, TCP (Transmission Control Protocol), UDP (User Datagram Protocol) are common protocols that are universally accepted by all manufacturers of Industrial Controllers. These protocols help in standardizing the data communication between different vendor controllers through the server–client architecture. In recent days, Open Platform Communications (OPC) have proven to be an effective technology to support interoperability and heterogeneity in control and automation applications. In this paper, a case study of common server–client communication protocols present in the industry through the implementation in industrial controllers has been presented. This research looks at the features of these communication protocols and their usage in the existing systems. OPC-UA communication has been compared with existing protocols such as Modbus, UDP, and TCP and its features to support Industry 4.0 are shown with comparative analysis.

Keywords Programmable logic controllers · OPC-UA · Modbus TCP · UDP · TCP/IP · Motion control

H. Ramesh (✉) · S. A. E. Xavier · R. P. Kumar · S. J. Fusic
Thiagarajar College of Engineering, Madurai, India
e-mail: rameshh@tce.edu

S. A. E. Xavier
e-mail: saexee@tce.edu

S. J. Fusic
e-mail: sjf@tce.edu

S. Rawat et al. (eds.), *Proceedings of First International Conference on Computational Electronics for Wireless Communications*, Lecture Notes in Networks and Systems 329,
https://doi.org/10.1007/978-981-16-6246-1_21

1 Introduction

The First Industrial Revolution in the late seventeenth and early eighteenth century was due to the development of steam engines which lead utilization of steam for power. The Second Industrial Revolution began in the 1870s, in which mass production of goods through assembly lines powered using electricity was established [1]. The Third Industrial Revolution began with the utilization of electronics into the automation industry and the development of a Programmable Logic Controller [2]. Moreover, utilization of IT-based solution such as ERP and MES with the automation industry has been achieved. Thus the use of automated control and intelligent robots for production has revolutionized the manufacturing industry [3]. Currently, the fourth industrial revolution based on the technologies of the internet of things, cyber-physical systems, and cloud computing to manufacture products has already begun [4]. Hanneman et al. [5] have identified four major components in Industry 4.0 scenario as cyber-physical systems, internet of things, internet of services and smart factories. The concept of Industry 4.0 was first introduced at the Hannover Fair in 2011. It has now taken the form of a buzzword to denote the current trend of industrial automation [6]. Kagerman et al. [7] proposed an idea of the factory of the future. By use of these new technologies, Industry 4.0 will lead to the development of new business models, work process, and development [8]. Industry 4.0 is developed on the basis of several current and trending technologies such as artificial intelligence, cloud computing [9, 10], mobile computing [11], big data [12, 13], machine learning [14], internet of things [15], etc. [3, 16].

The Automation Industry is prevailed by a large number of proprietary interfaces and devices. The number of devices from different vendors and newer fields such as wireless communication has resulted in a large number of platforms, protocols, and APIs. In a typical factory environment, a process control application will have a large number of controllers, servers, devices, components, etc., from various vendors. Most vendors provide their specific proprietary communication mechanism and interfaces [17]. Moreover, a large number of protocols and implementations which do the same functions have been developed by different groups [18]. Hence, in order to integrate the components to integrate a process control system, these problems of heterogeneity must be solved. The difficulties have led to efforts being taken to achieve interoperability in an easier and effective manner [17]. OPC-UA (Open Platform Communication-Unified Architecture) provides a suitable medium for interoperability at different levels of automation [19].

The main aim of this paper is to provide a broad outlook of commonly accepted server–client protocols present in the industrial controllers and the capability of OPC-UA to achieve seamless integration. This paper is organized as follows. Section 2 discusses the common Server–Client protocols available in industrial controllers and their implementation blocks. Section 3 is about the implementation of Server client protocol in Industrial Controllers. Section 4 deals with the comparison of OPC-UA with other protocols such as Modbus, TCP (Transmission Control Protocol), and UDP (User Datagram Protocol).

2 Features of Server–Client Protocols

Since 1970, more than 50 different protocols have been developed by manufacturers and vendors with most of them being proprietary and having proprietary interfaces. Of these protocols, only certain protocols have been accepted by most manufacturers. The server–client architecture is one of the most reliable communication methods for communication between devices. User Datagram Protocol (UDP), Transmission Control Protocol (TCP), Modbus, and OPC-UA are the most common Ethernet-based server–client architecture accepted by most manufacturers and vendors.

2.1 Modbus

The Modbus is a communication protocol developed by Modicon for use with Modicon Programmable Logic Controllers (PLC) and process control applications. Modbus has been accepted by about 30 manufacturers and many systems are in operation. Therefore, it has been regarded as a de facto industry standard and is now commonly used for communicating between industrial devices [23]. Modbus is based on Server client architecture where the server functions as master and the client functions as slaves. A single master can communicate with up to 247 slaves. Transaction between the master and slaves is based on query response type when only a single slave is addressed, while slaves do not give a response for broadcast messages. Slaves can create their own response and can only respond to a request initiated by the server [24].

A master's query consists of the slave address, function code, any required data, and error checking field. The function code depends on the data fields requested. The response of the slave consists of address, function code, data to be returned, and error checking field. If the request from the master contains any error or if the request is unable to be executed by the slave, the response from the slave will be an exception message. The error checking field is used to check if the contents of the message are valid [25].

Modbus is actually an application protocol that defines the rules for the data organization and interpretation and is independent of the underlying physical layers [24, 26]. It was originally designed for serial communication for RS232 and is now compatible with RS232/485. This serial communication is known as Modbus RTU. Modbus TCP/IP is simply a Modbus RTU wrapped into a TCP/IP frame and sent over the network cable instead of the serial line. Here, TCP/IP is used as a network layer protocol and the Ethernet as a physical layer [24, 25, 27].

In practice, Modbus TCP packets only contain the function code and data. Modbus checksum is not used and Ethernet TCP/IP checksum is used to check data integrity. The Modbus TCP protocol identifies two parts: PDU (Protocol Data Unit) and ADU (Application data unit) [28].

Transaction Identifier (2 byte)	Protocol Identifier (2 bytes)	Data length (2 bytes)	Unit Identifier (1 bytes)

Fig. 1 Modbus application header

The ADU has a 7-bit Modbus Application Protocol (MBAP) header as shown in Fig. 1 [3].

The Modbus Application Data is built into the data field of standard TCP/IP frame and is sent to port 502 via TCP. Modbus is an application layer protocol. While TCP/IP ensures the proper transmission of data, Modbus on the application layer is responsible for interoperability [25].

Modbus has a simple data structure of only four different data types [25]: Discrete Inputs, Coils, Holding registers, and Input Registers.

The request of Modbus transaction is made up of function code and additional data bytes which are based on the type of action to be performed and are largely the reference for the variables, mostly the registered address, as most operations on Modbus are done on the registers [25].

Similarly, the IL_ModbusTCPclient helps to create a Modbus slave. The IL_ModbusTCPServer and IL_ModbusTCPclient functions are realized using function blocks as shown in Fig. 2 [60].

TIA (Totally Integrated Automation) Portal by Siemens AG, is a total integrated solution for automation for Siemens products. It supports Modbus through the MB_SERVER and MB_CLIENT function blocks. The MB_SERVER function block acts as a Modbus TCP server and MB_CLIENT acts as Modbus TCP client and both are used to send, receive, and process Modbus information [61]. The MB_SERVER and MB_CLIENT are implemented using function blocks as shown in Fig. 3.

MATLAB by Math works Inc. has an Instrument Control Toolbox, which supports Modbus communication through TCP as well as Serial Port. It helps to connect to Modbus servers. It supports the read and write of all four basic data types [62].

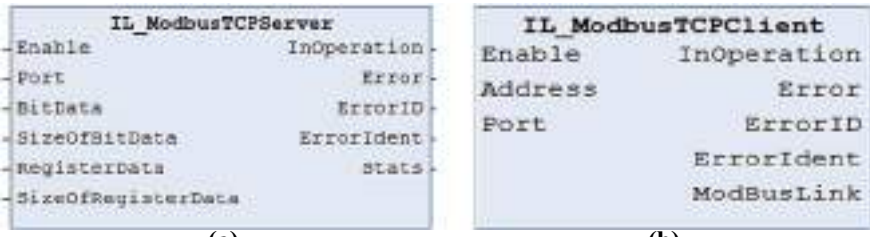

Fig. 2 **a** Modbus TCP Server in IndraWorks **b** Modbus TCP Client in IndraWorks

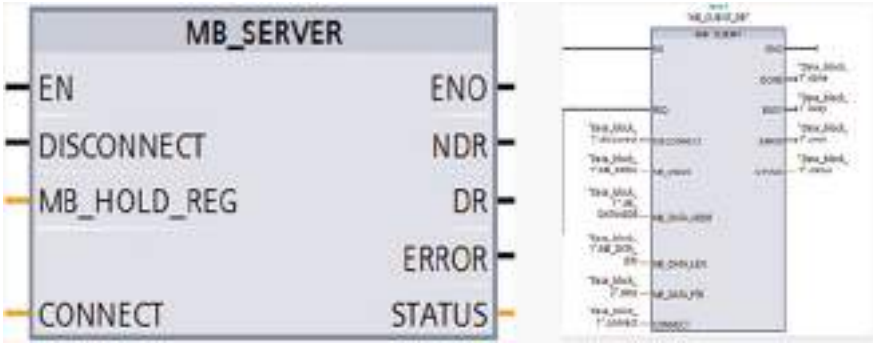

Fig. 3 **a** Modbus TCP server in TIA portal **b** Modbus TCP client in TIA portal

2.2 UDP (User Datagram Protocol)

UDP (User Datagram Protocol) is a simple communication protocol and it does not require a connection to be established beforehand as TCP [29]. It is used in applications where time delay in communication is critical. Unlike TCP, UDP does not guarantee data transmission and does not have well-defined handshaking messages. The messages in UDP are sent as a datagram and the messages are not guaranteed to be received in the same as order as sent. UDP, like TCP, operates in the transport layer which corresponds to the fourth layer of the OSI (Open Systems Interconnection) model [30]. UDP is a very lightweight protocol and hence the communication between devices using UDP is faster. There are error checking options available but retransmission of data is not possible [31, 32, 34].

In Bosch Rexroth, the functional blocks for implementing TCP communication are found in the RIL_SocketComm library. TCP communication is of two types: Synchronous and Asynchronous. In Asynchronous communication, IL_UDPSocketAsync or IL_UDPInitialAsync is used to create a new UDP connection and the connection created by IL_UDPInitialAsync can be closed by using IL_UDPCloseAsync. The server parameter in both IL_UDPSocketAsync and IL_UDPInitialAsync determines whether a UDP server or client is created [60]. The IL_UDP SocketAsync and IL_ UDPCloseAsync functions are realized using function blocks as shown in Fig. 4.

IL_UDPSendtoAsync and IL_UDPRecvfromAsyncare used to send and receive data packets using the UDP communication using block as shown in Fig. 5 [60]

Similarly, in TIA Portal by Siemens, TCON and TDISCON are used to create and disconnect a UDP connection. TUSEND is used to send and TURCV is used to receive data through UDP communication [61]. The TCON, TDISCON, TUSEND, and TURCV are implemented using function blocks as shown in Fig. 6.

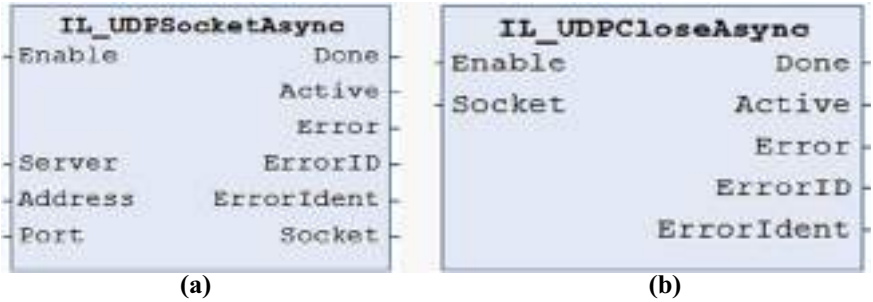

Fig. 4 **a** UDP connection start in IndraWorks **b** UDP connection close in IndraWorks

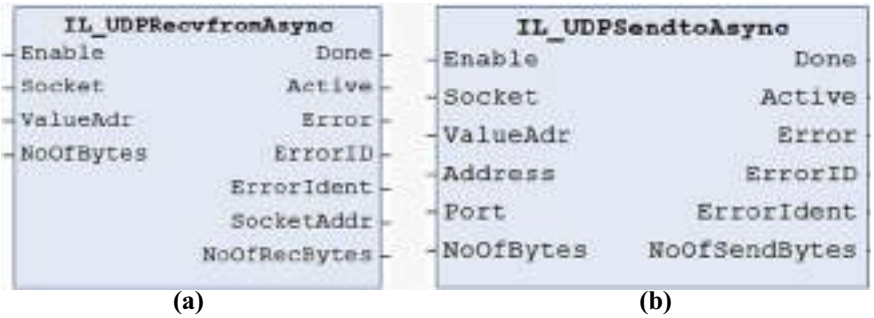

Fig. 5 **a** UDP receive in IndraWorks **b** UDP send in IndraWorks

2.3 TCP/IP (Transmission Control Protocol/Internet Protocol)

TCP/IP (Transmission Control Protocol/Internet Protocol) is a communication protocol that is connection oriented. TCP (Transmission Control Protocol) works in the transport layer which corresponds to the fourth layer of OSI (Open Systems Interconnection) model. It is responsible for the arranging of messages into data packets, their segmentation, etc. TCP requires a connection to be established before the data is transferred. This enables us to validate the messages as well as request to retransmit them in case of data packet loss [29]. TCP has acknowledgment messages which make it more reliable. Moreover, TCP has a mechanism which enables to send and receive the data in the correct order. The IP (Internet protocol) operates on the Transport layer or Layer3 of the OSI model. It provides for the transport of the byte data between the connected devices, by means of their IP address. TCP is generally used in cases where data reliability and data coherence are important [31, 32, 34].

In Bosch Rexroth PLCs, the functional blocks for implementing TCP communication are found in the RIL_SocketComm library. TCP communication is of two types: Synchronous and Asynchronous. In asynchronous communication,

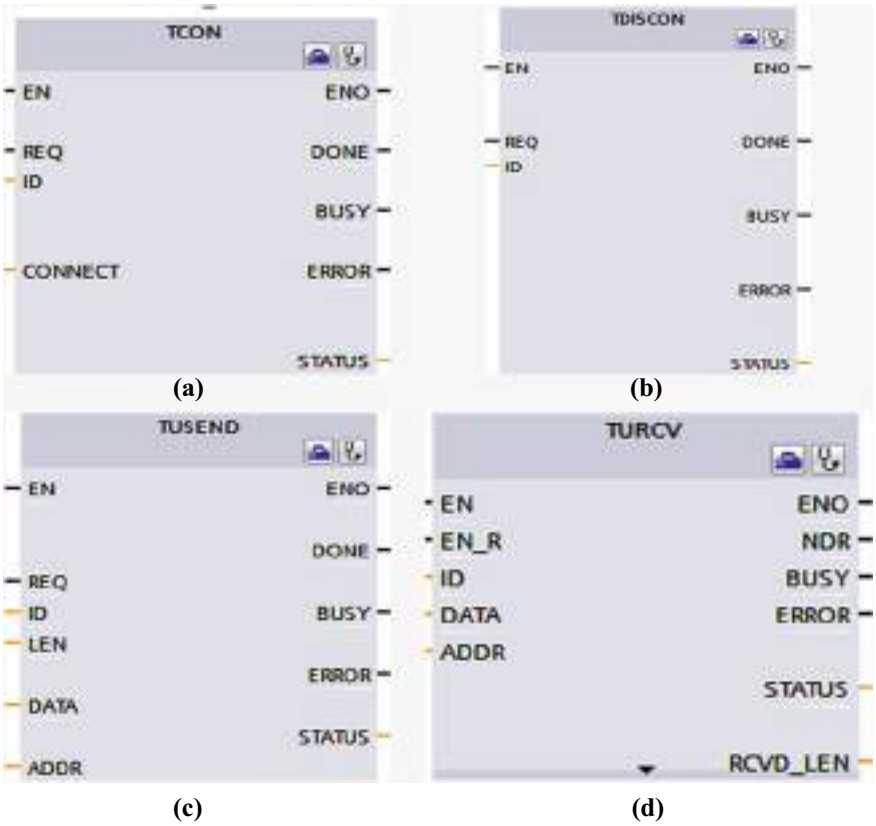

Fig. 6 **a** UDP connection start in TIA portal **b** UDP connection close in TIA portal **c** UDP send in TIA portal **d** UDP receive in TIA portal

IL_UDPSocketAsync or IL_UDPInitialAsync is used to create a new TCP connection and the connection can be closed by using IL_TCPCloseAsync. The server parameter in both IL_TCPConnectionAsync and IL_TCPInitialAsync determines whether a TCP server or client is created [60]. IL_TCPConnectionAsync and IL_TCPCloseAsync are implemented using function blocks as shown in Fig. 7.

IL_TCPSendAsync and IL_TCPRecvAsync are used to send and receive data packets using the TCP connection and are implemented using function blocks as shown in Fig. 8 [60].

In Tia Portal by Siemens, the TCON block is used to create a new TCP connection and TDISCON to disconnect it. Similarly, TSEND is used to send and TRCV is used to receive data packets through the established Connection [61]. The TCON, TDISCON, TSEND, and TRCV are implemented using function blocks as shown in Fig. 9.

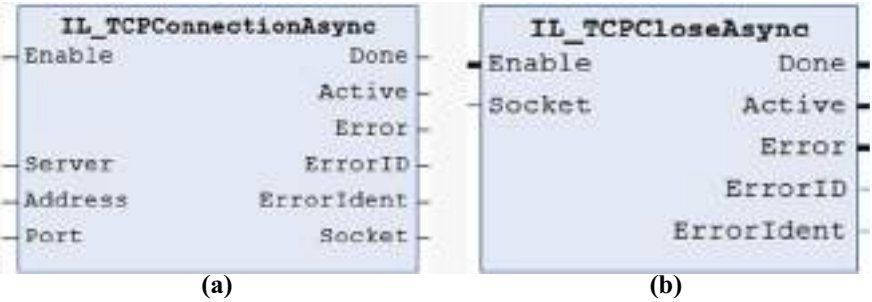

Fig. 7 **a** TCP connection start in IndraWorks **b** TCP Connection close in IndraWorks

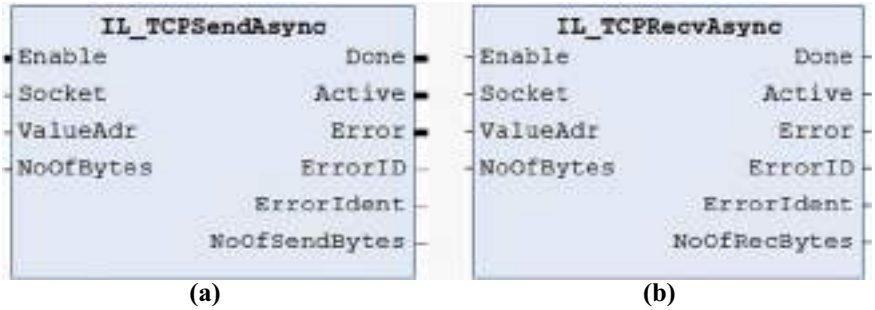

Fig. 8 **a** TCP send in IndraWorks **b** TCP receive in IndraWorks

In MATLAB by Mathworks Inc., TCP/IP communication is done using the Instrument control toolbox. TCP/IP is used to connect to both servers and clients and supports read as well as write functionality [62].

2.4 OPC-UA (OPC Unified Architecture)

OPC UA (OPC Unified Architecture) is the latest communication specification proposed by the OPC Foundation for secure, reliable, and interoperable transfer of information and between the various levels of the production environment from the shop floor to the planning departments [36]. In 1980, several organizations, educational institutions, and industrial organizations started to develop their own protocols and sets of standards [37–39]. In a short span of time, more than 50 types of protocols were developed [39], many specific for different applications such as the CAN for the automobile. Hence, to integrate the various components of an industrial scenario such as human–machine interface (HMI), supervisory control and data acquisition (SCADA), system were dependent on a large number of protocols [40]. Hence software for data conversion and other processes made the system error prone and was

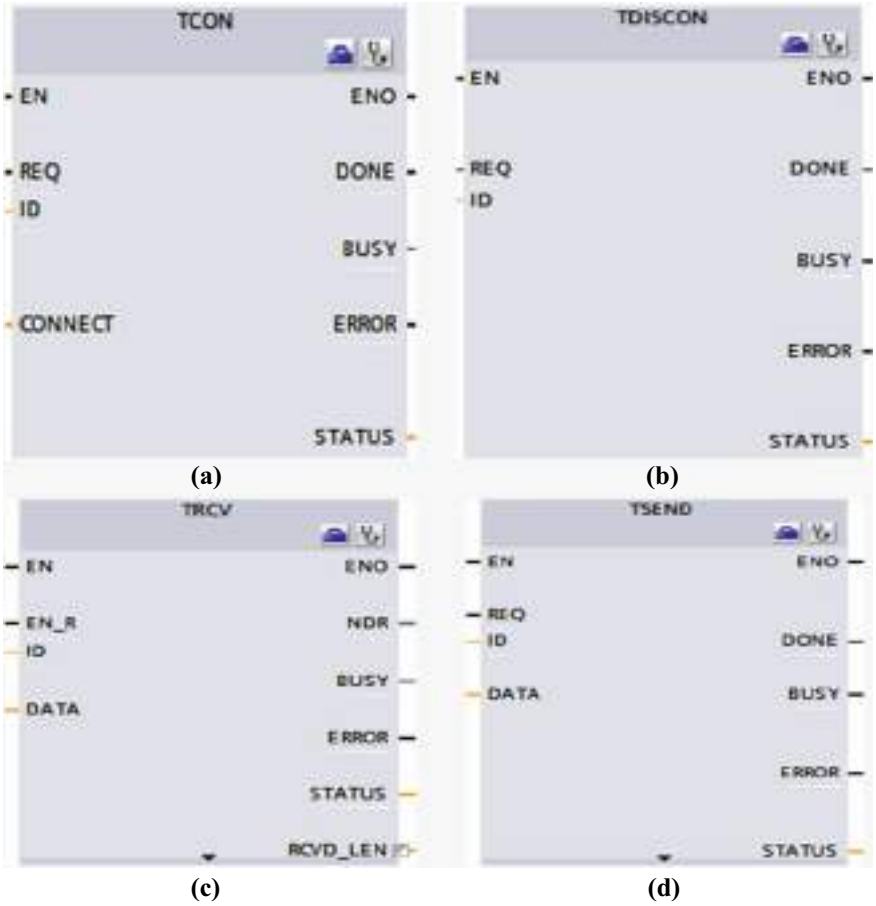

Fig. 9 **a** TCP connection start in TIA portal **b** TCP connection close in TIA portal **c** TCP receive in TIA portal **d** TCP send in TIA portal

a threat to its reliability [39]. To overcome this, The OPC foundation was formed by some companies such as Fisher-Rosemount, Intellution, Intuitive Technology, Opto22, Rockwell, and others [37, 38, 40]. In 1996, the first specification by the OPC Foundation called as OPC-DA (Data Access) was released which followed server–client architecture for communication [42].

OPC was originally meant as OLE for process control and was implemented on the basis of Microsoft's Object linking and embedding technology for object-oriented interactions and used the COM (Component Object Model)/DCOM (Distributed Component Object Model) technologies [37, 38, 41, 43]. The classic OPC however had a poor performance in certain aspects as in the Linux environment the COM/DCOM functionality had to be emulated which brought some problems [43].

In 2006, the OPC Foundation announced a new standard named OPC Unified Architecture (OPC-UA) and published a revision on it in 2009 [44]. Moreover, OPC-UA has been standardized as IEC62541 [42–44]. Lange et al., [41] have stated ten important reasons for the development of OPC-UA which include the need for internet enable communication; platform independence, and the fall in the life cycle of COM/DCOM technology are prominent. Zentralverband Elektrotechnik- und Elektronikindustriee.V (ZVEI), Verband Deutscher Maschinen- und Anlagenbau (VDMA), and Bundesverband Informationswirtschaft, Telekommunikation und neueMedien (BITKOM) have suggested a three-dimensional reference model for Industry 4.0-based production network called as Reference Architecture Model for Industry 4.0 (RAMI4.0) [45]. RAMI4.0 argues for OPC-UA for implying semantic understanding for communication between devices and virtual counterparts in the Industry 4.0 environment [46, 47].

The OPC foundation together with PLCOpen has created a specification for IEC61131-3 for mapping the OPC-UA information model to IEC 611313 standard [48, 49]. The client specification of PLCOpen maps OPC client features to functional blocks for accessing various OPC servers [50].

OPC-UA originally proposed a Server client model and has been extended and a Publisher/subscriber model called as PubSub has been developed. Recent specifications suggest the development of included time-sensitive Network with PubSub to cater to critical real-time processes [51]. OPC-UA has two types of encoding: Binary and XML. Two types of transport protocol are used: TCP and SOAP [52].

Interoperability of devices reckons on the consistent representation of data. OPC clients have the assurance that all OPC-UA servers use the same base model [53]. OPC-UA uses the object-oriented programming method to share information. The OPC-UA represents the information in the form of nodes. The nodes in the OPC server are represented by a model called Address Spaces, which shows the relations and references, method, and views between them [54]. The scope of OPC-UA allows scalability both horizontally (in the same level of automation) as well vertically (from PLC to MES or ERP) [3]. Imtiaz et al. discusses the possibility to scale the OPC UA protocol to chip-level devices [55].

Security is one of the parts of OPC-UA specification. First, both server and client establish mutual trust and start communication by using username password security or X.509V3 certificates. The messages are encrypted and signed to ensure confidentiality and integrity. Moreover, users can set specific privileges to the functions that can be performed on data [41, 43, 57, 58]. OPC-UA has enabled integration with common standards based on companion specifications which has been developed due to collaboration between the OPC Foundation and the standard's organization.

Both Siemens (S7 1500) and Bosch Rexroth PLCs have OPC-UA communication settings. In MATLAB, OPC-UA communication is provided by a separate OPC toolbox [60, 61, 63].

3 Implementation of Protocols in Industrial Computers

Motion control is a part of industrial automation, consisting of the systems and subsystems involved in the motion of parts of machines in a controlled manner. The main components of a motion control system are the controller, driver or power amplifier, one or more actuators. Motion control is of two types: open loop and closed loop. In an open loop, there is no feedback to the controller and hence the controller has no knowledge if the desired motion has been executed. In the case of a closed-loop system, sensors are employed which give info regarding the execution of motion.

For implementing motion logic applications, PLCOpen Motion library is required. The PLCOpen is based on IEC 61131 standard, and Part3-Programming Languages of PLCOpen provides the Logic for operations. The IEC 61131 is an International Standard that comprises a complete assemblage of standards on programmable controllers and their associated peripherals. Based on the needs of the application and specifications, it is required to use or choose a wide range of motion control hardware for meeting its goals. The PLCOpen motion standard Library offers a method to have standard application libraries that can be used for multiple hardware platforms. In addition to this, the effort required is lowered and the code is reusable across various platforms. In effect, the standardization of this library is done by defining libraries of reusable components. In this manner, the programming of the hardware becomes hardware independent and increases the reusability of the application software. Moreover, the support and training required are reduced and the motion control application is now scalable across various control platforms [59].

The various PLCOpen blocks used in the programming such as MC_Power, MC_MoveAbsolute, MC_MoveRelative, and MC_Stop.

3.1 Server–Client Protocol Implementation Using UDP, TCP, Modbus

Figure 10 explains the data sharing between two different manufacturers' PLC's through server–client architecture. In this case, the Siemens PLC (S7-1500) and Bosch Rexroth PLC (L65) act as servers and the MATLAB software is used as a client. The Servo drive start, stop, and motion parameters are sent from Siemens PLC to Rexroth servo drive and the status of motion parameters are sent back to Siemens PLC using this server–client architecture.

Using the different blocks available in the Siemens PLC, Bosch-Rexroth PLC, and MATLAB software, the data communication between them is established using TCP, UDP, and Modbus protocols.

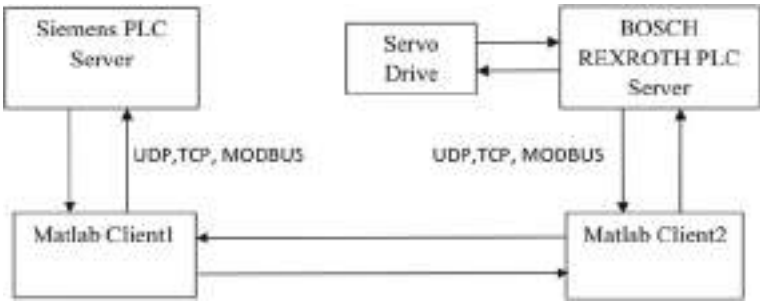

Fig. 10 Block diagram showing the data flow between Siemens and Bosch-Rexroth PLC using server–client protocol

3.2 Operation of Motion Control Programming Using OPCUA

Here, a sample setup is done using OPC-UA. The required parameter for motion control is made to transmit the data through OPC UA communication. The various parameters such as position, velocity, acceleration, and deceleration are obtained on the client side. These drive parameters can be shared between these two controllers (Bosch and Siemens) using the readValue and writeValue commands in MATLAB through OPCUA [63]. These motion parameters are varied based on our needs. Figure 11 shows a flowchart of how the program operates using OPCUA.

4 Comparison of Protocols

The Fig. 12 shows the data transfer between Bosch and Siemens PLC using OPC-UA protocol. Wire shark network analyzer is used to compare the performance of different protocols. Protocols are compared based on the time taken for data transfer and burst rate. Burst rate is a measure of maximum data transfer in a specified time frame [64].

Thus the time taken for communication and burst rate of data between server and client for motion control application using UDP, OPC-UA, TCP/IP, and Modbus TCP are noted and compared. In the case of OPC-UA, PLC is configured as server and MATLAB in PC is configured as client. Here the data transfer time is 4 ms and the burst rate is 0.6 packets per unit time. For TCP/IP communication, Server–Client communication is established between PLC and MATLAB. It has a data transfer time of 40 ms and burst rate of 0.4. In Modbus TCP communication, PLC is set as Modus server and MATLAB as a client. Here time taken for data transfer is approximately 60 ms and the burst rate is 0.2. For UDP communication the data transfer time is

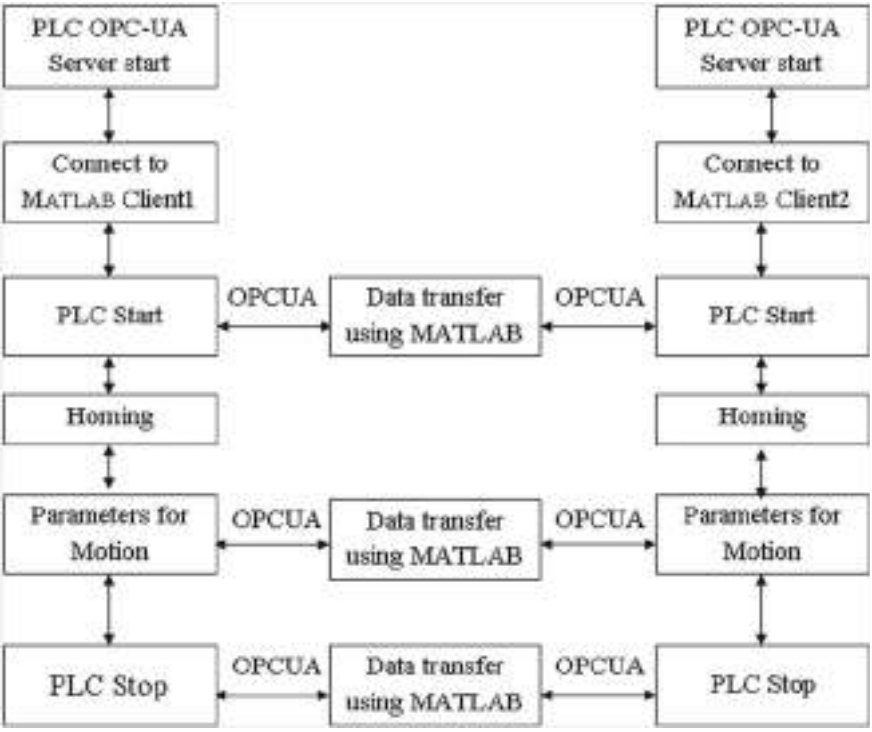

Fig. 11 Flowchart for motion program using OPC-UA

Fig. 12 Data for motion control transferred from Bosch PLC to Siemens using OPC-UA through MATLAB

approximately 0.2 ms and the burst rate is 0.41. The burst rate and data transfer time are compared for different protocols and graphs are drawn as shown in Figs. 13 and 14, respectively.

From the data transfer time, it is inferred that OPC-UA is faster than Modbus and TCP/IP but slower than UDP. Even though, UDP is faster than OPC-UA it is unreliable in the sense that it has no acknowledgment messages and handshaking. Moreover, OPC-UA has a better burst rate than all other protocols. Hence due to the

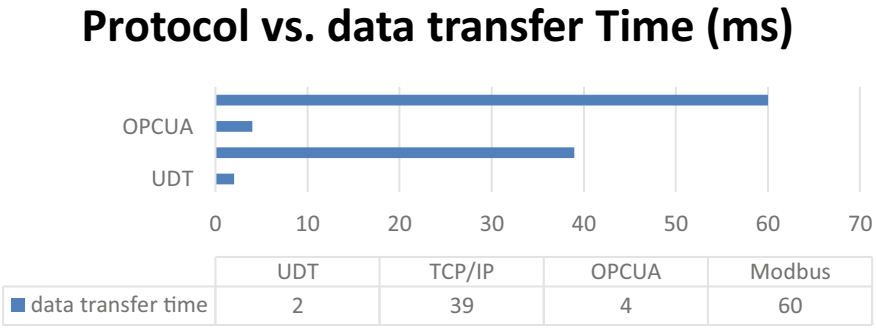

Fig. 13 Protocol versus data transfer time (ms)

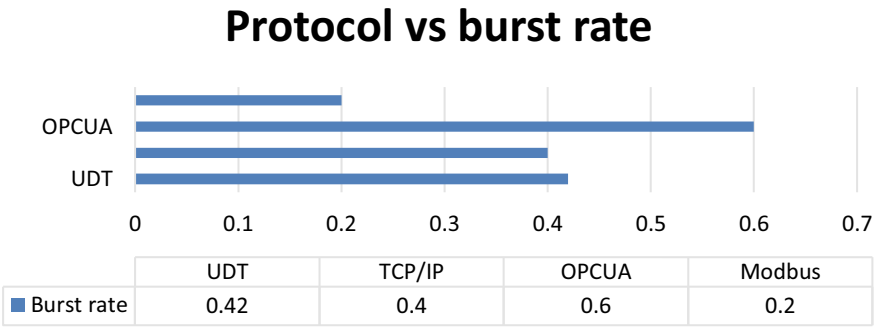

Fig. 14 Protocol versus burst rate

higher burst rate and less data transfer time, OPC-UA is found to be a preferred and effective communication protocol to solve the interoperability issues in the industrial environment in an easier way.

5 Conclusion

Thus OPC-UA communication has been compared with other protocols such as Modbus TCP, TCP/IP, and UDP and it has been found to be more suitable for solving interoperable issues in Industry 4.0. Moreover, the features of OPC-UA and its relevance to meet Industry 4.0 requirement has been studied. The advantages and disadvantages of common server–client protocols used in industries are studied practically which will help the user to select the proper communication protocol relevant to their applications. Further, this research can be extended to incorporate the data from the controllers to develop Digital Twins and by incorporating machine learning algorithm can be used in remote monitoring and predictive maintenance and thereby reducing the downtime of machines.

References

1. G. Schuh, T. Gartzen, T. Rodenhauser, A. Marks, Promoting work-based learning through industry 4.0. Procedia CIRP **32** 82–87 (2015). https://doi.org/10.1016/j.procir.2015.02.213
2. J. Greenwood, *The Third Industrial Revolution: Technology, Productivity, and Income Inequality*. (American Enterprise Institute for Public Policy Research, 1997)
3. R. Schmidt, M. Möhring, R.C. Härting, C. Reichstein, P. Neumaier, P. Jozinović, Industry 4.0—potentials for creating smart products: empirical research results. in *Business Information Systems. BIS 2015. Lecture Notes in Business Information Processing*, vol. 208, ed. by W. Abramowicz (Springer, Cham, 2015)
4. C.J. Bartodziej, The concept industry 4.0 an empirical analysis of technologies and applications in production logistics. (2017). https://doi.org/10.1007/978-3-658-16502-4_3
5. M. Hermann, T. Pentek, B. Otto, Design principles for industrie 4.0 scenarios, in *Proc. Annu. Hawaii Int. Conf. Syst. Sci. 2016* (2016), pp. 3928–3937. https://doi.org/10.1109/HICSS.2016.488
6. T.D. Oesterreich, F. Teuteberg. Understanding the implications of digitization and automation in the context of Industry 4.0. *Comput. Ind.* **83**, 121–139 (2016). https://doi.org/10.1016/j.compind.2016.09.006
7. H. Kagermann, W. Wahlster, J. Helbig, A. Hellinger, M.A.V. Stumpf, J. Blasco, H. Galloway, H. Gestaltung, Recommendations for implementing the strategic initiative INDUSTRIE 4.0. Report, the Industrie 4.0 Working Group of Acatech, (2013). http://www.acatech.de/fileadmin/user_upload/Baumstruktur_nach_Website/Acatech/root/de/Material_fuer_Sonderseiten/Industrie_4.0/Final_report__Industrie_4.0_accessible.pdf
8. V.R. Sreedharan, A. Unnikrishnan, Moving towards Industry 4.0: a systematic review. Int. J. Pure Appl. Math. **117**, 929–936 (2017). http://acadpubl.eu/jsi/2017-117-20-22/articles/20/84.pdf
9. X. Xu, From cloud computing to cloud manufacturing. Robot. Comput. Integr. Manuf. **28**, 75–86 (2012). https://doi.org/10.1016/j.rcim.2011.07.002
10. P. Mell, T. Grance, The NIST definition of cloud computing. http://csrc.nist.gov/groups/SNS/cloud-computing
11. G.H. Forman, J. Zahorjan, The challenges of mobile computing, Computer (Long. Beach. Calif). **27**, 38–47 (1994). https://doi.org/10.1109/2.274999
12. J. Wan, S. Tang, D. Li, S. Wang, C. Liu, H. Abbas, A.V. Vasilakos, A manufacturing big data solution for active preventive maintenance. IEEE Trans. Ind. Inform. **13**, 2039–2047 (2017). https://doi.org/10.1109/TII.2017.2670505
13. R. Schmidt, M. Möhring, Strategic alignment of cloud-based architectures for big data. in *2013 17th IEEE International Enterprise Distributed Object Computing Conference Workshops*, Vancouver, BC (2013), pp. 136–143.https://doi.org/10.1109/EDOCW.2013.22
14. S.R. Polyzotis, S.E. Whang, M. Zinkevich, Data management challenges in production machine learning, in *Proceedings of the* 2017 *ACM International Conference on Management of Data (SIGMOD'17)*. (ACM, New York, NY, USA, 2017), pp. 1723–1726. https://doi.org/10.1145/3035918.3054782
15. D. Zhang, J. Wan, Q. Liu, X. Guan, X. Liang, A taxonomy of agent technologies for ubiquitous computing environments. KSII Trans. Internet Inf. Syst. **6**, 547–565 (2012). https://doi.org/10.3837/tiis.2012.02.006
16. J. Ouyang, D. Li, C. Liu, S. Wang, An integrated industrial ethernet solution for the implementation of smart factory. IEEE Access. **5**, 25455–25462 (2017)
17. H.P. Breivold, K. Sandstrom, Internet of things for industrial automation-challenges and technical solutions, in *Proc.—2015 IEEE Int. Conf. Data Sci. Data Intensive Syst. 8th IEEE Int. Conf. Cyber, Phys. Soc. Comput. 11th IEEE Int. Conf. Green Comput. Commun. 8th IEEE Int.* (2015)
18. I. Ishaq, D. Carels, G. Teklemariam, J. Hoebeke, F. Abeele, E. Poorter, I. Moerman, P. Demeester, IETF standardization in the field of the internet of things (IoT): a survey (2013). https://doi.org/10.3390/jsan2020235

19. OPC UA, https://opcfoundation.org/about/opctechnologies/opc-ua/
20. L. Atzori, A. Iera, G. Morabito, The internet of things: a survey. Comput. Netw. **54**, 2787–2805 (2010). https://doi.org/10.1016/j.comnet.2010.05.010
21. D. Miorandi, S. Sicari, F. De Pellegrini, I. Chlamtac, Internet of things: vision, applications and research challenges. Ad Hoc Netw. **10**(7), 1497–1516 (2012)
22. L. Da-Xu, Enterprise systems: state-of-the-art and future trends. IEEE Trans. Ind. Inform. **7**, 630–640 (2011)
23. B. Drury, *Control Techniques Drives and Controls Handbook*, 2nd edn. (Institution of Engineering and Technology, 2009), pp. 508–510
24. Modicon Modbus Protocol Reference Guide Modicon Modbus Protocol Reference Guide, v1.1b. 51 p, (2006)
25. Acromag Inc., Introduction To Modbus Tcp/Ip, (2005) pp. 1–42. http://www.acromag.com
26. M. Rostan, Industrial Ethernet Technologies: Overview and Comparison. (2014), pp. 1–165. https://www.ethercat.org/download/documents/Industrial_Ethernet_Technologies.pdf
27. H. Koziolek, A. Burger, J. Doppelhamer, J. Pfrommer, A. Ebner, S. Ravikumar, B. Karunakaran, M. Wollschlaeger, T. Sauter, R. Ethernet, P. Danielis, J. Skodzik, V. Altmann, E.B. Schweissguth, F. Golatowski, D. Timmermann, P. Pop, M.L. Raagaard, M. Gutiérrez, W. Steiner, Survey on real-time communication via ethernet in industrial automation environments. Emerg. Technol. Fact. Autom. **1**, 55–61 (2018). https://doi.org/10.1109/ETFA.2018.8502479
28. Modbus-IDA, Modbus Messaging on TCP/IP Implementation Guide V1.0b, Hopkinton, Massachusetts (2006). www.modbus.org/docs/Modbus_Messaging_Implementation_Guide_V1_0b.pdf
29. Y.C. Lai, A. Ali, M.S. Hossain, Y.D. Lin, Performance modeling and analysis of TCP and UDP flows over software defined networks. J. Netw. Comput. Appl. **130**, 76–88 (2019). https://doi.org/10.1016/j.jnca.2019.01.010
30. E. Engineers, EtherNet/IP: Industrial Protocol White Paper, Coexistence. (2001)
31. F.T. Al-Dhief, N. Sabri, N.A. Latiff, N.N.N.A. Malik, M.A.A. Albader, M.A. Mohammed, R.N. Al-Haddad, Y.D. Salman, M.K.A. Ghani, O.I. Obaid, Performance comparison between TCP and UDP protocols in different simulation scenarios. Int. J. Eng. Technol. **7**, 172–176 (2018). https://doi.org/10.14419/ijet.v7i4.36.23739
32. S. Kumar, S. Rai, Survey on transport layer protocols: TCP UDP. Int. J. Comput. Appl. **46**(7), 20–25 (2012)
33. R. Alexsandro, M. Valentim, R. Viégas Jr, L. Affonso, H. Guedes, Performance analysis of protocols: UDP and RAW ethernet to real-time networks. Int. J. Eng. Technol. (2018)
34. S. Mackay, E. Wright, J. Park, D. Reynders, *Practical Industrial Data Networks: Design, Installation and Troubleshooting* (Elsevier Publication, 2003)
35. What is TCP? https://searchnetworking.techtarget.com/definition/TCP
36. OPC Foundation, www.opcfoundation.org
37. F. Iwanitz, J. Lange, OPC, Grundlagen, Implementation und Anwendung. (OPC Fundamentals, Implementation and Applications), 2nd edn. (Hüthig, 2002)
38. F. Iwanitz, J. Lange, OPC fundamentals, implementation, and application, 3rd edn. (Hüthig, Heidelberg, 2006)
39. Bernd Reissenweber, Feldbussysteme, Oldenbourg Wissenschaftsverlag (1998_
40. W. Mahnke, S.-H. Leitner, M. Damm, *OPC Unified Architecture* (Springer Verlag, Berlin Heidelberg, 2009)
41. J. Lange, F. Iwanitz, T.J. Burke, OPC: from data access to unified architecture. (Huethig, 2010)
42. M.H. Schwarz, J. Börcsök, A survey on OPC and OPC-UA: about the standard, developments and investigations, in *2013 XXIV International Conference on Information, Communication and Automation Technologies (ICAT)*, Sarajevo (2013), pp. 1–6. https://doi.org/10.1109/ICAT.2013.6684065
43. T. Hannelius, Integrating industrial information systems with OPC UA—A Java reference Implementation. Master Thesis, Tampere University of Technology, 2009

44. T. Hannelius, M. Salmenperä, S. Kuikka, Roadmap to adopting OPC UA, in *IEEE Int. Conf. Ind. Informatics.* (2008), pp. 756–761. https://doi.org/10.1109/INDIN.2008.4618203
45. P. Adolphs, H. Bedenbender, D. Dirzus, M. Ehlich, U. Epple, M. Hankel, R. Heidel, M. Hoffmeister, H. Huhle, B. Kärcher, H. Koziolek, R. Pichler, S. Pollmeier, F. Schewe, A. Walter, B. Waser, M. Wollschlaeger, Reference architecture model industry 4.0 (RAMI4.0), ZVEI and VDI, Status Report (2015)
46. F. Pauker, T. Frühwirth, B. Kittl, W. Kastner, A systematic approach to OPC UA information model design. Procedia CIRP **57**, 321–326 (2016). https://doi.org/10.1016/j.procir.2016.11.056
47. S. Cavalieri, M.G. Salafia, M.S. Scroppo, Integrating OPC UA with web technologies to enhance interoperability. Comput. Stand. Interfaces **61**, 45–64 (2019). https://doi.org/10.1016/j.csi.2018.04.004
48. EC 61131-3:2013, Programmable controllers - Part 3: programming languages. International Standard TC 65/SC 65B. International Electrotechnical Commission, Geneva, CH (2013)
49. PLCopen OPC UA Client for IEC 61131-3. https://www.plcopen.org/sites/default/files/downloads/plcopen_opc_ua_client_architecture.pdf
50. PLCopen and OPC Foundation: OPC UA Information Model for IEC 61131
51. https://www.plcopen.org/system/files/downloads/plcopen_opcua_information_model_for_iec_61131-3_version_1.01.09.pdf
52. OPCFoundation, OPC UA Part 14: Pub Sub Specification, Release 1.04, OPC Foundation (2018)
53. H. Haskamp, M. Meyer, R. Möllmann, F. Orth, A.W. Colombo, Benchmarking of existing OPC-UA implementations for Industrie 4.0-compliant digitalization solutions, in *2017 IEEE 15th International Conference on Industrial Informatics (INDIN)*, Emden (2017), pp. 589–594. https://doi.org/10.1109/INDIN.2017.8104838
54. M. Graube, S. Hensel, C. Iatrou, L. Urbas, Information models in OPC UA and their advantages and disadvantages, in *IEEE Int. Conf. Emerg. Technol. Fact. Autom. ETFA*. (2018), pp. 1–8. https://doi.org/10.1109/ETFA.2017.8247691
55. OPC Foundation, OPC UA Part 3: address space model specification, release 1.04, OPC Foundation (2017)
56. J. Imtiaz, J. Jasperneite, Scalability of OPC-UA down to the chip level enables "internet of Things, in *IEEE Int. Conf. Ind. Informatics.* (2013), pp. 500–505. https://doi.org/10.1109/INDIN.2013.6622935
57. OPC Foundation, OPC Unified Architecture Specification Part 2 Security Model, Version 1.01 (2009)
58. OPC Foundation, OPC UA Part 7 - Profiles 1.03 Specification.pdf (2015)
59. PLCOpen - Motion Control, https://plcopen.org/technical-activities/motion-control
60. Bosch Rexroth Indra Works Online Help, (2016)
61. Siemens S7-1500, ET 200MP, ET 200SP, ET 200AL, ET 200pro Communication Function Manual
62. Mathworks, Instrument Control Toolbox™ User's Guide R (2018b)
63. Mathworks, OPC Toolbox™ User's Guide R (2018b)
64. Wireshark User's Guide v3.1.0

Comparative Analysis on Diverse Heuristic-Based Joint Probabilistic Data Association for Multi-target Tracking in a Cluttered Environment

T. L. Purushottama and Pathipati Srihari

Abstract The target tracking using the passive multi-static radar system produces various detections via distinct signal propagation paths. Trackers solve the uncertainties that arise from the measurement path as well as the measurement origin. The existing multi-target tracking algorithms suffer from high computational loads, because they require the entire probable joint measurement-to-track assignments. This paper proposes to develop a comparative analysis on diverse heuristic algorithms for implementing the optimized JDPA model for tracking multiple targets using multi-static passive radar system in the presence of clutter. Here, the nature-inspired algorithms like Particle Swarm Optimization (PSO) and Grey Wolf Optimization (GWO) are used for analyzing the optimized JDPA model for tracking multiple targets in multi-static passive scenario. This paper further, aims to tune the position and velocity of the tracker towards the target using two heuristic algorithms, and intends to analyze the effect of those algorithms on improving the performance of multiple target tracking. The key objective of the proposed model is to minimize the Mean Absolute Error (MAE) between the estimated trajectory of the track and the true target state.

Keywords Mean absolute error · Joint probabilistic data association · Multi-target tracking · Grey wolf optimization · Particle swarm optimization

1 Introduction

The target tracking in the existence of cluttered measurements is a challenging problem due to measurement origin uncertainty. This problem gets further complex for multi-static passive scenario. Generally, there is a need to handle two problems [1]. The initial problem is the data association and the next problem is the False

T. L. Purushottama (✉) · P. Srihari
National Institute of Technology Karnataka, Surathkal, India

P. Srihari
e-mail: srihari@nitk.ac.in

S. Rawat et al. (eds.), *Proceedings of First International Conference on Computational Electronics for Wireless Communications*, Lecture Notes in Networks and Systems 329,
https://doi.org/10.1007/978-981-16-6246-1_22

Track Discrimination (FTD). The track component count of Joint Integrated Track Splitting (JITS), Integrated Track Splitting (ITS), and Multiple Hypotheses Tracking (MHT) increase in a sequential time, and the probabilistic data association (PDA) [2] is adopted to merge the tracked components into a single trajectory estimate having a Gaussian probability density function. Joint probabilistic data association (JPDA) [3] is employed for tracking multiple targets in the case of cluttered environments having known target counts. The JIPDA and JITS are the multitarget trackers that employ the optimal multiple target data association scheme of estimating and enumerating the entire possible joint measurement for tracking the associations [4]. Authors in [5], proposed two new composite methods for data association based on soft and evolutionary computing for tracking different targets in the existence of electronic countermeasures (ECM), clutter, and false alarms. In the presence of jamming, [6] proposed a novel clustering-based data association technique for tracking multiple targets.

Multiple target tracking (MTT) is a significant task in sonar, radar, and various surveillance systems. Generally, the measurements reported by the surveillance systems from the unintended sources are called as clutter. In recent years, passive radar gained significant interest in military and civilian applications [5]. The traditional transmitters (FM, DVB, etc.) are exploited by the passive radar in the form of opportunity illuminators. Hence, the additional hardware requirement and the frequency allocation are eliminated. So, in the passive radar, the target detection is continuous, covert, and inexpensive [7]. When multiple transmitters are exploited in a simultaneous manner, passive multi-static radar (PMSTR) is obtained. Here, the trajectory, as well as the location of a potential target, is defined by merging the measurements from various transmitter–receiver pairs having sharable coverage. As a result, the PMSTR provides noteworthy advantages [8].

Still, majority of the researches are dependent on the existing resampling mechanism and the weight degeneration problem is not handled in a fundamental manner. The detailed study of swarm intelligence optimization algorithm along with the particle filter is a novel technique for enhancing the performance of the Particle Filter (PF) [9, 10]. Few algorithms merge the PF with the generalized interactive genetic algorithm that may easily fall into premature convergence and leads to inaccurate filtering process. Therefore, there is a strong need to develop alternative heuristic-based data association techniques for PMSR scenarios.

The major contribution related to this paper is shown below:

- To implement the optimized JPDA model based on particle swarm optimization and grey wolf optimization for the tracking of multiple targets using passive radar with consideration of the constraints such as the position and the velocity.
- To minimize the MAE among the true target state and the estimated trajectory of track by tuning the position as well as the velocity.
- To perform the comparative analysis using diverse heuristic-based algorithms such as GWO, and PSO on JPDA for the multi-target tracking for PSMR scenario.

The organization of the paper is shown below: Sect. 2 describes a general JPDA-based target tracking algorithm for tracking multiple targets. Section 3 presents optimized JPDA based on diverse heuristic algorithms for tracking multiple targets. Section 4 highlights the simulation setup, plots, and briefs the results. Finally, Sect. 5 gives the conclusion remarks for the paper.

2 Optimized Joint Probabilistic Data Association Tracker for Multitarget Radar Tracking

2.1 JPDA-Based Tracking

Generally optimized JPDA algorithm is applied for multiple target tracking. In the initial step, the measurement model and motion models are defined. Thereafter, the multiple targets tracking algorithm is denoted. The track management is performed in three steps: initialization of the track initiation, updation of the track, and termination of the track. The track update is accomplished by the data association, which associates the measurements as whether these are target-originated or clutter-originated measurements to the existing tracks by means of the track filtering step [11].

Track Motion and Measurement Models: The vector denoting target state XC_{kc} at frame kc is defined into the Cartesian domain by including the target size as displayed in Eq. (1).

$$XC_{kc} \stackrel{\Omega}{=} \left[xc_{kc}^{\pi,\,pc},\ yc_{kc}^{\pi,\,pc},\ xc_{kc}^{\pi,\,vc},\ yc_{kc}^{\pi,\,vc},\ lc_{kc},\ wc_{kc}\right]^{TC} \tag{1}$$

In the above equation, the length and width of the target is defined by lc_{kc} and wc_{kc}, and the velocity and the position components are defined by $xc_{kc}^{\pi,vc}$,$yc_{kc}^{\pi,vc}$ and $xc_{kc}^{\pi,pc}$, $yc_{kc}^{\pi,pc}$ in the region of the $xc-$ and $yc-$ directions, respectively. The target dynamic is described by the nearly constant velocity model as shown in Eq. (2).

$$XC_{kc} = FCXC_{kc-1} + \theta\, wc_{kc} \tag{2}$$

The term FC is denoted in Eq. (3).

$$FC = \begin{bmatrix} IC_2 \otimes F\tilde{C} & 0_{4\times 2} \\ 0_{2\times 4} & IC_2 \end{bmatrix} \tag{3}$$

This equation denotes the state transition model, which is applied to the previous state XC_{kc-1} as displayed in Eqs. (4) and (5).

$$\theta = \begin{bmatrix} IC_2 \otimes \tilde{\theta} & 0_{4\times 2} \\ 0_{2\times 2} & IC_2 \end{bmatrix} \tag{4}$$

$$F\tilde{C} = \begin{bmatrix} 1 & TC_{sc} \\ 0 & 1 \end{bmatrix} \tag{5}$$

In the above equation, the term TC_{sc} denotes the sampling time, $\otimes$ denotes the Kronecker product, IC_{dc} denotes the unit matrix with dimension dc, $0_{r\times c}$ denotes the zero matrix with r rows and c columns, wc_{kc} denotes the process noise, which is forecasted to be drawn from a zero mean multivariate normal distribution with covariance QC, such that $wc_{kc} \approx \aleph(0_{4\times 1}, QC)$ and $\tilde{\theta} = \left[TC_{sc}^2/2, TC_{sc}\right]^{TC}$ as portrayed in Eq. (6).

$$QC = diag\left(\phi_{pc}^2, \phi_{vc}^2, \phi_{lc}^2, \phi_{wc}^2\right) \tag{6}$$

Here, the terms ϕ_{wc}^2, ϕ_{lc}^2, and ϕ_{vc}^2 define the variances for the width, length, and acceleration, and $diag(\bullet)$ defines the diagonal matrix. The measurement vector ZC_{kc} at frame kc is shown in Eq. (7).

$$ZC_{kc} \overset{\Omega}{=} \left[zc_{kc}^{rc}, zc_{kc}^{\rho}, zc_{kc}^{lc}, zc_{kc}^{wc}, zc_{kc}^{\theta}\right] \tag{7}$$

In the above equation, the terms zc_{kc}^{wc} and zt_{kc}^{lc} define the length of the minor and major axes, zc_{kc}^{ρ} and zc_{kc}^{rc} defines the azimuth and the range measurements of the ellipse center, which best fits the cluster, and zc_{kc}^{θ} defines the orientation of the ellipse. The measurements originated from the target are shown in Eq. (8).

$$ZC_{kc} = hc(XC_{kc}) + \omega_{kc} \tag{8}$$

Equation (9) defines the term $hc(XC_{kc})$.

$$hc(XC_{kc}) \overset{\Omega}{=} \left[\sqrt{xc_{kc}^2 + yc_{kc}^2},\ \arctan\left(yc_{kc}/xc_{kc}\right), lc_{kc}, wc_{kc}, \arctan\left(yc_{kc}^{\pi,vc}/xc_{kc}^{\pi,vc}\right)\right]^{TC} \tag{9}$$

The above equation denotes the measurement function and the instrumental noise vector is defined by ω_{kc}, which is presumed to be the Gaussian with zero mean as well as the covariance matrix as displayed in Eq. (10).

$$RC = diag\left(\phi_{rcrc}^2, \phi_{rc\rho}^2, \phi_{rclc}^2, \phi_{rcwc}^2, \phi_{rc\theta}^2\right) \tag{10}$$

Here, the terms ϕ_{rcwc}^2 and ϕ_{rclc}^2 define the variances for the two sizes, $\phi_{rc\theta}^2$ defines the variation for the orientation of the ellipse, and $\phi_{rc\rho}^2$, ϕ_{rcrc}^2 defines the variances in azimuth and range, respectively. The ETT takes the target orientation as logical with consideration to the motion orientation such as $\theta_{kc} = \arctan\left(\dot{yc}_{kc}/\dot{xc}_{kc}\right)$.

A random group of false or noisy clutter measurements is received by the sensor in every scan [12]. The noisy measurement count present in the surveillance space is designed using a Poisson distribution with known intensity called the clutter measurement density. The clutter measurement density having measurement $ZT_{kt,it}$ is represented with the help of the shortcut $\rho\left(ZT_{kt,it}\right)$. The amount of the surveillance space at time kt is denoted by VT_{kt}, and hence the probability that the clutter measurement count that equals mt in VT_{kt} at time kt tends to follow the Poisson distribution as in Eq. (11).

$$ut_{FT}(mt) = e^{-\int\limits_{VT_{kt}} \rho_{kt,it} dVT} \frac{\left(\int\limits_{VT_{kt}} \rho_{kt,it} dVT\right)^{mt}}{mt!} \tag{11}$$

In the above equation, the clutter measurement density is denoted by $\rho_{kt,it} = \frac{PT_{far}}{VT_{src}}$, where VT_{src} and PT_{far} represents the sensor resolution cell volume and probability of false alarm. The probability of false alarm persistently makes an effect on the clutter measurement count, meaning that when the probability of false alarm PT_{far} rises, the disorder measurement density $\rho_{kt,it}$ also rises, and the mean clutter measurement count present in the surveillance space VT_{kt} rises, thereby generating an enhanced clutter measurement count at every time kt. In the case of target tracking, the clutter measurement density describes either a priori known or an estimated priori in an adaptive manner on the basis of the current measurements.

Multiple Target Tracking Procedure: The tracking process works on the basis of the JPDA, where a Bayesian technique associates the checked measurements to the tracks by means of the probabilistic weights [13]. The management of the track follows the M/N logic. The filtering stage is performed by the unscented KF. The predicted or updated target state having its covariance at frame kc is defined by $XC^{jc}_{kc/kc}\left(XC^{jc}_{kc/kc-1}\right)$ and $PC^{jc}_{kc/kc}\left(PC^{jc}_{kc/kc-1}\right)$. At frame kc, a cluster of JC_{kc} active or preliminary tracks are described as $\mathrm{T}_{kc} = \left\{\mathrm{T}_1(kc), \ldots, \mathrm{T}_{jc}(kc), \ldots, \mathrm{T}_{JC_{kc}}(kc)\right\}$, where $\mathrm{T}_{jc}(kc)$ assumes the jcth track. A validation gate region ζ^{jc}_{kc} for each $jc \in [1, \cdots, JC_{kc}]$ is formed. The target-originated measurements denote the Gaussian that is spread on the outer of a predicted measurement $ZC^{jc}_{kc/kc-1}$ of the target jc, and then the gate is defined as displayed in Eq. (11).

$$\zeta^{jc}_{kc} = \left\{ZC : \left(ZC - ZC^{jc}_{kc/kc-1}\right)^{TC}\left(SC^{jc}_{kc}\right)^{-1}\left(ZC - ZC^{jc}_{kc/kc-1}\right) < \gamma\right\} \tag{12}$$

In the above equation, the threshold γ represents the gating probability PC_{GC}, and the innovation covariance that is the difference between the prediction and its measurement is defined by SC^{jc}_{kc}. The gating probability defines the probability, in which a measurement evolved by target jc is checked in an accurate manner.

2.2 Tracking Steps

The developed multiple target tracking system employs the optimized JPDA algorithm for handling the data association problem in the path of the targets of objects in an effective manner [14]. The different steps in the track management are shown in Fig. 1.

Initiation of Track: The association of measurement to $T_{jc}(kc)$ if it lies in the gated region. The unassociated measurement is termed as the initiator and a temporary track is generated. After detecting the initiator, the gate set up is started. If the detection lies in the gate region, then the track is called a preliminary track; elseways, it is referred to as dropped. The initialization of JPDA is done to set up the gate for the next frame. Beginning with the third scan, the logic of M detections out of N scans is utilized for the gates that follow. Finally, for the scan number $N + 2$, if the necessity of logic is completed, then the track is called as a confirmed or active track; elseways, it is called as a discarded track.

Termination of the Track: The track terminates when the following conditions are checked: no detection was validated in the previous $N*$ sampling times; the track uncertainty reached the threshold, and the output represents an impossible maximum velocity $vc_{\max}$.

Updation of the Track: All the tracks update the target state via the JPDA application rule. The updation of the state of the target is based on the measurement-to-track JPDA association rule and the prediction of the state of the target is considered from the motion model.

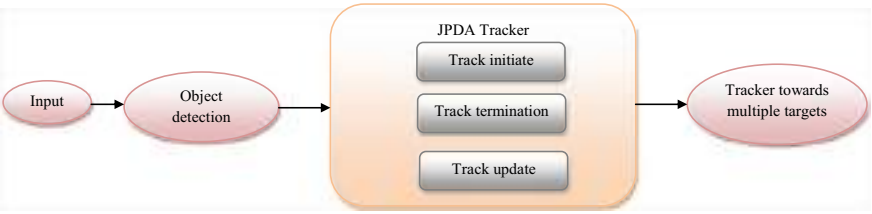

Fig. 1 Multi-target tracking model on the basis of the optimized JPDA algorithm

3 Contribution of Diverse Heuristic Algorithms for Target Tracking

3.1 Tracker Update and Objective

The position and the velocity of the object target are considered as $xc_{kc(u)}^{\pi,pc}$, $yt_{kc(u)}^{\pi,pc}$ and $xc_{kc(u)}^{\pi,vc}$, $yc_{kc(u)}^{\pi,vc}$, in which $u = 1, 2, \ldots, NV$, and NV denotes the total considered target count. Here, the tracker points with position as well as velocity are considered as $xc_{tr-kc(u)}^{\pi,pc}$, $yc_{tr-kc(u)}^{\pi,pc}$, and $xc_{tr-kc(u)}^{\pi,vc}$, $yc_{tr-kc(u)}^{\pi,vc}$, respectively. The position as well as the velocity of the tracker are updated by the heuristic algorithms in the path of the target. In every instant, the position as well as the velocity of the tracker in the path of the multiple targets are updated by the heuristic algorithms.

The major objective of updating the tracking points using the heuristic algorithms is to reduce the MAE among the targeted point and the tracked point. The novel position as well as velocity is used to track the position as well as the velocity. The MAE between the target as well as the tracked output is computed. The optimization happens for each time instance for reducing the error in each instance. The experiments are accomplished for 2 targets, 3 targets, and 5 targets. The objective model is displayed in Eq. (12).

$$Ob = \underset{\left\{xc_{kc(u)}^{\pi,pc}, yc_{kc(u)}^{\pi,pc}, xc_{kc(u)}^{\pi,vc}, yc_{kc(u)}^{\pi,vc}\right\}}{\arg\min}(MAE) \tag{13}$$

In the above equation, the objective model is described by Ob, the position of the object target is defined by $xc_{kc(u)}^{\pi,pc}$, $yc_{kc(u)}^{\pi,pc}$, and the velocity of the object target is defined by $xc_{kc(u)}^{\pi,vc}$, $yc_{kc(u)}^{\pi,vc}$. MAE is, "a measure of difference between two continuous variables", as shown in Eq. (13).

$$MAE = \frac{\sum_{kc=1}^{pc} \left| xc_{kc(u)}^{\pi,pc} - xc_{tr-kc(u)}^{\pi,pc},\ yc_{kc(u)}^{\pi,pc} -,\ yc_{tr-kc(u)}^{\pi,pc},\ xc_{kc(u)}^{\pi,vc} - xc_{tr-kc(u)}^{\pi,vc},\ yc_{kc(u)}^{\pi,vc} - yc_{tr-kc(u)}^{\pi,vc} \right|}{pc} \tag{14}$$

Here, the tracker points with position and velocity is defined by $xc_{tr-kc(u)}^{\pi,pc}$, $yc_{tr-kc(u)}^{\pi,pc}$ and $xc_{tr-kc(u)}^{\pi,vc}$, $yc_{tr-kc(u)}^{\pi,vc}$, respectively.

3.2 Comparative Heuristic Algorithms

The heuristic algorithms like PSO-based JPDA, GWO-based JPDA are compared with multi-target tracking using JPDA in terms of cost function and the mean absolute error.

GWO: GWO [6] is a novel meta-heuristic optimization algorithm. The major aim is to criticize the behaviour of the grey wolves for hunting in a cooperative manner. It represents a large-scale search technique that is centered on three optimal samples. To model the leadership structure, four sorts of grey wolves are considered: "alpha, beta, delta, and omega" "Hunting, looking for the prey, surrounding the prey, and assaulting the prey" are the three key processes employed here. It can also handle classical engineering design problems [17].

PSO: PSO [15] defines a population-oriented stochastic optimization algorithm. The structure is modified to attain the best performance. The distinct topology structures and various parameters configuration are also considered into effect. Hence, it is used for different application sectors. This algorithm initiates with the swarm population initialization and the particle fitness interpretation. Moreover, it also computes the swarm (global) optimal position and the individual (personal) best-suited position. It also updates the velocity of the position and the particle. This process stops when the most appropriate solution is achieved.

Target tracking can be thought of as a numerical optimization issue in which the local mode of the similarity measure is tracked using particle swarm optimization. The objective function is based on a multiple patch-based target representation and an area covariance matrix. The goal positions and velocities obtained in this manner are then used in a particle swarm optimization-based algorithm to optimize the paths obtained in the early step. After that, the final optimization is done using a conjugate process. To find strong local minima, the particle swarm algorithm is used, and the conjugate gradient is utilized to accurately identify the local minimum [16].

4 Results and Discussions

4.1 Simulation Setup

The DVB-based passive radar network which consists of four transmitters of opportunity located on ground is used for tracking multiple targets. Three different scenarios are considered for simulation: In scenario 1 two crossing targets moving with equal and uniform velocities are considered, scenario 2 presumes two crossing targets with an additional target moving along straight path and lastly scenario 3 five targets moving with uniform velocity are assumed. Further, it is assumed that all the targets appear simultaneously and are corrupted by heavy clutter and noise. Simulation of targets is carried out for 30 s with sampling period of 1 s and the simulation is carried out for 100 Monte Carlo runs. The heuristic algorithm-based JPDA for tracking multiple targets using multi-static passive radar system is implemented in MATLAB 2020a, and the results are tabulated and analyzed. The proposed variants of JPDA algorithms optimize the position and velocity of the targets for minimizing the MAE between the estimated trajectory of the track and the true target state.

4.2 Convergence Analysis

The convergence analysis of the suggested and existing heuristic-based JPDA for multiple targets tracking with passive radar system having multiple radar sites is portrayed in Fig. 2. From Fig. 2a for scenario 1, at 100th iteration, the cost function is better in the case of JPDA. Similarly, in Fig. 2b for scenario 2, at 100th iteration, the cost function is improved in the case of PSO-JPDA. Moreover, while considering Fig. 2c for scenario 3, at 100th iteration, the cost function is better with the PSO-JPDA. Hence, it is clear that cost function is better with distinct heuristic algorithms in considering the multi-target tracking scenarios. Also, from the convergence plots, we can infer that the PSO-based JPDA converges faster to the optimized range and velocity values even for complex scenarios like 2 and 3.

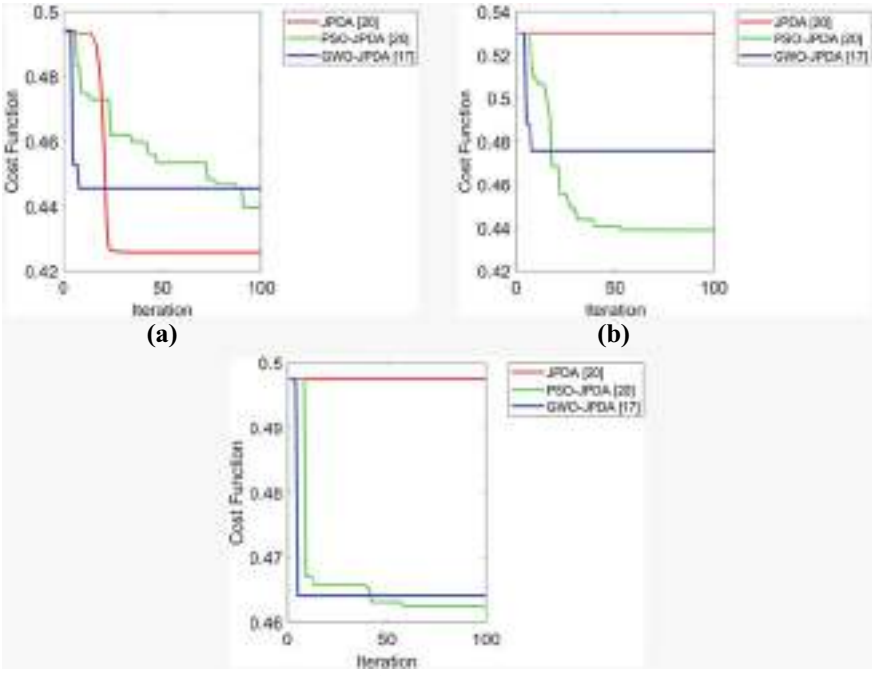

Fig. 2 Convergence analysis of the distinct heuristic-based JPDA for multiple target tracking with multi-static passive radar system for **a** Scenario case-1, **b** Scenario case-2, and **c** Scenario case-3

Table 1 Overall MAE analysis for multiple targets tracking using multistatic passive radar system for three different cases

Algorithm	Scenario 1	Scenario 2	Scenario 3
JPDA	0.52227	0.56051	0.56668
GWO-JPDA	0.5111	0.54319	0.55192
PSO-JPDA	0.4991	0.52483	0.53723

4.3 Overall MAE Analysis

The overall MAE analysis for the multiple targets tracking for the aforementioned three scenarios is portrayed in Table 1 and plotted in Fig. 3. MAE is a statistic that calculates the average magnitude of errors in a sequence of estimates without accounting for the course of the predictions. It is the average of the modulus of the differences between estimates and actual observations over the test sample, where all individual differences are given equal weight. Compared to MAE, the root mean square error (RMSE) is difficult to understand and does not adequately explain the average error. So in this work, we computed MAE instead of RMSE. The mean absolute error is calculated on the same scale as the data and hence called as scale-dependent accuracy. From the computed MAE, we can infer that for all scenarios the PSO-based JPDA gives the minimum mean absolute error and JPDA-based tracker has slightly higher MAE compared to the other two algorithms.

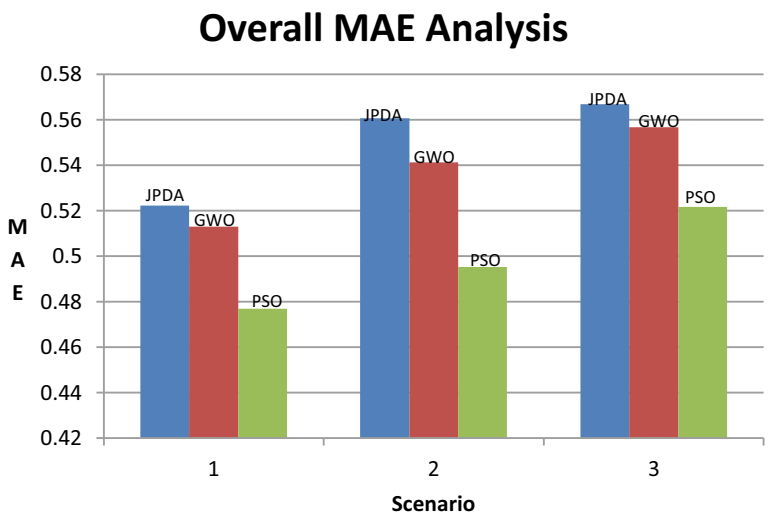

Fig. 3 Mean absolute error for JPDA, GWO-JPDA, and PSO-JPDA based multiple target tracking for Scenario case-1, Scenario case-2, and Scenario case-3

5 Conclusion

This paper has developed a comparative analysis on diverse heuristic algorithms for developing the optimized JDPA model for tracking multiple targets using a multi-static passive radar system in the presence of clutter. The algorithms such as GWO, and PSO were utilized for analyzing the optimized JDPA model for tracking multiple targets using passive radar system. It also tuned the position as well as the velocity of the tracker towards the target by means of distinct algorithms, and intended to analyze the effect of those algorithms on enhancing the multi-target tracking. As a major objective, it minimized the MAE between the estimated trajectory of track and the true target state. The cost function value for the scenario considering more than two targets is minimum for PSO-based JPDA and converges faster. The MAE for all the three scenarios under consideration is minimum for PSO-based JPDA making a good choice for multiple target tracking using optimal JPDA-based tracker. Further, the genetic algorithm-based optimization may be adopted for the data association in multi-target tracking and compared with the traditional JPDA.

Acknowledgements The authors would like to thank Mr. Pardhasaradhi, Research Scholar, Department of ECE, NITK, Surathkal for providing valuable suggestions while carrying out the research work.

References

1. D. Mušicki, B.L. Scala, Multi-target tracking in clutter without measurement assignment. IEEE Trans. Aerosp. Electron. Syst. **44**, 877–896 (2008)
2. X. Lyu, J. Wang, Sequential multi-sensor JPDA for target tracking in passive multi-static radar with range and doppler measurements. IEEE Access **7**, 34488–34498 (2019)
3. G. Vivone, P. Braca, Joint probabilistic data association tracker for extended target tracking applied to X-band marine Radar data. IEEE J. Ocean. Eng. **41**, 1007–1019 (2016)
4. F. Colone et al., A multistage processing algorithm for disturbance removal and target detection in passive bistatic radar. IEEE Trans. Aerosp. Electron. Syst. **45**, 698–722 (2009)
5. G.S. Satapathi, P. Srihari, Soft and evolutionary computation based data association approaches for tracking multiple targets in the presence of ECM. Exp. Syst. Appl. **77**, 83–104 (2017)
6. S. Mirjalili, S.M. Mirjalili, A. Lewis, Grey wolf optimizer. Adv. Eng. Softw. **69**, 46–61 (2014)
7. G.S. Satapathi, P. Srihari, All neighbor fuzzy relational data association for multitarget tracking in the presence of ECM, in *IEEE Annual India Conference (INDICON)*, Bangalore, India (2016), pp. 1–5
8. H. Kuschel, D. Cristallini, K.E. Olsen, Tutorial: passive radar tutorial. IEEE Aerosp. Electron. Syst. Mag. **34**, 2–19 (2019)
9. M. Tian, Y. Bo, Z. Chen, P. Wu, C. Yue, Multi-target tracking method based on improved firefly algorithm optimized particle filter. Neurocomputing **359**, 438–448 (2019)
10. D.B. Reid, An algorithm for tracking multiple targets. IEEE Trans. Autom. Control **6**, 843–854 (1979)
11. D. Mušicki, R. Evans, Multi-scan multi-target tracking in clutter with integrated track splitting filter. IEEE Trans. Aerosp. Electron. Syst. **45**, 1432–1447 (2009)
12. T. Fortmann, Y. Bar-Shalom, M. Scheffe, Sonar tracking of multiple targets using joint probabilistic data association. IEEE J. Ocean. Eng. **8**, 173–183 (1983)

13. T.L. Song, H.W. Kim, D. Musicki, Iterative joint integrated probabilistic data association for multitarget tracking. IEEE Trans. Aerosp. Electron. Syst. **51**, 642–653 (2015)
14. NATO science and Technology Organization, https://www.cmre.nato.int/
15. D. Wang, D. Tan, L. Liu, Particle swarm optimization algorithm: an overview. Soft Comput. **22**, 387–408 (2018)
16. B. Kwolek, A. Chatterjee, H. Nobahari, P. Siarry, Multi-object tracking using particle swarm optimization on target interactions. Adv. Heuristic Signal Process. Appl. Springer Chap **4**, 63–78 (2013)
17. M.W. Guo, J.S. Wang, L.F. Zhu, S.S. Guo, W. Xie, An improved grey wolf optimizer based on tracking and seeking modes to solve function optimization problems. IEEE Access **8**, 69861–69893 (2020)

Developing a Cost Model for a Multi-Controller Software-Defined Network Using M/M/c/K Queue with Retention of Reneged Flows

G. Uma Maheswari and K. Vasudevan

Abstract Flow Management is a key concern to ensure the Quality of Service in Software-Defined Network (SDN). This paper introduces an analytical model using M/M/c/K queueing where the arrival of flows is governed by Poisson process forming a single queue and there are 'c' number of controllers whose service times are exponential having a finite buffer 'K'. The loss due to Reneging and Retention of flows in a Multi-Controller SDN is initially evaluated. A Cost model has been formulated to estimate the effect of Retention of Reneged flows on Total Expected Cost per unit time. The results are simulated which validates that the Total Expected Cost per unit time is a function of service rate of the controller and M/M/c/K queueing model have significant influence on the performance of a Multi-Controller SDN.

Keywords Software-defined network · Multi-controller · M/M/c/K Queueing model · Loss rate · Cost model

1 Introduction

Software-Defined Networking (SDN) is a recent trend in networking, where forwarding is done by means of flows [1–3]. A set of packets between two endpoints can be termed as a flow. There is a logically centralized controller in SDN, which will decide about forwarding the incoming flows. The flows arriving at the networking devices are examined for finding a match in its flow table. The flow table consists of action to be performed for a particular match. The associated action is done when a match is found or else the networking device forwards the flow to the controller. The controller will then set up appropriate flows on the networking device. There lies a logical segregation between control plane and the Data plane in SDN. Researchers observed that the Multi-Controller SDN adequately helps to maintain

G. Uma Maheswari (✉) · K. Vasudevan
Thiagarajar College of Engineering, Madurai, India

K. Vasudevan
e-mail: kvasudevan@tce.edu

S. Rawat et al. (eds.), *Proceedings of First International Conference on Computational Electronics for Wireless Communications*, Lecture Notes in Networks and Systems 329,
https://doi.org/10.1007/978-981-16-6246-1_23

the QoS requirements with some additional operational cost. In a Multi-Controller SDN, it becomes inevitable to analyze the Loss Rate due to Reneging and Retention and Total Expected Cost.

An analysis of M/M/c queuing considering the conditions of reneging and balking was made [5]. The transient solution of system is obtained by means of a technique using the generating function. The transient probabilities are calculated by deriving a differential equation using the Bessel functions. A queueing system using M/M/c model having infinite capacity and c unreliable servers to verify the balking and reneging conditions was proposed [6]. The analysis is made with the help of quasi-birth-and-death (QBD) process to obtain the sufficient equilibrium condition of the system. The steady-state probability is obtained using matrix approach and the performance measures such as service rate, number of servers and repair rate are determined with the help of a cost model which results in minimal total expected cost per unit time. A study on finite capacity Markovian queueing model with multiple servers to verify the conditions of reneging, retention of reneged customers and discouraged arrivals was made [7]. The analysis of cost-profit model was determined by deriving the steady-state probabilities of system. A Feedback Markovian queuing model with multiple servers to check the conditions of customer impatience, encouraged arrivals, and retention of impatient customers was done [8]. The probabilities of the system were obtained and the necessary performance measures are calculated. A solution was provided for balancing the flows with guaranteed QoS among SDN controllers, for optimizing the provisioning costs of resources using M/M/1 model [9]. A solution was stated for the functioning of the network with reasonable cost and minimum resources and also guaranteed the QoS requirements of network. An analytical study was made on the dependency between the rate of arrival of flows, number of required resources and the cost due to controller's response time. The study revealed that the usage of resources was minimized, QoS was improved and cost was saved due to the balancing of flows. An analytical model to study the performance of Software-defined network (SDN) switches was made [10]. A model based on M/Geo/1 Queueing was exploited to study the parameters such as size of flow table, rate of arrival of packets, position and number of rules. An analytical model using M/M/c/K queuing was proposed to study the performance of Multi-Controller SDN [11]. The performance was studied based on the metrics such as Response Time (Flow setup time) and Waiting Time (Time spent in the Controller).

The comparison of performance analysis of SDN using various queueing models is shown in Table 1 (✓ means analysis is done and ✘ means analysis is not done). This paper proposes an analytical model by means of M/M/c/K queueing in which multi-controller queueing is implemented where each have a finite capacity and it can be used to analyze the performance of Multi-Controller SDN considering the loss due to reneging and retention of flows. The probabilities at the steady-state are determined considering c-controller queueing system with arrival rate having a Poisson distribution, service rate having an exponential distribution, and the controller has a limit on examining only K number of flows, such that $K \geq c$. The contributions done in this paper are an extension of [11] in which the performance measures like Response time and Waiting Time of the controller were analyzed in a Multi-Controller SDN. In

Table 1 Performance analysis in SDN using various queueing models

Performance measures analyzed	M/M/1 [9]	M/Geo/1 [10]	M/M/c/K [11]	M/M/c/K with retention of Reneged flows
		Existing		Proposed
Waiting time	✓	✓	✓	✘
Response time	✓	✓	✓	✘
Cost with additional resources	✓	✓	✓	✓
CPU utilization	✓	✓	✓	✓
Loss rate	✓	✓	✓	✓
Total expected cost	✓	✓	✓	✓

the proposed work, the performance measures of the controller are estimated considering the loss due to reneging and retention of flows and a Cost model is also derived which estimates the Total Expected Cost per unit time of the Multi-Controller SDN.

2 Analytical Model

A Multi-Controller SDN can be modelled as a M/M/c/K queueing system which dynamically manage the flows with the help of c number of controllers each having a finite buffer K. Let the rate of flows arriving at the controller can be denoted by λ and the rate of flows serviced by the controller can be denoted by μ. The controller stability can be estimated by $\rho = \lambda/\mu$. The controller stability is maintained such that, $\rho \geq 1$. The capacity of the Queueing system is finite and it can accommodate at most K number of flows at any time. Initially, the incoming flows have to join the queue to get the service. When the incoming flows arrive at the queue and there is no space in the queue to wait then reneging occurs, i.e., the flows leave the queue without getting service whose probability can be stated as p. Sometimes, the flows have to wait in the queue to get the service at the controller whose probability can be stated as q = (1-p) [7, 8] and [12]. The number of times the flows may leave the queue without getting service is considered to follow an exponential distribution which is mentioned by θ.

2.1 Steady-State Probabilities

Let $P_K(t)$ be the probability denoting K number of flows at time t in the system. The birth–death coefficients are used to derive the differential-difference equations which are stated as,

$$\frac{dP_0}{dt} = -\lambda P_0 + \mu P_1 \tag{1}$$

$$\frac{dP_K(t)}{dt} = \left(\frac{\lambda}{K-(c+1)}\right) P_{K-1}(t) - \{\mu c + (\xi p(K-c))\} P_K(t) \tag{2}$$

In the steady-state, $P_K(t) = P_K$. Therefore, the steady-state equations derived corresponding to differential-difference Eqs. (1) and (2) are,

$$0 = -\lambda P_0 + \mu P_1 \tag{3}$$

$$0 = \left(\frac{\lambda}{K-(c+1)}\right) P_{K-1}(t) - \{\mu c + (\xi p(K-c))\} P_K \tag{4}$$

Solving the Eqs. (3) and (4) iteratively, we obtain

$$P_K = \frac{1}{(K-(c+1))!} \prod_{x=(c+1)}^{K} \frac{\lambda}{\mu c + (\xi q(x-c))} \frac{\rho^c}{c!} P_0 \tag{5}$$

Using the normalization condition $\sum_{n=0}^{K} P_K = 1$, we get P_0 which can be stated as the probability denoting 0 number of flows in the controller and can be estimated by,

$$P_0 = \left[\sum_{n=(c+1)}^{K} \frac{1}{(n-(c+1))!} \prod_{x=(c+1)}^{n} \frac{\lambda}{\mu c + (\xi p(x-c))} \frac{\rho^c}{c!} + \sum_{(n=1)}^{c} \frac{\rho^n}{n!} + 1 \right]^{-1} \tag{6}$$

2.2 Controller Performance Metrics

Flows Expected to be Waiting. Let E(nfw) denotes flows expected to be waiting in the network and it can be stated as,

$$E(nfw) = \left[\sum_{n=(c+1)}^{K} n \frac{1}{(n-(c+1))!} \prod_{x=(c+1)}^{n} \frac{\lambda}{\mu c + (\xi p(x-c))} \frac{\rho^c}{c!} + \sum_{(n=1)}^{c} n \frac{\rho^n}{n!} \right] P_0 \tag{7}$$

Flows Expected to be Serviced. The flows expected to be serviced by the controller can be calculated from the flows expected to be waiting in the network. Let E(nfs) be the number of flows expected to be serviced by the controller and it

can be stated as,

$$E(nfs) = \left[\sum_{(n=1)}^{c} \mu n P_n + \sum_{n=(c+1)}^{K} \mu c P_n \right] P_0 \tag{8}$$

$$E(nfs) = \left[\sum_{n=(c+1)}^{K} \mu c \frac{1}{(n-c+1)!} \prod_{x=(c+1)}^{n} \frac{\lambda}{\mu c + (\xi p(x-c))} \frac{\rho^c}{c!} + \sum_{(n=1)}^{c} \mu n \frac{\rho^n}{n!} \right] P_0 \tag{9}$$

Reneging Rate. The Reneging rate (R_{re}) of the queueing system can be defined as the rate at which the incoming flows may renege or leave the Queue without getting service and it can be calculated by,

$$R_{re} = \sum_{n=1}^{K} (n-c)\xi p P_n \tag{10}$$

Retention Rate. The flows have to wait in the queuing system to get service, i.e., retention with a probability (q = 1-p). The Retention rate (R_{rt})of the queueing system can be stated as the rate at which the incoming flows may retain or hold the queue and it can be calculated by,

$$R_{rt} = \sum_{n=1}^{K} (n-c)\xi q P_n \tag{11}$$

Loss Rate. Due to the retention of reneged flows, there is a loss in the queueing system and the loss rate can be determined by,

Loss Rate = Reneging Rate + Retention Rate

$$L_R = \sum_{n=1}^{K} (n-c)\xi p P_n + \sum_{n=1}^{K} (n-c)\xi q P_n \tag{12}$$

Total Expected Cost. A Cost Model can be developed for a Multi-Controller SDN using M/M/c/K queueing considering the loss due to retention and reneging, which is a function of rate of flows serviced at the controller. The objective of the cost model is to reduce the cost per unit time. Let C_S can be considered as the Cost of providing service per unit time, C_W be the Cost associated with each incoming flow joining the queue and waiting for service and C_L can be considered as the Cost per unit time associated to each flow lost without getting service.

$$TEC = C_S P_B + C_W E(nfw) + C_L L_R \tag{13}$$

3 Performance Evaluation and Discussion

The simulations were done in a laptop computer having the specifications such as 16 GB RAM, intel core i7 processor operating at 2.50 GHz speed and 64-bit windows 10 operating system. The proposed scheme was validated using a discrete event simulation implemented in MATLAB. The following assumptions were made for doing the simulations such as the value of number of Controllers (c) = 3, value of K = 100,000, and rate of arrival of flows begins from $\lambda = 50{,}000$ flows per second and arrival rate is added by 5000 every time to get different simulation results. The analysis was done using 2 different rate of service such as $\mu = 50{,}000$ flows per second and $\mu = 70{,}000$ flows per second. The value of $\theta = 0.1$. It has been noted that as the rate of arrival of flows λ increases, the flows expected to be E(nfw) waiting in the queuing system also increases. This, in turn, increases the Reneging rate and Retention rate and thus the Loss rate also increases. The notations used in the proposed work and the values assumed are shown in Table 2.

Figure 1 shows the relationship between the rate of arrival of flows and the loss rate of the controller. It shows that the loss rate is being decreased when the service rate of the controller is increased from $\mu = 50{,}000$ flows per second to $\mu = 70{,}000$

Table 2 Notation used in the proposed work

Notations	Descriptions
λ	Rate of flows arriving at the controller (assumed range from 50,000 to 100,000)
M	Rate of flows serviced by the controller
C	Number of controllers (assumed c = 3)
K	Maximum number of flows satisfied by the Controller (assumed K = 100,000)
P	Controller Stability factor
P	Probability of incoming flows reneging or leaving the queue without getting service
Q	Probability of incoming flows retaining or holding the queue to get service
θ	Exponential distribution of number of times the flows may renege (assumed $\theta = 0.1$)
P_0	Probability denoting 0 number of flows in the Controller
P_K	Probability denoting K number of flows in the Controller
E(nfw)	Number of flows expected to be waiting
E(nfs)	Number of flows expected to be serviced
R_{re}	Reneging rate-rate at which the incoming flows may renege or leave the system
R_{rt}	Retention rate-rate at which the incoming flows may retain or hold the queue
L_R	Loss Rate due to Reneging and Retention
C_s	Cost of providing service per unit time (assumed $C_s = 30$)
C_w	Cost associated with each incoming flow joining the queue and waiting for service (assumed $C_w = 10$)
C_L	Cost associated to each lost flow per unit time. (assumed $C_L = 10$)
TEC	Total Expected Cost

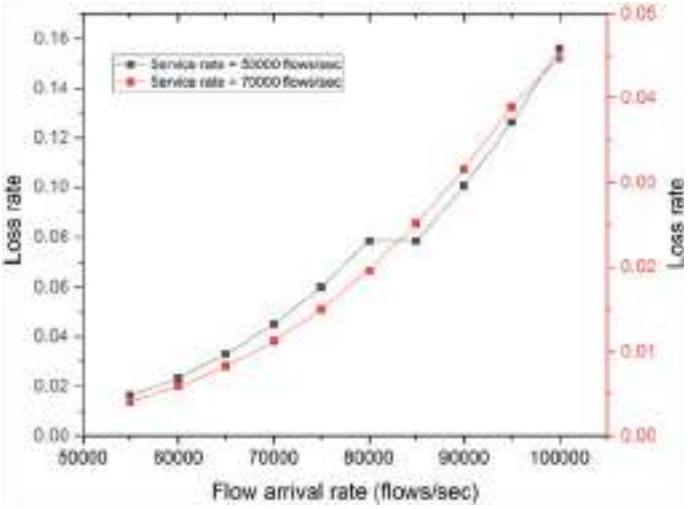

Fig. 1 Rate of arrival of flows vs Loss rate of the controller

flows per second. Initially, when the service rate is 50000 flows per second, the loss rate increases from 0 to 0.15. It is being reduced and the loss rate increases only up to 0.05 when the service rate is increased.

In Fig. 2, the effect on Total Expected Cost (TEC) due to the probability of retention of flows (q) is studied. The value of Cost of providing service per unit time (C_S) is considered as 30, Cost associated with each incoming flow joining the queue and waiting for service (C_W) is considered as 10 and Cost per unit time associated to

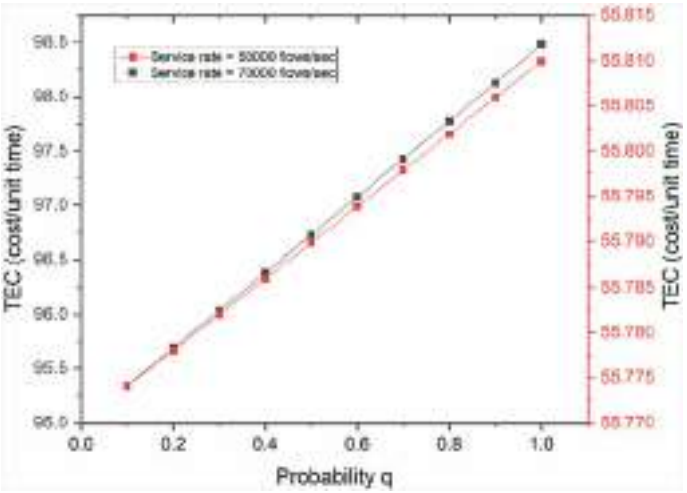

Fig. 2 Probability of Retention of flows (q) vs Total Expected Cost (TEC)

Table 3 Performance analysis of the controller

Service rate (flows/sec)	Loss rate	Total expected cost (cost/unit time)
50,000	0 to 0.15	95 to 98.5
70,000	0 to 0.05	o 55.81

each flow lost without getting service (C_L) is considered as 10. It has been observed that the Total Expected Cost of the system increases, as the probability of retention of flows increases. The graph shows that the increase in TEC is decreased when the rate of flows serviced is increased from $\mu = 50{,}000$ flows per second to $\mu = 70{,}000$ flows per second. Table 3 shows the values of loss rate and Total Expected Cost simulated when the service rate is $\mu = 50{,}000$ flows per second and $\mu = 70{,}000$ flows per second.

4 Conclusion

In this paper, an analytical model was proposed to study the performance of Multi-Controller SDN using M/M/c/K queueing to derive the loss rate due to retention and reneging of flows. The probabilities at the steady-state of the queueing system are determined and a Study was also made on the dependency between the Expected number of flows waiting, Reneging rate, Retention rate, and Total Expected Cost. A cost model is presented, which is a function of service rate of the controller to analyze the effect of Retention of Reneged flows with respect to Total Expected Cost per unit time in a Multi-Controller SDN. The study revealed that the service rate of controller mainly affects the performance of the network and the M/M/c/K queueing model has influence on Multi-Controller SDN.

References

1. P. Goransson, C. Black, *Software Defined Networks: a Comprehensive Approach*, (Elsevier Inc, Amsterdam, 2014)
2. H. Kim, N. Feamster, Improving network management with software defined networking. IEEE Commun. Mag. **51**(2), 114–119 (2013)
3. W. Xia, Y. Wen, C.H. Foh, D. Niyato, H. Xie, A survey on software defined networking. IEEE Commun. Surv. Tuts. 27–51 (2015)
4. D. Yue, W. Yue, Y. Sun, Performance analysis of an M/M/c/N queueing system with balking, reneging and synchronous vacations of partial servers, in *Sixth International Symposium on Operations Research and Its Applications*, (Xinjiang, China, 2006), pp. 128–143
5. R.O. Al-Seedy, A.A. El-Sherbiny, S.A. El-Shehawy, S.I. Ammar, Transient solution of the M/M/c queue with balking and reneging. Comput. Math. Appl. **57**, 1280–1285 (2009)
6. C.H. Wu, J.C. Ke, Computational algorithm and parameter optimization for a multi-server system with unreliable servers and impatient customers. J. Comput. Appl. Math. **2**(5), 547–562 (2010)

7. R. Kumar, S.K. Sharma, A multi-server Markovian queueing system with discouraged arrivals and retention of reneged customers. IJOR **9**(4), 173–184 (2012)
8. B.K. Som, S. Seth, M/M/c/N queuing systems with encouraged arrivals, reneging, retention and feedback customers. Yugosl. J. Oper. Res. **28**(3), 333–344 (2018)
9. K. Sood, S. Yu, Y. Xiang, H. Cheng, A general QoS aware flow-balancing and resource management scheme in distributed software defined networks. IEEE Access, 7176–7185 (2016)
10. K. Sood, S. Yu, Y. Xiang, Performance analysis of software-defined network switch using M/Geo/1 model. IEEE Commun. Papers, 2522–2525 (2016)
11. U.M. Gurusamy, K. Hariharan, M.S.K. Manikandan, Modelling and Performance Analysis of Flow Management in a Multi-Controller Software Defined Network Using M/M/c/K Model, in *15th IEEE India Council International Conference (INDICON)*
12. D. Gross, J.F. Shortie, J.M. Thompson, C.M. Harris, *Fundamentals of Queueing Theory*, 4th edn. (Wiley, Hoboken)
13. R. Kumar, S.K. Sharma, A multi-server markovian queueing system with discouraged arrivals and retention of reneged customers. Int. J. Operat. Res. **9**(4), 173–184 (2012)
14. J. Ansell, W.K.G. Seah, B. Ng, S. Marshall, Making queueing theory more palatable to SDN/OpenFlow-based network practitioners, in *NOMS 2016 IEEE/IFIP Network Operations and Management Symposium*, pp. 1119–1124 (2016)
15. Y. Goto, H. Masuyama, B. Ng, W.K.G. Seah, Y. Takahashi, Queueing analysis of software defined network with realistic openflowbased switch model, in *2016 IEEE 24th International Symposium on Modeling, Analysis and Simulation of Computer and Telecommunication Systems (MASCOTS)*, pp. 301–306 (2016)
16. J. Raychev, G. Hristov, D. Kinaneva, P. Zahariev, Modelling and evaluation of software defined network architecture based on queueing theory, in *28th EAEEIE Annual Conference (EAEEIE)*, pp. 1–5 (2018)
17. D. Singh, B. Ng, Y. Lai, Y. Lin, W.K.G. Seah, Modelling software defined networking: Switch design with finite buffer and priority queueing, in *IEEE 42nd Conference on Local Computer Networks (LCN)*, Singapore, pp. 567–570 (2017)

Multi-wave Effect Estimate of Pandemic on Population: A Prediction Model and IoT-Based Alerting

Ratnala Vinay, M. P. R. Prasad, and T. S. V. S. Vijaya Kumar

Abstract The current day scenario is all about the growing pandemic and a lot of possibilities arise regarding the resurgence of the pandemic in second and third waves which demands a good prediction model. The core idea of the project is around this. The aim of this project is to develop a prediction model which can provide an estimate of the effected population if second and third wave of resurgence occurs. The prediction model is based on the key behavior of the pandemic, which is a parabolic behavior. Considering this behavior, Numerical Methods have been used to find solution of Parabolic Differential Equations to arrive at an estimate simulated in the MATLAB tool. These can be of great use and provide accurate results if appropriate input parameters are provided. The IoT-based mechanism captures the outputs of the algorithm and provides a physical indicator through a dedicated device or mobile of the user.

Keywords Parabolic behavior · Prediction model · IoT · Numerical methods

1 Introduction

A lot of discussion has been going on flattening the curve. The curve is nothing but a parabola. Any pandemic outbreak in a single wave resembles a parabola. It initially peaks up and later starts to slow down. The idea is if framing of Parabolic Differential Equations is successful future estimates can be made when resurgence occurs with the data available from the first wave. The method in particular selected is explicit scheme of solving Parabolic Differential Equations [1–4]. The requirement to the solution is an increasing slope variable and a decreasing slope variable. Prediction models have the tendency to produce multiple results, so the methodology is also provided with an error estimation technique. There is a lot of data available online

R. Vinay · M. P. R. Prasad · T. S. V. S. Vijaya Kumar (✉)
NIT Kurukshetra, Kurukshetra, India

M. P. R. Prasad
e-mail: mprprasad@nitkkr.ac.in

S. Rawat et al. (eds.), *Proceedings of First International Conference on Computational Electronics for Wireless Communications*, Lecture Notes in Networks and Systems 329,
https://doi.org/10.1007/978-981-16-6246-1_24

through apps like Arogya Setu which is the input data used in this methodology. For the increasing slope, the doubling rate in various areas is considered. For the decreasing slope, the recovery rate is considered, the required slopes or mid values are obtained and processed in the parabolic differential equation to obtain solution [5, 6]. In the increasing slope estimate, a mapping scheme of different data is involved which is resolved by error estimation. The estimated answers are then worked on hardware to provide alerting.

2 Literature Review

A number of prediction models are studied [11–13]. A large number of methods proposed were demography oriented which were dependent on some features like the way some conventional diseases of that area spread [9, 10]. The method of analysis for current pandemic has become demography-oriented as there was no sufficient time from when the outbreak has occurred. This problem was effectively resolved in the proposed model which followed a data-driven approach. The algorithm made use of data from apps like Arogya Setu to develop an effective estimation methodology overcoming the problems faced by demography-based algorithms.

3 Methodology

3.1 Increasing Slope Estimate

The normalized value of each entry is considered in subintervals of 0.25. As a value comes in weight is given to the corresponding subinterval. Finally, two possible cases may arise an under peak or an over peak. The highest mapped sub interval in the under peak range and the highest mapped sub interval in the over peak range is considered for further computations and mid-value of the subinterval is used.

3.2 Decreasing Slope Estimate

The decreasing slope is obtained from the recovery rate data. The recovery rate of the cluster acts as the decreasing slope variable of the Parabolic Differential Equation. Flexibility in decreasing slope can be provided if we are analyzing post multiple input waves which give multiple recovery rates.

3.3 Error Estimation Analysis

In the increasing slope estimate, the most mapped entry is considered. This leads to scenario where entries are missed resulting in error. Thus, a Gaussian error estimate is constructed with the Centre being the mean which is the most repeated entry and the standard deviation being the permissible range for error. The unfavorable area gives us the error of the current estimation result [7, 8].

3.4 Result Analysis

The current estimation model is for third wave resurgence thus, four possible outcomes with their error are predicted. These scenarios are under peak followed by under peak. Under peak followed by over peak. Over peak followed by under peak and finally over peak followed by over peak [5, 6].

3.5 IoT-Based Working

The outputs of above algorithm are interfaced with an efficient hardware alerting system to represent the outputs in the most effective and useful manner. In this technique, the outputs of the MATLAB-based algorithm is transferred to a cloud-based IoT interface. At the user end, there must be a IoT compatible system to utilize the output. For the purpose of demonstration, Arduino is considered. The functionality is as follows. The inputs to be transferred to the cloud-based interface are the four results obtained in the algorithm, the outputs for under peak followed by under peak, under peak followed by over peak, over peak followed by under peak and finally over peak followed by over peak. Along with this, the initial doubling rate and the cluster number of the target cluster are also to be transmitted. The answers are further zoned to provide an alerting mechanism indicative to the user. The zones are such that they represent red, orange and green subdivisions. For physical indication, an alerting system is provided. If the predicted answer after transmission of results and mapping to cluster peaks fall in red zone then red-light glows as a physical indicator, if the result mapping falls in orange zone then orange light glows as a physical indication. If the result of mapping falls in green zone the alert is green light as a physical indication. Thus, when a user moves from place to place as the cluster entries change the alert is modified. This even gives a future indication of the zone the person is about to enter such that necessary precautions are taken.

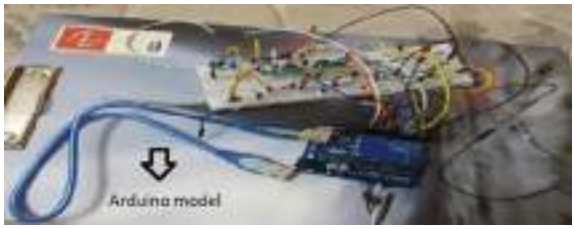

Fig. 1 Arduino alerting model developed

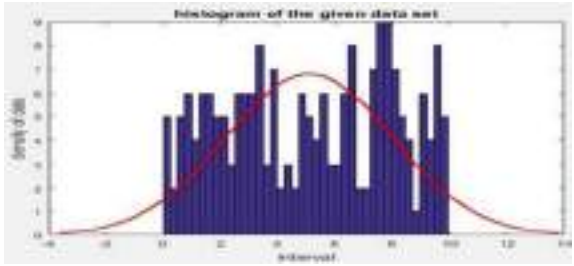

Fig. 2 The initial data set with normalized values

4 Results

4.1 Arduino-Based Model

The Arduino-based model as shown in Fig. 1 is the alerting system developed. It compromises of indicators which take the algorithm output as the input of the alerting system. Then based on the zone in which the result falls the corresponding indication is given by the system. This is a physical system which demonstrates the functionality of the algorithm. This mechanism can also be included into a mobile device with an application developed and interfaced to the algorithm by cloud interface.

4.2 Normalized Values

This is the histogram of the input data set which is normalized in the range 0 to 10 and divided into subintervals of 0.25. The occurrence of each subinterval is depicted in Fig. 2.

4.3 Under Peak Estimate

The error estimation of the input data set with the most occurring subinterval as mean and deviation being the error within permissible range estimated with the under peak

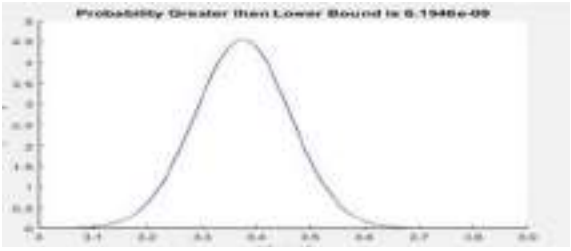

Fig. 3 Probability error estimate for under peak

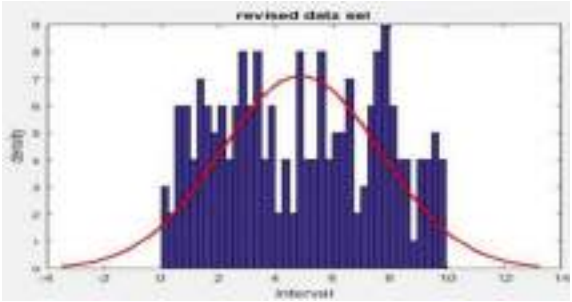

Fig. 4 Revised data set after under peak

cluster points in data is shown in Fig. 3. The values used are from the histogram plotted above (probability density as a function of normalized value in under peak).

4.4 Under Peak Normalized Data

The histogram of revised data set after initial assumption of under peak as per the outputs obtained after the first computation is shown in Fig. 4.

4.5 Error Estimation Scenario 1

The multi-season estimate of under peak followed by under peak with the mean being most repeated subinterval and standard deviation being the error within permissible range is shown in Fig. 5 (probability density as a function of normalized value in under peak followed by under peak).

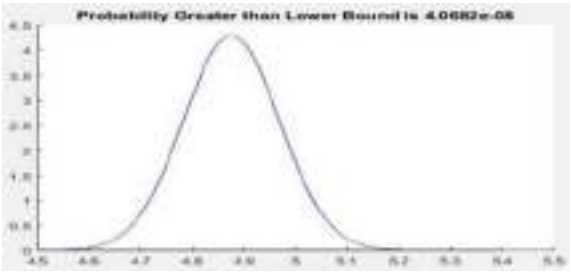

Fig. 5 Error estimation under peak followed by under peak

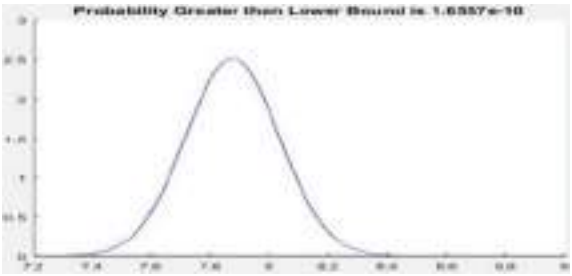

Fig. 6 Error estimation under peak followed by over peak

4.6 Error Estimation Scenario 2

The multi-season estimate of under peak followed by over peak with the mean being most repeated subinterval and standard deviation being the error within permissible range is shown in Fig. 6 (probability density as a function of normalized value in under peak followed by over peak).

4.7 Over Peak Estimate

The error estimation of the input data set with the most occurring subinterval as mean and deviation being the error within permissible range estimated with the over peak cluster points in data is shown in Fig. 7 (probability density as a function of normalized value in over peak).

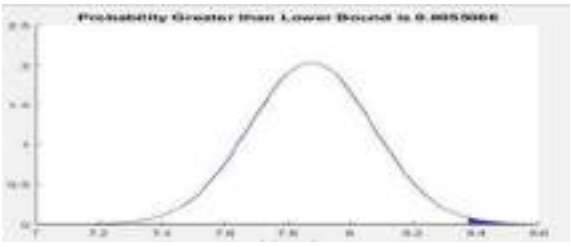

Fig. 7 Error estimation of over peak

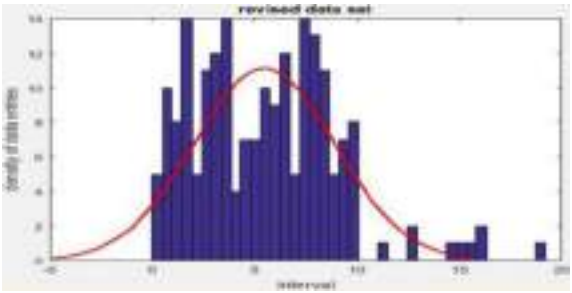

Fig. 8 Revised Data set for over peak

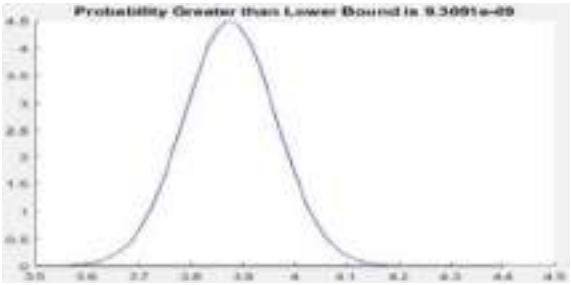

Fig. 9 Error estimation over peak followed by under peak

4.8 Over Peak Normalized Data

The histogram of revised data set after initial assumption of over peak as per the outputs obtained after first computation is shown in Fig. 8.

4.9 Error Estimation Scenario 3

The multi-season estimate of over peak followed by under peak with the mean being most repeated subinterval and standard deviation being the error within permissible range is shown in Fig. 9 (probability density as a function of normalized value in over peak followed by under peak).

4.10 Error Estimation Scenario 4

The multi-season estimate of over peak followed by over peak with the mean being most repeated subinterval and standard deviation being the error within permissible range is shown in Fig. 10 (probability density as a function of normalized value in over peak followed by over peak).

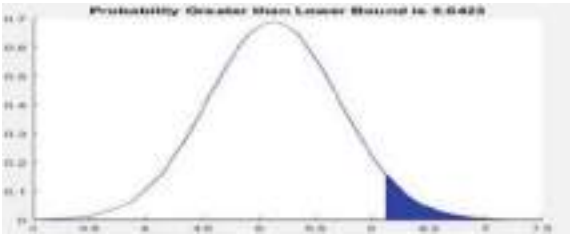

Fig. 10 Error estimation over peak followed by over peak

5 Computational Outputs

The outputs in Figs. 11 and 12 here depict the final value of population per 1000 in each of the four cases. The final results are as expected which gives the number of

```
The normalised value for under peak under peak estimate is :
    3.2861

The probability of error under peak under peak estimate is :
    4.6877e-08

The normalised value for under peak over peak estimate is :
    5.7080

The probability of error under peak over peak estimate is :
    6.3601e-09

The normalised value for over peak under peak estimate is :
    3.1788

The probability of error over peak under peak estimate is :
    0.0055

The normalised value for over peak over peak estimate is :
    4.1880

The probability of error over peak over peak estimate is :
    0.0478
```

Fig. 11 This is the normalized output value with error for each of the four cases

```
The population impact of under peak under peak estimate per 1000 :
  328.6123

The population impact of under peak over peak estimate per 1000 :
  570.7998

The population impact of over peak under peak estimate per 1000 :
  317.8504

The population impact of over peak over peak estimate per 1000 :
  418.8019
```

Fig. 12 The Final output

people effected per 1000 population if in the subsequent waves different patterns are followed of reaching or not reaching the expected peak.

6 Future Scope

The model suggested above is a real-time data-based prediction model working on increasing and decreasing slope estimates. The future of any data-driven algorithm is from the strength of the data. If we can improve the data size of the algorithm more efficient results can be obtained. With improved data sets more selective error correction techniques can be utilized improving the overall efficiency of the algorithm used here.

7 Conclusion

Numerical methods are one of the most powerful tools in estimation. It can be properly used to solve a large number of day-to-day problems. Any futuristic predictions can be achieved using Numerical methods, for example, the prediction of nutrition levels of a soil before and after using it for crops over some duration and finally helps the farmer to use only required set of fertilizers for boosting up the soil. The same estimate is applied and the resurgence effect of pandemic on population is estimated accurately. The data in analysis to improve the efficiency has been simulated taking into consideration from various reliable online data collection platforms available, on paper sources and apps like Arogya Setu. The inclusion of hardware-based alerting system makes the output more observable and useful for the end-user.

References

1. F.E. Browder, Linear parabolic differential equations of arbitrary order; general boundary value problems for the elliptic equations. Proc. Nat. Acad. Sci **39**, 185–190 (1953)
2. E.C.Du Fort, S.P. Frankel, Stability conditions in the numerical treatment of parabolic differential equations. Math. Tables Other Aids Comput. **7**(43), pp. 135–152 (1953)
3. H. Amann, Linear parabolic equations with strong boundary degeneration. J Elliptic Parabola Equ. **6**, 123–144 (2020). https://doi.org/10.1007/s41808-020-00061-1
4. D.W. Peaceman, H.H. Rachford, The numerical solution of parabolic and elliptic differential equations. J. Soc. Ind. Appl. Math. **3**(1)
5. B.S. Grewal, *Higher Engineering Mathematics*, 43rd edn.
6. Numerical Methods-Finite Difference Approach, NPTEL course
7. P.Z. Pebbels Jr, *Probability, Random Variables and Random Signal Principles*, 4th edn.
8. http://makeyourownneuralnetwork.blogspot.com/2015/01
9. M. Mandal, S. Jana, S. Kumar Nandi, A. Khatua, S. Adak, T.K. Kar, A model based study on the dynamics of COVID-19: prediction and control. Chaos, Solitons Fractals, **136**, 109889, ISSN 0960–0779 2020. https://doi.org/10.1016/j.chaos.2020.109889

10. K.C. Santosh, COVID-19 prediction models and unexploited data. J. Med. Syst. **44**, 170 (2020). https://doi.org/10.1007/s10916-020-01645-z
11. A. Bagula, H. Maluleke, O. Ajayi, Predictive models for mitigating COVID-19 outbreak. IEEE ISCC (2020)
12. S. Singh, P. Raj, R. Kumar, Prediction and forecast for COVID-19 outbreak in India based on enhanced epidemiological models. IEEE ICIRCA (2020)
13. J. Vakula Rani, A. Jakka, Forecasting COVID-19 cases in India using machine learning models. ICSTCEE (2020)

Latency and Power Improvement of Hardware Sequences Using Collapse and Evolve Approach: Nature-Inspired Methodology

Ratnala Vinay and M. P. R. Prasad

Abstract The main motivation of this work is from the extensive observation in the way tasks are implemented within hardware subsystems to achieve the desired functionality. In most of the scenarios for the completion of a particular computation a predetermined sequence is implemented. This in terminology of subsystem level implementation is called as hardware internal sequences. A lot of the steps which happen within the whole hardware sequence are redundant in nature. The target of optimization in this work is redundancy occurring in hardware sequences. To make the optimization methodology more compatible to the current trend of AI development, a nature-inspired methodology is proposed. The algorithm used here is called as collapse and evolve approach. The focus optimization parameters are latency and power consumed when the whole hardware sequence gets implemented. Nature or the process of evolution of nature is some hundreds of billion years old when compared to human evolution which is some tens of billion years old suggesting natural evolution to be a more advanced flow. So, focus is put on the natural evolution process to extract an efficient technique which can achieve our target optimization within the hardware sequences. The manner in which initial set of species survived and evolved frames the base of the hardware computational algorithm. The work suggested falls in the unison of a very interesting area of AI to hardware and nature-inspired computing which allows the outcomes of the work to be utilized in far more diversified areas. As a part of the study, the proposed algorithm is implemented on the power processing block of digital system.

Keywords Hardware sequence · Subsystem · Collapse and evolve · Latency · Power

R. Vinay (✉) · M. P. R. Prasad
NIT Kurukshetra, Kurukshetra, India

M. P. R. Prasad
e-mail: mprprasad@nitkkr.ac.in

S. Rawat et al. (eds.), *Proceedings of First International Conference on Computational Electronics for Wireless Communications*, Lecture Notes in Networks and Systems 329,
https://doi.org/10.1007/978-981-16-6246-1_25

1 Introduction

Hardware and computational algorithms are like two sides of the same coin. Improvement of one domain is highly dependent on the developments made in the other domain. Many of the cross-domain subjects like algorithms to architectures, computer system design focus on the point to improve efficiency of hardware development from computer algorithm perspective. So far this cross-domain development has mainly emphasized on improving micro-architectural algorithms for the development of computer hardware. With the current development, the trend has completely shifted to artificial intelligence in the software space. Huge emphasis has been made on the development of AI-based algorithms in the software domain. To make more and more efficient designs in hardware space it has become a need of the day for the cross-platform changes to be more AI-oriented so that the development in both the domains are on the same line. There are three phases of development of AI algorithms: analysis of conventional algorithms, data analytic for machine learning and deep learning techniques. The focus of AI development is to be made by considering all the above three steps. Deep learning has its extension in two main sub-domains brain-inspired development and nature or evolution inspired development. The algorithm proposed in the work specially falls into the nature or evolution inspired methodology of deep learning which can be used as a hardware performance improvement methodology inspired from AI algorithms [1, 2].

2 Literature Review

A system which implements the hardcoded sequential flow is the power core within the main processor which targets power reduction by focusing on a number of steps like peripheral bandwidth reduction, power modes to implement minimal static consumption and operating frequency to reduce dynamic power consumption [8]. To obtain an optimal number for the values of bandwidth, frequency and supply large number of sequential flows are involved which has a lot of redundancy [10]. These cores within hardware which use exclusive sequential flows are the target of development using proposed new flow. If collapse and evolve algorithm can be successfully implemented inside such cores having a lot of redundancies enhanced latency performance and power performance at an overall processor level can be obtained which is the motto of the proposed algorithm.

3 Methodology

3.1 Collapse and Evolve in Natural Evolution

Evolution is the most developed process which started from when life was existent on the planet. Collapse and evolve is one of the inspirations taken from the early stages of natural evolution. After water, sunlight and carbon-di-oxide were abundant on the planet. One of the first cells which originated are the plant parental cells from the process of photosynthesis. In general, intuition is the second set of species which started evolving are the animal parental cell. But this assumption is false. The true second set of species to originate are not the parental cells of animals. The second set of cells to develop are the parasitic cells which cannot survive independently for their food but are dependent on the plant cells. But as per the sequence of evolution the first stable system of species to evolve are plant and animal cells together. This suggests the system of plant cells and parasitic cells collapsed. This is because the parasitic species were totally dependent on the plant cells and after a point the equilibrium gets disturbed and the pair collapses. When the next cycle starts it again follows the same order of plant cell and parasitic cell. But if this might have continued forever then the evolution must have come to a halt. This is not the case which suggests after a few cycles of the plant and parasitic system the combination no longer existed. This became a part of permanent evolution exclusion and the pair no longer existed [3, 4]. This complete process is called as collapse and evolve approach in natural evolution as in Fig. 1.

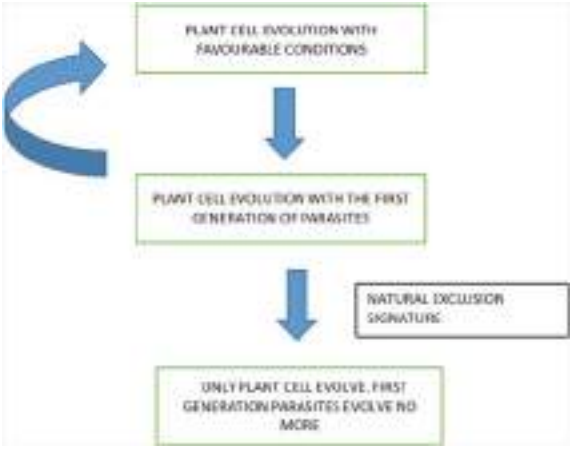

Fig. 1 Flow in natural evolution

3.2 Collapse and Evolve in Hardware Sequences

The aim of the work is to implement the collapse and evolve approach in hard ware sequences. The algorithm is developed on a model comprising of one input block, three decision blocks, two registers for each decision block and finally two output blocks. The whole algorithm is demonstrated on the patterns possible from this hardware design. The general way in which a sequence is implemented in above design is the input is triggered first. The control enters decision block1. If the decision is made the output is stored in the registers. Then control is transferred to decision block 2 waits for any decision, saves it in registers and then to decision block 3. After the control is out of decision block 3 then the data saved in two of the total 6 registers is implemented at the output. This is conventional method of hardware sequences implementation for the above design. Here a lot of redundancy is involved where even if decision is made in decision block 1 due to the sequential nature the flow runs through decision block 2 and 3. In the collapse and evolve algorithm the system initially operates in native mode. Native mode is when the system operates like the conventional system. As the native mode is ON the training module is up. When the training module reaches the pre-computed threshold the skip sequences are implemented and is called as skip mode. In skip mode when input is triggered the trained sequence is implemented.

Upon entry into skip mode, the feedback module goes up to track the missed input responses. If the feedback indicates the skip sequence fails above a threshold the system enters back to native mode. This is called as the collapse in hardware sequences. This is similar to the plant and parasitic system which collapses after the equilibrium gets disturbed. As cycle continuous in natural evolution. The hardware sequence in native mode gets the training module up and cycle between native and skip mode continuously. Each time collapse occurs an exclusion index is raised by one. When the exclusion index crosses the threshold then the skip mode becomes a permanent exclusion for the particular hardware sequence and only the native mode gets implemented. This resembles the evolve in natural evolution where plant and parasite system became a natural exclusion signature. Here the hardware sequence becomes an exclusion for the hardware model [5–7].Thus, efficiently implementing the natural evolution process on a hardware model as in Fig. 2.

3.3 Reliability Improvement Using Global Mutation Trigger

In AI algorithms reliability improvement improves the efficiency of the outputs. Global mutation trigger is one of the reliability improvement methods used. This is included in the algorithm to remove any early defects. If there is skip mode exclusion index raised to 1 where the exclusion should be 0 caused by a false early alarm. Global mutation trigger is a mechanism which captures the exclusion state of different systems using similar algorithm and computes a mean value of exclusion when trigger

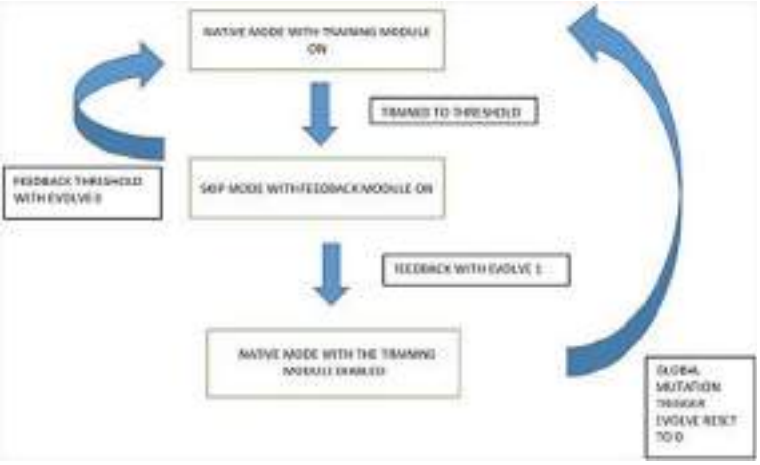

Fig. 2 Flowchart of the proposed algorithm

is raised. If the global exclusion sign is indicative of a false alarm then it re-triggers a signal that a false evolve has occurred and the system is reset to the native mode with the training module up and enable skip mode entry.

3.4 Algorithm Demonstration on Arduino-Based Model

The demonstration of the algorithm was performed by constructing an arduino-based model to implement the different hardware sequences as suggested above.

The input, decision block, registers and output blocks model was constructed. Arduino is coded with hardware sequences one by one to demonstrate the native mode then the skip mode and the evolve. The global trigger is finally implemented after the collapse and evolve processes ran successfully on the arduino model. The latency and power parameters are compared using the vivado tool by coding the hardware internal sequences in native and skip mode [8–10].

4 Results

4.1 Arduino-Based Implementation of Native Mode

In the arduino model is constructed as shown in Fig. 3. The code for the native mode sequence 1 is being implemented with the training module ON as shown in the figure below. The functionality obtained is as expected in the proposed flow of the

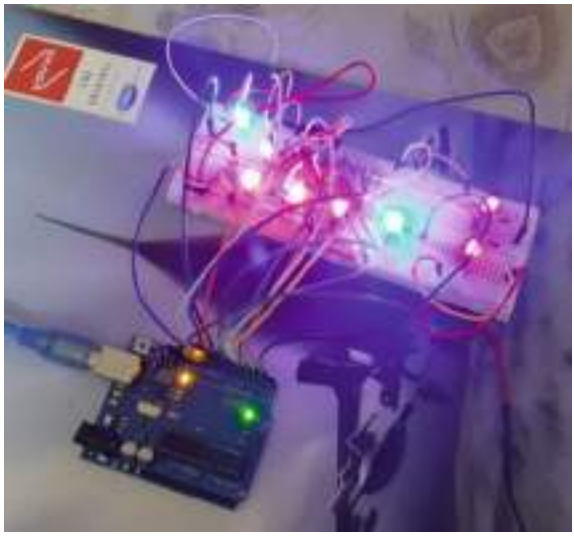

Fig. 3 Arduino-based model in native mode

algorithm. The flow started from the input block then the control went to the decision block with the temporary output being stored in the registers and the desired output mapping to sequence 1 being implemented.

4.2 Arduino-Based Implementation of Skip Mode

The skip mode is implemented on the arduino model for sequence 1 as shown in Fig. 4 below. The entry to skip mode after training module reached the predetermined threshold for switch from native mode to skip mode was proper and the sequence implementation in the skip mode was as expected proving the correctness of implementation of the proposed algorithm.

4.3 Latency Analysis of Both the Modes

Both the native mode and skip mode of hardware sequences are implemented by simulations on the Xilinx ISE tool to determine the time to produce stabilize outputs which becomes the latency in implementation of the sequence. Improved latency is observed in the skip mode. The observed latency of skip mode is 50ns and native mode is 80ns as shown in Figs. 5 and 6. Thus, the proposed algorithm helps in improving the latency.

Fig. 4 Arduino-based model in skip mode

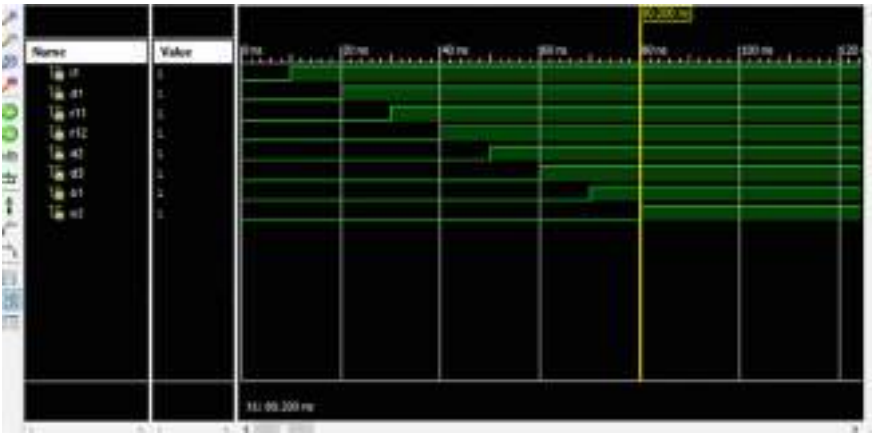

Fig. 5 Latency of nearly 80 ns in native mode

4.4 Power Analysis of Both the Modes

Both the native mode and skip mode of hardware sequence are implemented on the vivado tool to determine the power consumption of both sequences. The power consumption in native mode is around 0.274W whereas power consumption of skip mode is around 0.120W. Reduced power consumption is observed in the skip mode. This suggests that improved power consumption can be obtained by implementing

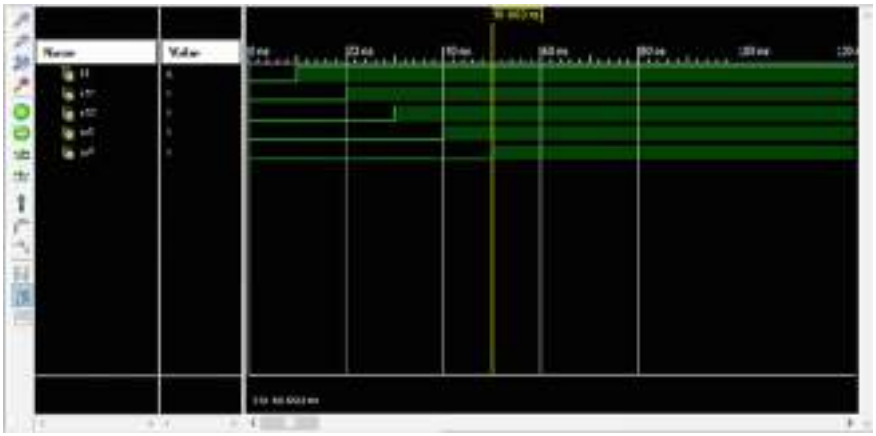

Fig. 6 Latency of nearly 50 ns in skip mode

Fig. 7 Power consumption in native mode

Total On-Chip Power (W)	0.274
Dynamic (W)	0.152
Device Static (W)	0.122
Total Off-Chip Power (W)	0.000
Effective TJA (C/W)	11.5
Max Ambient (C)	81.8
Junction Temperature (C)	28.2

Fig. 8 Power consumption in skip mode

Total On-Chip Power (W)	0.120
Dynamic (W)	0.000
Device Static (W)	0.120
Effective TJA (C/W)	11.5
Max Ambient (C)	83.6
Junction Temperature (C)	26.4

the proposed collapse and evolve algorithm over hardware sequences (Figs. 7 and 8).

4.5 Implementation of Global Mutation Trigger

To demonstrate the phenomenon of global mutation trigger a bluetooth module is interfaced with the arduino-based model developed. After interfacing of the bluetooth module normal and skip mode are implemented with the global mutation trigger ON

which helps to remove any false exclusions given by algorithm. Global mutation trigger is basically for re-entry of the subsystem back to native mode if any false permanent exclusions occur. The arduino model with blue-tooth interfaced implemented the native and skip modes as per the proposed flow suggesting the correctness in implementation of global mutation trigger shown in Figs. 9 and 10.

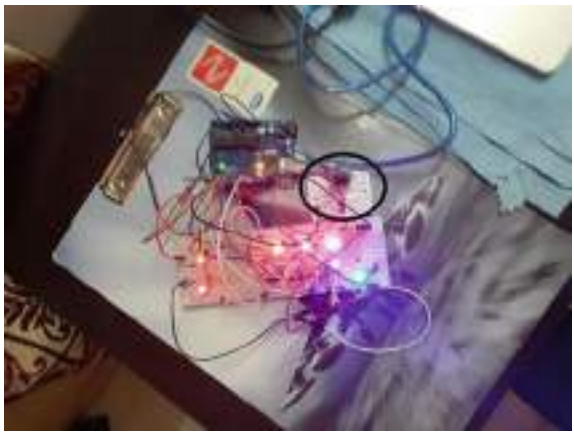

Fig. 9 Native mode with blue-tooth (encircled)

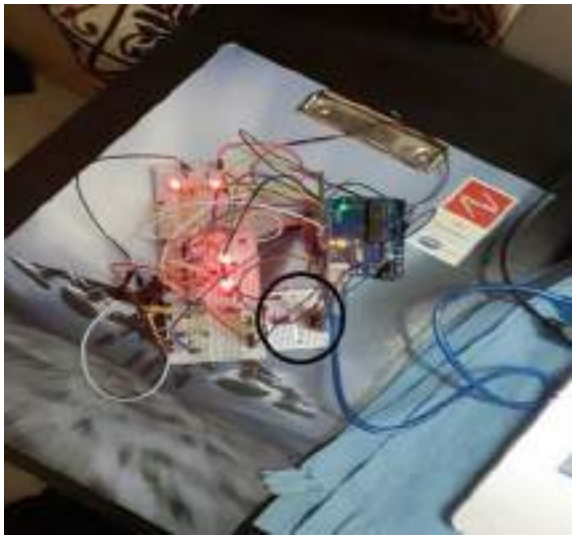

Fig. 10 Skip mode with blue-tooth (encircled)

Sequence number	Latency(ns)	Power consumption(W)
1	80	0.274
2	80	0.274
3	80	0.274
4	60	0.194
5	80	0.274
6	80	0.274
7	60	0.194
8	80	0.274
9	80	0.274
10	80	0.274
11	60	0.194
12	60	0.194
13	80	0.274
14	60	0.194
15	60	0.194
16	40	0.161

Fig. 11 Latency and power parameters in native mode for all the scenarios

4.6 Subsystem Level Regression Results of Latency and Power

The algorithm becomes an efficient and reliable methodology if all the possible sequences show the same latency and power improvement. For the arduino based model developed with one input block, three decision block and two output blocks a total combination of 16 hardware sequence were possible. The algorithm regression is run on all possible sequences and the net gain in latency and power are tabulated. Each and every possible sequence at a subsystem level has shown improvement in latency and power which indicates the efficiency of the proposed algorithm (Figs. 11 and 12).

5 Conclusion

Nature-inspired computing and algorithm development have been one of the fast-growing areas to improve the microarchitectural performance parameters of subsystems in the hardware domain. In the work carried out a keen observation is made on the collapse and evolve methodology occurring in nature and a computational algorithm flow and implementation is developed. This algorithm flow is then implemented on an arduino based hardware model to demonstrate the correctness of the algorithm and the hardware internal sequences which are improved are implemented using vivado tool. Finally, the performance parameters of latency and power consumption of the subsystem are compared in conventional method and collapse and evolve algorithm

Sequence number	Latency(ns)	Power consumption(W)
1	50	0.120
2	50	0.120
3	50	0.120
4	30	0.120
5	50	0.120
6	50	0.120
7	60	0.120
8	50	0.120
9	50	0.120
10	50	0.120
11	30	0.120
12	30	0.120
13	50	0.120
14	30	0.120
15	30	0.120
16	10	0.120

Fig. 12 Latency and power parameters in skip mode for all the scenarios

which is proposed as a part of the work. It can be clearly observed that there was a decrease in the latency and amount of power consumed for implementation of sequences within the subsystem in turn improving the overall performance of the subsystem which uses the collapse and evolve approach.

References

1. N. Siddique, H. Adeli, *Nature Inspired Computing: An Overview and Some Future Directions. Cognitive Computation* (Springer, Berlin, 2015)
2. E. Lopez-Rubio, E.J. Palomo, E. Dominguez, Bregman divergences for growing hierarchical self-organizing networks. Int. J. Neural Syst. **24**(4), 1450016 (2014). https://doi.org/10.1142/S0129065714500166
3. I. Prigogine, *The End of Certainty* (The Free Press, New York, 1996)
4. L.N. De Castro, Fundamentals of natural computing: an overview. Phys. Life Rev. **4**, 1–36 (2007). https://doi.org/10.1016/j.plrev.2006.10.002
5. L. Kari, G. Rozenberg, Many facets of natural computing. Commun ACM. **51**(10), 72–83 (2008). https://doi.org/10.1145/1400181.1400200
6. M. Ghosh, P. Sarkar, M. Saha, Nature-inspired computing behaviour of cellular automata, *in Evolving Technologies for Computing, Communication and Smart World*. Lecture Notes in Electrical Engineering, vol 694, ed by P.K. Singh, A. Noor, M.H. Kolekar, S. Tanwar, R.K. Bhatnagar, S. Khanna (eds) (Springer, Singapore, 2021). https://doi.org/10.1007/978-981-15-7804-5-11
7. W. Zhang, B. Gao, J. Tang et al., Neuro-inspired computing chips. Nat. Electron. **3**, 371–382 (2020). https://doi.org/10.1038/s41928-020-0435-7
8. J.S. Nagendra, N. Ramavenkateswaran, An overview of low power design implementation of a subsystem using UPF, in *2020 International Conference on Inventive Computation Technologies (ICICT)* (Coimbatore, India, 2020), pp. 1042—1047. https://doi.org/10.1109/ICICT48043.2020.9112524

9. P.V. Vimal, K.S. Shivaprakasha, IOT based greenhouse environment monitor- ing and controlling system using Arduino platform, in *2017 International Conference on Intelligent Computing, Instrumentation and Control Technologies (ICICICT)* (Kannur, 2017), pp. 1514–1519. https://doi.org/10.1109/ICICICT1.2017.8342795
10. D. Macko, K. Jelemensk´a, *Managing Digital-System Power at the System Level* (Africon, Pointe-Aux-Piments, 2013), pp. 1–5. https://doi.org/10.1109/AFR-CON.2013.6757781

Home Shanti (An Edge Computing-Based IoT System for Complete Home Security and Safety)

Atharv Tendolkar, Amit Choraria, K. S. Adithya, and Pramod Kumar

Abstract The post-COVID-19 era redefines safety and security for all of us. With increasing population, higher rate of unemployment and faster pace of life, we need a solution that can ensure safety as well as peace of mind for the family and their home. The proposed solution Home Shanti provides an integrated and holistic home management system which autonomously and remotely monitors the home without physical presence. It makes use of edge computing mechanisms to take on-board decisions via interaction with the sensors in the IoT environment. Smart home security is offered with a network of specific sensors. In addition, safety of the residents is taken care of in various regions of the house. The system is in constant touch with the owner through cloud, remote monitoring and real-time decision making. Hence, Home Shanti is the perfect solution for the safety and security of urban and rural home environments and its family, truly a 'shanti' peace of mind for the homeowner and his/her family.

Keywords IoT · Edge computing · Arduino · Thingspeak cloud · Sensorics · Safety · Security · Sustainable

1 Introduction

The idea behind Home Shanti bloomed after assessing the situation in urban home environments and need for safety and security. The inspiration was from 'Om Shanti', wherein we are protected and have a peace of mind. Building on this theme the solution offers not only security of the home but also safety of its residents. It offers a complete and holistic home management solution with varied capabilities. The module basically consists of a microcontroller-based central processing system with antennas for communicating with sensors and two-way data movement to user through cloud. It is shaped like a 'Trishul', which also signifies safety and protection of the house and its members. The system is able to analyze real-time data, perform

A. Tendolkar (✉) · A. Choraria · K. S. Adithya · P. Kumar
Department of Electronics and Communication Engineering, Manipal Institute of Technology, Manipal, India

S. Rawat et al. (eds.), *Proceedings of First International Conference on Computational Electronics for Wireless Communications*, Lecture Notes in Networks and Systems 329,
https://doi.org/10.1007/978-981-16-6246-1_26

on-device computed personalized feedbacks and alert the user through cloud-based architecture.

The house is monitored through a network of sensors placed at strategic locations to ensure optimal utilization, and maximize monitoring. Home Shanti measures the following including temperature, intrusion, gas leakage, smoke detection, flame detection and door ajar. In addition it also has a smart camera system embedded on the main entrance walls to detect the presence of someone at the door and record video based on motion detection. All the possible door entrances have magnetic strip sensors and vibration tamper alert sensors to detect instant door ajar. It makes use of infrared screens on windows for intrusion detection. All these provide a complete smart security solution for the home, but Home Shanti goes one step beyond and provides safety with its signature Home-Sense feature. This involves a network of sensors placed in the garage, kitchen and other areas where accidents may occur, and alerts the users in events of risk. What sets 'Home-Shanti' apart is that it can give personalized suggestions based on user usage patterns through a strong analytics feedback system. The entire system can be seamlessly integrated with existing house infrastructure and has multi-domain scaling ability. It has a thinking power of its own which enables it to take on-board decisions by itself and act on-site instead of consulting cloud-based processes. The owner has the ability to Arm/Dis-Arm the system as needed and access all the data real time through the mobile app via cloud. This fusion of a smart and real-time security monitoring with region-wise safety in the house provides the perfect solution for the modern-day homeowner and his/her family.

1.1 Literature Review

In order to ensure an efficient and sustainable monitoring of the home environment with minimum latency, we need systems that have intelligence at every node and not just at a central level. Currently, home security solutions are a costly proposition for most urban dwellers [1]. Moreover, these systems only provide cameras and motion detectors and do not provide a complete holistic security solution. Many a times the security cameras may detect the video, but no alerts will be given in real time. The available solutions today are not capable of mitigating the triggers on their own and only rely on reflecting sensor data to the owner. Moreover, these systems do not provide safety features which is a highly important function besides security of the home. This is where Home Shanti comes into picture, with the theme 'peace of mind for you and your home'. It offers a holistic real-time security monitoring along with the 'Home-Sense' feature that ensures the safety of the residents. Home Shanti has an intricate IoT network which offers a physical to digital mapping of the home environment. Data collection and processing play a key role in the development of this technology [2]. Sensory node information has to be transmitted across to the server or IoT platform over a secure and reliable network. Such a system provides remote accessibility and after analysis can notify the user accordingly. Designing

the right IoT framework is quintessential, which provides a better user experience along with reliability and security of the infrastructure. Home residents will thus be able to interact better with the sensorics and the home parameters. Furthermore, the framework allows for an intelligent data processing flow, and search-control capabilities [3]. Users can use the secure connection validated with system APIs and dual-step verification for critical information. Extrapolating on these ideas, the modern age solutions need efficient data points to work with triggers and sequence flow [4] (Table 1).

A Comparative Study between existing home security solutions and Home Shanti is shown in Table 2. What sets it apart is the affordability, convenience of remote monitoring and proudly 'Made in India'. Unlike the conventional solutions, Home Shanti has an edge computing ability that can take on-board decisions on the hardware and recommend personalized suggestions based on analytics. A user-friendly manual is complemented with the offering of Home Shanti for a better human-centered approach by providing targeted and successful implementations. This careful design offers the perfect niche solution for the urban dwellers and ensures their security and safety.

Table 1 Comparative study

Parameters	Home Shanti
Cost effective	Offers extensive Features at the right cost to the urban dwellers
User friendly	Simple and Ergonomic design
Less carbon footprint	Up-to 5% lesser power consumption than current imported alternatives
Multifunctional	Offers not just security but safety for the entire household

Table 2 Sensor data over a week at hourly frequency

	PIR Motion sensor (in Volts)	Magnetic strip sensor (in binary)	Vibration sensor (in Hz)	Temperature sensor (in °C)	Methane gas sensor (in ppm)
Min	0 (No motion detected)	0 (Door closed)	0 (No vibrations)	24	250
Max	2 (Motion Detected)	1 (Door Open)	50 k (High Vibrations)	32	450
Variation	2	1	50 k	8	200

2 Working and Modelling

2.1 System Architecture

The basic design structure of Home Shanti can be broadly divided into 4 levels. Each level forms an integral part of the entire structure and overall system that would collectively monitor a home which one can call Danger- Proof [5]. The 4 levels work seamlessly with each other as shown in Fig. 1. The above levels can be described as follows:

1. **Sensing**: This level forms the foundation of the infrastructure where different sensors collect real-time data from the physical environment.
2. **Processing**: The collected data signals then enter the brain of the system where they are converted into sensible information that is sent to the cloud for storage.
3. **Interfacing with Analytics**: The information sent to the cloud is processed upon and can be used for creating targeted analytics. The same can be accessed and monitored from the cloud and mobile application.
4. **Feedback**: User notifications are generated automatically from the brain of the system along with the cloud. Thus it gives warnings, when possible threat or risk is detected and can take action if the house owner fails to address the issue after a certain time to prevent the possibility of further damage.

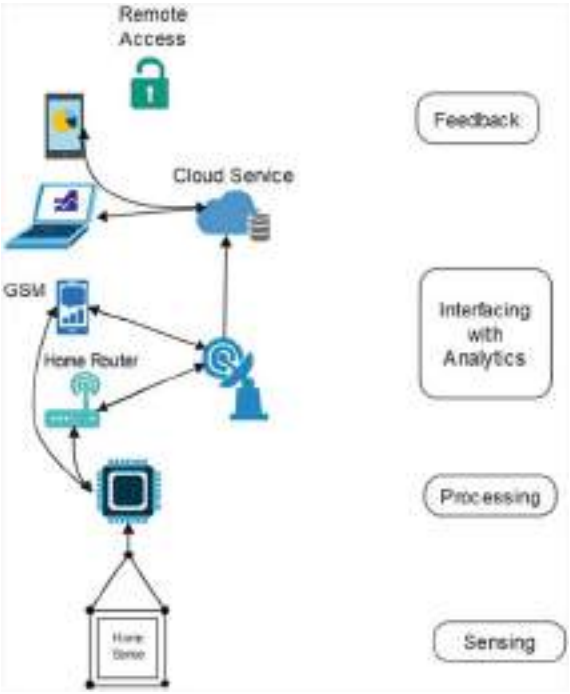

Fig. 1 System Architecture

2.2 Sensors

PIR Motion Sensor: The PIR HC-SR501 module senses motion of a human body within the sensor's range which is radially <140° and linearly 3m to 7m with an adjustable delay time of 5s to 200s. The working DC voltage and temperature range is 4.5V to 20V and 20°C to 80°C, respectively. Being placed at all the windows of the house it covers a good range of the entire room and can detect any motion in its proximity. The linearity error being < ±2% due to sudden heat changes makes it very accurate.

Magnetic Strip Sensor: A Door lock proximity switch placed at the door frame will sense if the door is opened and alarms the user of the activity. With a sensing distance of approximately 15–25mm and a linear error of <2%, it comes out to be very accurate.

Methane Gas Sensor: MQ-4 High Sensitivity Gas Methane (CNG) Detector Sensor Module with a detection range of 300~10000ppm and a resolution of 1ppm is placed on the ceiling of the kitchen. The sensor can detect if someone leaves the gas stove switched on but not in use, sending an emergency alert to the owner to prevent any fire hazard. With a sampling rate of 1s and an accuracy of 2% it is very sensitive to any such danger.

Flame Sensor: Also placed on the ceiling of the kitchen along with the methane gas sensor together acting as a fire-proof team in situations when MQ-4 sensor is active while the flame sensor is not sensing anything, it will immediately produce an alarm to the user thus preventing such fire hazards. It detects flame having wavelength within the range of 760nm to 1100nm from the light source. Detection range is up to 100cm with detection angle of about 60 degrees.

Vibration Sensor: Vibration sensor module alarm Motion sensor module vibration switch SW-420 module based on the vibration sensor concept and LM393 comparator is used to detect if there is any vibration that is beyond the threshold which can be adjusted using an onboard potentiometer. It is placed at the main door of the house to sense any physical impact or mechanical vibrations produced by any device used by the intruder trying to bypass the magnetic strip sensor.

Surveillance Camera: An ESP32 Camera placed at the main door of the house is used to capture the area of access. This feed is processed in real time through Arduino which helps to detect possible intrusions. The live feed is also transferred to the Thingspeak cloud platform through which it can be accessed for past footage if necessary. Since all these sensors are spread across the home at optimal positions, they are represented as the corners of the Home secured by the Home Shanti system as represented in Fig. 2. All these sensors with their individual accurate sensing capabilities combine to form a Home-Sense system which is foolproof and robust.

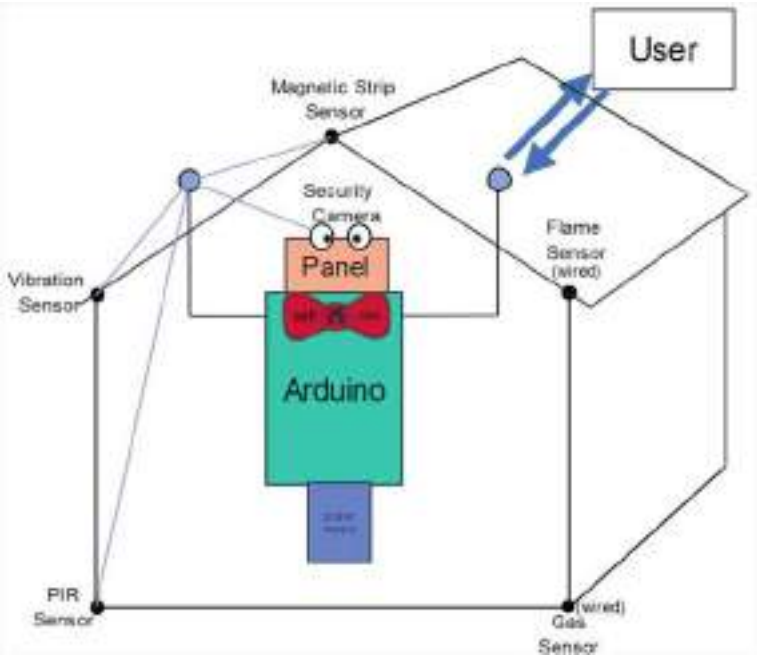

Fig. 2 Schematic of Home Shanti

2.3 Structure and Schematic of the Home Shanti

The module consists of wireless as well as wired sensors across every corner covering the entire house along with a surveillance camera to monitor and detect outsiders and warn the owner of possible chances of theft. It is also capable of saving rudimentary face profiles to auto-set the home features and access controls. Magnetic strip sensor and vibration alert sensor are placed on doors to detect intrusion, IR scanners on all windows and finally a combined kitchen safety module is what makes the system a complete home-safety monitoring one. Various sensor data from the different nodes are relayed to the cloud through the Central Arduino-based processor, wherein certain actions and triggers can be taken on the edge for faster response time capability. The data is sent to cloud through Wi-fi module in cities and GSM-based internet in places where Wi-fi capabilities may not be feasible. This data is then processed in the cloud and real-time house monitoring can be accessed by owner through cloud and mobile app from anywhere in the world. The display panel is for displaying information like date, alerts, reminders and sensor values. This summarizes the structure and schematic of the Home Shanti system.

2.4 Practical Development

- The idea that everyone needs a sense of security in the place where we live inspired the development of Home Shanti which uses parallel sense technique along with series coordination to achieve an automated 'Home Guard' system.

- The implementation of Home Shanti is being done module-wise for better system analysis and improved user experience. Figure 3 shows a rudimentary block diagram of the system showing how the sensors work simultaneously along with the necessary network communication with each other and interfacing with the Arduino.
- Subsequently, the processed data from the Arduino is sent via Wi-Fi or GSM module to the Thingspeak platform and then to a user-friendly interface application where the data is optimally represented and the user is notified of the threat.
- Writing the code: The Arduino IDE is used for programming and interfacing the Arduino to enable it to connect to the home Wi-Fi network and relay the collected sensor data real time to the cloud, via its appropriate Thingspeak Write API key. The data in the cloud can then be used for statistical analysis and to give targeted solutions.
- A smart relay-based emergency may be established to take certain preventive measures and inform concerned authorities if the owner fails to respond to the alerts so that situation can be controlled.

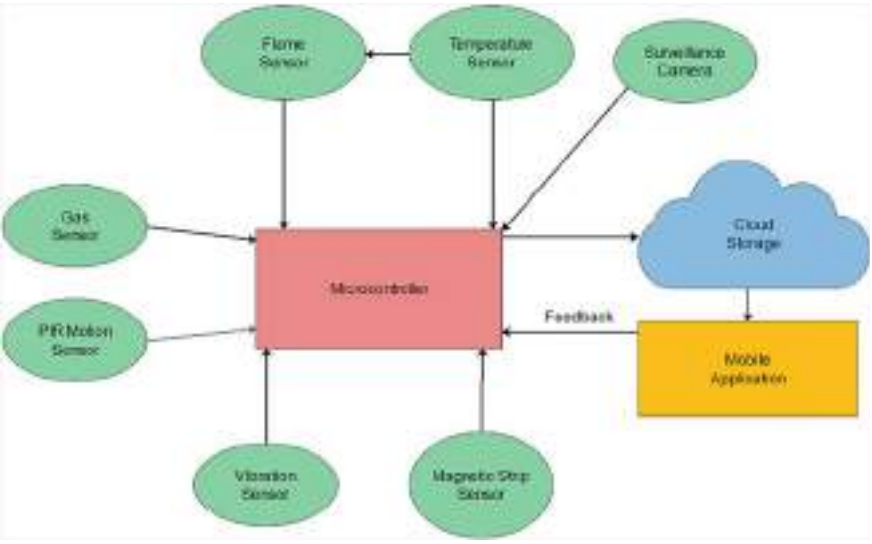

Fig. 3 Block representation of circuit

The block diagram and above description of the development help us to understand the blueprint of Home Shanti and the various modules involved to give a comprehensive home security analysis and real-time data logging of these parameters. The on-board intelligence is capable of taking decisions by itself as programmed by user. The robust system infrastructure adds to the reliability, safety and security aspect of the modules.

2.5 Circuit Development

The circuit development involves the sensor nodes like gas sensor, temperature sensor, magnetic sensors and more which are connected to the analog and digital pins of the Arduino. Meanwhile, the esp32 camera communicates with Arduino via TX and RX pins and thereafter image recognition takes place through cloud via Wi-Fi module. The Arduino sends the processed data to the Thingspeak platform via Wi-Fi module with the ESP8266 acting as a transceiver. The user interface and mobile application uses the pre-processed cloud data and takes the required action appropriately by notifying the user and waiting for the user to respond. If this remains unaddressed the automated system informs the required authority and takes edge computed based measures to prevent further mishap. The Home automated system, after taking the required actions keeps on updating the result real time to the cloud [6]. The complete security, Autonomy and error feedback mechanism on the Home Shanti make it a fool-proof, intelligent and trustworthy system which can think, as well as speak for itself [7]. The edge computing-based localized intelligence involves previous test cases and database through which it can take decision [8]. A detailed overview of the circuit involved in the design is shown in Fig. 4.

3 Results and Development

3.1 Circuit Realization

The overview of the Home Shanti system using Wi-Fi module interfaced with the Thingspeak cloud platform and user application completes the basic flow to rig up the actual circuit. Module-wise implementation of the system ensures that every module is properly tested and is reliably able to communicate with the Arduino. Fig. 5 is the circuit module for the Home-Sense of the entire house along with Arduino as the brain of the system and the Wi-Fi module as the communication channel to the cloud.

The sensors powered by the Arduino Uno board using its on-board 5V supply and GND connections. Analog port of the Arduino helps to import real-time sensed

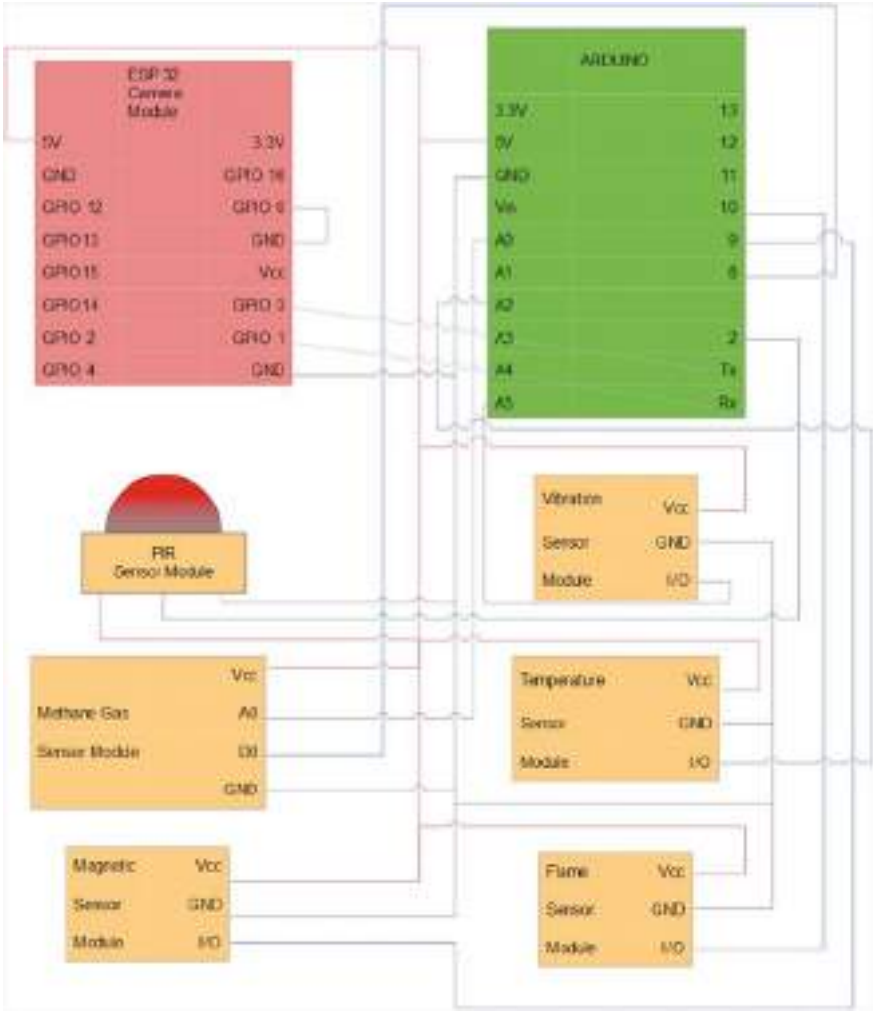

Fig. 4 Circuit Diagram Overview

data from the methane, temperature and vibration sensor and convert it to the corresponding calibrated values while the Digital port helps to import already processed data from the methane, flame and PIR sensor.

3.2 Interfacing on Thingspeak

- The platform Thingspeak being an IOT analytics platform in cloud storage that helps receive, visualize, analyze and work on the various sensor data.

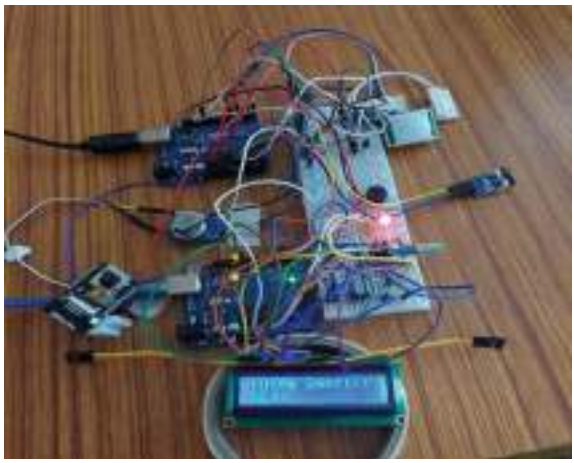

Fig. 5 Circuit Realization of Home Shanti

- Initial setup of our model requires signing up and creating various channel for each of our sensors [9].
- Each sensor is allotted a new channel which has a unique write and read API key that can allow our system to connect with Thingspeak platform accessible from anywhere over the internet through a user interface application.
- As shown in Table 2, the various sensors help to map the physical environment to digital.

3.2.1 Home-Sense and Safety

The Home Shanti system consists of Home-Sense feature for the Entry points and hazard safety features for the Kitchen which are explained in the following section :

Home-Sense for Entry points:

Windows: The PIR sensors as shown in Fig. 6 are placed on all the windows of the house thereby covering the entry point access areas. The graph attached indicates how the sensor value remains constant at 1 unit and falls to 0 units during the detection of any motion and trips the alarm thereby addressed to the user.

Room-Doors:

The Magnetic strip sensor module attached to the frame of all doors of the house is shown in Fig. 7. The sensor maintains 50% signal when the door remains closed while disconnects the circuit making the signal fall to 0% when the door is opened by the intruder thereby alerting the user via an alarm.

Main Door: Similar to the room doors, the main door has a magnetic strip sensor along with a Vibration sensor module on the inside while a ESP 32 camera module on the outside. The magnetic strip sensor will function similarly as it did for all the

Fig. 6 Home-sense for windows

Fig. 7 Home-sense for doors

room doors while the vibration and the camera module will provide further safety to the most probable entry point, functioning of which is mentioned in the following points.

- Vibration Sensor: The Vibration Sensor Module attached to the main door as shown in Fig. 8, will prevent any forced physical impact applied by the intruder. The graph attached shows that the circuit signal remains constant as long as there are no vibrations while signal suddenly oscillates indicating a physical impact to the door immediately alerting the user via an alarm.
- ESP32 Camera Sensor: A pre-trained camera module as shown in Fig. 9 is placed outside the main door of the house. Apart from providing the 24/7 live feed to the user which is accessible from anywhere it can recognize the homeowners through object detection mechanism, acting as a facial recognition module. Any new face will be considered as an intruder by the camera which then immediately sends an alert to the user via notification. The user can then access this footage through

Fig. 8 Home-sense for main door

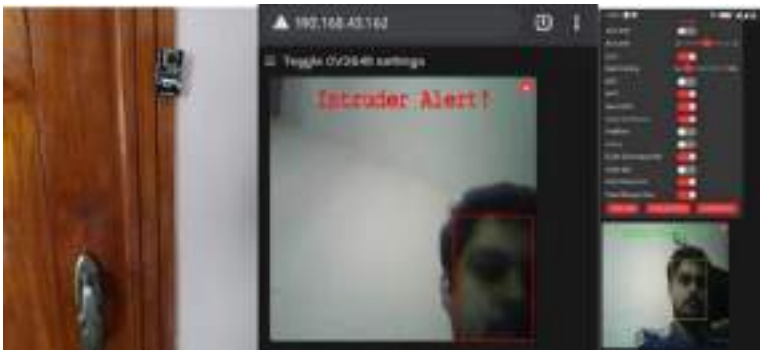

Fig. 9 An ESP32 camera module attached to the main door and its interface

cloud storage to verify the person's identity and use the module as an intercom as well.

Home Safety for Kitchen:

The Methane gas sensor as shown is placed in the proximity of the gas stove but at the same time at a sufficient distance from the flame. The sensor signal is transmitted wirelessly via the Wi-Fi module when shown in terms of a graph will maintain a constant signal of around 250 with occasional dips but rises as high as 400 when it senses methane gas within its proximity indicating a danger level [10]. As soon as this data crosses the threshold of 330 the system while in arm mode, it will trip an alarm alerting the user.

The temperature sensor LM35 is also placed alongside the gas sensor as shown in Fig. 10, the circuit signal of which is maintained with certain signal of which is maintained within certain range indicating room temperature until sudden rise above indicating presence of flame near it and tripping the alarm to alert the user when the system is in armed mode. The series dependency is shown between the temperature and gas sensor when in disarm mode. In this mode the gas sensor data if above the

Fig. 10 Home-sense for kitchen

threshold will also take account if the temperature sensor which if low indicating the absence of flame will trip the alarm alerting the user that the gas stove is on while nothing is being cooked. Hence, providing an additional safety feature to the intelligent Home-Sense.

4 Conclusion

After analyzing and looking at the process of development of Home Shanti, it is seen that this system provides the perfect home security and safety solution for today's home dweller. It is seen that this system has the ability to remotely manage homes and prevent possible thefts and intrusions. Moreover, it guarantees the safety of all members in the house by providing personalized feedback based on analytics and helps to reduce the possibility of accidents and dangers. This innovation will play a crucial part in modern era urban environments where cases of theft and accidents due to appliance failure still exist. The new age personal home assistant is not just the one that can talk with you, but a one that you can rely on for your home's safety and security, like Home Shanti. This will enable the urban dwellers to stay carefree whenever they go outside and even when they are inside.

4.1 Future Development

Home Shanti is in its final stages of development and testing. The entire process will involve thorough beta testing and calibration of all sensors for optimal event detection in its IoT environment. This will be followed by data transmission to the cloud along with adaptive sensor fusion through the edge. Many other need-based sensors will be added as per consumer requirement. The real-time events will be reflected with minimal latency in the cloud and mobile app which is under development. Data Analytics is going to play a key role in embedding intelligence and suggesting targeted personalized suggestions to enhance safety and security in the home. This

will involve analyzing the user patterns and detecting the accidents or threshold values, on which machine learning tools may be utilized to find out the possible faults and causes of the mishaps. The system will be able to offer recommendations and diagnosis through a continuously evolving case study algorithm. Strategic positioning of the sensors along with custom planning and modelling of the environment will be done. The brain of the system will be in an enclosed Trishul-shaped safety box that will be the hub for data transfer and control for the system. This will result in a prototype to industry-ready solution that can be deployed to ensure the security and safety of urban homes of today.

4.2 Future Scope

Home Shanti has a lot more features than what meets the eye. With its ability to be easily integrated into a variety of platforms, it has hassle-free installation and use, and can be scaled to provide various other multi-domain applications. It is basically a complete remote home management by itself. This module can be used to handle many autonomous applications in the house like smart lighting, robotic vacuum cleaners, automated washing machines and driers and even robotic kitchens. Any of these automated tasks can be integrated with the Home Shanti's' IoT network grid that can provide remote and complete house monitoring at fingertips for the right fingerprint. Dynamic system response and edge computed solutions result in intelligence at the processing level for faster performance and better sensor response management. Hence it is a very innovative and reliable device that will surely guarantee the safety and security of modern home dwellers. The fact that the device keeps on adapting with use provides better results with each use. It continuously has over the air updates for error-free and reliable operation. It is not just the technology but the results that one can rely on, a truly 'seeing is believing' example. Home Shanti makes home management hassle-free and creates a sense of trust in this technology. A low cost alternative that surely will be an integral part of today's modern homes. With rapid developments in edge computing and 5G rapid speeds, the urban dweller is rest assured to get faster computation and lower cost. Moreover, it provides the right data for the residents to take appropriate actions and preventive measures. The development of Home Shanti provided a gist of the technology behind it, electronics and design that was all seamlessly integrated to create your own complete home management system. A technical insight into how the variety of sensors were interfaced with the Arduino linked to the house-wide IoT network provides a real-time home system status right on the homeowners cell phone, one click away, from anywhere in the world.

Hence, the Home Shanti provides a sustainable, smart, ergonomic solution to the current safety and security in modern homes and with its multi-domain applicability, economic models and wide scalability it serves as a perfect home assistant for the urban age family.

References

1. N. Komninos, E. Philippou, A. Pitsillides, Survey in smart grid and smart home security: issues, challenges and countermeasures. IEEE Commun. Surv. Tutor. **16**(4), 1933–1954 (2014)
2. H. Huang, S. Xiao, X. Meng, Y. Xiong, A remote home security system based on wireless sensor network and GSM technology, in *2010 Second International Conference on Networks Security, Wireless Communications and Trusted Computing*, vol. 1 (IEEE, 2010), pp. 535–538
3. A.C. Jose, R. Malekian, Improving smart home security: Integrating logical sensing into smart home. IEEE Sens. J. **17**(13), 4269–4286 (2017)
4. D. Geneiatakis, I. Kounelis, R. Neisse, I. Nai-Fovino, G. Steri, G. Baldini, Security and privacy issues for an IoT based smart home, in *2017 40th International Convention on Information and Communication Technology, Electronics and Microelectronics (MIPRO).* (IEEE, 2017), pp. 1292–1297
5. L. Yang, S.H. Yang, F. Yao, Safety and security of remote monitoring and control of intelligent home environments, in *2006 IEEE International Conference on Systems, Man and Cybernetics*, vol. 2 (IEEE, 2006), pp. 1149–1153
6. X. Huang, P. Craig, H. Lin, Z. Yan, SecIoT: a security framework for the Internet of Things. Secur. Commun. Netw. **9**(16), 3083–3094 (2016)
7. A. Tseloni, R. Thompson, L. Grove, N. Tilley, G. Farrell, The effectiveness of burglary security devices. Secur. J. **30**(2), 646–664 (2017)
8. P. Kumar, A. Braeken, A. Gurtov, J. Iinatti, P.H. Ha, Anonymous secure framework in connected smart home environments. IEEE Trans. Inf. Forensics Secur. **12**(4), 968–979 (2017)
9. R.K. Kodali, V. Jain, S. Bose, L. Boppana, IoT based smart security and home automation system, in *2016 international conference on computing, communication and automation (ICCCA)* (IEEE, 2016), pp. 1286–1289
10. Q.I. Sarhan, Systematic survey on smart home safety and security systems using the arduino platform. IEEE Access **8**, 128362–128384 (2020)

Review of V2g System Considering the Grid Impact and Cost Benefit

Umme Kulsum, Ahmed Wasim, and Ravishankar Dudhe

Abstract As years pass by, the world is turning toward clean, renewable energy solutions and environmentally friendly practices. As a result, the use of Electric Vehicles (EVs) is being encouraged for sustainable transportation and they are also considered to be portable energy storing devices. It is highly expected of these EVs to make a major impact in the future grid stability which becomes a major concern when adopting renewable generation due to the intermittency of the sources. The concept of V2G (vehicle to grid) refers to the bidirectional integration between plug-in EVs and the grid which also allows the vehicle to contribute to reactive power support and active power regulation. Adding to that, filtering out harmonics, prediction of renewables' behavior and amending grid operations like stability, volatility, efficiency, etc., are also some features of V2G. This paper covers the overview of design, grid impact, and cost benefit of the V2G technology.

Keywords EVs · V2G · Smart grid · Battery Charging/Discharging · Off-board/On-board charger

1 Introduction

The recent past has brought to light issues concerning climate change and environmental pollution mainly due to energy produced using fossil fuels and natural gases. This has led to increased production and innovation of EVs all over the world [1, 2]. Since a considerable chunk of oil and gas usage has been due to motor vehicles, EVs are expected to reduce this dependency in order to reduce emissions by replacing these oils and gas-based vehicles [1, 3, 4]. Studies show that in a matter of 19 to 20 years, the international car sales will comprise of 30% of EVs. This

U. Kulsum (✉) · A. Wasim · R. Dudhe
Manipal Academy of Higher Education, Dubai, United Arab Emirates

R. Dudhe
e-mail: ravishankar.dudhe@manipaldubai.com

S. Rawat et al. (eds.), *Proceedings of First International Conference on Computational Electronics for Wireless Communications*, Lecture Notes in Networks and Systems 329,
https://doi.org/10.1007/978-981-16-6246-1_27

makes the total percentage of EVs in the world around 25% [5]. EVs have considerable amount of energy stored in them ranging from 10 to 60kWh. The charging and discharging of these EVs ought to overwork the system and deteriorate the life of the battery at some point of time. Such situations might require expensive modifications or upgrades and causes consistency issues. However, emerging concepts of smart grids, bi-directional chargers and battery technologies have introduced the concept of Vehicle-to-Grid (V2G), where EVs can not only draw power but they can also provide power back to the grid enabling efficient charging of EVs. This V2G technology takes into account network constraints by managing the generation dispatch, demand curve, taking peak loads into consideration, and also by regulating frequencies [6]. Adding on, V2G benefits the grid by increasing stability and efficiency whilst decreasing volatility caused by renewables. The bidirectional charger which is used comprises a DC link capacitor. This capacitor injects reactive power, Q into the grid to support the inductive devices demanding high reactive power [7]. This paper covers the overview of design, grid impact, cost benefits and power capacity of the V2G technology.

2 Framework of V2G

V2G is an extremely complicated yet tractable technology as compared to V2H system.V2G is generally avoided in small scale, therefore for large scale operation, it needs groups of GEVs such as GEVs in parking lots, charging stations, smart buildings and number of Vehicle-To-Home(V2H) systems. The framework consists of the following components [7]:

- GEV Charging stations
- GEV Battery swapping station
- Smart building /Parking lots
- Number of V2H systems
- Small renewable Energies
- Aggregators.

The GEVs can be grouped into three types depending on level of energy distribution. These are called clusters [7]. These clusters are mentioned below:

- First Cluster:

  GEVs which use Low-Voltage (LV) like for V2H and V2V systems. They're usually adaptable in residential zones, parking areas, smart buildings, etc.

- Second Cluster:

  GEVs which require Medium-Voltage (MV) like for V2G system. These GEVs correspond to GEV charging stations, such as fast charging stations.

- Third Cluster:

GEVs which also use MV network, but normally not preferred for V2G operation. These GEVs are found in battery stations. This is where discharged and recharged batteries are exchanged.

To make the entire system smart, the main component of the entire V2G system is the aggregator. This aggregator is the interface between EVs and grid and among multiple EVs as well. Therefore, aggregators are mediators between these individual systems and they can be designed uniquely for frequency regulation and managing the charging of the EVs.

3 Grid Impact in V2G System

In recent power electronic equipment, sensitivity to PQ irregularities is high, mainly to sags in voltage and interruptions [8, 10]. The EV batteries and EV charging are impacted due to disturbances caused in the grid. Since V2G deals with multiple GEVs, it is expected to alter the grid power flow, demand charge and demand pattern [11, 14].

These irregularities or disruptions due to PQ may affect the EV charger. This causes a bad impact on the charge current in the G2V through the battery. Contrary to this, the same issue will not be faced in the V2G model [8].

The Society of Automotive Engineers has published a standard J2894/2 that defines the following: suggestions on usage of on-board or off-board chargers (DC or AC) depending on PQ and grid impact due to EV, grid behavior that may reflect on EV charger or battery, values important for PQ stability, vulnerability and also to mention constraints related to controlling power as per recent standards [15].

Bi-Directional Charge system. Bi-directional converters are a vital link between the EV and grid. The charge–discharge mechanism depends on these converters. These bi-directional chargers comprise of a battery connected to a DC-DC converter. This DC-DC converter is further connected to a 3 phase DC-AC converter finally connecting to the 3 phase utility [22]**.**

The EV charger is prone to be interrupted by the voltage sag due to the grid in G2V mode. This poses a threat to the life of the battery which can reduce considerably. But, in the V2G mode, the disturbances are tolerated with less effect on the DC bus [22]**.**

As established before, V2G system is less susceptible to irregularities and disturbances in the grid in comparison to the G2V system that greatly impacts the charger over time. This is simply due to the fact that the energy stored in the G2V charger is entirely dependent on what it receives from the grid. This can also include those irregularities and disturbances in the grid that are transferred to the EV through the DC/DC bus and DC bus capacitor. Whereas in the V2G system, the charging system depends on the battery making it tough for energy to move in opposite direction of

the systems energy flow hence to reducing possibility of deteriorating the battery too soon.

Added advantages of the V2G chargers include their voltage balancing capability during times of dips. Voltage dips usually destabilize the flow due to the sudden increase and decrease, thus these chargers manage safer transitions between voltage values. Therefore, also contributing to reducing transient harmonics [23].

4 Cost Benefit

A report claims that around 2030, the UK power network could benefit by £270 million just by implementing V2G for a year. It also emphasizes that V2G could lead to a £200 million decrease in investment into the national distribution system. The report adds that this is possible by controlling charging times and also when the peak demand of the grid is reduced. An amount of £180 million could be saved by the implementation of EV's in just one year across the world's energy networks only if the timings on when to charge are controlled. By 2030, EV's in V2G could bring up the annual savings in a range of £40 to 90 million [32].

As established, the most effective way to gain considerable returns through implementation of V2G is to consider a fleet or group of EV's like in parking lots instead of independent vehicles. As an example, an entire parking lot owned and controlled by an individual can have the services necessary for successful V2G implementation resulting in an entire generation facility for the grid. These individuals are known as Electric Recharge Grid Operators (ERGO's). These car parking stations should have a minimum of 15 EV's to try to satisfy the 1MW requirement for a group of vehicles as per market conditions [35].

The total profit can be calculated using the following equation:

$$P = C_e * P_v * t \tag{1}$$

where P is the profit earned, C_e is the cost of supplied electricity, P_v is the power supplied by the vehicle and t is the duration of power flow.

In California, the returns are around 0.3$/kWh for over storage on days when there is excess energy to store, but that over storage is possible only during weathers other than summer amounting to around 10% days of the whole year [35].

Ancillary services:

In V2G system, Ancillary services provide balance in supply and demand, maintain grid reliability and facilitate transmission of power. These services not only improve the power system, they also provide cost benefits.

4.1 Voltage and Frequency Regulation

In order to maintain increased market value and ensure low strain on batteries, this is the first and foremost step to be taken in the V2G system [17, 24]. Frequency regulation is achieved when the demand and supply of active power, P is balanced. Such type of regulation is obtained using cyclic generators having high costs or implementing faster charge and discharge rates of batteries [16, 25].

Frequency regulation can be achieved throughout the day unlike overgeneration. Hence, there are higher chances for returns under frequency regulation for example when there's frequency regulation for over a period of 19–20 h, the returns are considerably satisfactory and as per a study, the profit comes up to $1,000. For shorter duration of frequency regulations, returns are neglectable [34, 35].

The highest profit-making potential of V2G reaches its peak when revenue is higher and the cost figures are at their lowest. A study concludes that over a period of 8 years. The net profit could sum up to more than $22,000 in such a case [35].

Consider the following cases for comparative study:

Case1: Frequency Regulation of 8 hours

Case2: Frequency Regulation of 22 hours

Case3: Storing over generated energy for 4 hours

Case4: Hybrid of overgeneration and frequency regulation for 4 and 18 hours respectively.

Profits can be accountable when the investment cost, battery maintenance/replacement cost, etc., are deducted.

Upon comparing the revenue/year and total costs, the profits obtained are as follows:

Case1: $-1,120

Case2: $1,008

Case3: $-2,865

Case4: $3,560.

Hence, we can conclude that frequency regulation of lesser time periods will yield lesser profits and can possibly cause losses. Whereas, longer hours of frequency regulation can yield higher profits. However, a combination of overgeneration storage and frequency regulation can harvest the highest profit approximately around $3,560 [35].

Voltage regulation is achieved when the demand and supply of reactive power, Q is balanced. An EV can respond immediately when regulation is necessary. The battery charger has an embedded voltage controller and is capable of reactive power compensation by varying phase angle of the current as per requirement [26].

Just by regulation, an EV can earn up to $1,250–$1,400 per year per vehicle, thus reducing cost of ownership by 9–10%. If just one vehicle reduces such amounts, then savings for groups of PEVs can be very much higher. Regulation up and Regulation down can be obtained by charging and discharging the EV respectively. In secondary and tertiary frequency control [28, 29], EVs are charged at lower cost whenever demand for regulation up arises.

Studies show that annual profits per vehicle in Denmark range from $80 to $2135. This was possible using secondary and tertiary frequency control.

4.2 Load Shifting

During the peak load time EVs can be used to give power to the grid and during the low demand time EVs can charge themselves. This charging and discharging pattern can be used to level the load on the power system.

In New York City (Level 2 charging simulation was carried out using 100,000 EVs), where an economic profit of $110 million/year can be obtained by providing up to 10% of peaking capacity has been given by EV at penetration levels around 50%. Another study elaborates that there is not much profit by increasing PEV usage when peak load is reduced using V2G [30].

Another simulation shows that using around 50,000 PEVs charged by renewable energy while being integrated with a smart grid saves $3.58 for a vehicle daily.

In another case over a period of 8 years, a vehicle owner can yield profits of $3,520 with an annuity and annual revenue of $427 and $2,583 [34].

Mode of operation of aggregators can benefit the EV user or owner in different ways when used in V2G system. The type of charging system and size of the EV along with its extra features decides the overall cost benefits of using the V2G system. To prove the same, a study was carried out comparing BYD e6, Beiqi EV200 and JAC iEV5 [27]. The result showed that the battery with low cost and high capacity as in the BYD e6 gives quite inconsiderable returns annually thus discouraging EV owners to indulge in the V2G system. Whereas for batteries with high cost and lower capacity as in the Beiqi EV200 and JAC iEV5, there is no possibility of returns at all in the case where all these types of EVs participate in the V2G mode. It was concluded that this is due to the high cost/kWh values. The ratio of peak valley electricity is very small therefore, these reasons influence the annual returns on V2G to be less. With rising manufacturers over the years, competition will also increase thus reducing the prices of batteries. Therefore, as the battery technologies continue to develop, the prices are guaranteed to decrease giving more reasonable cost/kWh rates hence increasing the profits from the V2G technology.

5 Future Scope

Seeing how fast the world is turning to renewable sources of energy, its grid integration brings with it issues concerning frequency regulation, intermittency, generation inconsistency, etc. This increases the necessity of storage systems for these renewables that can store and deliver energy immediately as and when required while maintaining the grid stability. Batteries of EVs can play a highly contributing role to these situations by their fast response and regulating capabilities. Soon, when

majority of the grid energy is supplied by renewable sources, the V2G technology will play a major role in balancing the electricity network and soon enough show potential in functions such as frequency regulation and acting as a reserve [33].

6 Conclusion

This paper has reviewed the V2G system considering the impact of grid in V2G system and the cost benefits by various ancillary services. The impact by the grid at G2V stage has shown levels which can damage the battery whereas at V2G level the grid fluctuation has less impact on the EVs.

References

1. M. Ehsani, Y. Gao, S.E. Gay, A. Emadi, *Modern Electric, Hybrid Electric, and Fuel Cell Vehicles* (CRC Press, Boca Raton, FL, 2005)
2. J. Larminie, J. Lowry, *Electric Vehicle Technology Explained* (Wiley, New York, 2003)
3. C.C. Chan, The state of the art of electric, hybrid, and fuel cell vehicles. Proc. IEEE **95**(4), 704–718 (2007)
4. K.T. Chau, C.C. Chan, Emerging energy-efficient technologies for hybridelectric vehicles. Proc. IEEE **95**(4), 821–835 (2007)
5. Bloomberg Energy Finance, Advanced Transport—Research Note, 25 Feb 2016
6. W. Choi, H. Tae, E-Truck Conversion with a Bi-Directional OBC, in *Transportation Electrification Conference and Expo Asia-Pacific (ITEC Asia-Pacific) 2019 IEEE* (2019), pp. 1–5
7. C. Liu, K.T. Chau, D. Wu, S. Gao, Opportunities and challenges of vehicle-to-home, vehicle-to vehicle and vehicle-to-grid technologies. Proc. IEEE **101**(11), 2409–2427 (2013)
8. X. Guo, J. Li, X. Wang, Impact of grid and load disturbances on electric vehicle battery in G2V/V2G and V2H mode, in *2015 IEEE Energy Conversion Congress and Exposition ECCE* (2015), 5406–5410
9. A. Thapar, T.K. Saha, Z.Y. Dong, Investigation of power quality categorisation and simulating it~s impact on sensitive electronic equipment. IEEE Power Eng. Soc. General Meet. **2**(1), 528–533 (2004)
10. E. Afshari et al., Control strategy for three-phase grid-connected PV inverters enabling current limitation under unbalanced faults. IEEE Trans. Ind. Electron. **64**(11), 8908–8918 (2017)
11. L. Held, M.R. Suriyah, E. Junge, S. Lossau, Impact of electric vehicle charging on low- voltage grids and the potential of battery storage as temporary equipment during grid reinforcement, in *1st EMobility Power System Interation Symposium* (2017), pp. 1–6
12. J.A.P. Lopes, F.J. Soares, P.M.R. Almeida, Integration of electric vehicles in the electric power system. Proc. IEEE **99**(1), 168–183 (2011)
13. W. Denholm, P. Short, An evaluation of utility system impacts and benefits of optimally dispatched plug-in hybrid electric vehicles, Technical Report. NREL/TP-620–40293, (2006), pp. 1–30
14. *Electrification Roadmap: Revolutionizing Transportation and Achieving Energy Security* (Electrification Coalition, Washington, DC, 2009)
15. The Society of Automotive Engineers, Power Quality Requirements for Plug-In Electric Vehicle Chargers J2894/1_201112 (2011)

16. W. Kempton, J. Tomic, Vehicle-to-grid power fundamentals: calculating capacity and net revenue. J. Power Sources **144**(1), 268–279 (2005)
17. J. Tomic, W. Kempton, Using fleets of electric-drive vehicles for grid support. J. Power Sources **168**(2), 459–468 (2007)
18. A.N. Brooks, *Vehicle-to-Grid Demonstration Project: Grid Regulation Ancillary Service with a Battery Electric Vehicle* (AC Propulsion Inc., San Dimas, CA, 2002)
19. A. De Los Rios, J. Goentzel, K.E. Nordstrom, C.W. Siegert, Economic analysis of Vehicle-to-Grid (V2G)-enabled fleets participating in the regulation service market, in *Rec. IEEE PES Innovative Smart Grid Technologies Conference (ISGT)* (2012)
20. R. Sioshansi, P. Denholm, The value of plug-in hybrid electric vehicles as grid resources. Energy J. **31**(3), 1–23 (2010)
21. D.S. Ochs, B. Mirafzal, P. Sotoodeh, A method of seamless transitions between grid-tied and stand-alone modes of operation for utility-interactive three-phase inverters. IEEE Trans. Ind. Appl. **50**(3), 1934–1941 (2014)
22. N. Koduri, S. Kumar, R.Y. Udaykumar, On-board Vehicle-to-Grid (V2G) integrator for power transaction in smart grid environment, in *2014 IEEE International Conference on Computational Intelligence and Computing Research*, 18–20 Dec. 2014 (2014)
23. V.A. Katić, M. Aleksandar, Stanisavljević ; Boris P. Dumnić ; Bane P. Popadić, Impact of V2G operation of electric vehicle chargers on distribution grid during voltage dips, in *IEEE EUROCON 2019-18th International Conference on Smart Technologies* (2019) , pp. 1–4
24. A. De Los Rios, J. Goentzel, K.E. Nordstrom, C.W. Siegert, Economic analysis of Vehicle-to-Grid (V2G)-enabled fleets participating in the regulation service market, in *Rec. IEEE PES Innovative Smart Grid Technologies Conference (ISGT)* (2012)
25. C. Wu, H. Mohsenian-Rad, J. Huang, Vehicle-to-aggregator interaction game. IEEE Trans. Smart Grid **3**(1), 434–442 (2012)
26. C. Wu, H.M. Rad, J. Huang, J. Jatskevich, PEV-based combined frequency and voltage regulation for smart grid, in *Rec. IEEE PES Innovative Smart Grid Technologies Conference (ISGT)* (2012)
27. Q. Cui, X. Bai, S. Zhu, B. Huang, Cost-benefit calculation and analysis of V2G system, in *2016 China International Conference on Electricity Distribution (CICED 2016) Xi'an* (2016), pp. 10–13
28. M.D. Galus, M. Zima, G. Andersson, On Iintegration of PHEVs into existing power system structures. Energy Policy **38**(11), 6736–6745 (2010)
29. Union for the Coordination of Transmission of Electricity (UCTE), Operation Handbook (2008)
30. C.D. White, K.M. Zhang, Using vehicle-to-grid technology for frequency regulation and peak-load reduction. J. Power Sources **196**(8), 3972–3980 (2011)
31. A.Y. Saber, G.K. Venayagamoorthy, Plug-in vehicles and renewable energy sources for cost and emission reductions. IEEE Trans. Ind. Elect. **58**(4), 1229–1238 (2011)
32. V2G 'Could Cut £270m a Year off Cost of Running UK Power System'—Utility Week. 2019. Utility Week (2019)
33. R.A. Raustad, The role of V2G in the smart grid of the future. Interface Mag. **24**(1), 53–56 (2015). https://doi.org/10.1149/2.f04151if
34. F. Galtieri, A. Neira, D. Propp, C. Protano, Vehicle-grid integration in California: a cost-benefit comparison study
35. J.C. Rafter, Vehicle to grid: an economic and technological key to california's renewable future. Pomona Senior Theses. Paper 146 (2016)

Energy-Efficient Cluster Head Rotation Using Fuzzy Logic

Jyoti Kumari, Amit Bhola, and Prabhat Kumar

Abstract A Wireless Sensor Network (WSN) consists of tiny sensor nodes possessing low power, storage capacity, computing capabilities, etc., that are spread in the sensing area to collect data. These sensor nodes can be grouped together to form clusters to ease communication and prolong network life. The coordinator node called Cluster Head (CH) plays the major role by collecting data from sensor nodes and sending it to the BS. The CH is either rotated or new CH is selected to use the network energy optimally. The CH rotation can be energy-based or time-based. The energy-based mechanism uses the remaining energy of the current CH whereas, the time-based mechanism uses the number of rounds after which CH needs to be changed. The paper proposes a dynamic time-driven CH rotation approach using fuzzy logic. The results demonstrate that the approach is more efficient.

Keywords Clustering · Cluster head rotation · Fuzzy Logic · Grid

1 Introduction

Wireless Sensor Networks typically consisting of huge number of sensor nodes with limited power, storage capacity, etc., are often considered as self-configured and infrastructure-less wireless networks [1]. These are used to observe and collect information from environment like temperature, vibration, motion, pressure, etc., and accordingly transfer their data to the central coordinator called sink or BS. The network knowledge can be obtained from BS through injecting queries. There are many approaches designed for self-configuration and information gathering. Among

J. Kumari (✉) · A. Bhola · P. Kumar
National Institute of Technology Patna, Bihar 800005, India
e-mail: jyoti.cse16@nitp.ac.in

A. Bhola
e-mail: amitb.phd19.cs@nitp.ac.in

P. Kumar
e-mail: prabhat@nitp.ac.in

S. Rawat et al. (eds.), *Proceedings of First International Conference on Computational Electronics for Wireless Communications*, Lecture Notes in Networks and Systems 329,
https://doi.org/10.1007/978-981-16-6246-1_28

these, clustering is the pioneer. In this, the nodes are grouped to form clusters based on some mechanism. The CH, among other nodes in the group is responsible for processing, aggregating, and transmitting the data collected from its cluster members (CM) to the BS [2]. The cluster formation has various advantages like increased energy efficiency, energy load balancing, prolonging the network lifetime [3, 12]. The cluster formation phase requires some intermediate processes like candidate CH selection, CH election, and CH declaration. All these processes require messages broadcasting by the sensor nodes and CH. Although clustering causes message overhead due to the CH selection procedure, it increases the network life to a greater extent [13–16]. The once selected CH cannot be retained till the end as it has to perform multiple works causing early energy drainage in comparison to the other sensor nodes. So, CH is rotated either statically or dynamically [4]. The CH rotation mechanisms can be categorized into energy-based and time-based [5]. The energy-based mechanisms use the remnant energy of the nodes to put the threshold for CH candidacy whereas, the time-based mechanisms put threshold using the number of rounds to be covered by a CH. Generally, the CHs are rotated in each round [15, 16]. This consumes greater energy and increases the message overhead. So, the CH needs to be rotated dynamically. The dynamic rotation of the CH reduces the message overhead, gives equal probability to each node of getting selected as CH, and balances the energy consumption.

Fuzzy logic can be defined as a multi-valued logic form where the truth value of a variable lies between 0 and 1 [6]. It is utilized to handle the partial truth construct, where the truth value ranges between utterly true and utterly false. In this paper, the threshold for the occurrence of CH rotation is determined by using fuzzy logic.

The remainder of the paper is structured as follows: Sect. 2 briefs the related works, Sect. 3 states the proposed methodology, Sect. 4 deals with the implementation part, Sect. 5 shows the result analysis, and finally, Sect. 6 concludes the paper.

2 Related Work

The efficient CH rotation is an important aspect for increasing the network lifetime and load balancing throughout the clusters. The message overhead generated during the clustering phase can be reduced by changing CH at different rounds.

In [15, 16], the authors have proposed fuzzy-based cluster head selection using different parameters. The approaches follow the principle of LEACH protocol where the CH is selected in each round.

Wu et al. [7] proposed LEast rotation Near-Optimal (LENO) strategy using dynamic programming method for cluster rotation. The law of conservation of energy is being used to determine the upper and lower bounds of the CH lifetime with the conclusion that it is skewed against the upper bound. This technique does not re-elect CH in each round rather it only performs the CH rotation.

Gamwarige et al. proposed [5] a distributed and energy-driven CH rotation. This scheme is governed by a dynamic threshold driven by the residual energy of CH. The

designated CH performs its duties until its energy drops below the threshold. In this scheme, the maximum residual energy component is figured out in second-degree neighborhood and searches for the new CH whenever the CH rotation is to be done.

In [8], a randomly generated number determines the probability of the CH and each node maintains a self-status record of being a CH in the previous rounds. The threshold value on addition controls the CH selection resulting in non-uniform clusters. The re-clustering is done each time the CH rotation occurs.

Hua et al. [9] proposed a Cluster Head Rotation Cooperative MIMO (CHR-CMIMO) scheme using the inner cluster selection process avoiding the re-clustering phase. The mCH (main CH) and aCH (assistant CH) are selected based on residual energy. The mCH performs its duties until its remaining energy drop below a predefined threshold and then chooses the next mCH and aCH having the highest and second-highest residual energies. They also proposed an Over-Jump method which is conducted when the next-hop CH is having lesser energy for communicating the data to a further level. The data is then transmitted to the next to next-hop CH. Only the residual energy of the CMs and the predefined threshold are considered in this scheme.

In [10], a centralized hybrid scheme combining the time-driven and energy-driven scheme is proposed. In this scheme, each CH calculates critical residual energy (Eri) and it is compared with its remnant energy. The energy-driven method is adopted when the residual energy is greater than Eri otherwise time-driven method is adopted. It also states that once a time-driven strategy is adopted, it fixes the clusters and is maintained until the network dies.

Chen et al. [11] proposed an asynchronous CH rotation scheme. In this scheme, the droppage of the remaining energy of the CH below threshold starts the CH rotation procedure. The remnant energy and initial energy are used to calculate the threshold value. The highest weighted CM node is chosen as next CH considering the energy, distance, and node density factors.

3 Proposed Methodology

System Model

The BS and the sensor nodes form the system infrastructure in a sensing area. The sensing area is dissected into square-shaped equal-sized grids also called clusters. The sensor node inside a grid can be either a CH node or a CM node. The CM node only senses the environmental information and transmits it to the CH rather than doing any processing work. Fewer superior nodes called CH, one in each group, transmits the data collected from its CMs to the BS.

In WSNs, a major portion of energy (CH and CMs) is consumed during data transmission that depends on transmission distance. Additionally, energy depletion during data collection and data aggregation also counts for the CH nodes. The radio energy dissipation model is a basic and simple model for energy dissipation caused

due to radio hardware, data transmitter, and receptor. Energy dissipation is proportional to the transmission distance (transmitter-receptor distance), i.e. d^2 in the case of free space propagation whereas, d^4 in the case of multipath fading. According to this model, for transmitting an m-bit message, the energy depletion can be calculated using Eqs. (1) and (2) [9].

$$E_t(m, d) = E_{elec}.m + E_{amp}.m \tag{1}$$

$$E_r(m) = E_{elec}.m \tag{2}$$

where, d denotes the distance between the transmitting and receiving sensor node, $E_t(m,d)$ denotes the transmission energy depletion of the sensor node while $E_r(L)$ denotes the receptor energy depletion. E_{elec} is the electronics energy depletion per bit during data transmission (transmission and reception both), due to digital coding, modulation, filtering, etc. E_{amp} is the amplifier energy consumed during data transmission as given by Eq. (3).

$$\begin{aligned} E_{amp} &= E_{fs}.d^2, when\ d \leq d_0 \\ &= E_{mp}.d^4, when\ d > d_0 \end{aligned} \tag{3}$$

Assumptions

- The sensor nodes are deployed randomly and are homogenous in nature.
- The BS is positioned at the center of the deployment area.
- The antenna of the sensor node is Omni-directional.
- The lifetime of the network is considered as when 90% of sensor nodes become dead [17, 18].

Phases of proposed work

There are three phases of the proposed work namely, cluster formation and cluster head selection, cluster head rotation, data transmission.

Cluster formation and CH selection

The sensing area is divided into square-shaped grids. The grid length is computed using transmission range. As shown in Fig. 1, the diagonal of the squared grid represents the transmission range, i.e. $a\sqrt{2} = r$, where a is the grid length. This grid represents a cluster. Initially, the geometric center of the cluster is selected as CH for each cluster due to the initial energy being equal for all sensor nodes. For the further rounds, the CH selection depends on the remnant energy and the position of the sensor nodes from the center of the cluster. As a result, such sensor node which is closest to the center of the cluster with highest energy is chosen as next CH.

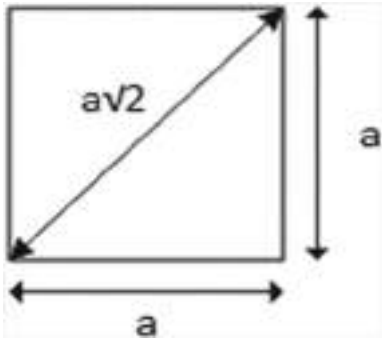

Fig. 1 Square Grid in the proposed scheme

CH rotation

The residual energy and the previous count of the selected node acted as a CH are taken as input to the fuzzy system and a fuzzy output is generated. This output gives the number of rounds the selected node will act as the CH. The selected node serves its purpose as the CH till the defined number of rounds. After that, the next CH is selected depending on the remnant energy and position from the center of the cluster. In this way, the CH is rotated after a dynamic number of rounds. This continues till the network dies.

Data transmission

In the data transmission phase, firstly, the CMs send their data to their respective CH using single-hop. The CH collects the data, processes it and then transmits it to the BS using single-hop communication. The CH to BS is single-hop communication is possible due to smaller sensing area. For larger area, multi-hop communication would be more efficient.

4 Implementation

The proposed protocol is tested using simulation tool MATLAB (Version R2017a) on Microsoft Windows 7 with an Intel Core i5-4990 processor, 3.6 GHz CPU, and 8 GB RAM. Multiple simulations are run for various network arrangements. Table 1 enlists the simulation parameters.

The sensing area is partitioned into square-shaped grids of size $50 \times 50\ m^2$. There are total 36 clusters formed by using transmission range as 70 m. Each node is having 1 J of energy. The sensor nodes know their position and cluster number to which they belong. The cluster nodes know their neighborhood information. The center of the grid is computed as the CH position. The next CH is selected depending on the remaining energy and distance of the CMs from the geometric center of the cluster. The proposed approach uses the fuzzy technique to estimate the threshold in terms of number of rounds for the CH to perform its duties. The input to the fuzzy is the

Table 1 Parameters and their values

Parameters	Parameter values
Sensing area	300 × 300 m^2
# of nodes	100–500
BS location	(150,150)
$E_{initial}$	1 J
E_{elec}	50 nJ/bit
E_{fs}	10 pJ/bit/m^2
E_{amp}	0.0013 pJ/bit/m^4
Transmission range	70 m
Data packet length	4000 bits
Control packet length	100 bits

remaining energy of the selected CH and the count to which it has already acted as CH in the previous rounds.

5 Result Analysis

Figure 2 demonstrates the random deployment of the sensor nodes in an area of 300 × 300 m^2 and the grid division of the sensing area. The sensing area is logically divided into 36 grids of size 50 × 50 m^2. Initially, the sensor node nearer to the centroid of the grid is selected as the CH of the grid. In Fig. 2, CH is represented by red star and the cluster member nodes are represented by blue dots. The word grid and cluster are used interchangeably.

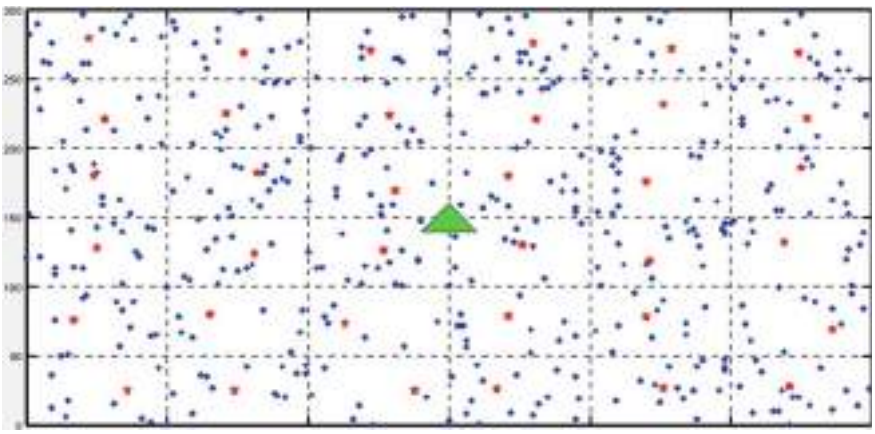

Fig. 2 The grid division and CH selection in the proposed scheme

Table 2 Fuzzy input and output

Residual energy	Previous count	Rounds
High	Large	LesserMed
High	Inter	LesserHigh
High	Small	HighlyHigh
Medium	Large	LesserLow
Medium	Inter	HighlyMed
Medium	Small	IntHigh
Low	Large	HighlyLow
Low	Inter	IntLow
Low	Small	IntMed

The information generated by the CM sensor node is transferred to the respective CH. The CH gathers information from respective CMs, process it, and sends it to the BS. Here, the CM-CH and CH-BS both communications are single-hop due to smaller network size. This task of current CH is performed till the round number generated by the Fuzzy System. The rules governing the Fuzzy System for our system are tabulated in Table 2. After that, new CH, among CMs, is selected depending on the remnant energy and distance from the center of the grid.

The input parameters namely residual energy and previous count of the nodes have been categorized into three namely high, medium, low and large, intermediate, small for the residual energy and previous count, respectively. There are nine outputs viz. lessermedium, lessershigh, highlyhigh, lesserlow, highlymedium, intermediatehigh, highlylow, intermediatelow and intermediatemedium corresponding to the inputs.

Figure 3 represents the overall Fuzzy system used in our system. After a CH rotation, the newly elected CH is nearer to the older one with the highest energy in the cluster/grid.

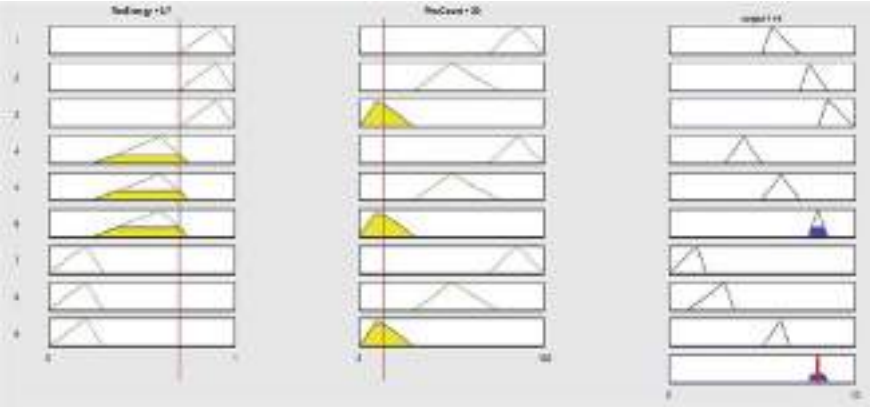

Fig. 3 The Fuzzy Logic for estimating the number of rounds of a CH

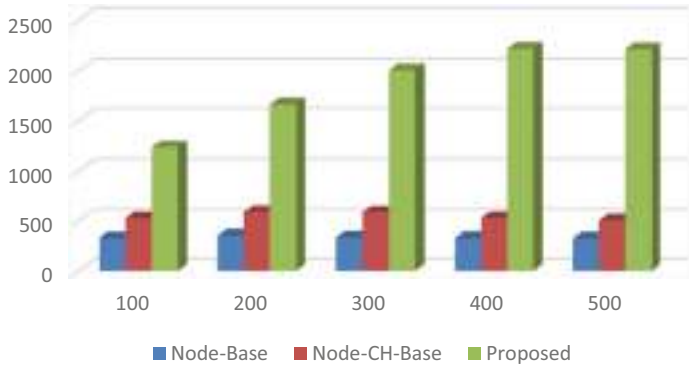

Fig. 4 First Node Dead v/s No. of nodes

The simulation has been performed by varying the node density keeping the same area. Figure 4. demonstrates the comparison of the first node dead (FND) of Node-Base, Node-CH-Base, and the proposed approach for 100, 200, 300, 400, and 500 nodes to the number of rounds in an area of 300 × 300 m^2 considering the maximum number of rounds as 100 in the Fuzzy system. Node-Base denotes the direct communication from the sensor node to the base station, i.e. single-hop communication. Node-CH-Base shows two-hop communication from sensor node to BS, i.e. CM to CH and from CH to BS. The CH is rotated in each round in this approach. While in proposed, the CH rotation is dynamic. It is clear from the figure that FND is the highest for the proposed approach irrespective of node density. The graph has been plotted after taking the average of the 50 simulation results.

Figure 5 shows the performance of the proposed scheme measured in three parameters namely FND, half node dead (HND), and last node dead (LND). The figure illustrates the comparison of FND, HND, and LND of the proposed scheme with

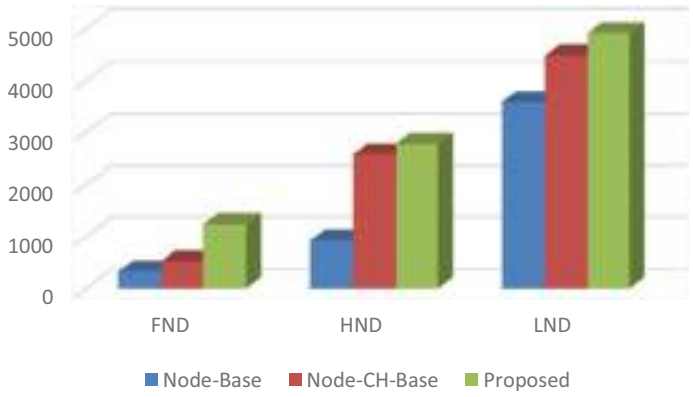

Fig. 5 Comparing the proposed scheme with Node-Base and Node-CH-Base

the Node-Base and Node-CH-Base in the sensing area of 300 × 300 m^2 with 100 sensor nodes. There is a larger difference between the Node-Base and the proposed scheme. The FND is the highest of the proposed among others. For the HND and LND, there is a slighter difference between the Node-CH-Base and the proposed since the cluster remained unchanged.

6 Conclusion

The proposed implementation of fuzzy logic for CH rotation provides a dynamic and efficient number of rounds for which a selected CH would perform its task. This threshold value is dependent on the remnant energy and the previous count of the selected CH. The proposed protocol can be used in various clustering protocols for improving the network lifetime.

At present, the above protocol is valid on a small area network, where each cluster is directly transmitting to the base station. In the future, an improved protocol would be worked on for enhancing the lifetime of the network for a large area network.

References

1. P. Rawat, K.D. Singh, H. Chaouchi, J.M. Bonnin, Wireless sensor networks: a survey on recent developments and potential synergies. J. Supercomput. **68**(1), 1–48 (2014)
2. A.A. Abbasi, M. Younis, A survey on clustering algorithms for wireless sensor networks. Comput. Commun. **30**(14–15), 2826–2841 (2007)
3. M.M. Afsar, M.H. Tayarani-N, Clustering in sensor networks: a literature survey. J. Netw. Comput. Appl. **46**, 198–226 (2014)
4. A. Kumar, V. Kumar, N. Chand, Energy efficient clustering and cluster head rotation scheme for wireless sensor networks. Int. J. Adv. Comput. Sci. Appl. (IJACSA) **3**(5), 129–136 (2011)
5. S. Gamwarige, E. Kulasekere, An algorithm for energy driven cluster head rotation in a distributed wireless sensor network, in *Proceedings of the International Conference on Information and Automation* (Colombo, 2005), pp. 354–359
6. G. Klir, B. Yuan, *Fuzzy Sets and Fuzzy Logic: Theory and Applications* (Prentice hall, New Jersey, 1995)
7. Wu, Y., Chen, Z., Jing, Q., Wang, Y.C..: LENO: LEast rotation near-optimal cluster head rotation strategy in wireless sensor networks, In: 21st International Conference on Advanced Information Networking and Applications (AINA'07), pp. 195–201, IEEE, Niagara Falls, Canada (2007).
8. W.B. Heinzelman, A.P. Chandrakasan, H. Balakrishnan, An application-specific protocol architecture for wireless microsensor networks. IEEE Trans. Wireless Commun. **1**(4), 660–670 (2000)
9. H. Hua, J. Qiu, S. Song, X. Wang, G. Dai, A cluster head rotation cooperative MIMO scheme for wireless sensor networks, in *International Conference on Wireless Algorithms Systems, and Applications* (Springer, Qufu, China, 2015), pp. 212–221
10. G. Ma, Z. Tao, A hybrid energy-and time-driven cluster head rotation strategy for distributed wireless sensor networks. Int. J. Distrib. Sens. Netw. **9**(1), 1–13 (2013)

11. C. Chen, F. Rao, X. Zhang, Y. Dong, An asynchronous cluster head rotation scheme for wireless sensor networks, in *International Wireless Communications and Mobile Computing Conference (IWCMC)* (IEEE, Dubrovnik, Croatia, 2015), pp. 551–556
12. B. Prince, P. Kumar, M.P. Singh, J.P. Singh, An energy efficient uneven grid clustering based routing protocol for wireless sensor networks, in *International Conference on Wireless Communications, Signal Processing and Networking (WiSPNET)* (IEEE, Chennai, India, 2016), pp. 1580–1584
13. P.S. Mehra, M.N. Doja, B. Alam, Fuzzy based enhanced cluster head selection (FBECS) for WSN. J. King Saud Univ.-Sci. **32**(1), 390–401 (2020)
14. T.M. Behera, S.K. Mohapatra, U.C. Samal, M.S. Khan, M. Daneshmand, A.H. Gandomi, Residual energy-based cluster-head selection in WSNs for IoT application. IEEE Internet Things J. **6**(3), 5132–5139 (2019)
15. H. El Alami, A. Najid, Energy-efficient fuzzy logic cluster head selection in wireless sensor networks, in *International Conference on Information Technology for Organizations Development (IT4OD)* (IEEE, Fez, Morocco, 2016), pp. 1–7
16. J. Wang, J. Niu, K. Wang, W. Liu, An energy efficient fuzzy cluster head selection algorithm for WSNs, in *International Workshop on Advanced Image Technology (IWAIT)* (IEEE, Chiang Mai, Thailand, 2018), pp. 1–4
17. Y. Padmanaban, M. Muthukumarasamy, Scalable grid-based data gathering algorithm for environmental monitoring wireless sensor networks. IEEE Access **8**, 79357–79367 (2020)
18. Y. Zhang, M. Liu, Q. Liu, An energy-balanced clustering protocol based on an improved CFSFDP algorithm for wireless sensor networks. Sensors **18**(3), 881 (2018)

Different Techniques in Neural Style Transfer-A Review

Kumarapu Jayaram, Malhaar Telang, Ravula Bharath Chandra Reddy, Yada Arun Kumar, Kore Shivanagendra Babu, Pooja Rana, Priyanka Chawla, and Usha Mittal

Abstract Neural Style Transfer is a very good example to show the capability of Convolutional Neural Network (CNN) to generated high-quality images. In style transfer algorithms two input images are present one is a content image and the other is a style image and it generates output in such a way that the output is a mix of both content and style image. There are different methods and approaches that can be used to implement the style transfer. This paper will focus briefly on neural networks and their architecture used in the approaches and briefly describe the important loss functions and the implementation of neural style transfer. This review paper will explain the four major approaches or techniques that have been used to implement neural style transfer, these approaches will also tell how they have improved on the original method put forward by Gatys et al. 2015 to produce good quality results and then find the advantages and disadvantages by comparison of each method that is explained. This paper aims to provide knowledge of how different approaches work.

Keywords Neural style transfer · Style image · Neural networks · Style transfer algorithms

1 Introduction

The deep learning framework has evolved over the years. The main approach toward image classification and image processing task was given by the convolutional neural network commonly known as CNN. The CNN is the base to produce high-quality images. Most of the recent advancements in style transfer are an improvement for the algorithm put forward by Gatys et al. 2015 [1]. Some focus on improving speed and some work to intelligently combine different styles. The separation of style and content from an image has proved that CNN and its related algorithms are capable

K. Jayaram · M. Telang · R. B. C. Reddy · Y. A. Kumar · K. S. Babu · P. Rana · P. Chawla · U. Mittal (✉)
School of Computer Science and Engineering, Lovely Professional University, Phagwara, Punjab, India
e-mail: usha.20339@lpu.co.in

S. Rawat et al. (eds.), *Proceedings of First International Conference on Computational Electronics for Wireless Communications*, Lecture Notes in Networks and Systems 329,
https://doi.org/10.1007/978-981-16-6246-1_29

to perform larger computation tasks to capture both high-level as well as low-level image features. Capturing their style and maintain the semantic features from the image is essential to produce a high-quality image, which the CNN [5] are capable to do. Not only on images the recent advancements in the field have extended the style transfer techniques on videos too. The major advantages of Style transfer algorithms are they can be used in photo and video editing, gaming and to save time to stylize arts on images. The four approaches that are have covered in this paper are. The first approach was put forward by Leon A. Gatys et al. in 2015 [1], feed-forward-based fast transfer method [7], Multi-Style transfer [10], and color preservation in style transfer [11]. Many researchers have either used a Visual Geometry Group (VGG) CNN or popularly known as VGG-16 or a VGG-19 algorithm, these are nothing but a pre-trained neural network. These are already trained on a large dataset with images and they can be used for any model. There are changes in the architecture of the different approaches. Each approach has its importance but the primary goal is to develop high-quality visually pleasing images. Some methods have updated the original method of Gatys et al. [1] and some have introduced new architecture and algorithms. Among all these, the function used to calculate loss is important because the quality of images depends on how well it has minimized a loss function.

2 Different Approaches in Neural Style Transfer

2.1 "A Neural Algorithm of Artistic Style"- by Leon a. Gatys Et Al in 2015 [1, 3, 5, 6]

Overview: The style transfer is a technique that consists of single content and style image. With this technique, style from the image is transferred into the content of the image in such a way that the resultant image is a blend of those two images which preserves the content from the first image while transferring the style from the second. Methodology: Neural Artistic Style Transfer was first put forward by Leon A. Gatys et al. in 2015 [1, 5] in his research paper "neural algorithm of artistic style". The key findings of the paper are it can decouple style and content representation of image inside CNN architecture. Conv nets played important role in this style transfer task. VGG 19 pre-trained neural network is employed in this method. VGG 19 [1] is a convolution neural network trained on an ImageNet for its object recognition and localization. This VGG 19 CNN performs exceptionally well in localization tasks. It can extract various features by taking the feature maps of certain layers while the images are feed into VGG. This method uses the per-pixel loss function they are mainly content and style loss. They can capture low-level image features the output is generated by minimizing the loss. The main goal is minimizing loss function and there should be a balance between both the losses to produce high-quality images. Gatys et al. process is slow as it uses backpropagation for updating weights for optimization.

This performs two tasks one is transferring the content from the first image then simultaneously transferring the style from the second image. In first task, the content of the image is feed into the VGG network similarly the Gaussian noise image is feed into the VGG and extracts the feature map matrix of certain layers. Now optimize the loss with the given function. [1, 3, 5, 6] (Figs. 1 and 2).

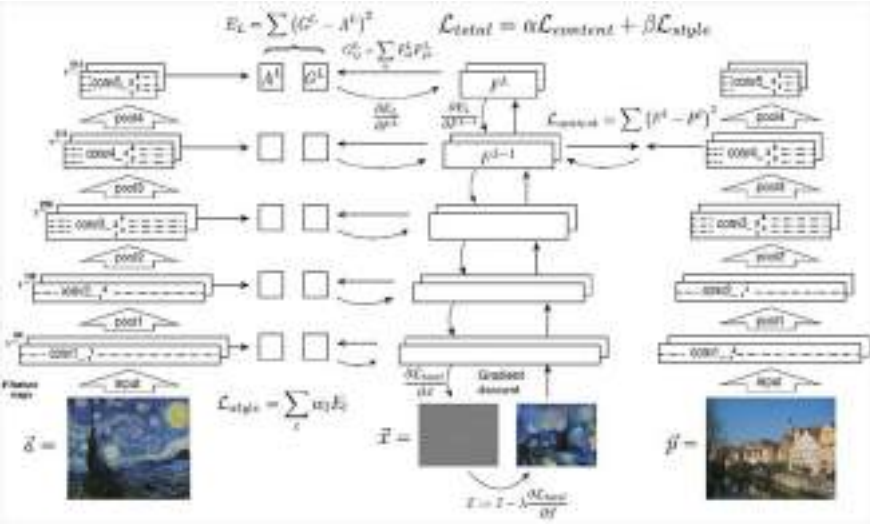

Fig. 1 Style transfer algorithm [5]

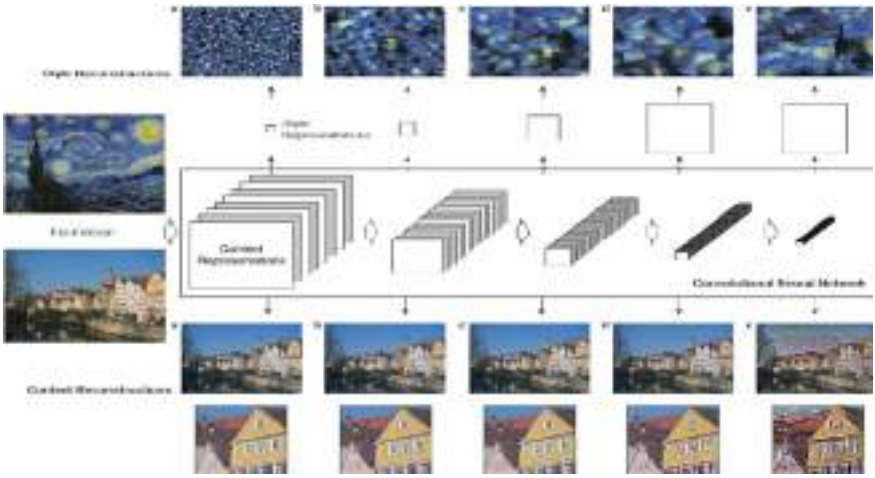

Fig. 2 CNN-content and style representation [1]

$$\mathcal{L}_{\text{content}}(\vec{p}, \vec{x}, l) = \frac{1}{2} \sum_{i,j} \left(F_{ij}^{l} - P_{ij}^{l}\right)^2$$

Simultaneously extract features maps from the content image but in the form of gram matrices. [1, 5, 6]

$$E_l = \frac{1}{4N_l^2 M_l^2} \sum_{i,j} \left(G_{ij}^{l} - A_{ij}^{l}\right)^2$$

$$\mathcal{L}_{\text{style}}(\vec{a}, \vec{x}) = \sum_{l=0}^{L} w_l E_l$$

Now combine the loss functions. [1, 5, 6]

$$\mathcal{L}_{\text{total}}(\vec{p}, \vec{a}, \vec{x}) = \alpha \mathcal{L}_{\text{content}}(\vec{p}, \vec{x}) + \beta \mathcal{L}_{\text{style}}(\vec{a}, \vec{x})$$

where the content and style weights are alpha and beta. In output content of the output image should be similar to the content taken from the content image and the style of the output image should be similar to the style taken from the style image.

2.2 *Fast Neural Style Transfer—by Justin Johnson et al in 2016 [7]*

Previous method given by Leon A. Gatys et al. shows how a style transfer algorithm works by optimization. Pixel to pixel loss was used in the algorithm. To enhance the image quality of output and show visually pleasing images a new approach is introduced which considers perceptual loss these are useful to extract high-level image features. It improves the primary algorithm put forward by Leon A. Gatys et al. in 2015 [1, 2], where it prefers to balance the style and content loss. This approach can perform the style transfer task by training the data on a feed-forward CNN using perceptual loss [7]. The perceptual loss means instead of extracting low-level features they extract high-level features. Perceptual loss can capture minute details. These pixel-to-pixel losses (per-pixel) are not useful in capturing high-level features. This approach is very good as it does the style transfer task at a comparatively very high speed. The perceptual loss capture image similarities more efficiently and while testing they transfer the style of the image in real-time. The perceptual loss directly transforms semantic network information to the transformation network from the loss network. The architecture of the Justin Johnson et al. 2016 method [7] is inspired by the method of semantic segmentation in CNN. There are some changes to the architecture as it has network downsampling this reduces the occupying space of the feature maps in addition to this it also includes network upsampling to produce a great quality output image.

Methodology: The Network consists of two main components the primary is the image transformation network f_W and the second is the loss network ϕ this loss network defines different loss functions applicable. This transformation network which is already a deep CNN improves the optimization algorithms of Gatys et al. [1, 3]. The input image given as (x) is passed to the network that helps to transform this image to the respective output image ($\hat{y}$). There are some weights associated with the network given by (W) generated by loss calculation with help of ($\hat{y}$) by comparing with y_s for style and y_c for content representation for the image [7].

To decrease total calculated weights of loss function used apply stochastic gradient descent:

$$W^* = \arg\min_W \mathbf{E}_{x,\{y_i\}}\left[\sum_{i=1} \lambda_i \ell_i(f_W(x), y_i)\right]$$

The loss network ϕ using the VGG-16 network. The main task for this network is to generate style and content representations for its respective style and content images, relu3_3 in the network is used for generating content representation, and the relu1_2, relu2_2, and relu3_3, relu4_3 from network generate its style representations. From this loss network with representations, there are two different types of loss function which are nothing but perceptual loss functions (Fig. 3).

These loss functions capture the semantic and also high-level perceptual features of any image. These loss functions are deep CNN because it makes use of ϕ as a loss network. These features are similar to the ones generated from the loss network ϕ. The CNN has already learned to store both semantic as well as high-level data measured from the loss function.

Feature reconstruction loss: Generated by output ($\hat{y}$) its respective content representation from relu3_3 it is squared normalized Euclidean distance, it tries to make output image and the target image to be similar. But it doesn't need to match exactly with the target image [7]. It is given by the formula:

$$\ell_{\text{feat}}^{\phi,j}(\hat{y}, y) = \frac{1}{C_j H_j W_j}\phi_j(\hat{y}) - \phi_j(y)_2^2$$

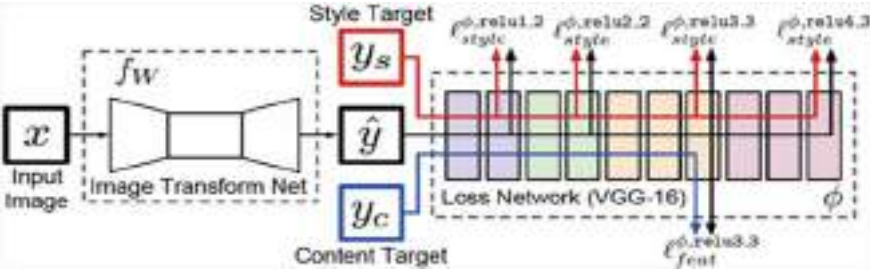

Fig. 3 Feed-forward method [7]

Style reconstruction loss: Generated by output (ŷ) from its respective content representation from layers that are relu1_2, relu2_2, and relu3_3, relu4_3 and it penalizes differences in styles for example take color, textures, and similar patterns, fine details, etc. when deviates from the target [7]. Its formula is:

$$\ell_{\text{style}}^{\phi,j}(\hat{y}, y) = G_j^{\phi}(\hat{y}) - G_j^{\phi}(y)_F^2$$

Working: The process for style transfer can be done only when the shape of inputs passed and output is 3 × 256x256. It also has residual connections. These kinds of layers make the process easy to learn to identify the function, this is important because it can share a common structure with the input image. Adding Upsampling and downsampling here for the style transfer process, two stride-2 is used for downsampling. Residual blocks are present after this, and two layers of CNN are provided with a stride of 1/2 to do upsampling there are few benefits of applying downsampling first and then upsampling. The main aim is to perform style transfer the target content image y_c provides the content and target style image y_s provides style. Then mix the content and style to produce the output image [7–9]. After training the network. By mixing content and style targets y_c and y_s. With the help of these, it can perform style as well as feature reconstruction. The output ŷ can be generated with the formula [7]:

$$\hat{y} = \arg\min_{y} \lambda_c \ell_{\text{feat}}^{\phi,j}(y, y_c) + \lambda_s \ell_{\text{style}}^{\phi,J}(y, y_s) + \lambda_{TV} \ell_{TV}(y)$$

λ_c, λ_s, and λ_{TV} are scalars, white noise is also present. This approach is a bit slow because it applies forward followed by backward passing in the loss network ϕ.

Result and discussion**:** The training has been done on the MS COCO dataset (2014) with over 80,000 images available for content images. Style images are selected with different artistic styles available. 80,000 images were trained, each batch has 4 images, this network is trained with two epochs and 40,000 iterations. Titan X GPU was used for training purposes which took close to 4 h of training. The language used is Torch. Since there are 2 epochs the model does not face overfitting issues thus no need for a dropout layer in the network. Coming to results obtained which are qualitatively near to the Gatys et al. method. The main outcome shown is capturing the semantic content of images. It could be possible because of preserving the VGG-16 features thus it can capture people and other background objects. Moving to quantitative results the developed style transfer algorithm has a speed much faster than Gatys et al. method and does style transfer in real-time. For 256 × 256 image size it just took 0.015 s, for 512 × 512 in just 0.05 s and for 1024 × 1024 in just 0.21 s [7]. Results can be seen in Fig. 4.

Fig. 4 Results of the method [7]

2.3 Multi-Style Transfer in 2017 by Brandon Cui et al. [10]

As discussed, the working of neural style transfer from the first approach, the second approach has improved the first approach and does style transfer in real-time using a feed-forward network and is very fast. In multi-style transfer, it applies style transfer to multiple styles. Many applications have worked on single style transfer that contains single style and content image. This method trains images to multiple styles. The primary steps taken in the paper [10] are first to implement the single style transfer and then train on a feed-forward CNN [7] which is then connected to the VGG-16 network [10] already pre-trained on the ImageNet dataset. It generated the style transfer image with high-quality visual output. It has also focused on improving the upsampling and instance normalization so that there is improved architecture. The Gatys et al. 2015 [1, 3–5] approach has a limitation that it can be trained on single image, that means it is trained on a single pre-trained network. These learn style from just one image and have many performance drawbacks. The primary focus of this technique is training multiple styles on a single content image this is done by maintaining a proper optimization of desired style and content image. In other words, makes a balanced combination of style and content loss function, this method has improved the feed-forward method by Justin Johnson et al. 2016 [7] by training on multiple images. This technique has used a VGG-16 pre-trained network, the dataset used is the MS COCO dataset which has 80,000 images.

Improvements: They have Improved the upsampling and instance normalization [10]. Other than referring to Gatys et al. approach [1, 3] and Johnson's approach [7] they have also done upsampling for the nearest neighbor. The problem solved is the convolution layers in it generated images with loosely packed pixels, by upsampling this is an efficient solution. The second important point is the images were trained individually but did not train images in batch this has been possible because of instance normalization [10]. The formula is given by:

$$(1)\ y_{tijk} = \frac{x_{tijk} - \mu_{ti}}{\sqrt{\sigma_{ti}^2 +}},\ \mu_{ti} = \frac{1}{HW}\sum_{l=1}^{W}\sum_{m=1}^{H} x_{tilm}$$

$$(2)\ \sigma_{ti}^2 = \frac{1}{HW}\sum_{l=1}^{W}\sum_{m=1}^{H}(x_{tilm} - \mu_{ti})^2$$

Content loss: It is content layer loss calculated by mean square error. It is given by the formula:

$$L_c = w_c \times \sum_{l \in CL}\sum_{i,j}\left(FC_{i,j}^{l} - FS_{i,j}^{l}\right)^2$$

Single style loss: Its style layer loss is calculated by the square error in gram matrices. It is calculated by the formula:

$$L_s = w_s \times \sum_{l \in SL}\sum_{i,j}\left(GC_{i,j}^{l} - GS_{i,j}^{l}\right)^2$$

Multi-style loss: Here in this consider the weighted average of all style loss to mix different styles each consists of blending weights. The style losses are modified. S stands for total multi-style loss [10] which is the weighted sum of multiple style images. It can choose the style layer and their weights independently as per our choice given by the formula: $L_s = \sum_{i=1}^{n} w_i L_{s_i}$ and Blended weights are calculated by:$w_i = \frac{L_{s_i}}{\sum_{i=1}^{n} L_{s_i}}$.

Discussion: As the main objective is to train a single content image to multiple styles, it is done using the basic Gatys et al. approach [1, 3] and fast style transfer method [7]. In the fast neural style transfer (feed-forward) it is by modifying the network in such a way that it will be able to train on multiple images in very little time. This has given appropriate results it has generated high-quality output even on multiple styles. It modified the neural network so that it can select a balanced combination of styles and content features automatically [10]. Even though the algorithm is modified it still chooses multiple styles of fixed size and takes a long time for training. Thus, interruptions in the middle of the training process can result in low-quality output. The output image quality is not at its best and it should not be allowed to train with more epochs because of non-overfitting. Here epoch means each time the network learns the properties of the input dataset. As this is a very large dataset, the network is hardly trained on 2 epochs. This training is not sufficient and also could not capture features properly. The dataset used was the MS COCO dataset.

2.4 *Preserving Color in Neural Artistic Style Transfer in 2016 Leon A. Gatys [11, 12]*

As discussed in the previous approaches the neural network transfers the style of the image into the content of the image. Whereas in color preservation neural artistic style transfer copies the color scheme of the content image and depicting the objects in the style of another image. This works by comparing statistics in a convolutional neural network that is trained in object recognition. There are two ways are used to keep the color of the style image in neural style transfer. They are.

A. Color Histogram matching.

B. Luminance only transfer.

Method A Color histogram matching [11, 12, 15]: In histogram matching the image represents the number of pixels in each color object. The components like Red, Green, and Blue cannot be used separately in Histogram equalization as it leads to significant changes in the color balance of an image. So, here ($C^{'}$) represents content image and ($S^{'}$) represents style image, the style image's colors are modified to match the colors of the content image. This generates a new style image (S*).

In particular let x = (R, G, B) represent each pixel of an image. Then each pixel is transformed given by $x_{S'} \leftarrow Ax_S + b$ Whereas, A is considered as a 3 × 3 matrix and b as a 3–vector.

This converts the mean and covariance of the RGB values into a new style image S* to match those in $C^{'}$. The mean of the color pixels is the average of all the pixels $\boldsymbol{\mu} = \sum_i \mathbf{x}_i / N$. The transformation is such that the mean and the covariance of the RGB values in the new style image ($S^{'}$) is similar to the original content image ($C^{'}$).

Method B Luminance only transfer [11, 12]: The use of luminance only transfer is that it maintains the colors of the content image exquisitely. So, the color channels are not more sensitive than the visual perception in luminance. To produce the output image, for this first extract L_S and L_C from the style and content images then by using YIQ color space apply the neural style algorithm to these images. If there is a significant difference within the content image and the style image, then compare the histogram of the content image L_C with the L_S style channel before transferring the style [12–14].

$$Ls' = \sigma_C/\sigma_S(L_S - \mu_S) + \mu_C$$

Here σ_C and σ_S are the mean luminance of the two images.

Discussion: These approaches have their pros and cons which are discussed as follows. For the Color Histogram matching & Luminance only transfer [12, 14, 15]. The color histogram matching explains how the style image color is transformed to match the color of the content image. The color distribution is often not fully matched, which leads to a discrepancy between the colors of the output image and the content image. The drawback of this method is that the color distribution to the content image is not fully transformed which leads to the discrepancy. In luminance only transfer [11] the color to the content image transforms flawlessly. However,

Fig. 5 Color preservation in style transfer [11]

there is a defect in that there is a mismatch between the content and style image. This fault is particularly noticeable, see the above Fig. 5 for example. In this image, there is a mismatch of colors that are not matching the stripes. This is explicitly noticeable with styles. In above Fig. 5, the colors are no longer match the stripes.

2.5 Practical Implementation

For this neural style transfer model MS COCO dataset is used for training which consists of 83,000 images the model gets trained on this dataset for a specific set of style. PyTorch data loader takes an image from the dataset and resizes it into 256 $\times$ 256 and concatenates it into batches and does image normalization. For the code implementation, its convention to use transform net and perceptual loss net (VGG16) and Adam optimizer. The next step is to load the style image to train the model for the specific style image. Subsequently, pass the style image through the perceptual map to find the style representation which is a collection of gram matrices. In the train loader, take one batch and pass it through the transform net. Here in content batch the images are collected from MS COCO dataset, next pass the images through the perceptual net and simultaneously pass the stylized batch coming out from the transform net through the perceptual net.

The target content representation is different for every single iteration whereas style representation is the same as the model is trained for a single style. Now calculate content loss and mean square error loss between target content representation and current content representation (Fig. 6).

Now find style loss by doing MSE on gram matrices. Combining content loss and style loss results in a total loss. While training from the dataset the first 20,000 images were used and one epoch. Now our model gets trained with a single style for 20,000 images. After training, save the model. Now use this model to do style transfer. Firstly, take a content image that is intended to do style transfer and use parser.add.argument

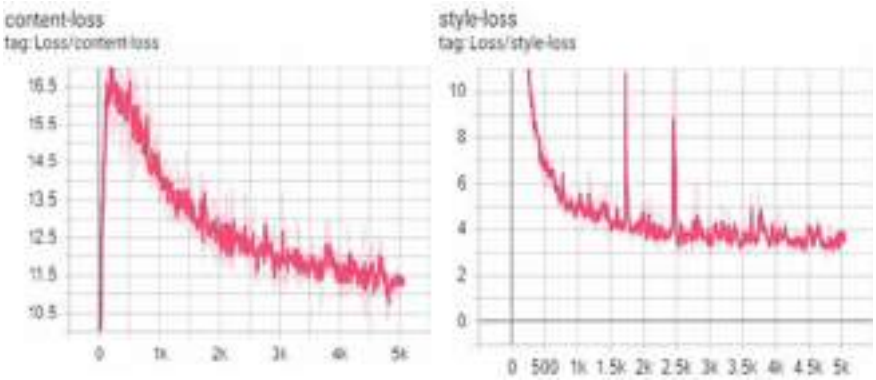

Fig. 6 Graph of implementation [17]

Fig. 7 Results of implementation [18]

then pass a content image and saved model. now create a function so that it takes the content image and saved model as an argument and the output result is the image that has the content of the content image and style of the style image in model which had been trained.

Results:

See Fig. 7.

3 Comparative Study

See Table 1 and 2.

Loss function: It gives the difference between predicted value and actual results (Table 3).

Table 1 Comparison of the approaches with their network, dataset used and time taken

Method with reference	Network used	Time taken for training/Getting results	Dataset
Gatys et al. method [1]	VGG 19	30 min-1 h to train depends on GPU Result-3.17 s	Content image (place) & Style image (art)
Fast style transfer [7]	VGG 16	4 h to train Result-0.015 s	MS COCO-For content and style (any art work)
Color preservation in style transfer [11]	VGG-16	training depends-CPU/GPU Results-unknown	Content image (place) & Style image (art)
Multi style transfer [10]	VGG 16	6 h training Results 3–5 s	MS COCO-For content, style image (any art work)
Practical implementation	VGG-16	1 h 45 min to train Results-3–7 s	MS COCO-For content and style (any art work)

Table 2 Comparison of approaches with the year first proposed, speed and loss used

Method with reference	Year	Remarks	Loss function used
Gatys et al. method [1]	2015	Slow	per-pixel loss—content and style loss
Fast style transfer [7]	2016	Very fast	Perceptual losses
Color preservation in style transfer [11]	2016	Slow-average speed	Per-pixel and others
Multi style transfer [10]	2017	Slow	Content, style and multi-style loss and perceptual losses
Practical implementation	2021	Slow-average	Perceptual loss net

Table 3 Comparison of approaches with their quality, advantages and disadvantages

Method with reference	Quality	Advantages	Disadvantages
Gatys et al. method [1]	Average-Good	No need of high GPU as uses optimization	Is a bit slow because of optimization
Fast style transfer [7]	Very high	Real-time & very fast	Needs GPU of high processing power
Color preservation in style transfer [11]	Average	Preserves the colors while transferring	Minor details are missing sometimes
Multi style transfer [10]	Average	Transfers style to multiple images	Slow and not efficient
Practical implementation	Good	Produces quality images on GPU	Takes some time for training

4 Conclusion and Future Scope

Transferring different styles on images gives an eye-pleasing experience. This paper gives a good understanding of how different techniques have been used in neural style transfer. These techniques enhance understanding of the working of CNN and different loss functions. Each discussed approach has something unique in it and some of them are an improvement of the previous techniques that were proposed. It gives a good knowledge of working of algorithms of different techniques and to know the importance of optimizing the loss function that was used. The main motto behind the improvement of the previously proposed method is to generate better quality output and also consume less time. Today many researchers are working toward finding new methods and techniques. Few recently introduced techniques are Video Style Transfer and Deformable Style Transfer. In style transfer algorithms optimize the loss to produce visually high-quality images. MS COCO dataset was used. Transferring style could be possible because of the computation ability of CNN. This paper has also given a comparison of different approaches with their advantages and disadvantages. The aim is to provide a comparison to identify the most efficient and quality method. In addition to all this paper includes practical implementation with results to add a better understanding. The future for CNN and style transfer algorithms has a lot of opportunities for researchers because there is a scope for improvement for the existing algorithms or developing new algorithms.

References

1. L.A. Gatys, A.S. Ecker, M. Bethge, A neural algorithm of artistic style (2015). https://arxiv.org/pdf/1508.06576.pdf
2. Y. Jing, Y. Yang, Z. Feng, J. Ye, Y. Yu, M. Song, Neural style transfer: a review. IEEE Trans. Visual Comput. Graphics **26**(11), 3365–3385 (2020). https://doi.org/10.1109/TVCG.2019.2921336
3. H. Li, A literature review of neural style transfer (2018). https://www.cs.princeton.edu/courses/archive/spring18/cos598B/public/projects/LiteratureReview/COS598B_spr2018_NeuralStyleTransfer.pdf
4. N. Makow, P. Hernandez, Exploring style transfer: extensions to neural style transfer (2017). http://cs231n.stanford.edu/reports/2017/pdfs/428.pdf
5. L.A. Gatys, A.S. Ecker, M. Bethge, Image style transfer using convolutional neural networks, in *IEEE Conference on Computer Vision and Pattern Recognition (CVPR)* (2016), pp. 2414–2423. https://doi.org/10.1109/CVPR.2016.265
6. A brief introduction to Neural Style Transfer, https://towardsdatascience.com/a-brief-introduction-to-neural-style-transfer-d05d0403901d
7. J. Johnson, A. Alahi, F.-F. Li, Perceptual losses for real-time style transfer and super-resolution (2016), https://arxiv.org/pdf/1603.08155, https://cs.stanford.edu/people/jcjohns/eccv16/, https://cs.stanford.edu/people/jcjohns/papers/eccv16/JohnsonECCV16.pdf
8. J. Johnson, Neural-style (2015). https://github.com/jcjohnson/neural-style
9. J. Johnson, Fast-neural-style (2016). https://github.com/jcjohnson/fast-neural-style
10. B. Cui, C. Qi, A. Wang, Multi-style transfer: generalizing fast style transfer to several genres (2017), http://cs231n.stanford.edu/reports/2017/pdfs/401.pdf

11. L.A. Gatys, M. Bethge, A. Hertzmann, E. Shechtman, Preserving color in neural artistic style transfer (2016). https://arxiv.org/pdf/1606.05897.pdf
12. L.A. Gatys, A.S. Ecker, M. Bethge, A. Hertzmann, E. Shechtman, Controlling perceptual factors in neural style transfer (2016). https://arxiv.org/pdf/1611.07865.pdf
13. Style in computer-vision neural style transfer, https://medium.com/datadriveninvestor/style-in-computer-vision-neural-style-transfer-c44da727f1c4
14. Style transfer w/color preservation on Mr. Bland, https://mspries.github.io/lemongang.html
15. Histogram matching, https://towardsdatascience.com/histogram-matching-ee3a67b4cbc1
16. Intuitive Guide to Neural Style Transfer, https://towardsdatascience.com/light-on-math-machine-learning-intuitive-guide-to-neural-style-transfer-ef88e46697ee
17. Figure 6-Graph obtained by tensorboard while practical implementation
18. Figure 7, https://github.com/gordicaleksa/pytorch-neural-style-transfer-johnson
19. S.S.Y. Kim, N. Kolkin, J. Salavon, G. Shakhnarovich, Deformable Style Transfer (2020). https://arxiv.org/pdf/2003.11038.pdf
20. D. Kadish, S. Risi, A.S. Løvlie, Improving object detection in art images using only style transfer (2021). https://arxiv.org/pdf/2102.06529.pdf
21. Jaejun Yoo, Youngjung Uh, Sanghyuk Chun, Byeongkyu Kang, Jung-Woo Ha.,**2019**. Photorealistic Style Transfer via Wavelet Transforms. arXiv:1903.09760 (https://arxiv.org/pdf/1903.09760.pdf)
22. D. Kotovenko, M. Wright, A. Heimbrecht, B. Ommer, Rethinking style transfer: from pixels to parameterized brushstrokes (2021). https://arxiv.org/pdf/2103.17185.pdf
23. H. Wang, Y. Li, Y. Wang, H. Hu, M.-H. Yang, Collaborative distillation for ultra-resolution universal style transfer (2020). https://arxiv.org/pdf/2003.08436.pdf

An Efficient Anonymous Authentication Scheme to Improve Security and Privacy in Large-Scale SDN-Based MANET

Suneel Miriyala and M. Satya Sai ram

Abstract Software-Defined Networking (SDN) is a traditionally used method in directly connected networks, and very recently onwards it was also used in some wireless networks. SDN's concept is to make the network more robust by leveraging the advantage of network interface re-programmability during initialization. In SDN-based networks, the control plane is transitioned to a level higher from the infrastructure to provide re-configuration. By having some input from nodes in the network, the SDN controller wants to change the configuration parameters. In Mobile Ad-hoc Network, the feedback may include insight into the quality of the connection and resources available, such as battery capacity and node position (hop count away from the destination). We introduce an anonymous authentication scheme to improve privacy inside SDN-based MANET along with which we proposed traffic monitoring system to avoid congestion and share the load from one controller to another controller. As our main contribution, a compact, stable authentication method with proper forward secrecy is developed, and what we consider to be a more interesting aspect is that it is possible to achieve user anonymity, perfect forward secrecy, and resistance to de-synchronization attacks at the same time. Our proposed work is implemented using ns-3 simulator and also proved that it was efficient by comparing with existing models.

Keywords MANET · Privacy · Security and SDN

1 Introduction

Mobile ad-hoc networks are adaptive structures made up of a variety of wirelessly transmitted mobile nodes that communicate. They are infrastructure-less networks that are self-organized, configured, and controlled. This form of network has the

S. Miriyala (✉)
College of Engineering and Technology, Acharya Nagarjuna University, Guntur, AP, India

M. S. Sai ram
ECE Department, RVR & JC College of Engineering, Guntur, AP, India

S. Rawat et al. (eds.), *Proceedings of First International Conference on Computational Electronics for Wireless Communications*, Lecture Notes in Networks and Systems 329,
https://doi.org/10.1007/978-981-16-6246-1_30

benefit of being able to be easily set up and distributed because it has an easy setup of equipment and no central administration. Examples are evident in the military or the emergency services [1].

Although devices used in wired networks get their power connection directly from accessible power grids, tiny batteries with a short lifetime are usually run in MANET nodes. This allows nodes reluctant for extended periods of time to execute intense computations. On the other hand, an attacker is usually capable of supplying adequate power and must be believed to be able to execute intense computations, implying that there is no level of attack and security in these networks.

The absence of centralized control in MANET renders detection mechanism a quite complicated problem. MANETs are extremely complex and high-scale and therefore cannot be reliably observed; benign MANET errors are reasonably common, such as disruption of transmission and loss of packets. It would be more difficult to detect intentional errors as a result. As security was an integral feature in a hostile area, these particular features of mobile ad-hoc networks pose problems that must be solved by security specifications. There has been extensive research in encryption of information, digital signature, key management, etc., by the scientific community that examines the secrecy of messages in transit over the unprotected network. However, several problems continue to arise, especially related to privacy and data confidentiality [2, 3].

This paper describes the important security and privacy concerns and current MANET strategies, in particular the field of MANET security that has not been commonly discussed. We propose a policy-based framework based on automated decision-making among nodes and focused on principles developed for other types of networks. The aim of this framework is not only to keep data confidentiality during conversation, but also after transmission to a different node. Work is on to ensure that perhaps a subset of nodes in MANETs established by the originator holds the content of communications confidential.

2 Importance of SDN-Based MANET

Software-Defined Networking (SDN) is referred to as an advanced, dynamic, controllable, cost-effective, and adaptable architecture, making it suitable for the latest applications. All networks are regulated and managed by software in this, we might conclude that all the networks are specified by software and stop the discussion. Here, the system architecture decouples the network's control and forwarding functions and enables the network control to become explicitly adaptive for applications and network services. The Open Flow protocol is a fundamental component of creating SDN solutions for different applications.

In the SDN-enabled MANET architecture, the SDN controllers are centrally located to control and manage the ad-hoc wireless network. Effectively, the controller is the network brain. The controller decides the network's collaborative actions and instructs the nodes involved about how to act. Network control functions are run by

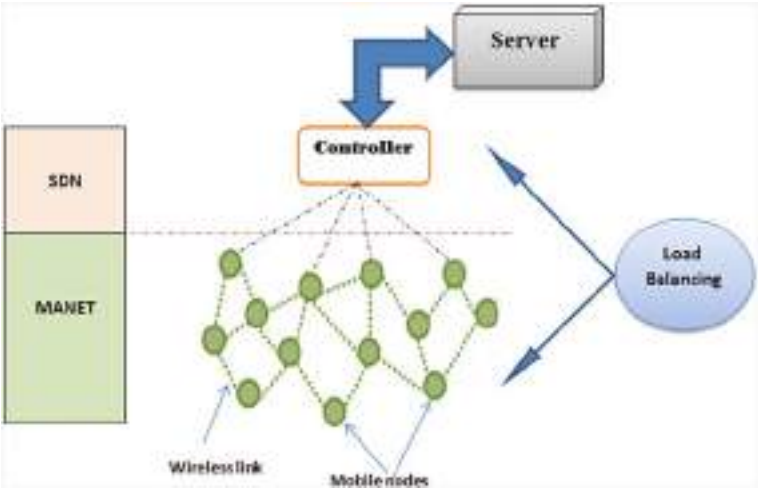

Fig. 1 SDN-based MANET environment for privacy and security

the controller and the control functions build the states on the nodes which is shown in Fig. 1.

Mobile devices, controllers, and a registration server are MANET components. The different data are processed and transmitted by the mobile devices. Before it can be used in SDN–MANET environments, all mobile devices must be registered with the registration server. The registration server monitors the identity of the mobile devices and maintains them.

It also retains a strong friendship with the monitor or responds to a request from the controller for mobile device verification. Mobile devices and the registration server will know the identity of the mobile devices because the mobile devices definitely know their identity and when the mobile devices sign for it, the registration server takes the identity of the mobile devices. The controller certifies the mobile devices unknown to the registration server without understanding the identity of the mobile devices. And it helps devices to connect securely with other mobile devices. When connecting to the controller for the first time, mobile devices carry out mutual authentication and key agreement with the controller using an unnamed verification process [4]. As this tip, the controller who is unaware of the identity of the mobile devices will check the mobile devices with the registration server service. Multiple sections of many mobile devices are based on one controller and consist of their own domain. In addition, we provide a load balancing algorithm to prevent network congestion due to the highly dynamic MANET environment.

Anonymous authentication and session key sharing via the same controller can be achieved by mobile devices in the same domain. A new verification scheme is proposed to ensure invisibility, confidentiality, and intractability in SDN–MANET environments using a secure double hiding privacy scheme. The proposed framework makes it safe for mobile devices to connect with each other in SDN MANET

environments. It also uses low-cost functions only to reduce the processing loads on the side of the mobile devices. Here, we had also used load balancing technique along with the proposed model to improve the network performance by managing queue size, transmission delay, packet loss, and power consumption.

3 Proposed Method for Security and Privacy in SDN-MANET

Although maintaining an accurate relationship, a registration server and a controller achieve reciprocal contact across the internet. On mobile devices, the registration server holds confidential details. The controller shapes its own domain and integrates the current mobile devices within its proper range. Let the mobile devices connect to the server of their registration. Mobile devices capture and generate different data and, if necessary, shared data with others. Several base stations are necessary to provide a reliable communication based on the amount of mobile devices within a domain.

The base stations do not participate directly in the joint process. Between the mobile devices and the controller, they only serve as mediators. If the communications channel stability is secured, many mobile devices will operate in one domain. Due to this, the mobile system only calculates low-cost tasks, while estimates of relatively high costs are up to controller. In other words, the careless number of mobile devices will build a domain. There are three phases to the proposed scheme: registration, enter, and contact. The mobile device SN_D, the controller CN, and the registration server SS are involved in each point. Using a safe process, such as the Diffie–Hellman key agreement protocol in advance, we presume that SS and CN share a similar secret key. And let us assume that time synchronization between SN_D, CN, and SS is defined.

SN_D securely signs for SS in the registration process. In the joining process, SN_D registered for SS usually joins CN's domain. CN will authenticate SN_D via SS in that process. The mobile devices that successfully entered the domain of CN can still not trust each other, although by sharing a shared secret key they are already developing a good relationship with CN. They conduct authentication and session key establishment processes when mobile devices choose to connect with each other securely.

Double hiding secure privacy scheme

Our proposed scheme mainly consists of three phases. They are:

i. Setup registration phase
ii. Joining into network phase
iii. Communication phase.

For MANET-based process, we have three devices like MANET node devices, Controller, and server (switch) nodes will be involved. In SDN-MANET environment, we have SDN Server (SS), Controller (CN), and SDN MANET Device (SN_D). Also, we consider some of the parameters like time stamp (Ttx), private key of I (PKi), Global id of I (GlobalIDi), and Local identity of I (LocalIDi).

The following assumptions we consider in the proposed work:

- SS and CN will exchange a common secret key through Diffie–Hellman key agreement protocol.
- In setup registration phase, SN_D will register for SS in a safe way. SN_D will join CN in the joining into network phase.
- In joining phase, CN will authenticate through SDN Server SS. The network device which joins inside the network, we can't believe completely as good. So, for this purpose, we bring trust management scheme. If they want to enter into communication phase with safety means, they want to carry authentication and session key which get from CN.

Setup registration phase

Firstly, the setup registration phase will be implemented using the following process:

- SN_D → registers with SS → SS provides Global identity.
- SN_D → receives that and store.

Then, the Global identity was generated using following step.

- Tt_st → starting time stamp
- Pk_SN_D → private key of wn D
- GlobalID SN_D = Hash(SN_D_id || Pk_SN_D||Tt_st).

The SDN Server will use this Global ID for verification process.

And SS stores SN_D s secret details like (SN_D_id, GlobalID, Pk_SN_D, Tt_st) in its storage and it will compute the hashing value of Hash(Pk_SN_D) and Hash (PK_SS) and give to SN_D as follows:

{SN_D_id, GlobalID SN_D, Pk_SN_D, hash(Pk_SN_D), hash(PK_SS), SS_id}.

After receiving this by SN_D will store it in its storage.

Joining into network phase

1. If SN_D wants to enter or join inside the Controller. Controller will authenticate SN_D using SS before providing services.

   CSK SS_CN → secret key used common between Controller and SDN Server.

   SI SN_D = GlobalID SN_D ⊕ hash(hash(PK_SS) || Tt SN_D).

   Here, we hide Global identity again using Local identity.

2. SN_D sends join request msg with MSG = (joinrequest, SI SN_D, SS_id, Tt SN_D) to CN. Which is network device request SS for authenticating CN and to provide CSK for joining CN.

3. After receiving Message. CN checks its Tt SN_D and generate new time stamp for CN as TtCN and it will do the hashing HCN as below.

HCN = hash(CSK SS_CN|| SI SN_D|| Tt SN_D|| TtCN). After generating this, it will send this AUTHREQ message ARM = (authrequest, SI SN_D, CN_ID, HCN, Tt SN_D, TtCN) to SS for authentication.

4. After receiving message ARM. SS checks CN id like whether it is a co-operate or not and also it checks TtCN for verifying its time period. After that it generates new message named Nmsg.
   Nmsg = hash(CSK SS_CN || Si SN_D || Tt SN_D|| TtCN).
   If this output is valid, then SS will generate timestamp Tss.
5. Then SDN Server ss creates GlobalID SN_Dnew by using received information and hash(Xss) as below.
   GlobalID SN_Dnew = LocalIDwn ⊕ hash(hash(Xss)|| Tt SN_D)
   And it gathers the secret information from its database using GlobalID SN_Dnew like (SN_D_id, Globalid_SN_D, Pk_SN_D,Tt_st). If GlobalID SN_Dnew and GlobalID SN_D are not the same, then SS rejects the request for authentication and it stops the communication with CN.
6. SS computes new global id as GlobalID_SN_Dnew2 = hash (SN_D_id || Pk_SN_D||Tt_st).
   After this new global id creation, SS created CSK to be communicated between CN and SN_D using SN_D private key PK_SN_D. And creates verification values like C1,C2 and C3 for SN_D and C4 for CN like.
   CSK CN_SN_D = hash(hash(PK_SN_D) || SN_D_id||CN_id||Tt SN_D|| Tt CN)
   C1 = hash(hash(PK_SN_D) || CN_id||Tt SN_D)
   C2 = hash(CSK CN_SN_D ||SS_id||Tt SN_D)
   C3 = hash(GlobalID_SN_Dnew2 ||SS_id||Tt SN_D)
   C4 = CSK CN_SN_D ⊕ hash(CSK CN_SS || Tt CN).
   After these steps, SS computes new Hash values Named HV = hash(CSK CN_SN_D || C1||C2||C3||C4||Tt_SS)
   This HV and Tt_SS will be used to check by CN when the MSG 3 receives and generates one more verification value C5 after generating CSK CN_SN_D. And sends the msg 4 to SN_D with (CN_id,C1,C2,C3,C5,TtCN,TtSS).
   CSK CN_SN_D = C4 ⊕ hash(CSK CN_SN_D || Tt CN). And C5 = CSK CN_SN_D ⊕ hash(CSK CN_SN_D|| Tt SN_D).
7. After receiving Msg4.SN_D checks Tt CN and then it creates C1new.
   C1new = hash(hash(PK_SN_D) || CN_id||Tt SN_D).
   And also creates CSK CN_SN_Dnew and C2new.
   CSK CN_SN_Dnew = hash(hash(PK_SN_D) || SN_D_id||CN_id||Tt SN_D|| Tt CN)
   C2new = hash(CSK CN_SN_Dnew ||SS_id||Tt SN_D).
   And SN_D creates GlobalID SN_Dnew and verify C3new as follows.
   GlobalID SN_Dnew = hash(PK_SN_D || SN_D_id || Tt SS)
   C3new = hash(GlobalID SN_Dnew || SS_id|| Tt SN_D).

If C3 and C3new is equal, SS computes SN_D's new GlobalID SN_Dnew and SN_D stores its New global id. So, now global id is updated by replacing old GlobalId.

And SN_D checks C5new = C5 after creating C5new = CSK CN_SN_Dnew ⊕ hash(CSK CN_SN_Dnew|| Tt SN_D).

This verification states that SN_D and CN share their Common secret key successfully.

Transmission Phase

In this phase, the network devices which are located inside the CN want to communicate with each other and share their session key for communication and it will make that communication as secure. In this, we made assumptions SN_D1 and SN_D2 already share their CSK named CSK_CN_SN_D1 and CSK_CN_SN_D2 with CN in joining phase.

The transmission between this SN_D1 and SN_D2 is as follows.

1. SN_D1 will generate time stamp Tt1 and create new LocalIDnew_SN_D1 = Globalid_SN_D1 ⊕ hash(hash(PK_SS) || Tt SN_D1). This is updated local id instead of old local id.
2. SN_D1 will verify C6 and HV1 using following equation.
   C6 = LocalIDnew_SN_D1⊕ hash(CSK CN_SN_D1 || Tt SN_D1)
   HV1 = hash(CSK CN_SN_D1|| LocalID_SN_D1||C6|| Tt SN_D1) and SN_D1 now sends request msg for communication with commmsg1 = (commreq, LocalID_SN_D1,ID_CN,C6,HV1, Tt SN_D1) to SN_D2.
3. T2 creates Tt SN_D2 after receiving commmsg1 and checking TtSN_D1 and creates new localid LocalIDnew_SN_D2 and C7 and HV2 as follows.
   LocalIDnew_SN_D2 = Globalid_SN_D2⊕ hash(hash(PK_SS) || Tt SN_D2).
   C7 = LocalIDnew_SN_D2 ⊕ hash(CSK CN_SN_D2 || Tt SN_D2).
   HV2 = hash(CSK CN_SN_D2 || Tt SN_D2||TtSN_D1||C6||C7||HV1|| LocalIDnew_SN_D2|| LocalIDnew_SN_D1)
   After generating these details, it sends auth req msg ARM1 to CN.
   ARM1 = (authreq,localid_SN_D1.localid_SN_D2,C6,C7,HV1,HV2,Tt SN_D1,Tt SN_D2)
   CN will check this Tt SN_D2, localid-SN_D1 and localid_SN_D2 to confirm SN_D1 and SN_D2 is authenticated in join phase and then it checks HV1 and HV2 is equal to HV1_new and HV2_new or not by using following equation.
   HV1_new = hash(CSK CN_SN_D1|| LocalID_SN_D1||C6|| Tt SN_D1)
   HV2_new = hash(CSK CN_SN_D2 || Tt SN_D2||TtSN_D1||C6||C7||HV1|| LocalIDnew_SN_D2|| LocalIDnew_SN_D1)
4. If above HV1 and HV2 are verified successfully, then CN creates new local id for wn D1 and SN_D2 by using C6,C7, CSK CN_SN_D1 and CSK CN_SN_D2.
   Localid_SN_D1new = C6⊕ hash(CSK CN_SN_D1 || Tt SN_D1)
   Localid_SN_D2new = C7⊕ hash(CSK CN_SN_D2 || Tt SN_D2)
   Now, this updated local_id will be taken instead of old local id.

Now generation of session key SK will be take place in CN with time stamp Tt CN_D1D2 and also it creates S1 and S2 using CSK CN_SN_D1 and CSK CN_SN_D2.

SK = hash(Localid_SN_D1 || Localid_SN_D2|| Tt SN_D1|| Tt SN_D2 ||CSK CN_SN_D1|| CSK CN_SN_D2||).

S1 = SK ⊕ hash(CSK CN_SN_D1|| Localid_SN_D2|| Tt SN_D1)

S2 = SK ⊕ hash(CSK CN_SN_D2|| Localid_SN_D1|| Tt SN_D2)

Now, CN computes hashing and verification values like C8,C9,HV3 and HV4.

C8 = hash(SK||ID_CN|| Tt SN_D1), C9 = hash(SK||ID_CN|| Tt SN_D2)

HV3 = hash(CSK CN_SN_D1||S1||C8|| Tt CN_D1D2)

HV4 = hash(CSK CN_SN_D2||S2||C9|| Tt CN_D1D2)

After this, CN sends messages to both SN_D1 and SN_D2 as follows.

Msg5 = (ID_CN,S2,C9,HV4, Tt CN_D1D2).

Msg6 = (ID_CN,S1,C8,HV3, Tt CN_D1D2).

6. After receiving this msg5 and msg6 wn D2 and SN_D1 will check HV3 and HV4 and both will generate new session keys separately SK_new like below.

SK_new = S2 ⊕ hash(CSK CN_SN_D2|| localid_SN_D1||Tt SN_D2) for SN_D2

SK_new = S1 ⊕ hash(CSK CN_SN_D1|| localid_SN_D2||Tt SN_D1) for SN_D1

And C8_new = hash(SK_new || ID_CN|| Tt SN_D2) for SN_D2

C9_new = hash(SK_new || ID_CN|| Tt SN_D1) for SN_D1

Here, SN_D1 and SN_D2 confirm C9_new and C8_new with C9 and C8 to check the session key computer by CN.

Finally, SN_D1 shares session key SK with SN_D2 successfully.

Here are several queue management approaches that will be introduced in the context of load balancing [5]; first, it will operate at the node level, then at the controller level, and a decision will be made appropriately. After receiving the warning message, the controller collects the parent list of child nodes that create queues at the congested gateway and requests that they get their queue level. At this stage, the controller will identify low queue parents of the child node(s) [6, 7].

4 Experimental Results

Here, we had used Network Simulator-3 for practical implementation of proposed method in SDN MANET environments. Also, the results are compared with the existing MANET security methods like Group key management SDN MANET [8] and Hybrid Encryption-based privacy in SDN MANET [9]. The proposed method shows good results with respect to all the network parameters using performance evaluation (Tables 1 and 2).

We evaluate the graphs by altering the size of attackers and nodes in the network. The parameters taken into account in the analysis performance of the proposed

Table 1 Comparing performance parameters with respect to number of attackers of proposed and various existing methods

Number of Attackers	Overheads		Packet delivery ratio		Delay	
	PRIVACY_ SDN_ MANET	SECURE_ AUTH_ PRIVACY_ SDN_ MANET	PRIVACY_ SDN_ MANET	SECURE_ AUTH_ PRIVACY_ SDN_ MANET	PRIVACY_ SDN_ MANET	SECURE_ AUTH_ PRIVACY_ SDN_ MANET
2	0.34	0.28	99.01	99.56	0.038	0.032
4	0.79	0.58	98.39	99.12	0.080	0.067
6	1.18	0.92	94.12	96.79	0.089	0.073
8	1.88	1.08	92.88	95.41	0.096	0.079
10	2.36	1.75	90.90	93.36	0.102	0.087

Number of Attackers	Loss		Throughput	
	PRIVACY_ SDN_ MANET	SECURE_ AUTH_ PRIVACY_ SDN_ MANET	PRIVACY_ SDN_ MANET	SECURE_ AUTH_ PRIVACY_ SDN_ MANET
2	0.95	0.67	29.45	32.59
4	1.53	0.85	27.39	30.15
6	6.12	3.21	26.26	28.53
8	8.54	4.69	25.54	28.21
10	10.42	6.64	24.94	27.83

Table 2 Comparing performance parameters with respect to number of nodes of proposed and various existing methods

Number of Nodes	Overheads		Packet delivery ratio		Delay	
	PRIVACY_ SDN_ MANET	SECURE_ AUTH_ PRIVACY_ SDN_ MANET	PRIVACY_ SDN_ MANET	SECURE_ AUTH_ PRIVACY_ SDN_ MANET	PRIVACY_ SDN_ MANET	SECURE_ AUTH_ PRIVACY_ SDN_ MANET
10	0.27	0.19	99.98	99.99	0.032	0.029
20	0.56	0.43	99.17	99.94	0.078	0.067
30	0.85	0.67	97.12	98.97	0.095	0.084
40	1.17	0.96	96.88	98.18	0.345	0.218
50	1.66	1.03	94.90	96.14	0.86	0.64

Number of Nodes	Loss		Throughput	
	PRIVACY_ SDN_ MANET	SECURE_ AUTH_ PRIVACY_ SDN_ MANET	PRIVACY_ SDN_ MANET	SECURE_ AUTH_ PRIVACY_ SDN_ MANET
10	0.87	0.83	30.06	33.10
20	0.97	0.86	28.14	32.53
30	1.56	0.95	28.76	30.88
40	3.47	1.23	27.65	30.05
50	7.27	2.11	27.53	29.75

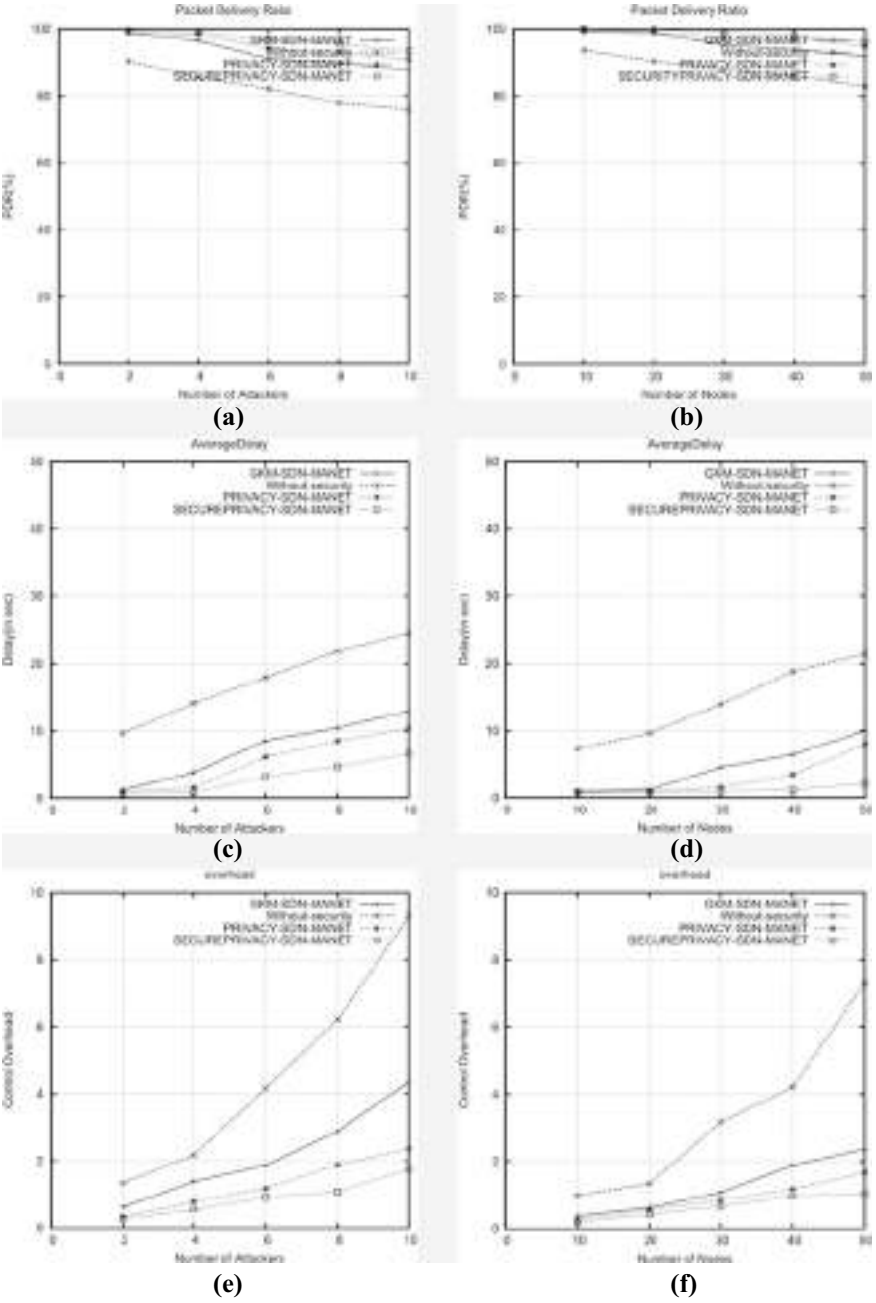

Fig. 2 Analysis of PDR (**a** and **b**), delay (**c** and **d**), overhead (**e** and **f**), throughput (**g** and **h**), and packet loss (**i** and **j**) with respect to nodes and attackers

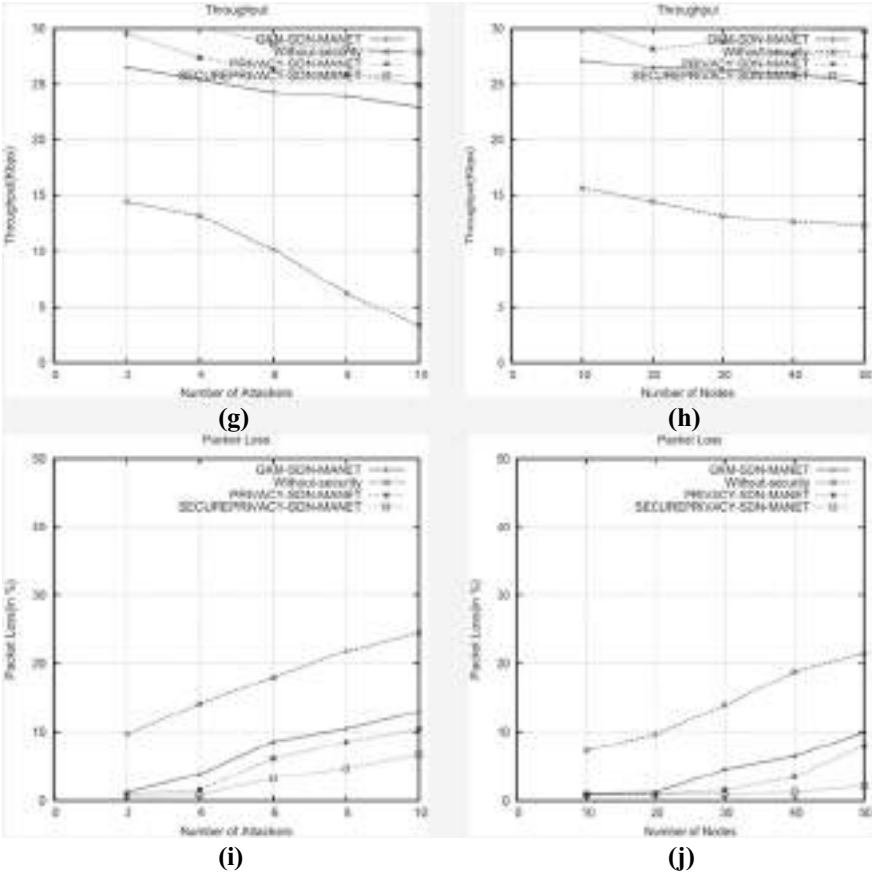

Fig. 2 (continued)

method are Packet Delivery Ratio (PDR), Average Delay, Control Overhead, Average Throughput, and Packet loss [10] (Fig. 2).

5 Conclusion

We propose a novel anonymous authentication scheme for security and privacy in SDN MANET. Here, the SDN controller plays a major role in the entire network. The experimental results also show that this method was best when compared with the existing techniques like Group key management SDN MANET and Hybrid Encryption-based privacy in SDN MANET. This method was more suitable to all the SDN-based MANETs to provide security and privacy.

References

1. K.A. Sliman, A. Yaklaf, Security routing protocols in ad hoc networks: challenges and solutions, in *International Conference on Recent Advances in Electrical Systems, Tunisia, 2016*
2. V.V. Sarbhukan, Ragha, establishing secure routing path using trust to enhance security in MANET. Wireless Pers. Commun. **110**, 245–255 (2020)
3. A. Ahmad, S. Ismail, User selective encryption method for securing MANETs. Int. J. Elect. Comput. Eng. (IJECE), p-ISSN 2088–8708, e-ISSN 2722–2578
4. Y. Chung, S. Choi, D. Won, Anonymous authentication scheme for intercommunication in the internet of things environments. Int. J. Distrib. Sensor Netw. (2015)
5. M.A. Salem, R. Yadav, Efficient load balancing routing technique for mobile ad hoc networks. Int. J. Adv. Comput. Sci. Appl. **7**(5) (2016)
6. H. Fotouhi, M. Vahabi, A. Ray, M. Bjorkman, SDN-TAP: an SDN-based traffic aware protocol for wireless sensor networks, in *IEEE 18th International Conference on e-Health Networking, Applications and Services (Healthcom), 2016*
7. S.V. Mallapur, S.R. Patil, J.V. Agarkhed, Load Balancing technique for congestion control multipath routing protocol in MANETs. Wireless Pers. Commun. **92**, 749–770 (2017)
8. S. Miriyala, M.S. Sairam, Lightweight group key management for data dissimilation for dynamic SDN MANET environments. J. Crit. Rev. **7**(3). ISSN-2394–5125
9. S. Miriyala, M.S. Sairam, Improving privacy in SDN based MANET using hybrid encryption and decryption algorithm, in *Microprocessors and Microsystems, 2020*
10. M. Chakraborty, M. Singh, *Introduction to Network Security Technologies Lecture Notes in Networks and Systems book Series* (LNNS), vol. 163, pp. 3–28
11. Manpreet, J. Malhotra, A survey on MANET simulation tools, in *International Conference on Innovative Applications of Computational Intelligence on Power, Energy and Controls with their Impact on Humanity (CIPECH14) 28 & 29 November 2014*

Drowsy Alarm System Based on Face Landmarks Detection Using MediaPipe FaceMesh

Aman and A. L. Sangal

Abstract The pandemic of 2020 has affected the every minor and major aspect of human life all over the world. The whole world went into lockdown, where socializing with other people was banned. Almost everything was being done online, whether it was the office work or classes. Schools and Colleges started conducting classes online through various video meeting apps, but this came with a lot of issues like students were losing interest in class, teachers were unable to see whether the students are paying attention in the class or not, etc. In this paper, a drowsy alarm system is proposed to tackle these issues which alerts the student as well as the teacher when a student is dosing off or losing interest in the class. MediaPipe FaceMesh, a lightweight Machine Learning (ML) face geometry solution, is used to create this system. With the help of Tensorflow.js, an ML library in Javascript, the system can be deployed in the web browser of any device whether it is a mobile or a computer. The system tracks the movement of eyes and mouth and alerts the person by starting the alarm if a closed eye or a yawn is detected. The effectiveness of the system when it runs on the WebGL, WebAssembly (WASM), and on computer's CPU (Central Processing Unit) is compared and the result has been shown.

Keywords MediaPipe · FaceMesh · Tensorflow.js · Landmarks · Face detection · Face tracker

1 Introduction

Due to the increase in online activity, the demand for Computer Vision (CV) is at its all-time high. Computer Vision (CV) is a field of study that tries to find or develop techniques that help computers understand and "see" digital images (videos and

Aman (✉) · A. L. Sangal
Dr. B R Ambedkar National Institute of Technology, Jalandhar, India

A. L. Sangal
e-mail: sangalal@nitj.ac.in

S. Rawat et al. (eds.), *Proceedings of First International Conference on Computational Electronics for Wireless Communications*, Lecture Notes in Networks and Systems 329,
https://doi.org/10.1007/978-981-16-6246-1_31

photographs) and their contents. It is an interdisciplinary field that could be generally referred to as the subfield of Machine Learning (ML) and Artificial Intelligence (AI), which may incorporate the use of specialized methods and the use of particular learning algorithms [1]. There is a plethora of research done in the area of Computer Vision over the last few years. A few of the popular CV applications are Face Detection, Face Recognition, Object Classification, Object Identification, Face Landmark Detection, etc.

Face detection is the building block of computer vision. Face detection is the prerequisite of any other computer vision applications involving faces [2]. Face detection has been studied in the last few years because of the increase in the interaction of humans and computers. Face detection is the subdomain or the subfield of object detection [2]. Due to its rapidly increasing use in a number of different applications, face detection is becoming a challenge. There are two types of errors in face detection, one is a false positive and the other is a false negative [3]. In a false positive, face is not detected although the face is present in an image or a video, and in a false negative, due to the low detection rate, faces are missed. There are a plethora of face detection algorithms present such as Viola Jones algorithm [2, 3], MediaPipe [4–6], Haar features [7, 8], SMQT Features and SNOW classifier [2], Neural Network-based face detection [2, 9], Support Vector Machine based face detection [2], etc.

In this paper, MediaPipe is used for face detection and face mesh prediction. Predicting the facial geometry or face mesh by face alignment or face registration has been a big issue in computer vision. For related work and for a good review on 2D and 3D face alignment or face mesh prediction problems, readers should read [10], the research is thorough and unique. Face mesh prediction is commonly done by locating very few (generally 68) landmarks, or key points [11]. But MediaPipe FaceMesh is a lightweight face geometry solution. As Fig. 1 shows, it estimates or predicts the 486 3D face landmarks to infer the estimated surface geometry of the human face in real-time [5, 11]. It uses ML to create 3D surface geometry, requiring only one camera input and does not need the customized depth sensor. Using the lightweight model architecture, the system provides the real-time performance necessary for the live experience.

This system is different from any typical face detection system. It can be deployed on the web browser and can be used everywhere while performing at a high speed. ML should not be restricted in the local systems only, as ML on the browser is the necessity of this day and age. To achieve this goal, tensorflow.js has been used in this system. Tensorflow.js is an ML library in Javascript. It comes up with the exact kind of hardware acceleration required using the Web GL layer, which is regarded as the web browser side Graphical Processing Unit (GPU) [12]. With the help of tensorflow.js and mediapipe facemesh, the proposed system tracks the movement of the eyes and mouth and starts the alarm if the eyes of the person are closed or the person yawns. The system can be deployed on the web browser of mobile or computer while performing at a high speed.

This paper is organized as follows: Sect. 2 provides a literature survey. Section 3 represents the methodology used. Section 4 gives the results. Section 5 presents the conclusions and Sect. 6 gives the future works.

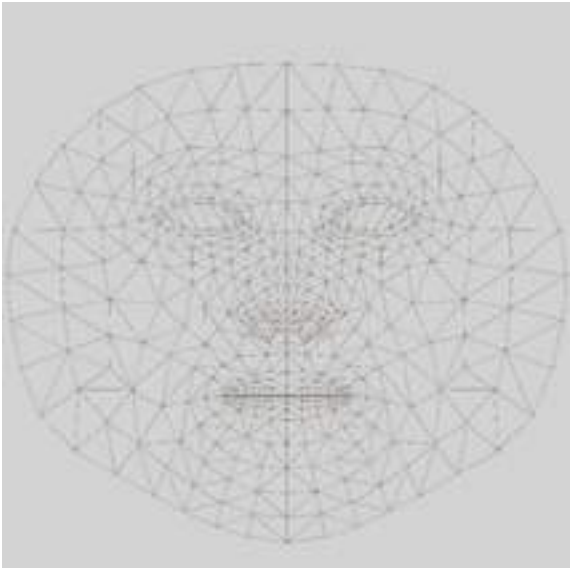

Fig. 1 The 486 3D face landmarks or keypoints map

2 Literature Survey

In this section of the paper, related work that is done in the area of face detection, face alignment or face mesh, and face tracker and eye tracker is discussed briefly. There has been extensive work done related to the areas mentioned above in the last few years.

In the area of face detection, many algorithms have been proposed and used in the past few years. Reference [3] has used the Viola Jones algorithm for face detection. Using the algorithm, Divya Meena and Ravi Sharan have demonstrated the technique where single as well as multiple human faces can be detected. To train the cascade technique, the above algorithm uses Adaboost which in turn makes the algorithm very efficient [3]. Due to its necessity in security applications, there have been a lot of algorithms proposed for face detection. References [7, 8] have used Haar features and Adaboost for face detection in videos. In the paper, S. V. Tathe, A. S. Narote, and S. P. Narote have made efforts to reduce the processing time for face detection. The system proposed in the paper detects and identifies the person in the camera view and raises the alarm if an unauthorized person is detected [7]. The Haar face detector proposed does not work if the face size is very small in the frame and it is unable to handle variations in the pose. Vinita Bhandiwad and Bhanu Tekwani have used neural networks for face detection [9]. They have used the ORL database which contains 400 images and used the MATLAB 2013 environment for implementing the results. The result showed that neural networks perform well for face detection purposes because of hidden layer processing. The system performed well even with the face which is not proper. Dwi Ana Ratna Wati and Dika Abadianto have used template matching algorithms for face detection and principal component analysis

(PCA) for face recognition to create a smart home security application system [13]. The template matching algorithm for face detection performs well in few conditions such as the colour of skin and shirt does not match, background colour and skin colour are different, part of the face is not covered with accessories, and distance between the camera and the person is less than 240 cm [13]. Kirti Dang and Shanu Sharma have compared the different face algorithms and presented the result [2]. Different face detection algorithms compared are Support Vector Machine, Neural Networks, Viola Jones, and SMQT features and SNOW classifier. To get accurate results, all the algorithms are compared using DetEval software based on recall and precision value. According to the results, Viola Jones has the highest value of precision and recall, and Support Vector Machine has the lowest value of precision and recall, so Viola Jones is the best face detection algorithm amongst these algorithms [2].

The work is done in the area of face landmarks detection, 2D and 3D face alignment, and face geometry discussed briefly in this part of the section. Yury Kartynnik, Artsiom Ablavatski, Ivan Grishchenko, and Matthias Grundmann have presented a model based on a neural network that predicts the face mesh of a human face using a single camera input [11]. The model shows a high prediction rate and works on mobile GPUs with high real-time inference speed. The model estimates or predicts the 486 3D face landmarks to infer the estimated surface geometry of the human face in real-time [11]. Adrian Bulat and Georgios Tzimiropoulos have presented a good review on 2D and 3D face alignment problems [10]. Landmark localization or face alignment is the area of computer vision in which a tremendous amount of research has been done in the last few years. Adrian Bulat and Georgios Tzimiropoulos have used Face Alignment Networks (FAN) for face alignment purposes [10]. Since there is a scarcity of 3D datasets for face alignment, they have used 2D to 3D FAN to construct the 3D face alignment dataset from the 2D face alignment dataset and used the 3D alignment dataset for 3D face alignment. The dataset does not contain some of the un-familiar poses. The result shows that the FAN works quite well and shows resilience to resolution, pose, and initialization. Dr. P. Shanmugavadivu and Ashish Kumar have used feature-based and part-based face detection techniques to address the Partially Occluded Face Detection (POFD) issue [14]. They have presented a system for face detection with loosely face geometry. The result presented shows the face that is partially occluded can be easily detected and annotated by using a detection method based on loosely face geometry in real time with fewer facial components [14].

The work is done in the area of human face tracker and eye tracker discussed briefly in this part of the section. Mandalapu Sarada Devi and Dr. Preeti R Bajaj have used the skin colour method to create a human face tracker that works in real-time [15]. The facial features extraction method is used to extract the position of the facial features in the human face. The human face tracking system can be used in various applications, one of the applications of human face tracker is video surveillance. Xiaosong Lan, Zhiwei Xiong, Wei Zhang, Shuxiao Li, Hongxing Chang, and Wenjun Zeng have presented a system for video surveillance using a human face tracker that accomplishes two things: it performs accurately for a long time even when a person moves in and out of the camera view constantly and it has very low complexity

which is very helpful in deploying the system in real-time [16]. Kanade-Lucas-Tomasi (KLT) feature tracker, and to decrease the computational complexity for online processing, HAKLT tracker has been used. HAKLT tracker is a simple tracker that is a combination of KLT and colour histogram [16]. Apart from the human face tracker, eye tracker is a very useful technology in the real world. It is a method that records the positions of eyes through a camera and converts it to the coordinates on a computer. Hong-Fa Ho has presented an eye tracker system that is of low cost and with better accuracy [17]. GazeTracker Opensource software and C# have been used to create the recording and analysis system. Divya Venugopal, Amudha J, and C. Jyotsna have proposed the usability, applications, and advantages of an eye tracker system [18]. Different applications of an eye tracker have been proposed in the paper such as stress analysis, advertising and marketing research, assistive technology, website usability, neuroscience and diagnostics, human behaviour, etc. [18]. This shows that there are many uses of face and eye tracker in the real world.

3 Methodology Used

In this section of the paper, all the methods used to create the drowsy alarm system have been discussed. The methods that have been used are MediaPipe Face Mesh and tensorflow.js to create an eye tracker and a yawn tracker which tracks the movement of the eye and the mouth of the person using the web camera of the device and the system is deployed on the web browser.

3.1 MediaPipe FaceMesh

MediaPipe Face Mesh is an ML pipeline that predicts the 486 3D face landmarks in real time as shown in Fig. 2a. This is a lightweight model architecture that runs easily on mobile devices, because of this reason the model gives the real-time performance necessary for a live experience. The model comes equipped with a triangular face mesh as shown in Fig. 2b and a face tracker as shown in Fig. 3a, b. A few of the ML solutions provided in MediaPipe are Face Detection, Face Mesh, Iris Tracker, Hands Tracker, Pose Tracker, Holistic, Object Detection, Hair Segmentation, Box Tracking, Objectron, KNIFT, and Instant Motion Tracking. In this paper, MediaPipe Face Mesh, MediaPipe Face Detection, and MediaPipe Face Tracker (Eye Tracker and Yawn Tracker) have been used to create the drowsy alarm system.

For geometry estimation or 3D facial landmarks estimation of a human face, MediaPipe Face Detection is required. For creating a face mesh, an accurate facial region of interest is required, which is provided by MediaPipe Face Detector. This detector is loosely based on BlazeFace. BlazeFace is a lightweight and good performing face detector which is created specifically for mobile GPU inference. This allows the

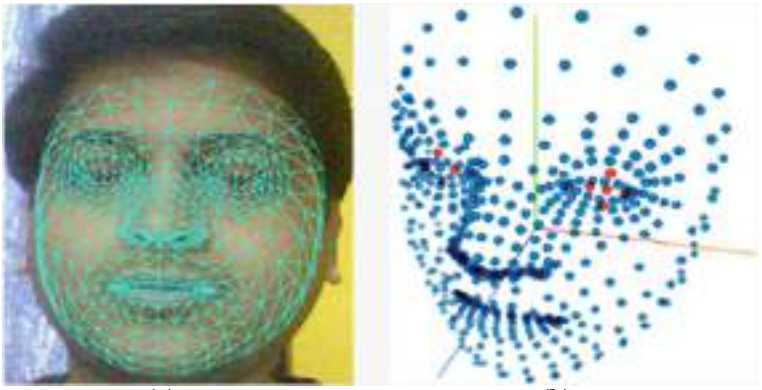

(a) **(b)**

Fig. 2 Showing the landmarks or keypoints of human face. **a** Face Mesh prediction over the face in real time. **b** Triangular Face Mesh in real time

mediapipe face detector to perform super well in real time which is very necessary for the live experience.

ML pipeline which is used in MediaPipe FaceMesh consists of two deep neural network models. These two models work together. The first model is a detector that works on the full image and calculates the face locations, and the second model is a 3D face landmark model that works on those face locations and with the help of regression anticipates the approximate surface geometry. By doing these processes, the face is accurately cropped which in turn drastically reduces the need for affine trans-formations (translation, rotation, scale change), instead, this allows the network to allocate most of its capability to coordinate prediction accuracy.

The mediapipe facemesh package used in the drowsy alarm system infers 3D face geometry from a video or an image. The package infers the 3D facial geometry using only a single camera without using any depth sensor. The 3D facial geometry locates facial features like nose, eyes, and lips including details like face silhouette and lip contours.

3.2 Eye Tracker

The eye tracker used in this paper to create the drowsy alarm system calculates the distance between the eyelids of both, right and left, eyes and if the distance calculated is less than the threshold value set, then it detects that the eyes are closed and starts the alarm. The threshold value can be adjusted according to the screen position and screen resolution of users. The alarm threshold value can be adjusted from 0 to 100, such that the alarm sounds only when the users close both the eyes. For the results shown in this paper, the threshold value for the eye tracker is set to 50. Keypoints

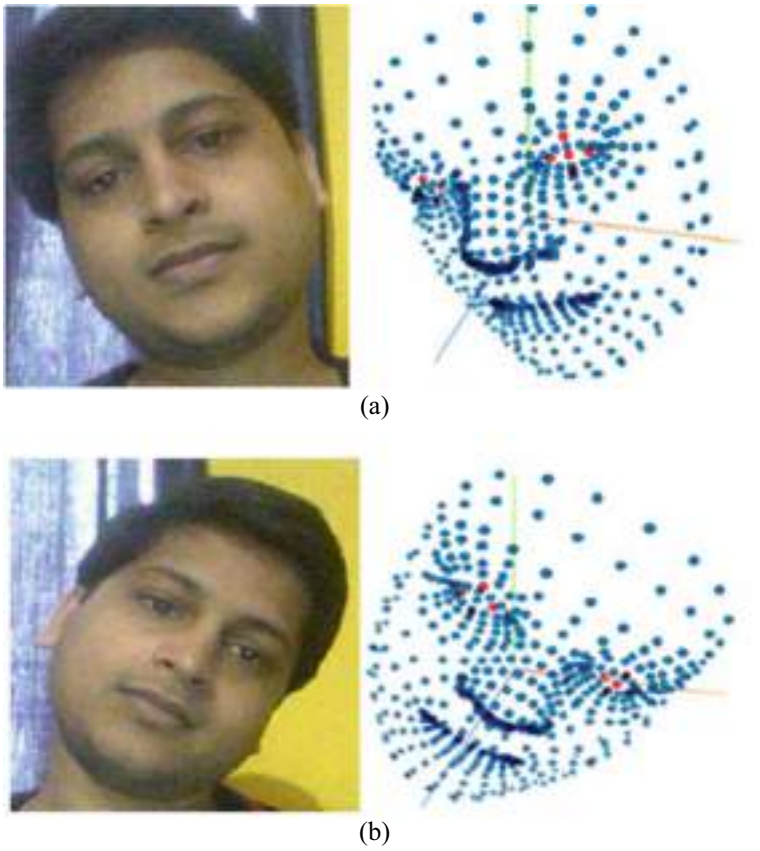

Fig. 3 Face movement tracker in real time. **a** Triangular face mesh tracking the left movement of the face. **b** Triangular face mesh tracking the right movement of the face

for eyes are shown as five red dots each for both the eyes in triangular face mesh as shown in Fig. 2b.

As shown in Fig. 4a, the distance between the vertical red dots in the triangular face mesh is greater than the threshold value set, which is 50 in this case, when the eyes of the person are open, and in Fig. 4b, the vertical red dots in the triangular face mesh are very close to each other, indicating that the distance measured is less than the threshold value, meaning both the eyes of the user are closed, thus starting the alarm.

The charts in Fig. 5a and b show the graph when both the eyes are open and when both the eyes are closed, respectively. The graph is created using CanvasJS which is a well-known library for creating charts or graphs in javascript.

The blue line in the chart is for the left eye and the red line in the chart is for the right eye. The chart shows the smoothed distance between the left and the right eyelids.

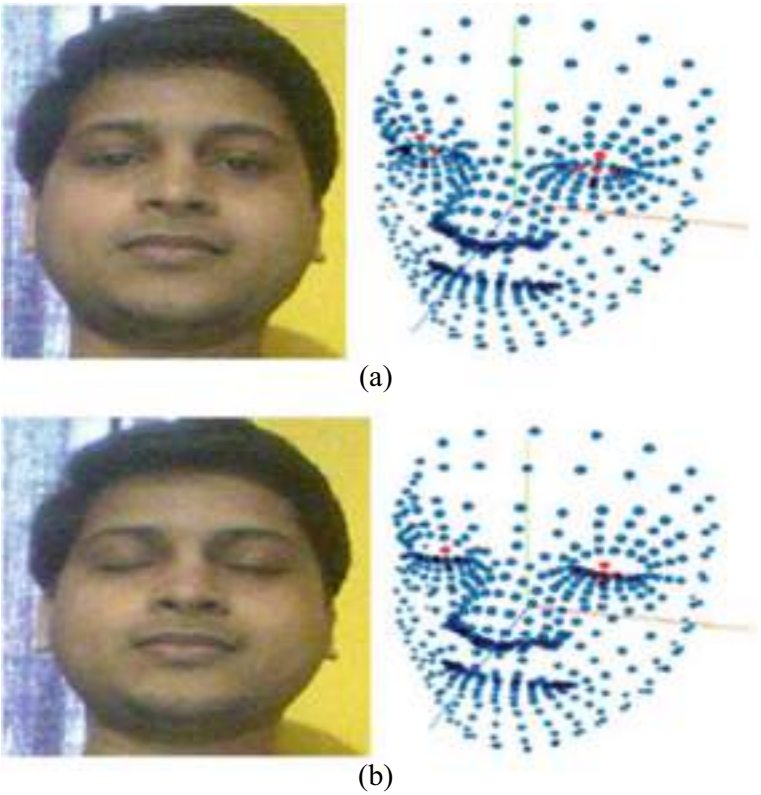

Fig. 4 The eyelids tracker. **a** Position of the red dots on the triangular face mesh when both the eyes are open. **b** Position of the red dots on the triangular face mesh when both the eyes are closed

In Fig. 5a, when both the eyes are open, the line in the graph is above 50 (threshold), and in Fig. 5b, the line in the graph is below 50, indicating both the eyes are closed, thus sounding the alarm.

3.3 Mouth Tracker or Yawn Tracker

The mouth tracker or the yawn tracker calculates the distance between the upper lip and the lower lip of a person. If the distance between the upper and the lower lip is greater than the set threshold value, then the system sounds the alarm indicating the person is yawning. The threshold value can be adjusted according to the screen resolution and screen position of users. The alarm threshold value can be adjusted from 100 to 500. For the results shown in this paper, the threshold value for the mouth tracker or the yawn tracker is set to 100.

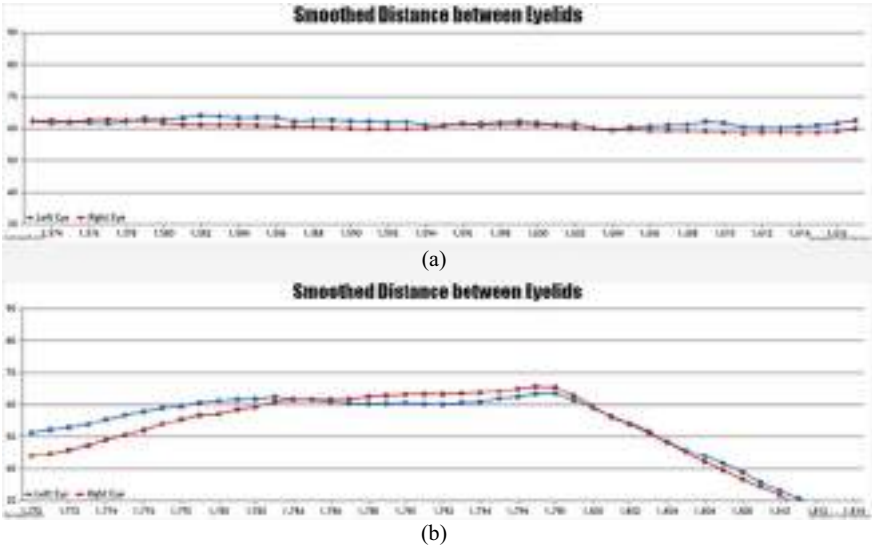

Fig. 5 Smoothed distance between eyelids. **a** When both the eyes are open. **b** When both the eyes are closed

While yawning, the keypoints around the lip area in the triangular face mesh and face mesh prediction over the face stretches are shown in Fig. 6. When the distance calculated is over the threshold value, which is 100 in this case, the system sounds the alarm alerting that the person is yawning. Base64 encoded string has been used for the beep or the alarm sound.

The charts in Fig. 7a and b show the graph when the mouth is open and when the mouth is closed, respectively. The graph is created using CanvasJS which is a well-known library for creating charts or graphs in javascript. The blue line in the chart is for the distance between the upper and the lower lip.

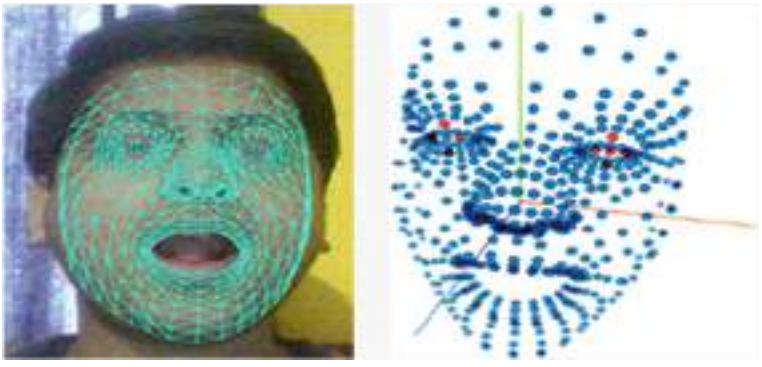

Fig. 6 The mouth tracker or the yawn tracker in real time

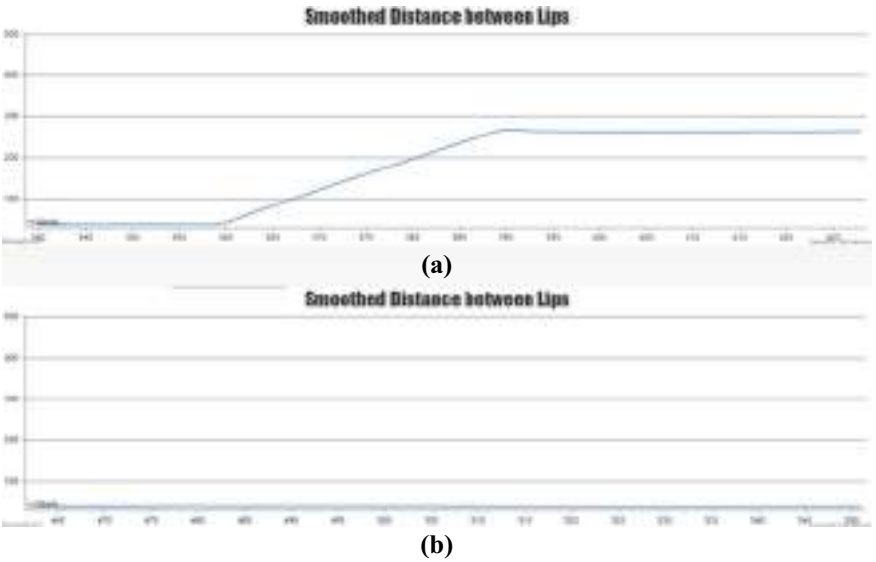

Fig. 7 Smoothed distance between lips. **a** When the mouth is open. **b** When the mouth is closed

3.4 TensorFlow.js

Tensorflow.js is a machine learning library in Javascript. It is a hardware-accelerated and open-source library for training and implementing machine learning models.

To build machine learning models from scratch by using high-level layers API or the low-level JavaScript, linear algebra library tensorflow.js can be used. It can be used to build machine learning in the web browser using intuitive and flexible APIs. Tensorflow.js model converters use pre-trained Keras or TensorFlow models in the web browser. By using sensor data that is connected to the web browser, it can even re-train models which existed before.

Tensorflow serving, a high-performance and flexible serving system for ML models, uses gRPC and Protobuf. gRPC uses HTTP/2 which keeps the basic postulates and standards of HTTP and removes the optional parts of HTTP1.1. gRPC takes full advantage of the capabilities of HTTP/2 and allows you to stream information on an ongoing basis. Protobuf is a binary format. It is used for the serialization of data. It is more effective than JSON. The performance of tensorflow serving is on par with the code written in C/C++.

Tensorflow.js comes up with the exact kind of hardware acceleration required using the WebGL layer, which is regarded as the web browser side Graphical Processing Unit (GPU).

Table 1 Performance of different devices

Devices	Performance (fps)
Dell (Windows)—WebGL	10
Dell (Windows)—WASM	5
Dell (Windows)—CPU	2
MacBook Pro—WebGL	40
MacBook Pro—WASM	22
MacBook Pro—CPU	18

Table 2 Performance of different model on windows

Model	Inference time (ms)
Mesh	215
Eye	185
Lips/Mouth	150

4 Result

A drowsy alarm system has been implemented that alerts the person if both the eyes are closed, i.e., person is sleeping or mouth is open, i.e., person is yawning. The system is specifically implemented keeping in mind about the online works, whether it be online class or online meeting. It is very hard to pay attention on every single person in online meeting or every single student in online class, but this system will help the meeting organizer or the teacher by starting the alarm if anyone starts to lose interest in the class or anyone is sleeping during the class. The system is implemented using the lightweight ML model so that it can work on low-end devices as well and it is easily deployable on the browser. In Table 1, the FPS is compared when it runs on WebGL, WASM, and CPU. The result in Table 1 is taken by deploying the system on MacBook Pro (a high-end device) and Dell Inspiron 15 3000 series (a low-end device) with windows as OS.

Table 2 demonstrates the performance of different models in our system in inference time (ms). As it is clear from Table 2 that the mouth tracker or yawn tracker model is faster than the eyelid tracker model in our system. The mouth tracker model is 23.4% faster than the eyelid tracker model. The mouth tracker and eyelid tracker models are 43.4% and 16.3% faster, respectively, than mesh model.

5 Conclusion

Using TensorFlow.js and MediaPipe FaceMesh, an ML model for a drowsy alarm system based on facial landmarks detection was created. Since tensorflow.js uses WebGL layer which is a browser side GPU, the system can be deployed on the browser of any device, whether it is a low-end device or a high-end device. MediaPipe

FaceMesh is a lightweight package which makes it ideal for real-time inference on variety of devices. The system is specifically implemented for alarming the teacher if any student is dosing off during the online class. After the pandemic of 2020, every college and school has started taking classes online, and it is very hard to keep an eye on each and every student in the online class. This system is a small effort to keep students attentive during online classes.

6 Future Works

The system implemented in this paper is a prototype, a more robust and accurate system can be created using the prototype system as a base. Using mediapipe facemesh, eyelids and mouth tracker were used for creating the alarm system. In future, other facial features and facial expressions can also be used for creating different applications like AR expression, etc. The 3D facial geometry can also be used for creating different AR effects in the same way it was used to create the drowsy alarm system.

Acknowledgements This research work was backed up/assisted in part by the Dr. B.R. Ambedkar National Institute of Technology, Jalandhar, India. Thanks to Professor Dr. A. L. Sangal for guiding me through this research work. Thanks to Ankur Shukla for helping with technical support.

References

1. J. Brownlee, A Gentle introduction to computer vision. Machine Learning Mastery, 19 March 2019 [online]. https://machinelearningmastery.com/what-is-computer-vision/. Accessed 12 Feb 2021
2. K. Dang, S. Sharma, Review and comparison of face detection algorithms, in *7th International Conference on Cloud Computing, Data Science & Engineering*, Confluence, Noida, 2017, pp. 629–633. https://doi.org/10.1109/CONFLUENCE.2017.7943228
3. D. Meena, R. Sharan, An approach to face detection and recognition, in *International Conference on Recent Advances and Innovations in Engineering (ICRAIE)*, Jaipur, 2016, pp. 1–6. https://doi.org/10.1109/ICRAIE.2016.7939462
4. MediaPipe Team, Face Mesh. Mediapipe, 2020 [online]. https://google.github.io/mediapipe/solutions/face_mesh.html. Accessed 8 Jan 2021
5. Annxingyuan, Tensorflow/Tfjs-Models. GitHub, 12 Oct. 2020 [online]. https://github.com/tensorflow/tfjs-models/tree/master/facemesh. Accessed 9 Jan 2021
6. A. Yuan, A. Vakunov Face and hand tracking in the browser with MediaPipe and TensorFlow.js. The TensorFlow Blog, 9 March 2020 [online]. https://blog.tensorflow.org/2020/03/face-and-hand-tracking-in-browser-with-mediapipe-and-tensorflowjs.html. Accessed 9 Jan 2021
7. S.V. Tathe, A.S. Narote, S.P. Narote, Face detection and recognition in videos, in *IEEE Annual India Conference (INDICON)*, Bangalore, India, 2016, pp. 1–6. https://doi.org/10.1109/INDICON.2016.7839098
8. D. Qu, Z. Huang, Z. Gao, Y. Zhao, X. Zhao, G. Song, An automatic system for smile recognition based on cnn and face detection, in *IEEE International Conference on Robotics and Biomimetics*

(ROBIO), Kuala Lumpur, Malaysia, 2018, pp. 243–247. https://doi.org/10.1109/ROBIO.2018.8665310
9. V. Bhandiwad, B. Tekwani, Face recognition and detection using neural networks, in *International Conference on Trends in Electronics and Informatics (ICEI)*, Tirunelveli, India, 2017, pp. 879–882. https://doi.org/10.1109/ICOEI.2017.8300832
10. A. Bulat, G. Tzimiropoulos, How Far are We from Solving the 2D & 3D Face Align-ment Problem? (and a Dataset of 230,000 3D Facial Landmarks), in *IEEE International Conference on Computer Vision (ICCV)*, Venice, Italy, 2017, pp. 1021–1030. https://doi.org/10.1109/ICCV.2017.116
11. Y. Kartynnik, A. Ablavatski, I. Grishchenko, M. Grundmann, Realtime facial surface geometry from monocular video on mobile gpus. arXiv:1907.06724 (2019)
12. S. Baldota, Optimizing face detection on your browser with Tensorflow.js. Medium, Towards Data Science, 18 June 2020 [online]. https://towardsdatascience.com/face-detection-on-the-browser-with-tensorflow-js-27846a5fe954. Accessed 12 Jan 2021
13. D.A.R. Wati, D. Abadianto, Design of face detection and recognition system for smart home security application, in *2nd International conferences on Information Technology, Information Systems and Electrical Engineering (ICITISEE)*, Yogyakarta, Indonesia, 2017, pp. 342–347. https://doi.org/10.1109/ICITISEE.2017.8285524
14. P. Shanmugavadivu, A. Kumar, Rapid face detection and annotation with loosely face geometry, in *2nd International Conference on Contemporary Computing and Informatics (IC3I)*, Noida, 2016, pp. 594–597. https://doi.org/10.1109/IC3I.2016.7918032
15. M.S. Devi, P.R. Bajaj, Active facial tracking, in *3rd International Conference on Emerging Trends in Engineering and Technology*, Goa, India, 2010, pp. 91–95. https://doi.org/10.1109/ICETET.2010.93
16. X. Lan, Z. Xiong, W. Zhang, S. Li, H. Chang, W. Zeng, A super-fast online face tracking system for video surveillance, in *IEEE International Symposium on Circuits and Systems (ISCAS)*, Montreal, QC, Canada, 2016, pp. 1998–2001. https://doi.org/10.1109/ISCAS.2016.7538968
17. H. Ho, Low cost and better accuracy eye tracker, in *International Symposium on Next-Generation Electronics (ISNE)*, Kwei-Shan Tao-Yuan, Taiwan, 2014, pp. 1–2. https://doi.org/10.1109/ISNE.2014.6839385
18. D. Venugopal, J. Amudha, C. Jyotsna, Developing an application using eye tracker, in *IEEE International Conference on Recent Trends in Electronics, Information & Communication Technology (RTEICT)*, Bangalore, India, 2016, pp. 1518–1522. https://doi.org/10.1109/RTEICT.2016.7808086

Siamese Network and Facial Ratios for Deformed Facial Matching

Ananya Sharma, Srikanth Prabhu, Aryamaan Yadav, P. Prithviraj, Vikas Venkat Sigatapu, and Pramod Kumar

Abstract Facial Recognition is a technique that uses the face and its features to identify/verify a person**.** It is a Biometric Application, which is playing an integral role in today's world in a wide variety of areas like Criminal Identification, Visitor Verification, and many other Real Time Identification systems. In this paper, we present a system that does facial matching for deformed faces. The proposed method combines the extraction of high-level feature representations using Deep Learning and the calculation of facial ratios using Image Processing to generate a robust model that can be used to identify/verify deformed faces. Whereas traditional face recognition systems show poor results when there is a face deformation. We use a function that tells us how similar or how different the two input images are. So, for this Siamese network is used. This network takes in an image as input and gives its feature vector. Then, we find the distance between the computed feature vectors of the two images which will give us a similarity score. Next, we use an Image Processing technique to calculate the facial ratios from macro features like eyes, lips, etc. These facial ratios are calculated based on facial landmarks spread across the face. We use multiple facial ratios, so even if deformities occur in a part of the face it will not have much effect on the system rendering it immune to facial changes. Hence, this paper tries to close the gap in the previously devised facial matching methods which were not designed for deformed faces.

Keywords Deformed faces · Siamese network · Image processing · Facial landmarks · Facial Ratios

A. Sharma · S. Prabhu (✉)
Department of Computer Science & Engineering, Manipal Institute of Technology, Manipal, India
e-mail: srikanth.prabhu@manipal.edu

A. Yadav · P. Prithviraj · V. V. Sigatapu · P. Kumar
Department of Electronics & Communication Engineering, Manipal Institute of Technology, Manipal, India

S. Rawat et al. (eds.), *Proceedings of First International Conference on Computational Electronics for Wireless Communications*, Lecture Notes in Networks and Systems 329,
https://doi.org/10.1007/978-981-16-6246-1_32

1 Introduction

Face Recognition is a method of identifying or verifying the identity of an individual using their face. Considerable amount of work is done in this particular field. It has been studied extensively in past years, and still a lot of exploration is being done in this field due to its numerous practical applications [1–12].

Deep models such as ConvNets [13] have proven to be very effective in capturing the high-level visual features of the face. These CNN models are also called end-to-end trainable systems. These features can be used for face verification later. In [14], an effective way to learn high-level overcomplete features with deep ConvNets is proposed. Each ConvNet takes in a face patch and computes the local low-level features from them. As the dimensions are reduced, more global and high-level features which are more prominent in distinguishing people are extracted from the final layers of the ConvNets. The training images are classified into one of 10,000 identities in [2]. Even though the task is challenging compared to binary classifiers, learned feature representations are generalized very well because of this. Training of binary classifiers is done in [3, 15, 16]. Instead of that, this approach is better as a strong regularization is added to the ConvNets preventing the model from overfitting. These features perform exceptionally well for verification tasks on a set of new faces unseen during the training, although they are learned through identification.

Enlarging the inter-personal variations while reducing the intra-personal variations poses a great deal of challenge for facial recognition. Sun et al. [4] argues that we need two supervisory signals, namely, face identification and verification signals to learn those features that enlarge the inter-personal variations. They referred to these features as Deep Identification-verification features (DeepID2). Since dissimilar DeepID2 features can be mapped to the same identity during identification, it will lead to problems if they are generalized to new tasks. A face verification signal solves this issue. It requires every two DeepID2 feature vectors of the same identity to be very close to each other while those feature vectors extracted from different identities are kept away. The extracted features from the identification model are concatenated and then reduced using PCA. Finally, a Joint Bayesian model [17] is used to train on the reduced features. Using an identification signal will allow the model to learn features that are very generalized as it trains on thousands of images. Using verification signals helps in reducing intra-personal variations. Hence, the paper states that both these signals are important for different aspects of feature learning and have to be employed together.

As a general rule of thumb, standard flow in facial recognition involves detection, alignment, representation, classification. DeepFace [5] has gone in the alignment and representation steps to make its own 3D face modeling system. This model helps to reduce the gap to human level performance in facial recognition systems, as the accuracy on the LFW database [18] reaches a record high of 97.35%.

Another paper which tries to develop a deep convolutional network is “Deeply learned face representations are sparse, selective, and robust” [19]. The authors of this paper have introduced DeepID2+, which is a high-performance deep convolutional

neural network. It is the successor of DeepID2 [4]. In this paper, the authors have proposed a compact and cheap network. This method achieved an accuracy of 99.47% on LFW dataset and 93.2% in YouTube Faces DB. However, they require additional post-processing such as concatenation of multiple models and PCA, as well as SVM classification and the FaceNet does a better job than this by directly learning the face embedding into a Euclidean space.

But the most recent advancement in this field has been achieved by FaceNet [20], which achieved an accuracy of 99.63% on LFW dataset and 95.12% in YouTube face DB. FaceNet generates a 128-dimensional embedding of faces which can be represented as a point in the Euclidean Space. The similarity or dissimilarity between faces can be quantified using the distances between these points which are mapped from the faces. FaceNet uses Triplet Loss to get the best possible embeddings of faces. The goal here is to use Triplet Loss to generate embeddings such that the Euclidean distance between faces of the same person is minimized and the Euclidean distance between faces of different identities is maximized.

Training the FaceNet made use of 100M–200M face thumbnails consisting of about 8M different identities. The training time required is extremely long and methods have to be devised to reduce this. As Triplet loss plays an important role in training, selecting the correct triplet is crucial for fast convergence. It is also advised to have "hard" triplets for training, but this criterion is infeasible to follow for the entire dataset.

In summary, we try to create a model which is robust and flexible enough to perform facial recognition on deformed faces. We try to achieve this by considering not just the results of our Siamese Network but also that of the facial matching using facial ratios.

2 Methodology

Facial Matching for Deformed Faces is implemented in two parts. First part consists of a deep learning model that is used to find the distance between two image vectors. The deep learning model is trained using a custom dataset of 16 pairs of the same person and 16 pairs of different persons. In the second part, we use Image Processing methods to calculate facial ratios of the classified image and the true image. After getting the facial ratios, we calculate another distance from these facial ratio vectors. We do this because the distance we get from the deep learning model will not be able to give good results if there are deformities in face. So, we combine it with the distance that we get with the facial ratios to normalize it.

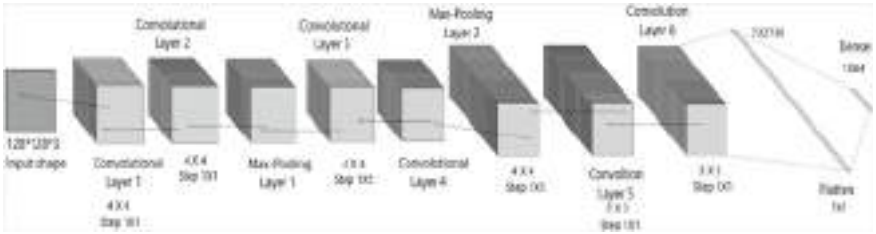

Fig. 1 Proposed architecture of CNN

2.1 Convolutional Network

We need a function that tells us how similar or how different the two input images are. So, for this we used a Siamese Network. This network takes in an image as input and gives its feature vector. In our model, we get a 64-dimensional encoding as output. Similarly, we send the second image and get its vector representation. We finally compute the distance (d1) between the two images by taking the norm of the encodings of the two images.

We train the model such that the distance (d1) is small for images of the same person and large for images of different persons. Our network consists of six convolutional layers followed by the fully connected layer. We use a kernel of 4×4 for the first four convolutional layers and 3×3 for the next two. The architecture for the proposed network is illustrated in Fig. 1. We have used the Rectified Linear Unit (RELU) as activation function for all the convolution layers. A Max-Pooling layer is introduced after every two convolution layers with pool size as 3×3 for the first two Max-Pooling layers and 2×2 for the last Max-Pooling layer. Pooling layers of CNN have zero padding. CNN has 47,001,408 trainable parameters.

2.2 Siamese Architecture

Two faces are taken as input for the system to give the score for similarity. If the score is less than the threshold, then the faces are considered to be similar, and if the score is greater than the threshold, then the faces are of two different persons. For pair classification and score calculation, we use the method proposed in [21] and [22]. We calculated the score by taking the difference of the features calculated from the two input images (Fig. 2).

After the fully connected layer, the sigmoid function is introduced as an activation function (Fig. 3).

For our purpose, we use ADAM (Adaptive momentum estimation) optimizer with learning rate as 0.0001. Instead of taking the predicted value, we formulated the following expression, which will be later used to calculate final score.

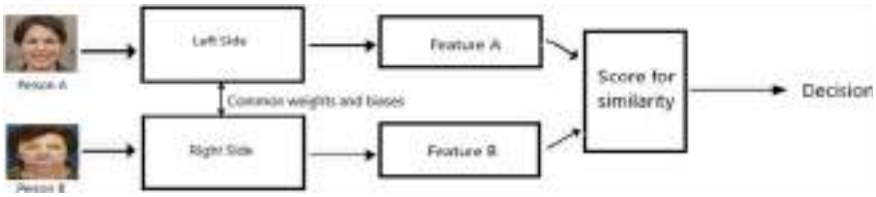

Fig. 2 Siamese architecture

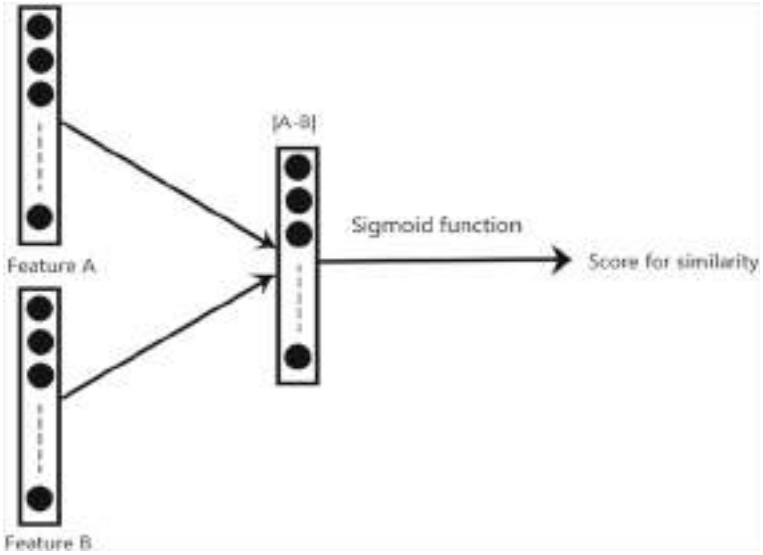

Fig. 3 Classification network for Siamese network

2.3 Feature Extraction

Facial Landmarks are certain key points in the face which are important for performing subsequent tasks focused on face like animation, face recognition, face tracking, gaze detection, expression recognition, gesture understanding, etc. These facial landmarks can be used for a discriminative role or as anchor points for a face graph.

We find a total of 68 facial landmarks, which includes two eye centers, nose tip, two mouth corners, etc. We later use some of these to calculate facial ratios.

Not all faces will be facing straight, there can be some faces tilted towards a particular direction. Locating the facial landmarks will be difficult for these cases.

We make use of the facial landmark detection implemented in the paper popularly known as *Kazemi's One Millisecond Face Alignment* [23] for this. In this paper, first, a mean shape estimate of landmarks is calculated and plotted on the face. Then,

Fig. 4 Landmark estimates in different stages of regressors. The input is initialized with a mean shape estimate. It can be seen that error is greatly reduced in the first stage

they extract 400 points from the face which are mostly concentrated around the eyes, mouth, and nose. For this, they use a probabilistic exponential prior. Next, a similarity transform is applied to all these 400 points with respect to the closest landmark coordinates to that particular point. Then, the images are passed through an ensemble of regression trees. Finally, with the help of a gradient boosting algorithm, the error is reduced as the image progresses through the regressors as shown in Fig. 4.

2.4 Facial Ratios

Using the extracted facial landmarks, the facial ratios are calculated. For example, we can use the landmarks 1, 17 and 37, 46 as shown in Fig. 5 in the last section to find the distance between them and get the ratio. Similarly, several different ratios are calculated. The ratios that can be calculated are mentioned in Table 1. Even if there is some face deformity, only the ratios which are calculated in that area get altered

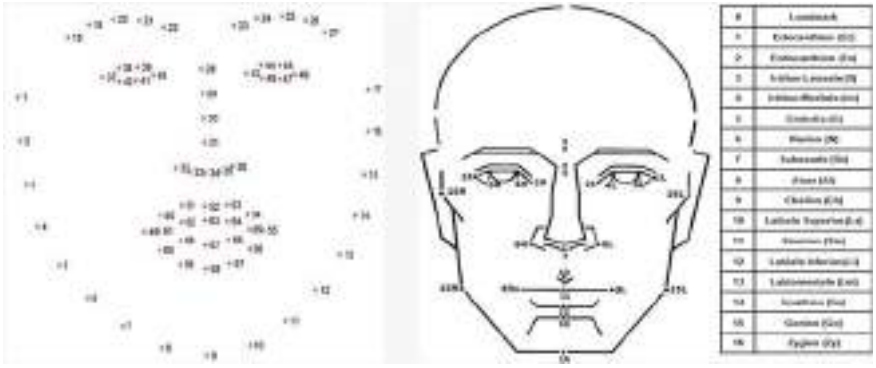

Fig. 5 **a** The 68 landmarks that we extracted from the image. **b** Some of the anthropometric facial landmarks and their locations

Table 1 Ratios and Indices that are considered and how they are calculated

Facial ratios	Calculation
1. Face ratio—1	$\frac{Maximum\ Face\ Height}{Maximum\ Face\ width\ and\ corresponding\ pt.}$
2. Face ratio—2	$\frac{Eye\ line\ to\ Mouth\ line\ distance}{Inter\ distances\ of\ Irises\ at\ Eye\ line}$
3. Eye line ratio	$\frac{Face\ Width\ at\ eye\ line}{Inter\ distances\ of\ Irises\ at\ eye\ line}$
4. Eye width ratio	$\frac{Face\ Width\ at\ Eye\ line}{Average\ Eye\ Width}$
5. Nose width ratio—1	$\frac{Maximum\ Face\ width\ and\ corresponding\ pt.}{Nose\ Width}$
6. Nose width ratio—2	$\frac{Face\ Width\ at\ Nasal\ Line}{Nose\ Width}$
7. Mouth width ratio—1	$\frac{Maximum\ Face\ width\ and\ corresponding\ pt.}{Mouth\ Width}$
8. Mouth width ratio—2	$\frac{Face\ Width\ at\ Mouth\ line}{Mouth\ Width}$
9. Ear width ratio	$\frac{Maximum\ Face\ width\ and\ corresponding\ pt.}{Average\ Ear\ Width}$
10. Ear height ratio	$\frac{Maximum\ Face\ Height}{Average\ Ear\ Height}$
11. Face height ratio (bisector)	$\frac{Height\ of\ upper\ face\ portion\ from\ Eye\ line}{Height\ of\ lower\ face\ portion\ from\ Eye\ line}$
12. Physiognomic facial index	$\frac{Pysiognomic\ Facial\ Height}{Breadth\ of\ Bizygomatic\ Arch} \times 100$
13. Morphological facial index	$\frac{Morphological\ Facial\ height}{Breadth\ of\ Bizygomatic\ Arch} \times 100$
14. Morphological upper facial index	$\frac{Morphological\ Upper\ Facial\ Height}{Breadth\ of\ Bizygomatic\ Arch} \times 100$
15. Inter-orbito jugular index	$\frac{External\ Biocular\ Breadth}{Breadth\ of\ Bizygomatic\ Arch} \times 100$
16. Sagittal naso-facial index	$\frac{Nasal\ Height}{Morphological\ Facial\ Height} \times 100$
17. Jugo-mandibular index	$\frac{Bigonial\ Breadth}{Breadth\ of\ Bizygomatic\ Arch} \times 100$
18. Jugo frontal index	$\frac{Minimum\ Frontal\ Breadth}{Breadth\ of\ Bizygomatic\ Arch} \times 100$
19. Nasal index	$\frac{Nasal\ Breadth}{Nasal\ Height} \times 100$
20. Relative chin height index	$\frac{Height\ of\ Lower\ Face}{Morphological\ Facial\ Height} \times 100$
21. Lip index	$\frac{Height\ of\ Integumental\ Lips}{Lip\ Length} \times 100$

but the other ratios remain the same. Hence, it is robust to any kind of deformations in the face (Fig. 6).

We calculate these ratios for both the deformed image that we sent as input to the deep neural network earlier and for the true image to which we are comparing it to. We compare the ratios of both the images and calculate the distance between them. The distance is very large for dissimilar images and less for the same images.

Fig. 6 Facial anthropometric measurements

2.5 Distance Calculation and Analysis

After getting the two distances, one from the Siamese network and the other from facial ratios, we take the weighted average of them.

Calculations for Ratio Measurement:

B = List of Landmark Pairs that are considered for calculating distance.
Pi = Face Landmark coordinates of the *i*th image.

Distance of *m*th point of *i*th image,

$$Distance(i, m) = \sqrt{(P(i)[B_m])^2 + (P(i)[B_m])^2}$$

Ratio of *p*th and *q*th distance in *i*th image,

$$Ratio(i, (p, q)) = \frac{Distance(i, p)}{Distance(i, (q))}$$

k = total number of distances.
Summation of all the distance errors,

$$distance\ error(facial\ ratio) = \sum_{l=0}^{k} \sum_{j=0}^{k-1-i} \left| (Ratio(1,(i,j)) - Ratio(2,(i,j))) / \left(Ratio(1,(i,j)) + Ratio(2,(i,j))^2 \right) \right|$$

$$Final\ distance\ error = \frac{2 \times (distance\ error((siamese)) + distance\ error(facial\ ratio)}{3}$$

3 Experimental Result

With Siamese architecture, we are able to reach an accuracy of 98.73% on training data. The image in Fig. 7 shows how the value of loss function decreases and accuracy increases with training time. When we input two images, the score received from the Siamese Network is further processed to get the total distance error. This distance error will be used in the final weighted average.

Examples of the 64-dimensional encodings are shown in Fig. 8. The features we obtain from the neural network are in one-dimension. We rearrange them as 2×32 for better visualization. We can observe that faces of the same identity have more commonly activated neurons than those of different identities. Hence, the Siamese model that is implemented can extract identity information.

Figure 9a, b are the faces of the same person, whereas Fig. 9b, c are the images of different people. Even though in Fig. 9a, the woman has a deformed nose, the ratio of distances between landmark points other than the ones considered near the nose on the face of that person will remain the same. But for the person in Fig. 9c, the ratio of distances will be different when compared to the ratio of distances of the person in Fig. 9b.

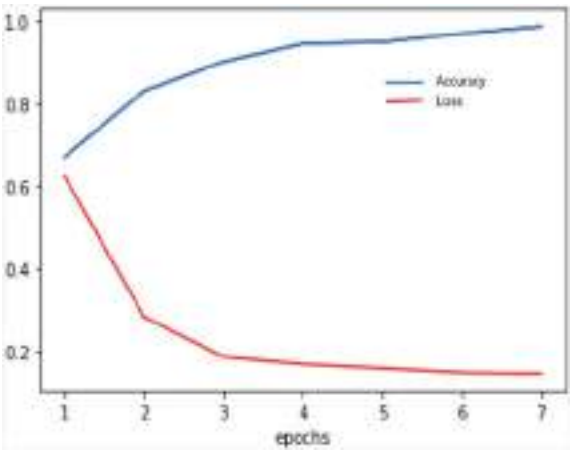

Fig. 7 Loss and accuracy rate through the training process

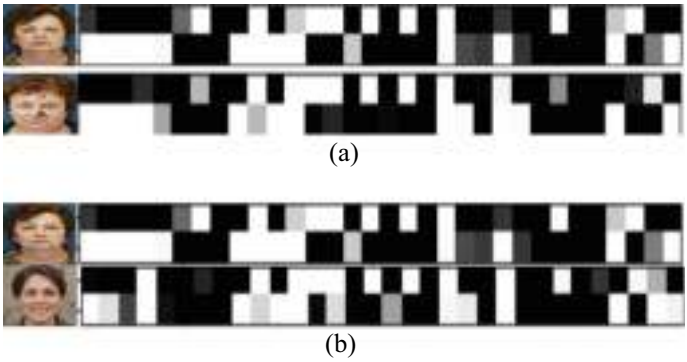

Fig. 8 Comparing the examples of the 64-dimensional encodings. The values in the feature vector are non-negative since they are taken from RELUs. The brighter squares indicate higher values. **a** Feature vector representations of the same person. **b** Feature vector representations of different persons

Fig. 9 **a** Deformed image of person A. **b** Normal image of a person A. **c** Image of a different person B

Figure 10a: Deformed Nose
Distance between 1 and 17: 433.1957
Distance between 37 and 46: 268.04663
Ratio: 1.626
Difference = 0.14605

Figure 10b: Normal Nose
Distance between 1 and 17: 394.045
Distance between 37 and 46: 244.032
Ratio: 1.47006

For different faces, i.e., Fig. 10b, c, the sum of difference between the ratio distances is 6.6065, whereas if it's the same face, i.e., Fig. 10a, b, the sum of difference between the ratio distance is 2.83065. The sum of ratios for different faces is twice as huge for similar faces.

The distance from the Siamese network, for similar faces (Fig. 10a, b) is 0.174926, whereas for different faces (Fig. 10b, c), the distance is 0.6255.

Table 2 shows the distance error from the Siamese Network, distance error from facial ratio, and final distance error for five pairs of images (two of same person and three of different person). Adding the weighted average enhances the final result and gives a better distance error when compared to only using the Siamese network. For the same person, two different images are taken, one is the normal image and the other one is with one deformed facial feature, adding the weighted average of facial ratio significantly reduces the distance error, hence increasing the prediction accuracy. Whereas for different persons, the error increases.

Fig. 10 Calculating the facial ratio by considering the two sets of landmarks 1, 17 and 37, 46 and finding the distance between them

Table 2 Experimental results

S no	Faces	Distance error (Siamese)	Distance error (facial ratio)	Final distance error
1	Similar	0.001259	0.00012	0.00087
2	Similar	0.16997	0.1067	0.14888
3	Different	2.32549	0.97345	1.8748
4	Different	0.49142	0.8864	0.62308
5	Different	0.42821	0.9331	0.59654

4 Conclusion

We have devised a method to perform facial matching with faces of individuals which could possibly be deformed. We do so by using a Siamese Network for getting the embeddings of the face and facial ratios to perform matching between faces with deformities. This is based on the idea that facial ratios do not tend to change even when a face is deformed say, due to an injury. The proposed method is expected to be of great use in fields like Forensic Sciences where situations may require identifying criminals who may be photographed when injured (with deformities). Also, the model that has been designed need not be re-trained when an image of a new person is added to the database. This can be considered as a major advantage over other traditional deep learning methods. In summary, this paper tries to close the gap in the previously devised facial matching methods which were not designed for deformed faces.

References

1. M. Wang, W. Deng, *Deep Face Recognition: A Survey* (2018)
2. Y. Sun, X. Wang, X. Tang, Deep learning face representation from predicting 10,000 classes, in *IEEE Conference on Computer Vision and Pattern Recognition* (2014)
3. Y. Sun, X. Wang, X. Tang, Hybrid deep learning for face verification, in *Proceedings of the ICCV* (2013)
4. Y. Sun, Y. Chen, X. Wang, X. Tang, *Deep Learning Face Representation by Joint Identification-Verification* (2014)
5. Y. Taigman, M. Yang, M.A. Ranzato, L. Wolf, DeepFace: closing the gap to human-level performance in face verification, in *IEEE Conference on Computer Vision and Pattern Recognition* (2014)
6. Z. Cao, Q. Yin, X. Tang, J. Sun, Face recognition with learning-based descriptor, in *Proceedings of the CVPR* (2010)
7. M. Guillaumin, J. Verbeek, C. Schmid, Is that you? Metric learning approaches for face identification, in *Proceedings of the ICCV* (2009)
8. Q. Yin, X. Tang, J. Sun, An associate-predict model for face recognition, in *Proceedings of the CVPR* (2011)
9. Z. Zhu, P. Luo, X. Wang, X. Tang, Deep learning identity-preserving face space, in *Proceedings of the ICCV* (2013)
10. Z. Zhu, P. Luo, X. Wang, X. Tang, Recover canonical view faces in the wild with deep neural networks. Technical report. arXiv:1404.3543 (2014)
11. Y. Taigman, M. Yang, M. Ranzato, L. Wolf, Web scale training for face identification. Technical report (2014)
12. Z. Zhu, P. Luo, X. Wang, X. Tang, Deep learning and disentangling face representation by multi-view perceptron, in *Proceedings of the NIPS* (2014)
13. Y. LeCun, L. Bottou, Y. Bengio, P. Haffner, Gradient-based learning applied to document recognition, in *Proceedings of the IEEE* (1998)
14. N. Kumar, A.C. Berg, P.N. Belhumeur, S.K. Nayar, Attribute and simile classifiers for face verification, in *Proceedings of the ICCV* (2009)
15. T. Berg, & P. Belhumeur, Tom-vs-Pete classifiers and identity preserving alignment for face verification, in *Proceedings of the BMVC* (2012)

16. T. Berg, P. Belhumeur, POOF: part-based one-vs-one features for fine-grained categorization, face verification, and attribute estimation, in *Proceedings of the CVPR* (2013)
17. D. Chen, X. Cao, L. Wang, F. Wen, J. Sun, Bayesian face revisited: a joint formulation, in *Proceedings of the ECCV* (2012)
18. G.B. Huang, M. Ramesh, T. Berg, E. Learned-miller, Labeled faces in the wild: a database for studying face recognition in unconstrained environments, in *ECCV Workshop on Faces in Real-life Images* (2008)
19. Y. Sun, X. Wang, X. Tang, Deeply learned face representations are sparse, selective, and robust (2014)
20. F. Schroff, D. Kalenichenko, J. Philbin, *FaceNet: A Unified Embedding for Face Recognition and Clustering* (2015)
21. J. Bromley, I. Guyon, Y. LeCun, E. Siickinger, R. Shah, Signature verification using a 'Siamese' time delay neural network (1994)
22. S. Chopra, R. Hadsell, Y. LeCun, Learning a similarity metric discriminatively, with application to face verification, in *IEEE Conference on Computer Vision and Pattern Recognition* (2005)
23. V. Kazemi, J. Sullivan, *One Millisecond Face Alignment with an Ensemble of Regression Trees* (2014)

Design of Novel Hamming Encoding and Decoding Circuits with Double Error Detection

Thanneru Chandrasekhar, M. P. R. Prasad, and Venkata Harish Babu Bhavanigari

Abstract In digital communication, transmitting data error-free is a major concern. The errors in data while transmitting results in wrong information at the receiving end. To protect the information in memories and register in digital circuits, error correction code plays an important role. Hamming code is one of such error-correcting codes used in digital transmission which can correct single-bit errors. Both even and odd parity checks can be used in the Hamming code. Here, even parity check method is used in implementing Hamming code encoding and decoding circuits. In Novel Hamming code, the parity bits are appended at the last to the data. Novel Hamming code requires less number of combinational gates than regular Hamming code. The pad-to-pad time delay is reduced in Novel Hamming encoding and decoding circuits as combinational gates are reduced while calculating parity bits. Here, both Hamming code and Novel Hamming code circuits are implemented in the Xilinx ISE Platform. A special redundant bit is used to spot the double-bit error.

Keywords Novel · Hamming · Double error · Error detection

1 Introduction

In digital transmission, environmental interference or noise is added during the transmission of data from the sender to receiver which generates errors. The accuracy and performance of the system are seriously affected by these errors. Therefore, error-free data transmission needs to be improved. To make the system work in real-time, it has to detect the error and correct the error. Hence, some error-correcting codes

T. Chandrasekhar · M. P. R. Prasad · V. H. B. Bhavanigari (✉)
NIT Kurukshetra, Kurukshetra, India
e-mail: bhavanigari_31911209@nitkkr.ac.in

T. Chandrasekhar
e-mail: thanneru_31911109@nitkkr.ac.in

M. P. R. Prasad
e-mail: mprprasad@nitkkr.ac.in

S. Rawat et al. (eds.), *Proceedings of First International Conference on Computational Electronics for Wireless Communications*, Lecture Notes in Networks and Systems 329,
https://doi.org/10.1007/978-981-16-6246-1_33

have to be used for error correction. To the data, one or more extra bits are added which generates a codeword.

HAMMING code is one such error-correcting codes well known for its double-bit error detection and single-bit error correction capability [1, 2]. It can detect a single-bit error and corrects at the receiver end. If multiple errors are present in the data, it will detect errors up to two bits and does not make any correction but indicates that the data is corrupted [3, 4]. Hamming code is invented by Richard Hamming. Detection of two-bit error can explained by SEDC-DED algorithm [5–7]. NOVEL HAMMING code [8, 9] is one that reduces the overhead at the transmitter side while calculating parity bits and does require correction at the receiver end if any [10, 11]. Verilog HDL is used to implement the hamming code using Xilinx ISE Design suite 14.3 [12, 13].

2 Hamming Code Algorithm

2.1 Encoder Algorithm

Hamming code supplies us the bit location where an error has occurred and its correction at the receiver end. Depending on the data bits, few extra bits are added at certain locations in the codeword which are called the parity bits. The parity bits are added at 2^n locations in the codeword where n = 0, 1, 2 … and so on. If the amount of bits is selected as X, then the amount of parity bits, P, is decided by the subsequent relationship.

$$2^P \geq X + P + 1. \tag{1}$$

For a 7-bit data, it requires 4 extra parity bits, and for 31-bit data stream, it needs 6 parity bits. Let's take the 7-bit data to be sender end is 0100100 and the parity bits are appended at locations 2^n 1, 2, 4, and 8 (where n = 0, 1, 2, 3). The eleven-bit Hamming codeword actually transmitted is PP0P100P100, where the P's are extra parity bits. The parity bits value calculation is explained below.

The first parity bit at location 1 is calculated by considering there is even parity at bit locations 1, 3, 5, 7, 9, and 11. Thus, the parity bit at location 1 will be 0. The second parity bit at bit location 2 is selected by considering there is an even parity at bit locations 2, 3, 6, 7, 10, and 11, and the value is 0. The third parity bit is calculated by considering there is an even parity at bit locations 4, 5, 6, and 7, and the value is 1. The last parity bit is calculated by considering there is an even parity at locations 8, 9, 10, and 11, and the value is 1. Thus the eleven-bit data actually podcasted is **00**1100**1**100.

While calculating parity bits at locations 1, 2, 4, and 8, the number of XOR operations are performed to check even parity is 6, 6, 4, and 4, respectively. Hence, a total of 20 XORs are required to generate Hamming code. For 31-bit data streams,

Table 1 Error detection and correction using Hamming code

Hamming code at receiving end											Status of parity check				Conclusion
1	2	3	4	5	6	7	8	9	10	11	C4	C3	C2	C1	
0	1	0	1	1	0	0	1	1	0	0	T	T	F	T	Error at bit location 2
0	0	0	1	1	0	1	1	1	0	0	T	F	F	F	Error at bit location 7
0	0	0	1	1	0	0	1	1	0	0	T	T	T	T	No error

the XORs involved in generating hamming code are 93. The error-detection and correction process is explained in detail in Table 1. For higher data streams, a lot of XORs are required in generating parity bits and their check for at receiving end for hamming code. Novel Hamming code reduces these combo-logic and pad-to-pad delay than regular Hamming code.

2.2 Hamming Decoder Using SEDC-DED Algorithm

The hamming code algorithm follows as explained below:

1. To the "X"-bit data word, "P" extra redundancy bits are added and generates a codeword of length X + P.
2. The LSB bit location value starts with 1 and ends with X + P.
3. The 2^n locations are reserved for parity bits and in remaining places data is appended.
4. Assuming even parity is present, these parity bits are calculated.

The method by which parity bits are calculated is as follows:

- P1 = (1^ 3^ 5^ 7^ 9^ 11^ 13…)
- P2 = (2^ 3^ 6^ 7^ 10^ 11…)
- P4 = (4^ 5^ 6^ 7^ 13)
- P8 = (8^ 9^ 10^ 11^ 12^ 13) where ^ means XOR

The regular Hamming code basically detects a 1-bit error only. To detect 2-bit errors, one more parity bit is added at the end of hamming code by making codeword length X + P + 1. For a 7-bit data, the Hamming code with double error detection is having length of 12 bits. This methodology is named as the SEDC-DED algorithm and is shown in Fig. 1. The extra parity bit is calculated by XORing all eleven-bits of Hamming code, i.e.,

P = 1^2^3^4^5^6^7^8^910^11

The detection and correction algorithm (SEDC-DED) works on the following "3" conditions:

1. If C = 0 and P = X, no error in data.

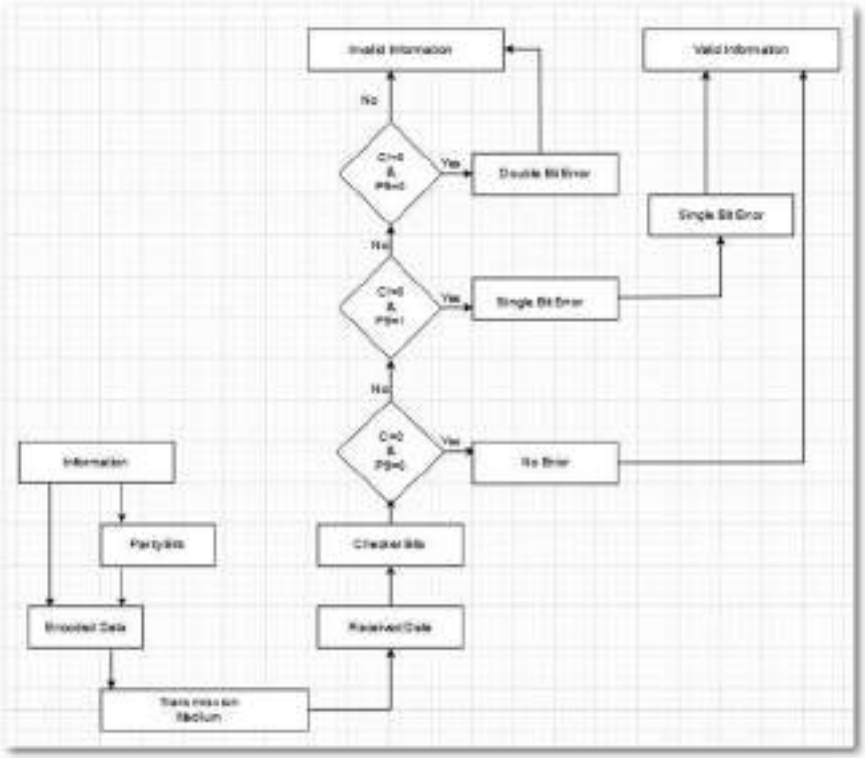

Fig. 1 Flowchart for SEDC-DED algorithm

2. If $C \neq 0$ and $P = 1$, single-bit error in data and corrected at the receiver end.
3. If $C \neq 0$ and $P = 0$, double-bit error occurred which is invalid data that can't be corrected. Here "C" indicates the 4 parity check bits (C4P3C2C1) calculated at the receiving end.

3 Novel Hamming Code

Let us consider the same 7-bit data taken for Hamming code, that is, 0010111. Formula to calculate number of parity bits is

$$2^{P-1} \geq N + 1 \tag{2}$$

satisfied, where P is the number of parity bits and N is the size of the Data stream. So, for 7-bit data, 4 parity bits are required. The extra bits needed during this approach

Table 2 Error detection and correction using improved novel method

Received data including parity bits											Status of parity check				Conclusion
1	2	3	4	5	6	7	8	9	10	11	C4	C3	C2	C1	
0	0	1	0	1	1	1	1	1	1	1	T	T	T	T	No error
0	0	1	0	1	0	1	1	1	1	1	T	F	F	T	Error at bit location 6
0	0	1	1	1	1	1	1	1	1	1	T	F	T	T	Error at bit location 4

is matching with legacy-hamming code for a few values of n. But in some cases, the novel hamming code requires one extra bit than hamming.

In this method, the parity bits are appended at the last after the regular data stream. Then, the eleven-bit data actually transmitted is 0010111EEEE, where the E's refer to the parity bits which are added at locations 8, 9, 10, and 11. The proposed method of calculating these parity bit values is illustrated below. The value for the 1st parity bit at location 8 is calculated by considering there is an even parity at bit locations 1, 3, 5, 6, and 8, and the value is 1. The value for the 2nd parity bit at location 9 is calculated by considering there is an even parity at bit locations 2, 3, 6, 7, and 9, and the value is 1. The value for the 3rd parity bit at location 10 is calculated by considering there is an even parity at bit locations 5, 6, 7, and 10, and the value is 1. The value for the 4th parity bit at location 10 is calculated by considering there is an even parity at all previously calculated parity bits, and the value is 1. Thus, the novel hamming code of eleven-bit data actually podcasted is 00101111111.

The number of comparisons required to calculate the value of parity bits at locations 8, 9, 10, and 11 is five, five, five, and four, respectively. So, a sum of 19 comparisons are involved in generating Novel Hamming code which is lesser than regular hamming code. The error-detection and rectification process in the novel method is as illustrated in Table 2.

Let's consider the codeword received is 00101**0**11111. We calculate checker bits as mentioned in the SEDC-DED algorithm. In Table 2, in the 2nd row, the C4, C3, C2, C1 are T, F, F, T, respectively, indicates there is an error at bit location 6. In received data, locations 1, 3, 5, 7, and 8 are not having any even parity error so that C1 is true (T). The bit locations 2, 3, 6, 7, and 9 are having even parity errors so that C2 is False (F). Similarly, there's even parity error at bit locations four, 5, 6, 7, and 10, and even parity happens at bit locations eight, 9, 10, and 11. Therefore, the standing of redundant check C3 is shown as F and C4 is shown as T. Considering F as 1 and T as 0, at bit location 6 error has occurred. The value received is 0 and is corrected as 1.

3.1 Novel Encoder Circuit

The Novel Encoder circuit takes the original data stream as input, performs XOR operation on bits, and generates parity bits. The data and parity bits are grouped to generate a hamming code. For example, a 7-bit data is given to the novel hamming encoder circuit which generates four extra parity bits making eleven-bit codeword. The eleven-bit encoded data is shown in Fig. 2 with 7-bit data (D1, D2, D3, D4, D5, D6, D7) and 4 parity bits (P1, P2, P4, P8) which is shown in Table 3.

The parity bits are calculated as below.

P1 = D1^D3^D5^D7
P2 = D2^D3^D6^D7
P4 = D4^D5^D6^D7
P8 = P1^P2^P3.

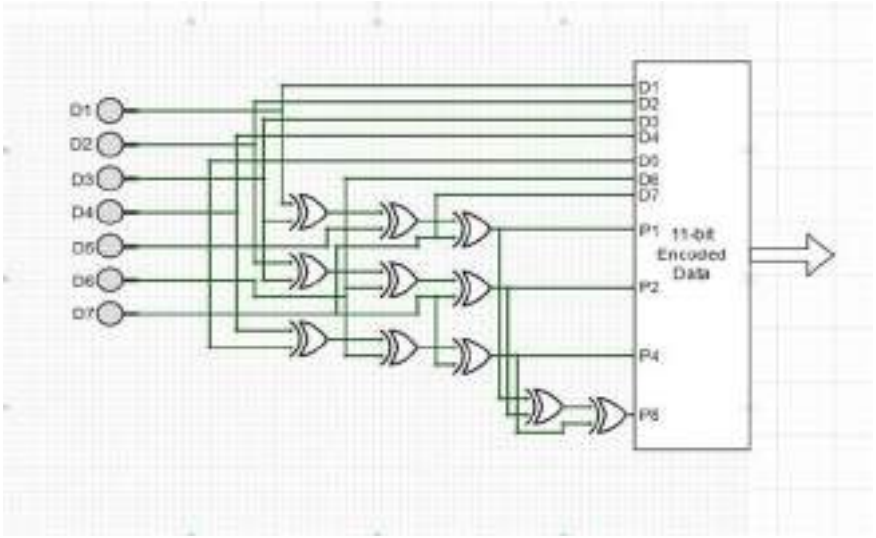

Fig. 2 Novel hamming encoder

Table 3 Eleven-bit encoded data

Bit location n	1	2	3	4	5	6	7	8	9	10	11
Codeword	D 1	D 2	D 3	D 4	D 5	D 6	D 7	P 1	P 2	P 4	P 8

3.2 Novel Decoder Circuit

The Novel Hamming decoding circuit is shown in Fig. 3. This circuit is having XOR gates, 4 to 16 decoder, and a parity checker block. It takes Novel hamming code generated by an encoder as input to the parity checker block which is made up of XOR combinational gates. The four parity checker bits are generated and feed to the 4 to 16 decoder. There are five unused outputs in the decoder which are 0, 12, 13, 14, and 15. The remaining outputs are XORed with the hamming code which gives us corrected data that is transmitted if it is having a single-bit error.

The checker bits are calculated as shown below.

C1 = (D1^ D3 ^D5^D7^D8)
C2 = (D2^D3^ D6^D7^D9)
C3 = (D4^D5^ D6^D7^D10)
C4 = (D8^D9^ D10^D11).

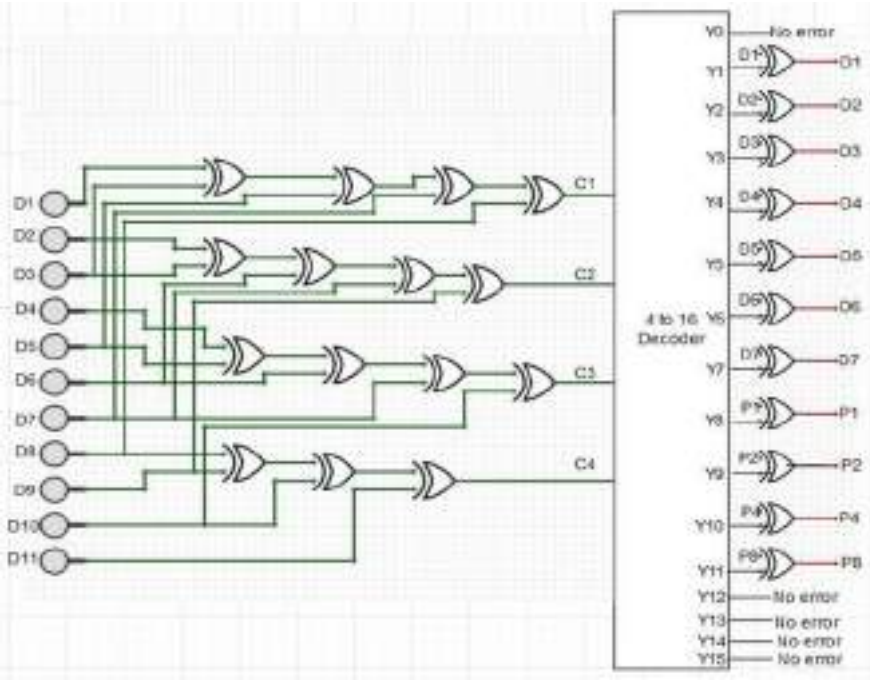

Fig. 3 Novel Hamming decoder

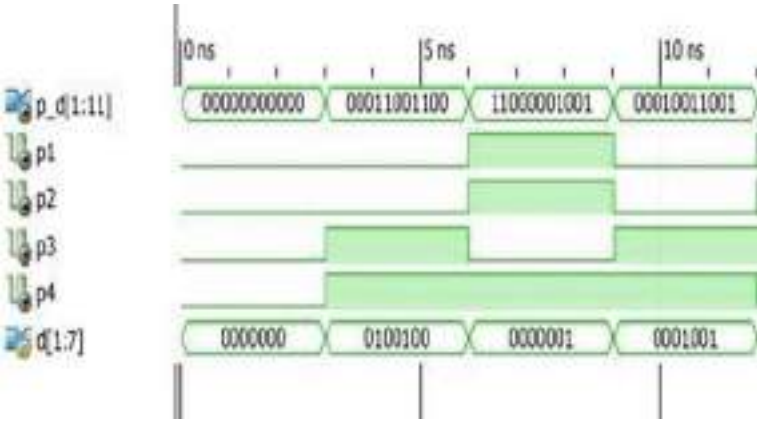

Fig. 4 Simulation output of Hamming encoder

4 Results and Comparison

4.1 Simulation Waveform of Hamming Encoder

The Hamming Encoder waveform is shown in Fig. 4. It is having 7-bit input data, 4 parity bits (p1, p2, p3, p4) which are added to the data, and generated 11-bit Hamming code ready for transmission.

4.2 Simulated Waveform of Hamming Decoder

The Hamming Decoder Waveform is shown in Fig. 5. The port p_d[1:11] is having 11-bit Hamming code received. The correction bits are calculated, and based on the position, correction is done if single-bit error is present. When the port two_error goes high, it indicates that we have more than one error, so we can see z's at output data.

4.3 Simulation Waveform of Novel Hamming Encoder

The Novel Hamming Encoder simulated waveform is shown in Fig. 6. To the 7-bit input data, 4 parity bits are added at the last and 11-bit Hamming code is generated.

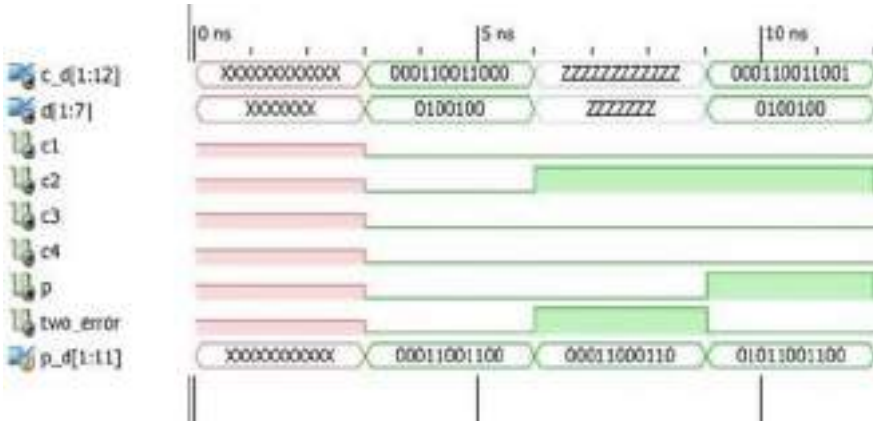

Fig. 5 Simulation output of Hamming decoder

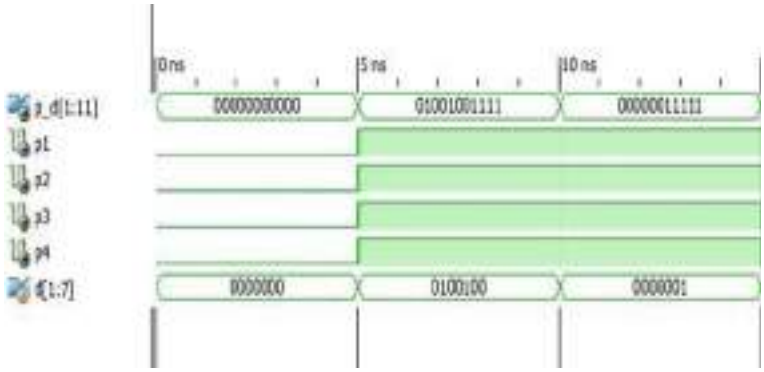

Fig. 6 Simulation output of novel Hamming encoder

4.4 Simulation Waveform of Novel Hamming Decoder

The Novel Hamming Decoder gets 11-bit hamming code as input. The 4 checker bits (c1, c2, c3, c4) are calculated. If the hamming code is having 1-bit error, based on checker value, the correction will happen accordingly. If more than 1-bit error occurs, it is indicated with port two_error and at output z's will come (Fig. 7).

4.5 Time Delay for Novel Hamming Circuits

The delay comparisons for Novel Hamming and Hamming are shown in Table 4.

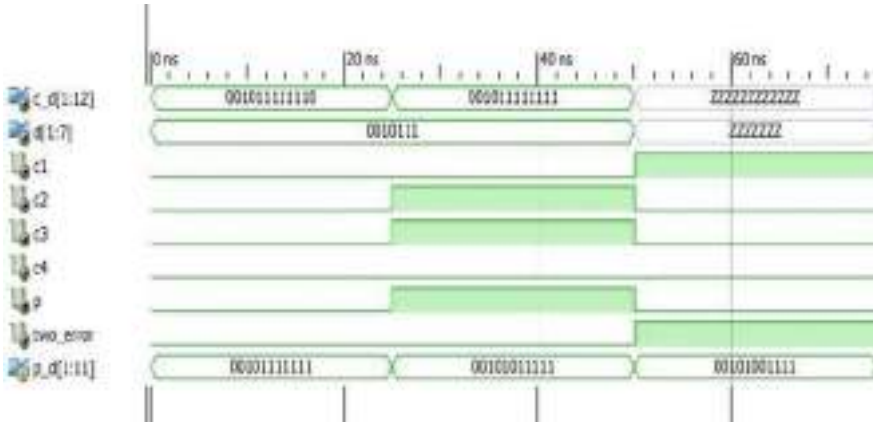

Fig. 7 Simulation output of novel Hamming decoder

Table 4 Pad-to-pad delay for 7-bit data

7-bit data timing report	Pad-to-pad delay in circuit (ns)
Hamming encoder	7.08
Novel Hamming encoder	6.821
Hamming decoder	13.59
Novel Hamming decoder	13.289

The Novel Hamming encoding and decoding circuits give less propagation delay than legacy Hamming circuits.

The Hamming Encoder pad-to-pad delay is shown in Fig. 8.

The Novel Hamming Encoder Circuit pad-to-pad delay is shown in Fig. 9.

5 Conclusion

For a 7-bit information signal, we have generated regular Hamming code and Novel Hamming code using Xilinx ISE. The Encoder and Decoder circuits are designed and implemented using Verilog in Xilinx ISE tool. The pad-to-pad delay is reduced in the Novel hamming code as the number of XOR gates is less than the Hamming code. The Decoder circuit detects the error in the hamming code and corrects it based on checker value. We have designed decoders such that they can detect multiple bit errors also with SEDC-DED algorithm. The effort needed in the calculation of parity bits is lower in the Novel method. Further improvements can be done in correcting multiple errors.

```
   Maximum combinational path delay: 7.086ns

Timing Detail:
--------------
All values displayed in nanoseconds (ns)

=========================================================================
Timing constraint: Default path analysis
  Total number of paths / destination ports: 55 / 15
-------------------------------------------------------------------------
Delay:               7.086ns (Levels of Logic = 4)
  Source:            d<5> (PAD)
  Destination:       p4 (PAD)

  Data Path: d<5> to p4
                                Gate     Net
    Cell:in->out      fanout   Delay   Delay  Logical Name (Net Name)
    ----------------------------------------  ------------
     IBUF:I->O             3   1.106   0.603  d_5_IBUF (p_d_5_OBUF)
     LUT4:I0->O            3   0.612   0.603  Mxor_p_d_11_xor0000_xo<0>1 (p_d_8_OBUF)
     LUT3:I0->O            2   0.612   0.360  Mxor_p4_xor0000_xo<0>1 (p_d_11_OBUF)
     OBUF:I->O                 3.169          p4_OBUF (p4)
    ----------------------------------------
    Total                      7.086ns (5.499ns logic, 1.587ns route)
                                       (77.6% logic, 22.4% route)
```

Fig. 8 Pad-to-pad delay for hamming encoder

```
   Maximum combinational path delay: 6.821ns

Timing Detail:
--------------
All values displayed in nanoseconds (ns)

=========================================================================
Timing constraint: Default path analysis
  Total number of paths / destination ports: 39 / 15
-------------------------------------------------------------------------
Delay:               6.821ns (Levels of Logic = 4)
  Source:            d<1> (PAD)
  Destination:       p1 (PAD)

  Data Path: d<1> to p1
                                Gate     Net
    Cell:in->out      fanout   Delay   Delay  Logical Name (Net Name)
    ----------------------------------------  ------------
     IBUF:I->O             2   1.106   0.632  d_1_IBUF (p_d_1_OBUF)
     LUT3:I0->O            3   0.612   0.418  Mxor_p1_xor0001_xo<0>1 (p1_xor0001)
     LUT3:I2->O            2   0.612   0.360  Mxor_p2_xor0000_xo<0>1 (p_d_2_OBUF)
     OBUF:I->O                 3.169          p2_OBUF (p2)
    ----------------------------------------
    Total                      6.821ns (5.499ns logic, 1.322ns route)
                                       (80.6% logic, 19.4% route)
```

Fig. 9 Pad-to-pad delay for novel Hamming encoder circuit

References

1. E. Khan, N. Pandey, N. Gupta, Review of binary codes for error detection and correction. Int. J. Innov. Res. Sci. Eng. Technol. **7**(4) (2018)
2. T. Fujiwara et al., Error detecting capabilities of the shortened Hamming codes adopted for error detection in IEEE Standard 802.3. IEEE Trans. Commun. **37**(9), 986–989 (1989)
3. S. Garg, A.K. Sharma. A.K. Tyagi, An introduction to various error detection and correction schemes used in communication. Int. J. Appl. Res. **2**(8), 216–218 (2016)

4. V. Badole, A. Udawat, Design of multidirectional parity code using Hamming code technique for error detection and correction **3**(5) (2014)
5. Neale, M. Sachdev, A new SEC-DED error correction code subclass for adjacent MBU tolerance in embedded memory. IEEE Trans. Device Mater. Rel. **13**(1), 223–230 (2013)
6. Y. Cui, M. Lou, J. Xiao, X. Zhang, S. Shi, P. Lu, Research and implementation of SEC-DED Hamming code algorithm, in *2013 IEEE International Conference IEEE Region 10*
7. P. Reviriego, S. Pontarelli, J.A. Maestro, M. Ottavi, Low-cost single error correction multiple adjacent error correction codes. Electron. Lett. **48**(23), 1470–1472 (2012)
8. Ahmadpou, A.A. Shal, M. Ziabari, A novel formulation of Hamming code, in *2009 6th International Conference on Electrical Engineering/Electronics, Computer, Telecommunications and Information Technology*
9. S. Lin, D.J. Costello, *Error Control Coding*, 2nd edn. (Prentice-Hall, EnglewoodCliffs, NJ, USA, 2004)
10. N. Shep, P.H. Bhagat, Implementation of Hamming code using VLSI, Department of Electronics & Telecommunication Dr B.A.M.U, Aurangabad Government College of Engineering Aurangabad (M.S.)
11. W. Xiong, D.W. Matolak, Performance of Hamming codes in systems employing different code symbol energies, in *IEEE Communications Society*, pp. 1055–1058 [Wireless and Communications and Networking Conference (WCNC)]
12. Verilog HDL: A Guide to Digital Design and Synthesis, 2nd edn. By Samir Palnitkar. https://d1.amobbs.com/bbs_upload782111/files_33/ourdev_585395BQ8J9A.pdf
13. Xilinx ISE 14.3 Software Manuals and Help. https://www.xilinx.com/support/documentation/sw_manuals/xilinx14_1/ise_tutorial_ug695.pdf

Performance Evaluation of Iterative SRP-PHAT Techniques for Acoustic Source Localization

Ritu Boora and Sanjeev Kumar Dhull

Abstract The Steered Response Power with Phase Transform (SRP-PHAT) is a widely preferred technique for acoustic source localization due to its robustness in a harsh environment. However, it necessitates exploring the search region on a computationally intensive grid to maintain its robustness, making it unsuitable for real-time applications. Modified SRP-PHAT introduced an effective strategy that considers the influential cubic volume around the grid location to compute the SRP functional. Consequently, the method allows examining the search region on a coarser spatial grid. However, the resolution of the technique is marginalized by the selected spatial grid step size. Thus, the Modified SRP-PHAT was further improved by employing an iterative grid decomposition strategy. However, in challenging environments, the performance deteriorates considerably with the iterative approach. Thus, the different implementations of the iterative SRP-PHAT techniques have been proposed in the literature. This paper presents a performance comparison of the Iterative Modified SRP-PHAT, Iterative Volumetric Reduction SRP-PHAT, Iterative Modified SRP-PHAT with adaptive search space, and conventional SRP-PHAT methods. These methods have been extensively tested on the simulated environment and SMARD database to confirm their validity and reliability. The results exhibit that the Iterative Modified SRP-PHAT with adaptive search space localizes the source with the least root mean square error in the practical reverberant environment. Furthermore, this localization accuracy is very close to densely computed SRP-PHAT with very small functional evaluations.

Keywords Sensor arrays · Source localization · SRP-PHAT · Modified SRP-PHAT · Iterative modified SRP-PHAT · GCC-PHAT

R. Boora (✉) · S. K. Dhull
Department of ECE, GJUS&T, Hisar 125001, Haryana, India

S. Rawat et al. (eds.), *Proceedings of First International Conference on Computational Electronics for Wireless Communications*, Lecture Notes in Networks and Systems 329,
https://doi.org/10.1007/978-981-16-6246-1_34

1 Introduction

Humans have become immensely reliant on machines for their convenience and quality of living. This dependency trend is continuously growing with the advancement of intelligent future technologies. Acoustic source localization is one such development that finds its significance in several new generation applications. These applications include video conferencing [1], hands-free communication, security surveillance [2, 3], speech enhancement system in automobiles [4, 5], robotics [6], voice capture in the reverberant environment, etc. The Steered Response Power with Phase Transform (SRP-PHAT) is a popularly used method for source localization owing to its proven robustness in challenging environments [7–11]. However, the search over a computationally intensive spatial grid limits its implementation for real-time systems [7, 12]. Work reported in [13] allowed the use of coarser spatial grids by evaluating the objective function as accumulated Generalized Cross Correlation (GCC) of the influential volume around the corresponding grid location. However, this approach was limited by its spatial resolution. Thus, an iterative technique with a Coarse-to-Fine strategy was implemented in work [14]. Regrettably, the iterative approach's performance degraded considerably in difficult acoustic conditions and, thus, lost the original robustness of SRP-PHAT. Therefore, to enhance the iterative approach's robustness, two different strategies have been proposed in the literature. Iterative Volumetric Reduction (IVR) SRP-PHAT [15] and Iterative Modified SRP-PHAT with adaptive search space (ISRP-A) [16] are the two improved strategies. This paper analyses and compares the performance of three iterative SRP-PHAT techniques with conventional SRP-PHAT (C-SRP) under different acoustic conditions. The work is arranged as follows: Sect. 2 briefly introduces the C-SRP and MSRP, while Sect. 3 explains iterative SRP methods. It is followed by a discussion on computational cost in Sect. 4 and, the experimental evaluations are conferred in Sect. 5.

2 Steered Response Power Techniques

Consider an acoustic localization system with M sensors and a sound source emitting signal $e(t)$ at an instant t. Thus, the received signal $s_i(t)$ at the ith microphone is given in Eq. (1) [17–19].

$$s_i(t) = h_i(t) * e(t) + \mathcal{N}_i(t); i \in \{1, 2, \ldots M\} \tag{1}$$

In Eq. (1), $h_i(t)$ is the impulse response from the source to the ith microphone, '*' denotes the convolution operator, $\mathcal{N}_i(t)$ is noise components at the ith channel.

Consider a sensor pair (l, k) such that $(l, k) \in 1, 2, ..M$ and v is the propagation speed of the signal in the medium. If the source is located at $X(x, y, z)$, the time difference of arrival (TDOA) of the signal at the two sensors positioned at X_k, X_l,

respectively, is evaluated from Eq. (2).

$$\tau_{kl}^{'}(\boldsymbol{X}) = round\left(\frac{\|\boldsymbol{X_l} - \boldsymbol{X}\| - \|\boldsymbol{X_k} - \boldsymbol{X}\|}{v}\right) \tag{2}$$

If the signal is sampled at a frequency of f_s Hz, the TDOA value can be represented in discrete-time samples (cf. Eq. (3)). The physically realizable delays for a sensor pair are bounded by the inter-sensor distance D and lies in the range $[-\tau_{\max}, \tau_{\max}]$ where $\tau_{\max} = round(f_s * D/v)$.

$$\tau_{kl}(\boldsymbol{X}) = round(\tau_{kl}^{'}(\boldsymbol{X}) * f_s) \tag{3}$$

The generalized cross-correlation between the two received signals of a sensor pair can be computed from Eq. (4) [20–22].

$$\boldsymbol{R}_{kl}(\tau) = \int_{-\infty}^{\infty} \frac{S_{kl}(\omega) S_{kl}^{*}(\omega)}{\left|S_{kl}(\omega) S_{kl}^{*}(\omega)\right|} e^{-j\omega\tau} d\omega \tag{4}$$

In Eq. (4), $S_{k,l}(\omega)$ and $S_{k,l}^{*}(\omega)$ are the FFTs of the two respective received signals, τ is the time lag, and the complex conjugate is denoted by *.

2.1 Conventional SRP-PHAT (C-SRP)

If P denotes the number of unique sensor pairs constituted from M sensors and, $\boldsymbol{R}_p$ is the Generalized Cross Correlation of the pth sensor pair, then the SRP value at a grid point $\boldsymbol{X}$ is evaluated from Eq. (5) [8, 23, 24].

$$W(\boldsymbol{X}) = \sum_{p=1}^{P} \boldsymbol{R}_p\left(\tau_p(\boldsymbol{X})\right) \tag{5}$$

The localization system selects the grid location ($\boldsymbol{X} \in \boldsymbol{J}_0$) with the maximum SRP functional value as an estimated source position $\boldsymbol{X}_{src}$ (cf. Eq. (6)), where $\boldsymbol{J}_0$ represents a set of contestant spatial positions in the search region.

$$\boldsymbol{X}_{src} = \underset{\boldsymbol{X} \in \boldsymbol{J}_0}{\arg\max}\, W(\boldsymbol{X}) \tag{6}$$

2.2 Modified SRP-PHAT (MSRP)

Several authors have proposed the objective function evaluation over small volumes to minimize the computational expense of SRP-PHAT. The Modified SRP-PHAT [13] is one such method that is based on the volumetric approach. The functional value at a contestant location $\boldsymbol{X}$ is measured by accumulating the GCC-PHAT over the associated delay interval of the symmetric volume surrounding it (cf. Eq. (7)).

$$W_{MSRP}(\boldsymbol{X}) = \sum_{p=1}^{P} \sum_{L_1^p(\boldsymbol{X})}^{L_2^p(\boldsymbol{X})} \boldsymbol{R}_p\big(\tau_p(\boldsymbol{X})\big) \tag{7}$$

The related delay interval for GCC accumulation of the pth sensor pair is denoted as $[L_1^p(\boldsymbol{X})L_2^p(\boldsymbol{X})]$. As an outcome, the full search space is explored on a coarser grid, and no candidate location is left unattended.

The lower and upper delay bounds for the contestant location are computed from Eqs. (8) and (9), respectively. In these expressions, $\nabla\tau_p(\boldsymbol{X})$ is the gradient vector (cf. Eq. (10)), and each component of the vector is determined from Eq. (11). The distance d in the gradient's direction from location $\boldsymbol{X}$ to the boundary of the influential cubic volume is evaluated by Eq. (12), where r is the grid step size.

$$L_1^p(\boldsymbol{X}) = \tau_p(\boldsymbol{X}) - \big|\big|\nabla\tau_p(\boldsymbol{X})\big|\big| \cdot d \tag{8}$$

$$L_2^p(\boldsymbol{X}) = \tau_p(\boldsymbol{X}) + \big|\big|\nabla\tau_p(\boldsymbol{X})\big|\big| \cdot d \tag{9}$$

$$\nabla\tau_p(\boldsymbol{X}) = \big[\nabla_x\tau_p(\boldsymbol{X}), \nabla_y\tau_p(\boldsymbol{X}), \nabla_z\tau_p(\boldsymbol{X})\big] \tag{10}$$

$$\nabla_\gamma\tau_p(\boldsymbol{X}) = \frac{\partial\tau_p(\boldsymbol{X})}{\partial\gamma} = \frac{1}{c}\left(\frac{\gamma-\gamma_{p1}}{\big|\big|\boldsymbol{X}-\boldsymbol{X}_{p1}\big|\big|} - \frac{\gamma-\gamma_{p2}}{\big|\big|\boldsymbol{X}-\boldsymbol{X}_{p2}\big|\big|}\right) \tag{11}$$

where $\gamma\epsilon\{x, y, z\}$

$$d = \frac{r}{2}\min\left(\frac{1}{|\sin\theta\cos\phi|}, \frac{1}{|\sin\theta\sin\phi|}, \frac{1}{|\cos\theta|}\right), \tag{12}$$

where $\theta = \cos^{-1}\left(\frac{\nabla_z\tau_p(\boldsymbol{X})}{||\nabla\tau_p(\boldsymbol{X})||}\right)$ and $\phi = a\tan_2\big(\nabla_y\tau_p(\boldsymbol{X}), \nabla_x\tau_p(\boldsymbol{X})\big)$. Similar to conventional SRP-PHAT, the candidate location with the highest SRP functional is selected as the source location.

Thus, MSRP explores the entire search region by accommodating the SRP functional computations to scalable spatial sampling. Thus, it allows the implementation of C-SRP on a coarser grid. However, the method's final localization accuracy is limited by the selected spatial resolution. Therefore, an iterative MSRP implementation was proposed in work [14], with an additional SRP functional variation.

3 Iterative SRP-PHAT Methods

3.1 Iterative Modified SRP-PHAT

The Iterative Modified SRP-PHAT (ISRP) [14] is a mean-based variant of the MSRP [13]. It decomposes the search space into smaller subvolumes in each iteration. The spatial grid is examined using mean modified SRP functional to search for the global maxima.

A sensor pair's spatial sensitivity is high along the line joining the two sensors and lessens gradually as the distance from this line increases [25, 26]. Therefore, the candidate locations lying in the higher sensitive region have large GCC summation intervals, leading to their higher SRP values due to accumulated noise. Thus, a mean-based functional (cf. Eq. (13)) is designed to mitigate the higher SRP values due to accumulated noise in the higher sensitive subregions [14, 27].

$$W_{MMSRP}(\boldsymbol{X}) = \sum_{p=1}^{P} \sum_{L_1^p(\boldsymbol{X})}^{L_2^p(\boldsymbol{X})} \frac{R_p(\tau(\boldsymbol{X}))}{L_2^p(\boldsymbol{X}) - L_1^p(\boldsymbol{X})} \tag{13}$$

Initially, the acoustic map is computed on a coarse grid and, the grid location with the highest functional values is selected. The influential volume around the chosen location is iteratively decomposed on a denser spatial grid to achieve a higher resolution. However, the mean operation of accumulated values reduces the highest SRP functional in the search map [27]. Therefore, the maximum SRP location on a coarser spatial grid may not correspond to a real source [15, 16]. Moreover, the approximations involved in calculating the associated delay bound of a discrete point may result in the exclusion of TDOA found and inclusion of TDOA not found in it [28]. Subsequently, it bounds the accurate estimation of the candidate locations' functional value. Therefore, for the ISRP approach, it is highly probabilistic to eliminate the global peak in the initial coarse iterations. It is demonstrated using Fig. 1a, where the true location doesn't correspond to the maxima. Henceforth, the selected region in Fig. 1b has missed the actual source location.

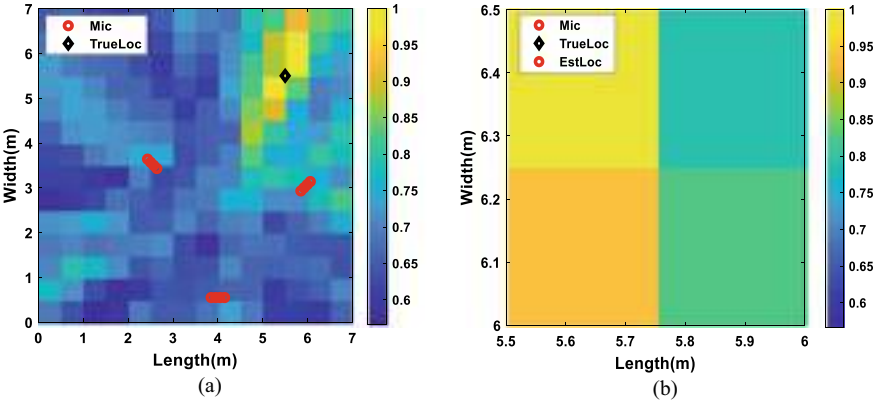

Fig. 1 SRP map using ISRP method. **a** Entire search region, $r_0 = 0.5m$. **b** Selected region, $r_1 = 0.25m$

3.2 Iterative Volumetric Reduction (IVR) SRP-PHAT

The iterative Volumetric Reduction (IVR) SRP-PHAT method [15] modified the ISRP approach. In this method, the search space is constrained to a higher probabilistic region after each iteration. The acoustic map is recomputed on a finer grid in the contracted search space in the successive iteration. These two steps are iterated to achieve the desired resolution.

The computed generalized cross-correlation (cf. Eq. (4)) is normalized as in Eq. (14). This step is worked out to ensure that the GCC value ranges [0, 1] and sums up to unity over the complete delay interval. Thus, it gives the probabilistic likelihood of a source with delay τ at pth sensor pair.

$$\overline{\boldsymbol{R}_p(\tau)} = \frac{\boldsymbol{R}_p(\tau) - \min\left(\boldsymbol{R}_p\right)}{\sum_{\tau=-\tau_{\max}}^{\tau_{\max}} \left(\boldsymbol{R}_p(\tau) - \min\left(\boldsymbol{R}_p(\tau)\right)\right)} \tag{14}$$

The SRP functional (cf. Eq. (15)) is evaluated for each grid location as the mean of accumulated GCC over its influential subvolume's associated delay. The computed map is normalized as in Eq. (16).

$$W^{'}(\boldsymbol{X}) = \sum_{p=1}^{P} \sum_{L_1^p(X)}^{L_2^p(X)} \frac{\overline{R_p(\tau(\boldsymbol{X}))}}{L_2^p(\boldsymbol{X}) - L_1^p(\boldsymbol{X})} \tag{15}$$

$$\overline{W}(X) = \frac{W'(\boldsymbol{X})}{\underbrace{\max W(\boldsymbol{X})}_{X \in J_i}} \tag{16}$$

The minimum and maximum delay bounds of the associated volume around the contestant location are computed from Eqs. (8) and (9), respectively. The estimated source location in the final contracted search volume is computed from Eq. (17).

$$\boldsymbol{X}_{src} = \arg\max\left(\overline{W}(\boldsymbol{X})\right), \boldsymbol{X} \in J_{I_{\max}-1} \tag{17}$$

3.2.1 IVR Algorithm

At the onset of the algorithm (cf. Table 1), set iteration $i = 0$, create a uniform spatial grid $\boldsymbol{J_i}$ with initial coarse grid resolution r_i in the given search volume $\boldsymbol{V}_i$. Define the maximum number of times to iterate the algorithm as $I_{\max}$ and desired resolution as r_{final}. Compute the objective function $\overline{W}(\boldsymbol{X})$ at all the grid points in the search region ($\boldsymbol{X} \in \boldsymbol{J_i}$) (cf. Eqs. (15) and (16)). Select the candidate locations with a likelihood higher than a specified threshold (0.95) from the computed map. Define the new contracted search volume $\boldsymbol{V}_{i+1}$ such that it constrained by the selected grid locations and their influential volume. Thus, the search volume is bounded by spatial location $[\boldsymbol{X}_{\min}, \boldsymbol{X}_{\max}]$ where $\boldsymbol{X}_{\min} = \left(x_{\min} - r_i/2, y_{\min} - r_i/2, z_{\min} - r_{i/2}\right)$ and $\boldsymbol{X}_{\max} = (x_{\max} + r_i/2, y_{\max} + r_i/2, z_{\max} + r_i/2)$. This procedure is repeated in the constrained volume with redefined grid resolution until the desired precision is accomplished.

The implementation of the IVR algorithm is demonstrated in Fig. 2. The objective function is evaluated over a coarser grid step size of $r_0 = 0.5m$ in Fig. 2a. As shown, the large subregions' likelihood function is not accurate. As this can entirely affect the system's performance, the IVR approach suggests re-evaluating higher probabilistic areas on a finer grid before pruning them. As displayed in Fig. 2b, the search region for the next iteration is such that it is bounded by the grid locations with the SRP

Table 1 IVR SRP-PHAT algorithm

1. Initialise: $iteration\, i = 0$, $grid\_resolution = r_i$, $Max\_Iterations = I_{\max}$, $spatial\_grid = \boldsymbol{J_i}$, $desired\_resolution = r_{final}$, search volume $V_{initial}$
2. Evaluate Objective Function: $\overline{W}(\boldsymbol{X}), \forall \boldsymbol{X} \in \boldsymbol{J}_i$ (cf. Eqs.(15) and (16))
3. Define: Threshold as Th
4. Sort: Sort and select the locations that have $\overline{W}(\boldsymbol{X}) > Th$
5. Redefine the search volume $\boldsymbol{V}_{i+1}$ bounded by $[\boldsymbol{X}_{\min}\boldsymbol{X}_{\max}]$
6. Check: if $i < I_{\max} - 1$ or $r_i > r_{final}$

i Redefine
$grid\_resolution\, r_{i+1}$, and,
$spatial\_grid\, \boldsymbol{J}_{i+1}$ in contracted search volume $\boldsymbol{V}_{i+1}$

ii Go to step 2

Else
Use Eq. (17) to estimate the source location
End

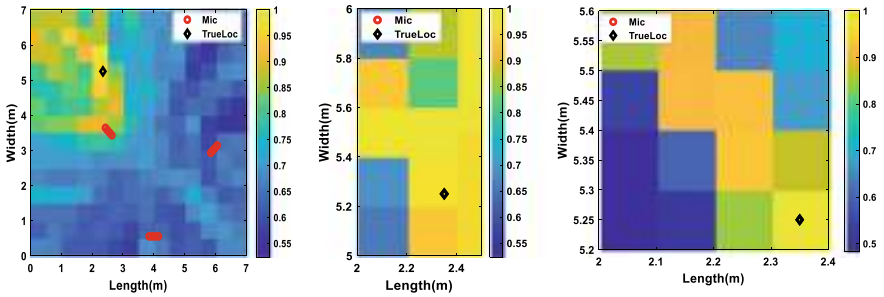

Fig. 2 SRP map using IVR for three successive iterations. **a** Initial search space. **b** Contracted region for i = 1. **c** Contracted region for i = 2

value higher than a threshold of Fig. 1a. The process of evaluating the SRP map and search volume reduction is repeated for the next iteration with a higher spatial resolution in Fig. 2c. When the map is calculated on a denser spatial grid $\boldsymbol{J}_2$ with $r_2 = 0.2m$, the map's accuracy is significantly improved to that of the previous ones.

3.3 Iterative Modified SRP-PHAT with Adaptive Search SPACE (ISRP-A)

Iterative Modified SRP-PHAT with Adaptive Search Space (ISRP-A) [16] is an upgraded ISRP method where the search space is adaptive to environmental conditions. The normalized GCC is computed at each sensor pair using Eqs. (4) and (14). The SRP functional at each grid location is the mean of accumulated GCC over its influential subvolume's associated delay (cf. Eqs. (15) and (16)). For the next iteration, the ISRP-A method suggests selecting all the grid locations with a likelihood higher than the threshold value. The search space for the next iteration is a set of distinct regions which accounted for the SRP functional of the selected locations. The threshold's optimum value is chosen as 0.94 after several experiments. The opted subregions are iteratively disintegrated and re-evaluated on a denser grid. The re-evaluation of high probabilistic regions on a denser grid ensures that the map's actual global peak is not missed in coarse acoustic maps during initial iterations.

Furthermore, there is a scope that the proposed method can also be extended to localize the multiple sources. It is illustrated using Fig. 3a, b, wherein the search space's acoustic map is computed for a grid step size of $0.5m$ and $0.1m$, respectively. It is observed from Fig. 3a that when the SRP map is calculated on a coarser grid, there are several locations with their functional value above the threshold. On the search space refinement, a sharp peak is witnessed at both the source locations in Fig. 3b, representing a possible extension of ISRP-A to multiple sources [29–31]. However, the dominating source makes the localization of submissive sources very challenging, necessitating further exploration of the method.

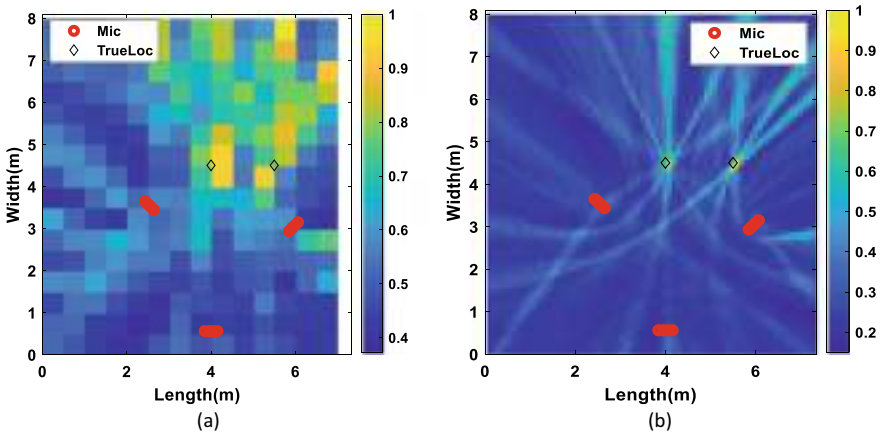

Fig. 3 Evaluation of SRP map with different spatial resolution. **a** r = 0.5 m. **b** r = 0.1 m

3.3.1 Algorithm

Initially, when $i = 0$, the algorithm is initialized with the following: coarse spatial resolution r_i, the initial set of candidate locations $\boldsymbol{J}_i$ in the original search volume $\boldsymbol{V}_i$, required spatial resolution r_{final}, maximum times to iterate in the algorithm as $I_{\max}$, and threshold Th. It is followed by computation of the objective function $W(\boldsymbol{X})$ for all the candidate locations $\boldsymbol{J_i}$ using Eq. (15) and Eq. (16). Among the evaluated locations, the ones with SRP functional higher than a threshold value are selected for the next iteration. After that, the search space for the next iteration is a set of distinct subregions which accounted for the functional value at the respective selected locations. In the successive iteration, the selected subregions are further disintegrated, and the energy map is computed on a denser spatial grid in each of them. The two steps, higher likelihood subregions selection and computing denser energy maps, are repeated recursively until the desired accuracy level is achieved. In the end, the locations with the highest SRP are estimated as source positions. ISRP-A algorithm is presented in Table 2.

3.3.2 Computation Cost

The computation cost of SRP-PHAT [13] is given by Eq. (18), where is the DFT's length, is the number of sensor pairs, and represents the average number of required functional evaluations to find the maximum power location. Suppose, the time to compute the accumulation limits for SRP functional is ignored. In that case, the computational cost of the ISRP, IVR, and ISRP-A only differs from the C-SRP in terms of the required functional evaluations. For ISRP and ISRP-A, the accumulation limits can be computed before running the localization algorithm to fasten the system. However, the same is not possible for the IVR algorithm where the contracted search

Table 2 ISRP-A algorithm

1. Initialise: iteration i = 0, grid_resolution = r_i, Max_Iterations = I_{max}, spatial_grid = J_i, $desired\_resolution = r_{final}$, Threshold = Th, search volume = $V_{initial}$
2. Evaluate the Objective Function: $\overline{W}(X), \forall X \in J_i$ (cf. Eqs. (15) and (16))
3. Selection: Select all $X \in J_i$ whose $\overline{W}(X) > Th$
4. Check: if $i < I_{max} - 1$ or $r_i > r_{final}$
i Redefine
a) grid_ resolution r_{i+1} such that $r_{final} \leq r_{i+1} < r_i$ and,
b) Redefine distinct search subregions around each selected grid point such that $X_{min} = X - r_i/2$ and $X_{max} = X + r_i/2$
c) define J_{i+1} candidate locations in each subregion with the spatial resolution r_{i+1}
d) i = i + 1
ii Go to step 2
Else
Use Eq. (17) to estimate source locations
End

region is uncertain [15].

$$SRPCost = \left[6.125P^2 + 3.75P\right]L\log_2 L + 15LP(1.5P - 1) + \left(45P - 30P^2\right)Fe \tag{18}$$

The required function evaluations for C-SRP and MSRP can be computed from Eq. (19).

$$Fe_{C-SRP/MSRP} = \frac{V_{initial}}{r_{final}^3} \tag{19}$$

In Eq. (19), is the initial search volume and is desired final resolution. As illustrated, the MSRP and C-SRP will have the same computational load for a similar grid size. However, C-SRP necessitates using the dense spatial grid to maintain its robustness, while MSRP allows the coarser spatial grids. Thus, the source's resolution is limited by the selected spatial grid in the MSRP approach. The required functional evaluations for ISRP and ISRP-A can be computed from Eq. (20) [15] and Eq. (21) [16].

$$Fe_{ISRP} = \frac{V_{initial}}{r_0^3} + \sum_{i=1}^{I_{max}-1}\left(\frac{1}{\alpha_i}\right)^3 \tag{20}$$

$$Fe_{ISRP-A} = \frac{V_{initial}}{r_0^3} + \sum_{i=1}^{I_{max}-1} \boldsymbol{J}_{i-1}^{Th}\left(\frac{1}{\alpha_i}\right)^3 \tag{21}$$

Here, is the initial grid resolution, is the number of grid point above the threshold selected for successive iteration, and is the spatial resolution for iteration, where.

The final spatial resolution of ISRP-A is

$$r_{final} = r_0 \prod_{i=1}^{I_{\max}-1} \alpha_i \tag{22}$$

4 Comparison of ISRP, IVR, and ISRP-A

The three iterative methods discussed above seem to be quite analogous, and hence for a better understanding, the difference between them is presented in Table 3.

Table 3 Difference between ISRP, IVR, and ISRP-A

	ISRP	IVR	ISRP-A
1	The grid location with the highest SRP functional is selected for successive iteration	The grid locations with the SRP functional above the threshold value of 0.95 are selected for the next iteration	The grid locations with the SRP functional above the threshold value of 0.94 are selected for the next iteration
2	The selected location's influential volume defines the search space for successive iteration	The selected locations constrain the contracted search space for the next iteration. Thus, the region encloses all the chosen grid locations	The selected locations with their influential volume define the discrete search subspaces for the successive iteration
3	The probability of missing the actual location in the initial coarse iterations is high	The probability of eliminating source location in the initial coarse iterations is low	The probability of eliminating source location in the initial coarse iterations is extremely low
4	The required functional evaluations are independent of the acoustic conditions	The required functional evaluations increase with degradation in acoustic conditions	The required functional evaluations are adaptive to acoustic conditions
5	Only the highest SRP subregion is explored on the finer grid in the successive iteration	The contracted Search region may enclose low probabilistic areas, and the distributed energy peaks may not allow efficient contraction	Only the subregions with significant SRP functional are explored on a finer grid
6	The method is not robust	The method is comparatively robust but still computationally inefficient	The method is robust and computationally efficient

(continued)

Table 3 (continued)

	ISRP	IVR	ISRP-A
7	The method can only be used for single source localization	The method can only be used for single source localization	The method can be used for multiple source localization

5 Experimental Evaluation

The performance of the above-discussed methods is tested on different simulated acoustic settings and the SMARD database.

5.1 Evaluation with Simulated Database

The experiments are carried out in an enclosed room with dimensions. The different reverberation settings required for experimental purpose are simulated using the Image Source Method (ISM) [17, 18]. The signal is received at three linear arrays, each consisting of three microphones, as shown in Fig. 2. The clean speech signals are taken from the TSP speech database and placed at several random locations in the room. The signals are digitized at a sampling rate of 44.1 kHz and processed with a frame length of 4096 samples and 50% overlap. The (Additive White Gaussian Noise) AWGN is added to the received signal to vary the SNR.

The iterative techniques are tested with a sequential grid resolution of (0.5, 0.1, 0.01 m) under different acoustic conditions. Figure 4 displays a performance comparison of Root Mean Square Error (RMSE) in localization of the discussed methods. As illustrated by the results, ISRP-A follows C-SRP very closely and shows superior results over the other two iterative techniques.

The threshold determines the success of the iterative approaches. The lower the threshold, the higher the accuracy, but at the price of increased computational

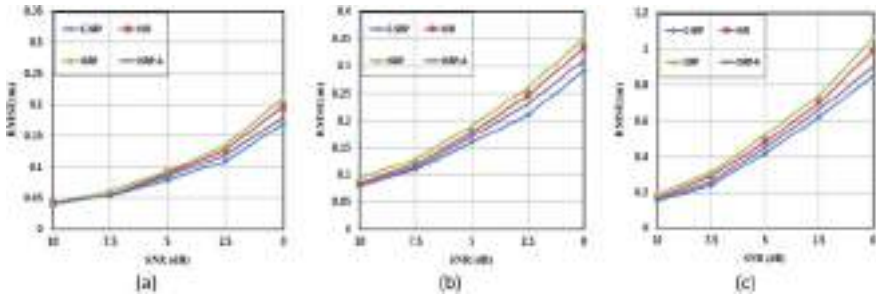

Fig. 4 Performance evaluation in terms of RMSE(m). **a** RT60 = 0.2 s. **b** RT60 = 0.5 s. **c** RT60 = 0.7 s

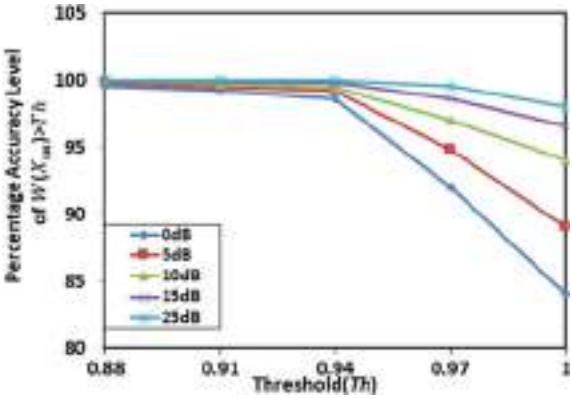

Fig. 5 Percentage accuracy of finding for a step size of 0.5 m, in different acoustic conditions

expense. Thus, the percentage accuracy of finding the source location's SRP value above the threshold (0.94) is experimentally verified and presented in Fig. 5.

The required average functional evaluations over random source locations are presented in Fig. 6. The grid step size used to evaluate the C-SRP is 0.01 m, while iterative methods are considered over the successive spatial resolution of (0.5, 0.1, 0.01 m). The reverberation's impact has been studied on IVR and ISRP-A methods with different acoustic settings.

As shown by the results, the computational cost of the methods is in the order. The computational cost of IVR approaches close to C-SRP in a challenging environment, while ISRP-A shows a small increase in required functional evaluations with the drop in SNR. Thus, a conclusion can be withdrawn from the experimental results that ISRP-A achieves accuracy close to densely computes C-SRP with only a marginal increase in computational cost to ISRP. Moreover, the computational requirement of ISRP-A is adaptive to environmental conditions.

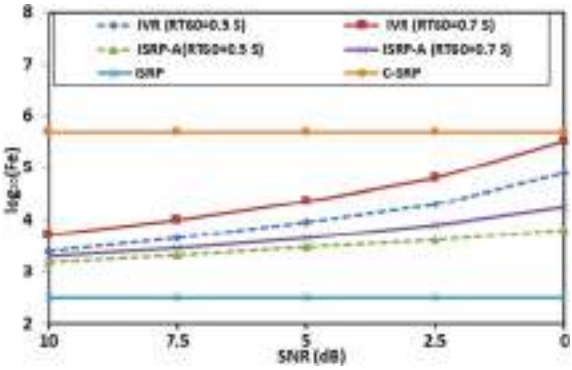

Fig. 6 Average computed functional evaluations (Fe) in different acoustic conditions

Table 4 Performance evaluation on SMARD database using configurations 0110 and 0111

Technique	Spatial resolution (m)	Anechoic signals		Reverberant signals	
		RMSE	Average Fe	RMSE	Average Fe
C-SRP	0.01	0.050	593,806	0.20	593,806
ISRP	[0.5, 0.1, 0.01] $I_{max=3}$	0.060	363	0.31	363
IVR	[0.5, 0.1, 0.01] $I_{max=3}$	0.050	3211	0.26	124,621
ISRP-A	[0.5, 0.1, 0.01] $I_{max=3}$	0.050	806	0.22	2218

5.2 Performance Evaluation on SMARD Database

An experimental evaluation of the iterative approaches and a finely computed C-SRP is performed on Single and Multichannel Audio Recordings Database (SMARD) [32]. The database contains the various recordings of the signals for different array configuration in a room of. The methods are tested using Omni-power 4296 sources over configurations 0111 and 0011. The RMSE and averaged functional evaluations for the anechoic and reverberant signal are presented in Table 4. As illustrated by the results, the ISRP-A method can attain an accuracy level very close to that of C-SRP with a significant computational cost reduction.

6 Conclusion

The paper presents the performance analysis and comparison of the SRP-PHAT methods, namely, ISRP, IVR, ISRP-A, and C-SRP. The performance of these methods is evaluated in several simulated environments and on the SMARD database. The results demonstrate that ISRP-A has succeeded in achieving localization accuracy close to densely computed C-SRP in unfavourable environments. Furthermore, the adaptive search space strategy of ISRP-A makes it a preferred choice over the other two iterative approaches. It helps the ISRP-A to vary the computational expense with the variation in environmental conditions.

References

1. A. Marti, M. Cobos, E. Aguilera, J.J. Lopez, Speaker localization and detection in videoconferencing environments using a Modified SRP-PHAT algorithm. Waves **3**, 40–48 (2011)
2. J.M. Badía, J.A. Belloch, M. Cobos, F.D. Igual, E.S. Quintana-Ortí, Accelerating the SRP-PHAT algorithm on multi- and many-core platforms using OpenCL. J. Supercomput. **75**, 1284–1297 (2019). https://doi.org/10.1007/s11227-018-2422-6

3. P. Pertilä, M. Parviainen, T. Korhonen, A. Visa, A spatiotemporal approach to passive sound source localization, in *IEEE International Symposium on Communications and Information Technologies*, pp. 1150–1154 (Sapporo, Japan, 2004). https://doi.org/10.1109/iscit.2004.1413899
4. R.S. Marinescu, A. Buzo, H. Cucu, C. Burileanu, Fast accurate time delay estimation based on enhanced accumulated cross-power spectrum phase, in *21st European Signal Processing Conference (EUSIPCO 2013)*, pp. 1–5 (Marrakech, Morocco, 2013)
5. J. Traa, D. Wingate, N.D. Stein, P. Smaragdis, Robust source localization and enhancement with a probabilistic steered response power model. IEEE/ACM Trans. Audio Speech Lang. Process. **24**, 493–503 (2016). https://doi.org/10.1109/TASLP.2015.2512499
6. A.Y. Majid, C. van der Horst, T. van Rietbergen, J.D. Zwart, R.V. Prasad, Lightweight audio source localization for swarm robots, in *IEEE 18th Annual Consumer Communications & Networking Conference (CCNC)*, pp. 1–6 (Las Vegas, NV, USA, 2021). https://doi.org/10.1109/CCNC49032.2021.9369572
7. M.A. Awad-Alla, A. Hamdy, F.A. Tolbah, M.A. Shahin, M.A. Abdelaziz, A two-stage approach for passive sound source localization based on the SRP-PHAT algorithm. APSIPA Trans. Signal Inf. Process. **9**, 1–12 (2020). https://doi.org/10.1017/ATSIP.2020.6
8. J.P. Dmochowski, J. Benesty, S. Affes, A generalized steered response power method for computationally viable source localization. IEEE Trans. Audio, Speech Lang. Process. **15**, 2510–2526 (2007). https://doi.org/10.1109/TASL.2007.906694
9. S. Delikaris Manias, D. Pavlidi, V. Pulkki, A. Mouchtaris, 3D localization of multiple audio sources utilizing 2D DOA histograms, in *24th—European Signal Processing Conference(EUSIPCO)*, pp. 1473–1477 (2016). https://doi.org/10.1109/EUSIPCO.2016.7760493
10. C. Zhang, D. Florêlncio, Z. Zhang, Why does PHAT work well in low noise, reverberative environments?, in *IEEE International Conference on Acoustics, Speech and Signal Processing (ICASSP)*, pp. 2565–2568 (2008). https://doi.org/10.1109/ICASSP.2008.4518172
11. F. Grondin, J. Glass, Fast and robust 3-d sound source localization with DSVD-PHAT. IEEE Int. Conf. Intell. Robot. Syst. 5352–5357 (2019). https://doi.org/10.1109/IROS40897.2019.8967690
12. D. Diaz-Guerra, A. Miguel, J.R. Beltran, Robust sound source tracking using SRP-PHAT and 3D convolutional neural networks. arXiv 1–12 (2020)
13. M. Cobos, A. Marti, J.J. Lopez, A modified SRP-PHAT functional for robust real-time sound source localization with scalable spatial sampling. IEEE Signal Process. Lett. **18**, 71–74 (2010). https://doi.org/10.1109/lsp.2010.2091502
14. A. Marti, M. Cobos, J.J. Lopez, J. Escolano, A steered response power iterative method for high-accuracy acoustic source localization. J. Acoust. Soc. Am. **134**, 2627–2630 (2013). https://doi.org/10.1121/1.4820885
15. Ritu, S.K. Dhull, Iterative Volumetric Reduction (IVR) steered response power method for acoustic source localization. Int. J. Sensors Wirel. Commun. Control. **10**, 1–9 (2020). https://doi.org/10.2174/2210327910999200614001049
16. R. Boora, S.K. Dhull, Iterative modified SRP-PHAT with adaptive search space for acoustic source localization. IETE Tech. Rev. (Institution Electron. Telecommun. Eng. India) **0**, 1–9 (2020). https://doi.org/10.1080/02564602.2020.1819895
17. E.A. Lehmann, A.M. Johansson, Prediction of energy decay in room impulse responses simulated with an image-source model. J. Acoust. Soc. Am. **124**, 269–277 (2008). https://doi.org/10.1121/1.2936367
18. E.A. Lehmann, A.M. Johansson, Diffuse reverberation model for efficient image-source simulation of room impulse responses. IEEE Trans. Audio Speech Lang. Process. **18**, 1429–1439 (2010). https://doi.org/10.1109/TASL.2009.2035038
19. J.B. Allen, D.A. Berkley, Image method for efficiently simulating small-room acoustics. J. Acoust. Soc. Am. **65**, 943–950 (1979). https://doi.org/10.1121/1.382599
20. M. Omologo, Acoustic event localization using a cross power-spectrum phase based technique, in *IEEE International Conference on Acoustics, Speech and Signal Processing (ICASSP)*, pp. 273–276 (Adelaide, SA, Australia, 1994). https://doi.org/10.1109/ICASSP.1994.389667

21. J.P. Dmochowski, J. Benesty, S. Affes, Fast steered response power source localization using inverse mapping of relative delays, in *ICASSP-IEEE International Conference on Acoustics, Speech and Signal Processing*, pp. 289–292 (2008)
22. A. Brutti, M. Omologo, P. Svaizer, Comparison between different sound source localization techniques based on a real data collection, in *Hands-free Speech Communication and Microphone Arrays (HSCMA)*, pp. 69–72 (2008). https://doi.org/10.1109/HSCMA.2008.4538690
23. H. Do, H.F. Silverman, Y. Yu, A real-time SRP-PHAT source location implementation using stochastic region contraction (SRC) on a large-aperture microphone array, in *IEEE International Conference on Acoustics, Speech and Signal Process (ICASSP)*, pp. 121–124 (2007). https://doi.org/10.1109/ICASSP.2007.366631
24. M. Ranjkesh, R. Hasanzadeh, A fast and accurate sound source localization method using the optimal combination of SRP and TDOA methodologies. J. Inf. Syst. Telecommun. **3**, 100–107 (2015). https://doi.org/10.7508/jist.2015.02.005
25. D. Salvati, C. Drioli, G.L. Foresti, Sensitivity-based region selection in the steered response power algorithm. Signal Process. **153**, 1–10 (2018). https://doi.org/10.1016/j.sigpro.2018.07.002
26. R. Boora, S.K. Dhull, A TDOA-based multiple source localization using delay density maps. Sadhana—Acad. Proc. Eng. Sci. **45**, 1–12 (2020). https://doi.org/10.1007/s12046-020-01453-8
27. M. Cobos, A note on the modified and mean-based steered-response power functionals for source localization in noisy and reverberant environments, in *IEEE 6th International Symposium on Communications, Control and Signal Processing*, pp. 149–152 (Athens, 2014). https://doi.org/10.1109/ISCCSP.2014.6877837
28. M.V.S. Lima, W.A. Martins, L.O. Nunes, L.W.P. Biscainho, T.N. Ferreira, M.V.M. Costa, B. Lee, Efficient steered response power methods for sound source localization using microphone arrays. IEEE Signal Process. Lett. **22**, 1–14 (2015). https://doi.org/10.1109/LSP.2014.2385864
29. B.G. Lee, J.S. Choi, Multi-source sound localization using the competitive K-means clustering, in *IEEE 15th Conference on Emerging Technologies & Factory Automation (ETFA)*, pp. 1–7 (Bilbao, 2010). https://doi.org/10.1109/ETFA.2010.5641169
30. A. Brutti, M. Omologo, E. Member, P. Svaizer, Multiple source localization based on acoustic map de-emphasis. EURASIP J. Audio, Speech, Music Process. **2010**, 1–17 (2010). https://doi.org/10.1155/2010/147495
31. A. Brutti, M. Omologo, P. Svaizer, Localization of multiple speakers based on a two step acoustic map analysis, in *IEEE International Conference on Acoustics, Speech and Signal Processing*, pp. 4349–4352. Las Vegas (2008). https://doi.org/10.1109/ICASSP.2008.4518618
32. J.K. Nielsen, J.R. Jensen, S.H. Jensen, M.G. Christensen, The single-and multichannel audio recordings database (SMARD), in *14th Int. Workshop on Acoust. Signal Enhancement-IWAENC*, pp. 40–44 (2014). https://doi.org/10.1109/IWAENC.2014.6953334

Software Test Automation Using Selenium and Machine Learning

Nisha Jha, Rashmi Popli, Sudeshna Chakraborty, and Pramod Kumar

Abstract Software testing has always been a crucial job in accomplishing and assessing the quality standards of a software product. Software testing is done to confirm the developed software product does what it is expected to do. However, testing is expensive in terms of time, effort, and is quite complicated. Studies report that software testing alone is responsible for almost half of the total budget incurred in software development. Additionally, manual testing is more prone to bugs and creating accurate and reliable software is an open issue. Specialists and experts have been exploring more effective and successful automation techniques for testing to deal with this issue. This paper is an endeavor to review the cutting edge of how machine learning and artificial intelligence have been figured out to automate and streamline software testing processes. It also provides an insight mapping of the research into these fields. Furthermore, a practical study on testing web applications is performed using selenium.

Keywords Software testing · Test automation · Machine learning · Artificial intelligence

1 Introduction

Test automation is employed to supplant or enhance conventional manual testing with the help of the test scripts suite. Benefits to Quality Assurance (QA) Engineers incorporate better software quality, decreased testing expenses, and repeatable test methods. Automated Software Testing is carried out to scale back testing timelines.

N. Jha (✉) · R. Popli
J.C. Bose University of Science and Technology, YMCA, Faridabad, India

S. Chakraborty
Sharda University, Greater Noida, India

P. Kumar
Department of Electronics & Communication Engineering, Manipal Institute of Technology, Manipal, India

S. Rawat et al. (eds.), *Proceedings of First International Conference on Computational Electronics for Wireless Communications*, Lecture Notes in Networks and Systems 329,
https://doi.org/10.1007/978-981-16-6246-1_35

An average automated test suite can be executed within a few hours. For a sophisticated product, manual testing may additionally need many human resources and comparatively more time to perform the same testing with consistency [1].

(a) Consistent test processes and methods
(b) Decrease in Quality Assurance Cost
(c) Boost in testing productivity
(d) Enhanced software product quality.

The following points need to be considered while choosing automation:

1. It is crucial to outline the motive of conducting test automation.
2. Building up a test automation procedure is highly essential in outlining what's to be automated, how it will be done, how the contents or scripts will be kept up, and what the standard costs and points of interest will be [2].
3. Countless testing 'devices' gave by merchants are exceptionally complex and use coding dialects. Treat the entire methodology of automated testing as you would any external software development effort. This fuse characterizing what should be automated (the prerequisites stage), planning test automation, composing the contents and test scripts, testing the contents, and so forth [3].
4. The test automation effort is speculation or investment which yields benefits in the long run. Additional time and assets are required [4]. The investment tur ns advantageous when these automated test scripts are executed again and again in every subsequent release. Therefore, it is quite essential to make sure that the scripts are adequately maintained.

2 Manual and Automated Software Testing

In case the test scripts need to be executed a couple of times, or the test is exceptionally costly to automate, it's presumably manual testing. Yet, of course, what desirable is stating "use common sense" once you got the opportunity to concoct a deterministic set of rules on how and when to automate? Manual testing permits the tester to perform more ad hoc or random testing. A large number of bugs are found via ad-hoc than via automation. Furthermore, the longer a tester goes through playing with the feature, the more the chances of detecting actual user bugs [5].

If test cases have to run again and again, test automation may be a significant success for the team. It offers the potential to execute automation against code that frequently changes to catch regressions in a well-timed manner. Automated test procedures are often executed simultaneously on various machines, whereas the manual tests would need to be run consecutively [6].

What comes off if a test cannot be automated?

Many scenarios cannot be automated, like usability testing cannot be automated, automation works only for predicted results and many more. That's why automation

is not a replacement for manual. Manual testing will never fade away. Software Testing can be viewed as a combination of Manual and Automation Testing.

3 Relationship Between Machine Learning and Software Testing

Artificial intelligence (AI) has successfully emerged as a warrior in decreasing the time, duration and effort required for many software engineering approaches [7]. Machine learning (ML), a sub-domain of AI only, can be used to automate various activities related to software engineering [8]. Additionally, the software is becoming more complex day by day, and traditional testing strategies are not able to scale well according to the complexity of these softwares. The ever- expanding intricacy of present-day programming frameworks has rendered ML-based strategies appealing.

A lot of research has been done on applications of ML algorithms that are applied to automatize the process of software testing. Whether the task is to generate the test cases, prioritize the test cases, or perform different types of testing like black box or white box, ML has proved its vitality [9].

ML techniques have been a promising method for automatizing testing related activities, construction, and evaluation of test oracle, and predicting the cost and time of testing.

That is the reason AI, which instructs frameworks to learn and apply that information, later on, makes programming analyzers think of more precise outcomes than conventional testing ever could [10]. Also, that the possibility of mistake isn't the sole factor that gets diminished. The time anticipated to play out testing of a product and discover the potential defects is additionally abbreviated, while the measure of information which should be taken care of can, in any case, increment with no strain on the testing group.

Since conventional software testing and ML testing are unique in many ways [11]. Table 1 can be viewed as a summarization of the key differences between traditional and ML testings.

Table 1 Comparison between conventional testing and machine learning testing

Conventional software testing	Machine learning testing
Test oracle is defined by the developers	Test oracle is described by the labeling companies and developers
The developer and tester generally does testing	Testing is conducted by data scientist, algorithm designer and developer
It mainly tries to find errors in coding	It focuses more on data, learning program and framework
Traditional software testing is generally done when requirements are fixed	The behavior keeps on changing due to frequent changes in the training data

The following points can be taken while incorporating machine learning to improve quality standards [12]:

1. Finding the patterns in the automated software testing cycles to get better results in regression testing or performance testing. And ML algorithms can pave an excellent way for pattern recognition.
2. Use ML to predict user behavior and change code in continuous testing, which can significantly reduce test cases without compromising test coverage.
3. Apply human creativity and imagination to complex algorithms.

There are various tools for ML testing like PyTorch, MLTest, Applitools, Testim, and many more.

4 Background and Related Work

An extensive literature review has been performed to explore the demand and implementation of ML approaches in the field of software test automation (Table 2). Databases like IEEE Explore, ACM Digital, Science Direct, Wiley Online, Springer have been looked for review.

Briand [23] gave a brief overview of the Ml applications applied in the domain of software testing on the basis of his personal experience. The author also emphasized the requirement for more research to enhance ML's potential from the software testing perspective.

Zhang et al. [11] coined two terms. First, ML Bug can be characterized as any defect in an AI framework that leads to a dissonance between the current and the essential conditions. Second, ML testing can be defined as any activity aimed to detect ML bugs.

Two key points that need to be considered for implementing ML and AI in software testing [24].

First, create automatic test cases by training ML.

Second, to make AI and ML systems think like human beings, i.e., deciding what to execute, what needs to be given more priority, what needs to be ignored and many more.

Figure 1 shows the steps which can be considered while testing ML systems [25].

5 Implementation Overview

For experimental setup, the login module of an e-commerce website, Amazon (https://www.amazon.in/) [26], has been tested using the Selenium testing tool.

The following terminologies are used while defining a test scenario and test case templates:

Table 2 Literature review

Authors	Premises	Verification
Zhang [13]	Machine learning methods have been applied to value-based software engineering. A framework has been proposed for value-based testing of software and generating test data	The proposed framework prioritizes testing decisions to achieve the most valuable objectives in a cost- effective manner
Silva et al. [14]	The work uses machine learning and artificial neural network tools to sort out the issue of functional test execution effort estimation	The experiments were performed on two real databases which use artificial neural networks. Different models like support vector machines and linear regression models have been compared
Cheatham et al. [15]	The work aims to find out the most important software testing attributes which can predict software testing cost and time using ML techniques	The methodology offers efficient testing time and cost management on the basis of some testing attributes taken as a training dataset for clustering. It also discusses the factors which affect the testing time
Lenz et al. [16]	The work presents an approach using machine learning clustering methods to link testing outputs from the applications of different fault-based and structural testing techniques	An experimental framework named RITA (Relating Information from Testing Activity) has been introduced to offer test case selection and prioritization
Meinke and Bennaceur [17]	The work gives an overview of some main techniques of ML and its applications in the field of software engineering	The paper extensively reviews the key challenges of the integration of ML in the area of software engineering
Amershi et al. [18]	The paper describes a study of how various Microsoft software teams develop softwares within an agile environment with AI and data features	A ML process maturity metric was proposed to guide teams to integrate AI features to make improvements in their softwares on the basis of information gathered by interviews and surveys
Ali and Gravino [19]	The systematic literature review discusses the software effort estimation models using ML techniques on the basis of a total of 75 primary studies from the time span of early 1991–2017	The result shows that ANN and SVM are the mostly used ML techniques. And COCOMO, NASA, and ISBSG are widely used datasets

(continued)

Table 2 (continued)

Authors	Premises	Verification
Kahles et al. [20]	The work offers an approach for the automation of analysis of root causes in agile software testing environment using ML	The prototype discussed collects data from interviewing various testing experts and provides a baseline for expert knowledge extraction
Rosenfeld et al. [21]	A novel approach for automation testing of Android applications was proposed applying various machine learning methods	A testing tool named ACAT was developed to find out more critical bugs in software
Grano et al. [22]	The work gives an overview of using machine learning models to predict branch coverage attained by testing tools	The results show that machine learning models like Huber Regression, Support Vector Regression, and Multilayer Perceptron are quite valuable for predicting branch coverage in automated testing But this type of prediction remains quite problematic due to the non-deterministic behavior of the algorithms

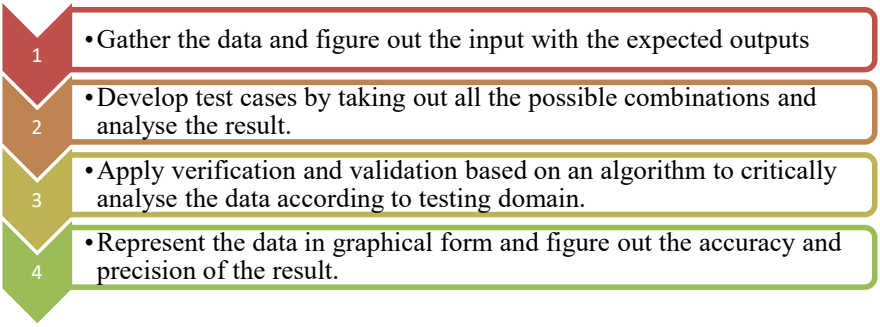

Fig. 1 Steps for ML testing

- TS_ID is a unique number associated with the test scenario.
- Test Scenarios are the high-level test cases that describe the different situations to test an application [27].
- Test Scenario Description describes the test scenarios.
- A test case refers to a set of situations or conditions that is used to test the functionality of an application.

The experiment tests the login module of the website with different test data. The login page first requires an email address or phone number and then sends a

one-time password to complete the authentication process. Once the authentication is successful, the user is transferred to the my_account page to perform several tasks like profile management, order management, and many more.

Selenium WebDriver is an open-source tool to test web applications. In Selenium WebDriver, the location of the web element is found and then desired actions are performed by calling different methods. To locate web elements, several options are available like id, name, Xpath, CSSpath, and many more. Selenium WebDriver is rich in a large set of inbuilt functions to test a web applications.

Selenium WebDriver in Python: A WebDriver driver instance is created as follows.

to execute the test cases [28]:
from selenium import webdriver
from selenium.webdriver.common.keys import Keys
driver = webdriver.Chrome("Path of the chromedriver")
driver.get("website URL")
driver.find_element_by_xpath('location of web element')

The following snapshot (Fig. 2) shows the login scenario for the website with incorrect login details:

Figure 3 demonstrates the login process with correct authentication details.

The testing process keeps a record of screenshot of the login attempts as follows [28]:

from PIL import Image
driver.save_screenshot("image.png")
image = Image.open("image.png")
image.show()

Fig. 2 Incorrect login

Fig. 3 Correct login credentials with password authentication

The dataset of login credentials, test cases, and screenshots can be used for ML and AI to measure user authenticity, forming the basis for future work.

5.1 Applying AI in Software Testing

An example of incorporating AI in software testing is to generate test cases by object detection and image classification in a web application. Here, the target is to strengthen ML to recognize web components based on models that have already been trained across various Systems Under Tests (SUT).

Using the feature of object recognition using ML-based approaches will take us one step closer to write test cases automatically irrespective of any test case-specific implementation details. The way automated test cases refer to objects using AI, the level of abstraction can be boosted. This approach is quite beneficial for the self-healing process to handle the dynamic changes in the application. Also, by raising the abstraction level, it becomes possible to reuse test cases across different SUTs. An ML model can be implemented by training enough to recognize various web application objects [29]. An example of webpage decomposition and object recognition is in Fig. 4.

The dataset can be prepared by collecting many images and related information of webpage objects. Frameworks like TensorFlow and Keras can then be used to train ML models using the training dataset. ML systems mainly depend on the data; data must be collected and prepared accurately for a better performing product.

Fig. 4 Object recognition

6 Conclusion

Although there are numerous benefits of ML-based testing, there are some flaws also. As discussed earlier, this ever-expanding multifaceted nature of present-day programming frameworks has rendered ML-based systems alluring in decision-making or automated test case generation.

With the continuous advancement in AI technologies, it is crucial to verify the systems' functionality, security, flexibility, performance, and availability. It means AI systems need to be tested thoroughly. But every coin has two sides. Briand [23] pointed out the non-availability of relevant data during testing activities is still one of the key drawbacks. Another limitation of it is being a machine. Everything can't be automated. There will always a need for skilled testers at every stage of Software testing.

Software testing will always be one of the non-negotiable processes to make AI and ML systems successful. Fortunately, researchers and practitioners have started recognizing AI and ML's potential to bridge the gap between human and machine-driven testing capabilities. The research has just begun, and it will only be taken ahead. A lot of research is still required to fully utilize the breakthrough combination of software testing and machine learning. One will have to be a constant learner with a critical thinking mindset.

References

1. R.M. Sharma, Quantitative analysis of automation and manual testing. Int. J. Eng. Innov. Technol. (IJEIT) **4**(1) (2014)

2. N. Bhateja, A study on various software automation testing tools. Int. J. Adv. Res. Comput. Sci. Softw. Eng. **5** (2015)
3. P. Rathi, V. Mehra, Analysis of automation and manual testing using software testing tool. Int. J. Innov. Advance. Comput. Sci. **4**, Special Issue March (2015)
4. A. Bertolino, Software testing research: achievements, challenges, dreams. FoSE 2007 Futur. Softw. Eng. (September) 85–103 (2007)
5. V. Kumar, Comparison of manual and automation testing. Int. J. Res. Sci. Technol. **1**(V) (2012)
6. Vishawjyoti, S. Sharma, Study and analysis of automation testing techniques. J. Global Res. Comput. Sci. **3**(12) (2012)
7. V.H.S. Durelli, Machine learning applied to software testing: a systematic mapping study. IEEE Trans. Reliab. **68**(3), 1189–1212 (2019)
8. M. Noorian, E. Bagheri, W. Du, Machine learning-based software testing: towards a classification framework, in *SEKE 2011—Proceedings of the 23rd International Conference on Software Engineering and Knowledge Engineering*, pp. 225–229 (2011)
9. R. Lachmann, Machine learning-driven test case prioritization approaches for black-box software testing, in *Proceedings of The European Test and Telemetry Conference—ettc2018*, pp. 300–309 (2018)
10. How machine learning and AI bring a new dimension to software testing. https://towardsdatascience.com/how-machine-learning-and-ai-bring-a-new-dimension-to-software-testing-7b2b6ea67b61?gi=e1cd2f5e488c. Last accessed 22 Apr 2020
11. J.M. Zhang, M. Harman, L. Ma, Y. Liu, Machine learning testing: survey, landscapes and horizons. IEEE Trans. Softw. Eng. https://doi.org/10.1109/TSE.2019.2962027 (2020)
12. Things to know when applying machine learning & artificial intelligence to QA test automation. https://www.blazemeter.com/shiftleft/3-things-know-when-applying-machine-learning-artificial-intelligence-qa-test-automation. Last accessed 22 June 2020
13. D. Zhang, Machine learning in value-based software test data generation, in *2006 18th IEEE International Conference on Tools with Artificial Intelligence (ICTAI '06)*, Arlington, VA, 2006, pp. 732–736 (2006)
14. D.G.e. Silva, M. Jino, B.T.d. Abreu, Machine learning methods and asymmetric cost function to estimate execution effort of software testing, in *2010 Third International Conference on Software Testing, Verification and Validation*, Paris, pp. 275–284 (2010)
15. T. Cheatham, J. Yoo, N. Wahl, Software testing: a machine learning experiment, pp. 135–141 (1995)
16. A. Lenz, A. Pozo, S. Vergilio, Linking software testing results with a machine learning approach. Eng. Appl. Arti. Intell. **26** (2013)
17. K. Meinke, A. Bennaceur, Machine learning for software engineering: models, methods, and applications, in *2018 IEEE/ACM 40th International Conference on Software Engineering: Companion (ICSE-Companion)*, Gothenburg, pp. 548–549 (2018)
18. S. Amershi et al., Software engineering for machine learning: a case study, in *Proceedings of the 41st International Conference on Software Engineering: Software Engineering in Practice (ICSE-SEIP' 19)*, pp. 291–300 (IEEE Press, 2019)
19. A. Ali, C. Gravino, A systematic literature review of software effort prediction using machine learning methods. J. Softw. Evolut. Process (2019)
20. J. Kahles, J. Törrönen, T. Huuhtanen, A. Jung, Automating root cause analysis via machine learning in agile software testing environments, in *2019 12th IEEE Conference on Software Testing, Validation and Verification (ICST)*, Xi'an, China, pp. 379–390 (2019)
21. A. Rosenfeld, O. Kardashov, O. Zang, Automation of android applications functional testing using machine learning activities classification, in *2018 IEEE/ACM 5th International Conference on Mobile Software Engineering and Systems (MOBILESoft)*, Gothenburg, pp. 122–132 (2018)
22. G. Grano, T.V. Titov, S. Panichella, H.C. Gall, How high will it be? Using machine learning models to predict branch coverage in automated testing, in *2018 IEEE Work-shop on Machine Learning Techniques for Software Quality Evaluation (MaLTeSQuE)*, Campobasso, pp. 19–24 (2018)

23. L.C. Briand, Novel applications of machine learning in software testing, in *2008 The Eighth International Conference on Quality Software*, Oxford, pp. 3–10 (2008)
24. Automated Software Testing in 2019: AI and ML, in *Traditional QA Out?* https://becominghuman.ai/automated-software-testing-in-2019-ai-and-ml-in-traditional-qa-out-dca3839d65. Last accessed 23 Apr 2020
25. Testing of machine learning systems—The new must have skill in 2018. https://www.capgemini.com/2017/12/must-have-testing-skills-in-2018/#. Last accessed 22 Apr 2020
26. Amazon. https://www.amazon.in/. Last accessed 8 Dec 2020
27. A. Adekanmi, Research on software testing and effectiveness of automation testing (2019). https://doi.org/10.13140/RG.2.2.30636.31365
28. Selenium Hq browser automation documentation. http://www.seleniumhq.org/. Last accessed 12 Nov 2020
29. D. Santiago, T.M. King, P. Clarke, AI-Driven test generation: machines learning from human testers, in *Proceedings of the 36th Pacific NW Software Quality Conference*, ed. by Proceedings of the 36th Pacific NW Software Quality Conference, pp. 1–14 (Portland, 2018)

Project Curative Collaborative and Sponsoring Platform

Rishabh Sharma, Ashreeya Pant, Sudeshna Chakraborty, C. M. Shahadat, Shahid Shabir Dar, and Vivek Kumar Singh

Abstract Nowadays, there are several types of ways to post your idea through social media or any kind of other funding platforms like Kickstarter, Indiegogo, Wishberry, RocketHub, and FundRazr. All these platforms raise funds for your Ideas and projects. However, these platforms do not evaluate or analyze your ideas. The analysis in our invention will provide the success percentage of the idea or project. Success percentage is the main factor to get your idea ready for funding. As mentioned in the terms and conditions in the existing applications, all of these charge for using their services. Some have a different charge for using the service without caring if your idea/project works or not, while some charge from the money that has been raised. These services do not guarantee your return on investments. This invention will provide a platform where anybody can share their thoughts and ideas. An AI algorithm will then assess these ideas and calculate how relevant the idea is as per the latest trends and requirements. The next algorithm in our application will also try and predict the chances of the project succeeding. It will also include a user rating feature where other users can rate the ideas and give opinions about them. Furthermore, our product will introduce a concept where the algorithm will give the idea a score based on the ratings and the results achieved by the other algorithms. Ideas will be ranked based on this score. In addition to this, our application will let users collaborate with other developers given that they have relevant skills. This will solve the first two shortcomings. For instance, you have an idea that you know is in demand and also a team capable of turning that idea into a reality. But how do you scale your product? This is where our final feature will come into play. Like normal users, potential investors can also go through the ideas and rate them. They can also choose to invest if there is an Idea/Product that captures their attention. Lastly, many features such as user sponsorship, product requests, and various other exciting features are being established to improve the experience of both the Users and the Investors.

Keywords Funding · Ideas · Invention · Collaborate · Potential investors · Sponsorship

R. Sharma (✉) · A. Pant · S. Chakraborty · C. M. Shahadat · S. S. Dar · V. K. Singh
Department of CSE, SET Sharda University, Greater Noida, UP, India

S. Rawat et al. (eds.), *Proceedings of First International Conference on Computational Electronics for Wireless Communications*, Lecture Notes in Networks and Systems 329,
https://doi.org/10.1007/978-981-16-6246-1_36

1 Introduction

Our App provides a platform where anybody can share their thoughts and ideas. An AI algorithm assesses their ideas and calculates how relevant their idea is as per the latest trends and requirements. Our algorithm also predicts the chances of the project succeeding. Other users can also rate the idea according to their opinion. Finally, we have another algorithm that gives the idea a score based on the ratings and the results achieved by our other algorithms. Ideas will be ranked based on this score. In addition to this, we also have a feature that lets users collaborate with other developers given that they have relevant skills [1]. Like normal users, potential investors can also go through the ideas and rate them. They can also choose to invest if there's an Idea/Product that captures their attention. Features such as User Sponsorship, Product Request, and many other exciting features improve the experience of both the Users and the Investors.

2 Literature Review

The world is advancing with new technologies and innovations every day. Some or the other people get new ideas everyday but have a barrier in front of them which doesn't let their ideas grow further. Most common concern is the concern about money to invest on their idea. Existing technologies do not have the capability of handling the needs of the user which may be due to high service charges, by not protecting the ideas of the user or by any other reasons [2]. There exist some platforms like Kickstart, Indiegogo, RocketHub, and so on which is used for crowd funding. For Instance, RocketHub is geared toward entrepreneurs who are searching for venture capital and have very high service charges. Similarly, Patreon is a membership platform that allows end users to support their favorite content creators and not on the basis of any projects or ideas. Furthermore, FundRazr allows users to create crowdfunding campaign about social issues like medical care, education, community help, and poverty alleviation. Next, Kickstarter is a funding platform for creative projects which provides space where people who are your known can work with you to support you. In Kickstarter, you can come up with your funding goals and deadline if your projects get the funding you will have to pay 5% as charge to the Kickstarter else there will be no charge [3].

3 Methodology/Planning of Work

Our first step was to identify the parameters that can help us identify and then differentiate a good idea from the bad one. Once we were done with that, we came up with an algorithm that would take these parameters and do computing with those parameters. Upon completion, it gave us a score that can signify how good the idea is and what are its chances of succeeding. Next, we created a model using this algorithm. Finally, we created the front end, which in our case would be an android and iOS application. The application would allow the user to enter and view different ideas. The application will also communicate with the server where our data model is and do the required operation. Once the idea is entered by the user will reflect a pending status and this will be visible in the admin panel of our application where the admin can see if the idea is passing all the parameters or not if the idea passes all the parameter the admin approves the idea and the status of that idea at user end changes from pending to approved. After getting approval idea becomes live and one can review the idea and add suggestions to it, also if someone is interested then he or she can become a sponsor for that idea by using the become sponsor button on the idea page.

Figure 1 shows the how the interaction works in our application, i.e., PCCASP.

Table 1 compares the drawback in the existing state of the art and shows how different our application is.

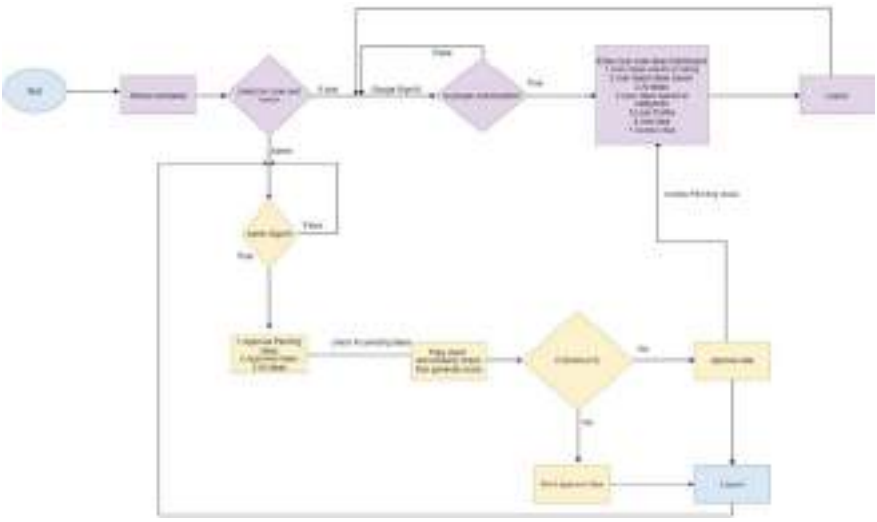

Fig. 1 Workflow of PCCASP

Table 1 Showing the uniqueness in our application

S no	Existing state of art	Drawbacks in existing state of art	Overcome
1	RocketHub doesn't check the originality and approval of the idea which may lead to things like online trolls, bad reviews on your business, or anonymous messages that make you feel bad [4]	I. If you reach your fundraising goal, you'll pay a fee of 4%, plus a 4% credit card handling fee. If you don't reach your goal, that fee jumps up to 8% plus the credit card handling fee II. RocketHub doesn't assure the success of the project III. RocketHub doesn't check the originality and approval of the idea which may lead things like online trolls, bad reviews on your business, or anonymous messages that make you feel bad	I. PCCASP which will not charge you that much and possibilities of success of the project will be calculated on early bases so that you don't have to lose your money II. PCCASP will be providing a realtime analysis of your idea with ratings from users III. PCCASP admin will only approve your idea to upload if it passes certain checks and analyses done by algorithms
2	Patreon is a membership platform that allows end-users to support their favorite content creators. The core functionality of the service is that users subscribe to their favorite content creators by paying a small recurring fee and receive some perks in return [5]	I. Patreon focuses mostly on content creators II. Patreon is a membership platform	I. PCCASP focuses on the ideas and projects the creator has to offer II. PCCASP is a sponsorship platform III. Other than providing sponsorship and connecting the users with the investors, our platform also enables collaboration IV. In our platform, you don't need to have an existing product or service to get funded
3	FundRazr allows users to create crowdfunding campaigns about social issues like medical care, education, community help, and poverty alleviation. It is working on a non-profitable design for creating help for the society [6]	I. It is an app that was designed to raise donations about social issues II. There is a chance of creating fake social issues and getting a donation	I. PCCASP is an application where potential developers having great ideas can get the investment II. PCCASP has a different algorithm that judges the success ratio of the ideas and attracts the investor

(continued)

Table 1 (continued)

S no	Existing state of art	Drawbacks in existing state of art	Overcome
4	Kickstarter is a funding platform for creative projects. Categories in which their deals are films, games, music, art, and technologies, etc., which provides space where people who are known can work with you to support you. In Kickstarter, you can come up with your funding goals and deadline if your projects get the funding you will have to pay 5% as a charge to the Kickstarter else there will be no charge [7]	I. In Kickstarter, you need a project, funding goals as well as a deadline to raise funds II. Kickstarter is a platform where you can get help from your known III. Kickstarter work on a model where you will have to pay 5% once funding is raised for your project	I. In PCCASP you just need an idea to rest everything develops later on II. In PCCASP, only experts will give you advice although you have a tremendous feature called 'Rating' where people who find your project interesting can rate it III. In PCCASP, you will get support from the expert for all the required amendments and you may get fund with 3% charges

4 Algorithms

We have introduced three unique algorithms in our application:

1. Similarity checker: It checks whether the ideas is plagiarised or not and generates the report.
2. Relevancy checker: It uses machine learning algorithms in order to generate a report on how likely an app is to be successful.
3. Unwanted words checker: It uses methods that is used to discard any idea that has unwanted/vulgar words.

5 Market Feasibility

1. Demand

After going through a few of the subreddits on reddit.com, we observed a slight demand for something that was slightly related to what we are trying to achieve. People, mostly students, and ones with less job experience, often tended to have some kind of hobby projects. They would discuss how they could proceed to scale up their product, and the financial aspects of it. There were a few other discussions too that were hovering around this topic. This showed that there were people who needed something that we can create, which means that there was a market for our product [8]. Or at least for the initial phase and beta testing so that we could later scale up the product once we perfected it to the market standards.

2. **Target**

There are two different kinds of use cases for our product. Given below are the targeted audience for each use case.

a. **Posting Ideas and Collaboration**

There are two demographics that we will be targeting here.

- **Group A**: This will consist of students who are looking for some hobby projects which they can add to their portfolio.
- **Group B**: This will consist of employed people who have been working on a side project and are now looking at ways to scale it up.

b. **Investors**

There's only one kind of group that we are targeting, at least for now.

- **Group A**: This consists of people with a few successful ventures who are looking for other potential prospects where they could benefit by investing.

3. **Competition**

There are a few existing platforms that do a little bit of what we already do.

- **Funding**: Sites like Kickstarter and Indiegogo allow users to post their products so that they can receive funding. But these are geared more toward public funding, rather than investments. However, there's a TV show "Shark Tank" where people can go to find investments for their products. But that is more geared towards businesses and not digital products. And not everyone can go there [10].
- **Collaboration**: We didn't come across any platforms that allowed users to find other partners with whom they can collaborate. Sites like Product Hunt and Patreon can be used for this product but they aren't very straightforward and would often require unnecessary additional effort [9].

a. **Technical Feasibility**

So, is it possible to achieve what we are trying to make with the help of existing technology? Yes, with a little effort from our side, and with the help of our mentors, we can develop this. We will however require or need to learn the following [11].

b. **Financial Feasibility**

- **Setup Cost**: Thanks to the AWS credits received, the initial setup costs should be very minor.
- **Operating Cost**: This will depend on the number of users. But the initial phase will be covered by the free AWS credits.

c. **Revenue Model**

Once we scale up, we will need a source of revenue to carry on. These are a few proposed revenue models we can implement.

- **Subscription Based**: We will introduce a subscription plan which will give additional benefits to the paying members.
- **Interest Based**: Once we have a few investors on board, we can take a small percentage of the amount that they invest as interest.
- **One Time Fee**: We might also add a one-time fee for taking advantage of the Sponsorships on our platform.

6 Results and Conclusion

Figure 2 shows the profile page of the user, where the user can edit his/her details and can see how they have interacted with the application. Figure 3 shows the categories screen in the application.

PCCASP is well optimized and performs smoothly. To some extent, due to some upgrades in the Flutter SDK, it might produce some errors. Some errors might also get produced because of the incompatibility of the mobile software. Any person with

Fig. 2 Profile page

Fig. 3 Categories screen

innovative ideas mainly students who seek for funds and Sponsors who seek for innovative ideas and are willing to fund are the targeted users for our application.

References

1. T.T. Wang, J.H. Xu, Automatic debugging of operator errors based on efficient mutation analysis, in *Multimedia Tools and Applications* (2018)
2. M. Alavi, Leidner, Review: knowledge management and knowledge management systems: conceptual foundations and research issues. MIS Quart. **25**(1), 107–136 (2001)
3. W. Ebner, J.M. Leimeister, H. Krcmar, Community engineering for innovations: the ideas competition as a method to nurture a virtual community for innovations. R&d Manage. **39**(4), 342–356 (2009)
4. A. Kankanhalli, M. Taher, H. Cavusoglu, Kim, Gamification: a new paradigm for online user engagement, in *Proceedings of the International Conference on Information Systems* (Orlando, FL, 2016)

5. H. Liu, J. Zhang, R. Liu, G. Li, A model for consumer knowledge contribution behavior: the roles of host firm management practices, technology effectiveness, and social capital. Inf. Technol. Manage. **15**(4), 255–270 (2014)
6. P.D. Morrison, J.H. Roberts, E. Von Hippel, Determinants of user innovation and innovation sharing in a local market. Manage. Sci. **46**(12), 1513–1527 (2000)
7. Y. Yoo, R.J. Boland Jr, K. Lyytinen, A. Majchrzak, Organizing for innovation in the digitized world. Organizat. Sci. **23**(5), 1398–1408 (2012)
8. K.E. Boyer, *Social Media and Nonprofits: Increasing Fundraising and Volunteerism for the Kahlo Cultural Center* (2011)
9. R. Hoefer, From web site visitor to online contributor: three internet fundraising techniques for nonprofits. Soc. Work **57**(4), 361–365 (2012)
10. N. Nichols, Understanding the funding game: the textual coordination of civil sector work. Canad. J. Sociol. **33**(1) (2008)
11. R.D. Waters, The value of relationship and communication management in fundraising: comparing donors' and practitioners (Views of Stewardship, 2010)

Home Automation Using Internet of Things: An Extensive Review

Ruchi Yadav, Nitin Yadav, Kartik Gupta, Rashmi Priyadarshini, Sudeshna Chakraborty, and Pramod Kumar

Abstract Internet of Things (IoT) is a dimension which permits the things to be detected, sensed, and to be accessed from remote locations. Pre-existing network architecture provides an opportunity for the combination of advanced monitoring system. This provides more accurate, efficient, and economical results. IoT is playing an active role in various fields of our life such as to assists chronic patients, smart transportation, smart grid, smart city, etc. In this research paper, we have explained the application of IoT in home automation and its role in sensing the environmental factors for improving energy efficiency and comfort of life. We have also discussed the various examples of IoT in home applications. Along with that a model has been discussed based on solar energy using IoT home automation. Primary objective of the research is focused on striking a balance between efficient power utilization and generation of power. Sensors and actuators are combined with the internet and are discussed here.

Keywords Internet of things (IoT) · Smart sensors · Home automation · Machine learning · Solar energy · Machine to machine · Auto ID labs

1 Introduction

There are numerous projects that are anticipated and are also currently working on various implementation of IoT for proper management of remote areas. For instance,

R. Yadav (✉) · N. Yadav · K. Gupta · R. Priyadarshini · S. Chakraborty
Sharda University, Greater Noida 201310, India

R. Priyadarshini
e-mail: rashmi.priyadarshini@sharda.ac.in

P. Kumar
Department of Electronics & Communication Engineering, Manipal Institute of Technology, Manipal, India
e-mail: p.kumar@manipal.edu

S. Rawat et al. (eds.), *Proceedings of First International Conference on Computational Electronics for Wireless Communications*, Lecture Notes in Networks and Systems 329,
https://doi.org/10.1007/978-981-16-6246-1_37

places like Songdo located in South Korea it is one of the examples of smart city application which is fully operated and well-equipped smart city. The complete automation concept is although not included in the Internet of Things (IoT) that includes ambient intelligence and automatic controls as they also do not require proper internet connections [1].

In future IoT may be a non-deterministic and open network in which auto-organized or intelligent entities web services, virtual objects also known as avatars will be interoperable and able to act independently pursuing their own objectives or shared ones depending on context, circumstances, or environments. Environmental monitoring applications [2] of IoT typically use sensors to assist in environmental protection by monitoring air or water quality, atmospheric, or soil conditions and could even include areas like monitoring movements of wildlife and their habitats. Usage of IoT devices for monitoring and operating infrastructure is likely to improve incident management and emergency response coordination, quality of service, up-times, and reduce costs of operation in all infrastructure-related areas [3].

The primary objective of doing research in home automation by using IoT integrating with the solar energy-based system. This utilizes the internet connection with sensors, actuators which together optimize the consumption of energy [4]. It is anticipated that the device will be inclusive of all the energy-consuming devices like power outlets, electric bulbs, switches, etc. It will be beneficial in balancing out the power generation and its usage with the help of effective communication with the utility supply company. The system uses IoT which is a network connection of physical devices, objects, buildings, vehicles, etc., which are integrated with various sensors, actuators, internet connectivity that helps in exchange and accumulation of data. IoT successfully allows various objects to be analyzed, sensed, and can be controlled from any remote areas across the complete architecture that includes the network architecture, generating more scope for direct combination of computer-related system and physical devices. This results in more efficient, accurate, and more computerized cyber-physical systems [5]. The IoT is augmented with the sensors and actuators combining with the internet make it a cyber physical system which includes various technologies like smart transportation, smart grids, smart cities, and more intelligent pollution control systems. Each and every entity in the system makes it a unique embedded computing system which is interoperate with the pre-existing network infrastructure. With an anticipate figure, it is said by the experts that IoT comprises of than 50 billion objects which uses this infrastructure [1].

The solar energy-based system that is adequate in size and properly installed system that needs much in management. So to make this clearer and present the complete system in a less complicated manner, we have divided it in three basic steps [6]. First of all, only three things are to be measured that are charge in the battery bank followed by charging power that is retained and the total power that is being used. These three parameters are measured in following units as Amp Hour Meter, Solar Amps Meter, and AC Amps Meter, respectively [7].

Kevish Ashton, a British Businessman, was the first one to coin the term Auto ID Labs which was originally called the Auto ID Centers that was in reference to the

RFID (Radio Frequency and Identification) in 1999. The connection of the objects (embedded devices) for exchanging of data with the help of IoT for offering advanced internet connectivity that also goes beyond M2M communications that includes various sets of rules and regulations, its domains, and various distinct applications [8]. The various devices also called the smart objects are anticipated to lead in automation in almost nearly all the domains like in the case of smart cities and enabling smart grid technologies. In IoT, the "Things" in the definition basically refers to the variety of devices like in the system of heart monitoring [2] that has bio chips transponders on animals, implants, coastal waters in electric claim, vehicles with the built in smart sensors, having various devices that monitors pathogens/food.environmental in which the DNA analyzing can be done even on the on field operational devices that helps in search of firefighters and various rescue related operations [9]. Some scholars advocate that "Things" in the acronym of IoT is basically refereeing to the in inextricable combination of various physical components like hardware, software and devices for providing data services. These components are primarily responsible for collection and accumulation of data with the contribution of various technologies already existing in the market. At present the market has ample of devices like smart thermostatic system, Wi-Fi systems for dryers and washers for the remote monitoring using IoT [10]. There are different areas of applications that help to generate huge amount of data from various places with the help automation established due to internet connectivity with the need of data aggregation and necessity of indexing, collecting, and storing of data more efficiently. As already explained IoT is a more effective and efficient platform responsible for today's Smart Energy, Smart Management System, Smart Transportation and pollution Control, Smart City, and various other fields [1].

2 Literature Review

One of the well known entrepreneurs Kevin Ashton coined a term in the 1990s called as the Auto ID Lab that was originated and inspired by an old term Automatic Identification using the Radio Frequency and Detection technique. This also used a similar technology like IoT called Machine-to-Machine (M2M) communications that established network connection and various protocols, applications, and various domains after rigorous study and development in that area [11].

3 General Architecture of IoT

There has been and still is much hype about the "Internet of Things". The idea of a globally interconnected continuum of devices, objects, and things in general emerged with the RFID technology [2] and this concept has considerably been extended to the current vision that envisages a plethora of heterogeneous objects interacting.

In the contemporary era, a huge number of distinct wearable are utilized to ensure the effective communication between the different types of heterogeneous devices collectively termed as "Interne of Things" that show the non horizontal silos that don't support the inter operability of the system [12]. Although the complete system leads to an effective viable solution to the holistic problem by balkanization of collective efforts. Adding further the pre- existing solutions do not fulfill the scalability needs of the future of IoT system. These systems provide a strong and basic block for governance and overlook the security and privacy in their present architectures [13]. For instance, a European-based Lighthouse-integrated system has proposed a model that is based on reference model set of key buildings with the combination of IoT architecture. With this combination of different models, they laid the foundations for increasing the growth of emerging technologies of IoT. By using the architecture paradigm based on IoT-A, having a top-down combination reasoning based on the architectural designs and based principles with the prototyping simulation and to explore the technical results of architectures [14].

Architecture of Internet of Things:

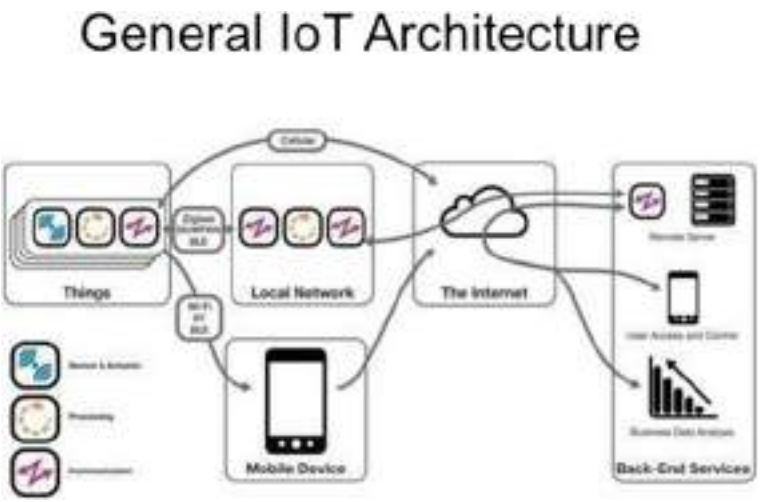

Various Layers of IoT:

1. **Objects**: Things or Objects that can be used in home appliances.
2. **Network**: Connecting objects within in the local network.
3. **Internet**: The Internet is provided by the local Internet Service Provider and also to provide the back end services.
4. **Mobile Devices**: The devices which are Hand held.
5. **Bank End Services**: This includes the collection of remote services and automation time.

4 Characteristics and Trends

IoT can also function as a tool that can save people money within their households. If their home appliances are able to communicate, they can operate in an energy efficient way. Finally, IoT can assist people with their everyday plans. A very interesting example that was given in a video was the communication between many devices that automatically adjusted to let an individual sleep in. Businesses can also reap many benefits from the IoT [14].

IoT can be useful in many different categories including asset tracking and inventory control, shipping and location, security, individual tracking, and energy conservation. As mentioned before, IoT allows for the communication between devices, commonly referred to as M2M communication [15]. With this being possible, physical devices are able to communicate to people letting them know their condition and where it is located. Devices such as trucks or ships allow for the maximum capacity to be filled by communication among devices and then relaying that information to a person to capitalize on the data supplied [24].

5 Intelligence

The control and intelligence of the devices are not a part of IoT. The autonomous controlling of devices and the ambient intelligence does not require the internet architecture. Although there is a research going on combination of these two wide areas of autonomous control and IoT so that the outcome of this driving force of objects is in the direction of autonomous IoT that is obtained from the integration of these branches [15].

It is considered widely that IoT is an open network and non-deterministic system. This system will be enable interoperability when various components like web services, SOA are combined with the virtual objects (Models) and will let it act independent of all other factors. This system depends on multiple factors like on the situations, context, or related environmental conditions. The modern day IoT devices uses the combination of different technologies like automation based on context being more sophisticated on the basis of its intelligence and requires sensors for the deployments in the real-time environmental conditions [12]. The autonomous behavior obtained through the collection and reasoning of the contextual information and with the capability to identify and detect the changes taking place in the environment, the major defects occurring in the sensors, providing the necessary mitigation solutions, and thus providing more reliability to IoT architecture.

6 Applications of IoT

- **Smart Healthcare**:

  The IoT has wide range of applications including healthcare like real-time monitoring of blood pressure and monitoring the heart rate using modern and more equipped devices also contributing in detection of special functioned implants like pacemakers, healthy fit bit wristbands, or the modern hearing aids equipment. IoT-integrated devices can be utilized to monitor health remotely and also notify the systems [15]. The special sensors can be used with the living spaces and help in real-time monitoring of the health, especially of old-aged people, making sure that the patient can be assisted and monitored to regain the lost movement with the effective therapy. The IoT-based healthcare devices are not only restricted to a set of patients it is also highly beneficial with the chronic and antenatal patients contributing in assisting them the basic vitalities and reminding the regular recurring medication necessities. These are also used as smart healthcare wearable for heart rate monitoring and resulting in more healthy living.
- **Smart Building and Smart Home Automation**:

  The IoT devices are also used for monitoring and controlling various systems like mechanical, electrical, and electronic-based systems. There are also used in various buildings like institutional, factories, private, public, residential, industrial, etc. [3].
- **Smart Transportation**:

  IoT highly contributes in the various fields like control and automation, communication, processing of data, and information also comprising of the field of smart transportation system. In smart transportation the interaction and exchange of data between these components enables the inter- and intra-communications involving the dynamic and rapid communications. This is also inclusive of smart controlling of traffic, smart parking, electrical toll system with the logistics and fleet managing techniques, vehicular control, road, and safety assistance [14].
- **Large-Scale Deployments**:

  There are numerous currently on going deployments based on IoT that enables to manage the places and large-scale deployments. For instance, like Songdo situated in South Korea which is a fully equipped wired smart city system almost in way of completion. Almost everything pre-planned in the city that is connected with the wired system and constrained into a sequence of data that can be studies and monitored by the set of computers with some or no human intervention.

  Other major applications is going on the project in Santader located in Spain. There are two different ways that have been used for deployment. The city constituted of 185,000 residents that have been seen in 18,500 cities by downloads of app in their mobile phones. The mobile application had already connected more than 10,000 sensors that contributed in making it a smart city. The places with the use of smart sensors included parking area, environment areas, and digitalized

cities. The location-based contextual data is utilized in the process of deployment to provide remunerations to the local merchants by dazzling deals that primarily focuses at increasing the impact [13].

- **Unique Addressability**:

The actual concept behind the Auto-ID Center is inspired from RFID-tags[2] and unique identification through Electronic Product Code although this will evolved into things comprising of various URL and IP address.

The retrospective perspective in the world of Semantic Web mainly included all the entities (not only the electronic related, RFID-enabled, smart sensor) addressable by already existing protocols. The entities themselves don't converse much, although they may not be represented by any third party agent, like a powerful centralized servers acting as owners [14].

The forthcoming decade of Internet applications utilizing the Internet Protocol Version 6 (IPv6) would help in effective communication with the various devices that are virtually connected with manmade things using huge addressed of IPv6 version. The current system will enable to envisage huge number of things/devices together [12].

An integration of such demonstrations can be easily found in the contemporary used GS1/EPC global Services (EPCIS) specification. It uses to identify objects in the range from aerospace to industries with the help of rapidly occupying the customer logistics and its products [14].

7 Benefits of Technology: IoT

There are numerous merits of incorporating IoT into our lives, which can help individuals, businesses, and society on a daily basis. For individuals, this new concept can come in many forms including health, safety, financially, and everyday planning. The integration of IoT into the health care system could prove to be incredibly beneficial for both an individual and a society. A chip could be implemented into each individual, allowing for hospitals to monitor the vital signs of the patient. By tracking their vital signs, it could help indicate whether or not serious assessment is necessary. With all of the information that is available on the Internet, it can also scare people into believing they need more care than what is really needed. Hospitals already struggle to assess and take care of the patients that they have. By monitoring individual's health, it will allow them to judge who needs primary attention. The IoT can also assist people with their personal safety. ADT, which is a home security system, allows individuals to monitor their security systems at home through their phones, with the ability to control it. Also, another technology that has already been released is GM On Star. This is a system that is embedded in GM cars that can detect if a crash has occurred and it automatically calls 9-1-1. It can also track the movement of the car [8].

All of these combined maximize revenue by cutting cost of inefficiencies within the business.

Another advantage of IoT is the ability to track individual consumers and targeting these consumers based on the information supplied by the devices. In a way, it provides a more "personalized" system that could potentially increase business sales and increases their demographic. Additionally, with the increased amount of devices connected to the Internet the Smart Grid expands, conserving more energy. Devices can make decisions and adapt without human guidance to reduce their energy usage. The IoT has many advantages to businesses, individuals, consumers, the environment, and society, but as with any technology, there are always repercussions and controversies that arise.

8 Future Scope

The system will likely be an example of event-driven architecture bottom-up made (based on context of processes and operations, in real time) and will consider any subsidiary level. Therefore, model-driven and functional approaches will coexist with new ones able to treat exceptions and unusual evolution of processes (Multi-agent systems, B-ADSc, etc.). In an IoT, meaning of an event will not necessarily be based on a deterministic or syntactic model but would instead be based on context of event itself: this will also be a semantic web.

9 Conclusion

The integration of solar-based energy system with IOT for home automation is a new idea. Integration of sensing and actuation system by connecting to internet is discussed here.

References

1. http://www.designnews.com/author.asp?section_id=1386&doc_id=276684
2. C.M. Shah, V.B. Sangoi, R.M. Visharia, Smart security solutions based on internet of things (IoT) electronics and telecommunication Engineering Department, D.J. Sanghvi College of Engineering, Vile Parle, Mumbai-4000056, India. Accepted 20 Sept 2014. 01 Oct 2014 **4**(5) (2014)
3. J.A. Stankovic, Research directions for the internet of things
4. R. Dickerson, E. Gorlin, J. Stankovic, Empath: a continuous remote emotional health monitoring system for depressive illness. Wireless Health (2011)
5. B. Brumitt, B. Meyers, J. Krumm, A. Kern, S.A. Shafer, Easyliving: technologies for intelligent environments. HUC (2000)

6. V.S. Narayanan, S. Gayathri, Design of wireless home automation and security system using PIC microcontroller. Int. J. Comput. Appl. Eng. Sci. **III** ISSN: 2231-4946, Special Issue, August 2013
7. http://iot-analytics.com/10-internet-of-things-applications
8. Y. Aguiar, M. Vieira, E. Galy, J. Mercantini, C. Santoni, Refining a user behavior model based on the observation of emotional states. Cognitive (2011)
9. https://en.wikipedia.org/wiki/Internet_of_Things
10. J. Lu, T. Sookoor, V. Srinivasan, G. Gao, B. Holben, J. Stankovic, E. Field, K. Whitehouse, The smart thermostat: using occupancy sensors to save energy in homes. ACM SenSys (2010)
11. M. Kay, E. Choe, J. Shepherd, B. Greenstein, N. Watson, S. Consolvo, J. Kientz, Lullaby: a capture & access system for understanding the sleep environment. UbiComp (2012)
12. M. Maroti, B. Kusy, G. Simon, A. Ledeczi, The flooding time synchronization protocol. ACM SenSys (2004).
13. S. Munir, J. Stankovic, C. Liang, S. Lin, New cyber physical system challenges for human-in-the-loop control, in *8th International Workshop on Feedback Computing* (2013)
14. S. Munir, J. Stankovic, DepSys: dependency aware integration of systems for smart homes, submitted for publication.
15. S. Ravi, A. Raghunathan, S. Chakradhar, Tamper resistance mechanisms for secure, embedded systems, in *Proceedings of 17th International Conference on VLSI Design*, p. 605 (2004)
16. A.R. Delgado, Rich picking and Vic Grout, remote-controlled home automation systems with different network technologies. Centre for Applied Internet Research (CAIR), University of Wales, NEWI, Wrexham, UK
17. C. Dixon, R. Mahajan, S. Agarwal, A. Brush, B. Lee, S. Saroiu, P. Bahl, An operating system for the home. NSDI (2012)
18. T. He, J. Stankovic, C. Lu, T. Abdelzaher, A Spatiotemporal communication protocol for wireless sensor networks. IEEE Trans. Parallel Distrib. Syst. **16**(10), 995–1006 (2005)
19. M. Huang, J. Li, X. Song, H. Guo, Modeling Impulsive Injections of Insulin: towards Artificial Pancreas. J. SIAM Appl. Math. **72**(5), 1524–1548 (2012)
20. A Liu, D. Salvucci, Modeling and prediction of human driver behavior, in *International Conference on HCI* (2001)
21. S. Mohammed, P. Fraisse, D. Guiraud, P. Poignet, H. Makssoud, Towards a co-contraction muscle control strategy for paraplegics. CDC-ECC (2005)

Clustering Protocol Based on Game Theory in Heterogeneous Wireless Sensor Networks

Mansi Gupta, Navneet Singh Aulakh, and Inderdeep Kaur Aulakh

Abstract Wireless sensor networks comprises of sensor nodes that consists of non-rechargeable batteries. The main constraint in WSNs is to develop energy-efficient protocols to save energy of sensor nodes to improve the existence of the network. Various energy-efficient clustering protocols have been developed as one of the solutions to energy efficiency. We propose and evaluate a new clustering protocol using game-theoretic approach based on probability for heterogeneous wireless sensor networks using two level nodes, i.e., standard and advanced nodes. In proposed protocol, cluster heads are elected using game theory in heterogeneous environment using various factors such as probability, initial energy, and residual energy. Finally, simulation experiments show that proposed protocol achieves more energy efficiency and enhances stability period, than other existing clustering protocols such as D-DEEC, SEP, LEACH in heterogeneous WSNs.

Keywords Clustering · Heterogeneity · Wireless sensor networks · Probability · Game theory

1 Introduction

Wireless sensor networks (WSNs) incorporate numerous autonomous devices known as sensor nodes that are widely used for various types of applications such as forest fire detection, monitoring environmental conditions, tracking purposes, etc. These sensor nodes are widely distributed in the region and all nodes send their sensed data

M. Gupta (✉) · N. S. Aulakh
CSIO Analytical Facilities, CSIR-Central Scientific Instruments Organization (CSIR-CSIO), Academy of Scientific and Innovative Research (AcSIR-CSIO), Chandigarh 160014, India
e-mail: mansigupta@csio.res.in

N. S. Aulakh
e-mail: aulakh@csio.res.in

I. K. Aulakh
University Institute of Engineering & Technology, Panjab University, Chandigarh 160014, India
e-mail: ikaulakh@pu.ac.in

S. Rawat et al. (eds.), *Proceedings of First International Conference on Computational Electronics for Wireless Communications*, Lecture Notes in Networks and Systems 329,
https://doi.org/10.1007/978-981-16-6246-1_38

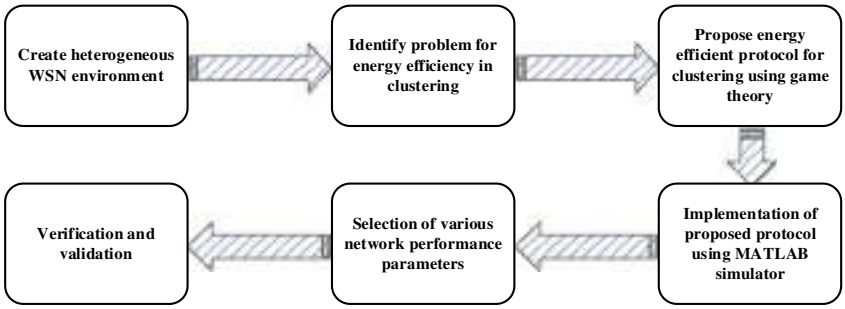

Fig. 1 Workflow diagram

to the base station (BS). Due to limited battery resource in sensor node, efficient use of power is a major constraint in WSNs. Major quantity of energy is used in data transmission between sensor nodes or from sensor node to base station. Clustering and routing protocols play a significant part in energy efficiency in WSNs [1, 2]. In clustering technique, clusters are formed by electing cluster heads (CHs). Remaining nodes join CHs as cluster members (CMs) and send their sensed data these CHs which further communicate this data to BS. WSNs can be homogeneous or heterogeneous in nature. In heterogeneous WSNs, all nodes are implemented with same amount of energy whereas in heterogeneous WSNs, some nodes are implemented with more initial energy. Implementation of few high energy nodes increases reliability and energy efficiency of the network. In this manuscript, an energy-efficient clustering protocol is proposed which utilizes game theory for clustering mechanism in heterogeneous WSNs that maximizes the lifespan of the network. Different clustering mechanisms using game theory have been proposed by various researchers in homogeneous environment [3–5]. Workflow diagram representing research in this paper is represented in Fig. 1. This paper proposes clustering protocol based on game theory in heterogeneous environment. In this approach, game theory is used to select CH by calculating probability of a node in heterogeneous network. Proposed protocol serves following objectives:

- In this paper, proposed protocol elects the best possible node to act as CH using threshold function that is formulated by probability function using game theory.
- It enhances the stability period as well as lifespan of network by election of optimized CHs.

In the rest of paper, in Sect. 2 related work of game theory clustering protocols is explained. In Sect. 3, proposed clustering protocol using game theory for heterogeneous WSN is elaborated. In Sect. 4, simulation experiments and results of proposed protocol are discussed in accordance with various performance parameters for its validation.

2 Related Work

Heinzelman et al. proposed clustering protocol, i.e., LEACH protocol in which random rotation of CHs is done to fairly allocate load between all sensor nodes of the network. LEACH leads to eight time less dissipation of energy than conventional protocols. LEACH algorithm operates in rounds. In its advertisement, cluster heads are elected using threshold-based function $T(j)$ using the probability of node to elect as CH that is determined as priori (5%), current round of the network, and the set of nodes that are not elected as CHs in previous rounds. After this, cluster heads send ADVT message to all nodes using CSMA MAC protocol, nodes will receive this message and decides to which cluster head it belongs. After cluster election is done, cluster formation phase starts. Each non-cluster head node acknowledges cluster heads by sending ADVT_ACK message using CSMA MAC protocol. In schedule creation phase, cluster heads assign time slots to all its cluster members when it can transmit its information using direct transmission. When all data has been transmitted by cluster members, CHs compress data and send to base station.

Younis et al. proposed effective topology control distributed clustering approach which uses hybrid of node's residual energy and degree of node for probabilistic selection of cluster heads periodically. This algorithm considers both inter-cluster and intra-cluster communication depending on type of application [10]. Few game theory-based clustering protocols of homogeneous and heterogeneous WSNs are represented in Table1.

Georgios Koltsidas et al. models a non-cooperative game theory clustering algorithm, i.e., CROSS in ad hoc and sensor networks. Nash Equilibria is provided for both pure and mixed strategies. All nodes in the network join clustering game with Equilibrium Probability to claim as cluster head [6]. Cost and payoff functions are calculated to determine energy consumption using radio model of energy. After calculating probability expected payoff and piece of anarchy is discussed. Then a clustering mechanism is designed using zero probability rule for cluster formation. Proposed protocol is compared with LEACH protocol and has more network lifetime than LEACH [1, 2].

3 Network Model

In this manuscript, proposed clustering protocol has following assumptions:

- Sensors nodes are not mobile and has fixed amount of energy.
- Each sensor node has its own identity, i.e., *id*
- Base station is fixed and has more energy
- Batteries of sensor nodes are irreplaceable.

Table 1 Comparison of game theory-based clustering protocols of homogeneous and heterogeneous WSNs

Protocols	Environment	Inter/Intra-cluster routing	Multi-hop	Game theory	Location-aware	Static/Dynamic	Mobility
CROSS [6]	HM	–	✗	Non-cooperative	✗	S	✗
LGCA [7]	HM	Intra	✗	Mixed strategy	✓	S	✗
ECAGT [8]	HM	–	✗	Localized Game theory	✗	S	✗
Lin [9]	HT	Inter	✗	Non-cooperative	✗	S	✗
Lin and Wang [3]	HT	–	✓	Sensor data reporting game	✗	S	✗

4 Energy Model for WSN

This energy model outlines the sum of energy dissipation in the network using free space or multipath propagation model [11]. If the communication distance is smaller i.e., $d < d_0$ free space model can be used else if $d < d_0$ multipath model can be used. Figure 2 shows the energy dissipation model for our network. The total number of bytes transmitting data are b bytes. The distance between transceiver and receiver node is denotes as d. E_{elec} is the energy dissipation between transmission and receiving of data. $\in_{mp1}$, $\in_{mp2}$ are the amplifying powers of free space and multi-path model [12, 13].

$$\mathrm{E_{Tr}(b,\,d)} = \begin{cases} b \cdot \mathrm{E_{elec}} + b \times \in_{\mathrm{mp'}} \times \mathrm{d}^2, d < \mathrm{d}_0 \\ b \cdot \mathrm{E_{elec}} + b \times \in_{\mathrm{mp''}} \times \mathrm{d}^4, d \geq \mathrm{d}_0 \end{cases} \tag{1}$$

Energy dissipation at receiver side is defined as

$$\mathrm{E_{Rx}(b)} = b \times \mathrm{E_{elec}} \tag{2}$$

Before the data from nodes is directed to sink, CH aggregates the data received from its cluster members. Energy dissipation in aggregation of data by CH is computed as

$$\mathrm{E_{agg}} = \mathrm{k}' \times b \times \in_{\mathrm{agg}} \tag{3}$$

where k' are the number of packets of length b.

Energy consumption if a sensor node is a CH is computed as

$$c = \mathrm{k}' \times \mathrm{E_{Rx}} + \mathrm{E_{ch,bs}} \tag{5}$$

Energy consumption if a sensor node is a standard node is computed as

$$\mathrm{c}' = \mathrm{E_{Tr}} + \mathrm{E_{i,ch}} \tag{5}$$

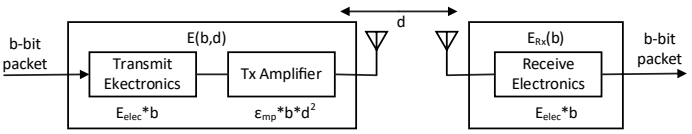

Fig. 2 Energy dissipation model

5 Proposed Protocol

Proposed protocol is designed such that it enhances the lifetime of the network. Energy model explained above calculates the energy dissipation on transmission, receiving, and aggregation of data. Proposed protocol operates in two phases, i.e., setup phase and steady phase. It performs the task of cluster formation, CH selection, and data transmission from CH to base station (BS). WSN used is heterogeneous in nature. It consists of standard nodes and advanced nodes. Heterogeneity nature of the network will enhance the network's performance due to advanced nodes with more initial energy. Advanced nodes have more energy than standard nodes and are less in number than standard nodes. In proposed protocol, CH selection is done in accordance with probability that is based on game theory.

5.1 Initial Phase

Depending upon the requirement of the application, nodes are deployed as advanced and standard nodes in which advanced nodes get some extra energy. After the nodes are deployed, nodes in this initial phase are divided into static clusters.

At initial stage, energy of the heterogeneous nodes is defined as
Energy of standard nodes $\mathrm{E_{std}} = \mathrm{E}'$
Energy of advanced nodes $\mathrm{E_{adv}} = \mathrm{E}'(1+\gamma)$
Sum of energy of the heterogeneous WSN is defined as

$$n \cdot \mathrm{E}'(1-\mathrm{x}) + n \cdot x \cdot \mathrm{E}'(1+\gamma) = n \cdot \mathrm{E}'(1+\gamma \cdot \mathrm{x}) \tag{6}$$

where E' denotes the standard energy of the node, n represents the total number of nodes, x denotes the no of advanced nodes provided with extra energy, and δ is extra energy factor of advanced nodes. Weighted probabilities for standard and advanced nodes are defined as

$$\mathrm{P_{std}} = \frac{\mathrm{P_{GT}}}{1+\gamma \cdot \mathrm{x}} \tag{7}$$

$$\mathrm{P_{adv}} = \frac{\mathrm{P_{GT}}}{1+\gamma \cdot \mathrm{x}}(1+\gamma) \tag{8}$$

where P_{GT} is the probability function generated using game theory that is defined in next section.

5.2 *Setup Phase*

In this setup phase, every node gathers the information of its neighboring nodes by broadcasting a HELLO message that comprises of ID of the node. When a HELLO message is received by its neighboring nodes, they send ACK message containing its ID of the node and its residual energy to the source node. Every node can then calculate its total number of neighboring nodes denoted as (Ne(i)) (Figs. 3, 4, 5, 6, 7, 8 and 9).

CH Selection

In each round, cluster head selection procedure is performed for all the clusters. Energy of all the nodes is considered as the major element for process of CH selection. Every node gets the opportunity to become cluster head. In our proposed protocol, a threshold function is devised which is a very challenging task for selection of

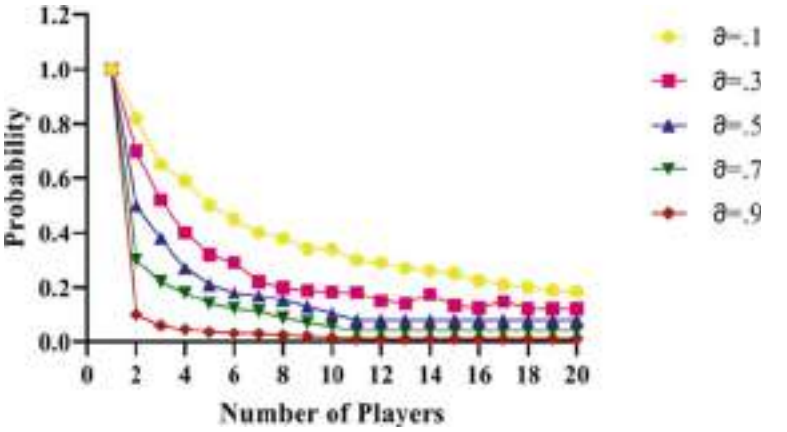

Fig.3 Probability of number of nodes to declare as CHs versus number of nodes for different values of τ

Fig. 4 Average residual energy when x = 0.2

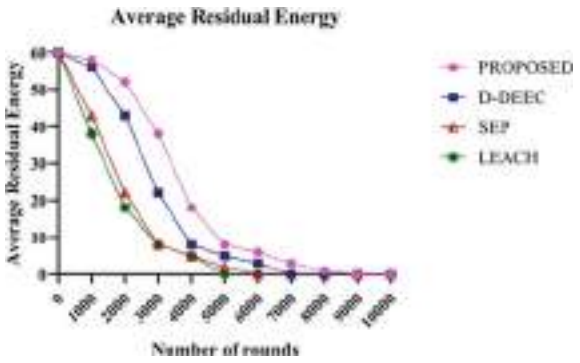

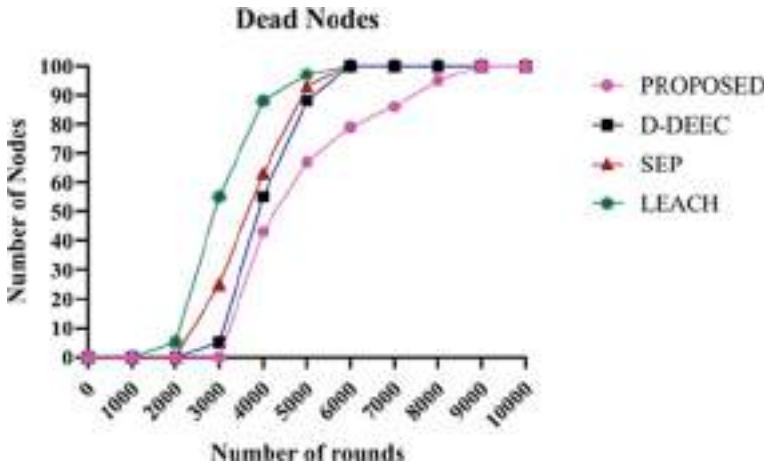

Fig. 5 Dead nodes when x = 0.2

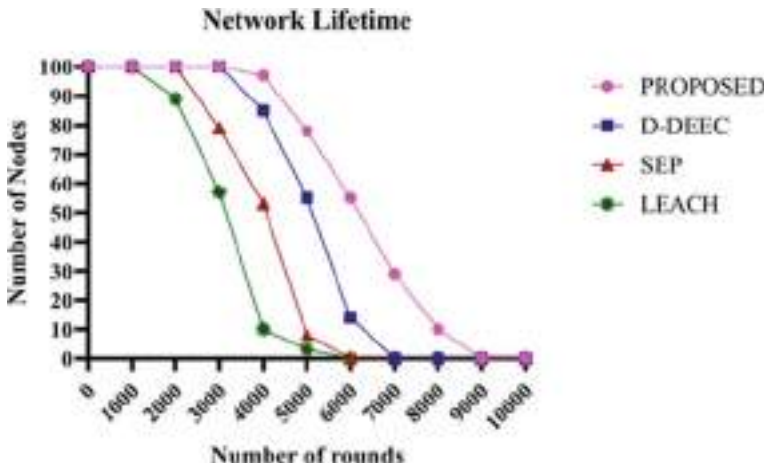

Fig. 6 Network lifetime when x = 0.2

cluster head in accordance with probability of node generated using game theory, initial energy, and residual energy of the node. All nodes participate in the process of cluster head selection but only few nodes are selected as CH [6]. Probability of node generated using game theory to select as CH is defined by function:

$$P_{GT} = 1 - \tau^{1/Ne(i)} \tag{9}$$

P_{nor} denotes the weighted probability of the standard node to select as cluster head is represented as

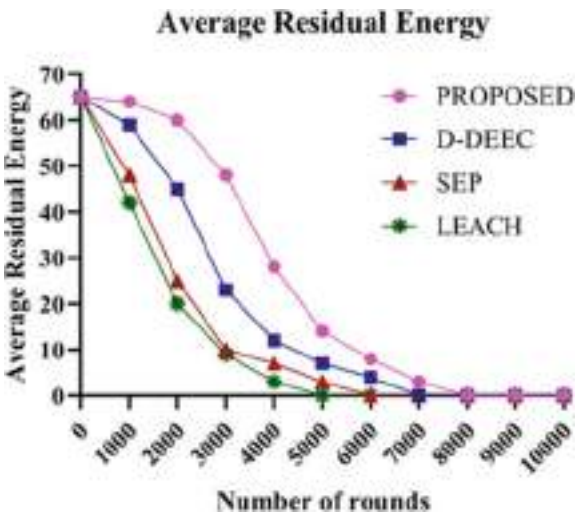

Fig. 7 Average residual energy when x = 0.3

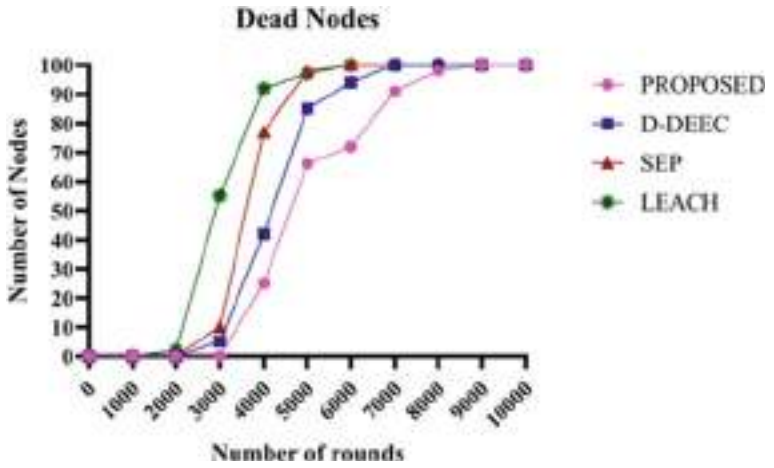

Fig. 8 Dead nodes when x = 0.3

$$\mathrm{P_{std}} = \frac{1 - \tau^{1/Ne(i)}}{1 + \delta \cdot x} \tag{10}$$

P_{adv} denotes the weighted probability of the advanced node to select as cluster head is represented as

$$\mathrm{P_{adv}} = \frac{1 - \tau^{1/Ne(i)}}{1 + \delta \cdot x}(1 + \delta) \tag{11}$$

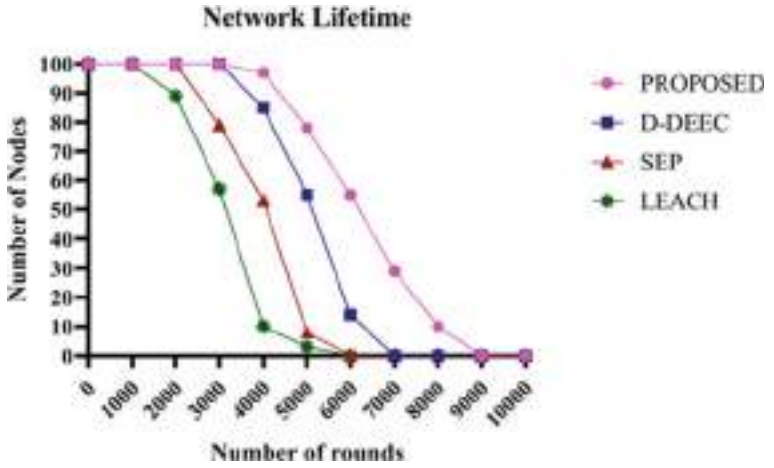

Fig. 9 Network lifetime when x = 0.3

Threshold functions for standard and advanced nodes can be defined as $T(N_{std})$ and $T(N_{adv})$.

Threshold function for standard nodes is given as

$$\mathrm{T(N_{std})} = \begin{cases} \frac{\mathrm{P_{std}}}{1-\mathrm{P_{std}}\left(\mathrm{r_0 mod}\,\frac{1}{\mathrm{P_{std}}}\right)} & if j \in G \\ 0 & otherwise \end{cases} \tag{12}$$

where r_0 are the number of rounds.

Threshold function for advanced nodes is given as

$$T(\mathrm{N_{adv}}) = \begin{cases} \frac{\mathrm{P_{adv}}}{1-\mathrm{P_{adv}}\left(\mathrm{r_0 mod}\,\frac{1}{\mathrm{P_{adv}}}\right)} if j \in G \\ 0 otherwise \end{cases} \tag{13}$$

For node to be selected as CH, it must satisfy conditions of threshold function, if it does not it becomes cluster member.

Cluster Formation

When all CHs are selected, they send a message to announce their selection. When this message is received by standard nodes they respond to their nearest CH and joins it as cluster member. Hence, clusters are formed.

Transmission phase

After the formation of clusters, CHs allot time slots to its cluster members. All standard nodes accumulate the sensed data and transmit it to their respective CH. When cluster head receipt data from all its respective cluster members, it performs

function of aggregation and compression on sensed data and direct it to BS. After this, network again reverts to setup phase and process goes on till whole energy of heterogeneous network is exhausted.

6 Simulation Results and Discussions

For analyzing the proposed protocol, experiments are performed on MATLAB simulator. Proposed protocol is then compared with existing techniques in accordance with various performance parameters such as network lifetime, throughput to verify its efficiency.

6.1 Simulation Parameters

Network lifetime

It is described as the total number of rounds from beginning of operation until the last node dies in the network.

Average Residual Energy

It defines the average of left-over energy of the sensor nodes in the WSN.

Stability Period

It is described as the period starting with the beginning of the WSN until the death of the first node.

Table 2 Values of simulation parameters

Energy parameters	Value
Number of nodes	100
Base station position	100 * 100
Sensing field	50,175
Initial energy	0.5 J
γ	1
x	0.1, 0.2, 0.3
b	4000 bits
E_{agg}	5 nJ/bit/signal
E_{elec}	50 nJ/bit
$\in_{mp1}$	10 pJ/bit/m^2
$\in_{mp2}$	0.0013 pJ/bit/m^4

6.2 Discussions

Standard parameters that are used for simulation experiments in MATLAB are discussed in Table 2. Two cases are considered for determining energy efficiency in which all parameters are same except the value of x which is a heterogeneity factor. Figure 3 represents the probability of number of nodes declare as CHs versus number of nodes with different values of parameter τ.

Case 1: When value of x = 0.2

If the value of x = 0.2, it means number of advanced nodes in the network are 20%. In case 1, total energy of the network is 60 J as 20% nodes have extra energy. Proposed protocol is compared with existing approaches such as D-DEEC, SEP, and LEACH protocol to analyze its performance. In Fig. 4, residual energy of 100 nodes is considered to observe the performance of the network. It represents the average residual energy of the nodes for 10,000 rounds. Network with proposed protocol survives for longer time as compare to D-DEEC, SEP, and LEACH protocol. Figure 5 represents the stability period of the network through number of dead nodes for each round. Stability period is determined from the beginning of the rounds till the first dead node. Stability period of our proposed energy-efficient protocol is more than D-DEEC, SEP, and LEACH protocol which is around 3200 rounds. Figure 6 illustrates the network lifetime of the proposed protocol in respect of the number of the rounds. Network Lifetime of our proposed protocol is better than D-DEEC, SEP, and LEACH protocol which is around 8100 rounds. Analysis of all above parameters shows that proposed protocol enhances the energy efficiency of the WSN in comparison to existing techniques.

Case 2: When value of x = 0.3

If the value of x = 0.3, it means number of advanced nodes in the network are 20%. In case 1, total energy of the network is 65J as 30% nodes have extra energy. Proposed protocol is compared with existing approaches such as D-DEEC, SEP, and LEACH protocol to analyze its performance. In Fig. 7, residual energy of 100 nodes is considered to observe the performance of the network for heterogeneity factor x = 0.3. Graph represents the average residual energy of the nodes for 10,000 rounds. The proposed protocol survives for longer time as compare to D-DEEC, SEP, and LEACH protocol. Figure 8 represents the stability period of the network through number of dead nodes for each round network for heterogeneity factor x = 0.3. Stability period is determined from the beginning of the rounds till the first dead node. Stability period of proposed clustering protocol outer performs D-DEEC, SEP, and LEACH protocol which is around 3000 rounds. It means first node of proposed protocol dies after 3000 rounds, whereas first dead node of other protocols is much earlier. Figure 9 shows the network lifetime of the proposed clustering protocol with respect to the number of the rounds network for heterogeneity factor x = 0.3. Network Lifetime of our proposed protocol outperforms D-DEEC, SEP, and LEACH protocol which is around 8000 rounds. Analysis of all above parameters with heterogeneity

factor x = 0.3 validates that proposed protocol enhances the energy efficiency of the WSN in comparison to existing techniques.

7 Conclusion

In this research, an energy-efficient clustering protocol formulated using game theory for heterogeneous WSNs is presented. Selection of optimal CHs is a crucial part as it effects the energy efficiency of the network directly. In this research, selection of optimal CHs is done using game theory in heterogeneous WSN. In this research, all nodes take part in the process of clustering game and only few nodes become eligible to be real CHs. Weighted probability of standard and advanced nodes is designed that is based on the probability function which is formulated using game theory. Then, a threshold function is formulated on the basis of weighted probability for standard and advanced nodes. Simulation results reveal that proposed protocol outperform existing clustering approaches D-DEEC, SEP, and LEACH in accordance with various network parameters.

8 Future Scope

In future work, more levels of heterogeneity in WSNs can be considered for this proposed game theory clustering protocol and more network parameters can be added to enhance proposed protocol.

References

1. I.F. Akyildiz, W. Su, Y. Sankarasubramaniam, E. Cayirci, Akyildiz et al., Wireless sensor networks a survey.pdf **38**, 393–422 (2002)
2. G. Anastasi, M. Conti, M. Di Francesco, A. Passarella, Energy conservation in wireless sensor networks: a survey. Ad Hoc Netw. **7**(3), 537–568 (2009). https://doi.org/10.1016/j.adhoc.2008.06.003
3. X.H. Lin, H. Wang, On using game theory to balance energy consumption in heterogeneous wireless sensor networks, in *Proceedings of Conference Local Computer Networks, LCN* (2012), pp. 568–576. https://doi.org/10.1109/LCN.2012.6423676.
4. B. Elbhiri, S. Rachid, S. El Fkihi, D. Aboutajdine, Developed distributed energy-efficient clustering (DDEEC) for heterogeneous wireless sensor networks, in *2010 5th International Symposium on I/V Communications and Mobile Network, ISIVC 2010* (2010), pp. 1–4. https://doi.org/10.1109/ISVC.2010.5656252
5. N. Javaid, T.N. Qureshi, A.H. Khan, A. Iqbal, E. Akhtar, M. Ishfaq, EDDEEC: enhanced developed distributed energy-efficient clustering for heterogeneouswireless sensor networks. Procedia Comput. Sci. **19**, 914–919 (2013). https://doi.org/10.1016/j.procs.2013.06.125

6. G. Koltsidas, F.N. Pavlidou, A game theoretical approach to clustering of ad-hoc and sensor networks. Telecommun. Syst. **47**(1–2), 81–93 (2011). https://doi.org/10.1007/s11235-010-9303-5
7. D. Xie, Q. Sun, Q. Zhou, Y. Qiu, and X. Yuan, An efficient clustering protocol for wireless sensor networks based on localized game theoretical approach. Int. J. Distrib. Sens. Netw. **2013** (2013). https://doi.org/10.1155/2013/476313
8. Q. Liu, M. Liu, Energy-efficient clustering algorithm based on game theory for wireless sensor networks. Int. J. Distrib. Sens. Netw. **13**(11) (2017). https://doi.org/10.1177/1550147717743701
9. X.-H. Lin, Y.-K. Kwok, A game theoretic approach to balancing energy consumption in heterogeneous wireless sensor networks. Wirel. Commun. Mob. Comput. 170–191 (2015). https://doi.org/10.1002/wcm
10. O. Younis, S. Fahmy, A comment on 'HEED: a hybrid, energy-efficient, distributed clustering approach for ad hoc sensor networks. IEEE Trans. Mob. Comput. **4**(3), 366–379 (2004). https://doi.org/10.1109/TMC.2006.141
11. D. Kumar, T.C. Aseri, R.B. Patel, EEHC: energy efficient heterogeneous clustered scheme for wireless sensor networks. Comput. Commun. **32**(4), 662–667 (2009). https://doi.org/10.1016/j.comcom.2008.11.025
12. H.Y. Shi, W.L. Wang, N.M. Kwok, S.Y. Chen, Game theory for wireless sensor networks: a survey. Sensors (Switzerland) **12**(7), 9055–9097 (2012). https://doi.org/10.3390/s120709055
13. R. Machado, S. Tekinay, A survey of game-theoretic approaches in wireless sensor networks. Comput. Netw. **52**(16), 3047–3061 (2008). https://doi.org/10.1016/j.gaceta.2008.07.003

Data Variance-Based Distributed Outlier Detection in Wireless Sensor Networks

Yogita and Vipin Pal

Abstract Outlier detection is a key component for the proper functioning of a wireless sensor network. It helps in identifying malicious events taking place in the field and faulty sensors. This paper presents a distributed outlier detection technique that separates outlying cases from normal data locally at sensors and sends only the summarized information of data to sink nodes to minimize the communication overhead in the resource-constraint wireless sensor network. The proposed solution employs variance of normal data as a measure to identify outliers. The performance of the proposed method has been evaluated on real-world datasets collected by WSN deployment projects. Experimental results prove the effectiveness of the proposed method in terms of higher outlier detection rate, lower false alarm rate and lower communication overhead as compared to the simulated centralized approach.

Keywords Data variance · Outlier detection · Wireless sensor networks

1 Introduction

Wireless sensor networks (WSNs) are composed of battery-powered sensor nodes distributed over a large area and one or more sink nodes for accumulating sensed information of sensor nodes [1]. The gathered data provides real-time information of the monitored area and an analysis of it helps in making time-critical intelligent decisions and countering the unwanted events in a wide range of applications. Outliers [2] in WSNs may arise due to noise and errors, change in the observed phenomenon, malicious attacks and faulty sensors. The occurrence of outliers heavily demean the quality of data and subsequently the analysis results. Timely and accurate identification of outlying data objects is very essential for improving the quality of sensed

Yogita · V. Pal (✉)
National Institute of Technology Meghalaya, Shillong, India
e-mail: vipinpal@nitm.ac.in

Yogita
e-mail: yogitathakran@nitm.ac.in

S. Rawat et al. (eds.), *Proceedings of First International Conference on Computational Electronics for Wireless Communications*, Lecture Notes in Networks and Systems 329,
https://doi.org/10.1007/978-981-16-6246-1_39

data. Finding outliers also assists in spotting interesting events that take place in the monitored zone. Outlier detection in WSNs is a topic of current importance and is also very challenging owing to the limited resources and dynamic nature of the network.

Most of the existing techniques that have been proposed in the literature for finding outliers in WSNs data follow a centralized processing model, where data of all sensor nodes must be transferred to a central location like sink node [3–7]. This transfer of data results in very large communication overhead and rapidly depletes the battery of sensor nodes that leads to a shortened lifespan of the network. Though some work has been done under the distributed model of outlier detection which reduces the communication by building normal data model locally at sensor nodes and then sending only the summarized parameters of it to a central location, these methods have their own limitation of being sensitive to parameters like cluster width and number of nearest neighbours. Other than this, these methods assume the static behaviour of data and process it in batches without adapting the data model over multiple batches. Such techniques suffer from poor performance on real-world dynamic data (changes in the monitored environment) [8, 9]. So this area needs to be further investigated to design and develop outlier detection techniques suitable for WSNs so that the power of concealed information of sensed data can be fully optimized.

In this paper, a distributed outlier detection technique has been proposed that employs data variance as a measure for separating outliers from normal data. It is unsupervised in nature as it does not require any prior knowledge and labelled data to generate normal data model. The proposed approach maintains and updates the normal data model of sensor nodes over multiple data windows to incorporate the essence of new data and to limit the effect of old data in finding outliers to handle dynamic changes. To address the issue of limited resources, the proposed method do all computations incrementally and only summarized information of data windows is stored at sensor nodes. Initially, it identifies outliers locally at sensor nodes from incoming data window and then a summary of normal data model is passed to other nodes. Sending only summary of data as oppose to whole data reduces the communication overhead. The proposed method does not implore the parameters like cluster width or the number of clusters. The efficiency and effectiveness of the proposed method have been evaluated and compared with the centralized method [10] on publicly available real-world datasets of sensor network projects.

The remaining part of this paper has been organized as follows: the review of related work has been given in Sect. 2, network model and problem definition has been drafted in Sect. 3, the proposed approach has been presented in Sect. 4, experimental results have been discussed in Sect. 5 and Sect. 6 concludes the work of the paper.

2 Related Work

Outlier detection in WSNs is of great significance for secure and reliable functioning of network [1, 11]. Finding outliers in traditional datasets has been highly researched by data mining and machine learning community [3, 4]. However, these techniques assume the availability of considerable computational and memory resources and are hence not viable in resource-constrained scenarios of WSN.

Existing outlier detection techniques can be classified as supervised or unsupervised depending upon whether they need labelled data or not [3, 5, 12, 13]. Unsupervised approaches do not need pre-labelled data to build a normal data model and can detect new types of abnormal behaviours (outliers) [3] whereas supervised approaches demand pre-labelled normal and outlying (abnormal) data. In the context of many real-life WSN applications neither pre-labelled data is always available nor it is easy to collect. Even the dynamic nature of data imposes frequent retraining of classifier which is not feasible due to limited resource availability with sensor nodes. So in WSN set-up, unsupervised approaches are much more suitable than supervised ones.

The following two types of processing models have been suggested in the literature to identify outliers in WSNs: centralized and distributed. The majority of outlier detection techniques fall in centralized group [3]. These techniques demand the presence of the entire dataset at a central location [14, 15]. Accumulating data of whole network or a subset of nodes at a single location is not practical for resource-restrained WSNs. It increases the communication in the network and quickly exhausts energy (battery power) of sensor nodes. As opposed to this, distributed techniques reduce the data communication by building a normal reference model locally at sensor nodes to identify outliers and then just share the summarized information with other nodes.

Chatzigiannakis et al. have proposed a principal component analysis-based (PCA) centralized mechanism for identifying outliers from WSNs data [6]. Gupta et al. [7] have also given a centralized method for detecting fail-stop failures and routing protocol attacks in WSNs. Both of these techniques generate high communication overhead in the network. Branch et al. [16] have proposed a nearest-neighbour-based unsupervised outlier detection algorithm to identify the top-n outliers in WSN data. First, it detects candidate outliers locally at sensor nodes and then identifies top-n outliers of a node. Then a subset of data is broadcasted to its neighbouring nodes to find global top-n outliers. Though it is a distributed algorithm, it involves several rounds of data communication among sensor nodes.

Fixed-width clustering-based unsupervised outlier detection techniques have been presented in [8, 9] by Rajasegarar et al. These techniques work in a distributed fashion and largely reduce communication overhead by clustering and summarizing data before sending it to the sink node. But these methods ask users to set width of clusters and the number of nearest-neighbour clusters parameters. Setting these parameters is not easy in a dynamic environment of WSNs, and if parameters are not defined accurately, then it results in poor performance of the proposed method.

These techniques perform outlier detection on a time window data measurements at a time and do not consider the adaptability of the clustering model over multiple windows to handle the issue of dynamic data (changes in the monitored environment). Another fixed-width clustering-based approach combined with nearest-neighbor-based approach for detecting and classifying outliers as noise data or interesting event is given by Fawyz et al. [17]. It also faces the problem of setting cluster width and nearest-neighbour parameters.

After having a close look at the state of the literature on outlier detection in WSNs, it can be concluded that this area needs to be explored further to address the open research challenges pertaining to this field.

3 Network Model

A wireless sensor network (WSN) is made up of a set of sensor nodes $S = \{S_i | i = 1, 2\ldots, s\}$ which collect data from the monitored field and send aggregated data to the sink node (gateway node). Sink node (gateway) is much more powerful than sensor nodes in terms of computational capabilities, storage space and energy. All sensors are time-synchronized. A WSN may be of flat or hierarchical topology. In flat topology all sensors send data directly to the sink node. On the other hand, in hierarchical topology nodes send data through intermediate level nodes to the sink node; an example of it is shown in Fig. 1. Flat topology can be assumed equivalent to a one-level hierarchical topology.

At a fixed $\leq$t interval of time, each senor node S_i measures a multidimensional data vector from the area under observation. In this way, over a window of N measurements, each sensor possess a set of data vectors $X_i = \{X_{it} | t = 1, 2, \ldots, N\}$ and N is referred to as data window size in the present work.

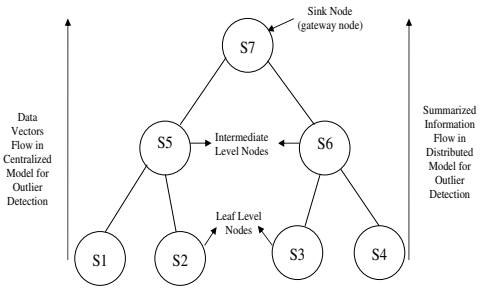

Fig. 1 A two-level wireless sensor network hierarchical topology and conceptual difference in two outlier detection models

4 The Proposed Outlier Detection Technique

In the proposed scheme, the outlier detection process has been distributed among all sensor nodes. The overall working architecture of the proposed outlier detection technique for a two-level hierarchy topology comprising seven nodes is graphically summarized in Fig. 2. It also shows the main algorithmic steps that take place at sensor nodes of a level and the type of data communicated between different levels.

At every data window of size N, the following functions are carried out:

Step 1: Each sensor S_i applies the proposed outlier detection algorithm to divide current window data into normal data cluster and candidate outliers cluster. A normal cluster consists of those data vectors that are consistent with the previously observed patterns of sensed data. A candidate outlier is a data measurement that shows anomalous behaviour in the context of currently available normal data model of the same sensor node on which it is present. But its outlying behaviour is further verified on higher levels of hierarchy up to sink node to declare it as an outlier. It has been applied to minimize the false alarms by exploiting the spatial correlation of sensor network data. If at any level candidate outlier fails to satisfy the outlying criterion, it has been removed from the candidate outliers set. Node-level detection of candidate outliers is very necessary to maintain the integrity of accumulated data.

Step 2: Sensor S_j generates the summary of a normal cluster. Summary of a normal cluster comprises of its mean, variance and size.

Step 3: Sensor S_j sends candidate outliers and normal data cluster summary to its corresponding intermediate node (parent) at the next level of hierarchy. For example, sensors S1 and S2 send summary and candidate outliers to sensor S5. Sending summarized cluster representation to other sensor nodes instead of raw data vectors minimizes the communication overhead in network and prolongs the lifetime of wireless sensor networks.

Step 4: Intermediate node (parent node) S_P merges its own normal cluster summary with normal cluster summaries it has received from lower-level nodes (child node). For example, node S6 merges normal cluster summaries of sensors S3 and S4 with its own normal cluster summary. Anomalous behaviour of candidate outliers is tested against a new normal cluster (produced after merging) to exploit the spatial correlation of sensor nodes to trim down the false alarms. If a candidate does not sat-

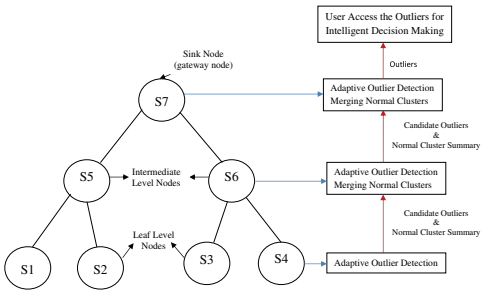

Fig. 2 The working architecture of the proposed outlier detection technique

isfy the outlying criterion then it is added to the normal cluster summary and removed from the candidate outliers set. This reduces the unnecessary communication of false alarms to the sink node.

Step 5: Intermediate nodes further send merged normal cluster summary and candidate outliers to their corresponding intermediate node (parent) at the next level of hierarchy.

Step 6: This process continues recursively up to sink node. Sink node also merges the normal cluster summaries and test candidates against a new normal cluster. If a candidate reaches the sink node and also satisfies outlying criterion at the sink node, then that is finally declared as an outlier.

Candidate outlier detection computational cost is $O(NP)$ and summary generation and updates process involves very small computation. Let it be G and U, respectively. Computational complexity of leaf nodes for each data window is $O(NP + G + U)$, and that of an intermediate node is $O(NP + G + U + KP)$, where K is the number of candidate outliers at a node. It is equivalent to O(N+K)P.

The proposed scheme is flexible to work in scenarios where one or more than one sink nodes are present in the deployed region.

5 Evaluation

The proposed method has been compared to an unsupervised centralized outlier detection method, presented in [10], because centralized models provide a baseline for comparing outlier detection accuracy of distributed approaches [18]. For comparison purposes we have taken top 20% objects. For experimental purpose data window size has been taken as 100 data points and data history size as 500 data points.

For performance assessment of the proposed method, two metrics, namely *Outlier Detection Rate* (ODR) and *False Alarm Rate* (FAR), have been examined. ODR and FAR are defined as follows:

$$\text{Outlier Detection Rate} = \frac{\text{No. of Outliers Detected}}{\text{Total Outliers}} \tag{1}$$

$$\text{False Alarm Rate} = \frac{\text{No. of False Alarms}}{\text{Total Normal Data Objects}} \tag{2}$$

5.1 Datasets

The following two real-world datasets have been used for experimental analysis.

1. *SensorScope Project Dataset*: This dataset has been collected from a wireless sensor network which was deployed at Grand-St-Bernard under SensorScope Project funded by NCCR MICS [19]. This network was composed of seven sensors nodes which were numbered from 1 to 7 and each sensor collected values of ambient temperature, soil moisture, solar radiation, relative humidity and watermark measurements over an interval of two minutes. In our experiments, we have used two attributes, namely ambient temperature and relative humidity for each sensor. Data corresponding to each attribute for all sensors is mapped to a range of [0, 1]. Data labelling has been done by using visualization technique [20].

2. *ISSNIP Dataset*: This data has been made publicly available by the Australian Research Council Network on Intelligent Sensors, Sensor Networks and Information Processing (ISSNIP) [21]. It corresponds to a wireless sensor network deployed using TelosB sensors for monitoring temperature and humidity. It comprises 4690 observations per sensor collected over a period of 6 h. It is a labelled dataset and outliers were introduced artificially by adding a source of hot water and steam within the monitored environment.

5.2 Results and Discussion

The performance of the proposed method has been analyzed in terms of outlier detection rate and false alarm rate. Outlier detection rate should be high and the false alarm rate should be low for accurate detection and to avoid consumption of resources in investigating false alarms.

It can be seen from Table 1 that ODR for SensorScope sensors is very high ranging from 0.917 to 1.0 and false alarm rate is very low ranging from 0.005 to 0.014. It shows the effectiveness of the proposed scheme. String "NAN" under the outlier detection rate column signifies that corresponding sensor data does not have any outlier, hence outlier detection rate is undefined.

It can be observed from Table 2 that, in case of ISSNIP dataset, ODR for sensor 3 is 0.96, which is fairly high. For sensor 1, ODR is 0.672 owing to the fact that even very small deviations have been artificially labelled as outliers for sensor 1 data. In the literature, a maximum of 0.6207 outlier detection rate has been reported for sensor 1, which is much smaller than ODR of the proposed method. It indicates the capability of the proposed method to attain a high outlier detection rate. The false alarm rate is very small for this dataset ranging from 0.004 to 0.007.

The percentage (%) reduction in communication overhead for two datasets has been given in Tables 3 and 4, respectively. In centralized method, sensor node sends all data vectors to the sink node but in the proposed approach only summary of normal data cluster and candidates outliers are passed to sink node to minimize the

Table 1 Outlier detection rate of the proposed technique on SensorScope project dataset

Sensor	No. of outlier detected	No. of false alarms	Total outlier	Total normal objects	Outlier detection rate	False alarm rate
Sensor 1	100	79	100	6516	1	0.012
Sensor 2	0	90	0	6616	NAN	0.014
Sensor 3	0	36	0	6616	NAN	0.005
Sensor 4	29	42	30	6586	0.967	0.006
Sensor 5	77	83	84	6532	0.917	0.013
Sensor 6	0	35	0	6616	NAN	0.005
Sensor 7	0	76	0	6616	NAN	0.011

Table 2 Outlier detection rate of the proposed technique on ISSNIP dataset

Sensor	No. of outlier detected	No. of false alarms	Total outlier	Total normal objects	Outlier detection rate	False alarm rate
Sensor 1	39	18	58	4632	0.672	0.004
Sensor 2	0	34	0	4690	NAN	0.007
Sensor 3	96	26	100	4590	0.96	0.006
Sensor 4	0	29	0	4690	NAN	0.006

Table 3 Percentage (%) reduction in communication overhead of network for SensorScope project data

Sensor	No. of data vectors transmitted by sensor in centralized by sensor in distributed approach	No. of data vectors transmitted approach	% Reduction in communication overhead
First level of hierarchy			
Sensor 1	6116	338	94.4735
Sensor 2	6116	197	96.7789
Sensor 3	6116	147	97.5965
Sensor 4	6116	203	96.6808
Second level of hierarchy			
Sensor 5	18348	635	96.5391
Sensor 6	18348	370	97.9834

Table 4 Percentage (%) reduction in communication overhead of network for ISSNIP data

Sensor	No. of data vectors transmitted by sensor in centralized approach	No. of data vectors transmitted by sensor in distributed approach	% reduction in communication overhead
First level of hierarchy			
Sensor 1	4190	198	99.0375
Sensor 2	4190	176	99.032
Sensor 3	4190	262	99.053
Sensor 4	4190	238	99.0473

communication overhead. The subset of data used in initialization has not been considered in communication overhead analysis. Also, gateway node has been excluded from the analysis of communication overhead as it does not send data to other nodes, but only receives. Intermediate nodes also send data of their child nodes along with their own data. Hence the number of data vectors transferred by intermediate nodes is approximately three times the number of data vectors transmitted by leaf-level nodes. The percentage reduction in communication overhead is calculated as per (3):

$$\%\ \text{Reduct. in Comm. OH} = ((X - Y)/X) \times 100 \tag{3}$$

where X is the number of data vectors transmitted by the sensor in a centralized approach, and Y is the number of data vectors transmitted by the sensor in a distributed approach

It is evident from Tables 3 and 4 that the percentage (%) reduction in communication overhead is very large from centralized method to distributed proposed approach. It varies from 94.47 to 97.98 and from 99.03 to 99.05 for SensorScope and ISSNIP datasets, respectively, corresponding to different sensors. It shows that the proposed technique involves much smaller data communication as opposed to centralized approach. The comparison of the proposed distributed method and centralized method [10] in terms of outlier detection rate and false alarm rate has been provided in Figs. 3 and 4 for two datasets. It can be concluded from Tables 3, 4, Figs. 3 and 4 that the proposed technique has attained ODR and FAR close to the ODR and FAR achieved by centralized approach with remarkable reduction in communication overhead. It proves the appropriateness of the proposed scheme for finding outliers in resource-constrained WSNs.

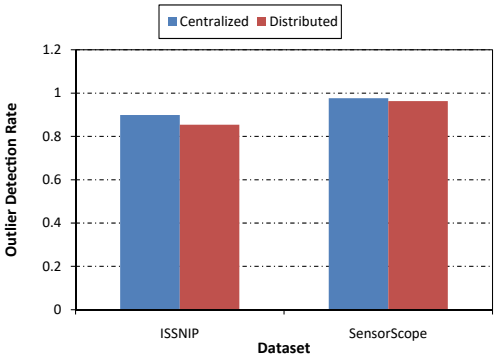

Fig. 3 Comparison of outlier detection rate

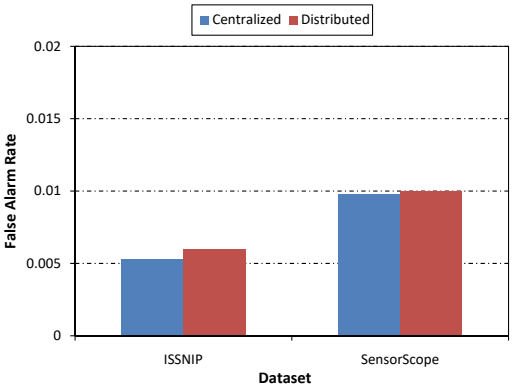

Fig. 4 Comparison of false alarm rate

6 Conclusion

In this paper, a distributed outlier detection technique for wireless sensor networks has been presented that employs normal data variance to identify outliers and exploits the temporal and spatial correlation of sensors nodes by maintaining normal data model over data of multiple windows and by retesting outlierness of candidate outliers against merged normal clusters. Experimental results concluded that the proposed technique has attained ODR and FAR close to the ODR and FAR achieved by centralized approach with a remarkable reduction in communication overhead.

References

1. Y. Zhang, N. Meratnia, P. Havinga, Commun. Surv. Tuts. **12**(2), 159 (2010)
2. D. Hawkins, *Identification of Outliers*. Monographs on Applied Probability and Statistics (Chapman and Hall, London [u.a.], 1980)
3. V. Chandola, A. Banerjee, V. Kumar, ACM Comput. Surv. **41**(3), 15:1 (2009)

4. M. Gupta, J. Gao, C.C. Aggarwal, J. Han, IEEE Trans. Knowl. Data Eng. **99**(PrePrints), 1 (2013)
5. V.J. Hodge, J. Austin, Artif. Intell. Rev. **22**, 2004 (2004)
6. C. Chatzigiannakis, S. Papavassiliou, IEEE Sens. J. **7**, 637 (2007)
7. S. Gupta, R. Zheng, A.M.K. Cheng, in *Proceedings of MASS* (IEEE, 2007), pp. 1–9
8. S. Rajasegarar, C. Leckie, M. Palaniswami, J. Parallel Distrib. Comput. **74**(1), 1833 (2014)
9. S. Rajasegarar, C. Leckie, M. Palaniswami, J. Bezdek, in *ICCS 2006, 10th IEEE Singapore International Conference on Communication Systems* (2006), pp. 1–5
10. M. Amer, M. Goldstein, in *Proceedings of the 3rd RapidMiner Community Meeting and Conferernce (RCOMM 2012)*, ed. by S. Fischer, I. Mierswa (Shaker Verlag GmbH, 2012), pp. 1–12
11. M. Xie, S. Han, B. Tian, S. Parvin, J. Netw. Comput. Appl. **34**(4), 1302 (2011). Advanced Topics in Cloud Computing
12. P.N. Tan, M. Steinbach, V. Kumar, *Introduction to Data Mining* (Pearson Education, 2006)
13. Y. Thakran, D. Toshniwal, in *Proceeding of ISDA* (2012), pp. 947–952
14. E.M. Knorr, R.T. Ng, in *Proceedings of the 24rd International Conference on Very Large Data Bases* (Morgan Kaufmann Publishers Inc., San Francisco, CA, USA, 1998), VLDB '98, pp. 392–403
15. S. Ramaswamy, R. Rastogi, K. Shim, in *Proceedings of the 2000 ACM SIGMOD International Conference on Management of Data* (ACM, New York, NY, USA, 2000), SIGMOD '00, pp. 427–438
16. J. Branch, C. Giannella, B. Szymanski, R. Wolff, H. Kargupta, Knowl. Inf. Syst. **34**(1), 23 (2013)
17. A. Fawzy, H.M. Mokhtar, O. Hegazy, Egypt. Inform. J. **14**(2), 157 (2013)
18. M. Moshtaghi, J.C. Bezdek, T.C. Havens, C. Leckie, S. Karunasekera, S. Rajasegarar, M. Palaniswami, Wirel. Commun. Mob. Comput. (2012)
19. Sensorscope system. http://sensorscope.epfl.ch/index.php/MainPage
20. S. Takianngam, W. Usaha, in *International Symposium on Intelligent Signal Processing and Communications Systems (ISPACS)* (2011), pp. 1–6
21. S. Suthaharan, M. Alzahrani, S. Rajasegarar, C. Leckie, M. Palaniswami, in *Proceedings of the Sixth International Conference on Intelligent Sensors, Sensor Networks and Information Processing (ISSNIP 2010)* (2010)

Single-Image Super-Resolution Using Rational Fractal Interpolation and Adaptive Wiener Filtering

Ruchika Dhawan and Umesh Ghanekar

Abstract In this paper, we have propounded a neoteric procedure for the super-resolution of an image using a single image. An image of low resolution is given as input which is upscaled to an image while preserving the information that is stored in textural and structural details of an image. The image provided as input which is of low resolution is segregated into two sections, namely textured and non-textured according to the features of the image. Rational fractal interpolation is employed in the section of the image considered as textured and rational interpolation is employed in the remaining image which is considered to be non-textured. Thereafter, pixel mapping is performed. The result obtained from interpolation is found to contain Gaussian noise. To subdue the effect of this noise, an adaptive Wiener filter is applied. Finally, an image of high resolution is obtained. Profound simulations and assessments demonstrate that competitive performance is achieved by our algorithm. The mean square error reduces approximately up to 5%, whereas the structural similarity index improves marginally.

Keywords Single-image super-resolution · Rational fractal interpolation · Gaussian noise · Wiener filter

1 Introduction

Among the major tools used during the process of image restoration is super-resolution (SR). Due to the manufacturing limitations that are incurred in an imaging system, the quality of the image gets degraded which can be restored and enhanced by using the process of SR. The procedure of acquiring an image of high resolution (HR) from the available images of low resolution (LR) is termed SR. When

R. Dhawan (✉) · U. Ghanekar
Department of Electronics and Communication, National Institute of Technology, Kurukshetra, Kurukshetra, Haryana 136119, India
e-mail: ruchika_31905125@nitkkr.ac.in

U. Ghanekar
e-mail: ugnitk@nitkkr.ac.in

S. Rawat et al. (eds.), *Proceedings of First International Conference on Computational Electronics for Wireless Communications*, Lecture Notes in Networks and Systems 329,
https://doi.org/10.1007/978-981-16-6246-1_40

a single image of LR is used for obtaining an image of HR, it is defined as single image super-resolution (SISR). For better visual effects and scientific applications [1] such as biometric, remote sensing, face hallucination, satellite communication, and surveillance, land cover analysis of HR images is often required. The mathematical representation [1, 2] of it is modeled in (1)

$$P = BCDL + N \tag{1}$$

The HR image is denoted by "*P*", and "*L*" represents the image of LR. The decimation factor is represented by "*D*", and "*B*" denotes the geometric transformation metric or warping, and the metric used for blurring is represented by "*C*". "*N*" is the noise addition that is conventionally studied as white Gaussian noise. Prevailing methods employed for SR perhaps are arranged into three primary classes where the techniques are based on interpolation, reconstruction, and learning [3]. Techniques based on learning and reconstruction rely on the source of patches employed for training, whereas techniques based on interpolation extract information of the patch from the image of LR. In the techniques based on interpolation, the pixels that are unknown in the grid of the HR image are estimated by using their neighborhood pixels. Techniques employed for interpolations are categorized into basic and edge-directed. Techniques employed for interpolation that is basic can further be categorized into linear or nonlinear. Equations that are linear are computed in linear interpolation techniques which are the same as evaluating interpolation that is one-dimensional, for example, bilinear, nearest neighbor. Techniques involving nonlinear interpolation comprise cubic, bicubic, spline, polynomial, and further modifications of it [4, 5]. The above methods are fast in execution but incur artifacts such as blurring and ringing effects [5], particularly regions comprising edges and high texture. Different edge-directed interpolation techniques were introduced to overcome the above deficiencies [6–8]. These techniques succeed in evaluating the edge structure but introduce speckle-noise around texture areas. The ideal kernel function which is approximated through the rational function [6] has been implemented in the following image interpolation [9]. Rational function interpolation often produces visual results that are good when compared to other basic interpolation techniques. But textural details are not preserved on a satisfactory level through rational interpolation function.

An efficient tool widely used for representing the texture, classification, and segmentation of an image is fractal. A multifractal spectrum based on texture [10] was introduced. The multifractal analysis was employed in wavelet pyramids for describing textural details in an image in which the information from both domains was implicitly combined [11]. In [12], the dynamic classification of texture was presented based on dynamic fractal analysis. A popular technique employed for filtering and denoising the image is Wiener filtering [13]. The tradeoff that occurs between inverse filtering and smoothing of noise is balanced through it by eliminating additive noise. The concept of the Wiener filter was propounded by Nobert Wiener [14]. Wiener filter is a type of linear filter. This paper propounds a new procedure to enhance the performance of SISR which is based on rational fractal interpolation by

deploying an adaptive Wiener filter. In this algorithm, the first step is the division of the region of the LR image which is achieved by deploying the isoline method which helps in detecting the information stored in the textural and structural details of an image. The difference between the values of pixels helps in evaluating the textural details. Rational fractal interpolation is employed in the section of the image considered as textured and rational interpolation is employed in the remaining image which is considered to be non-textured. Then pixel mapping is done. To obtain an image of HR adaptive Wiener filtering is performed which is illustrated in Sect. 2. In Sect. 2, the complete process of rational fractal interpolation employed in the SISR algorithm is discussed. Section 3 comprises the experimental findings and interpreting the efficacy of the algorithm. In Sect. 4 conclusions are presented.

2 Proposed Framework for SISR

Different structural characteristics are inhibited by different regions of an image. In the proposed model, different interpolation techniques are employed depending upon the texture of the region. A crucial procedure in the process of interpolation is the division of regions. The quality of interpolation is straight away influenced by the efficacy of the division of regions. For the division of regions, structural and textural information needs to be detected which is carried out through the isoline method [15]. In a given input image of LR, to detect the textural details a 5×5 patch is considered. If the size of the patch is too small it results in noise sensitivity. A few regions considered to be textured will be evaluated as non-textured regions if the size of the patch of image considered is too large. The differences between the values of pixels help in evaluating the textural details. Each 5×5 patch of the image is grouped into four 3×3 sub-blocks. The average of all the pixels considered in the 5×5 patch $\boldsymbol{R}$ is evaluated through Eq. (2).

$$R = \begin{bmatrix} l_{(1,1)} & l_{(1,2)} & l_{(1,3)} & l_{(1,4)} & l_{(1,5)} \\ l_{(2,1)} & l_{(2,2)} & l_{(2,3)} & l_{(2,4)} & l_{(2,5)} \\ l_{(3,1)} & l_{(3,2)} & l_{(3,3)} & l_{(3,4)} & l_{(3,5)} \\ l_{(4,1)} & l_{(4,2)} & l_{(4,3)} & l_{(4,4)} & l_{(4,5)} \\ l_{(5,1)} & l_{(5,2)} & l_{(5,3)} & l_{(5,4)} & l_{(5,5)} \end{bmatrix},$$

$$\alpha = \frac{\sum_{p=1}^{5} \sum_{q=1}^{5} l_{p,q}}{5 \times 5}, \tag{2}$$

where the pixel value at the point (p, q) is represented by $l_{p,q}$. The image is segregated into two different regions mainly textured and non-textured based on the following formula:

$$\Delta j_{p,q} = l_{p,q} - \alpha \tag{3}$$

If $\Delta j_{p,q}$ is greater than or less than zero the region is considered to be non-texture. The complexity of the texture is reflected through the scaling factors. The values of the scaling factor directly affect the output of interpolation. If the region is textured, the scaling factors $\left(d_{x,y}, x, y = 1, 2\right)$ are evaluated through Eq. (6). If the region is non-textured, the value of $d_{x,y} = 0 \leq x, y = 1, 2$. Consider the first sub-block $\left(l_{p,q}, p, q = 1, 2, 3\right)$. Equation (4) represents the average of all the pixels contained in the first sub-block.

$$a = \frac{l_{1,1} + l_{1,2} \cdots l_{3,3}}{9} \tag{4}$$

$$b = \left|l_{1,1} - a\right| + \left|l_{1,3} - a\right| + \left|l_{3,1} - a\right| + \left|l_{3,3} - a\right| \tag{5}$$

$$d_{1,1} = \frac{\left|l_{1,1} - a\right|}{b},$$

$$d_{1,2} = \frac{\left|l_{1,3} - a\right|}{b},$$

$$d_{2,1} = \frac{\left|l_{3,1} - a\right|}{b},$$

$$d_{2,2} = \frac{\left|l_{3,3} - a\right|}{b} \tag{6}$$

The process of interpolation is comprehended to the whole image of LR where each patch is traversed in a raster scan order. Then pixel mapping is applied through which amplification of the image can be achieved at an integral multiple [16]. The image obtained from interpolation is subtracted from the original image. The resultant image obtained is found to have Gaussian distribution which is shown in Fig. 1. Therefore, to subdue the noise in the interpolated image, an adaptive Wiener filter is employed. It is a type of linear filter which adapts itself to the variance of the image [17]. Little smoothing is performed by the filter where the variance of the image is large whereas more smoothing is performed where the variance of the image is small. This methodology produces better results when compared with linear filters by preserving edges and high-frequency components of an image [18]. From the interpolated image denoted as Z local mean and variance represented as μ_Z and ${\sigma_Z}^2$ is evaluated around each pixel which is represented as

$$\mu_Z = \frac{1}{R \times S} \sum_{t_1, t_2 * \varphi} z(t_1, t_2) \tag{7}$$

$${\sigma_Z}^2 = \frac{1}{R \times S} \sum_{t_1, t_2 * \varphi} z^2(t_1, t_2) - {\mu_Z}^2 \tag{8}$$

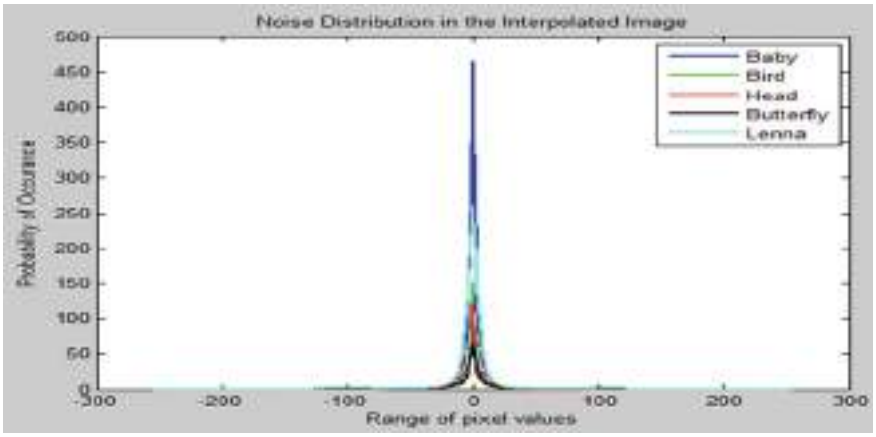

Fig. 1 Distribution of noise in the interpolated image

where φ is the $R \times S$ neighborhood of each pixel in the interpolated image Z. Pixel-wise estimate is obtained as follows:

$$P(t_1, t_2) = \mu_Z + \frac{{\sigma_Z}^2 - {n_z}^2}{{\sigma_Z}^2}(z(t_1, t_2) - \mu_Z) \tag{9}$$

where ${n_z}^2$ represents the variance of the noise. As the variance of the noise is unknown, it is evaluated as the average of all the local variances which is represented as

$${n_z}^2 = \frac{1}{R \times S} \sum_{t_1, t_2 * \varphi} {\sigma_Z}^2(t_1, t_2) \tag{10}$$

The algorithm comprises the following steps:

(i) Divide the image of LR into 5×5 patches.
(ii) Further, divide each 5×5 patch into four 3×3 sub-blocks.
(iii) Evaluate the average of all pixels contained in the 5×5 patch.
(iv) In the sub-block, to evaluate the value of each pixel subtract the value of the pixel from the average value of the considered 5×5 patch.
(v) Further, segregate the image into texture and non-texture regions based on the isoline method. If the value of a pixel in the sub-block is greater than or less than zero, it is considered to be a non-texture region.
(vi) Rational fractal interpolation is employed in the section of the image considered as textured and rational interpolation is employed in the remaining image which is considered to be non-textured.
(vii) The interpolated image is subtracted from the original image. The resultant image is found to have Gaussian distribution.

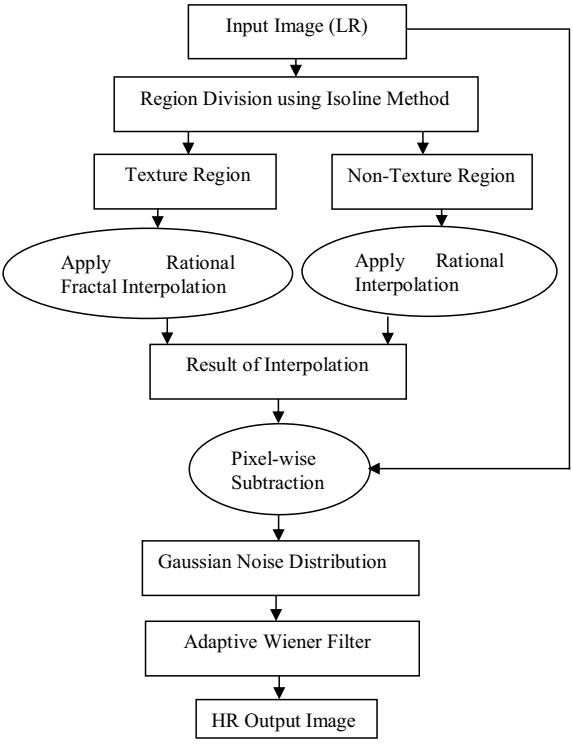

Fig. 2 Schematic diagram for the propounded technique

(viii) To subdue the effect of noise adaptive, the Wiener filter is employed. It adapts itself to the variance of the image.
(a) Local mean and variance are evaluated around each pixel which is denoted by Eqs. (7) and (8).
(b) Pixel-wise estimate is evaluated which is represented by Eq. (9).
(c) As the variance of the noise is unknown, Eq. (10) is employed in evaluating it.
(ix) Finally, an HR image is obtained.

The complete schematic diagram is given in Fig. 2.

3 Simulations and Results

Diverse experiments are implemented to analyze the efficacy of the algorithm that is presented. The test images used for the experiment are shown in Fig. 3. The images employed in evaluating the performance are gathered from Set5 [19]. Images of LR are acquired by down-sampling images of HR. Both horizontal and vertical directions employ the process of down-sampling. The scaling factor considered here

Fig. 3 (Color online) Test images employed for the experiment (from left to right): Baby, Bird, Butterfly, and Head

is 2. Images of LR are also obtained by downscaling operators that are unknown to introduce more realistic conditions. The human perception is more sensitive to the luminance channel as compared with the other two chrominance channels. Therefore, the RGB color space is transformed into YCbCr color space and all the techniques that are compared are conducted in the Y channel. The other channels are directly upscaled through bicubic interpolation. The performance of the method is collated with other techniques based on three indices that are used for objective assessment. They are mean square error (MSE), peak signal to noise ratio (PSNR), and structural similarity (SSIM) [20]. The expressions employed for evaluating PSNR and SSIM are stated by Eqs. (11) and (12).

$$PSNR = 10\log_{10}\left(\frac{V^2}{mse}\right) \tag{11}$$

where *PSNR* is represented in *dB*, the maximum pixel value is denoted by V, and *mse* is the mean square value.

$$SSIM\,(e,f) = \frac{\left(2\mu_e\mu_f + y_1\right)}{\left({\mu_e}^2 + {\mu_f}^2 + y_1\right)} \tag{12}$$

where μ_e, μ_f indicate local means for images e and f. The above *SSIM* formula indicates the luminance term.

In a given input image of LR, to detect the roughness of texture a 5×5 patch is considered. Each 5×5 patch of the image is grouped into four 3×3 sub-blocks. The average of all the pixels considered in the 5×5 patch is evaluated. In the sub-block, to evaluate the value of each pixel subtract the value of the pixel from the average value of the considered 5×5 patch. Further, segregate the image into texture and non-texture regions based on the isoline method. If the value of a pixel in the sub-block is greater than or less than zero, it is considered to be a non-texture region. Rational fractal interpolation is employed in the section of the image considered as textured and rational interpolation is employed in the remaining image which is considered to be non-textured. The interpolated image is subtracted from the original image. The

type of noise in the resultant image is found to be Gaussian in nature. To decrease the effect of noise in the interpolated image adaptive Wiener filter is employed. The filter adapts itself to the variance of the image. The value of $R \times S$ neighborhood employed is 3×3. Little smoothing is performed by the filter where the variance of the image is large, whereas more smoothing is performed where the variance of the image is small. This methodology produces better results when compared with linear filters by preserving edges and high-frequency components of an image. The efficacy of the method is presented by collating its performance with bicubic interpolation, BMF in which for preprocessing of image median filtering is applied following which bicubic interpolation is implemented, ICBI [21], and rational fractal interpolation which are shown in Tables 1, 2, 3 and 4 with reference to MSE, PSNR, and SSIM, respectively.

The propounded technique is better with reference to MSE, PSNR, and SSIM which can be inferred from the tables mentioned above. The visual characteristics of the presented algorithm along with other compared techniques are shown in Fig. 4. The image considered for comparing the visual characteristics is that of a "bird".

Table 1 Objective quality evaluation of various techniques for baby

	Bicubic	BMF	ICBI	Rational fractal	Proposed
MSE	31.137	48.104	14.161	13.721	12.965
PSNR	33.198	31.309	36.620	36.757	37.003
SSIM	0.967	0.922	0.984	0.984	0.985

Table 2 Objective quality evaluation of various techniques for bird

	Bicubic	BMF	ICBI	Rational fractal	Proposed
MSE	41.752	74.111	11.012	15.128	14.121
PSNR	31.924	29.432	37.712	36.333	36.632
SSIM	0.941	0.888	0.977	0.979	0.979

Table 3 Objective quality evaluation of various techniques for butterfly

	Bicubic	BMF	ICBI	Rational fractal	Proposed
MSE	226.246	366.505	90.465	78.105	72.875
PSNR	24.585	22.490	28.566	29.204	29.505
SSIM	0.880	0.815	0.935	0.950	0.951

Table 4 Objective quality evaluation of various techniques for head

	Bicubic	BMF	ICBI	Rational fractal	Proposed
MSE	40.270	55.282	27.674	23.333	22.171
PSNR	32.081	30.705	33.710	34.451	34.673
SSIM	0.804	0.742	0.840	0.857	0.857

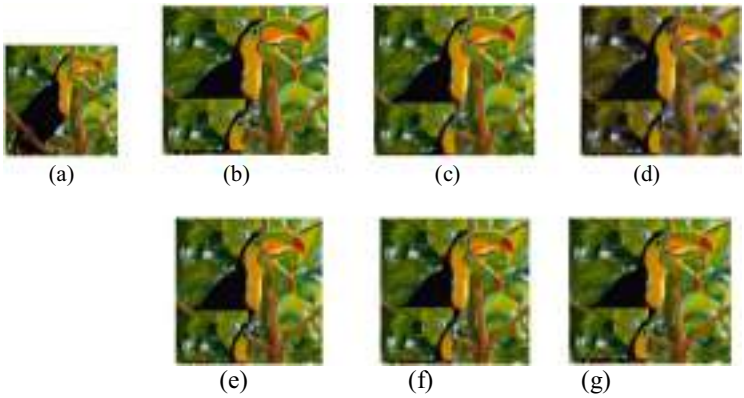

Fig. 4 Comparison of SISR techniques for S = 2 on image "Bird". **a** LR input image, **b** original HR image, **c** bicubic, **d** BMF, **e** ICBI, **f** rational fractal, **g** proposed method

The figure represents that the image of HR obtained from the presented algorithm is visually better when compared to other techniques.

4 Conclusions

This paper presents single-image super-resolution formulated on rational fractal interpolation combined with an adaptive wiener filter. First, for each patch of the LR image, the isoline method is used to detect texture. After detecting the texture the image is segregated into texture and non-texture regions. For the texture region, a rational fractal interpolation model is employed, and for the non-textured region, rational interpolation model is employed. The interpolated image is found to contain noise which has Gaussian distribution. To reduce the effect of noise, an adaptive Wiener filter is employed which adapts itself to the variance of the image. The usefulness of the proposed technique is testified via the simulation results. The performance of the propounded algorithm can be further ameliorated by designing a more effective filter to suppress the Gaussian noise.

References

1. K. Nasrollahi, T. Moeslund, Super-resolution: a comprehensive survey. Mach. Vis. Appl. **25**(6), 1423–1468 (2014)
2. S.C. Park, M.K. Park, M.G. Kang, Super-resolution image reconstruction: a technical overview. IEEE Signal Process. Mag. **20**(3), 21–36 (2003)
3. G. Pandey, U. Ghanekar, A compendious study of super-resolution techniques by single image. Optik. 166 (2018). https://doi.org/10.1016/j.ijleo.2018.03.103

4. J. Shi, S.E. Reichenbach, Image interpolation by two-dimensional parametric cubic convolution. IEEE Trans. Image Process. **15**(7), 1857–1870 (2006)
5. P. Thévenaz, T. Blu, M. Unser, I. Bankman, Image interpolation and resampling, in *Handbook of Medical Image Processing and Analysis* (Academic Press, 2000), pp. 393–420
6. X. Li, M.T. Orchard, New edge-directed interpolation. IEEE Trans. Image Process. **10**(10), 1521–1527 (2001)
7. D. Zhou, X. Shen, W. Dong, Image zooming using directional cubic convolution interpolation. IET Image Proc. **6**(6), 627–634 (2012)
8. D. Zhang, W. Xiaolin, An edge-guided image interpolation algorithm via directional filtering and data fusion. IEEE Trans. Image Process. **15**(8), 2226–2238 (2006)
9. S. Carrato, L. Tenze, A high quality 2X image interpolator. IEEE Signal Process Lett **7**(6), 132–134 (2000)
10. Y. Liu, Z. Yunfeng, G. Qiang, Z. Caiming, Image interpolation based on weighted and blended rational function, in *ACCV Workshops* (2014)
11. Y. Xu, X. Yang, H. Ling, H. Ji, A new texture descriptor using multifractal analysis in multi-orientation wavelet pyramid, in *IEEE Computer Society Conference on Computer Vision and Pattern Recognition*, San Francisco, CA (2010), pp. 161–168
12. Y. Xu, Y. Quan, H. Ling, H. Ji, Dynamic texture classification using dynamic fractal analysis, in *International Conference on Computer Vision,* Barcelona (2011), pp. 1219–1226
13. R.C. Gonzalez, R.E. Woods, S.L. Eddins, *Digital Image Processing Using MATLAB* (Prentice Hall, 2004)
14. N. Wiener, *Extrapolation, Interpolation, and Smoothing of Stationary Time Series* (Wiley, 1949)
15. S. Osher, J.A. Sethian, Fronts propagating with curvature-dependent speed: Algorithms based on Hamilton-Jacobi formulations. J. Comput. Phys. **79**(1), 12–49 (1988)
16. Y. Zhang, Q. Fan, F. Bao, Y. Liu, C. Zhang, Single-image super-resolution based on rational fractal interpolation. IEEE Trans. Image Process. **27**(8), 3782–3797 (2018)
17. J.S. Lee, Digital image enhancement and noise filtering by use of local statistics. IEEE Trans. PAMI **2**(2), 165–168 (1980)
18. J.S. Lim, *Two-Dimensional Signal and Image Processing* (Englewood Cliffs, NJ, Prentice Hall, 1990), p. 548. Equations 9.44, 9.45, and 9.46
19. M. Bevilacqua, A. Roumy, C. Guillemot, M.-L. Alberi-Morel, Low-complexity single image super-resolution based on nonnegative neighbor embedding, in *Proceedings of the British Machine Vision Conference* (2012), pp. 135.1–135.10
20. W. Zhou, A.C. Bovik, H.R. Sheikh, E.P. Simoncelli, Image quality assessment: from error visibility to structural similarity. IEEE Trans. Image Process. **13**(4), 600–612 (2004)
21. A. Giachetti, N. Asuni, Real-time artifact-free image upscaling. IEEE Trans. Image Process. **20**(10), 2760–2768 (2011)

High-Performance Wallace Tree Multiplier Design Using Novel 8-4 Compressor Implementation for Image Processing

Saher Jawaid Ansari, Priyanka Verma, and Surya Deo Choudhary

Abstract Multipliers can generate a significant performance in designing filters, MAC units, memories, and image processing applications. Several multipliers have been designed and implemented for various applications. However, the main issue was the latency which is increasing as the number of bits increasing. Multipliers with compressors help in the reduction of latency of partial product which in turn helps in reducing the summation of adders in the final summation stage. In the proposed design of 8 * 8 Wallace tree multiplier, 16 partial products have been obtained by multiplication of operands and multiplicand. In the proposed Wallace tree multiplier design with 8–4 compressor, multiplication operation has been obtained in less number of steps as compared to conventional multiplier without compressors in which the number of stages is reduced from 16-12-8-6-4-3-2. The proposed 8 × 8 Wallace tree multiplier with an 8-4 compressor requires 24.7 ns for completion of the multiplication operation. It thus achieved a 43% reduction in delay as compared to the conventional Wallace tree multiplier (WTM). The simulation result also proves that the proposed design has achieved a 27% reduction in total power dissipation. Thus, the proposed Wallace tree multiplier (WTM) exhibits better interpretation in terms of latency as well as power dissipation, and hence, it can be used for high-performance image processing implementation. The proposed Wallace tree multiplier (WTM) is simulated using ModelSim Student Edition tool and synthesized using Xilinx ISE 14.7 navigator tool.

Keywords Wallace tree multiplier · Compressor · High performance · Latency

1 Introduction

Multipliers are most widely used for arithmetic operations. Wallace tree multiplier uses adders, both half adders as well as full adders, for tree formation to reduce the number of partial products. The focus of the paper is to optimize the partial products,

S. J. Ansari (✉) · P. Verma · S. D. Choudhary
Department of Electronics & Communication Engineering, Noida Institute of Engineering and Technology, Greater Noida, India

S. Rawat et al. (eds.), *Proceedings of First International Conference on Computational Electronics for Wireless Communications*, Lecture Notes in Networks and Systems 329,
https://doi.org/10.1007/978-981-16-6246-1_41

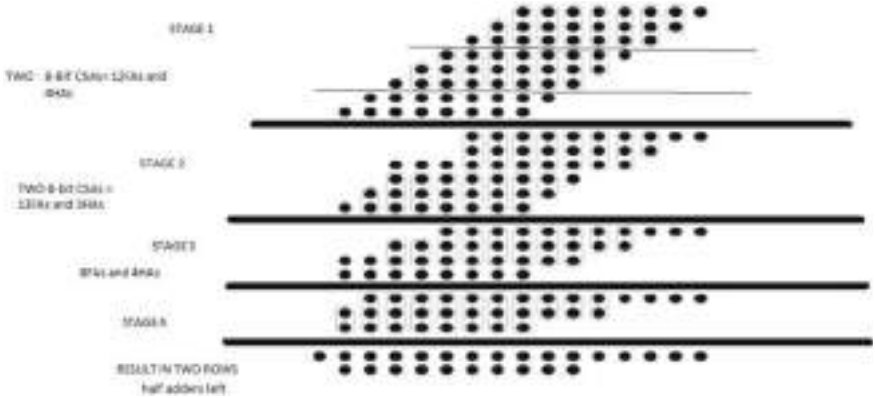

Fig. 1 Diagram of Wallace tree multiplier

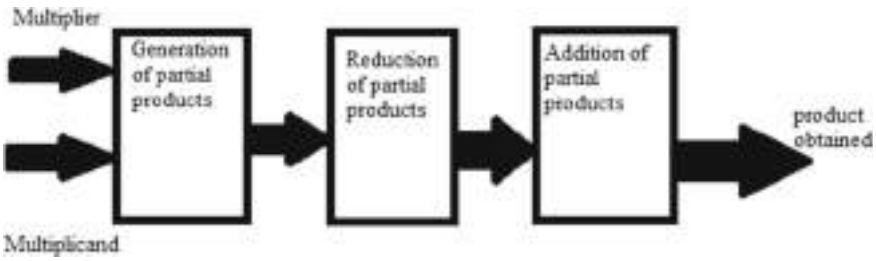

Fig. 2 Basic stages of Wallace tree multiplier

hence the number of stages is reduced in multiplication [1, 2]. The basic architecture of the Wallace tree multiplier at different stages is given in Fig. 1.

The three phases of Wallace tree multiplier architecture are as follows [3]:

- The first stage of WTM is the generation of partial products (PP).
- Collection of partial products (PP) is the second stage
- Finally, additional stage in which the last two rows are summed using an adder.

We can refer to Fig. 2 for more assistance of the three phases of the Wallace tree multiplier.

2 Conventional Wallace Reduction Method

This paper contributes to the design of WTM by proposing a policy to reduce the delay and area of the multiplier. In the conventional WTM, the first step is to form the arrays of partial products [4–6]. In the second step, we have to group three adjacent rows each, and these three rows are reduced using half adders and full adders. The

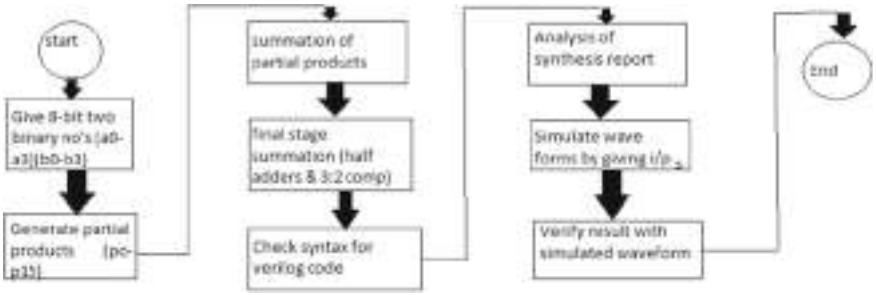

Fig. 3 Proposed algorithm

number of adders is used accordingly in a column-wise manner. If there are three bits in a column we will use a full adder for it and if there are two bits in a column then we will use half adder for it.

In this process, the carry-out of the previous adder will be treated as the carry input bit of the present adder. Hence, the proposed algorithm for the reduction process of WTM is shown in Fig. 3.

In conventional Wallace tree multiplier (WTM), the strategy is given in Eq. (1) [7] as

$$\begin{aligned} &P_j + 1 = 2\left[P_j/3\right] + P_j \bmod 3 \\ &P0 = N = 9,\ P1 = 6,\ P2 = 4,\ P3 = 3,\ P4 = 4. \end{aligned} \tag{1}$$

3 Compressor

A compressor is an adder that takes bits of the same weight and adds them to produce the sum signals. Compressors are mostly used for reducing and accumulating inputs to the smaller number of inputs in a manner that less number of partial products is obtained in the first stage. The main application of compressors within a multiplier is that a huge number of partial products is reduced concurrently. There are several types of compressors used in the multiplier to speed up multiplication. Carry signals are required if variables of sum input ($\sum$inputs) are greater than the sum of variables of output ($\sum$outputs).

The m:2 compressors are mostly used due to their high bit-rate compression. It is well described in [7, 8] that show m:3 compressors accelerate the phase of partial product reduction.

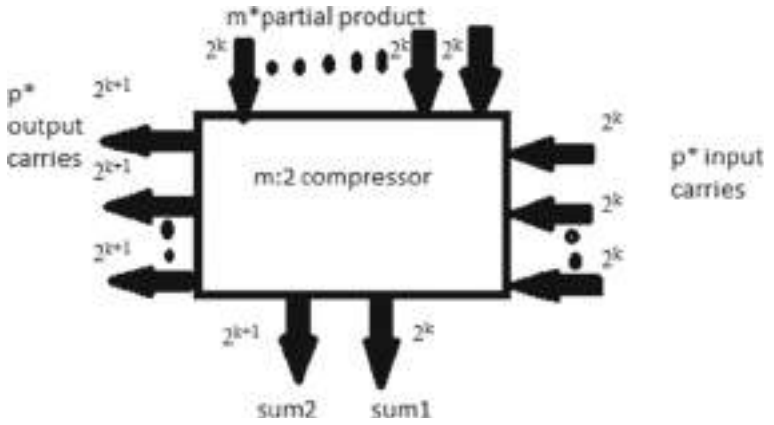

Fig. 4 The basic structure of an m:2 compressor

4 m:2 Compressors

The basic structure of an m:2 compressor is shown in Fig. 4, where the weights of the partial products obtained are indicated differently. It takes m equally weighted input signals and returns two main outputs as sum1 and sum2. In this, m:2 compressor takes p inputs of different weights and gives outputs of different weights [9].

$$\sum_{i=1}^{2} outputs + \sum_{i=1}^{p} output\ carries = \sum_{i=1}^{m} partial\ products + \sum_{i=1}^{p} input\ carries \tag{2}$$

$$2^k + 2^{k+1} + p * 2^{k+1} = (m + p) * 2^k \tag{3}$$

$$(2p + 3) * 2^k = (m + p) * 2 \tag{4}$$

$$p = m - 3p \geq 0 \tag{5}$$

Equation (2) demonstrates p = m − 3.

5 Compressor Implementation

If a column has one partial product then it is shifted to the next stage without any carry. But on the other hand, a half adder has one significant drawback [10]. Therefore, half adder has no input for the carry-out of the previous adder. Hence, to overcome this

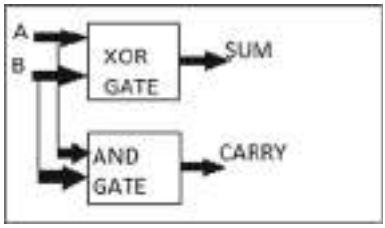

Fig. 5 Logic diagram of half adder

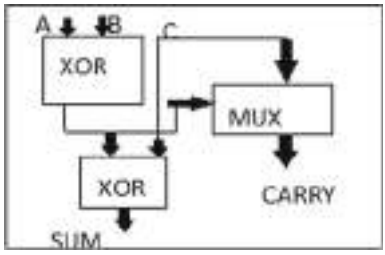

Fig. 6 Logic diagram of 3-2 compressor

drawback we require a combinational circuit that takes three inputs A, B, C (carry inputbit) from the previous adder and we named it a full adder (Figs. 5 and 6).

A full adder uses three inputs, each of one bit to perform the addition operation. In full adder, the three bits of inputs are to refer as an operand, and output is known as sum and carry [10–12].

5.1 3-2 Compressor

This compressor takes three inputs L_1, L_2, and L_3 that generate outputs as sum and carry [13, 14].

The basic conventional architecture of 3-2 compressor is given in Fig. 7. The basic equation of 3-2 compressor is given by Eqs. (6)–(8) (Figs. 8, 9 and 10)

$$L_1 + L_2 + L_3 = \text{sum} + 2 * \text{carry} \tag{6}$$

The 3-2 compressor output equation states are as follows:

$$\text{Sum} = L_1 \hat{} L_2 \hat{} L_3 \tag{7}$$

$$\text{Carry} = (L_1 \hat{} L_2) * L_3 + (L_1 \hat{} L_2)' * L_1 \tag{8}$$

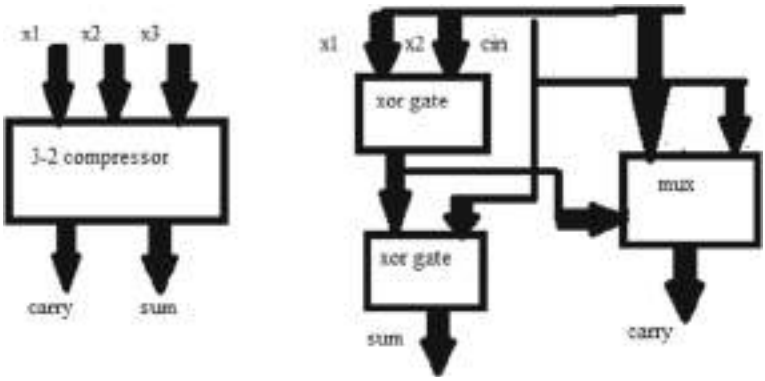

Fig. 7 **a** Symbol of 3-2 compressor. **b** Basic diagram of 3-2 compressor

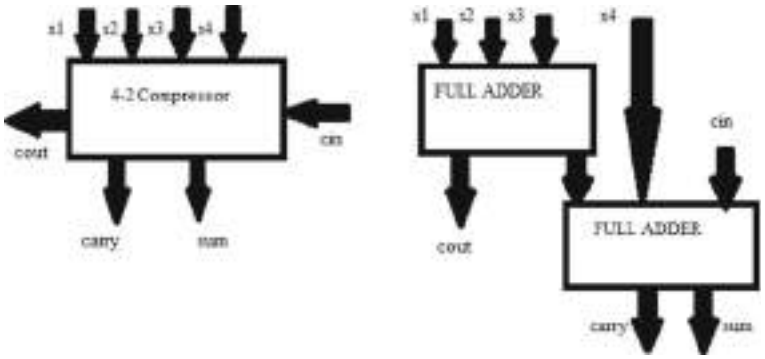

Fig. 8 Basic diagram of 4-2 compressor

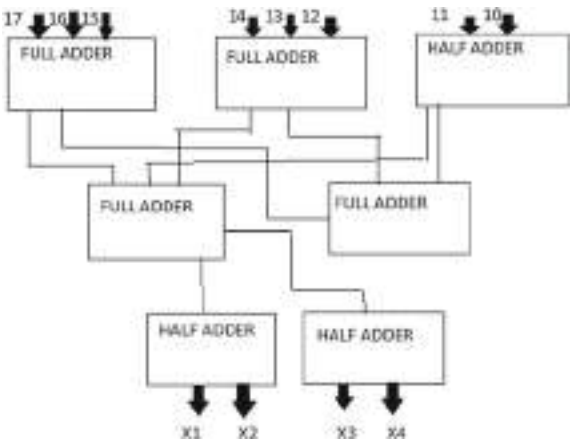

Fig. 9 (8-4) compressor design

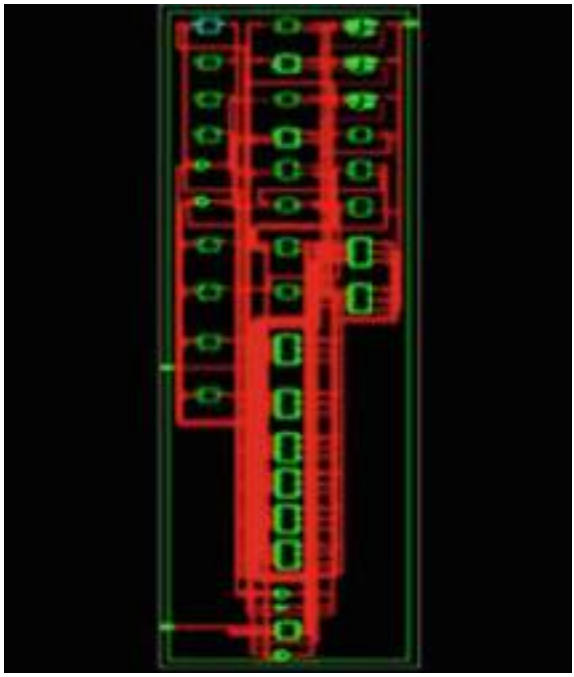

Fig. 10 RTL schematic diagram of 8 × 8-bit WTM using 8-4 compressor

5.2 4-2 Compressor

This compressor has four inputs T_1, T_2, T_3, and T_4, and outputs sum and carries along with carry-input and carry-output as given in Fig. 11. The basic equations of 4-2 compressor are given in (15) and (16):

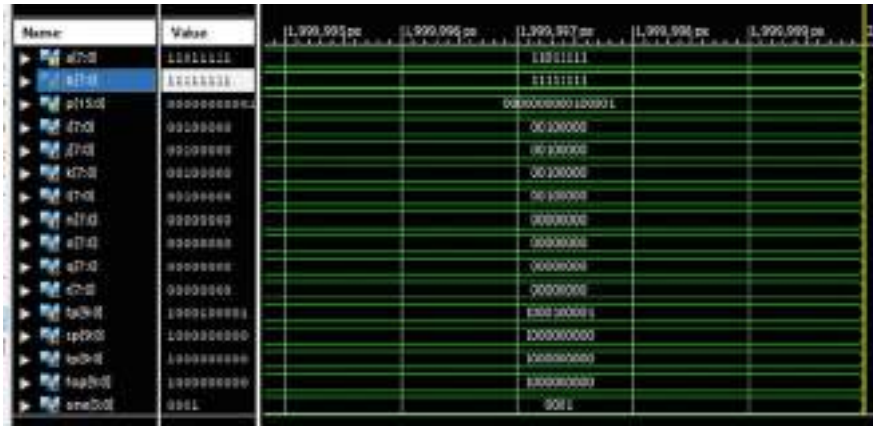

Fig. 11 Waveform of 8-bit Wallace tree multiplier using 8-4 compressor

$$T_1 + T_2 + T_3 + T_4 + C_{\text{in}} = \text{sum} + 2 * \left(C_{\text{arry}} + C_{\text{out}}\right) \tag{9}$$

where

$$\text{Sum} = T_1 \hat{} T_2 \hat{} T_3 \hat{} T_4 \hat{} C_{\text{in}} \tag{10}$$

$$C_{\text{out}} = (T_1 \hat{} T_2) * T_3 + (T_1 \hat{} T_2)' * T_1 \tag{11}$$

$$C_{arry} = (T_1 \hat{} T_2 \hat{} T_3 \hat{} T_4) * C_{\text{in}} + (T_1 \hat{} T_2 \hat{} T_3 \hat{} T_4)' * T_4 \tag{12}$$

5.3 8-4 Compressor

The proposed 8-3 compressor design is shown in Fig. 9, which illustrates a basic implementation of m:4 compressors. The performance result with a carry adder is shown in Table 1, indicating IOs, logic level, number of transistors used, number of LUTs and slices used in connections compared to the 4-2 compressor. The basic equations proposed in 8-4 compressor architecture are given in (17) and (18)

$$P_1 = J \hat{} K \hat{} L \tag{13}$$

$$P2 = ((JK)|(JL)|(KL)) \hat{} \left(M \hat{} N \hat{} O\right) \tag{14}$$

$$P_3 = ((JK)|(JL)|(KL)) \,\&\, (M \hat{} N \hat{} O)) \hat{} (MN)|(MO)|(MO) \tag{15}$$

Table 1 Performance comparison of Wallace tree multiplier with 8-4 compressor and without compressor (delay analysis and power analysis)

Parameters	Employing 8-4 compressor	Employing 4-2 compressor	Employing 3-2 compressor	Conventional WTM multiplier
Maximum combinational path delay (ns)	72.172	89.205	118.631	126.618
Logic delay (ns)	24.057	29.735	39.54	31.654
Route delay (ns)	48.115	59.47	79.091	94.964
Total delay (ns)	144.004	151.508	176.848	252.64
Leakage power (W)	0.03	0.03	0.05	0.05
Static power (W)	0.35	0.392	0.455	0.471
Total power (W)	0.380	0.422	0.505	0.521

$$P_3 = ((JK)|(JL)|(KL)) \,\&\, (M\hat{}N\hat{}O))\&(MN)|(MO)|(MO) \tag{16}$$

where

$$J = Q_0\hat{}Q_1 \tag{17}$$

$$M = Q_0\& Q_1 \tag{18}$$

$$K = Q_2\hat{}Q_3\hat{}Q_4. \tag{19}$$

$$N = ((Q_2 \,\&\, Q_3) \,|\, (Q_2 \,\&\, Q_4) \,|\, (Q_3 \,\&\, Q_4)) \tag{20}$$

$$L = Q_5\hat{}Q_6\hat{}Q_7 \tag{21}$$

$$O = ((Q_5 \,\&\, Q_6) \,|\, (Q_5 \,\&\, Q_7) \,|\, (Q_6 \,\&\, Q_7)) \tag{22}$$

The main advantages of 8-4 compressors are as follows:

- The partial product is reduced in number as compared to conventional WTM.
- Occupies a smaller area in comparison to a conventional multiplier.
- Occupies less number of logic gates.

6 Simulation

See Figs. 10, 11, 12, 13, 14 and 15, Table 1.

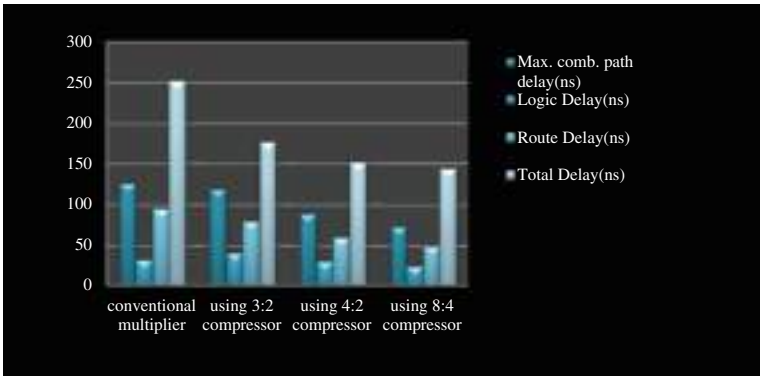

Fig. 12 Delay analysis of conventional and proposed multiplier

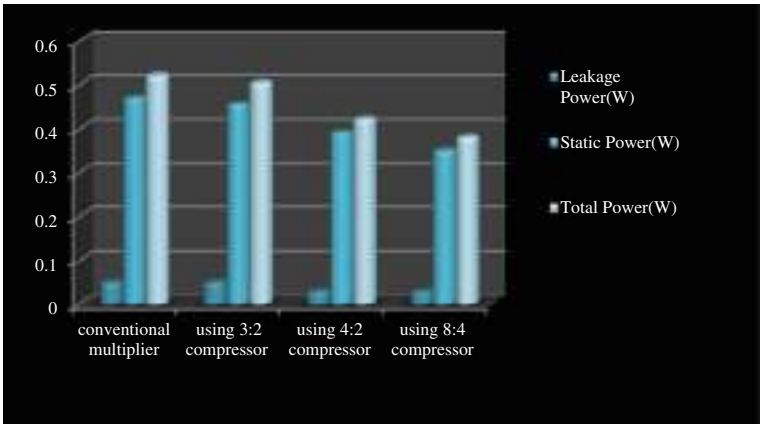

Fig. 13 Power analysis of conventional and proposed multiplier

Fig. 14 Total delay analysis of the conventional and proposed multiplier

7 Results and Discussion

The feasibility of compressors is authentic using Xilinx ISE 14.7 synthesis tool detailing them in VERILOG HDL language. The RTL schematic diagram of the 8-bit WTM is demoed in Fig. 11 and the simulation waveform of the 8-4 compressor is shown in Fig. 12. Table 2 illustrates various delay (ns) and power (W), respectively. The total delay in terms of logic delay, combinational path delay, and route delay is shown in Fig. 13.

The comparison of the result of WTM using compressors (8-4) as compared to WTM with (3-2, 4-2) compressors and conventional Wallace tree multiplier is elaborated in Figs. 13 and 14. In Fig. 13 the graphical representation of delay comparison is shown between the conventional multiplier and different multipliers with

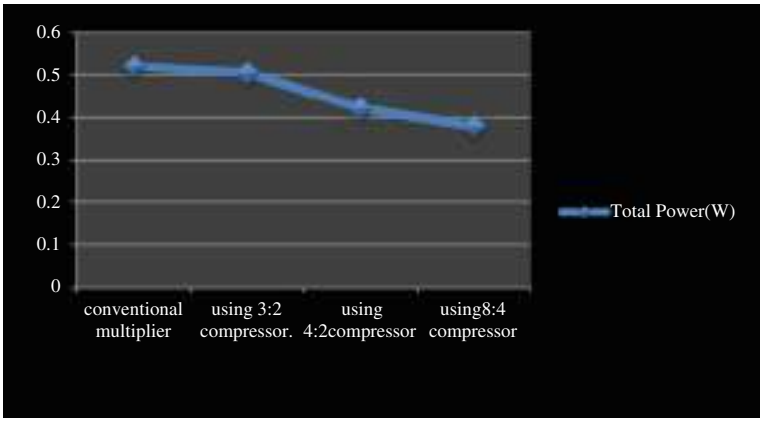

Fig. 15 Total power comparison for conventional multipliers with the proposed multiplier

compressors in terms of total delay which illustrates that using 8-4 compressor gives a minimum of delay for all above delays. Similarly, Fig. 14 elaborates the graphical representation of power dissipated with reference to leakage power, static power, and total power for multiplier with compressors and conventional multiplier. Therefore, the total delay as shown in Fig. 15 clearly shows that 8-4 compressor requires a delay of 24.7 ns which is a 43% reduction as compared to the conventional WTM. In Fig. 15 total power dissipation has been compared. It shows a reduction of 27% total power dissipation in the proposed WTM as compared to the conventional WTM.

8 Conclusion and Future Scope

The proposed 8 × 8 Wallace tree multiplier with 8-4 compressor requires 24.7 ns for completion of the multiplication operation. It thus achieved a 43% reduction in delay as compared to the conventional Wallace tree multiplier. The simulation result also proves that the proposed design has achieved a 27% reduction in total power dissipation [19].

In the DSP processor, multiplication is done by the multiplier. This paper presents a technique to modify a structure using Wallace tree multiplier with compression technique used to amplify the speed and reduce power and area and thus improving signal processing. The future scope of this paper is to apply an image processing algorithm and implement it on field-programmable gate arrays (FPGAs). The use of WTM in image processing is effectively used to reduce the total design time of a system. It is possible to carry out our research work further with WTM using compressors in the future to implement an FIR filter which can help in improving the performance of the filters at the receiver by reducing the area, power, and delay [20].

Technological systems are one of the poles of the advanced findings of the community that depends upon digital image processing. There is a wide range of uses for filtering in image processing. In a further research paper, a low-power design technique of FIR filter used for image processing which can be implemented using the clock gating technique will be considered.

References

1. H.R. Mahdiani, A. Ahmadi, S.M. Fakhraie, C. Lucas, Bio-inspired imprecise computational blocks for efficient VLSI implementation of soft-computing applications. IEEE Trans. Circuits Syst. **5**, 850–862
2. V.G. Oklobdzija, D. Villager. S.S. Liu, IEEE transactions on method for speed optimized partial product reduction andgeneration of fast parallel multipliers using an algorithmic approach (IEEE). **4**, 249–306 (2019)
3. S. Vaidya, D. Dandekar, Delay-power performance comparison of multipliers in VLSI design circuit. Int. J. Comput. Netw. Commun. (IJCNC) **2**, 440–690 (2019)
4. V. Gupta, D. Mohapatra, S.P. Park, A. Raghunathan, K. Roy, Impact IMPrecise adders for low-power approximate computing, in *International Symposium on Low Power Electronics and Design (ISLPED)*, vol. 2 (2019), pp. 450–553
5. D. Baran, M. Aktan, V.G. Oklobdzija, Energy-efficient implementation of parallel multipliers with improved compressors. IEEE Trans. Electron. Des. (IEEE) **2**, 147–152 (2018)
6. M.H. Rashid, IEEE Trans. Power Electron. Circuits Dev. Appl. Pearson Education Inc. (IEEE) **5**, 1600–2400 (2017)
7. M. Margala, N.G. Durdle, Low-power low-voltage 4–2 compressors for VLSI applications, in *Proceedings IEEE Alessandro Volta Memorial Workshop Low-Power Design (IEEE),* 15–19 Oct 2015*,* vol. 3 (2015), pp. 2600–3200
8. Y.-H. Chen, An accuracy adjustment fixed-width array multiplier based on multilevel conditional probability. IEEE Trans. Very Large Scale Integr. (VLSI) Syst. (IEEE) **23**, 1800–1890 (2015)
9. M.D. Ercegovac, T. Lang, Digital arithmetic. Trans. Digit. Arith. Mult. (Elsevier). **16**, 1100–1354 (2013)
10. S.R. Rijal, S.G. Mungale, Design and implementation of 8*8 truncated multiplier on FPGA. Int. J. Sci. Res. Publ. (IJSRAT) **3**, 2200–3100 (2012)
11. A. Dandapat, P. Bose, S. Ghosh, P. Sarkar, D. Mukhopadhyay, A 16*16 bit binary multiplier using high speed compressors. Int. J. Electr. Comput. Syst. Technol. (IJECT) **4**, 234–339 (2011)
12. K. Prasad, K. Parhi, Low power 4–2 and 5–2 compressors, in *Proceedings of the Conference Record of the 35th Asilomar Conference on Signal and Systems and Computer*s, vol. 5 (IEEE Explore Press, 2011), pp. 129–133
13. Z. Wang, G.A. Jullien, W.C. Miller, A new design technique for column compression multipliers. IEEE Trans. (IEEE) **4**, 962–970 (2010)
14. D. Radhakrishnan, A.P. Preethy, Logic 4–2 compressor for high-speed multiplication, in *Proceedings 43rd IEEE Midwest Synopsis. Circuit System* (IEEE)*,* vol.3 (2010), pp. 1296–1299
15. S. Veeramachaneni, K.M. Krishna, L. Avinash, S.R. Puppala, and M.B. Srinivas, Novel architectures for high-speed and low-power 3-2, 4-2 and 5-2 compressors*,* in *Proceedings of 20th International Conference on VLSI Design (ICVD),* vol. 2 (2009), pp. 324–329
16. R. Menon, D. Radhakrishnan, High performance 5:2 compressors architectures, Circuits Dev. Syst. (IEEE) **153**, 447–452 (2008)
17. N.K. Gahlan, P. Shukla, J. Kaur, Implementation of Wallace tree multiplier using compressor. Int. J. Comput. Technol. Appl. (IJCT) **3**, 256–552 (2006)

18. M. Othman, M.A.M. Ali et al., High performance parallel multiplier using Wallace tree algorithm. Semicond. Electron. (IEEE) **3**, 433–436 (2005)
19. N. Nagdeve, V. Moyal, A. Fande, A simulation based evaluation of different compressors for fast multiplication. Int. J. Sci. Eng. Res. (IJSR) **3**, 250–256 (2004)
20. R.V.K. Pillai, D. Al-Khalili, and A.J. Al-Khalili, Energy delay analysis of partial product reduction methods for parallel multiplier implementation, in *International Symposium on Low Power Electronics and Design (ISLPED)*, vol. 23 (2003), pp. 201–204

Vital Signs Monitoring Using FMCW Radar for Different Body Orientations in the Presence of Random Body Movement

G. N. Rathna and Deepchand Meshineni

Abstract In this paper, the discussion is on non-contact vital signs monitoring using a frequency-modulated continuous-wave (FMCW) radar. Here, we analyze the phase of the intermediate frequency (IF) signal in detail. Any human or clutters exposed to the FMCW radar signal can reflect the chirp. The reflected chirp goes to the mixer to produce an IF signal. This paper deals with extracting vital signs such as breathing rate and heart rate from a subject who sits in front of the radar irrespective of the chest orientation toward the radar. The phase of the IF signal is processed to obtain the spectrum in the desired range-bin. The spectrum is further subjected to filtering and thresholding as will be detailed. Random body movements are detected, and those samples are discarded for the calculation of heart rate.

Keywords Vital signs · Breathe rate · Heart rate · FFT · Phase · Unwrapping · Chirp

1 Introduction

Non-contact vital-sign monitoring gains even more importance in the context of COVID-19. In this technique, one can continuously monitor vital signs by adhering to the protocols of social distancing [1]. Currently, millimeter-wave radars are used in medical, diagnostic applications to derive relevant information from reflected chirps [2–5]. This radar also has other applications in drowsiness detection, monitoring burn victims, and monitoring neonatal units, among others [6, 7]. In this work, we wish to extract information on vital signs using a millimeter-wave FMCW sensor that utilizes frequencies in the range of 76–81 GHz. We will process the unwrapped phase of the intermediate frequency (IF) signal for calculations.

G. N. Rathna (✉) · D. Meshineni
Department of Electrical Engineering, IISc, Bengaluru, India
e-mail: rathna@iisc.ac.in

D. Meshineni
e-mail: meshinenid@iisc.ac.in

S. Rawat et al. (eds.), *Proceedings of First International Conference on Computational Electronics for Wireless Communications*, Lecture Notes in Networks and Systems 329,
https://doi.org/10.1007/978-981-16-6246-1_42

Breathing and heartbeat activity will lead to the displacement of the chest cavity. The effect of heartbeat and breathe on the frequency of unwrapped phase of IF signal will be difficult to resolve in data capture of few seconds only [8–10]. Typically, these activities will take some time to settle down to a rhythm and then they discernibly change the frequency of the unwrapped phase of the IF signal. In this paper, we deal only with the phase of the IF signal at the selected range-angle-bin. In Sect. 3 we explain the step-by-step procedure for extracting vital signs from the reflected waves within the radar field. A chirp is generated by the synthesizer and is transmitted by the TX antenna. This signal interacts with the objects in its path and gives rise to multiple reflections that reach the receiver. The time taken for reflection to reach the receiver contains the distance information of the object from the radar viewpoint [11, 12].

2 Concept

The transmitted chirp is reflected by the objects in the surroundings and the RX antenna captures these reflected chirps and then relays them to the mixer for down-conversion. This also reduces the sampling_rate. The down-converted signal has a constant frequency w.r.t fast time-axis as shown in Fig. 1, where 'τ' is the round-trip delay and S is the slope value. The received chirp is also shown. Of interest to us is the IF signal [13, 14].

'Sτ' is the intermediate frequency. T = 2d/c; here 'd' is the distance between the radar and the object, and 'c' is the speed of light. The transmitted signal from the

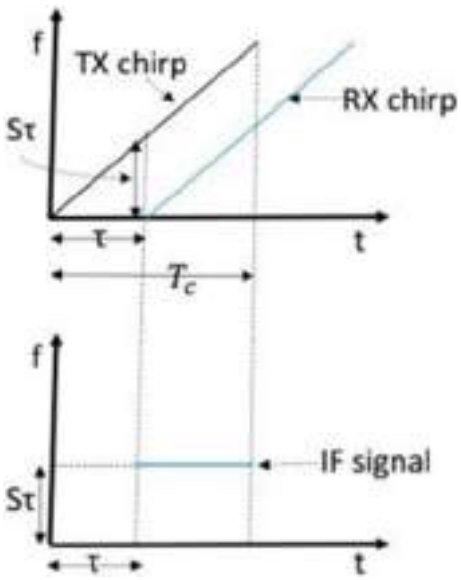

Fig. 1 IF signal after down-conversion

FMCW radar can be modeled as given in Eq. 1:

$$Y_T(t) = \leq_T \cos\left(2\pi f_c t + \frac{B}{T_c}\pi t^2 + \varphi(t)\right) \tag{1}$$

where fc is the starting frequency of the chirp, B is the bandwidth of the chirp, Tc is the chirp time duration, Tf is the fast time-axis ADC sampling interval, and Ts is the slow time-axis sampling interval.

The reflected signal from the object can be modeled as in Eq. 2:

$$Y_R(t) = \leq_T \cos\left(2\pi f_c(t - t_d) + \pi \frac{B}{Tc}(t - t_d)^2 + \varphi(t - t_d)\right) \tag{2}$$

where td = 2R(t)/c, R(t) is the distance between the radar and the object.

After sending the TX signal to the mixer, the resultant signal can be modeled as in Eq. 3:

$$Y(t) = A\cos(2\pi f_b t + \varphi_b(t) + \Delta\varphi_b(t)) \tag{3}$$

The phase noise $\Delta\theta(t)$ can be neglected for short-range applications. The IF signal after I/Q sampling can be modeled as the nth ADC sample and mth chirp, as described in Eq. 4:

$$Y[n, m] = A\cos\left[2\pi f_b n T_f + \left[\frac{4\pi R\sum n T_f + mT_s}{\lambda}\right]\right] \tag{4}$$

If there are multiple reflections for the transmitted chirps, then the mixer output will be the sum of the multiple reflected signals after being down-converted in the mixer. The single reflected chirp has a phase of Eq. 4 described in Eq. 5.

$$\varphi_b\left[\sum n T_f + mT_s\right] = \left[\frac{4\pi R\sum n T_f + mT_s}{\lambda}\right] \tag{5}$$

If only slow time-axis sampling is chosen for our application, the desired signal separates further away from the frequency band. Fast time-axis ensures that high-frequency data are sampled appropriately without any loss in the required data. The equations mentioned in this section of the paper are borrowed from references. Depending on the sampling, the time-axis can be chosen [15–17].

Since chest displacement is of smaller magnitude (<10 mm) and low frequency (<4 Hz), the change in fast time (chirp time) is negligible. So, it is sufficient to check the phase values for the chirp time interval, then this means whenever chirp touches the chest of the human unless the complete chirp is reflected from the chest, the distance between the chest and the radar is constant, i.e., the chest is stationary at

the starting time of the chirp and ending time of the chirp. So, we measure phase for each chirp only once w.r.t to slow time-axis (number of chirps per second); therefore,$\varphi_b(mT_s) = \frac{4\pi R_0}{\lambda} + \frac{4\pi R(mT_s)}{\lambda}$, where R0 is a constant [15–17].

3 Signal Acquisition Parameters

The starting frequency of the chirp used is 77 GHz and the radar transmits 20 chirps/second, in which each chirp has a duration of 50 μs and fast time-axis sample rate is 2 MSps. The slow time-axis sampling rate must satisfy Nyquist criteria, and the maximum frequency of interest that the vital sign contains is 4 Hz. It is ideal to take sampling rate Fs >8 Hz. We choose Fs = 20 Hz [18].

4 Vital Signs Estimation

The output of the mixer is used to estimate vital signs. The first step we use to estimate vital signs is by performing FFT across all the transmitter and receiver pairs. The frequency where the maximum peak occurs is proportional to the distance between the radar and the object. After selecting range-angle-bin, we calculate the phase of each desired range-angle-bin peak in different time intervals (slow axis time intervals). If the variation of the phase exceeds a certain threshold, we select it as a valid range-angle-bin [19, 20]. In this way, we can eliminate reflections due to static clutter and make clutter-resistant estimation. In Fig. 2 the initial subject orientation and the corresponding unwrapped phase are shown.

In Fig. 3, we can see the representation of an unwrapped phase signal and its frequency along with the differential phase signal. Observe the waveform in Fig. 3d: the vertical line separates the heartbeat signal into two segments. The segment to the right of the line is dominated by body movement. Figures 4, 5 and 6 show the

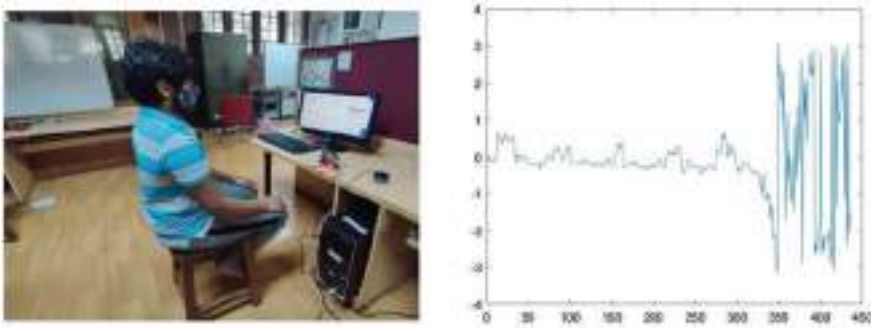

Fig. 2 Subject orientation and extracted phase

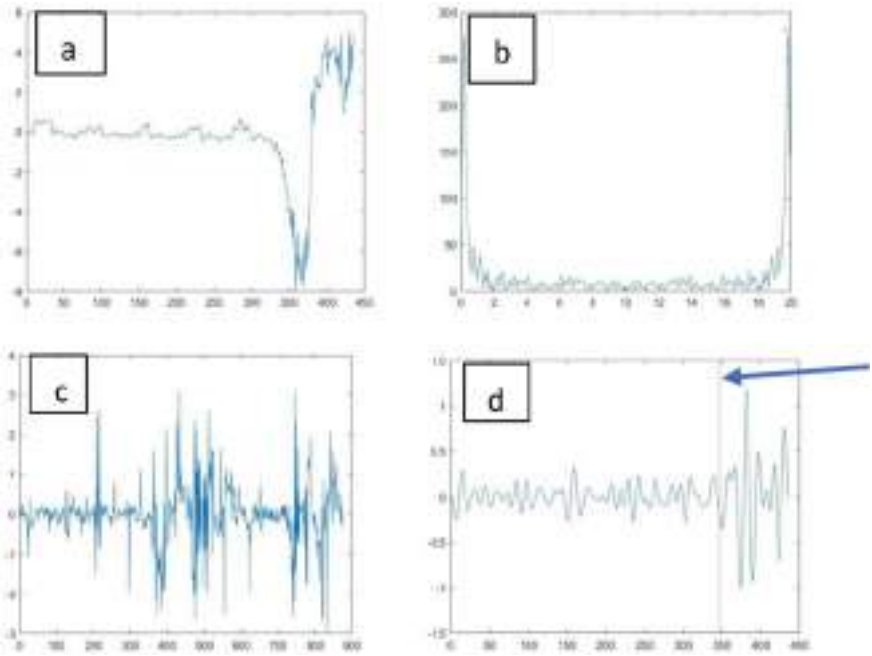

Fig. 3 Unwrapped **a** phase signal, **b** frequency response of unwrapped signal, **c** differential phase signal, **d** heartbeat signal

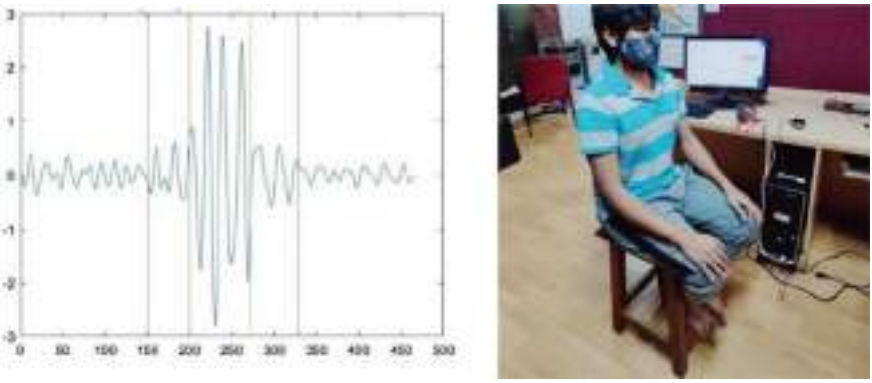

Fig. 4 Left profile orientation

subject-oriented in different directions to FMCW radar. The waveform captures the minor and larger body movements as is depicted by the different segments separated by the vertical lines. It is highlighted by the pointing arrow in Fig. 3d.

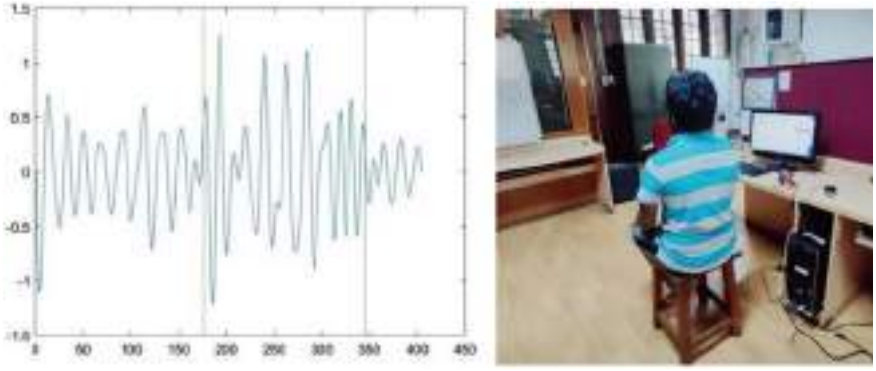

Fig. 5 Right profile orientation

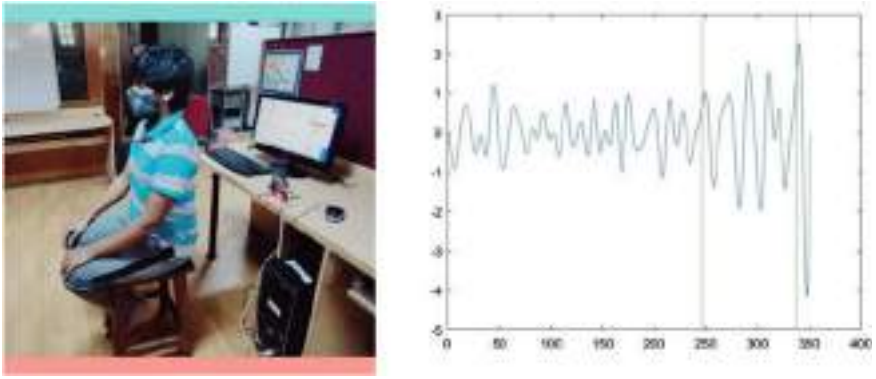

Fig. 6 Back profile orientation

First, we compute the phase of the intermediate frequency (IF) signal and then we unwrap it. After successfully unwrapping the phase, to remove phase drifts and in suppressing breathing, phase sample difference is computed.

Then the IIR bandpass filter is applied for the breathing region spectrum [0.1–0.5] Hz and cardiac region spectrum [0.8–4.0] Hz. Then a statistical-based segment approach is used for computing random body movement, i.e., we define a window of user-defined size and then we compute RMS values of signal for each window. The vertical lines are drawn where the maximum change in RMS occurs. In Fig. 3d, the line separates the heartbeat signal and heartbeat with random body movement. Here the subject is subjected to move randomly within the same range bin. In Fig. 4 waveform, we can see four change points in heartbeat signal out of five segments: first and last are due to a heartbeat; the second and third segment has random body movement; and the second and fourth segment has small body movement compared to the third segment. Similarly, in Fig. 5, the second segment has random body movement. In Fig. 6, the second and third segment has random body movement;

therefore, while computing heart rate we can discard the segment which is distorted with body movement.

As we know that the number of peaks per minute in the heart waveform is heart rate and the number of peaks per minute in the breathing waveform is called breathing rate, appropriate interpeak distance should be calculated from both breathing and heart rate waveforms Minimum interpeak distance for breathing signal is 1/fbmTs where fbm is the maximum frequency breathing spectrum. Ts is slow time-axis sampling rate.

The maximum interpeak distance for breathing signal is 1/fbsTs, where fbs is the minimum frequency in the breathing spectrum and maximum interpeak distance for heartbeat signal is 1/fhsTs where fhs is the minimum frequency in the cardiac spectrum. The minimum interpeak distance for the heartbeat signal is 1/fhmTs, where fhm is the maximum frequency in the cardiac spectrum.

The primary reason for taking the unwrapped phase is because the phase function computes the four-quadrant wrapped phase in [− ,] range. If the difference between two successive phase samples is greater than then the phase sample is subtracted by 2 . Similarly, if the difference between successive samples is less than − then we add 2 .

While analyzing the cardiac spectrum or breathing spectrum, if there is a single dominant peak at any frequency then the resultant waveform would be approximately sinusoidal. Here, we easily calculate the heart rate and breathing rate, i.e., the number of peaks per second is equal to the dominant frequency. Baseline-wandering cannot be seen in the waveforms because the subject was in a fixed position from the radar and was performing the breathing task in a stable environment [21].

5 Future Scope

1. Data collection to be done in a different scenario, to simulate real-time use-case.
2. Bandpass filter is to be designed.
3. Threshold on the amplitude of reflected waves to detect the prominent peak needs to be calculated based on the type of data in the context of recording environment.
4. Filtered waveform and the unwrapped phase waveform are to be correlated to find the similarity index among the waves.
5. A physical unit of acquisition board loaded with optimized parameters and code is to be installed at the entrance of major buildings to monitor the visitors for their vital parameters.

6 Conclusion

FMCW radar is a good choice for acquiring reflected waveforms and the same is used for extracting valuable information such as breathing rate and heart rate. An optimized signal processing chain with the right choice of bandpass filtering, accurate thresholding, and high correlation can provide the values of vital parameters with improved accuracy. This paper highlights the FFT operation on the received waveform, the resulting spectrum, and subsequent extraction steps for obtaining the heart rate and breathing rate waveforms. The unwrapped phase signal can also be averaged to remove certain undesirable higher frequency components. We must ensure that the system is not subjected to power-line interference by provisioning an on-board power supply. The work includes mentioning minimum peak distance, detecting random body movements, accommodating different orientations of the subject as compared to reference [22] among other such works published on the same topic.

References

1. A. Ahmad, J.C. Roh, D. Wang, A. Dubey, Vital signs monitoring of multiple people using a FMCW millimeter-wave sensor. in *2018 IEEE Radar Conference (RadarConf18)* (2018), pp. 1450–1455. https://doi.org/10.1109/RADAR.2018.8378778
2. M. Alizadeh, Remote vital signs monitoring using a mm-wave FMCW radar. p. 102, 2019
3. M. Alizadeh, G. Shaker, J.C.M. De Almeida, P.P. Morita, S. Safavi-Naeini, Remote monitoring of human vital signs using mm-Wave FMCW Radar. IEEE Access **7**, 54958–54968 (2019). https://doi.org/10.1109/ACCESS.2019.2912956
4. L. Ding, M. Ali, S. Patole, A. Dabak, Vibration parameter estimation using FMCW radar Texas instruments, Dallas, Texas university of Texas at Dallas, Richardson, Texas. Icassp **2016**(1), 2224–2228 (2016)
5. G.W. Fang, C.Y. Huang, C.L. Yang, Simultaneous detection of multi-target vital signs using EEMD algorithm based on FMCW radar. in *IEEE MTT-S 2019 International Microwave Biomedical Conference (IMBioC 2019)—Proceedings* (2019), pp. 1–4. https://doi.org/10.1109/IMBIOC.2019.8777810
6. M. He, Y. Nian, Y. Gong, Novel signal processing method for vital sign monitoring using FMCW radar. Biomed. Signal Process. Control **33**, 335–345 (2017). https://doi.org/10.1016/j.bspc.2016.12.008
7. X. Hu, T. Jin, Short-range vital signs sensing based on EEMD and CWT using IR-UWB radar. Sensors (Switzerland) **16**(12), (2016). https://doi.org/10.3390/s16122025
8. H. Lee, B.H. Kim, J.K. Park, S.W. Kim, J.G. Yook, A Resolution enhancement technique for remote monitoring of the vital signs of multiple subjects using a 24 GHz bandwidth-limited fmcw radar. IEEE Access **8**, 1240–1248 (2020). https://doi.org/10.1109/ACCESS.2019.2961130
9. J. Liu, Y. Wang, Y. Chen, J. Yang, X. Chen, and J. Cheng, Tracking vital signs during sleep leveraging off-the-shelf WiFi. in *Proceedings of the 16th ACM International Symposium on Mobile Ad Hoc Networking and Computing* (2015), pp. 267–276. https://doi.org/10.1145/2746285.2746303
10. J. M. Munoz-Ferreras, Z. Peng, R. Gomez-Garcia, and C. Li, Random body movement mitigation for FMCW-radar-based vital-sign monitoring. in *BioWireleSS 2016—Proceedings, 2016 IEEE Topical Conference on Biomedical Wireless Technologies, Networks, and Sensing Systems (BioWireleSS)* (2016), pp. 22–24. https://doi.org/10.1109/BIOWIRELESS.2016.7445551

11. J. M. Munoz-Ferreras, J. Wang, Z. Peng, R. Gomez-Garcia, and C. Li, From Doppler to FMCW radars for non-contact vital-sign monitoring. in *2018 2nd URSI Atlantic Radio Science Meeting (AT-RASC)* (2018), pp. 2018–2021. https://doi.org/10.23919/URSI-AT-RASC.2018.8471575
12. J.M. Muñoz-Ferreras, J. Wang, Z. Peng, C. Li, R. Gómez-García, FMCW-radar-based vital-sign monitoring of multiple patients. in *IEEE MTT-S International Microwave Biomedical Conference (IMBioC) 2019—Proceedings* (2019), pp. 2019–2021. https://doi.org/10.1109/IMBIOC.2019.8777845
13. Z. Peng et al., A portable FMCW interferometry radar with programmable Low-IF architecture for localization, ISAR imaging, and vital sign tracking. IEEE Trans. Microw. Theory Tech. **65**(4), 1334–1344 (2017). https://doi.org/10.1109/TMTT.2016.2633352
14. G. Sacco, E. Piuzzi, E. Pittella, S. Pisa, An FMCW radar for localization and vital signs measurement for different chest orientations. Sensors (Switzerland) **20**(12), 1–14 (2020). https://doi.org/10.3390/s20123489
15. A. Shrestha, H. Li, J. Le Kernec, F. Fioranelli, Continuous human activity classification from FMCW Radar with Bi-LSTM Networks. IEEE Sens. J. **20**(22), 13607–13619 (2020). https://doi.org/10.1109/JSEN.2020.3006386
16. E. Turppa, J.M. Kortelainen, O. Antropov, T. Kiuru, Vital sign monitoring using fmcw radar in various sleeping scenarios. Sensors (Switzerland) **20**(22), 1–19 (2020). https://doi.org/10.3390/s20226505
17. K. van Loon et al., Wireless non-invasive continuous respiratory monitoring with FMCW radar: a clinical validation study. J. Clin. Monit. Comput. **30**(6), 797–805 (2016). https://doi.org/10.1007/s10877-015-9777-5
18. D. Wang, S. Yoo, S.H. Cho, Experimental comparison of ir-uwb radar and fmcw radar for vital signs. Sensors (Switzerland) **20**(22), 1–22 (2020). https://doi.org/10.3390/s20226695
19. F.K. Wang, T.S. Horng, K.C. Peng, J.K. Jau, J.Y. Li, C.C. Chen, Detection of concealed individuals based on their vital signs by using a see-through-wall imaging system with a self-injection-locked radar. IEEE Trans. Microw. Theory Tech. **61**(1), 696–704 (2013). https://doi.org/10.1109/TMTT.2012.2228223
20. P. Wang et al., Method for distinguishing humans and animals in vital signs monitoring using IR-UWB radar. Int. J. Environ. Res. Public Health **16**(22), 1–21 (2019). https://doi.org/10.3390/ijerph16224462
21. S. Wang et al., A novel ultra-wideband 80 GHz FMCW radar system for contactless monitoring of vital signs. in *37th Annual International Conference of the IEEE Engineering in Medicine and Biology Society (EMBC)* (Novem, 2015), pp. 4978–4981. https://doi.org/10.1109/EMBC.2015.7319509
22. G. Sacco et al., Vital signs monitoring for different chest orientation using an FMCW radar. in *Proceedings of URSI GASS* (Rome, Italy, 2020)

A Comparative Approach for Opinion Spam Detection Using Sentiment Analysis

Ashish Singh and Kakali Chatterjee

Abstract The most important sources of information about the products or services are online reviews. People trust online review comments while purchasing electronics items, hotel booking, college admission, movies, etc. Sometimes it has been intentionally written by the fake reviewers for monetary gain, business rivalry, etc. Many times, these messages were found fake after the judgments. The fake reviews transmission has a significant social and economic impact on society. Hence, an accurate detection mechanism must be there to identify fake reviews. In this paper, the opinion spam detection mechanism is proposed using sentiment analysis (SA) for content-based applications. In this technique, the sentiment score of the sentences is computed. It is detected as fake or not fake, depending on the sentiment score of reviews. The work also proposed a Long Short-Term Memory (LSTM) based deep learning approach to identify the topic of fake reviews. Combining these two approaches provides a more accurate opinion spam detection rate compared to other existing models. On the benchmark "Deceptive Opinion Spam Corpus v1.4" dataset is used. Our model's accuracy is 92.46% with 9.23% of the false acceptance rate and 5.50% of the false rejection rate.

Keywords Sentiment analysis · Fake reviews · Opinion spam detection · Deep learning

1 Introduction

Today's digital world is mainly based on the Internet, which offers various services such as commercial, cultural, political, and educational services. The information

A. Singh (✉)
School of Computer Engineering, KIIT Deemed To Be University, Bhubaneswar, Odisha 751024, India

K. Chatterjee
Department of Computer Science and Engineering, National Institute of Technology, Patna, Bihar 800005, India
e-mail: kakali@nitp.ac.in

S. Rawat et al. (eds.), *Proceedings of First International Conference on Computational Electronics for Wireless Communications*, Lecture Notes in Networks and Systems 329,
https://doi.org/10.1007/978-981-16-6246-1_43

collected from the Internet or any other sources is not entirely trusted. People spend more time on the e-commerce site to purchase the products because it is more effective to visualize the product in different ways. Online reviews are often shared as blogs, articles, or tweets on numerous Internet channels such as e-commerce sites, discussion boards, review pages, news sites, or other social networking websites [8]. But sometimes, this kind of reviews is not authentic. The customer can write a review of the product to express its opinion and share the experiences of the product or services online. Customers go through all the product reviews before purchasing the product. Hence, illegal activities such as writing fake reviews, fake comments, fake social network postings, fake blogs, deceptive messages, and bogus reviews that try to mislead readers are known as "Opinion Spam".

Online reviews can be expressed in various ways, such as text, audio, video, image, and gesture. Fake reviews can be content based [1], metadata based [6], and user based [20]. User-based detection is mainly concern with tracking bots and spam, bio information, etc. Metadata-based detection is concerned with device sources, friends, and followers in the social network, etc. This paper deals with content-based detection techniques containing text, images, GIFs, and videos under content-based fake reviews. Most of the content is in text format. Thus, the work mainly focuses on text content-based applications.

The identification of emotions can be performed as positive, negative, and neutral in the text analysis approach [13]. SA has been performed primarily on three levels: Document, Sentence, and Aspect level [14]. The contributions of the work in this paper are as follow:

- The work proposed a fake review detection model based on SA for content-based applications.
- The work also illustrated LSTM-based deep learning techniques for the detection of fake reviews.
- The model's performance is calculated by using different measurement metrics. The achieved results demonstrated better performance when the detection model uses LSTM-based deep learning approach.

The rest of the entire paper is structured as follows: the literature works are discussed in Sect. 2. The proposed work related to SA and LSTM-based deep learning is described in Sect. 3. The implementation and result analysis of the proposed model are discussed in Sect. 4. Finally, conclude the work in Sect. 5.

2 Literature Work

Opinion spam detection has become a major issue at present to validate online opinions and obtain consumer confidence. Jindal et al. [7] led research on the issue of opinion spam by analyzing the dataset of Amazon product reviews. Researchers have described opinion spam detection in three different ways: opinion spam [21], opinion spammer [4], and network of opinion spammer [23]. There are various effective spam

features, such as review-content-based features [7], reviewer behavior-based features [22], and review-reviewer network-based features [2], that have been used to detect spam reviews. Some other methods used by the researchers include machine learning techniques [19], and Natural Language Processing (NLP) [12] that have provided good results to detect false reviews.

3 Proposed Model

The work developed LSTM-based deep learning model that is shown in Fig. 1. The proposed SA model has consisted of four phases: fetch the dataset, identification of the topic and tokenizing the content, calculate sentiment score [5], and visualization of the result in terms of score. In this process, TextBlob and VADER libraries [3] are used. The working of the proposed model is presented in Algorithm 1.

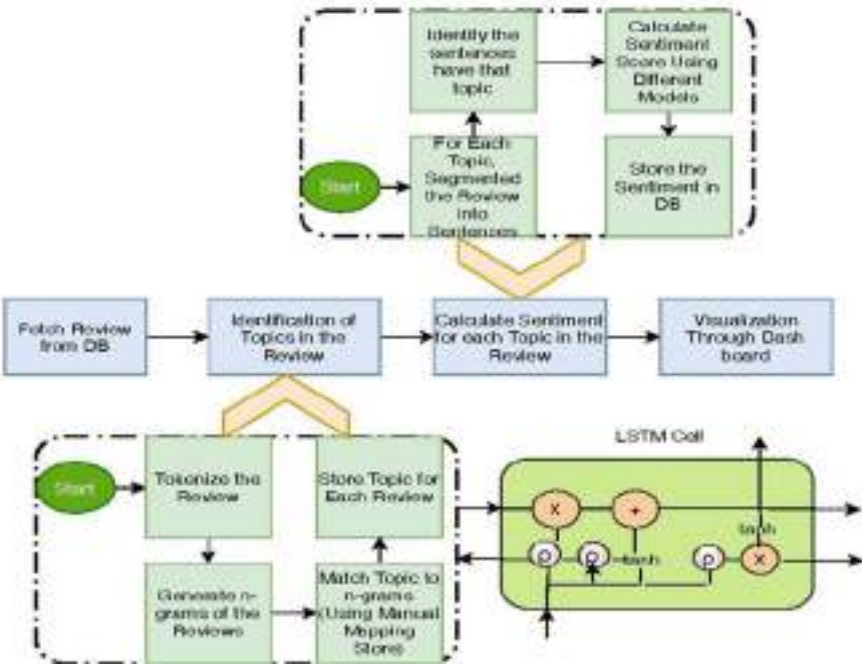

Fig. 1 Architecture of proposed SA-based model

Algorithm 1 Algorithm for Sentiment Analysis

```
INPUT: Fetch Reviews
OUTPUT: Visualization of Result Based on Sentiment Score.
procedure
    Fetch the Reviews from Data Base
    Identification of the Topic Using LSTM Model
    { Load the labelled data set for training
    Convert Dictionary words into embedded vector using n-gram technique [18]
    Design LSTM model for fake review [17]
    Tune the Parameters of model
    Training and Testing the Model for the Data Set
    Evaluate the Performance of the model }
    Now, Calculate Sentiment Score
    hui.li.postive = scan('database/opinion-lexi-English/pos-words.txt', what = 'char',comment.char=';')
    hui.li.neg = scan('database/opinion-lexi-English/neg-words.txt',what = 'char',comment.char = ';')
    positive.word = char(hui.li.positive)
    negative.word = char(hui.li.negative)
    sentiment.score = fun(sentences, positive.word, negative.word, progress='none') {
    require(plyr)
    require(stringr)
    sentiment.score = laply(sentences, fun(sentence, positive.word, negative.word)
    sentence = sub('[[:punction:]]', '', sentence)
    sentence = sub('[[:ccntrol:]]', '', sentence)
    sentence = sub('d+', '', sentence)
    sentence = lower(sentence)
    word.list = str_split(sentence, 's+')
    positive.match = match(word, positive.word)
    negative.match = match(word, negative.word)
    positive.match = !is.ya(positive.match)
    negative.match = !is.ya(negative.match)
    sentiment.score = sum(positive.match)-sum(negative.match)
    return(sentiment.score)}
    (positive.word, negative.word, progress = progress )
    scores.ss = data.frame(score=scores, text=sentences)
    return(scores.ss)
    Visualise the Result Based on Sentiment Score
```

4 Implementation Results and Performance

The work created a model for the identification of fake reviews. This prototype is developed using Python language (version 3.7.7) on a Jupyter notebook (version 6.0.3) by using Keras library. Keras is an open-source API for the processing of neural networks and deep learning. It can run Tensorflow on top of API. The work is implemented our model on four dataset which is downloaded from different sources.

Table 1 Dataset description

Dataset	Year	Users	Hotels	Reviews
Dianping SequentialRec [9]	2019	6,16,331	10,979	38,68,306
Dianping SocialRec [11]	2015	1,47,918	11,123	21,49,675
Dianping SocialRec [10]	2014	11,352	10,657	5,01,472
Opinion Sspam [15, 16]	2011, 2013	40	20	1600 (Deceptive, Truthful, +ve, −ve)

- Dianping SequentialRec (2019) [9]: It consists of 6,16,331 customers, 10,979 restaurants, and 38,68,306 actions from April 2003 to November 2013 in Shanghai, China.
- Dianping SocialRec (2015) [11]: It consists 1,47,918 customers, 11,123 restaurants, and 21,49,675 actions from April 2003 to November 2013 in Shanghai, China.
- Dianping SocialRec (2014) [10]: It contains 11,352 users, 10,657 restaurants, and 5,01,472 actions from April 2003 to November 2013 in Shanghai, China.
- Deceptive Opinion Spam Corpus v1.4: It is created by Ott et al. [15, 16]. There are two forms of the dataset: Truthful Review and another is Deceptive Review. The dataset is also defined as per the sentiment review (Positive and Negative). For the experiment purpose, 70% of the dataset is used to train the model, and 30% of the dataset is used to test the model shown in Table 1.

The performance of our model is measured. It is based on Accuracy (Acc) Eq. 1, Precision (Pre) Eq. 2, Recall (Rec) Eq. 3, F-score Eq. 4, False Acceptance Rate (FAR) Eq. 5, and False Rejection Rate (FRR) Eq. 6. The computation mechanism is described in Table 2. The confusion metric is shown in Table 3 for the dataset [9–11, 15, 16].

The LSTM-based deep learning model is achieved Acc (92.46%), Pre (93.04%), Rec (94.49%), and F-Score (93.75%), FAR (9.23%), and FRR (5.50%) for the dataset [15, 16]. For the dataset [10], the acc is 87.16%, Pre is 88.96%, Rec is 90.52%, F-Score is 89.73%, FAR is 11.03%, and FRR is 9.47%. The dataset [11] gives 89.74% acc, Pre is 90.51%, Rec is 92.01%, F-Score is 91.25%, FAR is 13.43%, and FRR is 7.98%. For the dataset [9], acc is 90.34%, Pre is 92.13%, Rec is 90.06%, F-Score is 91.08%, FAR is 9.33%, and FRR is 9.93% which is shown in Table 4. The achieved result shows that the LSTM-based deep learning model has maximum Acc, Pre, Rec, F-Score, and minimum FAR and FRR in the case of "Deceptive Opinion Spam Detection" dataset. The LSTM-based deep learning model has achieved maximum improvement with respect to the NB model in terms of Acc (90.40%), Pre (80.66%), Rec (68.25%), F-Score (74.52%), FAR (78.16%), and FRR (87.45%) for the dataset [15, 16] that is shown in Table 5. The chart in Figs. 2, 3, 4 and 5 illustrates the comparative analysis of various algorithms. The performance of the LSTM-based deep learning model is evaluated on different dataset shown in Fig. 6. The achieved results say that the performance of the Deceptive opinion spam dataset [15, 16] is better than other dataset [9–11].

Table 2 Performance measurement metric

Evaluation metric	Detailed description	Used formula
Acc	Accuracy is the sum of *Tp* and *Tn* divided by Total value (*Tp*, *Tn*, *Fn*, *Fp*)	$Acc = \frac{T_p+T_n}{T_p+T_n+F_n+F_p}$ (1)
P re	Precision (Specificity) is the ratio of *Tp* to sum of *Tp* and *Fp*	$\Pr e = \frac{T_p}{T_p+F_p} * 100$ (2)
Rec	Recall (Sensitivity) is the ratio of *Tp* to sum of *Tp* and *Fn*	$\text{Rec} = \frac{T_p}{T_p+F_n} * 100$(3)
F-Score	F-Score (F1-Score) is the average weighted of *P re* and *Rec*. It is also called F-Measure	$F - Score = \frac{2*\Pr e*\text{Rec}}{\Pr e+\text{Rec}}$ (4)
FAR	It is the percentage of detection cases in which unauthorized users are wrongly accepted	$FAR = \frac{F_p}{F_p+T_n} * 100$ (5)
FRR	It is the percentage of detection cases in which authorized users are wrongly rejected	$FAR = \frac{F_n}{T_p+F_n} * 100$ (6)

5 Conclusion and Future Scope

SA is an area of research that analyzes people's beliefs, perceptions, or emotions against particular objects. The literature survey found many fake review identification methods, but the detection rate is not adequate. To resolve such issues, SA and LSTM based on deep learning techniques have been developed. For this, the datasets have been downloaded from various sources. The downloaded dataset is applied to the SA and LSTM models. SA has led to the development of better products and sound business management reviews. The work found that the LSTM-based deep learning model has performed better in terms of Acc, Pre, Rec, F-Score, FAR, and FRR than other pre-trained models. The result shows that FAR and FRR are less and Acc, Pre, Rec, and F-Score are high compared to the existing model. In the future, the work is extended to detect opinion spam in other types of information like images and videos. The model can be improved by using other deep learning models.

Table 3 Confusion metric for dataset

Classifier	Dianping SequentialRec [9]				Dianping SocialRec [11]				Dianping SocialRec [10]				Deceptive Opinion [15, 16]			
	Tp	Fp	Fn	Tn	Tp	Fp	Fn	Tn	Tp	Fp	Fn	Tn	Tp	Fp	Fn	Tn
NB	14,54,676	8,77,149	4,95,713	10,40,768	6,27,907	4,19,745	4,66,966	6,35,027	1,60,125	1,07,880	1,05,497	12,797	478	450	373	299
KNN	15,10,309	6,41,519	5,05,439	12,11,044	7,92,662	4,20,990	4,09,430	5,26,593	2,11,513	96,748	90,451	1,02,759	594	382	238	386
SVM	14,63,894	13,10,841	7,04,161	3,89,418	8,80,744	3,58,105	3,12,594	5,98,232	2,13,954	82,543	78,881	126,094	505	307	414	374
DT	15,53,227	6,14,698	4,62,239	12,38,142	9,10,119	3,75,945	2,40,794	6,22,814	2,20,417	75,175	73,462	1,32,418	619	234	320	427
RF	18,98,772	2,91,271	2,27,469	14,50,794	10,71,125	1,90,807	1,50,562	7,37,181	2,51,487	51,236	35,268	1,63,481	887	119	82	512
LSTM	19,10,634	1,62,997	2,10,682	15,83,993	11,51,703	1,20,623	99,934	7,77,415	2,81,501	34,932	29,456	1,55,501	910	86	53	569

Table 4 Performance metric for dataset

Classifier	Dianping SequentialRec [9]						Dianping SocialRec [11]						Dianping SocialRec [10]						Deceptive Opinion [15, 16]					
	Acc	Pre	Rec	F-Score	FAR	FRR	Acc	Pre	Rec	F-Score	FAR	FRR	Acc	Pre	Rec	F-Score	FAR	FRR	Acc	Pre	Rec	F-Score	FAR	FRR
NB(%)	64.50	62.38	74.58	67.63	45.73	25.41	58.75	59.93	57.34	58.60	39.79	42.65	57.45	59.74	60.28	60.00	45.74	39.71	48.56	51.50	56.16	53.72	60.08	43.83
KNN(%)	70.35	70.18	74.92	72.47	34.62	25.07	61.37	65.31	65.94	65.62	44.42	34.05	62.67	68.61	70.04	69.31	48.49	29.95	61.25	60.86	71.39	65.70	49.73	28.60
SVM(%)	71.73	67.52	78.98	72.80	34.95	21.10	68.80	71.09	73.80	72.41	37.44	26.19	67.81	72.16	73.06	72.60	39.56	26.93	54.94	62.19	54.95	58.34	45.08	45.04
DT(%)	72.16	71.64	77.06	74.25	33.17	22.95	71.31	70.76	79.07	74.68	37.64	20.92	70.36	74.56	75.00	74.77	36.21	24.99	65.39	72.56	65.92	69.08	35.04	34.07
RF(%)	86.59	86.70	89.30	87.98	16.71	10.63	84.12	84.87	87.67	84.24	20.56	12.32	80.75	83.07	87.70	85.32	23.86	12.29	87.45	88.17	91.53	89.81	18.85	8.84
LSTM(%)	90.34	92.13	90.06	91.08	9.33	9.93	89.74	90.51	92.01	91.25	13.43	7.98	87.16	88.96	90.52	89.73	11.03	9.47	92.46	93.04	94.49	93.75	9.23	5.50

Table 5 Improvement of LSTM model with respect to other models

Classifier	Dianping SequentialRec [9]					Dianping SocialRec [11]					Dianping SocialRec [10]					Deceptive Opinion [15, 16]				
	NB	KNN	SVM	DT	RF	NB	KNN	SVM	DT	RF	NB	KNN	SVM	DT	RF	NB	KNN	SVM	DT	RF
Acc(%)	40.06	28.42	25.94	25.19	4.33	52.75	46.23	30.44	25.84	6.68	51.71	30.08	28.54	23.88	7.94	90.40	50.96	68.29	41.40	5.73
Pre(%)	47.69	31.28	36.45	28.60	6.26	51.03	38.59	27.32	27.91	6.65	48.91	29.66	23.28	19.31	7.09	80.66	52.88	49.61	28.22	5.52
Rec(%)	20.76	20.21	14.03	16.87	0.85	60.46	39.54	24.67	16.37	4.95	50.17	29.24	23.90	20.69	3.22	68.25	32.36	71.96	43.34	3.23
F-Score(%)	34.67	25.68	25.11	22.67	3.52	55.72	39.06	26.02	22.19	8.32	49.55	29.46	23.60	20.01	5.17	74.52	42.69	60.70	35.71	4.39
FAR(%)	79.60	73.05	73.30	71.87	44.17	66.25	69.77	64.13	64.32	34.68	75.89	77.25	72.12	69.54	53.77	78.16	73.62	70.90	62.56	30.40
FRR(%)	60.92	60.39	52.94	56.73	6.59	81.29	76.56	69.53	61.85	35.23	76.15	68.38	64.83	62.10	22.95	87.45	80.77	87.79	83.86	37.78

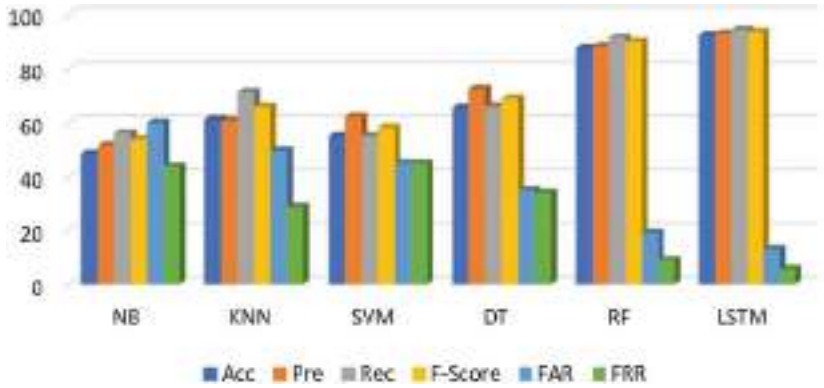

Fig. 2 Performance of dataset [16]

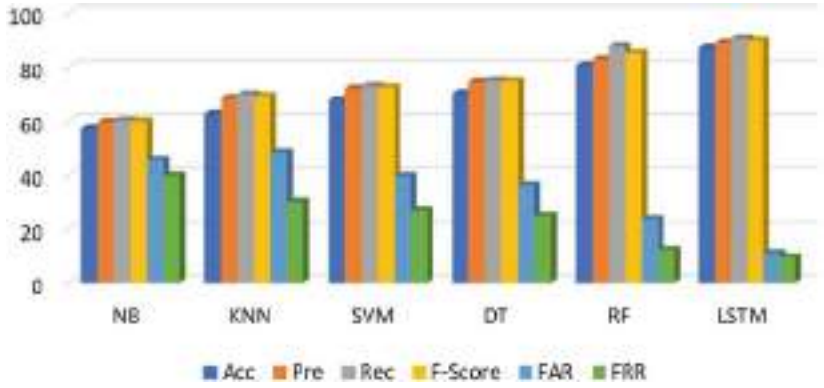

Fig. 3 Performance of dataset [10]

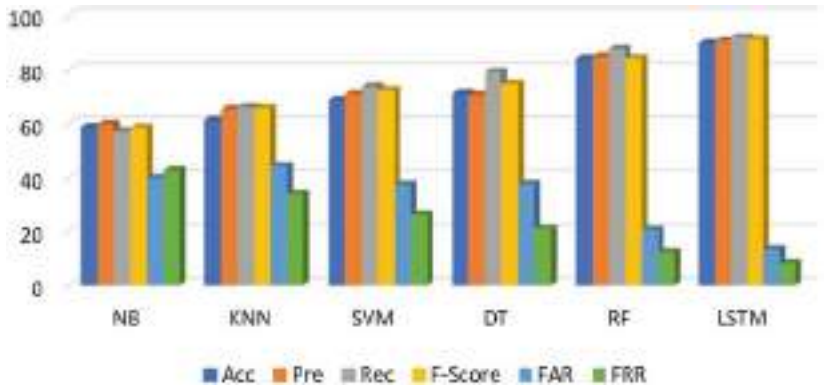

Fig. 4 Performance of dataset [11]

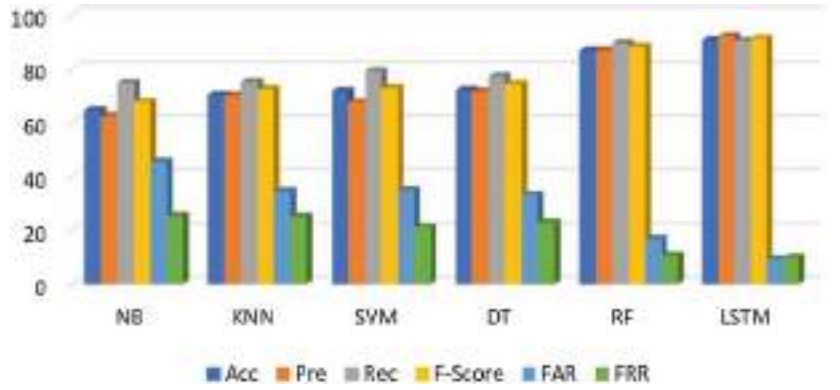

Fig. 5 Performance of dataset [9]

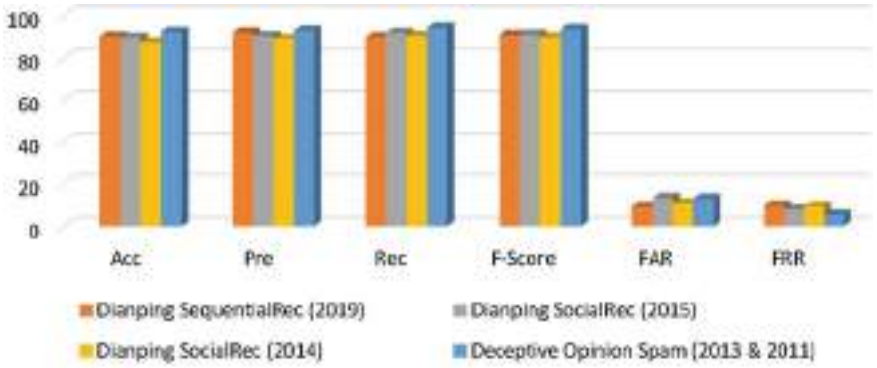

Fig. 6 Performance of LSTM model

References

1. O. Ajao, D. Bhowmik, S. Zargari, Fake news identification on twitter with hybrid cnn and rnn models. in *Proceedings of the 9th International Conference on Social Media and Society* (2018), pp. 226–230
2. L. Akoglu, R. Chandy, C. Faloutsos, Opinion fraud detection in online reviews by network effects. in *Proceedings of the International AAAI Conference on Web and Social Media*, Vol. 7, No. 1. (2013)
3. V. Bonta, N.K.N. Janardhan, A comprehensive study on lexicon based approaches for sentiment analysis. Asian J. Comput. Sci. Technol. **8**(S2), 1–6 (2019)
4. G. Fei, A. Mukherjee, B. Liu, M. Hsu, M. Castellanos, R. Ghosh, Exploiting burstiness in reviews for review spammer detection. in *7th International AAAI Conference on Weblogs and Social Media* (2013)
5. M. Hu, B. Liu, Mining and summarizing customer reviews. in *Proceedings of the 10th ACM SIGKDD International Conference on Knowledge Discovery and Data Mining*, pp. 168–177
6. Z. Jin, J. Cao, Y. Zhang, J. Luo, News verification by exploiting conflicting social viewpoints in microblogs. in *Proceedings of the AAAI Conference on Artificial Intelligence*, Vol. 30, No. 1

7. N. Jindal, B. Liu, Analyzing and detecting review spam. in *Seventh IEEE International Conference on Data Mining (ICDM 2007)* (IEEE, 2007), pp. 547–552
8. P. Kalaivani, K.L. Shunmuganathan, Sentiment classification of movie reviews by supervised machine learning approaches. Indian J. Comput. Sci. Eng. **4**(4), 285–292 (2013)
9. H. Li, Y. Liu, N. Mamoulis, D.S. Rosenblum, Translation-based sequential recommendation for complex users on sparse data. IEEE Trans. Knowl. Data Eng. **32**(8), 1639–1651 (2019)
10. H Li, D. Wu, N. Mamoulis, A revisit to social network-based recommender systems. in *Proceedings of the 37th International ACM SIGIR Conference on Research & Development in Information Retrieval* (2014), pp. 1239–1242
11. H. Li, D. Wu, W. Tang, N. Mamoulis, Overlapping community regularization for rating prediction in social recommender systems. In *Proceedings of the 9th ACM Conference on Recommender Systems* (2015) pp. 27–34
12. J. Li, C. Cardie, S. Li, Topicspam: a topic-model based approach for spam detection. In *Proceedings of the 51st Annual Meeting of the Association for Computational Linguistics*, Vol. 2. (2013), pp. 217–221
13. J. Malbon, Taking fake online consumer reviews seriously. J. Consum. Policy **36**(2), 139–157 (2013)
14. W. Medhat, A. Hassan, H. Korashy, Sentiment analysis algorithms and applications: a survey. Ain Shams Eng. J. **5**(4), 1093–1113 (2014)
15. M. Ott, C. Cardie, J. Hancock, Negative deceptive opinion spam. in *Proceedings of the 2013 Conference of the North American Chapter of the Association for Computational Linguistics: Human Language Technologies* (2013), pp. 497–501
16. M. Ott, Y. Choi, C. Cardie, J.T. Hancock, Finding deceptive opinion spam by any stretch of the imagination. in *Proceedings of the 49th Annual Meeting of the Association for Computational Linguistics: Human Language Technologies* (2011), pp. 309–319
17. S. Pal, S. Ghosh, A. Nag, Sentiment analysis in the light of LSTM recurrent neural networks. Int. J. Synth. Emot. (IJSE) **9**(1), 33–39 (2018)
18. J. Pennington, R. Socher, C.D. Manning, Glove: Global vectors for word representation. in *Proceedings of the 2014 Conference on Empirical Methods in Natural Language Processing (EMNLP)* (2014), pp. 1532–1543
19. M. Crawford, T.M. Khoshgoftaar, J.D. Prusa, A.N. Richter, H. Al Najada, Survey of review spam detection using machine learning techniques. J. Big Data **2**(1), 1–24 (2015)
20. S. Vosoughi, D. Roy, S. Aral, The spread of true and false news online. Science **359**(6380), 1146–1151 (2018)
21. S. Xie, G. Wang, S. Lin, P.S. Yu, Review spam detection via temporal pattern discovery. In *Proceedings of the 18th ACM SIGKDD International Conference on Knowledge Discovery and Data Mining* (2012) pp. 823–831
22. S. Xie, G. Wang, S. Lin, P.S. Yu, Review spam detection via time series pattern discovery. in *Proceedings of the 21st International Conference on World Wide Web* (2012), pp. 635–636
23. J. Ye, L. Akoglu, Discovering opinion spammer groups by network footprints. in *Joint European Conference on Machine Learning and Knowledge Discovery in Databases* (Springer, Cham, 2015) pp. 267–282

Image Dehazing Based on Colour Ellipsoid Prior and Low-Light Image Enhancement

Balla Pavan Kumar, Arvind Kumar, and Rajoo Pandey

Abstract The images in hazy environment are not clearly visible due to atmospheric light scattering. Hence, image dehazing is required to reduce the haze effect. In this paper, a colour ellipsoid prior-based model is utilized for image dehazing. After dehazing, the output appears dark and with less contrast. These images experience with low brightness and may downgrade the performance for computer vision systems. The LIME (low-light image enhancement) is implemented in our proposed work, to avoid the over-dark and less-contrast outcome. The image enhancement scheme is implemented for the dehazed image using LIME. For a dehazed image, the Illumination Map (IM) is computed and it is further refined by using structure prior. Through the refined IM, the dehazed image can be enhanced effectively. For the proposed method, the experimental results show better qualitative and quantitative results when compared to the state-of-the-art methods.

Keywords Image dehazing · Colour ellipsoid prior · Low-light image enhancement · Illumination map · Structure prior

1 Introduction

In this digital world, an image plays a pivotal part in the field of digital communication. The images that are obtained by the camera in hazy environments are severely affected because of dissipation of atmospheric light. Due to this, an image is not clearly visible and causes loss of information. In order to avoid this scenario, an image dehazing algorithm has to be proposed to improve the image details and reduce the effect of haze.

A dehazing algorithm is available in [1] which uses the technique of Dark Channel Prior (DCP) and atmospheric scattering model [2]. The atmospheric light is obtained

B. P. Kumar (✉) · A. Kumar · R. Pandey
NIT, Kurukshetra, Kurukshetra, India

A. Kumar
e-mail: arvind_sharma@nitkkr.ac.in

S. Rawat et al. (eds.), *Proceedings of First International Conference on Computational Electronics for Wireless Communications*, Lecture Notes in Networks and Systems 329,
https://doi.org/10.1007/978-981-16-6246-1_44

by evaluating the highest intensity value in dark channel. Using atmospheric light and refined transmission map, the dehazed image is retrieved. Non-local dehazing method [3] works on the principle of colour distribution in RGB colour space. In the RGB colour space, the colour clusters are appeared for haze-free image and haze lines appeared for hazy image. By recognizing the haze lines and calculating per-pixel transmission, the dehazed image can be recovered. Based on colour attenuation prior method [4], the scene depth is assumed to be proportional to the difference among saturation and brightness of corresponding pixel intensities. Another dehazing method which is on the basis of BCCR (boundary constraint and contextual regularization) is proposed in [5]. It is based on the concept of DCP; transmission map is calculated by presuming that haze-free image bounded with $C_0 < J(x) < C_1$; here C_0, C_1 are the constant intensity vectors, J is haze-free image, and x is the pixel coordinate. The contextual regularization is performed to lessen the halo artefacts. Dehazenet method [6] is implemented for image dehazing which is based on convolutional neural networks (CNN). It is implemented by haze-relevant feature extraction, multi-scale mapping, local-extremum, and non-linear regression.

A colour ellipsoid prior-based dehazing method is available in [7] which is based on atmospheric model and dichromatic analysis. In [7], a colour ellipsoid is developed from pixel intensity values, for better analytics. Ellipsoid framework is utilized to compute the prior vector. The lowest colour ingredient from the measured prior vector is used for contrast maximization of hazy pixels. The obtained dehazed outcome is over-dark and low contrast.

In this paper, firstly, the image dehazing is implemented using colour ellipsoid prior model [7] as mentioned above. To overcome the problem of over-dark and low-contrast dehazed outcome, Low-light IMage Enhancement (LIME) algorithm [8] is applied to the dehazed output, as the part of post-processing. The LIME works on the principle of illumination map estimation to enhance an image. In R, G, B channels of a degraded image, the peak pixel intensity value is utilized to generate illumination map. The illumination map is refined using structure-wise smoothing. From the refined illumination map, an image can be enhanced. In this paper, the LIME algorithm [8] is applied to the dehazed image which is obtained from method [7]. By applying LIME algorithm to that dehazed output, the over-dark and low-contrast output can be avoided which results in better brightness and contrast. The proposed technique produces good qualitative and quantitative results when compared with the above-mentioned existing methods.

2 Background

As described by the Koschmieder in [2], a hazy image can be mathematically represented as given below:

$$I(x) = J(x).t(x) + A(1 - t(x)) \tag{1}$$

where x is the pixel location, I is hazy image, J is haze-free image, t is transmission map and A is atmospheric light. The transmission map can be represented as given below:

$$t(x) = e^{-\beta.d(x)} \tag{2}$$

Here d is the distance from camera to the scene and β represents the attenuation constant.

3 Methodology

3.1 Colour Ellipsoid Prior (CEP)

The hazy image is dehazed using CEP as given in [7]. Figure 1 shows the step-by-step procedure to dehaze a hazy image using CEP [7]. An ellipsoid is constructed to mathematically approximate the cluster vectors. As given in [7], the ellipsoid (Ω_i) is expressed as given below:

$$\Omega_i = \{z|(z-\mu_i)^T \sum\nolimits_i^{-1} (z-\mu_i) \leq 1\} \tag{3}$$

where z denotes vector in RGB space as given in [9], $z = [z_r\ z_g\ z_b]^T$;

$\overline{x_j}$ denotes the normalized pixel as given in [10], $\overline{x_j} = \left[\frac{x_{r,j}}{A_r}\ \frac{x_{g,j}}{A_g}\ \frac{x_{b,j}}{A_b}\right]^T$;

μ_i denotes the mean vector as given in [7], $\mu_i = \frac{1}{|\Delta_i|} \sum\limits_{j \in \Delta_i} \overline{x_j} = [\mu_{r,i}\ \mu_{g,i}\ \mu_{b,i}]^T$;

$\sum_i$ denotes the covariance matrix as given in [7],

$$\sum\nolimits_i = \frac{1}{|\Delta_i|} \sum_{j \in \Delta_i} (\overline{x_j} - \mu)(\overline{x_j} - \mu)^T = \begin{bmatrix} \Sigma_{r,i}^2 & \Sigma_{rg,i} & \Sigma_{rb,i} \\ \Sigma_{gr,i} & \Sigma_{g,i}^2 & \Sigma_{gb,i} \\ \Sigma_{br,i} & \Sigma_{bg,i} & \Sigma_{b,i}^2 \end{bmatrix}$$

The vector with least colour element in Ωi is considered as CEP vector. As given in [7], CEP vector is expressed as follows:

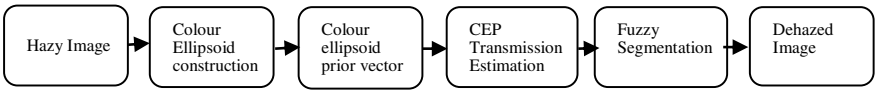

Fig. 1 Block diagram of colour ellipsoid prior method for image dehazing

$$\theta_i = \min_{z \in \Omega_i} \left\{ \min_{c \in \{r,g,b\}} z_c \right\} \tag{4}$$

It can be further expressed as follows:

$$\theta_i = \min_{c \in \{r,g,b\}} \left\{ e_c^T z_c^* \right\} = \min_{c \in \{r,g,b\}} \left\{ \mu_{c,i} - \Sigma_{c,i} \right\} \tag{5}$$

where e_c^T is the unit colour component vector, e_c ($c \in \{r, g, b\}$), $e_r = [1\,0\,0]^T$, $e_g = [0\,1\,0]^T$, $e_b = [0\,0\,1]^T$. z_c^* ($c \in \{r, g, b\}$) denotes minimizing vector. As given in [7], the transmission estimation for colour ellipsoid prior is expressed as follows:

$$t_i = 1 - \alpha\theta_i = 1 - \alpha \min_{c \in \{r,g,b\}} \left\{ \mu_{c,i} - \Sigma_{c,i} \right\} \tag{6}$$

To elude the halo artefacts, the hazy image is segmented based on the fuzzy logic as given in [7],

$$t_i = 1 - \alpha \left\{ \hat{\mu}_{c^*,i} - \hat{\Sigma}_{c^*,i} \right\} \tag{7}$$

where $\hat{\mu}_{c^*,i}$, $\hat{\Sigma}_{c^*,i}$ denote the cluster classified mean and variance, respectively, as given in [7]. From Eqs. (1), (7) calculating atmospheric light A, the dehazed image (J) can be recovered by

$$J(x) = \frac{I(x) - A}{t_i(x)} + A \tag{8}$$

3.2 *Low-Light Image Enhancement*

The dehazed image (J) appears dark and with low contrast. It has to be processed further to enhance the intensity levels and contrast of dehazed image (J). In this paper, as the part of post-processing, the dehazed image is enhanced using Low-light IMage Enhancement (LIME) of [8] as shown in Fig. 2. The LIME framework mainly relies on illumination map (τ). As given in [8], the low-light image (in this paper, dehazed image J is considered as low-light image) is defined as follows:

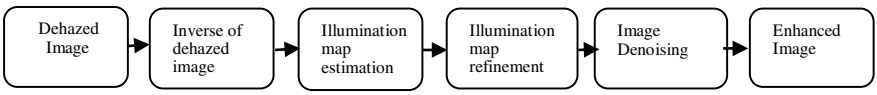

Fig. 2 Block diagram for post-processing of image dehazing using LIME

$$J = I \circ \tau \tag{9}$$

where I denotes the desired enhanced image and $\circ$ operator denotes multiplication (element-wise).

An assumption is made in [8] where the inverted low-light image (dehazed image J) can be considered as hazy image which can be expressed based on Eq. (1) as follows:

$$1 - J = (1 - I) \circ \widetilde{T} + a(1 - \widetilde{T}) \tag{10}$$

where a is atmospheric light, $(1 - J)$ denotes inverted low-light image and $\widetilde{T}$ denotes transmission map.

The illumination map is estimated by adopting the initial illumination map as given in [8]:

$$\widetilde{T}(x) \leftarrow \max_{c \in \{r,g,b\}} J^c(x) \tag{11}$$

For inverse low-light image, the transmission map estimation is expressed as given in [8]:

$$\widetilde{T}(x) \leftarrow 1 - \min_c \frac{1 - J^c(x)}{a} = 1 - \frac{1}{a} + \max_c \frac{J^c(x)}{a} \tag{12}$$

From Eqs. (10) and (12), the recovered image can be expressed as given in [8]:

$$I(x) = \frac{J(x) - 1 + a}{(1 - \frac{1}{a} + \max_c \frac{J^c(x)}{a} + \varepsilon)} + (1 - a) \tag{13}$$

Here ε denotes arbitrary constant to avoid invalid outcome. The above recovered image is from the raw illumination map, it has to be considered in better way in order to get finer output. The local regularity is considered to estimate the illumination map as given in [8]:

$$\hat{T}(x) \leftarrow \max_{y \in \Omega(x)} \max_{c \in \{R,G,B\}} J^c(y) \tag{14}$$

Here $\Omega(x)$ indicates local region. The above consideration increases local regularity but doesn't take the structures into consideration. In order to conserve the structure details, the below optimization has to be considered as given in [8]:

$$\min_T \left\| \hat{T} - T \right\|_F^2 + \alpha \| W \circ \nabla T \|_l \tag{15}$$

Here $\hat{T}$ indicates initial transmission map, T denotes refined transmission map, α denotes the balance coefficient, F and l denote the Frobenius and $l1$ norms, respectively. From the above optimization, the refined transmission map can be obtained. Gamma transformation is applied to refined transmission map T as given in [8] for better enhancement. But, due to gamma transformation, the noise particles present in the dark regions are also enhanced. In order to remove those unwanted noise particles, denoising is applied based on [11]. The final enhancement result as given in [8] is given below:

$$I_f \leftarrow I \circ T + I_d \circ (1 - T) \tag{16}$$

where I_f denotes final enhanced image and I_d denotes denoised image. The final enhanced image is produced with better contrast and visibility.

4 Experimental Results

4.1 Objective Evaluation

Our proposed method is tested with RESIDE [12], Densehaze [13], I-Haze [14], NH-Haze [15] and O-Haze [16] databases. Firstly, the image quality is evaluated using reference parameters—PSNR, SSIM and no-reference parameters—computational time, Naturalness image quality evaluator (NIQE). Tables 1, 2, 3, 4 and 5 shows the image quality parameter values of state-of-the-art methods and proposed method

Table 1 Image quality parameter values for 0002_0.8_0.08 image (from RESIDE database)

Parameters	DCP [1]	NLD [3]	CAP [4]	BCCR [5]	D-net [6]	CEP [7]	Proposed
Computation time	572.36	10.72	0.4564	6.193	7.7307	0.125	0.774
SSIM	0.0031	0.8588	0.6938	0.9121	0.8458	0.606	0.5151
PSNR	5.6547	16.9184	16.1585	18.3194	20.5843	12.475	12.6821
NIQE	3.8385	2.3789	2.3824	2.2819	2.1815	2.4168	3.1498

Table 2 Image quality parameter values for 02_*hazy* image (from Densehaze database)

Parameters	DCP [1]	NLD [3]	CAP [4]	BCCR [5]	D-net [6]	CEP [7]	Proposed
Computation time	354.29	6.58	3.9151	11.9591	0.565	0.042	0.432
SSIM	0.0085	0.4868	0.4041	0.4427	0.3477	0.4504	0.4196
PSNR	11.6674	17.4747	17.1304	14.4992	15.5656	16.3104	12.6081
NIQE	4.1002	4.1322	3.3712	3.4562	6.3554	3.4482	5.1345

Table 3 Image quality parameter values for 01_*indoor _haz y* image (from I-Haze database)

Parameters	DCP [1]	NLD [3]	CAP [4]	BCCR [5]	D-net [6]	CEP [7]	Proposed
Computation time	70.01	1.34	3.2409	8.9211	0.4750	0.033	0.412
SSIM	0.0021	0.7575	0.7049	0.767	0.7309	0.5725	0.7688
PSNR	5.6854	13.6141	12.5014	13.2628	14.9755	9.9484	16.1482
NIQE	18.8746	5.1698	2.1988	2.1356	4.4816	3.2227	4.0758

Table 4 Image quality parameter values for 08_*hazy* image (from NH-Haze database)

Parameters	DCP [1]	NLD [3]	CAP [4]	BCCR [5]	D-net [6]	CEP [7]	Proposed
Computation time	314.11	5.87	4.096	10.7218	1.1767	0.06	0.64
SSIM	0.001	0.7853	0.6163	0.6666	0.6433	0.7411	0.7865
PSNR	6.235	14.6019	12.9838	11.9862	14.6309	13.0859	17.4795
NIQE	5.763	1.6018	1.7238	1.7118	4.289	5.2356	4.9260

Table 5 Image quality parameter values for 01_*out door _haz y* image (from O-Haze database)

Parameters	DCP [1]	NLD [3]	CAP [4]	BCCR [5]	D-net [6]	CEP [7]	Proposed
Computation time	153.56	2.94	4.8177	11.388	0.8701	0.039	0.479
SSIM	0.0015	0.6369	0.3884	0.6762	0.6786	0.4856	0.5751
PSNR	7.61	13.3637	11.231	14.5734	15.1592	11.3712	13.6840
NIQE	18.8834	3.398	2.0487	2.8418	3.5725	3.0856	4.9912

for different images from different databases. The image quality parameters are calculated for the hazy images from different databases.

4.2 Subjective Evaluation

The proposed method produces results with better brightness and contrast when compared with algorithms in [1, 3–7]. The dehazed image outputs of state-of- the-art methods and proposed method are shown in Figs. 3, 4, 5, 6 and 7. All the methods are tested with hazy images from different databases.

For the image 0002_0.8_0.08 in Fig. 3, the dehazed output appears dark and with low contrast for state-of-the-art methods ([1, 3–5, 7]), less haze is removed for method [6], as shown in Fig. 3. Our proposed algorithm overcomes the failures of state-of-the-art methods and appears better as shown in Fig. 3h.

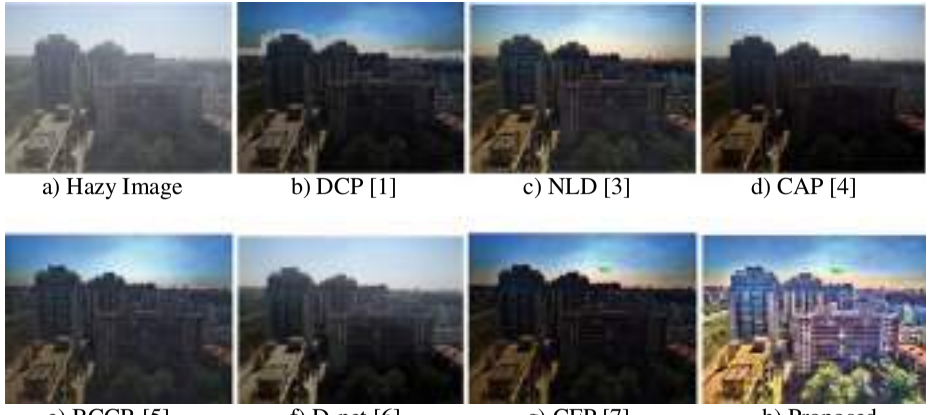

Fig. 3 **a** Hazy image '0002_0.8_0.08' image (from RESIDE database). **b–h** Dehazed output of existing methods—[1, 3–6] and [7]. **h** Dehazed output of proposed method

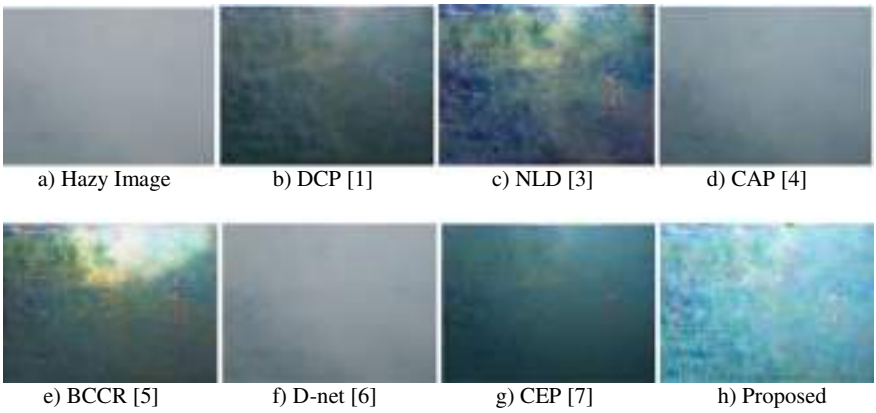

Fig. 4 **a** Hazy image '02_hazy' image (from Densehaze database). **b–h** Dehazed output of existing methods—[1, 3–6] and [7]. **h** Dehazed output of proposed method

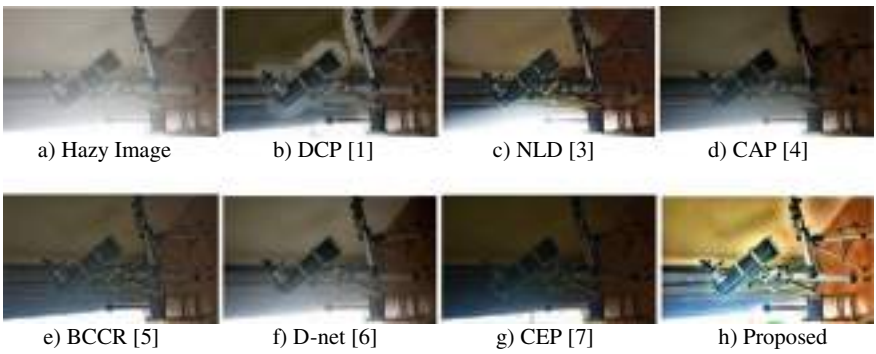

Fig. 5 **a** Hazy image—'01_indoor_hazy' image (from I-Haze database). **b–h** Dehazed output of existing methods—[1, 3–6] and [7]. **h** Dehazed output of proposed method

5 Conclusion

Colour ellipsoid prior model is used in this paper for image dehazing. The dehazed output obtained appears dark and with low contrast. In order to avoid that, the dehazed image is enhanced using Low-light IMage Enhancement (LIME) technique to improve the brightness and contrast of dehazed image. In LIME method, illumination map estimation, illumination map refinement, and image denoising operations are performed. By applying LIME algorithm to that dehazed output, the over-dark and low-contrast output can be avoided which results in better brightness and contrast. The image quality metrics and dehazed output image of the proposed method are compared with the state-of-the-art methods. The proposed method produces the results than previous methods.

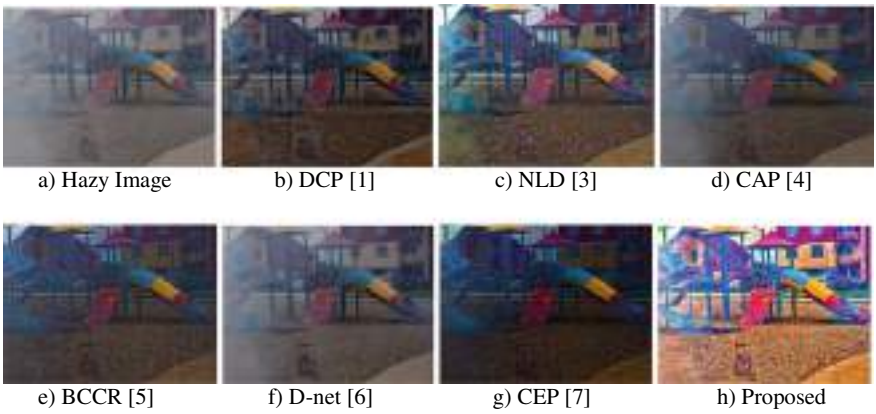

Fig. 6 **a** Hazy image.—'08_hazy' image (from NH-Haze database). **b–h** Dehazed output of existing methods—[1, 3–6] and [7]. **h** Dehazed output of proposed method

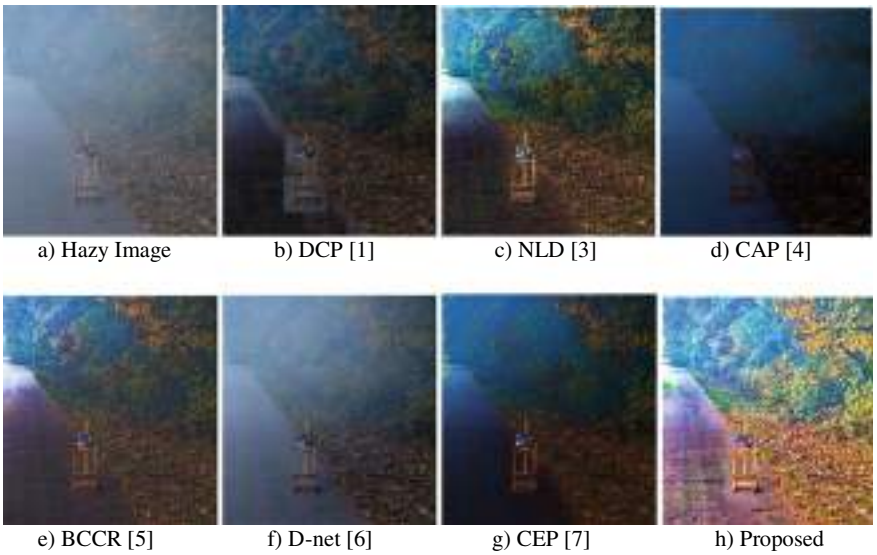

Fig. 7 **a** Hazy image—'01_outdoor_hazy' image (from O-Haze database). **b–h** Dehazed output of existing methods—[1, 3–6] and [7]. **h** Dehazed output of proposed method

References

1. K. He, J. Sun, X. Tang, Single image haze removal using dark channel prior. IEEE Trans. Pattern Anal. Mach. Intell **33**(12), 2341–2353 (2011)
2. E. J. McCartney, *Optics of the Atmosphere: Scattering by Molecules and Particles* (Wiley, New York, USA, 1976), pp. 1–42
3. D. Berman, et al., Non-local image dehazing, in *Proceedings of IEEE Conference on Computer*

Vision and Pattern Recognition (2016), pp.1674–1682
4. Q. Zhu, J. Mai, L. Shao, A fast single image haze removal algorithm using colour attenuation prior. IEEE Trans. Image Process. **24**(11), 3522–3533 (2015)
5. G. Meng, Y. Wang, J. Duan, S. Xiang, and C. Pan, Efficient image dehazing with boundary constraint and contextual regularization, in *Proceedings of IEEE Conference on Computer Vision and Pattern Recognition* (2013), pp. 617–624
6. B. Cai, X. Xu, C. Jia, K.and Qing, D. Tao, Dehazenet: an end-to end system for single image haze removal. IEEE Trans. Image Process **25**(11), 5187–5198 (2016)
7. T. M. Bui et al., Single image dehazing using colour ellipsoid prior. ÌEEE Trans. Image Process. **27**(2), 999–1009 (2018)
8. X. Guo, LIME: a method for low-light image enhancement. arXiv (2016), pp. 87–91. https://doi.org/10.1145/2964284.2967188.
9. K. B. Gibson, T. Q. Nguyen, An analysis of single image defogging methods using a colour ellipsoid framework. EURASIP J. Image Video Process. **2013**, 37 (2013)
10. W. J. Kuo, R. F. Chang, Approximating the statistical distribution of colour histogram for content-based image retrieval, in *Proceedings of IEEE ICASSP*, vol. 4 (2000), pp. 2007–2010
11. K. Dabov, A. Foi, V. Katkovnik, K. Egiazarian, Image denoising by sparse 3d transform-domain collaborative filtering. IEEE Trans. Image Process. (TIP) **16**(8), 2080–2095 (2007)
12. B. Li, W. Ren, D. Fu, D. Tao, D. Feng, W. Zeng, Z. Wang, Benchmarking single-image dehazing and beyond. IEEE Trans. Image Process. **28**(1), 492–505 (2019)
13. C. O. Ancuti et al., Dense haze: a benchmark for image dehazing with dense-haze and haze-free images. arXiv:1904.02904 (2019)
14. C. O. Ancuti et al., I-HAZE: a dehazing benchmark with real hazy and haze-free in-door images, in *International Conference on Advanced Concepts for Intelligent Vision Systems* (Springer, Cham, 2018)
15. C. O. Ancuti, C. Ancuti, R. Timofte, NH-HAZE: an image dehazing benchmark with non-homogeneous hazy and haze-free images, in *IEEE CVPR NTIRE Workshop* (2020)
16. C. O. Ancuti, C. Ancuti, R. Timofte, C. De Vleeschouwer, O-HAZE: a dehazing bench-mark with real hazy and haze-free outdoor images, in *IEEE/CVF Conference on Computer Vision and Pattern Recognition Workshops (CVPRW)*, Salt Lake City, UT (2018), pp. 8670–8678

A Fuzzy AHP Approach for Prioritizing Fog Computing Security Parameters

Jasleen Kaur, Alka Agrawal, and Raees Ahmad Khan

Abstract Cloud computing provides many facilities such as storage, computing, analytics, scalability, etc. But, it also suffers from issues like traffic congestion, high latency and increased communication cost. Fog computing was introduced by Cisco Systems as an alternative to cloud computing. It acts as a mid-layer between user devices and cloud level thereby helps in managing the cons of the latter. However, the introduction of fog layer casts doubt on the security of data travelling through it. Security, being multidimensional in nature, can be handled in an efficient manner, if addressed through its dependent factors and sub-factors in a hierarchical manner. Hence, a hierarchical structure representing corresponding factors and sub-factors related to fog computing security is presented and the same have been prioritized deploying Fuzzy Analytical Hierarchy Process (FAHP). The obtained solutions have been compared to those obtained through classical AHP and are observed as coordinated in nature.

Keywords Cloud computing · Fog computing · Security · Analytical hierarchy process · Fuzzy

1 Introduction

The sharing of storage and processing power among the Internet-enabled devices in a centralized fashion has become possible through cloud computing [1]. The introduction of Internet of Things (IoT) has led to the addition of several smart devices to the web that has affected the cloud processing power with respect to condensed traffic, latency, etc. This consequently has had an adverse imapct on Quality of Service (QoS). Instantaneous results are demanded in case of latency-sensitive applications The presence of a middle layer between the and users that is capable of performing minimal processing operations was thought to be useful in this regard. Real-time analytics was the basic idea behind the introduction of fog

J. Kaur (✉) · A. Agrawal · R. A. Khan
Department of Information Technology, Babasaheb Bhimrao Ambedkar University (A Central University), Lucknow, India

S. Rawat et al. (eds.), *Proceedings of First International Conference on Computational Electronics for Wireless Communications*, Lecture Notes in Networks and Systems 329,
https://doi.org/10.1007/978-981-16-6246-1_45

computing concept. Fog computing may be defined as an extension to cloud concept that brings computation, storage and control closer to the end user. It is ideal for latency-sensitive sectors such as healthcare, finance, etc. [2].

However, the fog scenario presents its unique issues and challenges because of its distinctive features such as location awareness, mobility support, etc. [3]. Security being one of the critical issues. This is so because users' data travels through fog layer before reaching the cloud, and thus raises question about the security of the data. Fog is closer to the end devices and hence is more vulnerable to malicious activities [4]. Fog security solutions need to be different from the available cloud and IoT security solutions because of latency considerations. Hence, the pre-existent security mechanisms need to be revisited with reference to fog characteristics [5]. In other words, it may be said that fog computing security needs to be considered from the scratch.

Security, being multidimensional in nature, can be handled in an efficient manner, if addressed through its dependent factors and sub-factors in a hierarchical manner. This makes security assessment at fog level a multi-criteria decision-making problem [6]. Hence, as the proposed work, a hierarchical structure with fog computing security dependent factors and sub-factors has been presented. Further, the identified factors have been ranked using FAHP. The results obtained by the proposed technique have been compared to those obtained through classical approach and are observed as coordinated in nature.

The organization of the rest of the paper is as follows: the related work forms Sect. 2. Section 3 describes the hierarchical structure of security factors. Section 4 is about the methodology and its implementation. Section 5 is the comparison and the paper concludes with Sect. 6.

2 Related Work

Since the inception of fog computing in 2016, the Internet has been filled with research dealing with its different issues and challenges. One of the major issues that has been addressed by various reserachers is security provided by the layer [2–6]. The reserachers have devised a security and privacy scheme for fog-enabled VANET [7]. In 2020, the reserachers have analysed techniques for data security at fog layer [8]. In 2019, Abbas et al. [9] have given a mechanism for securing smart applications deployed at fog layer. The technique is based on identity-based encryption and signature and has been evaluated using OPNET simulator. Other researchers have also stressed about the security of data at fog level in various sensitive areas such as healthcare, finance, etc. [10, 11]. The authors have described intelligent techniques for security at fog layer [12]. Ali et al. [13] have described privacy and security issues in fog paradigm. Similarly, security challenges have been discussed by the authors alongwith some countermeasures in fog era [14]. Through the above researches, it is evident that the research community is considering security at fog layer at a huge pace.

Some researchers are deploying AHP methodology to access security attributes in dfferent sceanrios. Say, Alenezi et al. [15] have evaluated the impact of software security design tactics. Similarly, Kumar et al. [16] have estimated the usable-security of helathcare web applicaion through hybrid MCDM techniques. Agrawal et al. [17] have measured the sustainable security of different web applications through hybrid AHP-TOPSIS methodology.

Hence, we observed that the researchers are considering security in the area of fog computing paradigm as a reserach problem. Hence, in view of the above-mentioned explanation, various fog computing security factors along with their sub-factors have been presented in a hierarchical manner to contribute towards security monitoring in fog environment systematically.

3 Fog Computing Security

Security of any system or scenario needs to be managed from the very basic level. It is something that cannot be treated as an add-on. It needs to be throughly studied step by step or level by level. For efficient management of security attributes at fog level, the authors have devised some dependent factors and sub-factors [6]. The hierarchical representation of identified fog computing factors is shown in Fig. 1.

The figure describes the security factors as level 1 and level 2 factors, respectively. The level 1 factors (A1–A5) are said to be directly dependent on fog computing security while the level 2 sub-factors (A11–A53) are believed to indirectly impact the security at fog level.

Fig. 1 A hierarchical structure of fog computing security parameters

4 Fuzzy AHP Methodology and Implementation

The quantitative estimation of corresponding fog security factors is considered a challenging task. However, the empirical analysis is indispensible in proper estimation of fog computing security. Ranking or prioritization will help the researchers and academicians in dealing with the security in the given environment in a systematic and efficient way. Hence, the ranking of fog security factors and sub-factors may be considered as a Multi-Criteria Decision-Making (MCDM) problem. This methodology is deployed to evaluate the various cross-cutting criteria and provide a legitimate decision [18]. MCDM problems are widely solved using AHP problem [19]. It provides the decision tool for MCDM problems using the pair-wise comparison matrix.

Satty developed the FAHP technique that is being used by different researchers to reduce the ambiguities in the academicians' and experts' judgements [20]. The integration of fuzzy with AHP helps in dealing with issue of ambiguity. Linguistic variable, triangular fuzzy numbers represented as (l, m, u) is used for the pair-wise comparison of the criterion [21]. The authors have discussed the methodology step-wise. Buckley's [22] method has been implemented to calculate the relative importance and weights of the criteria.

Step 1. The required data is collected through questionnaire in the linguistic form based on the topic from 42 academicians and experts. The received data is then altered to the numerical form (see Table 1).

Step 2. The obtained data from the different experts has been aggregated and $\left(\overset{*}{\boldsymbol{d}}_{ij}\right)$ is computed via Eq. 1 and shown in Table 2.

$$\left(\tilde{d}_{ij}\right) = \sum_{k=1}^{n} \tilde{d}_{ij}^{k}/n \tag{1}$$

(n = number of experts).

Table 1 Fuzzy AHP-related linguistic scale values

Linguistic scale	Fuzzy triangular scale
Completely High (CH)	(5, 7, 9)
Vastly High (VH)	(3, 5, 7)
High (H)	(1, 3, 5)
Mediumly High (MH)	(1, 1, 3)
Exactly Equal (EE)	(1, 1, 1)
Mediumly Low (ML)	(1/3, 1/1, 1/1)
Low (L)	(1/5, 1/3, 1/1)
Vastly Low (VL)	(1/7, 1/5, 1/3)
Completely Low (CL)	(1/9, 1/7, 1/5)

Table 2 Aggregated pair-wise comparison matrix

	A1	A2	A3	A4	A5
A1	(1, 1, 1)	(3, 5, 7)	(1, 3, 5)	(0.155, 0.235, 0.60)	(2.57, 3.6, 4.665)
A2	(0.155, 0.235, 0.60)	(1, 1, 1)	(1.6, 2.65, 4)	(0.155, 0.235, 0.60)	(1, 1, 1)
A3	(0.20, 0.33, 1)	(0.57, 1.6, 2.665)	(1, 1, 1)	(1, 2, 3)	(4, 6, 8)
A4	(3, 5, 7)	(3, 5, 7)	(0.60, 0.655, 1)	(1, 1, 1)	(4, 6, 8)
A5	(1.55, 2.57, 3.6)	(1, 1, 1)	(0.125, 0.17, 0.265)	(0.125, 0.17, 0.265)	(1, 1, 1)

Step 3. As per Buckley's method, the aggregated pair-wise comparison matrix is used to calculate the geometric mean of fuzzy numbers using

$$\tilde{r}_i = \left(\prod_{j=1}^{n} \tilde{d}_{ij} \right)^{\frac{1}{n}} \tag{2}$$

where i = 1, 2, 3…n and $\tilde{r}_i$ is a triangular number. The geometric mean values are shown in Table 3.

Step 4. The addition of two TFNs is done using:

$$\begin{aligned} \tilde{A}_{\mathrm{m}} \surd \tilde{A}_{\mathrm{n}} &= (l_{\mathrm{m}}, m_{\mathrm{m}}, u_{\mathrm{m}}) \surd (l_{\mathrm{n}}, m_{\mathrm{n}}, u_{\mathrm{n}}) \\ &= (l_1 + l_2, m_1 + m_2, u_1 + u_2) \end{aligned} \tag{3}$$

Deploying this, the vector summation of each $\tilde{r}_i$ is calculated.

Step 5. To arrange the triangular numbers in ascending order, their inverse is calucated using Eq. 4:

$$\begin{aligned} A^{-1} &= (l_1, m_1, u_1)^{-1} \\ &= \frac{1}{u_1}, \frac{1}{m_1}, \frac{1}{l_1} \end{aligned} \tag{4}$$

Table 3 Fuzzy comparison values' geometric mean

	Geometric mean of fuzzy comparison values		
A1	1.5051	1.6660	1.787800
A2	1.31351	1.38601	1.484110
A3	1.4659	1.6133	1.733740
A4	1.632644	1.775917	1.888175
A5	1.306040	1.374726	1.437110

Table 4 Triangular fuzzy weights of each criterion

	Fuzzy weights $\tilde{w}_i$		
A1	0.208371	0.213154	0.214598
A2	0.181845	0.177331	0.178144
A3	0.202944	0.206411	0.208109
A4	0.226028	0.227216	0.226646
A5	0.180812	0.175887	0.172503

Step 6. Equation 5 shows the multiplication formula.

$$\begin{aligned} \tilde{A}_{\mathrm{m}} \geq \tilde{A}_{\mathrm{n}} &= (l_{\mathrm{m}}, m_{\mathrm{m}}, u_{\mathrm{m}}) \geq (l_{\mathrm{n}}, m_{\mathrm{n}}, u_{\mathrm{n}}) \\ &= (l_{\mathrm{m}} * l_{\mathrm{n}}, m_{\mathrm{m}} * m_{\mathrm{n}}, u_{\mathrm{m}} * u_{\mathrm{n}}) \end{aligned} \tag{5}$$

$$\begin{aligned} \tilde{w}_i = \tilde{r}_i &\geq (\tilde{r}_1 \sqrt{} \tilde{r}_2 \sqrt{} \cdots \sqrt{} (\tilde{r}_n)^{-1} \\ &= (lw_i, mw_i, uw_i) \end{aligned} \tag{6}$$

Table 4 shows the fuzzy weights of each criteria.

Step 7. Now, it is known that w_i is a TFN, hence, for defuzzification, CoA method is used. This method is given by [23], as shown in the given equation.

$$m_i = \frac{= (lw_i, mw_i, uw_i)}{3} \tag{7}$$

Step 8. Finally, through Eq. 8, the final criteria weights are calculated.

$$N_i = \frac{m_i}{\sum_{i=1}^{n} m_i} \tag{8}$$

The above-mentioned steps are carried out over the data collected for both the levels. Finally, the respective ranks and weightages are calculated. The final weights of level 1 and level 2 criteria thus obtained are given in Tables 5, 6, 7, 8, 9 and 10.

The responses received by the experts were undergone through the above steps. The prioritization of the factors and sub-factors was achieved by FAHP approach.

Table 5 Final weights of level 1 attribute

Level 1 criteria	Weights	Rank
Access control (A1)	0.35	2
Integrity (A2)	0.17	3
Data protection (A3)	0.07	5
Privacy (A4)	0.42	1
Intrusion detection (A5)	0.13	4

Table 6 Final weights of A1

	Weights	Rank
Authentication policy (A11)	0.07	4
Authorization (A12)	0.53	1
Identification (A13)	0.17	3
Trust (A14)	0.25	2

Table 7 Final weights of A2

	Weights	Rank
Non-repudiation (A21)	0.58	1
Credibility (A22)	0.13	3
Delegation (A23)	0.24	2

Table 8 Final weights of A3

	Weights	Rank
Insider threats (A31)	0.24	2
Secure transmission protocol (A32)	0.63	1
Redundancy (A33)	0.10	3

Table 9 Final weights of A4

	Weights	Rank
Anonymization (A41)	0.15	3
Obfuscation (A42)	0.45	1
Encryption (A43)	0.39	2
Aggregation (A44)	0.05	4

The results show that according to the opinion of the experts, privacy needs to be given utmost importance while considering different aspects of security at fog level.

5 Comparison

This section is about the comparison of the results obtained from FAHP technique with those obtained from classical approach. The same prioritization was done using

Table 10 Final weights of A5

	Weights	Rank
Detection algorithm (A51)	0.69	1
Verifiability (A52)	0.12	3
Alert generation (A53)	0.32	2

the classical AHP technique and both the results were compared using correlation coefficient given by Spearman. The correlation coefficient given by Spearman was chosen because of its efficiency to deal with the ordinal data [24]. The correlation value was found to be 0.892 which clearly depicts that the results are highly correalted in nature. The value of the correlation coefficient also shows that the results obtained by the researchers have been validated.

6 Conclusion

In the presented research endeavour, the authors have ranked the identified fog computing security factors and sub-factors using Fuzzy Analytical Hierarchy Process (FAHP) based on the opinions of 42 experts and academicians. The fog computing security factor 'privacy' is found to be highly prioritized by the experts which clealry symbolizes the need to preserve the anonymity of the user content that flows through the fog layer. Hence, in the future, the researchers may deploy a hybrid approach for ranking the fog computing security factors and devise a technique for privacy preservation at fog level.

References

1. L. Wang, G. Von Laszewski, A. Younge, X. He, M. Kunze, J. Tao, C. Fu, Cloud computing: a perspective study. New Gener. Comput. **28**(2), 137–146 (2010)
2. R. Verma, S. Chandra, Security and privacy issues in fog driven IoT environment. Int. J. Comput. Sci. Eng. **7**(5), 367–370 (2019)
3. J. Kaur, A. Agrawal, R.A. Khan, Security issues in fog environment: a systematic literature review. Int. J. Wirel. Inf. Netw. **27**, 467–483 (2020)
4. M. Mukherjee, R. Matam, L. Shu, L. Maglaras, M.A. Ferrag, N. Choudhury, V. Kumar, Security and privacy in fog computing: challenges. IEEE Access **5**, 19293–19304 (2017)
5. R. Verma, S. Chandra, a systematic survey on fog steered IoT: architecture, prevalent threats and trust models. Int. J. Wirel. Inf. Netw. **28**(1), 116–133 (2021)
6. J. Kaur, A. Agrawal, R.A. Khan, Security assessment in foggy era through analytical hierarchy process, in *2020 11th International Conference on Computing, Communication and Networking Technologies (ICCCNT)* (IEEE, 2020), pp. 1–6
7. S.A. Soleymani, S. Goudarzi, M.H. Anisi, M. Zareei, A.H. Abdullah, N. Kama, A security and privacy scheme based on node and message authentication and trust in fog-enabled VANET. Veh. Commun. **29**, 100335 (2021)
8. A. Murugesan, B. Saminathan, F. Al-Turjman, R.L. Kumar, Analysis on homomorphic technique for data security in fog computing. Trans. Emerg. Telecommun. Technol. e3990 (2020)
9. N. Abbas, M. Asim, N. Tariq, T. Baker, S. Abbas, A mechanism for securing IoT-enabled applications at the fog layer. J. Sens. Actuator Netw. **8**(1), 16 (2019)
10. Y. Guan, J. Shao, G. Wei, M. Xie, Data security and privacy in fog computing. IEEE Netw. **32**(5), 106–111 (2018)
11. J. Kaur, R. Verma, N.R. Alharbe, A. Agrawal, R.A. Khan, Importance of fog computing in healthcare 4.0, in *Fog Computing for Healthcare 4.0 Environments* (Springer, Cham, 2021), pp. 79–101

12. M. Qiu, S.Y. Kung, K. Gai, Intelligent security and optimization in Edge/Fog computing (2020)
13. A. Ali, M. Ahmed, M. Imran, H.A. Khattak, Security and privacy issues in fog computing. Fog Comput. Theory Pract. 105–137 (2020)
14. Z. Ashi, M. Al-Fawa'reh, M. Al-Fayoumi, Fog computing: security challenges and countermeasures. Int. J. Comput. Appl. **975**, 8887 (2020)
15. M. Alenezi, A.K. Pandey, R. Verma, M. Faizan, S. Chandra, A. Agrawal, R.A. Khan, *Evaluating the Impact of Software Security Tactics: A Design Perspective*
16. R. Kumar, A.I. Khan, Y.B. Abushark, M.M. Alam, A. Agrawal, R.A. Khan, An integrated approach of fuzzy logic, AHP and TOPSIS for estimating usable-security of web applications. IEEE Access **8**, 50944–50957 (2020)
17. A. Agrawal, M. Alenezi, R. Kumar, R.A. Khan, Measuring the sustainable-security of Web applications through a fuzzy-based integrated approach of AHP and TOPSIS. IEEE Access **7**, 153936–153951 (2019)
18. M. Abdel-Basset, G. Manogaran, M. Mohamed, A neutrosophic theory based security approach for fog and mobile-edge computing. Comput. Netw. **157**, 122–132 (2019)
19. C. Kahraman, S.C. Onar, B. Oztaysi, Fuzzy multicriteria decision-making: a literature review. Int. J. Comput. Intell. Syst. **8**(4), 637–666 (2015)
20. T.L. Saaty, *The Analytic Hierarchy Process* (McGraw-Hill, New York, 1980)
21. O. Kilincci, S.A. Onal, Fuzzy AHP approach for supplier selection in a washing machine company. Expert Syst. Appl. **38**(8), 9656–9664 (2011)
22. J.J. Buckley, Fuzzy hierarchical analysis. Fuzzy Sets Syst. **17**(3), 233–247 (1985)
23. S.W. Chou, Y.C. Chang, The implementation factors that influence the ERP (enterprise resource planning) benefits. Decis. Support Syst. **46**(1), 149–157 (2008)
24. Online availabe at: https://www.questionpro.com/blog/spearmans-rank-coefficient-of-correlation/

A Review on Local Binary Pattern Variants

Aditya Singh, Ramesh K. Sunkaria, and Anterpreet Kaur

Abstract In spite of successful and remarkable advancement made in current studies on local binary methods, it requires groundbreaking research into theoretical perspectives as well as required more efficient approaches on algorithm to concern about the real-world problems occurring in natural images. The research indicated a precise indication of the target for texture characteristics and allowed the application to expand the LBP method into practical engineering, while optimizing theoretical analyses. The LBP method is relatively straightforward and uncomplicated for texture analysis, but also has an invariance of rotation, grayscale invariance, and other important benefits. In terms of precision of texture analysis based on LBP having multiple applications, the conventional local binary model (LBP) approach was to calculate the value of each pixel of an image and assign the model's binary value with their specified based on their relationship to neighboring pixels. In consideration of situation on real time images that are having efficient operator on texture analysis for images, this paper covers the various strains of local binary patterns with their area of application, benefit, and their disadvantages for future shortcomings.

Keywords Local binary pattern · Image retrieval · Facial recognition · Texture analysis · Local features

1 Introduction

In this era of technology, images are coming up as a vast database and it becomes quite problematic to deal with such large amount of data. Hence, it results in the need of a technique through which huge database of images can be efficiently looked upon. A technique which can perform an automatic search of a particular required image from the huge database is needed. This process of retrieving images related to the desired one, which is a query in the large database, is called image retrieval [1]. Nowadays, in the field of image processing, image retrieval is a topic which is

A. Singh (✉) · R. K. Sunkaria · A. Kaur
Dr. B. R. Ambedkar National Institute of Technology, Jalandhar 144011, India

S. Rawat et al. (eds.), *Proceedings of First International Conference on Computational Electronics for Wireless Communications*, Lecture Notes in Networks and Systems 329,
https://doi.org/10.1007/978-981-16-6246-1_46

being researched and studied actively. The image retrieval method can be carried out in two ways: first one is text-based image retrieval and the other is content-based image retrieval (CBIR) [1]. In case of images which need to be retrieved through text attributes like keywords, text and metadata are brought up in use. But the image retrieval by text-based method requires image indexing manually which is surely a time-consuming task. So this makes the traditional method for image retrieval to have lost its place in case of large database [2]. In this world of technology, an efficient and less time engaging method should be considered for the retrieval process. This could be achieved by a technique called CBIR which was introduced in 1922 by Kato. CBIR is more efficient in contrast to the traditional text-based technique.

The CBIR technique focuses on low-level visual feature extraction for retrieving the image [2]. This step is followed by comparing these extracted features with the query for more resemblance resulting in relative image retrieval. This proposed technique by Kato is much nearer to human understanding regarding visual representation.

2 Texture Analysis

Texture is one of the more popular methods being used for image retrieval. It can deal with differentiation among images. It results in surface features as it differs with local intensities of image. These features are detected by properties like coarseness, smoothness, and regularity. This method uses signal processing as the bases of feature extraction. It includes various mathematical transformations in the image. These transformations further result in coefficients which are the image features. The texture feature extraction includes transforms like Gabor filters, discrete wavelet transform [3, 4], etc. The texture feature extraction can be carried out in one more way which includes method related to model. Initially, in such techniques, an assumption model for an image is made. Then the parameters of the assumed model undergo estimation and such parameters are said to be texture descriptor features. There is a commonly known method called Markov random field [3]. Also, the texture method includes another way called structural analysis. The texture primitives having large description and are individually segmented along with uniform patterns can undergo this technique. In the approached texture, we talk about the basic LBP method from which most methods are extended for use and research is carried out on an ongoing basis, and we thank their exceptional performance as we benefit from it. Ojala et al. [4] introduce the LBP methodology in 2002. After the introduction of its LBP operator, some ongoing research on the basis of LBP studies has been carried out in texture analysis.

3 Local Binary Pattern

Local binary pattern operator consists of eight pixels in neighborhoods and one at the center in a 3 × 3 pixel matrix where the point of center pixel is used as threshold [5]. If the intensity of the neighboring pixels is greater than the center pixel value then one is assigned in matrix otherwise it is zero. Then concatenation process is done considering each pixel in clockwise direction. To provide labels to the given pixels the decimal values related to it are used. LBP codes are also known as derivative binaries [6]. The disadvantage of this method is the small size of neighborhood, i.e., 3 * 3 as it is not able to characterize the main features in large dimension images. In later stage, this operator was made to work on different scale images to overcome the disadvantage.

4 LBP Strain

LBP did not have the capacity to take all discriminatory facts; it is regarded as evidence of differences in the different neighborhoods. With the change of several pixels taking place have caused variations of LBP. LBP enhances the performance across a variety of applications.

Ojala et al. [7] introduced the uniform LBP, the main purpose of which is to decrease how many local binary models exist. From observing, only certain binary models occur more commonly, and in some cases over 90% of all models. If the number of transition changes in binary form then the pattern is said to be uniform.

Liao [8] proposed the dominant local binary patterns (DLBP) in which they considered the method of classification of the texture. In this approach, it is able to represent the dominant models in texture pictures, to maintain the equalization properties of rotational invariants, and histograms of the conventional LBP approach. It is simple and computationally efficient. Results from the experiment show that it possesses a good classification of texture.

Biancon proposed DLBP [9], a dominant LBP that used models occurring more frequently for capturing certain information from image. The features of DLBP are less susceptible to noise and histogram equalization and more robust when image rotation is performed.

Guo et al. [10] introduced the LBP-TOP variants called multi-frame LBP-TOP to find the exact matching pair of the images that are matching by video texture synthesis. The objects and their visual motifs in the video textures are characterized by dynamic ways. Dynamic texture analysis can provide useful guidance to a wide range of applications such as video compression and recovery.

Fehr [11] introduced a new idea for an invariant rotation calculation function from the local and invariant model of the histogram. In this approach which are applied on the descriptor LBP at the same time static and dynamic. When referring to the

texture in static mode, the presentation of the local binary model histogram in Fourier functions.

3-D-LBP, an extended LBP, was proposed by Huang et al. [11]. It is similar to ELBP which captures anisotropic structures more efficiently. Schema of median binary was introduced in [11]. By multiplying pixels corresponding to local median local characteristics were determined.

For capturing macro-structure information in an image, a new descriptor median robust extended local binary pattern was presented by Liu et al. [12]. Comparison values of median patches and derivation from the local patches were done instead of raw pixel intensity. The resulting pattern is less noise sensitive and can efficiently capture micro- and macro-structures. FbLBP which is a feature-based LBP with low dimensionality and less illumination sensitivity was proposed. Both magnitude and sign differences were considered. Mean and variance were used to describe the magnitude portion of the difference vector and the classic LBP described the significant portion.

A second-order LTrP was proposed by Murala [12]. It is calculated using vertical and horizontal derivatives. For calculating directionality of pixels, it uses 0–90° derivatives of LDP. Analysis of performance of combination of LTrP and GT is also done.

Transition Local Binary pattern (LTBP): Here, the transition-encoded LBP binary value is a clock comparison of neighboring pixels for all pixels except the middle.

Volume Local Binary Pattern (VLBP) [13]: VLBP with texture in dynamic nature is a set of volume with space from (X, Y, T). The representation of the X- and Y-coordinates for the spatial domain and T shows the frame index.

Local Ternary Pattern (LTP), a variant proposed by Rassem [14], has proven to have less sensitivity to noise and more discriminant power than the basic local binary pattern. 3—valued coding is involved in which gray-level differences in the kernel are calculated considering threshold about zero.

Modified Local Binary Models (MLBP) [15]: In this paper, MLBP works on the principle of making a comparison between the neighboring pixel values with the mean of the matrix value in the m * n matrix. The main purpose of this method (MLBP) is image feature extraction having better characteristics. It was checked on various types and sizes of images and then contrasts it to older methods. The vicinity AdaBoost as far as I know, in the images first time seeing the research area where LBP are applying in 3D mode.

Local Derivative Pattern (LDP) is introduced by the Suruliandi et al. [16] where information regarding local feature of higher order is acquired. The different spatial relationships in local regions are understood and encoded. In some applications like recognition of face, a better performance is offered as the descriptor uses two-level computations.

Sorted LBP was proposed by Ryu et al. [17], which encoded patterns without considering spatial transition. The descriptor sorts consecutive patterns to create rotational invariance. Also, encoding of all the binary patterns having any number of spatial transitions was done by the descriptor. Summing up of all consecutive bit neighborhood patterns and sorting the result into zero and one bit were done.

Table 1 Various variants of LBP

LBP variant	Description	Pros	Application	Cons
LBP	Scaling and counting the number of bit for transitions	Illumination of intensity was changed and computational accuracy was improved	Texture analysis	Discriminative information was losses
Multiscale LTP	Depicting images at different scales at high dimensionality coupled with the small size of the maximum number 3	Conversing the large spatial area	Facial analysis	Accuracy is enhanced, but histogram performance compromises
Opponent color LBP	Extraction of the internal and inter-channel characteristics for the classification of the color texture	Color images included with help of LBP	Recognize the facial color, expression	The segregation of color and texture has been disregarded
SLBP	Fuzzy adhesion functionality is used	Get a higher level of recognition when comparing with the original LBP and the co-occurrence of LBP soft	Face recognition	Computer efficiencies were lower than expected
Transition LBP	Comparison of neighboring pixels clockwise for all pixels with the exception of center	Greater accuracy for moveable things that have speed	Car detection and recognition	Sensitive to noise causing trouble
Modified LBP	Combines the sign and amplitude of facial texture with random forest technology	Covers the texture in the color images	Facial identification with the aid of iris	Reduction of the vector characteristic of the recognition precision

(continued)

Table 1 (continued)

LBP variant	Description	Pros	Application	Cons
Dominant LBP	Utilizes the most common LBP models	Approximately reaches the threshold value any frequent and sorted construction patterns	Fingerprint recognition	Accuracy
Multiframe LBP	Provide continuous and infinitely variable flow of frameworks	Ability to recover pictures while playing the video	Video texture analyzing	The blur appeared in the images
Volume LBP	By combining the motion of the image with the tighter look	Real-time application	Gender recognition and lip reading	Accuracy compromised
Hybrid LBP	The use of a genetic algorithm optimized the characteristics of the pictures	Noise is suppressed and takes account of overall characteristics	Facial recognition on broadband television	The precision was not reached because the threshold is given
Local derivative pattern	Encodes various distinct spatial relations contained directional calculation within the edges of four direction angles	Automatically switch to the threshold values for the directional value	Face recognition	Noise sensitive and considers only the local characteristics
2D and 3D LBP	The SVM algorithm is used for the 3D extension, which are values computed in rotation in the neighbor sphere	Human perception are covers	Facial recognition	The length of the characteristic vectors takes but has not given a lot of information about this document
MRELBP	The local plot median values are compared	Face detection performance has been improved and there is flexibility in the structures	Texture classification	Filtration has been slow
LTP	Comparison by threshold of the values with the value of the central pixels—1, 0, 1	Robust with the noise	Facial classification	It is difficult to define absolute thresholds

(continued)

Table 1 (continued)

LBP variant	Description	Pros	Application	Cons
LTrP	Encodes the relation between the values of the pixels with the neighbor according to the direction on vertically and horizontally	Give the most accurate values according to the directorates	Fingerprint and facial classification	Just consider vertical and horizontal directions, ignoring diagonal directions

In [18] Bello, the introduction of new research into the field of LBP which is a hybrid type of LBP scheme to exploit the information is locally and globally for texture pictures. The major contribution to image orientation, based on texture, was the estimation of the LBP histograms that can be aligned. The histogram is used to measure the dissimilarities among the images (Table 1).

5 Conclusion

LBP method used is in an effective and successful way for their communication gap benefits with the application of computer vision. The flexibility of LBP makes its use easier for a variety of applications. The LBP has produced various good results and has been frequently used to predict and detect image linkage as well as car tracking and biological image processing. In this article, it is addressed about various descriptors in local binary whose strains are used for different types of applications such as texture analysis, facial grading, fingerprinting, video analysis, and so on. Therefore, the LBP operators examined herein are a good starting point for various applications.

References

1. M. Garg, G. Dhiman, A novel content-based image retrieval approach for classification using GLCM features and texture fused LBP variants. Neural Comput. Appl. **33**, 1311–1328 (2021)
2. S. Gupta, P. Roy, P. Dogra, Retrieval of colour and texture images using local directional peak valley binary pattern. Pattern Anal. Appl. **23**, 1569–1585 (2020)
3. N. Alpaslan, K. Hanbay, Multi-resolution intrinsic texture geometry-based local binary pattern for texture classification. IEEE Access **8**(3205122), 54415–54430 (2020)
4. S. Chen-Ke, Y.-H. Yun, C.-H. Wen, X. Zhang, Research and perspective on local binary pattern. Acta Autom. Sinica **39**(6), 730–744 (2013)
5. A.K. Bedi, R.K. Sunkaria, S.K. Randhawa, Local binary pattern variants: a review, in *2018 First International Conference on Secure Cyber Computing and Communication (ICSCCC)* (2018), pp. 234–237

6. J. Yuan, D. Huang, H. Zhu, Y. Gan, Completed hybrid local binary pattern for texture classification, in *2014 International Joint Conference on Neural Networks (IJCNN)* (2014), pp. 2050–2057
7. T. Ojala, M. Pietikainen, T. Maenpaa, Multiresolution gray-scale and rotation invariant texture classification with local binary patterns. IEEE Trans. Pattern Anal. Mach. Intell. **24**(7), 971–987 (2002)
8. S. Liao, X. Zhu, Z. Lei, L. Zhang, S.Z. Li, Learning multi-scale block local binary patterns for face recognition, in *Advances in Biometrics. ICB 2017*, ed. by S.W. Lee, S.Z. Li. Lecture Notes in Computer Science, vol. 4642 (2017)
9. F. Bianconi, E. González, A. Fernández, Dominant local binary patterns for texture classification: labelled or unlabelled. Pattern Recogn. Lett. **65**, 8–14 (2015)
10. Y. Guo, G. Zhao, Z. Zhou, Video texture synthesis with multi-frame LBP-TOP and diffeomorphic growth model. IEEE Trans. Image Process. **22**(10), 3879–3891 (2013)
11. J. Fehr, H. Burkhardt, 3D rotation invariant local binary patterns, in *2008 19th International Conference on Pattern Recognition* (2008), pp. 1–4
12. S. Murala, R.P. Maheshwari, R. Balasubramanian, Local tetra patterns: a new feature descriptor for content-based image retrieval. IEEE Trans. Image Process. **21**(5), 2874–2886 (2012)
13. K. Kiruba, E.D. Shiloah, R. Raj, C. Sunil, Hexagonal volume local binary pattern (H-VLBP) with deep stacked autoencoder for human action recognition. Cogn. Syst. Res. **58**, 71–93 (2019)
14. T.H. Rassem, B.E. Khoo, Completed local ternary pattern for rotation invariant texture classification. Sci. World J. **2014**, 373254 (2014)
15. O. Connor, B. Roy, Facial recognition using modified local binary pattern and random forest. Int. J. Artif. Intell. Appl. (2013)
16. B. Zhang, Y. Gao, S. Zhao, J. Liu, Local derivative pattern versus local binary pattern: face recognition with high-order local pattern descriptor. IEEE Trans. Image Process. **19**(2), 533–544 (2010)
17. J. Ryu, S. Hong, H.S. Yang, Sorted consecutive local binary pattern for texture classification. IEEE Trans. Image Process. **24**(7), 2254 (2015)
18. N.R. Bello, Improved opponent color local binary patterns: an effective local image descriptor for color texture classification. Electron. Eng. (2017)
19. J. Trefný, J. Matas, *Extended Set of Local Binary Patterns for Rapid Object Detection* (2010)

Auto-luminance-Based Face Image Recognition System

Anurag Verulkar and Kishor Bhurchandi

Abstract For getting the improvement over the recognition accuracy of face recognition system, a method based on auto-luminance is proposed. Firstly, the face is detected from the query via input images, real-time web cam using the Viola–Jones face detection algorithm, then detected face is pre-processed with auto-luminance and histogram equalization method. Then, we use HOG feature descriptor measuring gradient amplitude and the orientation of the gradients. These features with the description are then classified with the help of SVM machine learning classifier to discriminate the different classes. By using this approach of auto-luminance with histogram equalization and HOG feature extraction when performed at input images, live web cam and the well-known ORL cropped face database, it is cogitated that this algorithm has a higher face recognition rate than the conventional one when applied pre-processing on them.

Keywords HOG · Face recognition · Viola–Jones algorithm · Face detection · Feature extraction · Pre-processing

1 Introduction

Biometrics is the process of recognizing and authenticating the individuals through specific and singular biological characteristics. On the basis of recognizable and verifiable data, a person gets identified and then authenticated for different purposes. This information based on biological characteristics are then transformed for digital processing. The most typical use cases of biometric technologies are found in healthcare and subsidies, public security, military services, border travel and migration cases, civil recognition, physical and logical access for authentication, and some

A. Verulkar (✉) · K. Bhurchandi
Visvesvaraya National Institute of Technology (VNIT), Nagpur, Nagpur, India

S. Rawat et al. (eds.), *Proceedings of First International Conference on Computational Electronics for Wireless Communications*, Lecture Notes in Networks and Systems 329,
https://doi.org/10.1007/978-981-16-6246-1_47

other commercial applications areas. There are different types of biometric identification techniques such as face recognition, DNA matching, finger geometry recognition, eyes-iris recognition, typing recognition, voice-speaker identification, and hand geometry recognition.

Face recognition identification technique is focused in this paper. Basically, face recognition is an approach of recognizing and affirming the identity of an individual person using their face. People in photos, video, or in real-time-based manner are identified by the face recognition systems. For more than 10 years until now, face recognition technology has existed and evolved. It is becoming more and more a necessity in today's world than other biometrics due to its non-contact process [1]. Many researchers have researched thoroughly and after the continuous improvement, many traditional recognition algorithms have come forth in the field of face recognition, with the likes of wavelet transform, the principal component analysis (PCA), the hidden Markov model, the face feature based, etc. Many facial feature extraction methods based on local image form for extracting object features such as visual features like GIST, HOG (histogram of oriented gradient), and LBP (local binary pattern) have been also used because of the low automation [2]. In recent years, because of its high robustness and high accuracy, the artificial neural network has shown massive advantages [3].

Face recognition system presented in this paper can be generally break down into three modules, namely, face detection, face feature extraction, and face recognition. Mainly the applications of face recognition such as security authorized control access, criminal record identification, tracking school, and industrial attendance, recognizing specific people for special events and many other commercial applications are concentrated here. It is the method of detecting objects as faces from still pictures, video footages, etc. We can extract the facial characteristics of people by this procedure. Different kinds of approaches for face detection have evolved [4]. These approaches are Viola–Jones, SMQT features and SNOW classifier, support vector machine-based face detection, and neural network-based face detection, and Viola–Jones algorithm is one of the best algorithms based on the F1-score and the timing analysis of inputs [5] is discussed in detail in the next section. Face feature extraction is also crucial in face recognition system. For that an effective descriptor for characterizing and distinguishing the different features of people is a necessity for this process. With the help of feature points classifying facial behavior into variance categories, the objective of this is to make the local image as distinguishable as possible while keeping the characteristics versus different type of modifications. Some robust descriptor for face recognition such as LBP and HOG are demonstrated here in this paper. The next step involves recognition, which classifies the facial image as per the features which match with face database and identify the person belongs to which class. With the face contents available in the face database this face feature content is compared for face recognition. This involves in which face matching of one-to-many elements with authentication provided to one. Basically face recognition is a perceptual structure recognition for facial cases, implemented to classify the known face and unknown face from the database.

2 Theory

2.1 Viola–Jones Algorithm

Capturing the face in input images is the first and the most important start in this face recognition process. Viola–Jones algorithm [6] has been utilized here which minimizes system computation time and is achieving more detection precision and accuracy than other detection methods. Haar features with a cascade of classifiers are some of the requirements for this algorithm to identify the objects. As we know, human faces have different facial region properties such as nose, eye, mouth, etc. which are compared using the Haar features with the Haar basis functions. Generally, there are three types of features deployed for face detection named as two-rectangle, three-rectangle, and four-rectangle diagonal features as shown below.

These Haar features are then computed by using the integral image. This integral image at location (a, b) contains the summation of the pixels over and to the left side of that particular (a, b) location.

$$J(a, b) = \sum_{i=1}^{a} \sum_{j=1}^{b} I(i, j);\ 1 \leq a \leq M,\ 1 \leq b \leq M \tag{1}$$

where J is the integral image as shown above. The next process involves adaptive boost also known as AdaBoost algorithm which chooses the best features needed. Some redundant features are eliminated using the threshold value and setting the selected specific features, and Viola–Jones uses this machine learning classification algorithm AdaBoost which combines weak classifiers to make a strong classifier. In every stage, this procedure takes place and there is a succession of such stages. AdaBoost must select a handful of the weak classifiers and add weight to any just classifier so that in every stage, discarded objects are unnecessary ones only. Thus, the more the number of levels of stages, the better will be the superiority and degree of accuracy of face detection. The next process is cascading which is a hierarchical classification. Each classifier has features built-in. By adding more and more features in every consequent stages, complexity of classifier raises. Next stage gets the input from preceding stage, the detected area which is disapproved or unaffectedly passed

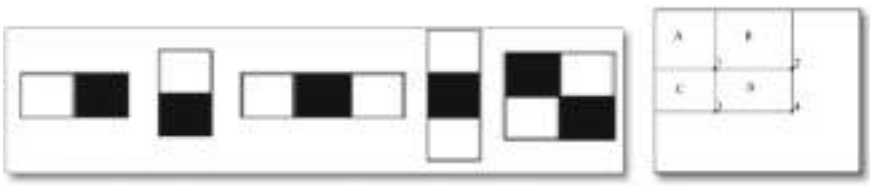

Fig. 1. **a** Different Haar features **b** integral image formation

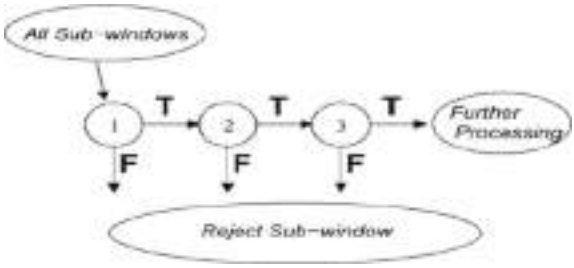

Fig. 2 Cascaded classification

on. Thus, as shown in Fig. 2, at the end only the area which successfully passes all the stages of cascading remains.

2.2 Histogram of Oriented Gradients

For face recognition based on facial extraction [7], HOG feature descriptors are used [8], in which counting the gradient magnitude and direction occurrence of the local image is done by capturing the features. Conventionally, HOG splits the image into different blocks of cells and examines a histogram of oriented gradients over them. The basic idea of HOG features is that from the concentration of the local intensity gradients or edge directions from the posture variations for the given images, the local object appearances and shape can be characterized to a great extent. Due the translational invariance of histogramming, the orientation measurement analysis is subjected to lumenal changes which includes brightness and contrast of images. The measurement concentrations within the image regions with the histograms summarized by the HOG features are extensively used for recognition of distorted shaped textured objects. Each primal point of an image determines the original HOG feature. The corresponding region around each primal point is divided into some uniformly spaced block of cells and over all the pixels of the cell for each cell gradient directions or edge location aggregates a local 1-D histogram. Forming of feature takes the histogram measurements of all cells around one primal point and then as displayed in Figs. 3 and 4. The formation of image representation takes such collective histogram features of all primal points.

The HOG feature computations involve some procedure. Firstly, the input image gradient amplitude in the direction of horizontal and vertical is computed with the orientation of the gradient β.

$$|\alpha| = \sqrt{\text{Img(x)}^2 + \text{Img(y)}^2} \tag{2}$$

$$\beta(\text{x},\ \text{y}) = \tan^{-1}(\text{Img(x)}/\text{Img(y)}), \tag{3}$$

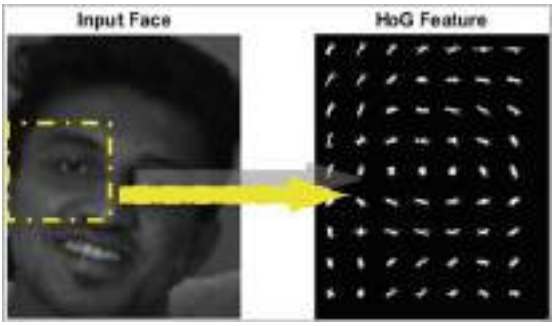

Fig. 3 Final histogram feature of small spatial regions (block of cells)

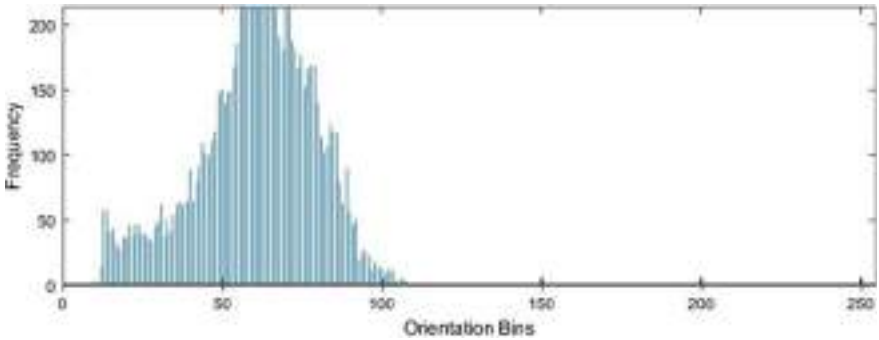

Fig. 4 Histogram representation of the marked small block of cells

where Img is a given image, $|\alpha|$ is the gradient magnitude, and β is the orientation of the gradient. $\beta \in [-180, 180]$, $\text{Img(x)} = \text{Img} * \text{K(x)}$, $\text{Img(y)} = \text{Img} * \text{K(y)}$, where $\text{K(x)} = [-1\ 0\ 1]$, $\text{K(y)} = [-1\ 0\ 1]^{\text{T}}$, and "*" is the convolution operation. Collective aggregation of the magnitude of a gradient for each orientation into bins is then done for the measurement of histogram orientation for each cell. Signed gradient and unsigned gradient spread histogram channels 0°–360° and 0°–180°, respectively. In a single vector, after combining all histograms, the image feature is constructed by normalizing histograms within each block of cells.

2.3 Support Vector Machine

The prediction of the class of given data points is known as the classification process [9]. A mapping of input variables (i) to the discrete variables (j) is roughly estimated by classification predictive modeling. Support vector machine classifier has been used with the HOG face feature descriptor which maximizes the geometric margin and

minimizes the classification error by creating a barrier hyperplane in the feature point space domain. The maximum margin is calculated by two parallel hyperplanes being constructed, one on each side of the individual one. A good distance of separation is achieved by the hyperplane which has the largest distance of separation to the neighboring support vectors of both classes, so if new examples come, they are then mapped into the same space region and predicted to belong to a category in which side of the gap it falls in. So there would be more chance that unknown sample approaches to be classified correctly if these parallel hyperplanes are having clear gap as wide as possible.

3 Proposed Method

Depending on the face recognition workflow this proposed system is broadly divided into two sections: training and recognition.

3.1 Training

MATLAB 2016a software has been used for the deployment of system. For object detections, MATLAB software has in-built Computer Vision System Toolbox. For Viola–Jones algorithm, the toolbox comprises many in-built cascade object detectors, viz., faces, eyes, mouth, nose, etc. Therefore, a customized detector to detect objects has been created. To do so a neural network has been trained. The task of this unsupervised neural network is to capture the required entity in the given image and return its localization, x- and y-coordinates, width as well as height of the box around the objects. With the help of a MATLAB function, the system is trained with positive and negative images, and this MATLAB function is called "trainCascadeObjectDetector". Basically, the required object in the image somewhere inherently presents and contained by the positive images and the negative images are the ones who don't have the objects placed in the images. The required object in the positive images has a region/boundary of area marked around the objects known as Region Of Interest (ROI). After the successful training of the system, an .xml file is generated. This .xml file is then fed to the "vision.CascadeObjectDetector" MATLAB system object in workspace to detect the objects in the test enquired images.

In this case, objects are faces from the input images. These faces are cropped with the size of 92×112 (width $= 92$, height $= 112$) dimensions to form a face database/gallery of faces. These cropped faces then go for pre-processing activity. Pre-processing is a crucial part in this proposed system. Firstly, the low/high threshold values are selected. These are then multiplied with row and column values of an image to get two limits which are lmin and lmax. The matrix is calculated for the NTSC color space. Basically it contains the NTSC luminance (γ) related to brightness and chrominance (I and Q) related to color components information as columns which

have an equivalence to the colors in the RGB colormap. Then the processed image is calculated as

$$\text{Pimg} = {}^{(img - lmin)}/_{(lmax - lmin)} \tag{4}$$

where img is the original image value. Now histogram equalization is the next processing stage for the image [10]. First, we obtain the probability distribution of all gray levels after converting RGB image into grayscale image in turn.

$$\text{P}(\text{g}_\text{i}) = {}^{\text{ni}}/_{N}, \text{i}(0, 1, 2, ..., 255) \tag{5}$$

where $\text{P}(\text{g}_\text{i})$ shows the *i*th gray level of the frequency, g_i is the gray level, n_i is the number of occurrences of the *i*th gray level, and N indicates the total number of pixels. Therefore, calculating the cumulative distribution function:

$$\text{C}_\text{k} = \sum_{\text{i}=0}^{\text{k}} \text{P(gi)} \tag{6}$$

Now, histogram equalization is defined by h after the gray level,

$$\text{h}_\text{i} = \text{INT}(\text{hmax} - \text{hmin})\text{C}_\text{k} + \text{hmin} + 0.5 \tag{7}$$

where INT is used for rounding the equation. The mapping of g_i and hi is histogram equalization. Evenly distribution of the grayscale of image is performed after the equalization process, and the contrast of the image is increased and fed to the next process for algorithm of face recognition. The next process includes feature extraction. HOG feature face descriptor is used in this paper [11]. Size of HOG cell [8 8] is demonstrated for the results shown in the experimental results section. Increasing the cell size allows to capture prominent scale spatial information. But increasing the cell size may end up losing the small-scale details. Prior to this, the face database is portioned into training and testing cases with 80–20 sharing. About 4680 HOG features are extracted from the training face database and then classified by a machine learning classification algorithm SVM with labeled description of training images to discriminate classes. This concludes training process of the proposed system workflow.

3.2 Recognition

Now the next task is face recognition. The faces from the inputs, viz., pictures, video footages, live webcam, etc. are first detected and again pre-processed using the same method as done with training process. Faces are subjected to face detection, cropping into 92 × 112 pixel dimensions, and then auto-luminance, histogram equalization

before feature extraction. HOG feature face descriptor is used for the feature extraction for the input query [11]. Now depending on the features of cropped input face and the classifier model used for the face classification, the proposed system predicts the matched face to the enquired face and decides whether the cropped pre-processed face is a known face or a unknown face for the face database available to the system.

3.3 Proposed Algorithm

Following steps define the proposed method:

Step 1: Positive and negative images training by the neural network creating .xml file.

Step 2: Viola–Jones face detection algorithm exercised for detecting faces from input image.

Step 3: Crop the detected face.

Step 4: Pre-process the cropped faces with auto-luminance and histogram equalization.

Step 5: Extracting HOG features from processed faces.

Step 6: Fitting into suitable face classifier for different classes.

Step 7: Reading the input image and cropping the faces using face detection algorithm.

Step 8: Pre-process the cropped faces with auto-luminance and histogram equalization.

Step 9: Extracting HOG features from processed enquired face.

Step 10: Predicting matched face to the enquired face.

4 Experimental Results

The experiment results have been carried out on the MATLAB 2016a software by considering the equations and theory mentioned earlier. The existed HOG feature-based algorithm and the proposed algorithm results are displayed in the succeeding figures. A comparison of the results of face recognition algorithms is also shown. Face recognition workflow results for different ways of inputs can also be seen.

In Figs. 5 and 6, the HOG features visualization with original detected input face and HOG features visualization with pre-processed detected input face of ORL face database are shown, respectively. It can be seen from the figures that there are different orientations of gradients in both the cases. In Fig. 7, we can see the histogram representation of collective block of cells in an input face image which is not evenly distributed as compared to histogram representation of pre-processed input face image as shown in Fig. 8.

Face recognition workflow results for different ways of inputs such as input image from photos, live web cam, and face image from ORL database are shown in Figs. 9

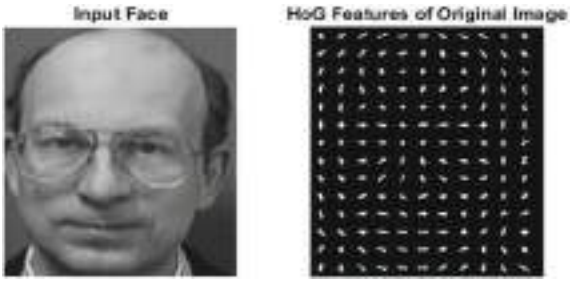

Fig. 5 HOG feature visualization with original detected input face

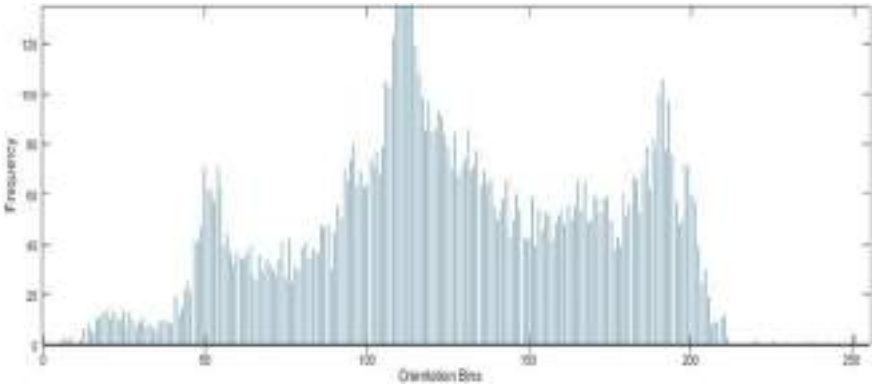

Fig. 6 Histogram representation of original detected input face

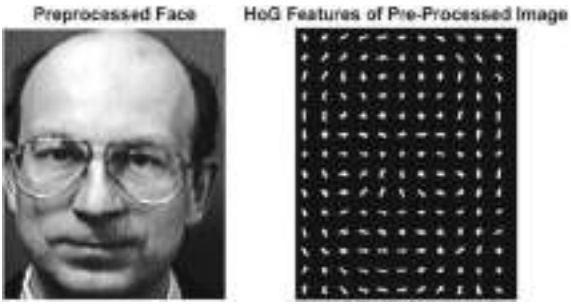

Fig. 7 HOG features visualization with pre-processed detected input face

and 10 as well as in Fig. 11, respectively. The enquired faces are well pre-processed with auto-luminance and histogram equalization functions so as to get maximum accurate result as the predicted face.

Different face recognition algorithms are also shown in Table 1. It is seen that the presented face recognition algorithm which is a combination of pre-processing, HOG feature extraction with SVM classifier yields the more accurate results than with other alliance. It has been seen that when the method is deployed with 320

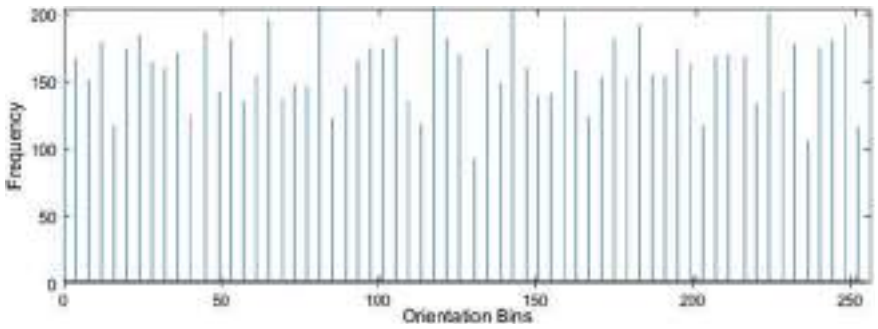

Fig. 8 Histogram representation of pre-processed detected input face

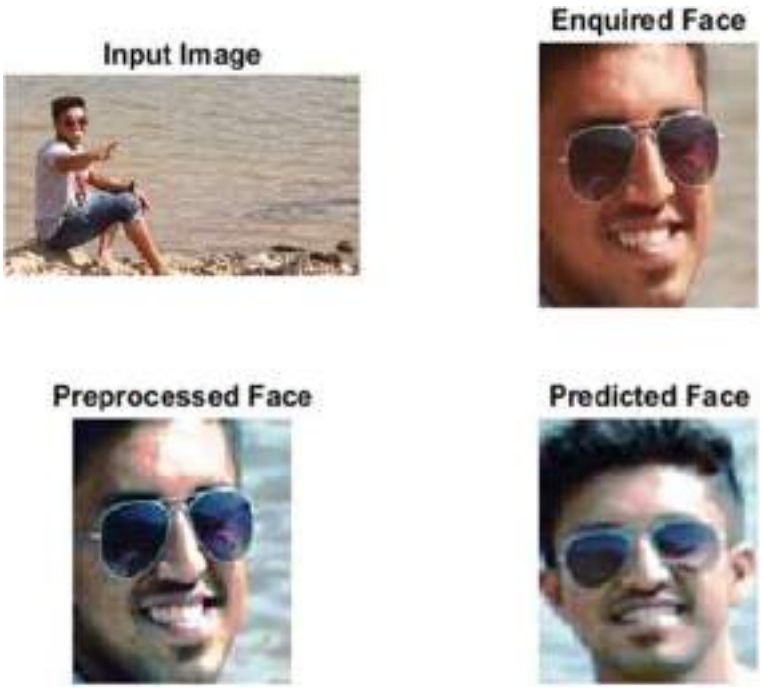

Fig. 9 **a** Input image **b** detected input face, **c** pre-processed face, **d** predicted face

training cases and demonstrated on 40 test cases of ORL database it has shown a betterment of more than 2.7%.

Fig. 10 **a** Input image from live web cam **b** detected input face **c** pre-processed face **d** predicted face

Fig. 11 **a** Input query face from ORL database **b** pre-processed face **d** matched class

Table 1 Face recognition accuracy when subjected to 40 different test cases of ORL database compared with different face recognition algorithms with pre-processing

Face recognition algorithms	Recognition accuracy over ORL database %
LBP + SVM + Pre-processing	0.650
LBP + KNN + Pre-processing	0.800
HOG + KNN + Pre-processing	0.875
HOG + Naive Bayes + Pre-processing	0.900
HOG + SVM + Pre-processing	0.925
Proposed algorithm	0.950

5 Conclusion

The auto-luminance-based face image recognition using HOG features is demonstrated. The new method workflow for face recognition is proposed, which is an improvisation over the existing face recognition using HOG feature descriptors. The comparison of different face recognition methods is demonstrated by comparing the feature selection scheme such as LBP and HOG with different face classifiers like kNN, SVM, Naive Bayes. It is demonstrated that face recognition accuracy of this approach has acquired 95% when subjected to 40 different test cases of ORL face database.

References

1. B. Heisele, P. Ho, J. Wu, T. Poggio, Face recognition: component-based versus global approaches. Comput. Vis. Image Underst. **91**(1/2), 6–21 (2003)
2. H.T.M. Nhat, V.T. Hoang, Feature fusion by using LBP, HOG, GIST descriptors and canonical correlation analysis for face recognition, in *2019 26th International Conference on Telecommunications (ICT)*, Hanoi, Vietnam (2019), pp. 371–375. https://doi.org/10.1109/ICT.2019.8798816
3. E. Jiang, A review of the comparative studies on traditional and intelligent face recognition methods, in *2020 International Conference on Computer Vision, Image and Deep Learning (CVIDL)*, Chongqing, China (2020), pp. 11–15. https://doi.org/10.1109/CVIDL51233.2020.00010
4. M.H. Yang, D.J. Kriegman, N. Ahuja, Detecting faces in images: a survey. IEEE Trans. Pattern Anal. Mach. Intell. **24**(1) (2002)
5. K. Dang, S. Sharma, Review and comparison of face detection algorithms, in *2017 7th International Conference on Cloud Computing, Data Science & Engineering—Confluence*, Noida, India (2017), pp. 629–633. https://doi.org/10.1109/CONFLUENCE.2017.7943228
6. P. Viola, M. Jones, Rapid object detection using a boosted cascade of simple features, in *Proceeding of International Conference on Computer Vision and Pattern Recognition (CVPR)*, Kauai, HI,USA (2001)
7. N. Dalal, B. Triggs, Histograms of oriented gradients for human detection, in *CVPR* (2005), pp. 886–893
8. O. Deniz, G. Bueno, J. Salido, F. De la Torre, Face recognition using histograms of oriented gradients. Pattern Recogn. Lett. **32**(12), 1598–1603 (2011)

9. N. Sabri et al., A comparison of face detection classifier using facial geometry distance measure, in *2018 9th IEEE Control and System Graduate Research Colloquium (ICSGRC)*, Shah Alam, Malaysia (2018), pp. 116–120. https://doi.org/10.1109/ICSGRC.2018.8657592
10. P. Chang, Y. Chen, C. Lee, C. Lien, C. Han, Illumination robust face recognition using spatial expansion local histogram equalization and locally linear regression classification, in *2018 3rd International Conference on Computer and Communication Systems (ICCCS),* Nagoya, Japan (2018), pp. 249–253. https://doi.org/10.1109/CCOMS.2018.8463262
11. T. Do, E. Kijak, Face recognition using co-occurrence histograms of oriented gradients, in *2012 IEEE International Conference on Acoustics, Speech and Signal Processing (ICASSP)*, Kyoto, Japan (2012), pp. 1301–1304. https://doi.org/10.1109/ICASSP.2012.6288128

A Novel Approach of Mutual Authentication in Fog Computing

Sameer Farooq and Priyanka Chawla

Abstract Today, security is a major issue in the cyberworld. The data generated by the devices are more susceptible to threats and attacks than being used. The emergence of cloud computing and IoT changed the whole concept of handling and interacting with data. The framework that we proposed for the security of data, which is being generated by IoT devices is divided into multiple phases. The first starting phase is mutual authentication. This phase guarantees the communicating parties are genuine. The paper presents the novel scheme for mutual authentication between two parties that are IoT device and Fog system. In the paper, we discuss and figure out how the IoT device and the Fog system will interact with each other and authenticate each other.

Keywords Mutual authentication · Fog system · IoT · MD5 · MITM

1 Introduction

The development of novel computing technologies like cloud computing, IoT and Fog computing has shifted the paradigm of working and security of existing technologies. The organizations are migrating from standalone networks to cloud networks for better availability, security, reliability and scalability. To achieve the secure remote communication, the mutual authentication plays the vital role. The mutual authentication is fundamental block for secure communication in client–server remote environments. It enables client and server to communicate with each other securely. As we are in era of information age, the cloud computing, Fog computing and IoT networks are growing with tremendous speed, the attacks and means of attacking are also getting sophisticated. The hackers are using complex codes and tools to steal user data from server databases.

The client–server environment of wireless networks is facing more challenges. They are prone to more attacks as they are part of insecure public channels. The

S. Farooq · P. Chawla (✉)
Lovely Professional University, Phagwara, Jalandhar 144401, Punjab, India

S. Rawat et al. (eds.), *Proceedings of First International Conference on Computational Electronics for Wireless Communications*, Lecture Notes in Networks and Systems 329,
https://doi.org/10.1007/978-981-16-6246-1_48

attacker may impersonate as the registered client and request for the resources and services from the server. This will cause the security breach in the whole network. The sensitive information of other clients may be extracted from the database by adversary and later use it for some malicious intent. The mutual authentication is the only way to address the above problem. To protect the user's privacy, the identities of client and server must be hidden while communication. The proposed scheme uses the hash function and the XOR operation to make communicating message complex and difficult for cryptanalysis if intercepted by intruder.

The work that is being presented here is actually the first phase of the framework that is being presented by the author for securing data while transmission between IoT devices and cloud. The name of the framework is 'Novel Hybrid Encryption Framework to secure data transmission between IoT and Fog System'. The proposed framework is divided into four phases:

i. Mutual authentication.
ii. Key generation.
iii. Encryption.
iv. Decryption.

In this paper, we are discussing the first phase of the framework that is mutual authentication. The author proposes the novel approach on how to achieve mutual authentication between two parties without using PKI, in case of resource-sensitive environments. The reason for proposing the new work is because PKI is not suitable in low-powered and resource-constraint environments. The PKI consumes more resources because of its complexity, while the proposed work will authenticate two sides without consuming many resources, thus suitable for resource-constraint environments like WSN and IoT.

Figure 1 shows a simple IoT-Fog network, and this network secures the devices on both ends have to mutually authenticate each other. Fog system is placed at the edge of the network, so whatever data is collected or generated by the IoT devices that are sent to the cloud indirectly via the Fog system after analytics and error removal. The reason for analytics is that the data collected by the IoT devices may have some unnecessary or erroneous data, so sending all this to the cloud will be a

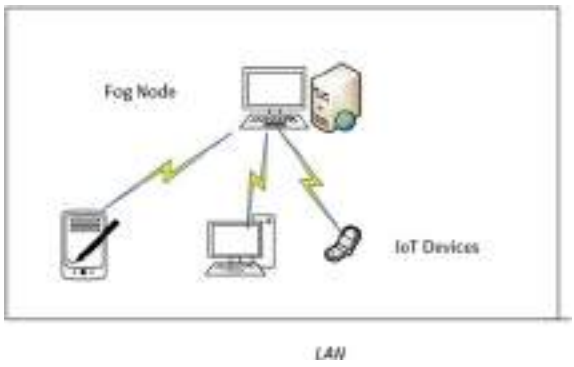

Fig. 1 Fog network in LAN

wastage of time, bandwidth, cloud storage and obviously money. The best solution to this problem is to filter all the data that is generated by the IoT devices inside LAN using the Fog system. The solution is good but the issue arises when we consider the security of data inside LAN, that is, who is going to process data and whose data is to be processed.

2 Literature Review

The authentication is main issue when it comes to security concern of IoT, Fog computing or cloud computing. Whether the communicating partner is legitimate or not is an issue in every security-vulnerable network. The researchers of different areas proposed various concepts of how to achieve the security goals. The cloud architecture is different than Fog architecture and so there security parameters are. The cloud is less vulnerable as compared to Fog, the various threats that exists in Fog do not exists in cloud at all, because the Fog is located towards the edge of network.

Lamport [1] proposed password-based authentication scheme using password table for credential storage. The table was used for users' authentication while users requests any service from server. However, Mitchell and Chen [2] and Chen and Ku [3] noted weakness of integrity attack and impersonate host attack in the scheme proposed by Lamport [1]. Hwang et al. [4] proposed Shamir's ID-based signature scheme for authentication using smart cards. Hwang and Li [5] proposed ElGamal-based remote authentication scheme using smart cards without authentication table. The log requests and passwords were verified by the system. However, the vulnerabilities of system were found by Chan and Cheng [6] and Shen et al. [7]. Chien et al. [8] presented solution to the shortcomings of Sun's [9] scheme, an efficient practical solution that does not allow users to freely choose credentials by its own and perform mutual authentication. Ku and Chen [10] and Hsu [11] identified various possible attacks on Chien et al. [8] who proposed system like parallel session attack, insidious attack and reflection attack. Lee et al. [12] proposed modified Chien et al. [8] scheme by removing parallel session attack. However, Yoon and Yoo [13] pointed flaws of masquerading server attack and insidious server attack on Lee et al. [12] system. Lee and Chiu [14] presented authentication method based on password and claimed it to be improvement of system proposed by Wu and Chieu [15]. However, Xu et al. [16] pointed out forgery attack on Lee et al. [14] system and password guessing attack on Lee et al. [17]. Song [18] pointed various possible attacks on Xu et al. [16] system and suggested new password-based protocol for authentication using smart cards. Li et al. [19] pointed various vulnerabilities in Kim and Chung [20] system and proposed new efficient system based on discrete logarithm properties of ECC without timestamp value. Tang et al. [21] pointed possible attacks on scheme proposed by Awasti et al. [22] and proposed new mutual authentication scheme based on timestamp value using ECC and smart card. Shen and Du [23] after analysing Kim and Chung [20] improved scheme proposed by Li and Lee [24] which inherited weakness of smart card security breach. Jiang et al. [25] proposed scheme using

password-based authentication; however, scheme is vulnerable to basic password guessing attack.

In the modern information era, the user can access multiple services simultaneously. Most of the authentication algorithms are based for single server environments. The issues are the user has to register and store respective credentials of all servers that increase credential managing burden on the user. Li et al. [26] proposed neural network password authentication scheme for multi-server environments and claimed the user has to register once for multiple server and services access. Lin et al. [27] to improve efficiency of Li et al. [26] proposed new ElGamal signature-based scheme. Jaung et al. [28] proposed scheme using symmetric encryption and hash function for authentication in order to decrease the computational cost of algorithm. However, Ku et al. [29] pointed out insidious attack in Juang [28] scheme and claimed it cannot give required forward confidentiality. Lio and Wang [30] proposed scheme for multi-server authentication environment based on password and smart card using dynamic identity. However, Hsiang and Shih [31] pointed out weaknesses of Lio and Wang [30] system like forgery, impersonation and insidious attack. They proposed their own system Hsiang and Shih [31] to overcome its vulnerabilities. Sood et al. [32] noted vulnerabilities in system proposed by Hsiang and Shih [31] like impersonation attack, replay attack and card stolen attack. Various biometric systems were also proposed to achieve remote mutual authentication like Odelu et al. [33] who proposed biometric smart card-based authentication for multi-server environments. He and Wang [34] proposed scheme for multi-server environment using three-factor authentication with ECC. Lu et al. [35] consider the authentication as the main security issue at the different levels of Home Area Network (HAN). Author also mentions that the PKI-based infrastructure cannot be applied to Fog as it is not efficient to Fog due to scalability of Fog users. Kumar [36, 37], Lu et al. [38], Tsai [39] focused on password-based authentication technique as utilized in clouds but Fog is not cloud so it is not feasible to use them. Another disadvantage is that passwords are susceptible to dictionary attacks and it is not feasible to keep multiple lists of passwords for each Fog user who communicates with different servers of multiple Fog networks. Next issue to consider in password-based authentication is entropy of passwords, and to overcome entropy there is session key management but that requires complex arithmetic computations. Ibrahim [40] proposed the concept of single lived master key that allows user to connect with any Fog server and mutually authenticate it. The vulnerability is, if this master key gets compromised, it means attacker can get access to any Fog server throughout the network. The algorithm used by author is AES for encryption and SHA-356 for authentication. While sending '*KFu*' from generator to user there may be MITM attack. Sameer and Prashar [41] proposed in his work mutual authentication technique, in which he is using Registration ID of patient and Server ID along with Tm [timestamp value]. The timestamp value is used to check message freshness, so as to avoid session hijacking. All three values are hashed with Md5 hashing algorithm and sent on either side. Papers not complying with the LNNS style will be reformatted. This can lead to an increase in the overall number of pages. We would therefore urge you not to squash your paper.

3 Proposed Methodology

The To design an algorithm that provides Mutual authentication in data transmission between IoT devices, Fog systems, and Cloud servers.

The Fog computing includes different set of IoT nodes that are placed in some environment either to generate the data by sensing various environmental factors or to transmit the data generated by the various sources to the base station. All these nodes, whether it is collection of sensors or a group of any other electronic data processing gadgets, are known with one name, that is, Internet of Things (IOT) and the paper presents one of the objectives of the algorithm that secures the data transmission between the IoT devices and the Fog system.

There isn't any proper security architecture for Fog computing, the reason is novelty and dynamic heterogeneous nature. Fog computing consists of multiple nodes [IoT devices] which may or may not be connected with each other. All the data which are generated by these devices are sent to the cloud via Fog system which is located at the edge of LAN. The reason behind using Fog as intermediary for transmission is because at this location [Fog] some data analytics and processing of collected data are done, which improves resources management like bandwidth, battery power, storage capacity, processing power, etc. Depending upon the number of nodes and the types of nodes, the number of Fog devices in LAN may vary from one to many.

The need for mutual authentication is because of wireless communication among the nodes [IoT devices]. We know board-casting characteristic that is inherited by the wireless communication is prone to almost every possible attack. Thus, in Fog computing, there is a need of such a security architecture that will not only protect the data generated by IoT devices but also protect the network nodes. To protect the data the solution is to encrypt it as soon as it leaves the node which generates it. And to protect the nodes, the solution is mutual authentication before communication with base station. The proposed framework will mutually authenticate the sink node [IoT device] with base station [Fog system] and vice versa. The algorithm that is used for authentication depends on two prerequisites that are User_ID and Node_ID. Both IDs are provided by the Fog service provider [FSP] to its clients for individual identification of each node in the LAN. The algorithm is divided into two phases:

3.1 Registration phase.
3.2 Authentication phase.

3.1 Registration Phase

The registration phase is the first step of the whole framework that is used by author to secure the data transmission between the IoT device and the Fog system. The customer who wants to use the Fog service in his network has to first register his devices [IoT devices] with Fog service provider [FSP]. The FSP on registering will provide the user with unique id [User_ID] for his identification and for identification

of each device there will be separate Ids [Reg_ID] for each device. Thus, each device on network will hold two attributes that are who owns it [User_ID] and who it is [Reg_ID]. The details of customer with his respective devices that are using Fog service are added in the database of the FSP for later verification of nodes while mutual authentication between base station and sink node. It is important to note that the User_ID and Reg_ID both are confidential to the user and must not be disclosed to the third party by any means.

Node identification:

Device identification	Reg_ID
Owner Identification	User_ID

In case if there is some customer of FSP who owns multiple devices, so in that case the User_ID will be same while the Reg_ID for each device will be different.

The Fog system will calculate the hash values from the respective node IDs and perform other necessary operation too and then save the results in the database that will be used while authentication.

3.2 Authentication Phase

This phase includes various steps that mutually authenticates IoT devices and the Fog system with each other. After the registration phase, each IoT device is associated with two attributes User_ID and Reg_ID, and on the other hand the Fog system is storing the details of each node in its database shown in Table 1.

The following steps are used by algorithm to mutually authenticate IoT device with the Fog system:

1. The first step is to calculate the md5 hash of User_ID and Reg_ID by the IoT device:

$$h1 = Md5\ (User\_ID + Reg\_ID)$$

2. The second step is to perform the XOR operation between calculated hash '***h1***' and Reg_ID by the IoT device.

$$h2 = (h1 \hat{} Reg\_ID)$$

Table 1 Hash value table

User_ID	Node_ID	h1 = md5(User_ID + Node_ID)	h2 = h1^User_ID
A101X	001AX101AX	cbd342553de457ac…	5ac4fcf56224…
A101X	002AX101AX2	43fac32453de…	Ac32567434…
S904Z	001S904ZAX2	cdsfbd3425fd…	Zg5432453de…

3. The calculated XOR value '***h2***' is sent to the base station that is in actual the Fog system by the IoT device.

Now by chance if any intruder gets that '***h2***', that is, useless because it is just the hash stream which he can't decrypt by any mean, as the generated value is dependent on the various parameters which are only known to the user device and the Fog server.

4. On receiving the '***h2***' hash value the Fog system examines it and then searches for it in its database. If value matches the process goes further otherwise process is terminated and communicating node is blocked. If it is present that means communicating node is genuine, as only genuine node can calculate the accurate hash value.
5. The Fog system will search for the '***h2***' vale in its database to get the respective Reg_ID. After that the XOR operation will be performed between '***h2***' and fetched Reg_ID value to get the '***h1***' value.

$$h1 = (h2 \leq Reg\_ID)$$

6. After extracting '***h1***', the Fog system will calculate the md5 hash of User_ID and Reg_ID of respective '***h2***' value.

$$h3 = Md5\ (User\_ID + Reg\_ID)$$

7. Now the extracted value '***h1***' will be compared with the calculated value '***h3***', if the values are equal that means the sender is genuine node, so sender, i.e. IoT device is authenticated.

```
If (h1 == h3)
        S1 -> Sender Authentication Successful.
else
        S3 ->  Sender Authentication Failed.
        S4 ->  Terminate connection.
```

8. When IoT device (sink node) is successfully authenticated by the Fog system (bases station), the next step is the base station will calculate the '***h4***' that is md5 hash of Reg_ID and then performs XOR operation between calculated '***h4***' and User_ID to get '***h5***'. Now this '***h5***' value will be sent to the sender side (IoT device/sink node) for receiver side (Fog system/base station) authentication.

$$h4 = Md5(Reg\_ID)$$
$$h5 = (h4 \leq User\_ID)$$

While communication if intruder intercepts communication channel he will get hash stream of ***'h5'*** that will be useless as it contains no information.

9. On receiving '***h5***' the IoT will perform XOR operation between '***h5***' and User_ID to extract '***h4***'. After that the IoT device will calculate '***h6***', i.e. md5 hash of Reg_ID.

$$h4 = (h5 \overset{\wedge}{} \text{User\_ID})$$
$$h6 = \text{Md5}(\text{Reg\_ID})$$

10. If the calculated value is equal to the extracted value that means server is genuine, because only server can generate accurate hash as it is the only entity which owns User_ID and Reg_ID details of IoT device.

If (h4 == h6)
    S1 −> Fog system Authentication Successful.
else
    S3 −> S Authentication Failed.
    S4 −> Terminate connection.

11. When both sides will mutually authenticate each other successfully that means the mutual authentication is successful.

4 Algorithm for Mutual Authentication

```
Client side = IoT Device / Sink Node.
Server side = Fog System / Base Station.

INPUT:
       Reg_ID / Node_ID
       User_ID / Owner_ID

START:
CLIENT-SIDE (IoT Device):
1. Compute ccH_N+R = md5(Reg_ID+ User_ID).
2. Calculate   ccH^Reg_ID = ccH_N+R ^ Reg_ID.
3. SEND ccH^Reg_ID to Fog System.
```

SERVER-SIDE (Fog System):

4. RECIEVED $^{cc}H_{\hat{}Reg\_ID}$.
5. Fetch Reg_ID from database and perform XOR between $^{cc}H_{\hat{}Reg\_ID}$ and Reg_ID to extract $^{cc}H_{N+R}$.
6. Calculate $^{sc}H_{N+R}$ = md5(Reg_ID+ User_ID).
7. If $^{cc}H_{N+R}$ = = $^{sc}H_{N+R}$

   "….. *IoT device is authenticated*.

8. Calculate $^{sc}H_{Reg\_ID}$ = md5(Reg_ID).
9. Calculate $^{sc}H_{\hat{}User\_ID}$ = $^{sc}H_{Reg\_ID}$ ^ User_ID.
10. SEND $^{sc}H_{\hat{}\ User\_ID}$ to IoT Device.

CLIENT-SIDE (IoT Device):

11. RECEIVED $^{sc}H_{\hat{}\ User\_ID}$
12. Perform $^{sc}H_{\hat{}\ User\_ID}$ XOR User_ID to extract $^{sc}H_{Reg\_ID}$.
13. Calculate $^{cc}H_{Reg\_ID}$ = md5 (Reg_ID).
14. If $^{cc}H_{Reg\_\_ID}$ = = $^{sc}H_{Reg\_ID}$.

    "….. *Fog System is Authenticated*.

***……Mutual Authentication Successful*.

5 Results and Discussions

The novel mutual authentication approach method proposed by author is implemented in Visual Studio 2015. The code is simulated using Microsoft IIS manager, which hosts web application that contains codes of algorithm proposed by author.

Fig. 2 Homepage interface

The IoT device we use here is smartphone which acts as IoT node that is mutually authenticated with the server node (PC) using the new algorithm for mutual authentication.

Below given are snapshots of various results that we got while authenticating IoT node with server node.

Figure 2 shows the homepage interface of web application that is used for mutual authentication testing between IoT node and server node. On connecting the Fog network to utilize Fog services the user will first get this interface in which he can either register or authenticate his given credentials provided to him by Fog service provider.

On clicking the Registration button next interface will be available as shown in Fig. 3, and the user has to fill all the details that are being asked for, including User_ID and Reg_ID that is provided to him manually by the Fog service provider while opting for Fog service.

This above interface could be managed by Fog service provider independently if he doesn't want user's interaction. The best idea is that it should be managed by the service provider only, and the user should only be able to authenticate his credentials provided to him by the service provider as shown in Fig. 4. So, in Fig. 3, interface will not be available to the user in our case as we want no interaction of user while storing data in database or generating respective hashes. So, user while getting home interface will have only one option that will be 'Authentication' button for login purpose.

Figure 4 shows the authentication interface that will be available to user after homepage interface. The user has to enter the credentials, i.e. User_ID and Reg_ID as provided by the service provider, after that he has to click on 'Authenticate' button

Fig. 3 Registration interface

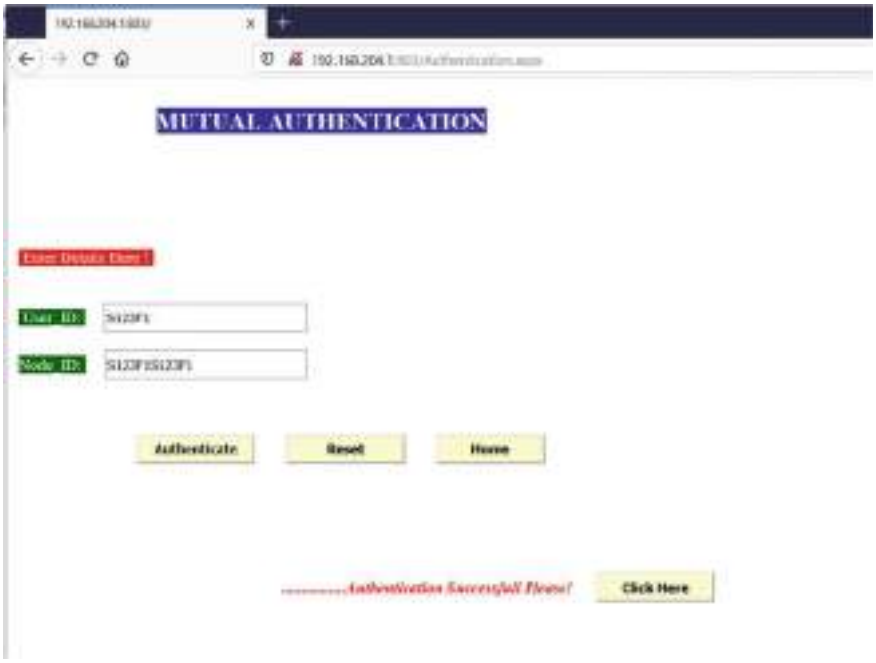

Fig. 4 Mutual authentication interface

Fig. 5 Key generation interface

and if details are correct the new button will appear on screen 'Click Here' that will ask user to click on button. Once user clicks on the Respective button he will be redirected to another interface, that is, key generation interface, next boarder step of proposed framework, namely, 'Novel Hybrid Encryption Framework to secure data transmission between IoT and Fog System'.

In the above case, when user will click on 'Authenticate' button, the algorithm code will run in backend as explained in proposed section that will mutually authenticate both if details are correct. Both will authenticate each other if server is some proxy server or if node is not legitimate node then connection will be terminated.

Figure 5 shows the key generation interface that will be available to the user to generate keys for encryption decryption of data only after successful mutual authentication of IoT device with Fog server.

Figure 6 shows the virtual IoT device connected with the Fog server. The devices successfully get connected with the server and then works perfectly with the proposed methodology.

6 Conclusion

The motive of proposing this algorithm is to overcome the flaws of traditional authentication algorithms that may be present in terms of complexity or security. The mutual authentication is the most important step in any security framework. In case

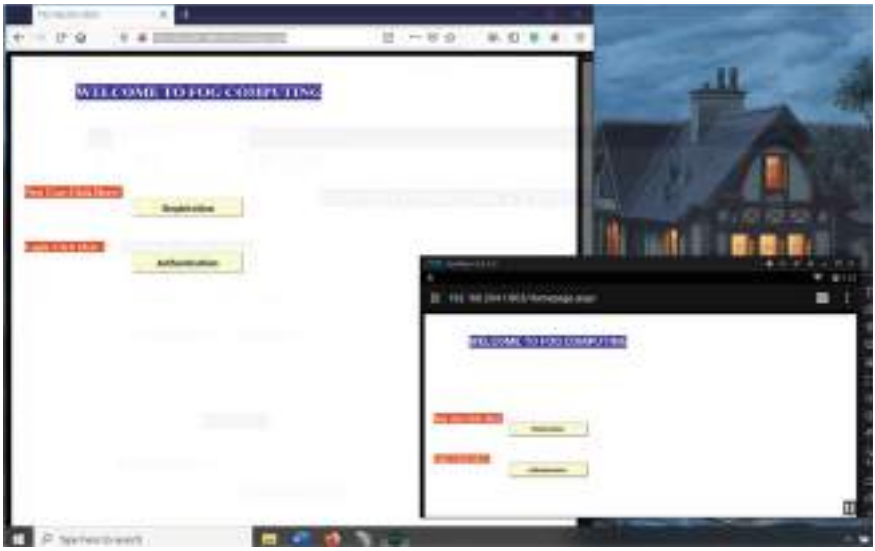

Fig. 6 IoT device connected with Fog server

of cloud and Fog computing using the traditional methods like PKI for authentication don't work, because both are resource-constrained networks and utilizing any framework that consumes higher resources isn't feasible here. The algorithm that we proposed is simple and less complex and reliable to resource-constrained networks. It uses hashing techniques and with simple mathematical operations to achieve mutual authentication from both sides.

References

1. L. Lamport, Password authentication with insecure communication. Commun. ACM **24**(11), 770–772 (1981)
2. C.J. Mitchell, I. Chen, Comments on the S/KEY user authentication scheme. ACM SIGOPS Oper. Syst. Rev. **30**(4), 12–16 (1996)
3. C.M. Chen, W.C. Ku, Stolen-verifier attack on two new strong-password authentication protocol. IEICE Trans. Commun. **E85-B**(11), 2519–2521 (2002)
4. T. Hwang, Y. Chen, C.S. Laih, Non-interactive password authentications without password tables, in *Proceedings of IEEE Region 10 Conference on Computer and Communication Systems* (1990), pp. 429–431
5. M.S. Hwang, L.H. Li, A new remote user authentication scheme using smart cards. IEEE Trans. Consum. Electron. **46**(1), 28–30 (2000)
6. C.K. Chan, L.M. Cheng, Cryptanalysis of a remote user authentication scheme using smart cards. IEEE Trans. Consum. Electron. **46**, 992–993 (2000)
7. J.J. Shen, C.W. Lin, M.S. Hwang, A modified remote user authentication scheme using smart cards. IEEE Trans. Consum. Electron. **49**(2), 414–416 (2003)
8. H.Y. Chien, J.K. Jan, Y.M. Tseng, An efficient and practical solution to remote authentication: smart card. Comput. Secur. **21**(4), 372–375 (2002)

9. H.M. Sun, an efficient remote user authentication scheme using smart cards. EEE Trans. Consum. Electron. **46**(4), 958–961 (2000)
10. W.C. Ku, S.M. Chen, Weaknesses and improvements of an efficient password-based user authentication scheme using smart cards. IEEE Trans. Consum. Electron. **50**(1), 204–207 (2004)
11. C.L. Hsu, Security of Chien et al.'s remote user authentication scheme using smart cards. J. Comput. Stand. Interfaces **26**(3), 167–169 (2004)
12. S. Lee, H. Kim, K. Yoo, improved efficient remote user authentication scheme using smart cards. IEEE Trans. Consum. Electron. **50**(2), 565–567 (2004)
13. E. Yoon, K. Yoo, More efficient and secure remote user authentication scheme using smart cards, in *Proceedings of 11th International Conference on Parallel and Distributed System* (2005), pp. 73–77
14. N.Y. Lee, Y.C. Chiu, Improved remote authentication scheme with smart card. J. Comput. Stand. Interfaces **27**(2), 177–180 (2005)
15. S.T. Wu, B.C. Chieu, A user friendly remote authentication scheme with smart cards. J. Comput. Secur. **22**(6), 547–550 (2003)
16. J. Xu, W.T. Zhu, D.G. Feng, An improved smart card-based password authentication scheme with provable security. J. Comput. Stand. Interfaces **31**(4), 723–728 (2009)
17. S.W. Lee, H.S. Kim, K.Y. Yoo, Improvement of Chien et al.'s remote user authentication scheme using smart cards. J. Comput. Stand. Interfaces **27**(2), 181–183 (2005)
18. R. Song, Advanced smart card-based password authentication protocol. J. Comput. Stand. Interfaces **32**(5), 321–325 (2010)
19. X. Li, F. Wen, S. Cui, A strong password-based remote mutual authentication with key agreement scheme on elliptic curve cryptosystem for portable devices. J. Appl. Math. Inf. Sci. **6**(2), 217–222 (2012)
20. S.K. Kim, M.G. Chung, More secure remote user authentication scheme. J. Comput. Commun. **32**(6), 1018–1021 (2009)
21. H.B. Tang, X.S. Liu, L. Jiang, A robust and efficient timestamp-based remote user authentication scheme with smart card lost attack resistance. Int. J. Netw. Secur. **15**(6), 360–368 (2013)
22. A.K. Awasthi, K. Srivastava, R.C. Mittal, An improved timestamp-based remote user authentication scheme. Comput. Electr. Eng. **37**(6), 869–874 (2011)
23. J. Shen, Y. Du, Improving the password-based authentication against smart card security breach. J. Softw. **8**(4), 979–986 (2013)
24. C.T. Li, C.C. Lee, A robust remote user authentication scheme against smart card security breach, in *Proceedings of the 25th Annual IFIP WG 11.3 Conference on Data and Applications Security and Privacy* (2011), pp. 231–238
25. Q. Jiang, J. Ma, G. Li, L. Yang, Robust two-factor authentication and key agreement preserving user privacy. Int. J. Netw. Secur. **16**(4), 321–332 (2014)
26. L. Li, I. Lin, M. Hwang, A remote password authentication scheme for multi-server architecture using neural networks. IEEE Trans. Neural Netw. Learn. Syst. **12**(6), 1498–1504 (2001)
27. I.C. Lin, M.S. Hwang, L.H. Li, A new remote user authentication scheme for multi-server architecture. Futur. Gener. Comput. Syst. **19**(1), 13–22 (2003)
28. W.S. Juang, Efficient multi-server password authenticated key agreement using smart cards. IEEE Trans. Consum. Electron. **50**(1), 251–255 (2004)
29. W.-C. Ku, H.-M. Chuang, M.-H. Chiang, Cryptanalysis of a multi-server password authenticated key agreement scheme using smart cards. IEICE Trans. Fundam. Electron. Commun. Comput. Sci. **E88-A**(11), 3235–3238 (2005)
30. Y.P. Liao, S.S. Wang, A secure dynamic ID based remote user authentication scheme for multi-server environment. Comput. Stand. Interfaces **31**(1), 24–29 (2009)
31. H.C. Hsiang, W.-K. Shih, Improvement of the secure dynamic ID based remote user authentication scheme for multi-server environment. Comput. Stand. Interfaces **31**(6), 1118–1123 (2009)

32. S.K. Sood, A.K. Sarje, K. Singh, A secure dynamic identity-based authentication protocol for multi-server architecture. J. Netw. Comput. Appl. **34**(2), 609–618 (2011)
33. V. Odelu, A.K. Das, A. Goswami, A secure biometrics-based multi-server authentication protocol using smart cards. IEEE Trans. Inf. Forensics Secur. **10**(9), 1953–1966 (2015)
34. D. He, D. Wang, Robust biometrics-based authentication scheme for multi-server environment. IEEE Syst. J. **9**(3), 816–823 (2015)
35. R. Lu, X. Li, X. Liang, X.S. Shen, X. Lin, GRS: the green, reliability, and security of emerging machine to machine communications. IEEE Commun. Mag. **49**(4), 28–35 (2011)
36. M. Kumar, An enhanced remote user authentication scheme with smart card. Int J. Netw. Secur. **10**(3), 175–184 (2010)
37. M. Kumar, A new secure remote user authentication scheme with smart cards. Int. J. Netw. Secur. **11**(2), 88–93 (2010)
38. R. Lu, Z. Cao, Z. Chai, X. Liang, A simple user authentication scheme for grid computing. Int. J. Netw. Secur. **7**(2), 202–206 (2008)
39. J.L. Tsai, Efficient nonce-based authentication scheme for session initiation protocol. Int. J. Netw. Secur. **9**(1), 12–16 (2009)
40. M.H. Ibrahim, Octopus: an edge-fog mutual authentication scheme. IJ Netw. Secur. **18**(6), 1089–1101 (2016)
41. F. Sameer, D. Prashar, Hybrid encryption algorithm in wireless body area networks (WBAN), in *Intelligent Communication, Control and Devices* (Springer, Singapore, 2018), pp. 401–410

A Robust Massive MIMO Detection Based on Conjugate Gradient Approach

Mitesh Solanki and Shilpi Gupta

Abstract The neighborhood search algorithms recently emerged as a promising low-complexity detection algorithm for massive multiple-input, multiple-output (MIMO) wireless systems have fascinated recent research attention. They iteratively perform searches in a constrained Maximum-likelihood (ML) space for the solution vector. In addition, they execute with a complex matrix inversion an immense number of computations, resulting in higher complexity within a massive MIMO configuration. Motivational by these, we focus on unconstrained minimization problems to quickly decline in an ML cost function and devise for updating rules to improve performance. Using this robust approach and the reduction of the ML cost function concerning the descent direction, we propose a computationally efficient Conjugate Gradient-based local neighborhood search (CGLS) detection algorithm. The proposed CGLS detection algorithm is employed to give the most reduction in the ML cost metric by determining in a decent direction update within an unconstrained neighborhood. It gains acceleration for convergence with few iterations. Simulation results show that the proposed CGLS detector outperforms the counterpart detector.

Keywords Massive MIMO · Constrained maximum-likelihood (ML) space · Conjugate gradient (CG)

1 Introduction

The recent trend toward massive Multiple-Input-Multiple-Output (MIMO) currently has a leading physical layer technological candidate that can offer high spectral efficiency with higher throughput in the 5G wireless standard system. Consequently, massive MIMO has fascinated attention from both academics and industry [1, 2].

M. Solanki (✉) · S. Gupta
Sardar Vallabhbhai National Institute of Technology, Surat 395007, India
e-mail: ds16ec001@eced.svnit.ac.in

S. Gupta
e-mail: sgupta@eced.svnit.ac.in

S. Rawat et al. (eds.), *Proceedings of First International Conference on Computational Electronics for Wireless Communications*, Lecture Notes in Networks and Systems 329,
https://doi.org/10.1007/978-981-16-6246-1_49

In massive MIMO systems have key concept is an equipped base station (BS) with many antenna arrays, and it serves multiple users simultaneously. Diversity and multiplexing gain lead to service authenticity and high data rate for the base stations with large antennas in massive MIMO system [2]. However, in practice, some critical factors like complexity of architecture, high power demand, processing delay, and MIMO antenna size are associated with this system [3]. Amidst these challenges, reliable signal detection at receiver with less complexity is a crucial task in the way of sturdy receiver design [4, 5]. To fulfill the requirement of high data throughput demand of recent wireless applications, all mentioned challenges are to be tackled efficiently.

The maximum-likelihood (ML) is the optimal detector, but it follows an exhaustive search as a result increases computational complexity with the number of antennas with higher order modulation. Consequently, it becomes unmanageable in massive MIMO systems rather than its higher computational complexity [6]. Sphere decoder reports its performance close to ML detector. However, it can only be practical solution for small-scale MIMO systems [7]. Various low-complexity detection algorithms are devised for conventional and large MIMO systems. Such detectors are based on neighborhood search algorithm [8, 9], such as lattice reduction-based detector [10], sparsity-based MIMO detection [11], Gibbs sampling-based detector [12], and interference cancellation-based detector [13]. Due to additional cost constraints these can't be directly applicable for massive MIMO systems in spite of their performance improvement.

Another interesting category of the neighborhood search-based algorithm is likelihood ascent search (LAS), which achieves a better performance-complexity tradeoff in massive MIMO systems [8]. Further, the finding solution vector is conceded within the ML unconstrained space; the error performance can be further improved. With these ideas, the author has proposed an unconstrained LAS (ULAS) detection algorithm [9]; however, it has a highly complex structure and involves inversion of the matrices. In massive MIMO systems, it results in having massively computational complexity.

This detection problem motivates the robust design and development of a new detection scheme that can provide a better alternative in achieving fewer computations inversion less detection algorithms. However, the concept of finding a solution vector within a fixed neighborhood is constrained. Thus, research to find massive MIMO detection is to solve the unconstrained optimization problem using alternate linear solver and iterative search methods. We propose a computationally efficient conjugate gradient-based local neighborhood search (CGLS) detector. The architecture of CGLS is an integration of an evolutionary version of the LAS algorithm and inspired by the conjugate gradient (CG) approach in which added the parameters for speed up convergence. Our simulation results show that CGLS achieves near-optimal performance with high parallelism with fewer iterations than the traditional detection algorithms.

The paper structure is organized as follows: In Sect. 2, we present the system model of a massive MIMO system and propose a signal detection algorithm named

CGLS in Sect. 3. Section 4 provides some simulation results to demonstrate the performance of the proposed CGLS detector. Finally, Sect. 5 describes conclusions.

2 System Model

We discuss the system model of downlink massive MIMO system where a base station (BS) employed with n_t antenna is communicating with a piece of user equipment (UE) with n_r antennas (where $n_r \checkmark n_t$). The transmitted data stream vector is denoted by $\overline{x} = \left(\overline{x}_1, \overline{x}_2, \ldots, \overline{x}_{n_t}\right)^T$, where $\overline{x}_i \epsilon \mathbb{C}^{n_t \times 1}$. The received signal vector is indicated by $\overline{y} = \left(\overline{y}_1, \overline{y}_2, \ldots, \overline{y}_{n_r}\right)^T$, $\overline{y}_i \epsilon \mathbb{C}^{n_r \times 1}$, where the system model is represented by mathematically as

$$\overline{y} = \overline{H}\overline{x} + \overline{n}, \tag{1}$$

where $\overline{n} = \left(\overline{n}_1, \overline{n}_2, \ldots, \overline{n}_{n_r}\right)^T \epsilon \mathbb{C}^{n_r \times 1}$ denotes the additive white Gaussian noise vector at the receiver, with each element having the Gaussian distribution with mean zero and variance σ_n^2. Moreover, $\overline{H} \epsilon \mathbb{C}^{n_r \times n_t}$ is the channel matrix, with each element having the independent and identically distributed $(i.i.d.)$ complex zero mean and variance unity. $\overline{x}$ is the map with quadrature amplitude modulation $\mathcal{M}$-QAM constellation scheme; the $\overline{x}$ entries are taken values from $\{\mathcal{A}_m, m = 1, \ldots, \mathcal{M}\}$, where $\mathcal{A}_m = (2m - 1 - \mathcal{M})$. To simplify the process of signal detection, we avoid forming complex symbols by forming equivalent real-valued presentations, i.e., switching from a complex k-dimensional to a real $2k$-dimensional one [8, 9]. Thus, the real equivalent system model can be written as follows:

$$y = Hx + n, \tag{2}$$

where

$$y = \begin{bmatrix} \Re\{\overline{y}\} \\ \Im\{\overline{y}\} \end{bmatrix} \epsilon \mathbb{R}^{2n_r \times 1}, \quad x = \begin{bmatrix} \Re\{\overline{x}\} \\ \Im\{\overline{x}\} \end{bmatrix} \epsilon \mathbb{R}^{2n_t \times 1},$$

$$n = \begin{bmatrix} \Re\{\overline{n}\} \\ \Im\{\overline{n}\} \end{bmatrix} \epsilon \mathbb{R}^{2n_r \times 1}, \qquad H = \begin{bmatrix} \Re\{\overline{H}\} & -\Im\{\overline{H}\} \\ \Im\{\overline{H}\} & \Re\{\overline{H}\} \end{bmatrix} \epsilon \mathbb{R}^{2n_r \times 2n_t}.$$

For simplicity, we consider the real equivalent system model (2). Our main intention is to find the solution vector from the set of all possible transmit vectors $\left(\log_2 \mathcal{M}\right)^{2n_t}$ that is close to the receive signal vector y, which provides a reduction in ML cost. Thus, it can be defined mathematically as follows

$$\widehat{x}_{ML} = \arg \min_{x \epsilon \mathcal{A}_m^{2n_t}} \|y - Hx\|^2, \tag{3}$$

it indicates ML detection. We express the objective ML cost function as

$$\phi(x) = \|y - Hx\|^2 = \sum_{i=1}^{2n_r} \left| y_i - \sum_{j=1}^{2n_t} h_{ij} x_j \right|^2. \tag{4}$$

As the size of the system goes larger, the ML detector is stringently becoming burdensome that makes it infeasible for implementation in the real systems. By definition of the neighborhood search algorithm, there is execution with some policy of neighborhoods [9]. In the next section, we are reformulated the ML problem using an unconstrained optimization problem.

3 Proposed Conjugate Gradient-Based Local Neighborhood Search Algorithm

3.1 Conjugate Gradient Method

A computationally efficient linear solver Conjugate Gradient (CG) approach can evaluate a system linear equation with low computations [14, 15]. Let us defining of the solution vector start of the iteration (k)th as $x^{(k)}$ and it will end of $(k+1)$th iteration as $x^{(k+1)}$. Now, the ML cost metric of $x^{(k+1)}$ represented it with the help of Taylor series expansion [9]. Now, considering the basic concepts of the iterative solver method for a smooth unconstrained optimization problem. Usually, our main intent in diminishing the ML cost metric is to ensure that movements from iteration (k)th to $(k+1)$th are only allowed to reduce ML cost. Thus, the solution update vector on (k)th iteration decreases ML cost metric at an optimum update point. Therefore, this optimal update is not limited to constrained space but is anywhere in a full ML space. So now, we refer to this update as the unconstrained symbol update. Thus, the ML solution would achieve through this unconstrained optimization problem. We apply this Conjugate Gradient (CG) approach to the objective ML cost function for a solution. The ML cost function (3) is formulated using an unconstrained optimization problem. The ML cost function can be expressed with linear expression with an unconstrained optimization problem as follows:

$$\hat{x}_{ML} = \arg\min_{x \epsilon \Omega^{2n_t}} \left\{ \frac{1}{2} x^{(k)^T} W x^{(k)} - f^{(k)^T} x^{(k)} \right\}, \tag{5}$$

where $W = H^T H$ presents symmetric positive semidefinite matrix, $f^{(k)} = \left(y - Hx^{(k)}\right)^T H$. Therefore, the gradient of ML cost metric (5) at the optimum point will be zero, i.e., $Wx^{(k)} - f^{(k)^T} = 0$. So now, we can define the conjugate direction as $\mathcal{D} = \left[d_{(0)}, d_{(1)}, \ldots, d_{(l-1)}\right]$ concerning with given W, i.e., as $d_{(i)}^T W d_{(j)} = 0, \forall i \neq j$.

The main advantage of the CG approach is the fact that the CGLS algorithm convergence and iteration process with a few iterations comes close to the exact optimal point. Therefore, we can reduce the cost function within l steps by progressively diminishing its l individual conjugate direction in $\mathcal{D}$. In the evaluation of the gradients of the objective function, we can set a new conjugate descent direction to reduce subsequent iterations, and so we can achieve faster convergence. The formation of conjugate directions and development is based on the Fletcher-Reeves approach [16]. The CGLS algorithm can find the solution vector within the l iterations. Therefore, the next symbol update by lth iterations can be written as follows:

$$x_{(l+1)}^{(k)} = x_{(l)}^{(k)} + \lambda_{(l)} d_{(l)}, l = 0, 1, 2, \ldots, kmax, \tag{6}$$

where l indicates iteration index, $kmax$ is the iteration number, and $\lambda_{(l)}$ is the learning parameter that describes the optimum step length with $d_{(l)}$. The flowchart of the CGLS detector is presented in Fig. 1.

Furthermore, we consider a negative gradient of (5) is equal to the residual $r_{(l)}$ of a linear system, i.e.,

$$r_{(l)} = f^{(k)^T} - W x_{(l)}^{(k)}. \tag{7}$$

In the proposed CGLS algorithm to calculate the iteration and parameters, initial settings are required, such as $x^{(0)}$; η is the indicate algorithm stopping tolerance; and $d_{(l)} = r_{(l)}$. Determine the update residual vector for the update descent direction of the next step, which reduces the ML cost very quickly. It takes a step length $\lambda_{(l)}$ by the learning rate until the solution comes close to the vector. Finally, it sets the approximate step size $\beta_{(l)}$ parameter for the new search direction.

3.2 Pre-processing

The CGLS starts with an initial solution vector as $x^{(0)}$. For the initial solution vector, we can use such as Matched-Filter (MF), or Zero forcing (ZF), or Minimum Mean Square Error (MMSE), which can mathematically be expressed as follows:

$$x_{MF}^{(k)} = \lceil H^T y \rfloor_{\mathcal{A}_m}$$

$$x_{ZF}^{(k)} = \lceil \left(H^T H\right)^{-1} H^T y \rfloor_{\mathcal{A}_m}$$

$$x_{MMSE}^{(k)} = \lceil \left(H^T H + \sigma^2 I\right) H^T y \rfloor_{\mathcal{A}_m}, \tag{8}$$

where $\lceil . \rfloor_{\mathcal{A}_m}$ represents the element-wise rounding from the set of $\mathcal{A}_m$. In the iterative process, the initial solution can lead to increased detection accuracy for a final solution

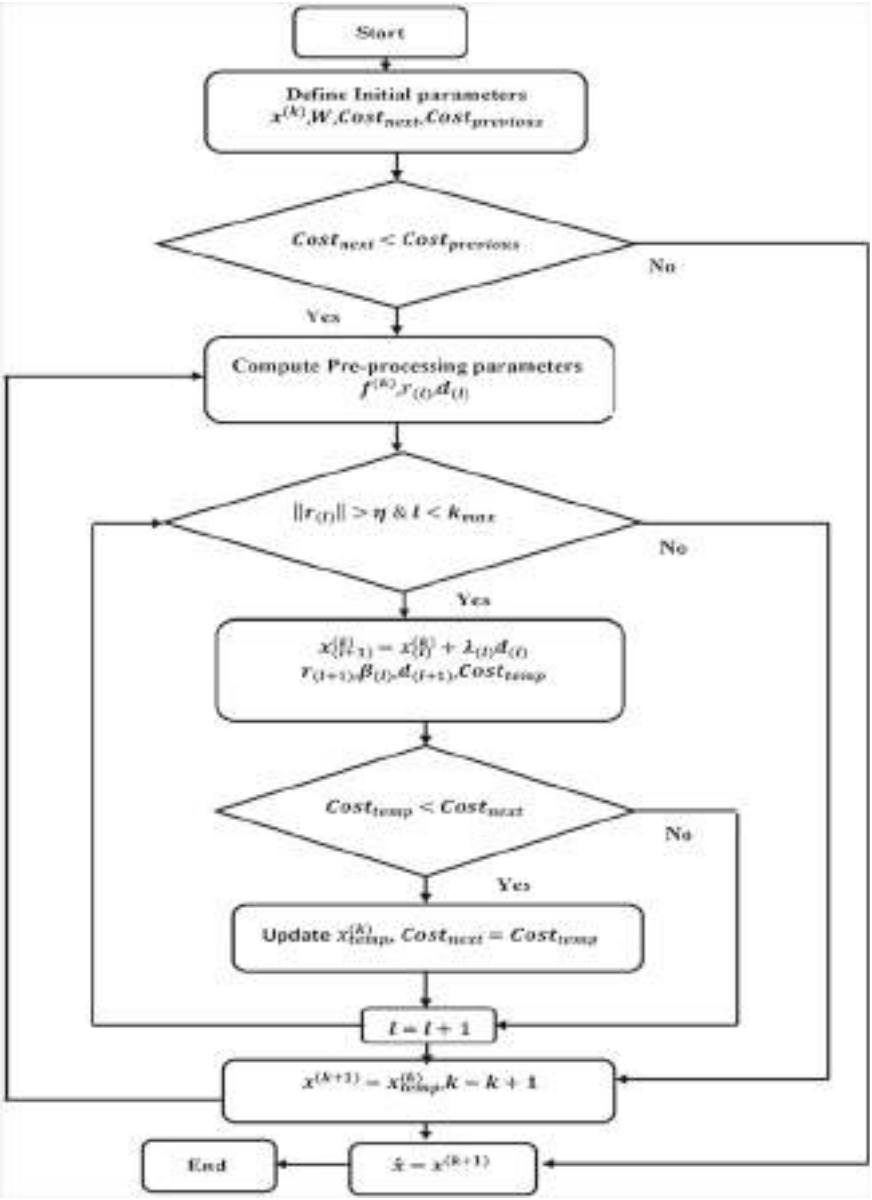

Fig. 1 The CGLS detector flowchart

with a few iterations. In our study, we have chosen the MMSE initial solution vector. This advantage is important in detection accuracy [17].

4 Simulation Results

In this section, the performance of the proposed CGLS detector for massive MIMO systems has been investigated. We evaluate the BER performance of the CGLS detector via comprehensive simulation and compare its counterpart detector as ULAS [9]. The simulations for plotting the BER curve are obtained for 4-QAM, and 16-QAM modulations, massive MIMO configurations such as $n_t = n_r = 8, 16$. We consider up to the transmission data frame length is equal to 1024; the stopping tolerance of the algorithm is $\eta = 10^{-4}$; the number of iterations is $k_{max} = 3$, and taken MMSE solution as the initial vector.

4.1 Analysis of BER Performance

The BER performance of the proposed CGLS has been evaluated with respect to ULAS detector, as shown in Figs. 2 and 3, respectively. From the figure, it can be seen that the proposed CGLS achieves better performance than ULAS one. For example, compared to ULAS, CGLS requires 1.4 dB and 1.6 dB less SNR to achieve a BER of 10^{-3} for 8×8 MIMO systems using 4-QAM and 16-QAM modulations, respectively.

We can also see that, for $n_t = n_r = 16$, the CGLS much better emulates the performance of a ULAS. These figures show clearly the effectiveness of the CGLS detector.

In summary, the simulation results are proved that CGLS can achieve better performance with significantly faster convergence. Therefore, CGLS achieves advantages over related work in terms of parallelism and detection accuracy.

5 Conclusion

This paper proposes a near-optimal low-complexity MIMO detector based on the Conjugate gradient approach. The proposed CGLS detector is derived as an expression for minimizing ML cost through the formulation of an unconstrained optimization problem. A linear solver CG method based on the search for the optimal point is further used to keep the matrix inversion-free operation in the iterative process. We explicated, with simulation results, that our proposed CGLS exhibits a significant performance improvement, especially when higher order modulation and increases

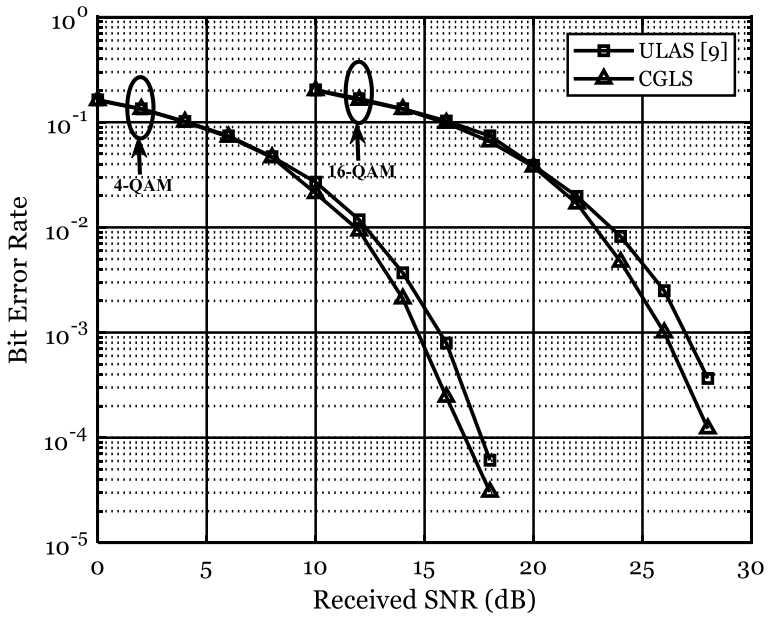

Fig. 2 The BER versus SNR: comparison of the proposed Conjugate Gradient-based local neighborhood search (CGLS) and conventional ULAS; 4-QAM and 16-QAM over 8×8 MIMO systems

the number of antennas with few iterations. Hence, our robust CGLS detector is more implementation-friendly for massive MIMO systems.

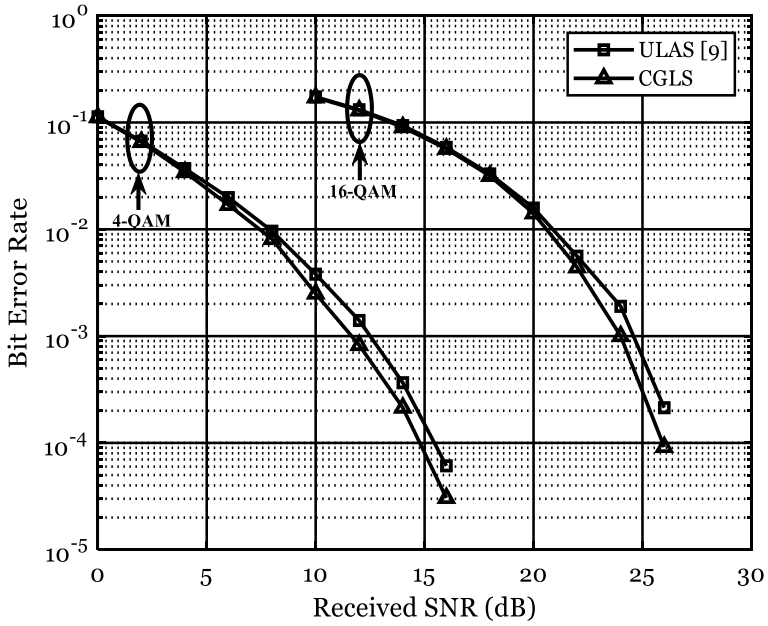

Fig. 3 The BER versus SNR: comparison of the proposed Conjugate Gradient-based local neighborhood search (CGLS) and conventional ULAS; 4-QAM and 16-QAM over 16 × 16 MIMO systems

References

1. S. Yang, L. Hanzo, Fifty years of MIMO detection: the road to large-scale MIMOs. IEEE Commun. Surv. Tutor. **17**(4), 1941–1988 (2015)
2. E.G. Larsson, O. Edfors, F. Tufvesson, T.L. Marzetta, Massive MIMO for next generation wireless systems. IEEE Commun. Mag. **52**(2), 186–195 (2014)
3. F. Rusek et al., Scaling up MIMO: opportunities and challenge with very large arrays. IEEE Signal Process. Mag. **30**(1), 40–60 (2013)
4. E.G. Larsson, MIMO detection methods: how they work [lecture notes]. IEEE Signal Process. Mag. **26**(3), 91–95 (2009)
5. M. Wu, B. Yin, G. Wang, C. Dick, J.R. Cavallaro, C. Studer, Large-scale MIMO detection for 3GPP LTE: algorithms and FPGA implementations. IEEE J. Sel. Top. Signal Process. **8**(5), 916–929 (2014)
6. A. Chockalingam, B.S. Rajan, *Large MIMO Systems* (Cambridge University Press, 2014)
7. L.G. Barbero, J.S. Thompson, Fixing the complexity of the sphere decoder for MIMO detection. IEEE Trans. Wirel. Commun. **7**(6), 2131–2142 (2008)
8. K.V. Vardhan, S.K. Mohammed, A. Chockalingam, B.S. Rajan, A low-complexity detector for large MIMO systems and multicarrier CDMA systems. IEEE J. Sel. Areas Commun. **26**(3), 473–485 (2008)
9. A.K. Sah, A.K. Chaturvedi, An unconstrained likelihood ascent based detection algorithm for large MIMO systems. IEEE Trans. Wirel. Commun. **16**(4), 2262–2273 (2017)
10. Q. Zhou, X. Ma, Element-based lattice reduction algorithms for large MIMO detection. IEEE J. Sel. Areas Commun. **31**(2), 274–286 (2013)
11. Y. Fadlallah, A. Aïssai-El-Bey, K. Amis, D. Pastor, R. Pyndiah, New iterative detector of MIMO transmission using sparse decomposition. IEEE Trans. Veh. Technol. **64**(8), 3458–3464 (2015)

12. A.M. Mussi, T. Abrão, Multiple restarts mixed Gibbs sampling detector for large-scale antenna systems. IET Signal Proc. **13**(3), 273–285 (2019)
13. P. Li, R.C. de Lamare, R. Fa, Multiple feedback successive interference cancellation detection for multiuser MIMO systems. IEEE Trans. Wirel. Commun. **10**(8), 2434–2439 (2011)
14. M.R. Hestenes, E. Stiefel, Methods of conjugate gradients for solving linear systems. J. Res. Natl. Bur. Stand. **49**(6), 409–436 (1952)
15. B. Yin, M. Wu, J.R. Cavallaro, C. Studer, Conjugate gradient-based soft-output detection and precoding in massive MIMO systems, in *IEEE Global Communications Conference*, *Austin* (2014), pp. 3696–3701
16. R. Fletcher, C.M. Reeves, Function minimization by conjugate gradients. Comput. J. **7**(2), 149–154 (1964)
17. L. Liu, G. Peng, P. Wang, S. Zhou, Q. Wei, S. Yin, S. Wei, Energy- and area-efficient recursive-conjugate-gradient-based MMSE detector for massive MIMO systems. IEEE Trans. Signal Process. **68**, 573–588 (2020)

Performance Analysis of LAS Algorithm in Massive MIMO with Imperfect CSI

Mitesh Solanki and Shilpi Gupta

Abstract Likelihood Ascent Search (LAS) algorithm is a low-complexity detection algorithm that emerges as an optimistic in massive multiple-input multiple-output (MIMO) systems. In real-time scenarios, channel estimation is challenging in wireless communication systems. This paper proposes a lattice reduction-based LAS (LR-LAS) detector for efficient detection under the assumption of imperfect channel state information. Our proposed LR-LAS detector takes computing the maximum likelihood (ML) cost in the ubiquity of a medium-to-strong estimation error. Our approach presents a novel training-based channel estimation and detection framework. Simulation results on the performance of the Bit Error Rate (BER) of LR-LAS are compared by drawing useful insights for massive antennas.

Keywords Likelihood ascent search · Massive MIMO · Lattice reduction · Imperfect channel state information · Maximum likelihood cost function

1 Introduction

The recent trend toward leading technological candidates as massive multiple-input multiple-output (MIMO) systems requires vast enhancement in network throughput and efficiency to achieve performance demanding by consumers in the 5G era [1, 2]. In massive MIMO features, deploy base stations with massive antennas that serve simultaneously communicate with many users. The maximum likelihood (ML) is the optimal detector, but it follows an exhaustive search, as a result, increases computational complexity with the number of a transmitter antenna and constellation size. Consequently, it becomes unmanageable in massive MIMO systems because of increasing growth complexity [3]. Sphere decoder reports its performance close

M. Solanki (✉) · S. Gupta
Sardar Vallabhbhai National Institute of Technology, Surat 395007, India
e-mail: ds16ec001@eced.svnit.ac.in

S. Gupta
e-mail: sgupta@eced.svnit.ac.in

S. Rawat et al. (eds.), *Proceedings of First International Conference on Computational Electronics for Wireless Communications*, Lecture Notes in Networks and Systems 329,
https://doi.org/10.1007/978-981-16-6246-1_50

to ML detector. However, it can only be a practical solution for small-scale MIMO systems [4, 5]. The neighborhood search algorithms recently emerged as a promising low-complexity detection algorithm suitable candidates near-optimal performance alternatives for massive MIMO systems. The integrated linear minimum mean square error (LMMSE) multi-user detection views and a joint of single user message passing decoder have proposed a solution that maintains low complexity and performance in [6]. A well-known algorithm finds the optimum but has high complexity for hardware implementation. One of the most important parts to pay attention in massive MIMO systems is the design of an efficient low-complexity detection algorithm [7, 8]. Performance investigation and system design for massive MIMO systems are under acceptance with channel state information (CSI) is fully known at the receiving end. This channel information is unrealistic for most practical communication systems, especially in fast-fading channels [9, 10].

In massive MIMO systems, the achievable higher throughput with imperfect CSI has been rigorously reported for fading channels. Moreover, an iterative channel estimation approach has been proposed for massive MIMO systems with least square (LS) estimation and spare message passing (SMP) algorithms [11]. The iterative channel estimation and detection are an encouraging approach to enhancing the accuracy of detection by iterations. This approach can be made obtainable via the exploitation of both training-based approach and detection. It is attention to use a lattice reduction-based detector with lower computational complexity in an iterative detection/estimation approach in massive MIMO systems [12].

Another fascinating class of neighborhood search-based algorithm is likelihood ascent search (LAS) algorithm, which obtains much better balance in performance and complexity trade-off across massive MIMO systems. Most LAS algorithms introduced are a design with uncorrelated MIMO channels on the receiver under consideration of accurate CSI [13, 14]. In [14], the authors have proposed a space–time block code (STBC) and an iterative channel estimation/detection scheme, the LAS detector has been investigated with imperfect CSI. One paper has addressed a LAS detector using a basic least square (LS) channel estimator for the MIMO system [8, 15]. However, for large-scale systems, a new approach to improving the quality of channel estimation is still needed. Newly, the growing interest in training-based channel estimation has become one of the most popular approaches to solving problems of massive MIMO systems. In [5, 16], how best to choose optimal training sequence for the implementation of training-based channel estimators such as linear LS and minimum mean square error (MMSE) has been investigated for both multiple transmission and single receiver antennas.

In the present work, we have developed a robust approach to training-based estimation with a LAS detector in a massive MIMO system even with incomplete CSI. Here, generic system model is being considered that accounts for the occurrence of channel estimation error on the user equipment (UE) side. We use MMSE, the most widely used linear channel estimation scheme. To aid channel estimation at the UE, the base station (BS) simultaneously transmits a specific length of the mutual orthogonal training sequences. Thus, projections on the signal received from the known training matrix are conditional, which is naturally advantageous for channel

statistics. The main contribution of this paper is to propose the adoption of an LR scheme to alleviate the effects of channel estimation error in system performance. We propose a lattice reduction-based LAS (LR-LAS) algorithm to improve the detection accuracy and reduction of ML cost. We consider a training-based channel estimator for detection/estimation framework in massive MIMO systems. We first estimate the channel matrix by MMSE estimator based on the known at the receiving signal. Then, LR-LAS detector uses the estimated channel matrix with LR-based initial solution vector in the detection process. The LR method provides an orthogonal basis and consequently improves performance under imperfect CSI conditions.

The paper structure is formed as follows: In Sect. 2, we present the signal system model of massive MIMO systems with a training-based channel estimation and discuss the iterative LAS algorithm with accurate CSI. Section 3 introduces the proposed LR-LAS algorithm with imperfect CSI and reformulates ML cost. Section 4 provides some simulation results to demonstrate the performance of LR-LAS detector. Finally, Sect. 5 concludes.

2 System Model and Channel Estimator

2.1 System Model

We discuss the signal system model of block fading massive MIMO systems a base stations (BS) employed with n_t antenna is communicating with a piece of user equipment (UE) with n_r. Thus, during the data-symbol transmission stage, the $n_r \times 1$ complex received-signal vector $y_c \beta \mathbb{C}^{n_r \times 1}$ can be expressed mathematically as

$$y_c = H_c x_c + n_c, \tag{1}$$

where $x_c \beta \mathbb{C}^{n_t \times 1}$ is the $n_t \times 1$ is denoted transmitted data stream vector, $n_c \beta \mathcal{CN}\left(0, \alpha_n^2 I_{n_r}\right)$ is the $n_r \times 1$ complex Gaussian noise vector, and $H_c \beta \mathbb{C}^{n_r \times n_t}$ indicates the complex channel-gain matrix. x_c is the map with quadrature amplitude modulation (*M-QAM*) constellation schemes; the x_c entries are taken values from $\{\mathcal{A}_m, m = 1, \cdots, M\}$, where $\mathcal{A}_m = (2m - 1 - M)$ [14]; and those transmitted symbols are equally probable and independent, with $\mathbb{E}\left[x_c x_c^{\mathcal{H}}\right] = E_s I_{n_t}$, where E_s indicates average transmitted energy. For the channel-gain matrix, we adopt the spatial correlation channel model [16], an important MIMO channel model in which

$$H_c = R_{n_r}^{\frac{1}{2}} H_w^c R_{n_t}^{\frac{1}{2}}. \tag{2}$$

Here $H_w^c \beta \mathbb{C}^{n_r \times n_t}$ denotes random matrix, with each element having the independent and identically distributed $(i.i.d.)$ complex zero-mean circular symmetrical complex Gaussian (ZMCSCG) with variance unit. $\mathrm{R}_{n_r} \beta \mathbb{C}^{n_r \times n_r}$ and $\mathrm{R}_{n_t} \beta \mathbb{C}^{n_t \times n_t}$ both represent receiving and transmitting correlation matrices, respectively. To simplify

the process of signal detection, we avoid forming complex symbols by forming equivalent real-valued presentations, i.e., switching from a complex k-dimensional space into a real 2 k-dimensional one. Then Eq. (1) can be rewritten as [14]

$$y = Hx + n, \tag{3}$$

where

$$n = \begin{bmatrix} \Re\{n_c\} \\ \Im\{n_c\} \end{bmatrix} \beta \mathbb{R}^{2n_r \times 1}, \; H = \begin{bmatrix} \Re\{H_c\} & -\Im\{H_c\} \\ \Im\{H_c\} & \Re\{H_c\} \end{bmatrix} \beta \mathbb{R}^{2n_r \times 2n_t},$$
$$y = \begin{bmatrix} \Re\{y_c\} \\ \Im\{y_c\} \end{bmatrix} \beta \mathbb{R}^{2n_r \times 1}, \; x = \begin{bmatrix} \Re\{x_c\} \\ \Im\{x_c\} \end{bmatrix} \beta \mathbb{R}^{2n_t \times 1}. \tag{4}$$

According to Eqs. (2) and (4), we can write $H = R_{H,n_r}^{\frac{1}{2}} H_w R_{H,n_r}^{\frac{1}{2}}$, where

$$\mathrm{R}_{\mathrm{H,n_r}} = \begin{bmatrix} \mathrm{R}_{\mathrm{n_r}} & 0_{\mathrm{n_r}} \\ 0_{\mathrm{n_r}} & \mathrm{R}_{\mathrm{n_r}} \end{bmatrix} \quad \text{and} \quad \mathrm{R}_{\mathrm{H,n_t}} = \begin{bmatrix} \mathrm{R}_{\mathrm{n_t}} & 0_{\mathrm{n_t}} \\ 0_{\mathrm{n_t}} & \mathrm{R}_{\mathrm{n_t}} \end{bmatrix}. \tag{5}$$

2.2 Channel Estimator

We describe the estimate of channel matrix using the popular training sequence approach. We assume that the frame of the channel $\left(L_p + L_d\right)$ is fading with time variations, where L_p refers to symbol intervals in the pilot sequence, and L_d to those in data transmission. For a linear MMSE channel estimator, any training sequence matrix $\mathrm{X}_p \beta \mathbb{C}^{n_t \times L_p}$ with an orthogonal rows and same norm which is optimal in terms of reducing mean square estimation error [5]. According to (1), the received-signal matrix $\mathrm{Y}_p \beta \mathbb{C}^{n_r \times L_p}$ during the training sequence transmission is given by [5]

$$Y_p = H_c X_p + N_p, \tag{6}$$

where $N_p \beta \mathbb{C}^{n_r \times L_p}$ indicates additive white Gaussian noise matrix with each element $N_p \sim \mathcal{CN}\left(0, \alpha_n^2 \mathrm{I}_{n_r}\right)$. Therefore, we assume that X_p satisfies $\mathbb{E}\left[X_p X_p^{\mathcal{H}}\right] = E_p L_p I_{n_t}$, where E_p is the energy of each training symbol. Knowing X_p and Y_p, using MMSE channel estimation, the estimated channel matrix given in [5] is as follows:

$$\widehat{H}_{MMSE} = Y_p \left(X_p^{\mathcal{H}} R_{H_c} X_p + \alpha_n^2 n_r I_{n_r}\right)^{-1} X_p^{\mathcal{H}} R_{H_c}, \tag{7}$$

where $\mathrm{R}_{H_c} = \mathbb{E}\left\{H_c^{\mathcal{H}} H_c\right\}$ indicates the matrix of channel correlations. Therefore, the estimated channel matrix is $\widehat{H}_{MMSE} = H_c + E$, where channel estimation error matrix E is a ZMCSCG with $E \sim \mathcal{CN}\left(0, \alpha_e^2\right)$ elements [5]. The variance of E is

given by [17]

$$\alpha_e^2 = \alpha_n^2/(L_p \mathrm{E}_p). \tag{8}$$

Furthermore, E is uncorrelated to the channel matrix [17], i.e., $\mathbb{E}\left[E^{\mathcal{H}} H_c\right] = 0$. Therefore, channel estimation error in [5] gives the association of the covariance matrix,

$$R_E = \mathbb{E}\left[EE^{\mathcal{H}}\right] = \left(R_{H_c}{}^{-1} + \frac{1}{\alpha_n^2 n_r} X_p X_p^{\mathcal{H}}\right)^{-1}. \tag{9}$$

Thus, the mean square error J_{MMSE} can be calculated as [5]

$$J_{MMSE} = tr\{R_E\} = tr\left\{\left(R_{H_c}{}^{-1} + \frac{1}{\alpha_n^2 n_r} X_p X_p^{\mathcal{H}}\right)^{-1}\right\}. \tag{10}$$

Now, using an eigenvalue decomposition of R_{H_c} in the form $R_{H_c} = U\omega U^{\mathcal{H}}$, where ω and U are defined as diagonal matrix and unitary eigenvector matrix with a positive eigenvalue of R_{H_c}, respectively. Consequently, the mean square error, J_{MMSE}, (10) gives [5]

$$J_{MMSE} = tr\left\{\left(\omega^{-1} + \tilde{X}_p \tilde{X}_p^{\mathcal{H}}\right)^{-1}\right\}, \tag{11}$$

where $\tilde{X}_p = \frac{1}{\sqrt{\alpha_n^2 n_r}} U^{\mathcal{H}} X_p$.

2.3 LAS Detector with Perfect Channel State Information

In this section, we describe LAS detector. Using the real equivalent signal system model (3) and assuming perfect CSI, the mathematical expression in [13, 14] of the ML solution is

$$\hat{x}_{ML} = \underset{x\beta\mathcal{A}_m^{2n_t}}{arg\ min} \|y - Hx\|^2. \tag{12}$$

LAS algorithm is a local-search-based iterative detector that starts with an initial solution vector $x^{(0)}$ (in our case, MMSE solution) and then generates different vectors in the same neighborhood. In the next step, the algorithm seeks the vector in the neighborhood with the lowest ML cost. If such a vector is found, it is treated as a new solution vector and next iteration is performed. If, however, a further reduction in ML cost is not found, then algorithm terminates, and current vector is considered

as a final solution vector. The initial solution vector begins with the k th iteration as $x^{(k)}$. It terminates at the end of $x^{(k+1)}$ from the $(k+1)$th iteration to refine the solution with LAS [14]. The ML cost at the k th iteration $C\left(x^{(k)}\right)$ is written as [13]

$$C\left(x^{(k)}\right) = x^{(k)^T} H^T H x^{(k)} - 2y^T H x^{(k)}. \tag{13}$$

3 Proposed LR-LAS Detector with Imperfect CSI

We use the LAS detector to minimize the ML cost and update the current solution. LAS is favorable for Lattice Reduction (LR) as its aid in attaining alternatives leading to further improvements in error performance with imperfect CSI [12]. The MMSE solution $\tilde{x}_{LR-MMSE}$ to a modified channel matrix $\widehat{H}_{MMSE}$ is expressed as [12]

$$\tilde{x}_{LR-MMSE} = Wy, \tag{14}$$

where $W = \left(\widehat{H}_{MMSE}^T \widehat{H}_{MMSE} + \alpha_n^2 I_{2n_r}\right)^{-1} \widehat{H}_{MMSE}^T$. This result will be extremely important for enabling the LAS detector to accommodate the initial MMSE solution.

3.1 Mathematical Formulation

In applying the LR technique with imperfect CSI, we consider estimated channel matrix is known on receiver and that an initial value given to LAS detector by MMSE receiver is given by (14) with [12]

$$W = \left(\widehat{H}_{MMSE}^T \widehat{H}_{MMSE} + \alpha_n^2 I_{2n_r}\right)^{-1} \widehat{H}_{MMSE}^T. \tag{15}$$

LR method provides reduction of the basis of the channel matrix, and find a new, almost orthogonal basis. The lattice itself remains the same, but now with $\tilde{H}_{LR-MMSE} = \widehat{H}_{MMSE}\widehat{T}$, where $\widehat{T}$ is a unimodular matrix [18]. Let W denote the MMSE solution that gives suppression in interfering signals and provides the detection of $\tilde{x}_{LR-MMSE}$ as follows [18]:

$$\hat{x} = \widehat{T}^{-1} \tilde{x}_{LR-MMSE}.$$

The LR detection vector is $\hat{x}$, after the scaling and shifting operations are straightforward. Let $\hat{x} = \left[\hat{x}_1, \hat{x}_2, \cdots, \hat{x}_{2n_t}\right]^T$ be the MMSE solution. We can formulate the ML cost (12) as

$$C_0\left(\hat{x}^{(k)}\right) = \hat{x}^{(k)^T}\widehat{H}_{MMSE}^{T}\widehat{H}_{MMSE}\hat{x}^{(k)} - 2y^T\widehat{H}_{MMSE}\hat{x}^{(k)}. \quad (17)$$

4 Analysis of Simulation Results

In this section, the performance of the training-based MMSE estimation with the proposed LR-LAS detector is investigated and compared with counterpart LAS detectors. We analyze the performance of the LR-LAS algorithm by comprehensive simulations and compare its BER with closely related state-of-the-art schemes. Throughout the simulation, we consider the channel elements are stationary in the transmitting end. We consider a massive MIMO system with $n_t = n_r = 4, 8, 16$; a 4-QAM modulation scheme; training sequence lengths $L_p = n_t$; $\alpha_e^2 = 0.02$, and frame time slot $L_p + L_d = 1024$. We start by comparing the LR-LAS detector with the conventional LAS detector [14, 15], taking the MMSE solution as the initial vector.

4.1 Result Discussion

We examine the proposed LR-LAS detector with conventional space–time block code STBC LAS for 4×4, and 8×8 MIMO system with 4-QAM modulation scheme. BER performance of LR-LAS and modified LAS detector has also been shown for 4-QAM with $n_t = n_r = 16$. The proposed LR-LAS detector BER performance is illustrated in Fig. 1. The performance of the LAS detector with accurate CSI provides a benchmark reference curve. From the figure, it can be observed that the LR-LAS performs much better than STBC LAS for $n_t = n_r = 4, 8$.

The BER performance of LR-LAS and conventional LAS with the MMSE estimation scheme and modified LAS is also shown for 16×16 MIMO system in Fig. 1. It can be observed that the proposed LR-LAS required only 10.2 dB SNR to achieve 10^{-3} BER, whereas the conventional LAS scheme required 11.3 dB SNR and modified LAS scheme required 10.8 dB SNR. Thus, the proposed algorithm significantly outperforms the conventional LAS. By increasing $n_t = n_r$, the proposed LR-LAS more closely emulates the performance of the perfect CSI LAS detector. Thus, the LR-LAS detector shows strong candidature for use in massive MIMO systems.

5 Conclusion

This paper has discussed lattice reduction-based LAS (LR-LAS) detection algorithm with massive MIMO systems. The effect of channel estimation error due to the

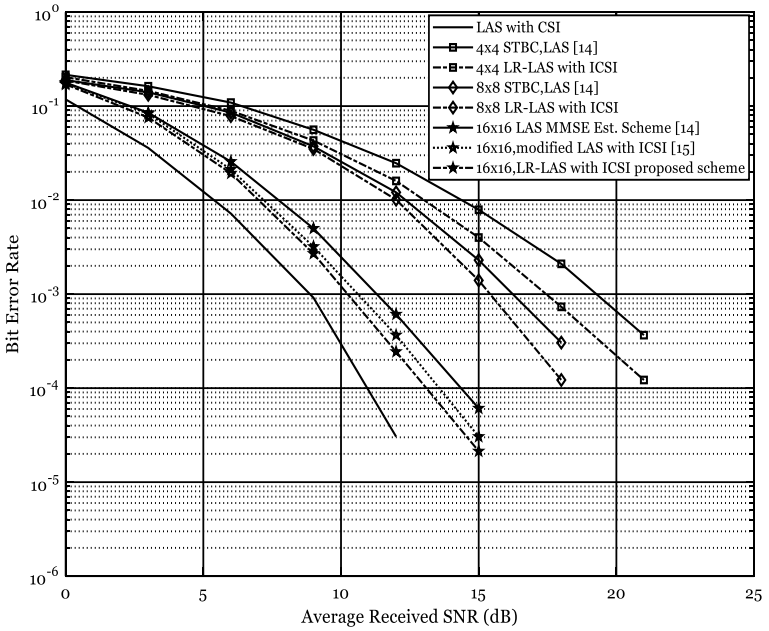

Fig. 1 Comparison of proposed lattice reduction-based likelihood ascent search (LR-LAS) and conventional LAS, with perfect and imperfect channel state information (CSI and ICSI) cases; 4-QAM over 4×4, 8×8, and 16×16 MIMO systems

inaccuracy in channel estimation has been investigated using LR approach. The proposed LR-LAS detector has achieved a significant improvement in performance over conventional LAS algorithms, even with imperfect CSI. Simulation results show that LR-LAS detector improves the performance of massive system under imperfect CSI. Therefore, our proposed LR-LAS can be used as efficient means of detecting the signal with imperfect CSI in massive systems.

References

1. F. Rusek, D. Persson, B.K. Lau et al., Scaling up MIMO: opportunities and challenges with very large arrays. IEEE Signal Process. Mag. **30**(1), 40–60 (2013)
2. D.C. Araujo, T. Maksymyuk, A.L.F. de Almeida, T. Maciel, J.C.M. Mota, M. Jo, Massive MIMO: survey and future research topics. IET Commun. **10**(15), 1938–1946 (2016)
3. A. Švač, F. Meyer, E. Riegler, F. Hlawatsch, Soft-heuristic detectors for large MIMO systems. IEEE Trans. Signal Process. **61**(18), 4573–4586 (2013)
4. A. Chockalingam, B.S. Rajan, *Large MIMO Systems* (Cambridge University Press, New York, 2014)
5. M. Biguesh, A.B. Gershman, Training-based MIMO channel estimation: a study of estimator tradeoffs and optimal training signals. IEEE Trans. Signal Process. **54**(3), 884–893 (2006)

6. Y. Chi, L. Liu, G. Song, C. Yuen, Y.L. Guan, Y. Li, Practical MIMO-NOMA: low complexity and capacity-approaching solution. IEEE Trans. Wirel. Commun. **17**(9), 6251–6264 (2018)
7. E. Bjornson, P. Giselsson, Two applications of deep learning in the physical layer of communication systems [lecture notes]. IEEE Signal Process. Mag. **37**, 134–140 (2020)
8. I. Chihaoui, M.L. Ammari, P. Fortier, Improved LAS detector for MIMO systems with imperfect channel state information. IET Commun. **13**(9), 1297–1303 (2019)
9. E. Björnson, L. Sanguinetti, H. Wymeersch, J. Hoydis, T.L. Marzetta, Massive MIMO is a reality—what is next? Five promising research directions for antenna arrays. Digit. Signal Proces. **94**, 3–20 (2019)
10. A. Elghariani, M. Zoltowski, Low complexity detection algorithms in large-scale MIMO systems. IEEE Trans. Wirel. Commun. **15**(3), 1689–1702 (2016)
11. C. Huang, L. Liu, C. Yuen, S. Sun, Iterative channel estimation using LSE and sparse message passing for MmWave MIMO systems. IEEE Trans. Signal Process. **67**(1), 245–259 (2019)
12. L. Bai, S. Dou, Q. Li et al., Low-complexity iterative channel estimation with lattice reduction-based detection for multiple-input multiple-output systems. IET Commun. **8**(6), 905–913 (2014)
13. K.V. Vardhan, S.K. Mohammed, A. Chockalingam, B.S. Rajan, A low-complexity detector for large MIMO systems and multicarrier CDMA systems. IEEE J. Sel. Areas Commun. **26**(3), 473–485 (2008)
14. S.K. Mohammed, A. Zaki, A. Chockalingam, B.S. Rajan, High-rate space-time coded large-MIMO systems: low-complexity detection and estimation. IEEE J. Sel. Topics Signal Process. **3**(6), 958–974 (2008)
15. I. Chihaoui, M.L. Ammari, LAS detector with soft-output MMSE initialization under imperfect channel estimation and channel correlation. Wirel. Pers. Commun. **108**(1), 213–220 (2019)
16. E. Bjornson, B.A. Ottersten, Framework for training-based estimation in arbitrarily correlated Rician MIMO Channels with Rician disturbance. IEEE Trans. Signal Process. **58**(3), 1807–1820 (2010)
17. J. Wang, O.Y. Wen, S. Li, Soft-output MMSE MIMO detector under ML channel estimation and channel correlation. IEEE Signal Process. Lett. **16**(8), 667–670 (2009)
18. J. Park, J. Chun, Improved Lattice reduction-aided MIMO successive interference cancellation under imperfect channel estimation. IEEE Trans. Signal Process. **60**(6), 3346–3351 (2012)

An Efficient Deep Neural Networks-Based Channel Estimation and Signal Detection in OFDM Systems

A. Krishnama Raju, Shilpi Gupta, and Akriti Jaiswal

Abstract This article represents an improvement in the efficiency of Deep Neural Networks (DNN) employed in OFDM systems for estimation of channel, detection of symbols by using Hyperparameter tuning. Deep learning is increasing its popularity in each field and it's a set of Artificial Intelligence (AI). Deep Neural Network (DNN) model is completely different from traditional Orthogonal Frequency Division Multiplexing (OFDM) receiver in such a way that OFDM receiver has to estimate the channel state information separately then it is able to detect the transmitted signal, but DNN model will be trained offline by simulated data over various channel statistics then directly employed in online for detection of the transmitted signal directly. Deep learning gives a performance better than traditional methods, i.e., Minimum Mean Square Error (MMSE) of channel estimation and symbol detection in wireless communications. First, we have analyzed the performance of traditional methods, i.e., MMSE over Winner II channel without deep learning by observing BER with cyclic prefix and without Cyclic Prefix (CP) and with variation in number of pilot carriers. Thereafter we will deploy hyperparameter tuning with proposed DNN model in OFDM for estimation of channel and detection of symbols in the winner II channel mainly for the Urban power delay profile using QPSK modulation. Here, we have claimed that by reducing the no of epochs from 20,000 to 10,000, training period will be reduced from 52 to 26 h, i.e., 50% while maintaining the almost same BER performance.

Keywords Hyperparameter tuning · Deep neural networks (DNN) · Orthogonal frequency division multiplexing (OFDM)

1 Introduction

Orthogonal Frequency Division Multiplexing (OFDM) is a modulation scheme commonly used in wireless systems to counter selective fading in wireless networks.

A. Krishnama Raju · S. Gupta (✉) · A. Jaiswal
Sardar Vallabhbhai National Institute of Technology, Surat 395007, India
e-mail: sgupta@eced.svnit.ac.in

S. Rawat et al. (eds.), *Proceedings of First International Conference on Computational Electronics for Wireless Communications*, Lecture Notes in Networks and Systems 329,
https://doi.org/10.1007/978-981-16-6246-1_51

Channel State Information (CSI) is very important for channel estimation and coherent signal detection OFDM systems. Channel State Information (CSI) is extracted by means of pilot carriers inserted during the transmission of OFDM blocks. Estimated CSI will be used for signal detection in OFDM systems. By analyzing various attempts in channel estimation and signal detection in OFDM systems to mimic the cyclic channel variation, a blind estimation method is proposed by Musolino [5]. The conventional channel estimation methods like Minimum Mean Square Error (MMSE) have employed in OFDM at various channel environments [4].

Nowadays AI, machine learning, deep learning methods in various communications problems employed and DNN, ANN models are used in end-to-end manner for reducing various hardware complexities and effective utilization of resources. DNN and ANN models are applied in channel decoding [8], localization using Channel State Information (CSI) [1], signal detection [6]. The AI is expanding wings due to various large data processing units like GPUs and larger quantity of data for training DNN models.

Here, this work is an attempt to prove that the DNN model has the ability to combat the frequency-selectivity of wireless channels in such a way that this will modify the architecture according to dynamics encountered in the channel, i.e., distortion and interference. To optimize the architecture, hyper-parameters like leaky ReLU, Dropout after every hidden layer, Huber loss/Smooth mean absolute error, learning rate, etc. are tuned. Finally, simulation results are compared with MMSE channel estimator.

2 Channel Details

The main purpose of WINNER is to build a single universal radio access system flexible to a wide range of mobile scenarios from a short-range to a wide range. This is mainly based on radio access technology with improved capabilities compared to existing mobile systems or their evolutions. WINNER II is a sequence of the WINNER-I project, which enhanced the overall system concept [7]. The software interface addresses device issues beyond 3G. It is flexible in the bandwidth and frequency spectrum of the carrier.

The device design embraces a wide range of radio environments that offer substantial reliability and service quality (QoS) improvements. The radio interface optimizes the use of spectral resources, e.g., by using current channel conditions and multiple antenna technology. WINNER II channel model is not only applicable to system level but also applicable to all RF channels of bandwidth up to 100 MHz and frequency range of 2–6 GHz. It will support multiple users, different polarization, and multiple cell communication networks. In this work, focus is on the B1 hotspot scenario which included both Line of Sight (LOS) and Non-Line of Sight (NLOS) components (Table 1).

Table 1 Propagation scenarios specified in WINNER II channel [7]

Scenario	Definition	Mobility (km/hr)	Frequency (GHz)
A1	Indoor office/residential	0–5	2–6
A2	Indoor to outdoor	0–5	2–6
B1	Typical urban microcell	0–70	2–6
B2	Bad urban microcell	0–70	2–6
B3	Large indoor hall	0–5	2–6

3 Architecture

Deep learning is applied in all areas successfully with higher performance improvements includes speech recognition [9], computer vision [3], natural language processing [2], and now the field of wireless communications too. The structure of the deep learning model is shown in Fig. 1. In order to improve the ability of recognition and representation we have to increase the number of hidden layers in the DNN model; so, we consider DNN as a Deep version or subset of ANN. Each layer output in DNN is a nonlinear function of the weighted sum of perceptrons or neurons in the preceding layer as shown in Fig. 1. Model is either sigmoid function or leaky ReLU function defines as $F_s(a) = 1 - 1/(e^{-a} + 1)$ and $F_r(a) = \alpha a$ if $\alpha \leq 0$, otherwise a, respectively. So, output is cascaded of the nonlinear transfer function of input data. Mathematically expressed as

$$z = f(I, \theta) = f^{(L-1)}\big(f^{(L-2)}\big(\cdots f^{1}(I)\big)\big), \tag{1}$$

where L is a total number of layers, θ is the total number of weights in the DNN model. The parameters to a model mean that are weights to neurons, which are going to be optimized offline for online detection and channel estimation. The optimal

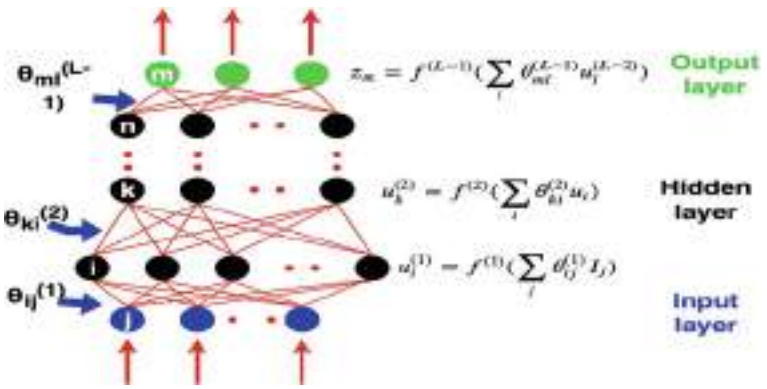

Fig. 1 A multi-layer deep neural network structure

values of weights we will get by perfectly training the DNN model by a sufficient number of epochs with prior known desired outputs. The architecture for simulation of the DNN model in estimation of channel and detection of symbols is shown in Fig. 1. The OFDM signal processing is similar like the conventional system [10]. The length of CP, in this case, should be greater than 16 microseconds because that is the maximum delay spread; we have taken at the system environment setup. The modeling of the multipath channel used in this system is described in terms of complex variable $h(n)$.

The received signal $y(n)$ will be modeled as

$$y(n) = x(n) * h(n) + w(n), \tag{2}$$

where $*$ is circular convolution, $x(n)$ is transmitted signal, $w(n)$ represents the AWGN noise. After pre-processing means removing the cyclic prefix, DFT is applied on the received signal

$$Y(k) = X(k)H(k) + W(k), \tag{3}$$

where $Y(k)$ is DFT of $y(n)$, similarly $X(k), H(k), W(k)$ are the DFTs of $x(n), h(n), w(n)$, respectively.

In this, we are taking the first block as pilot symbols then data blocks. One OFDM block will contain the pilot symbol and more data symbols this will be called one frame. we have to divide the data and make the frame duration such a way that during the transmission of the frame channel behavior is constant. But the channel is varying from one frame to another frame. During the training period we are taking one pilot block followed by one data block then we are trying to detect the transmitted data in the winner channel in an end-to-end manner. In system architecture Fig. 2 We are training in effective way means we are training using the same model for channel estimation and detection means 2 stages in one model. Stage 1 is offline in this we are training the DNN model. The received OFDM samples are generated across various dynamic channel scenarios, i.e., urban or rural power delay profile with various statistical properties and variations in received samples are used for adjusting the weights and biases of the DNN model. Stage 2 is the online DNN model which will recover the transmitted data without any knowledge of channel information (explicitly channel estimation not needed).

3.1 DNN Model Training

In the training period of the DNN model, we will consider OFDM modulation and wireless communication channels as block boxes. We will get the many channel models for channel state information, it will easily mimic the real channels in terms of channel characteristics. By using this model, we will simulate and get the required training data for training the DNN model. Every time doing the simulation generates

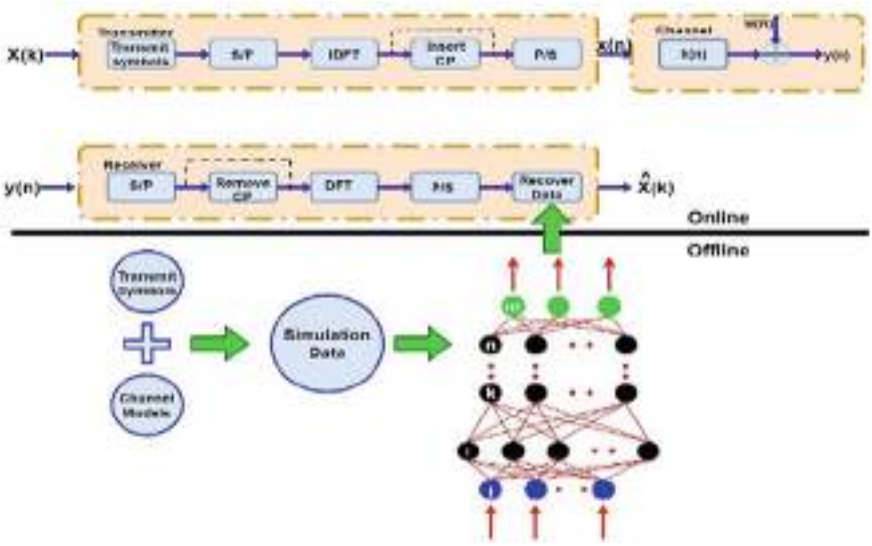

Fig. 2 DNN modeled system architecture with offline training and online testing stages

the random data then insert pilots into this up to the OFDM frame will form then apply to the DNN model just take the received samples and compare with the transmitted data sequence update the weights and biases in DNN model. The received OFDM signal is based on various channel conditions in our case it is an urban power delay profile. To evaluate the performance of the model we are choosing Huber loss function, which is defined as

$$L_{\delta}\left(\widehat{X}(K), X(k)\right) = \frac{1}{2}\left(\widehat{X}(K) - X(k)\right)^2, For\left|\widehat{X}(K) - X(k)\right| \leq \delta$$
$$= \delta\left|\widehat{X}(K) - X(k)\right| - \frac{1}{2}\delta^2 otherwise, \quad (4)$$

where $\widehat{X}(K)$ is detected and $X(k)$ is transmitted message.

The DNN model will contain 5 layers in this 3 of them are hidden layers. The number of neurons present in each layer is 256, 500, 250, 120, 16, respectively. The real and imaginary parts are incorporated in the input layer. The OFDM block contains pilot and data block, respectively. Every 16 bits of data will form one group and be detected in the part of the training. Then all data outputs are concatenated at the final output. Leaky ReLU is an active function in all middle or hidden layers but at the output layer, sigmoid is output activation function used for mapping the data in an interval of (0, 1).

4 Hyper-parameters

4.1 Learning Rate

Learning rate is step size at the end of each iteration while traveling toward minima or optimizing point. There will be always a trade-off between overshooting and convergence rate. Here in our experiment we chose learning rate as 0.01.

4.2 Number of Epochs

Here batch size means before updating the training weights how many samples we have to process. Epochs are defined as a number of times we have to pass through training data set before updating the internal model weights. In our experiment we chose 10,000 number of epochs and batch size is 254.

4.3 Loss Function and Activation Function

Huber loss will act as both L1 and L2 loss according to the value of delta. Getting minima is not guarantee if we will use Mean Absolute Error for training neural networks due to large gradient descent. But this problem won't occur while we are using mean squared error because gradient descent value will reduce as it is approaching minima value. Compared to Mean Square Error, the Huber loss is more robust to outliers present in the data. Huber loss will contain both the good properties of MAE and MSE. The only disadvantage for Huber loss, we have to find the value of delta iteratively or by training the model iteratively.

4.4 Bias and Variance

For best model always bias and variance values should be less. Choosing the best model includes checking the training set and testing set error. some points to keep in mind about choosing the model.

1. If test set error is greater than train set error then the model is represented as overfitting and it has high variance.
2. If test set and train set error both are having high value then the model is represented as underfitting and it has a high bias.
3. If the training set error is more than test set error then the model has high variance and high bias.

4. Train set and test set error both are small then data is fitted reasonably, hence model as low variance and low bias.

We are getting high train set error means it has high bias, then for fixing this problem we have to increase the number of hidden layers or we have to increase the network size.

4.5 Dropout

Dropout can be defined as at the end of each hidden layers how many inactive nodes are eliminated. So, in order to improve the learning speed dropout is very important. In our experiment we taken 20% as dropout rate.

5 Results

The simulation parameters are shown in Table 2. If we will train the network using fewer epochs then underfitting of data will leads to a decrease in accuracy. To get maximum accuracy on the given training set we have to use a greater number of epochs then we get an optimal solution. To explore this statement, we initially fixed SNR to 20 dB and number of pilots to 64 for QAM then performing only 20 epochs we get the prediction and mean error 0.100877, 0.04962, respectively. For comparison of Reference work [10] the same setup with their parameters if we use 20,000 epochs

Table 2 Simulation environment details

Parameter	Remark
Number of subcarriers	64
Length of CP	16
Channel used	WINNER II
Scenario	B1 (typical urban microcell)
Number of paths	24
Maximum delay	16 μs
Model	DNN (TensorFlow)
Number of training epochs	10,000
Batch size	256
Activation function	Leaky RELU, Sigmoid
Loss function	Huber loss
Learning rate	0.01
Platform	Ubuntu 16.04

then prediction and mean error will be achieved as 0.004367, 0.003125, respectively. For 20,000 epochs training, the model will take 52 h.

To reduce the training period to half only 10,000 epochs have been used with the trade-off in BER. At the same time, hyperparameter tuning has been incorporated to reduce trade-off in BER. If the proposed model is run for 20,000 epochs then BER (SNR 20 dB and 64 pilots with CP) will be 0.003842 as prediction which is better than reported work. By using 10,000 epochs with hyperparameter tuning we will get prediction and Mean Square Error is 0.004609, 0.003375, respectively. By comparing above we decided to fix a number of training epochs as 10,000 with a trade-off in a bit accuracy in BER but very less impact on receiving blocks because change will occur in the 4th decimal point, i.e., 10^{-4} in BER. Hence, we will get the benefit from half of the training period will be reduced. Finally, the training period is 26 h.

5.1 Effect of Number of Pilots on DNN Performance

Pilots are overhead subcarriers used for estimation of the channel that is phase shift present in each subcarrier and equalizer gain, etc. As shown in Fig. 3 MMSE 64 Pilots and deep learning 64 Pilots are approximately giving the same results. Here our main target is to reduce the number of Pilots and we have to study the impact on received symbols. In MMSE if we use only 8 pilots instead of 64 pilots as shown in the graph after 15 dB signal-to-noise ratio BER versus SNR curves will become flatten. By employing trained deep learning architecture, we can see that if we use 8 Pilots also, we are getting almost results as MMSE 64 pilots. Due to this overhead caused by the Pilots in the subcarriers is reduced by almost 77%. Reason for the selection of 64 pilots and 8 pilots is extreme cases considered for showing the overhead reduction

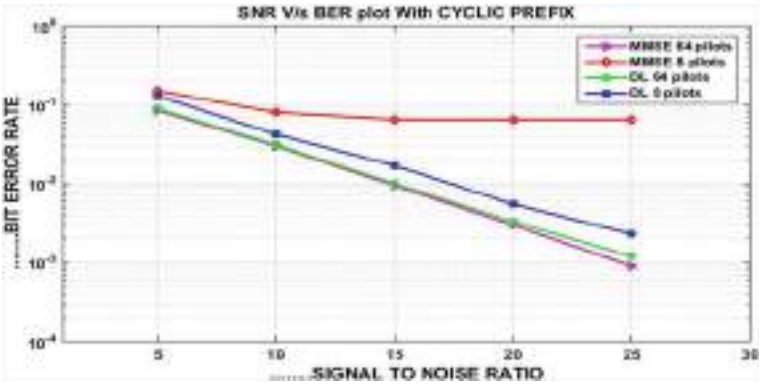

Fig. 3 Impact of the number of pilots on BER performance for DNN-based model and conventional MMSE-based OFDM system

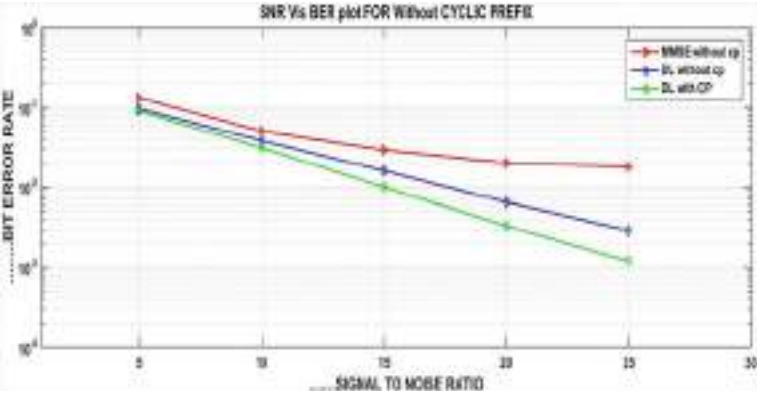

Fig. 4 Impact of cyclic prefix on BER performance of DNN-based system

in a better manner. Hence, we can prove that deep learning architecture is robust in case the channel is noisier and we can reduce the number of Pilots also with a little sacrifice of BER which is worth compared to overhead present in the subcarriers. Various samples with mean square error, with 64 pilots and 8 pilots, are included in Fig. 3.

5.2 Performance of DNN with Respect to Cyclic Prefix

Cyclic Prefix is needed for converting linear convolution to circular convolution of the given physical channel to combat the Inter Symbol Interference (ISI). But this increases the energy and time for transmission. As shown in Fig. 4 MMSE cannot estimate the channel effectively without Cyclic Prefix. The BER gets saturated while increasing SNR more than 15 dB. However, DNN model even without Cyclic Prefix performs well. This result shows that wireless channel characteristics have been revealed and can be learned in training by Deep Neural Networks. It can be observed from Fig. 4 that DNN model is very robust. If a comparison is made between the systems: OFDM system with MMSE and DNN-based OFDM system, then it can be found that in the absence of CP later gives good BER performance than former.

Even DNN model with CP does not have much variation than the model without CP. Hence, it can be inferred that CP has not much impact on the DNN-based system.

5.3 Robustness of DNN Model

MMSE and deep learning architecture have been compared in the case of channel estimation and detection in OFDM systems.

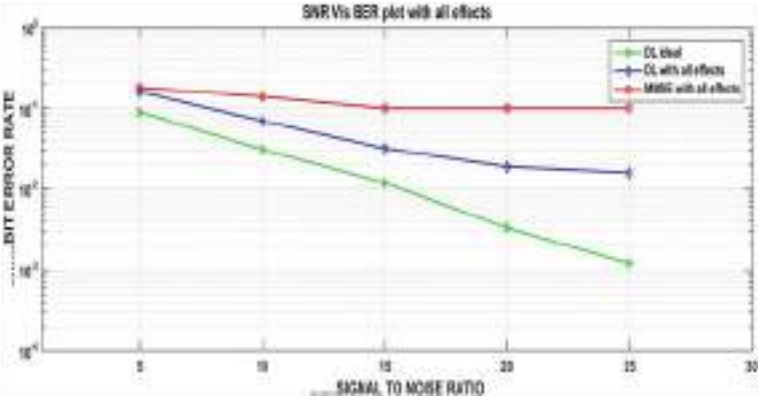

Fig. 5 BER performance for showing robustness of DNN model

Using deep learning architecture, the number of pilots used for signal detection can be reduced and cyclic prefix is also avoided. Due to this activity overhead in OFDM transmission is going to reduce significantly. As shown in Fig. 5 deep learning with 8 pilots is better than MMSE with 8 pilots but there is a negligible degradation in the performance of OFDM systems observed. In the above work offline trained deep learning architecture has the same statistics as online deployed deep learning architecture. But in the real case, there is a lot of difference or mismatches observed between online and offline deployment of deep learning architecture because while training the architecture model we are fixing SNR to particular values like 5, 10, 15, 20, 25 dB. We have to take care trained model has to withstand the mismatches between the two stages. Most of the time mismatch occurred due to maximum delay spread and a number of paths encountering in the channel bandwidth. These two parameters are different from the trained model in the offline stage and the online deployment stage has different maximum delays and a number of paths while testing. Care should be taken proper matching of offline trained stage and online deployment stage.

6 Conclusion

By observing the results, it can be concluded that whenever wireless communication channels are affected with severe distortion and severe interference then deep learning is very useful. For reducing the training period, hyperparameter tunning is being applied. Unlike the MMSE 8 pilots model (saturates after 15 dB), the DL model will not saturate up to 25 dB SNR. Impact of CP is more in the case of MMSE compared to the DNN model. Results suggest that CP can be completely removed that too with the negligible trade-off of BER using the DNN model. Almost all performance of MMSE with CP and DNN model without CP give the same performance. Here,

including all effects means by omitting cyclic prefix (CP) and reducing the number of pilots DL give better performance compared to MMSE. The future work can be extended to real time scenario where online and offline stages need to be matched properly.

References

1. S. Chen, G. Gibson, C. Cowan, P. Grant, Adaptive equalization of finite non-linear channels using multilayer perceptrons. Signal Process. **20**(2), 107–119 (1990)
2. K. Cho, B. Van Merrienboer, C. Gulcehre, D. Bahdanau, F. Bougares, H. Schwenk, Y. Bengio, Learning phrase representations using rnn encoder-decoder for statistical machine translation (2014). arXiv:1406.1078
3. A. Krizhevsky, I. Sutskever, G.E. Hinton, Imagenet classification with deep convolutional neural networks, in *Advances in Neural Information Processing Systems* (2012), pp. 1097–1105
4. Y. Li, L.J. Cimini, N.R. Sollenberger, Robust channel estimation for ofdm systems with rapid dispersive fading channels. IEEE Trans. Commun. **46**(7), 902–915 (1998)
5. A. Musolino, M. Raugi, M. Tucci, Cyclic short-time varying channel estimation in ofdm power-line communication. IEEE Trans. Power Deliv. **23**(1), 157–163 (2007)
6. E. Nachmani, Y. Be'ery, D. Burshtein, Learning to decode linear codes using deep learning, in *2016 54th Annual Allerton Conference on Communication, Control, and Computing (Allerton)* (IEEE, 2016), pp. 341–346
7. M. Narandzic, C. Schneider, R. Thoma, T. Jamsa, P. Kyosti, X. Zhao, Comparison of scm, scme, and winner channel models, in *2007 IEEE 65th Vehicular Technology Conference-VTC2007-Spring* (IEEE, 2007), pp. 413–417
8. X. Wang, L. Gao, S. Mao, S. Pandey, CSI-based fingerprinting for indoor localization: a deep learning approach. IEEE Trans. Veh. Technol. **66**(1), 763–776 (2016)
9. C. Weng, D. Yu, S. Watanabe, B.H.F. Juang, Recurrent deep neural networks for robust speech recognition, in *2014 IEEE International Conference on Acoustics, Speech and Signal Processing (ICASSP)* (IEEE, 2014), pp. 5532–5536
10. H. Ye, G.Y. Li, B.H. Juang, Power of deep learning for channel estimation and signal detection in ofdm systems. IEEE Wirel. Commun. Lett. **7**(1), 114–117 (2017)

Optimization of Channel Capacity of MmWave Massive MIMO Using Hybrid Precoding

A. Mounika Durga and Shaik Jakeer Hussain

Abstract mmWave communication system encounters the higher path loss than the microwave communication system due to the high-frequency band. To defeat the path loss problem massive number of antennas with low wavelength are deployed at the transmitter and receiver side. To transmit multiple data streams and to get better spectral efficiency and capacity precoding is required. Developing the hybrid Precoding is economically high and consumes more power and it is divided into analog and digital parts. Due to the presence of large antennas and analog part in the hybrid precoding, mmWave massive MIMO requires some special algorithms to do the channel estimation and precoding. To construct the sparse precoding and combining problems in mmWave massive MIMO, channel is considered as -sparse channel. In this paper sparse precoding is designed based on the orthogonal basis pursuit algorithm for mmWave massive MIMO by using dictionary which consists of array response vectors of angle grid points.

Keywords mmWave Massive MIMO · Channel estimation · Precoding · Sparse · Orthogonal basis pursuit

1 Introduction

In future 5G is expected to give 1000 times capacity more than the present 4G. To get this lot of technologies has been proposed. In that mmWave is one of the technology playing crucial role [1] in 5G cellular mobile communications, because of availability of large bandwidth. Major difference between the mmWave and the present wireless communication system is the carrier frequency. Carrier frequency in the mmWave is ten times greater than the present wireless systems. It causes the more path loss in mmWave systems. However it is the drawback in the mmWave systems but the interesting point is wavelength of antenna which is very low. So we can place more number of antennas arrays. mmWave combining with massive MIMO

A. M. Durga (✉) · S. J. Hussain
Department of ECE, VFSTR, Guntur, Vadlamudi Andhra Pradesh, India

S. Rawat et al. (eds.), *Proceedings of First International Conference on Computational Electronics for Wireless Communications*, Lecture Notes in Networks and Systems 329,
https://doi.org/10.1007/978-981-16-6246-1_52

improves the beam forming gain, spectral efficiency [2, 3] and helps to overcome the path loss in the mmWave system. Initially conventional MIMO exploits the digital precoder to transmit data, it controls both signal's amplitude and phase. In digital precoder structure each and every antenna requires one RF chain compulsory. There are several digital precoding techniques that are introduced. In that simplest one is the Matching Filter (MF) precoding [4]. In the MF precoding SNR rate is increased at the mobile station side. But the drawback is interference which is high between the input data streams. Zero forcing (ZF) precoding [4] is introduced to overcome the interference problem in MF, but performance loss is more. To get high SNR and low interference wiener filter (WF) [4] is introduced. There are still more digital precoding methods known as optimal DPC, near optimal Tomlinson Harashima precoding [5] are introduced, but they are very difficult to compute. Digital precoding fulfills the requirement to get better performance by controlling both signals amplitude and phase but it consumes more power and hardware cost is high because, requirement of more number of RF chains. Analog beam forming is implemented with less number of RF chains by using phase shift networks [7–9] and it is developed initially for point to point communication systems [6]. Drawback of analog beam forming is, it can manipulate only phase.

To defeat the issues in analog beam forming and digital precoding new era is introduced, that is hybrid precoding [10]. Hybrid precoding is divided into two parts, one is the digital precoder which is used to remove the interference between the data streams and the other part is analog beam former used to gain the more antenna gain. Basically Hybrid beamforming structure is two types, they are spatially sparse hybrid precoding and successive interference cancelation (SIC). Spatially sparse precoding is the fully connected architecture [4] in which the every RF chain is connected to all base station antennas through the phase shifts. SIC is the sub-connected architecture [11] in which RF chain is connected to only subset of antennas. Several authors carry out research on hybrid precoding. Considering the hardware limitations by using more RF chains and analog to digital converters precoding in [1] is implemented by using phase shift networks and finite precision ADCs for processing the signal at receiver. In [2] DFT-based processing is used for hybrid precoding where the base station knows perfectly about the channel and zero forcing method is used for precoding to get better spectral efficiency. In this paper we are designing precoder by taking input as optimal unconstrained precoder, and combining is designed by considering MMSE receiver.

The subsequent sections of this paper are arranged as follows. Introduction of mmWave massive MIMO system and channel model is provided in Sect. 2. In Sect. 3, designing of precoder using optimal unconstrained precoder is explained. Combiner design for mmWave massive MIMO using MMSE receiver is presented in Sect. 4. Simulation results are presented for different types of antenna array dimensions in Sect. 5.

2 System and Channel Model

Let us consider single user mmWave massive MIMO system which is shown in Fig. 1 in [4] contains transmitter with N_T antennas, receiver with N_R antennas. Here transmitter transmits the N_S data streams to the receiver. To allow multi-data stream transmission transmitter is endow with N_T^{RF} chains with condition $N_S \sim N_T^{RF} \sim N_T$. In this architecture transmitter applies baseband precoder $\mathrm{F_B}$ of size $N_T^{RF} \times N_S$ by using N_T^{RF} RF chains, followed by RF precoder $\mathrm{F_R}$ of size $N_T \times N_T^{RF}$ and it is implemented by using phase shift networks. Input data stream S is the size of $N_S \times 1$ and it should satisfy the condition $\mathrm{E[SS}\surd] = \frac{\mathrm{I_{Ns}}}{\mathrm{N_S}}$. After precoding the signal which is to be transmitted to the receiver is in form of discrete time can be defined as $\mathrm{X} = \mathrm{F_R F_B S}$. Elements of the RF precoder has to satisfy $\left(\mathrm{F_R^{(i)} F_R^{(i)}}\surd\right)_{l,l} = \mathrm{N_T^{-1}}$ that means all elements in the RF precoder matrix should have equality in the norm. Power constraint of transmitter is done by normalizing baseband precoder and the condition to satisfy is $\|\mathrm{F_R F_B}\|_F^2 = N_s$.

For our simplicity, we are considering the narrowband system [3] because the mmWave systems coherence bandwidth is large. Then received signal $N_R \times 1$ can be represented as

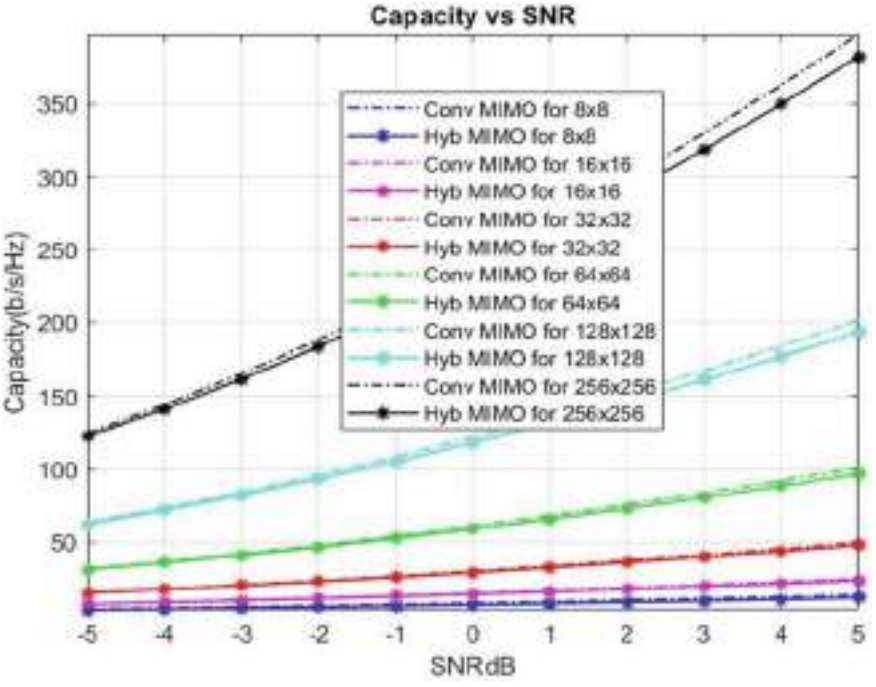

Fig. 1 Comparison for capacity of conventional MIMO and hybrid MIMO for different antenna array dimensions

$$y = \sqrt{\pi}\mathrm{HF_R F_B S} + \mathrm{n} \tag{1}$$

Here H is channel matrix of size $N_R \times N_T$ and it has to satisfy condition $\mathrm{E}[\|\mathrm{H}\|_F^2] = N_T N_R$, n is noise with mean 0 and variance φ_n^2, $CN(0, \varphi_n^2)$ and π is average of received power. In mmWave to allow precoding the transmitter and receiver should perfectly familiar with channel H. In real time systems receiver should know the channel state information by doing some training methods and that information shares with transmitter. Receiver is constructed with N_R^{RF} RF chains with size of $N_S \sim N_R^{RF} \sim N_R$ and phase shifters to receive the precoding signal and that is

$$\tilde{y} = \mathrm{W_B W_R H F_R F_B S} + \mathrm{W_B W_R n} \tag{2}$$

Here $\mathrm{W_R}$ is the RF combining matrix of size $N_T \times N_T^{RF}$ and $\mathrm{W_B}$ is the baseband combiner matrix at receiver side similar to base station. Elements of $\mathrm{W_{RF}}$ matrix should have equal norm same as analog RF precoding. When the signal is transmitted over the mmWave massive MIMO channel capacity can be represented as

$$R = \log_2\left(\left| I + R_n^{-1} \mathrm{w_B W_R H F_R F_B F_B F_R H W_R W_B} \right|\right) \tag{3}$$

where R_n is noise covariance matrix and it will get after the combining procedure at receiver side. Here we are considering narrowband channel because path loss is more in mmWave system due to high carrier frequency and antenna correlation is occurred when a large number of antennas are placed at the transmitter and also the combination of mmWave and massive MIMO causes fading. In narrow band clustered channel model, channel matrix H is represented as

$$H_N = \Delta \sum_{l=1,\ldots L} \lambda_l a_R(\theta_l^R) a_T^H(\theta_l^T) \tag{4}$$

$$H = \sum_{i=1}^{L} A_R(\phi)\, H A_T^H(\phi)$$

where Δ is the normalization factor, defined as $\Delta = \sqrt{N_T N_R / L}$ and λ_l is the gain of the lth path. Where θ_l^R is the angle of arrival. θ_l^T is angle of departure. $a_R(\theta_l^R)$, $a_T(\theta_l^T)$ are the transmitter and receiver antenna array responses. Where $A_R(\phi) = \left[a_R(\theta_1^R), \ldots a_R(\theta_L^R)\right]$ is the receive antenna array response matrix which are complex Gaussian random variables. Similarly $A_T(\phi) = \left[a_T(\theta_1^T), \ldots a_T(\theta_L^T)\right]$ is the transmit antenna array response matrix which are complex Gaussian random variables. Here we are considering the angular grid of size G, it should be greater than or equal to the number of transmitting antennas. Transmitting array response is taken as

$$A_T(\phi) = \left[a_T(\theta_1^T), \ldots a_T(\theta_G^T)\right]$$

and $H = \sqrt{\frac{N_T N_R}{L}}\, diag(\lambda_1, \ldots \lambda_L)$.

Antenna array responses are a function of transmitter and receiver antenna array structure. There are two types of antenna array structures existing, they are uniform linear array and uniform planar array. ULA is only two-dimensional and UPA is 3D. Array response for N elements with respect to y-axis is defined as

$$a_{ULA} = \frac{1}{\sqrt{N}}\left[1, e^{jkd\sin(\phi)}, \ldots, e^{j(N-1)kd\sin(\phi)}\right]^T \tag{5}$$

Array response vector for N = W * H elements with respect to y- and z-axis defined as

$$a_{UPA}(\phi, \theta) = \frac{1}{\sqrt{N}}\begin{bmatrix} 1, \ldots, e^{jkd(m\sin(\phi)\sin(\theta)+n\cos(\theta))}, \ldots, \\ e^{j(W-1)kd\sin(\phi)\sin(\theta)+(H-1)\cos(\theta))} \end{bmatrix}^T \tag{6}$$

Here m, n are the index for y- and z-axis.

3 Sparse Precoding Problem Formulation

Here we are designing mmWave massive MIMO precoder to get maximum capacity. In this we are not directly maximizing optimization of precoder to increase spectral efficiency by using Eq. (3), it requires joint optimization because, existence of four matrix variables of precoder and combiner to maximize spectral efficiency. So we are decoupling the transmitter and receiver optimization problem for simplification and concentrating on precoder design initially. We are designing precoder to maximize the mutual information obtained by Gaussian signal over clustered channel.

$$I(\mathrm{F_R F_B}) = \log_2\left(\left|\mathrm{I} + \frac{1}{\mathrm{N_S}\varphi_{\mathrm{n}}^2}\mathrm{H F_R F_B F_B^{*} F_R^{*} H^{*}}\right|\right) \tag{7}$$

Designing of precoder problem in mmWave massive MIMO by using optimization technique can be expressed as

$$\begin{aligned} \left(\mathrm{F_R^{opt}}, \mathrm{F_B^{opt}}\right) &= \arg\max_{\mathrm{F_B}, \mathrm{F_R}} \mathrm{I}(\mathrm{F_R}, \mathrm{F_B}), \\ \text{s. t}\ \ \mathrm{F_R} &\in \mathrm{F_R} \\ \|\mathrm{F_R F_B}\|_{\mathrm{F}}^2 &= \mathrm{N_S} \end{aligned} \tag{8}$$

where f_R is set of realizable precoders. There are no solutions to found for approximation (8) for feasibility constraint of non-convex. So here we are finding near

optimal precoder to the approximations (8). Here we have to find optimal unconstrained precoder of channel F_{opt}. To do the precoder we have to find singular value decomposition of channel. Mutual information of SVD of channel can be expressed as

$$I(F_R F_B) = \log_2\left(\left|I + \frac{\pi}{N_S \varphi_n^2} \sum^{2} V_{\surd} F_R F_B F_{\mathbb{B}} F_{\mathbb{R}} V\right|\right) \tag{9}$$

Here $\sum$ is the diagonal matrix consisting of two elements $\sum_1$ and $\sum_2$ of size $N_S \times N_S$. And $V = [V_1\ V_2]$ of dimension $N_T \times N_S$. Optimal unconstrained precoder of channel H is defined as $F_{opt} = V_1 = F_R F_B$. Here we are considering the eigen values of matrix I_{N_S} are small [4] that means $V_{\mathbb{1}} F_R F_B F_{\mathbb{B}} F_{\mathbb{R}} V_1$ are small. In mmWave massive MIMO precoding it is expressed as $V_{\mathbb{1}} F_R F_B \approx I_{N_S}$. And singular values of $V_{\mathbb{2}} F_R F_B$ are small that means $V_{\mathbb{2}} F_R F_B \approx 0$. Finally the mutual information can be expressed as

$$I(F_R, F_B) = \log_2\left(\left|I + \frac{1}{N_S \varphi_n^2} \sum_{1}^{2}\right|\right) - \left(N_S - \left\|V_{\mathbb{1}} F_R F_B\right\|_F^2\right) \tag{10}$$

Here to get maximum mutual information we have to maximize the $\mathrm{tr}(V_{\mathbb{1}} F_R F_B)$. Instead of maximizing the trace we can also minimize $\left\|F_{opt} - F_R F_B\right\|_F$. Precoder problem can be restated as

$$\begin{aligned} \left(F_R^{opt}, F_B^{opt}\right) &= \arg\min_{F_B, F_R} \left\|F_{opt} - F_R F_B\right\| \\ &\text{s.t } F_R \in F_R \\ &\|F_R F_B\|_F^2 = N_S \end{aligned} \tag{11}$$

Here set of precoders are restricted to take from the array response of elevation and azimuthal angle of departure. And the above problem (11) can be rewritten as

$$\begin{aligned} \left(F_R^{opt}, F_B^{opt}\right) &= \arg\min_{F_B, F_R} \left\|F_{opt} - F_R F_B\right\| \\ &\text{s. t } F_R \in \left\{a_T\left(\theta_l^T\right) 1 \sim 1 \geq G\right\} \\ &\|F_R F_B\|_F^2 = N_S \end{aligned} \tag{12}$$

Algorithm to find spatial sparse precoding using orthogonal matching pursuit:

Input: F_{opt}

1: F_R = empty matrix

2: $F_{re} = F_{opt}$

3: for $i \sim N_T^{RF}$ do

4: $\psi = A_T F_{re}$

5: $k = \underset{l=1,\ldots,G}{\arg\max} (\phi\phi)_{l,l}$

6: $F_R = \left[F_R l A_T^k\right]$

7: $F_B = (F_R F_R)^{-1} F_R F_{opt}$

8: $F_{re} = \frac{F_{opt} - F_R F_B}{\left\| F_{opt} - F_R F_B \right\|_F}$

9: end for

10: $F_B = \sqrt{N_S} \frac{F_B}{\|F_R F_B\|_F}$

11. return $F_R F_B$

4 Sparse Combiner Problem Formulation

In the previous section we have discussed the precoder design that increases the mutual information at the transmitter side. In this section we are going to design the combiner. Receiver decodes the signal with help of $N_R \times 1$ the dimension receive signal. In massive MIMO systems using such type of decoder increases complexity, so to overcome this problem we are using MMSE receiver. Here we have to design combiners, which reduces the mean square error between the transmitted signal and processed signal. Combiner problem can be expressed as

$$\begin{aligned} \left(W_R^{opt}, W_B^{opt}\right) &= \underset{W_R, W_B}{\arg\max}\, E\left[\left\| S - W_B W_R y \right\|_2^2\right] \\ &\text{s. t } W_R \in W_R \end{aligned} \tag{13}$$

W_R is the set of combiners and exact solution for the above problem in Eq. (3) can get by using MMSE [5] and the solution is $W_{MMSE} = (F_B F_R H H F_R F_B + \varphi_n^2 N_S I)^{-1} F_B F_R H$ (14).

By using MMSE we can rewrite the combiner optimization problem (13) as follows

$$\begin{aligned} \left(W_R^{opt}, W_B^{opt}\right) &= \underset{W_R, W_B}{\arg\min} \left\| R_{yy}^{1/2} (W_{MMSE} - W_R W_B \right\|_F \\ &\text{s. t } \quad W_R \in \{a_R(\theta_l^R), 1 \sim l \geq G\} \end{aligned} \tag{14}$$

Algorithm to find MMSE spatial sparse combining using orthogonal matching pursuit:

Input: W_{MMSE}

1: W_R = empty matrix

2: $W_{re} = W_{MMSE}$

3: for $i \sim N_R^{RF}$ do

4: $\psi = A_R^H E[yy^H] W_{re}$

5: $k = \underset{l=1,\ldots,G}{\arg\max} (\phi\phi^H)_{l,l}$

6: $W_R = \left[W_R 1 A_R^k\right]$

7: $W_B = (W_R^H R_{yy} W_R)^{-1} W_R^H R_{yy} W_{MMSE}$

8: $W_{re} = \frac{W_{MMSE} - W_R W_B}{\|W_{MMSE} - W_R W_B\|_F}$

9: end for

10: return $W_R W_B$

5 Simulation Results

In this section we are going to discuss the simulation results obtained by doing the precoding in Sect. 3 and combining in Sect. 4. Figure 1 shows the mmWave massive capacity for both hybrid MIMO and conventional MIMO for different antenna array dimensions like 8×8, 16×16, 32×32, 64×64, 128×128, and 256×256. From Fig. 1 we can observe that when SNR is increased, the capacity also increased and along with the increment in antenna dimensions there is an increment in channel capacity also (Tables 1, 2, 3, 4, 5, and 6).

Table 1 Capacity of hybrid and massive MIMO for 8×8 antenna array dimension

SNR dB	Hybrid MIMO capacity	Conventional MIMO capacity
−5	3.5168	4.1294
−4	4.0938	4.8079
−3	4.7288	5.5550
−2	5.4261	6.3688
−1	6.1786	7.2466
0	6.9903	8.1847
1	7.8593	9.1783
2	8.7793	10.2223
3	9.7486	11.3114
4	10.7576	12.4400
5	11.8135	13.6030

Table 2 Capacity of hybrid and massive MIMO for 16 × 16 antenna array dimension

SNR dB	Hybrid MIMO capacity	Conventional MIMO capacity
−5	7.5025	7.7174
−4	8.6529	8.9199
−3	9.9127	10.2388
−2	11.2781	11.6732
−1	12.7508	13.2208
0	14.3205	14.8783
1	15.9927	16.6411
2	17.7538	18.5038
3	19.6073	20.4601
4	21.5477	22.5033
5	23.5650	24.6265

Table 3 Capacity of hybrid and massive MIMO for 32 × 32 antenna array dimension

SNR dB	Hybrid MIMO capacity	Conventional MIMO capacity
−5	15.1900	15.5233
−4	17.5227	17.9469
−3	20.0770	20.6061
−2	22.8504	23.4993
−1	25.8325	26.6224
0	29.0226	29.9684
1	32.4085	33.5280
2	35.9761	37.2902
3	39.7273	41.2420
4	43.6563	45.3694
5	47.7462	49.6579

Table 4 Capacity of hybrid and massive MIMO for 64 × 64 antenna array dimension

SNR dB	Hybrid MIMO capacity	Conventional MIMO capacity
−5	31.0042	31.6945
−4	35.7318	36.6130
−3	40.8942	42.0046
−2	46.4899	47.8660
−1	52.5003	54.1883
0	58.9231	60.9573
1	65.7558	68.1541
2	72.9520	75.7558
3	80.5159	83.7363
4	88.4201	92.0671
5	96.6337	100.718

Table 5 Capacity of hybrid and massive MIMO for 128 × 128 antenna array dimension

SNR dB	Hybrid MIMO capacity	Conventional MIMO capacity
−5	62.3047	63.5459
−4	71.7564	73.3618
−3	82.0602	84.1162
−2	93.2384	95.8034
−1	105.256	108.4061
0	118.0908	121.8971
1	131.7196	136.2399
2	146.1170	151.3904
3	161.2141	167.2980
4	176.9548	183.9069
5	193.3098	201.1581

Table 6 Capacity of hybrid and massive MIMO for 256 × 256 antenna array dimension

SNR dB	Hybrid MIMO capacity	Conventional MIMO capacity
−5	122.4549	124.5906
−4	141.1364	143.9509
−3	161.5506	165.1801
−2	183.6748	188.2684
−1	207.4966	213.1844
0	232.9450	239.8764
1	259.9800	268.2750
2	288.5091	298.2955
3	318.4541	329.8401
4	349.7228	362.8012
5	382.2315	397.0640

References

1. V. Venkateswaran, A.-J. van der Veen, Analog beamforming in MIMO communications with phase shift networks and online channel estimation. IEEE Trans. Sig. Process. **58**(8), 4131–4143 (2010)
2. W. Tan, M. Matthaiou, S. Jin, X. Li, Spectral efficiency of DFT-based processing hybrid architectures in massive MIMO. IEEE Wireless Commun. Lett. **6**(5), 586–589 (2017)
3. D. Tse, P. Viswanath, *Fundamentals of Wireless Communication* (Cambridge University Press, 2005)
4. O. El Ayach, S. Rajagopal, S. Abu-Surra, Z. Pi, R.W. Heath, Spatially sparse precoding in millimeter wave MIMO systems. IEEE Trans. Wireless Commun. **13**(3), 1499–1513 (2014)
5. T. Kailath, A.H. Sayed, B. Hassibi, *Linear Estimation*, vol. 1 (2000)
6. J. Wang, Z. Lan, C.-W. Pyo, T. Baykas, C.-S. Sum, M.A. Rahman, J. Gao et al., Beam codebook based beamforming protocol for multi-Gbps millimeter-wave WPAN systems. IEEE J. Select. Areas Commun. 27(8), 1390–1399 (2009)
7. C.H. Doan, S. Emami, D.A. Sobel, A.M. Niknejad, R.W. Brodersen, Design considerations for 60 GHz CMOS radios. IEEE Commun. Mag. **42**(12), 132–140 (2004)
8. Z. Pi, F. Khan, An introduction to millimeter-wave mobile broadband systems. IEEE Commun. Mag. **49**(6) (2011)
9. A. Valdes-Garcia, S.T. Nicolson, J.-W. Lai, A. Natarajan, P.-Y. Chen, S.K. Reynolds, J.-H. Conan Zhan, D.G. Kam, D. Liu, B. Floyd, A fully integrated 16-element phased-array transmitter in SiGe BiCMOS for 60-GHz communications. IEEE J. Solid-State Circ. **45**(12), 2757–2773 (2010)
10. Y. Zeng, R. Zhang, Millimeter wave MIMO with lens antenna array: a new path division multiplexing paradigm. IEEE Trans. Commun. **64**(4), 1557–1571 (2016)
11. C. Cordeiro, D. Akhmetov, M. Park, IEEE 802.11 ad: Introduction and performance evaluation of the first multi-Gbps WiFi technology, in *Proceedings of the 2010 ACM International Workshop on mmWave Communications: From Circuits to Networks* (ACM, 2010), pp. 3–8

A WDM-Based Optical Wireless Converged Architecture for Traffic Balancing

Abhishek Gaur and Vibhakar Shrimali

Abstract A consolidated nomenclature for LTE wireless networks is proposed in which wavelength division multiplexing PONs are arranged in a ring topology. The setup is completely dynamic so that various base stations in the particular network may communicate over a dedicated λ_{LAN} channel. The irregularity in traffic of downstream channels may be monitored in this architecture. Traffic balancing may be achieved in this proposed work.

Keywords NG (Next Generation) · PON (Passive Optical Networks) · OLT (Optical Line Terminal) · ONU (Optical Network Unit) · TDM (Time Division Multiplexing) · WDM (Wavelength Division Multiplexing) · eNB (Evolved Node-B) · 10GEPON (10 Gb Ethernet Passive Optical Networks) · LTE (Long Term Evolution) · QoS (Quality of Service) · WLAN (Wireless Local Area Networks) · WBAN (Wireless Broadband Access Networks) · WiMAX (Worldwide Interoperability for Microwave Access)

1 Introduction

Undoubtedly PON technology is considered as a valuable solution for NG communication networks [1] since the demand for greater bandwidth is growing continuously among the subscribers. The service provider requires the need of backhauling traffic from next generation wireless broadband access architectures. The traffic may be managed by the effective use of this architecture. Conventional technologies such as circuit switched, packet switched, wire line used for conventional third-generation network infrastructures are not meeting the present day user requirements of new 5G access networks [2]. Therefore, an up-gradation is needed in existing Telecom

A. Gaur (✉)
USICT, GuruGobindSinghIndraprasthaUniversity, Delhi, India
e-mail: abhishek.usict.010164@ipu.ac.in

V. Shrimali
GB Pant Govt. Engg. College, Delhi, India

S. Rawat et al. (eds.), *Proceedings of First International Conference on Computational Electronics for Wireless Communications*, Lecture Notes in Networks and Systems 329,
https://doi.org/10.1007/978-981-16-6246-1_53

infrastructures. Therefore NG PONs is considered as a reliable solution for the implementation of the mobile backhaul networks due to its improved capacity, wider range, and economical installation. TDM-based EPONs are considered to be more effective as compared to other PON schemes, since in such schemes all Network Units of Optical Network (ONUs) shares a single wavelength during upstream transmission based on a TDMA technique which is implemented by the Optical Line Terminal (OLT). For enhancement in capacities, 10GE-PONs have been proposed and recently standardized [1]. In new deployments, NG-PON architectures may be considered more efficient [3]. In reference to Next Generation Wireless Broadband Access Networks (NG-WBANs), mobile WiMax and LTE are considered as two promising technologies that are expected to support higher data rates. Moreover, LTE-A networks have the capability of supporting higher data rates up to 1 Gbit/s along with latency of less than 10 ms [4]. LTE exploits the existing Telecom infrastructure, which is used by most of the mobile operators [2]. Therefore, building a new network infrastructure may not be advisable, due to which LTE Technology is widely acceptable. Future converged architectures are capable of supporting the communication among the LTE Base Stations. A wavelength division multiplexing-passive optical network is a ring topology-based converged architecture which supports communication with a WLAN channel [5]. A new converged architecture based on Tree Topology is proposed [6], in which all ONUs communicate with each other which belong to the same PON. In this paper, a new PON-LTE system hierarchy has been proposed for backhauling the LTE networks, using ring topology. Such kind of system may be considered as suitable for supporting the improved capacity, service availability, and QoS offered by ring-based WDM Networks. The inter-communication between optical network units are performed via the optical line terminal leading to packet delay and bandwidth wasting during the upstream and the downstream broadcasting. To overcome these problems, ring topology-based WDM architecture has been proposed [7–10].

2 Ring Architecture and Proposed Converged Architecture

The proposed converged access architecture (Fig. 2) employs WDM rings (Fig. 1) of ONUs for interconnection of LTE base stations in the similar Network area. Every WDM ring is connected to its corresponding optical line terminal with the help of a fiber cable and a 3-port circulator. Access gateways may be implemented in OLTs and at the core sites of the evolved packet core. Every WDM optical network unit serves as one LTE eNB, while both ONUs and eNBs are supporting an interface. The intermediate ONUs are allowed to bypass in this new architecture so that excess traffic may be re-routed in the network. A unidirectional transmission is observed at the ring in which data packets are routed in the similar direction. EPS bearers are deployed to support end-to-end communication. Each bearer consists of a unique QoS identifier and some identifying parameters. Bearers are classified as GBR (Guaranteed/Assured Bit Rate) where blocking prefers over dropping of data packets. Since the backhaul

network is not being able to see EPS bearer so the gateway provides layer 2 frames with a 3-bit class-of-service value, carried at the "User Priority bits" of the Ethernet frame header.

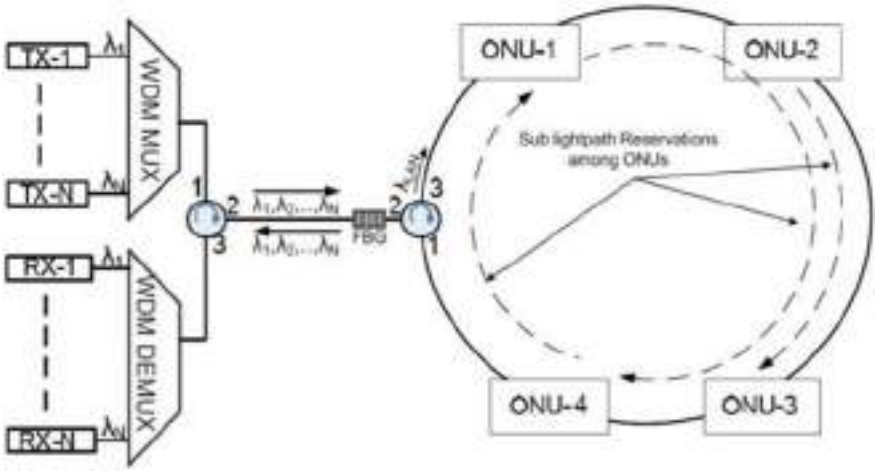

Fig. 1 WDM-based ring architecture

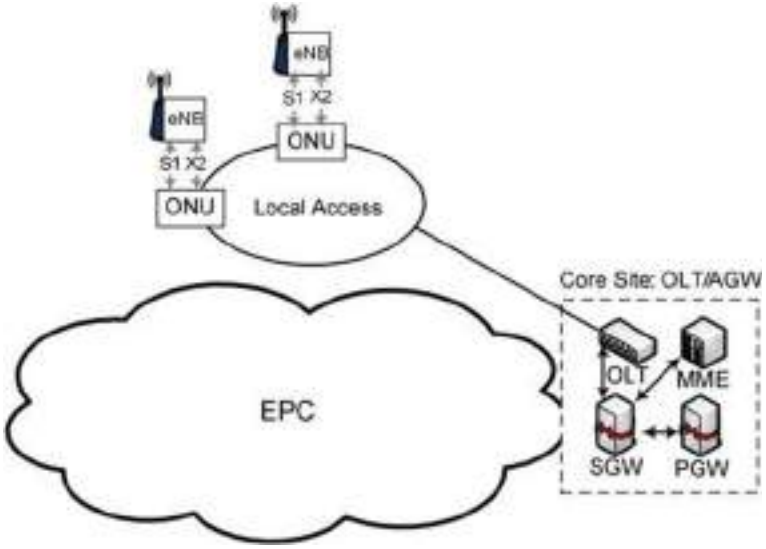

Fig. 2 Proposed converged architecture

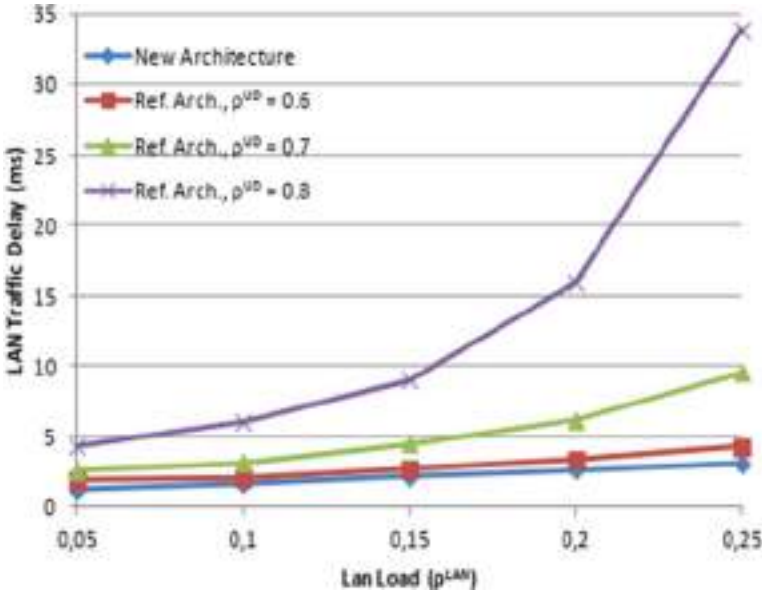

Fig. 3 Traffic delay vs. LAN load for different upstream/downstream channel loads

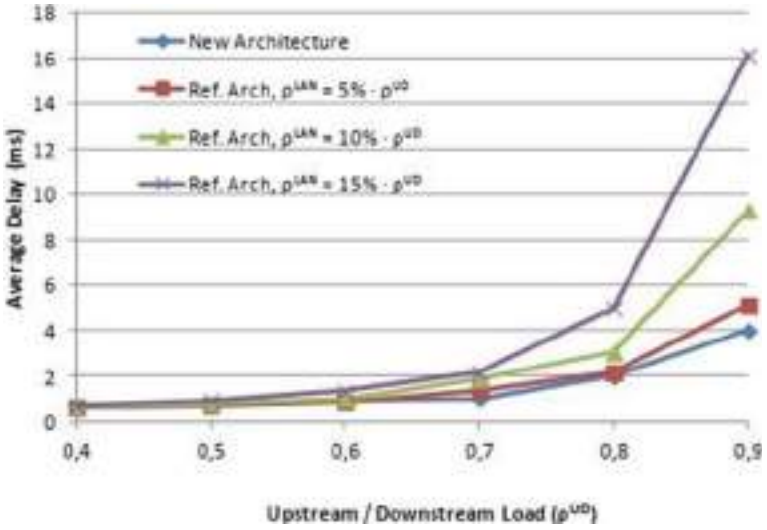

Fig. 4 Average traffic delay vs. load for different LAN traffic Loads

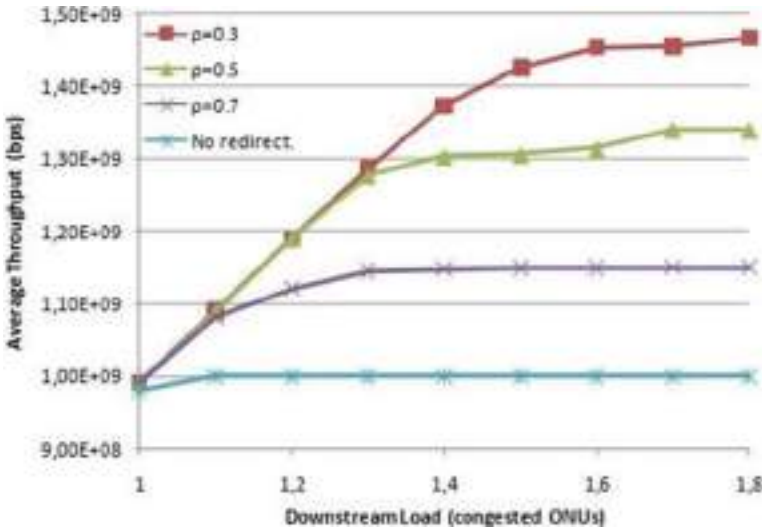

Fig. 5 Congested ONUs average throughput vs. traffic load in downstream

3 Dynamic Bandwidth Allocation/Reallocation

In this architecture, inter-optical network unit communication is performed at the common wavelength λ_{LAN}. Full meshing among the LTE base stations of the same ring is allowed, for direct exchange of data traffic via X2 interface. The excess traffic may be offloaded from congested downstream channels with the help of this additional wavelength, and re-directing it through less congested one (s). Therefore dynamic reallocation may be achieved in the network and downstream wavelengths are allowed to share their capacity. Time is digitized and quantized to next level in fixed time duration. Time division multiple access scheme is used in this scheme.

4 Dynamic Traffic Re-Direction

Traffic re-direction may be achieved by providing re-direction of traffic from those optical network units which are congested to that optical network units which are less congested on priority basis. An efficient algorithm is required in this regard. In this architecture, a hash-based technique is used for offloading the traffic [11]. This technique is calculation-based fingerprint value. The hash algorithm has been used for finding the origin and terminal address, origin and terminal port, and serial no.

5 Performance Evaluation

The performance of proposed architecture has been analyzed by series of simulations in NS-2 software. We simulated a ring topology-based LTE-Fiber converged network with 8 ONU/eNBs. An optical line terminal is being connected with a multidirectional feeder fiber. We modeled our architecture in such manner so that LAN traffic routes through X2 interface. Without loss of generality, we limit this set of measurements to one pair of ONUs and assume symmetric upstream/downstream traffic load. After achieving the simulation results, we compared the proposed design with reference design in which all inter-optical network units traffic routes through the optical line terminal via the dedicated LAN wavelengths. As a result, the packet delay in proposed ONU design may be reduced. It may be observed that new architecture posses lesser packet delay as compared to that of the reference architecture. Figure 4 displays the average delay of upstream/downstream traffic vs. the traffic load, for different LAN loads. It is observed that the average traffic delay of the proposed architecture remains unaffected by the LAN traffic, as the latter is transmitted in a separate channel. On the other hand, at the reference architecture LAN traffic wastes resources of the upstream/downstream channels, which leads to an increased delay. To this end, we may argue that the addition of a single wavelength, λ_{LAN}, significantly improves delay characteristics and offloads traffic from inter-eNB communication (Figs. 3 and 5).

Therefore, the QoS has been maintained when rerouting of excess traffic is managed properly. Moreover, it has been observed that the ideal bandwidth capacity of the WLAN channel may be engaged for downstream communication (Fig. 6).

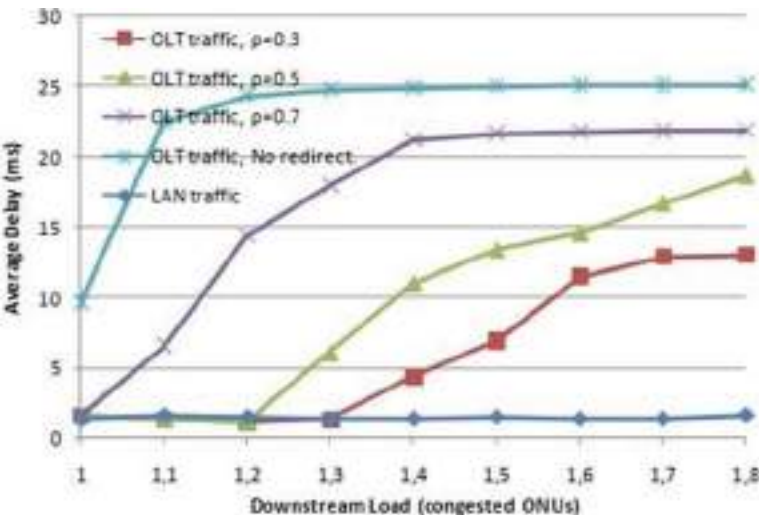

Fig. 6 Average delay vs. downstream load

6 Conclusion

In this paper, an innovative next generation converged architecture for wireless backhaul networks has been implemented which employs ring topology-based wavelength division multiplexing passive optical networks. The suggested architecture supports load balancing as well as inter-base station communication by dynamically re-allocating and sharing the downstream wavelengths. Intermediate ONUs has been bypassed for avoiding unnecessary traffic delay. An allocation scheme has been proposed for resource sharing of LAN traffic. The simulation results of the proposed architecture clearly show improved average delay characteristics and better traffic off-loadings among enBs. The suggested scheme effectively exploits ideal bandwidth capacity thereby implementing traffic rerouting.

References

1. M.D. Andrade et al., Evaluating strategies for evolution of passive optical networks. IEEE Comm. Mag. **49**(7), 176–184 (2011)
2. E. Dahlman, in *HSPE & LTE for Mobile Broadband* (Academic Press, 2008)
3. D. Breuer, Opportunities for next-generation optical access. IEEE Comm. Magazine **49**(2), 16–24 (2011)
4. Parkvall et al., Evolution of LTE toward IMT-Advanced. IEEE Comm. Magazine **49**(2), (2011)
5. G. Ellinas et al., Complete fixed-mobile convergence. IEEE/OSA J. Light. Technol. **28**(16), 2343–2357 (2010)
6. C. Ranaweera et al., Next generation optical-wireless converged network architectures. IEEE Network **26**(2), 22–27 (2012)
7. K. Ramantas et al., Efficient resource management via dynamic bandwidth sharing in a WDMPON ring-based architecture. in *Proceedings of IEEE ICTON*, 2012
8. Y. Chen, Optical burst switching: a new area in optical networking research. IEEE Network **18**(3), 16–23 (2004)
9. H. Erkan et al., A ring-based WDM-PON access architecture for the efficient network resources utilization. in *Proceedings of IEEE ICC*, 2008, pp. 5175– 5181
10. Norros et al., Theory of connectionless networks on the basis of fractional Brownian motion. IEEE J. Sel. Areas Commun. **13**(6), 953–962 (1995)
11. Z. Cao et al., Performance of hashing-based schemes for internet load balancing. in *Proceedings of IEEE INFOCOM*, 2000

Key Pre-distribution Scheme for Wireless Sensor Networks Using Combinatorial Design

Lakshmi Jayant Kittur and Alwyn Roshan Pais

Abstract Considering Wireless Sensor Networks (WSNs) usage in sensitive applications, providing secure communication between the sensor nodes is of utmost importance. The key pre-distribution technique allows the sensor nodes to encrypt the messages employing the secret key to uphold the network security. Having limited computational powers and storage capacity are the constraints of sensor nodes. In this work, Combinatorial Design (CD) is employed to propose a deterministic scheme for key pre-distribution in WSNs wherein keyrings are generated from a given keypool. The network region is divided into many same-sized cells with regular sensor nodes and cell leaders deployed in each cell. The cell leaders possess higher resource and computational capabilities than the regular sensor nodes and thus are used for communication between cells. Whenever the regular sensor nodes need to establish communication links with other regular sensor nodes in the same cell, they can do so directly using the common secret key. The key pre-distribution scheme proposed for cell leaders is highly scalable. A detailed study of the scalability, the resiliency of the proposed scheme is also presented. The resiliency accomplished is comparable to other existing schemes. Still, at the same time, the given scheme provides full connectivity, high scalability without a significant increase in the storage overhead of the sensor nodes.

Keywords Combinatorial design · Wireless networks · Key pre-distribution · Wireless sensor networks · Network security

1 Introduction

WSNs are a collection of distributed sensor nodes communicating with each other using wireless links. The sensor nodes gather information about the surroundings and then transmit the sensed data to a base station. The sensor nodes have limited

L. J. Kittur (✉) · A. R. Pais
Information Security Research Lab, Dept. of Computer Science and Engineering, National Institute of Technology Karnataka, Surathkal, Mangalore, Karnataka, India

S. Rawat et al. (eds.), *Proceedings of First International Conference on Computational Electronics for Wireless Communications*, Lecture Notes in Networks and Systems 329,
https://doi.org/10.1007/978-981-16-6246-1_54

storage space, battery-powered, limited capacity for computation, and their communication is often limited to the Radio Frequency (RF) range [1]. Typically, WSNs provide features to monitor environmental conditions and hence find usage in a wide variety of applications like human/machine health monitoring, military intelligence, industrial process monitoring, etc. [1–3]. In many situations, the sensor nodes are positioned in some hostile environments, and hence they are more susceptible to node capture attacks. Since the sensor nodes have limited memory and computing power, symmetric encryption techniques are more suitable for securing communication links. If every pair of nodes receive a unique secret key for communication, then the keyring size of each node increases as the sensor nodes in the network increases, which is not feasible if the network size is huge. Hence, combinatorial designs (CD) are good candidates for providing symmetric keys to the sensor nodes. From a given keypool, keyrings are derived such that keys are repeated in the key rings, which act as a common secret key between the sensor nodes. These keyrings are then assigned to the sensor nodes before stationing them in the deployment region. This process is known as key pre-distribution.

In this paper, we propose key pre-distribution scheme for heterogeneous networks consisting of regular sensor nodes and cell leaders. The cell leaders possess more resource capabilities than the regular sensor nodes and hence are used for inter-cell communication. The deployment region is cleft into same-sized areas called cells with regular sensor nodes and cell leaders stationed in each cell. The proposed design aims to provide high scalability without hampering the connectivity and making the network resilient toward the node capture attacks.

The remaining of the paper is organized as follows. The key pre-distribution scheme-related papers are discussed in Sect. 2. Section 3 presents the preliminary necessary to understand the scheme. The proposed scheme is described in Sect. 4. A detailed analysis of the presented scheme is performed in Sect. 5. Whereas Sect. 6 presents the comparative study of the proposed scheme with other schemes, and finally, in Sect. 7, the conclusion is presented.

2 Literature Survey

Key pre-distribution schemes are widely organized into three categories: probabilistic, deterministic, and hybrid schemes [4]. A random pairwise key pre-distribution scheme was put forward by Liu et al. [5] which used deployment knowledge. Huang et al. [6] adopted multi-space Blom [7] scheme and also took deployment knowledge into consideration while assigning the keys. Many deterministic schemes using CD have been presented recently. Camtepe and Yener [8] proposed a scheme for key pre-distribution using the symmetric design and Generalized Quadrangles to produce keyrings for the sensor nodes. Lee and Stinson [9] used Transversal Design to generate keyrings. Using the scheme of [9], Simonova [10] proposed another scheme for homogeneous network and considered location information to distribute keyrings. Ruj and Roy [4] adopted the scheme of [8] to distribute keyrings to the

sensor nodes within a cell and Transversal Design for generating keyrings for the cluster heads. On similar grounds, Bag [11] proposed a scheme that determined the number of cluster heads per cell according to the grid's size. Kumar et al. [12] proposed a scheme (CDKPD and CDRKPD) motivated by [4] scheme that improved the network's resiliency. Kumar et al. [13] proposed another scheme wherein the keys were assigned to only 3/4th of the cluster heads of each type/kind and did not use any information related to the location of sensor nodes positioned in the network. A hybrid scheme was proposed by Kumar et al. [14] which used a combination of both combinatorial and pairwise keys to assign keyrings to the nodes and reduced the storage overhead of the cluster heads. Bechkit et al. [15] proposed a scalable approach using combinatorial design to generate keys to the sensor nodes. Modiri et al. [16] proposed the usage of scalable design called Residual design to generate keyrings. Morshed Aski [17] proposed a scalable and fully connected combinatorial design scheme for IoT network.

3 Preliminaries

3.1 Design

A combinatorial design [18] is a pair *(X, A)* wherein *X* is pool of elements and *A* is a multiset consisting of subsets of *X*. *X* is called as points and *A* is called as blocks. A (v, k, λ)-Balance Incomplete Block Design known as BIBD is a design that meets the following conditions:

1. $|X| = v$
2. Every block has k points, and
3. Every pair of points is present in precisely λ blocks.

Example 1: A BIBD with $v = 7$, $k = 3$ and $\lambda = 1$

$X = \{10, 20, 30, 40, 50, 60, 70\}$, and

$A = \{(10,20,30), (10,40,50), (10,60,70), (20,40,60), (20,50,70), (30,40,70), (30,50,60)\}$.

The notations used in this paper are described in Table 1.

Table 1 Notations

N	Number of cells
n	Sensor node count in each cell
Q	Sensor node count in the network
q, *k*	Prime power
Rl(P)	Local resiliency when *P* regular sensor nodes are hacked
Rg(K)	Global resiliency when *K* cell leaders are hacked

4 Proposed Method

In the proposed scheme, the network area is divided such that there are equi-sized regions called cells. The regular sensor nodes are stationed in each cell, and the keys are assigned to them using symmetric design. Tables 2 and 3 depict the correspondence between CD and key pre-distribution for regular sensor nodes and cell leaders, respectively. The sensor nodes present in a cell use shared keys to communicate with each other directly. For inter-cell communication, cell leaders stationed in each cell are used. The keyrings are assigned to the cell leaders using two SBIBDs by taking the cartesian product of the keyrings generated by each SBIBD. This technique of generating the keyrings is highly scalable as the number of cell leaders supported for a prime power k is of the order of k^4, and the keyring size is $2(k + 1)$. The network is also resilient to attacks wherein nodes are captured by the adversary, and connectivity of 1 is maintained throughout the network.

4.1 Key Pre-Distribution Within a Cell

The sensor nodes within each cell are assigned keyrings using a deterministic approach through combinatorial design. The sensor nodes are assigned the keyrings derived from the keypool. The sensor nodes then communicate using the common keys present in their keyrings. Symmetric design as in [8] is employed to generate the keyrings. For a given prime power q, q^2+q+1 keyrings of symmetric design, each of size $q+1$ are obtained. Thus, the prime power q should be chosen such that the sensor node count(n) within each cell is $q^2+q+1 \geq n$. Different key pools are used for each cell so that one cell's compromise does not affect other cells. This is particularly

Table 2 Correspondence between block design and key pre-distribution for regular sensor nodes

Design	Key Pre-distribution
Set of points $= q^2+q+1$	Keypools $= q+q+1$
Blocks $= q^2+q+1$	Keyring $= q+q+1$
Elements in a block	Keys in a keyring
Size of each block $= q+1$	Size of keyring $= q+1$

Table 3 Correspondence between block design and key pre-distribution for cell leaders

Design	Key Pre-distribution
Set of points $= (k^2+k+1)^2$	Keypools $= (k^2+k+1)^2$
Blocks $= (k^2+k+1)^2$	Keyring $= (k^2+k+1)^2$
Elements in a block	Keys in a keyring
Size of each block $= 2(k+1)$	Size of keyring $= 2(k+1)$

useful in battlefields wherein the compromised cell's isolation is possible without affecting the other cells in the network.

4.2 Key Pre-Distribution for Cell Leaders

To assign the keyrings to the cell leaders, the key pre-distribution technique as proposed in [17] is employed. Consider a network of size N (number of cells). An appropriate value for k that is a prime power is decided to satisfy the condition that $(k^2+k+1)^2 \geq N$. Then keyrings are generated from two SBIBD's derived from two different pools such that SBIBD_1 $({k_1}^2+k_1+1, k_1+1, 1)$ and SBIBD_2 $({k_2}^2+k_2+1, k_2+1, 1)$ where $k_1 = k_2 = k$. A cartesian product of (k^2+k+1) keyrings each of SBIBD_1 and SBIBD_2 is calculated, thus generating $(k^2+k+1)^2$ number of keyrings each of size $2(k+1)$. An example is shown in Table 4. The generated keyrings are then assigned to the N cell leaders. This method is highly scalable as for a given keyring size of $2(k+1)$, it generated $(k^2+k+1)^2$ keyrings, i.e., of the order k^4, whereas just using SBIBD produces $O(k^2)$ keyrings. At the same time, the connectivity maintained is 1. There is a tradeoff between resiliency and keyring size space. In the proposed scheme, through experimentation, we considered four cell leaders per cell. Thus providing a resilient, scalable network without increasing the storage overhead for the sensor nodes. The four types of cell leaders are namely *Type w*, *Type x*, *Type y*, *Type z* derived from four different keypools. The keyrings generation and assignment process is the same for each type and is summarized in Algorithm 1. For communication between the cells, regular sensor nodes can utilize any of the four cell leaders. A cell leader of a given type in a cell can communicate only with the cell leaders of the same type in other cells using the common secret key. Through the key pre-distribution design proposed for cell leaders, any two cell leaders of a given type can have either two or $k+2$ keys in common. Hence, the hash of the common keys

Table 4 Keyrings for cell leaders generated from two SBIBDs (7,3,1) with keypools {0,1,2,3,4,5,6} and {8,9,10,11,12,13,14}

0 8 1 9 3 11	0 9 1 10 3 12	0 10 1 11 3 13	0 11 1 12 3 14	0 12 1 13 3 8
0 13 1 14 3 9	0 14 1 8 3 10	1 8 2 9 4 11	1 9 2 10 4 12	1 10 2 11 4 13
1 11 2 12 4 14	1 12 2 13 4 8	1 13 2 14 4 9	1 14 2 8 4 10	2 8 3 9 5 11
2 9 3 10 5 12	2 10 3 11 5 13	2 11 3 12 5 14	2 12 3 13 5 8	2 13 3 14 5 9
2 14 3 8 5 10	3 8 4 9 6 11	3 9 4 10 6 12	3 10 4 11 6 13	3 11 4 12 6 14
3 12 4 13 6 8	3 13 4 14 6 9	3 14 4 8 6 10	4 8 5 9 0 11	4 9 5 10 0 12
4 10 5 11 0 13	4 11 5 12 0 14	4 12 5 13 0 8	4 13 5 14 0 9	4 14 5 8 0 10
5 8 6 9 1 11	5 9 6 10 1 12	5 10 6 11 1 13	5 11 6 12 1 14	5 12 6 13 1 8
5 13 6 14 1 9	5 14 6 8 1 10	6 8 0 9 2 11	6 9 0 10 2 12	6 10 0 11 2 13
6 11 0 12 2 14	6 12 0 13 2 8	6 13 0 14 2 9	6 14 0 8 2 10	

acts as the secret key between the two cell leaders. This makes the network more resilient as the adversary need to capture all the common keys between the two cell leaders to hamper the communication link between them.

Algorithm 1: Key assignment for cell leaders
Result: N keyrings for cell leaders
1. Find prime power k, such that $(k^2+k+1)^2 \geq N$
2. Generate $SBIBD_1$ and $SBIBD_2$ with different keypools as SBIBD $(k^2+k+, k+1, 1)$. Let the keyrings of $SBIBD_1$ be denoted by A and that of $SBIBD_2$ by B
3. Take cartesian product of the keyrings generated from $SBIBD_1$ and $SBIBD_2$ as $C = A \times B$ where $\|C\| = z = (k^2+k+1)^2$
4. Assign the generated $z = (k^2+k+1)^2$ keyrings to the N cell leaders

5 Analysis

In this section, the security and scalability analysis of the proposed scheme is presented.

5.1 Scalability

Scalability is the network's maximum ability in terms of the number of sensor nodes it can support. For a given keyring size of $2(k+1)$, the number of cell leaders generated by the proposed design is $(k^2+k+1)^2$ which is of the order k^4, and it is of the order k^2 using SBIBD. Thus, the proposed scheme provides high scalability without hampering the connectivity than other techniques that use SBIBD.

5.2 Resiliency

The adversary gets hold of the keyrings of the sensor node by attacking it. Thus making all the keys present in that keyring unusable for securing communication elsewhere in the network. The network's resiliency is given as

$$R(s) = \frac{\text{Count of links affected when s nodes are hacked}}{\text{Total count of links in the network}} \tag{1}$$

where *R(s)* gives the resiliency of the model when s nodes are attacked.

Local Resiliency. The keyring size of a regular sensor node is $q+1$ where $q^2+q+1 \leq n$, where n is sensor node count per cell. Each key is present in $q+1$ keyrings. Hence, exposing a single key compromise $(q+1)\,(q)/2$ intra-links. Thus, if an attacker captures a regular sensor node, he exposes $q+1$ keys and thereby compromising $((q+1)^2)\,(q))/2$ intra-links. When the attacker captures P regular sensor nodes in the whole region, then the count of intra-links disrupted is

$$Rl(P) = \frac{P(q(q+1)^2/2)}{N(q^2+q+1)(q^2+q)/2} \tag{2}$$

where N is cell count. However, actual value may be lesser than this as number of unique keys exposed may be much lesser. The theoretical and experimental values of Local Resiliency are given in Table 5.

Global Resiliency. Global resiliency is the ratio of the number of links between cells compromised to the total number of links existing between the cells. There exist primary and secondary links between the cells in the network. The cell to cell communication link is the primary link, and the secondary links represent the communication link between the same type of cell leaders. Thus, in the proposed scheme, one primary link and four secondary links exist between any two cells. Each key in the proposed key-distribution scheme for cell leaders is present in $(k+1)$ (k^2+k+1) keyrings. The keyring size for the cell leader is $2(k+1)$. Whenever a cell leader is attacked, then the keys present in its keyring get exposed. A primary link between two cells is said to be broken only when all the four secondary links between them are damaged/broken. It is impossible to determine precisely the count of secondary links damaged when certain cell leaders are compromised since we cannot determine the number of unique keys captured. Also, between any two cell leaders, two or $k+2$ keys are shared, and a hash of these shared keys acts as the secret key between them. Hence, we cannot give an exact count of secondary links broken when a certain key is compromised. Thus, in turn, it is impossible to determine the total number of primary links affected theoretically. Table 6 presents the experimental

Table 5 Theoretical and experimental values of Local Resiliency *Rl(P)* where N is the cell count in whole network, n is the count of sensor nodes per cell, $q+1$ gives the key ring size, P is the count of regular sensor nodes attacked

N	n	q	P	*Rl(P)* theoretical	*Rl(P)* experimental
9	7	2	5	0.2380	0.2222
25	13	3	20	0.2461	0.2256
49	57	7	50	0.1432	0.0841
121	133	11	200	0.1491	0.1388
289	307	17	400	0.0811	0.0779
506	553	23	700	0.0600	0.0582
961	993	31	1000	0.0335	0.0331

Table 6 Estimation of Global resiliency (*Rg(S)*) where *N* is the cell count, *k* is prime power, *S* is the count of cell leaders attacked

N	*k*	*S*	*Rg(S)*
49	2	5	0.0012
169	3	7	0.0009
961	5	25	0.0577
3249	7	50	0.2091

values of global resiliency that has been calculated for varying sizes of the network. It is evident that the proposed method is highly resilient to node capture attacks.

6 Comparative Analysis

The proposed scheme has significant advantages over the other schemes. The proposed scheme is highly scalable, producing keyrings of the order k^4 for a prime power k and at the same time maintains the connectivity of 1 throughout the network. Keypools used for generating keyrings for each cell and cell leaders are different. Thus, compromising a cell leader or sensor node does not hamper the whole network but only to a small portion of the network.

Further, in the presented method, four cell leaders are stationed in each cell. Hence, a cell is isolated from the other parts of the network only when all the four cell leaders get compromised and this makes the network robust and resilient. Also, a hash of the common keys shared between cell leaders is performed to obtain a common secret key. This further enhances the model's resiliency as the adversary cannot disrupt a communication interlink until he gets hold of all the common keys shared. The key storage overhead for cell leader is $\sqrt[4]{N}$ and for regular sensor node is $\sqrt{n}$ where n is the regular sensor node count for each cell and N is the cell count.

Figure 1 shows the comparison of our scheme with the existing schemes. It can be seen that the resiliency of the presented scheme is comparable to other standard schemes, but our scheme also offers high scalability, full connectivity.

7 Conclusion

In the proposed article, a deterministic approach for generating keyrings is presented. The network is divided into cells of the same size with regular sensor nodes and cell leaders deployed in each cell. The technique of combining two symmetric designs is highly scalable and at the same time maintains a connected network. Sensor nodes within a cell communicate directly with each other and employ cell leaders for inter-cell communications. The resiliency achieved from the presented scheme is comparable to existing schemes without hampering the connectivity and also provides good scalability. In the future, the keys can be distributed to the sensor nodes taking into

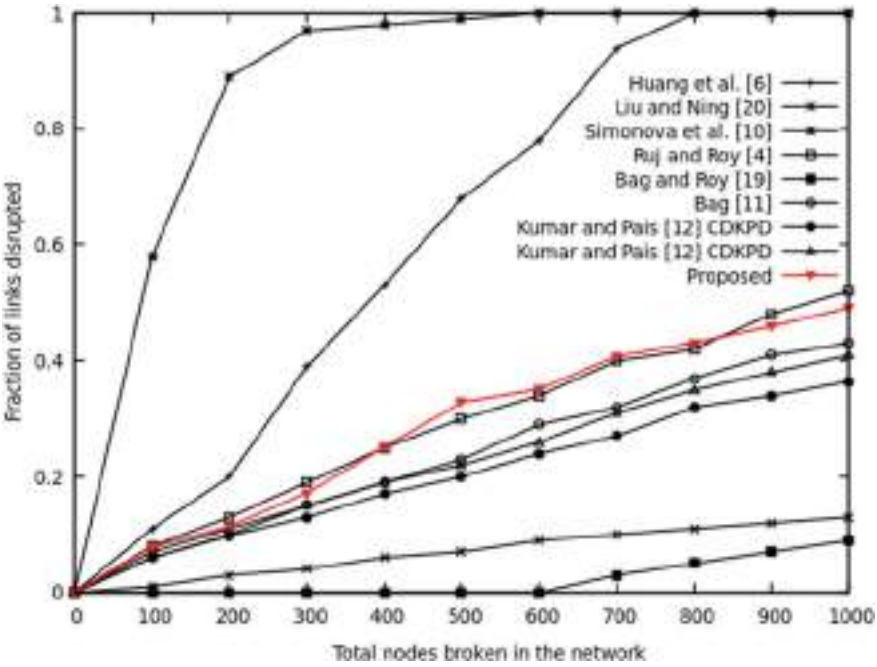

Fig. 1 Comparison for various schemes Ruj et al. [4] ($k = 12$ and $Q = 16{,}093$), Bag [11] ($q = 13$ and $Q = 16{,}055$), Bag and Roy [19] ($p = 11$, $c = 4$ and $Q = 16{,}093$), Simonova [10] ($k = 16$, $p = 11$ and $Q = 12{,}100$), Huang et al. [6] ($\theta = 7$, $\varphi = 1$, $\gamma = 8$, $\tau = 2$, $n_z = 100$ and $Q = 10{,}000$), Liu and Ning [20] ($m = 60$, $L = 1$, $k = 200$ and $Q = 10{,}000$), CDKPD [12] ($k = 12$ and $Q = 16{,}093$) and CD-RKPD [12] ($\rho = 4$, $k = 12$ and $Q = 16{,}093$), proposed scheme (q = 3, k = 11 and Q = 16,093) (Q = sensor node count in a WSN)

consideration their resource constraint of communication range, and the number of cluster heads per cell can be reduced without affecting the resiliency of the model.

References

1. C. Zhu, C. Zheng, L. Shu, G. Han, A survey on coverage and connectivity issues in wireless sensor networks. J. Netw. Comput. Appl. **35**(2), 619–632 (2012)
2. I.F. Akyildiz, W. Su, Y. Sankarasubramaniam, E. Cayirci, A survey on sensor networks. IEEE Commun. Mag. **40**(8), 102–114 (2002)
3. A. Kumar, A.R. Pais, En-route filtering techniques in wireless sensor networks: a survey. Wirel. Pers. Commun. **96**(1), 697–739 (2017)
4. S. Ruj, B. Roy, Key predistribution using combinatorial designs for grid-group deployment scheme in wireless sensor networks. ACM Trans. Sens. Netw. (TOSN) **6**(1), 4 (2009)
5. D. Liu, P. Ning, Location-based pairwise key establishments for static sensor networks. in *Proceedings of the 1st ACM workshop on security of ad hoc and sensor networks*, 2003, pp. 72–82

6. D. Huang, M. Mehta, D. Medhi, L. Harn, Location-aware key management scheme for wireless sensor networks. in *Proceedings of the 2nd ACM workshop on security of ad hoc and sensor networks*, 2004, pp. 29–42
7. R. Blom, An optimal class of symmetric key generation systems. in *Workshop on the Theory and Application of Cryptographic Techniques* (Springer, 1984) pp. 335–338
8. S.A. Camtepe, B. Yener, Combinatorial design of key distribution mechanisms for wireless sensor networks. IEEE/ACM Trans. Netw. **15**(2), 346–358 (2007)
9. J. Lee, D.R. Stinson, A combinatorial approach to key predistribution for distributed sensor networks. in *IEEE wireless communications and networking conference*, 2005 (IEEE, 2005), pp. 1200–1205
10. K. Simonova, A.C. Ling, X.S. Wang, Location-aware key predistribution scheme for wide area wireless sensor networks. in *Proceedings of the fourth ACM workshop on Security of ad hoc and sensor networks*, 2006, pp. 157–168
11. S. Bag, A new key predistribution scheme for grid-group deployment of wireless sensor networks. Ad Hoc Sens. Wirel. Netw. **27**, (2015)
12. A. Kumar, A.R. Pais, A new combinatorial design based key pre-distribution scheme for wireless sensor networks. J. Ambient. Intell. Humaniz. Comput. **10**(6), 2401–2416 (2019)
13. A. Kumar, N. Bansal, A.R. Pais, New key pre-distribution scheme based on combinatorial design for wireless sensor networks. IET Commun. **13**(7), 892–897 (2019)
14. A. Kumar, A.R. Pais, A new hybrid key pre-distribution scheme for wireless sensor networks. Wirel. Netw. **25**(3), 1185–1199 (2019)
15. W. Bechkit, Y. Challal, A. Bouabdallah, V. Tarokh, A highly scalable key pre-distribution scheme for wireless sensor networks. IEEE Trans. Wirel. Commun. **12**(2), 948–959 (2013)
16. V. Modiri, H.H.S. Javadi, M. Anzani, A novel scalable key pre-distribution scheme for wireless sensor networks based on residual design. Wirel. Pers. Commun. **96**(2), 2821–2841 (2017)
17. A.M. Aski, H.S. Javadi, H. Shirdel, A full connectable and high scalable key pre-distribution scheme based on combinatorial designs for resource-constrained devices in iot network. Wirel. Person. Commun. **114**, 2079–2103 (2020)
18. D. Stinson, Combinatorial designs: constructions and analysis. Springer Sci. Bus. Media (2007)
19. S. Bag, B. Roy, A new key predistribution scheme for general and grid-group deployment of wireless sensor networks. EURASIP J. Wirel. Commun. Netw. **2013**(1), 145 (2013)
20. D. Liu, P. Ning, Improving key predistribution with deployment knowledge in static sensor networks. ACM Trans. Sens. Netw. (TOSN) **1**(2), 204–239 (2005)

Performance of Kalman-Based Precoding in Millimeter-Wave Communication

Divya Singh

Abstract Millimeter-wave (30–300 GHz) communication entails a large number of transmitting and receiving antennas to accomplish high beamforming gains, so as to minimize the high path loss. Digital precoding/combining suffers from complex hardware due to the requirement of an enormous number of antenna arrays, and analog precoding/combining suffers from a poor performance rate. Therefore, hybrid precoding is a trade-off between analog and digital precoding/combining, when the number of users increases. This paper carries Kalman-based analog/digital, i.e. hybrid precoding to increase spectral efficiency in the case of multiuser system. Simulation results show the improved average achievable rate in millimeter-wave multiuser system.

Keywords Millimeter wave · Kalman filter · Hybrid beamforming · MIMO

1 Introduction

Mm-wave communication is a main empowering innovation for understanding the spectrum mash in the future 5G framework. Because of restricted accessible range in the mm-wave band, traditional cell and WiFi-based arrangements can't be scaled up to encounter the ever-developing information requests of organization densification, and rising applications related to server farms and cell phones [1]. Millimeter-wave communication in the as of late opened up adjacent square of unlicensed range in the 57.1–71.0 GHz territory is an open door for accomplishing Gbps information rates [2]. In reality, the present standards working in these groups permit up to 2 GHz-wide channels for short-length communication [3–6].

While the equipment support from a huge number of antenna terminals for beamforming capacities is as of now accessible, the high operating frequency, estimated sampling rates and bandwidth of channel make it hard to send conventional completely digital beamforming arrangements [7–11]. Hence, analog beamforming

D. Singh (✉)
Department of Electronics and Communication, GLA University, Mathura, India
e-mail: divya.singh@gla.ac.in

S. Rawat et al. (eds.), *Proceedings of First International Conference on Computational Electronics for Wireless Communications*, Lecture Notes in Networks and Systems 329,
https://doi.org/10.1007/978-981-16-6246-1_55

strategy is a potential option in mm-wave communication, which arranges the phases of different signals from antenna through simple phase shifters of analog type. But this type of strategy cannot increase the beamforming gain. Therefore, hybrid beamforming is an emerging solution that incorporates the advantages of analog and digital solutions and minimizes the limitations of both solutions. There are a number of existing solutions for multiuser hybrid mm-wave system [12, 28–34]. Two-stage-based hybrid precoding is proposed in ref. [12]. In single user system, the base station and mobile station together prefer a 'best' blend of radio frequency (RF) beamformer/combiner so as to amplify the channel gain to that particular MS [13–16]. To minimize interference among users, the effective channel is inverted at the base station in ZF hybrid precoding [28]. Earlier works have created calculations to increase the average achievable rate instead to limit the bit error rate (BER) execution [18, 25–29]. Few BER improvement arrangements incorporate works, for example, [30] and [32].

In Kalman filter-based algorithm, the value of unknown variables is estimated using previous measurements of those unknown variables over time. Kalman filters have been showing their value in different applications. Kalman filters have generally straightforward shape and require little computational force. However, it is as yet difficult for individuals who are inexperienced with estimation theory to comprehend and actualize the Kalman filters. While there exist some great research works, for example, [1] describing theory and related derivations of Kalman filter. This paper focuses on Kalman-based hybrid precoding in Mm-wave systems.

2 System Model

A system of hybrid precoder for single users is shown in Fig. 2 consisting N_s data streams per user. This system also consists of N_t antennas at the BS, equal number of RF chains at BS and MS and N_r antennas at the receiver. N_s data streams on each subcarrier are bounded to [9]:

$$N_s \leq N_{RF} \leq N_t$$

The baseband precoder F_D with dimension $N_{RF} \times N_s$ and analog RF precoder and F_A with dimension $N_t \times N_{RF}$ are used at downlink to transmit the signal x [15–18]. This transmitted signal in the complex vector form is given by:

$$x = F_A F_D s \forall x \in \mathbb{C} N_t \times 1 \tag{1}$$

where, s denotes the $N_s \times 1$ size transmitted symbol matrix.

The received signal by the user is:

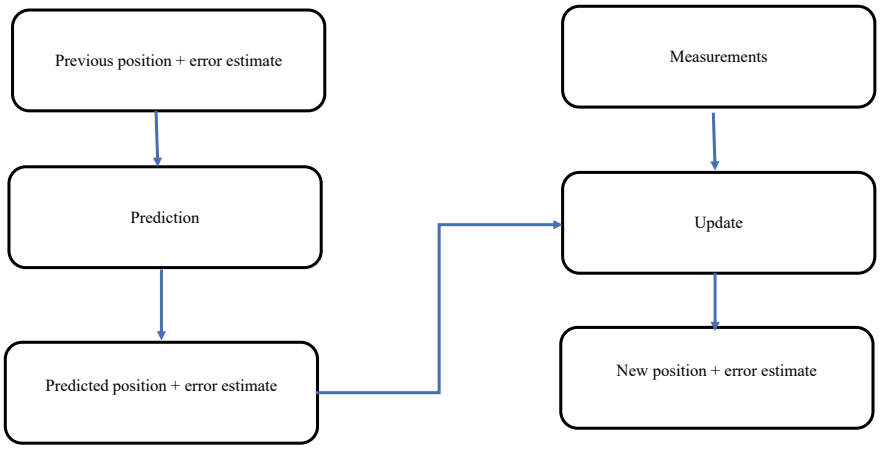

Fig. 1 Estimation process using Kalman filter

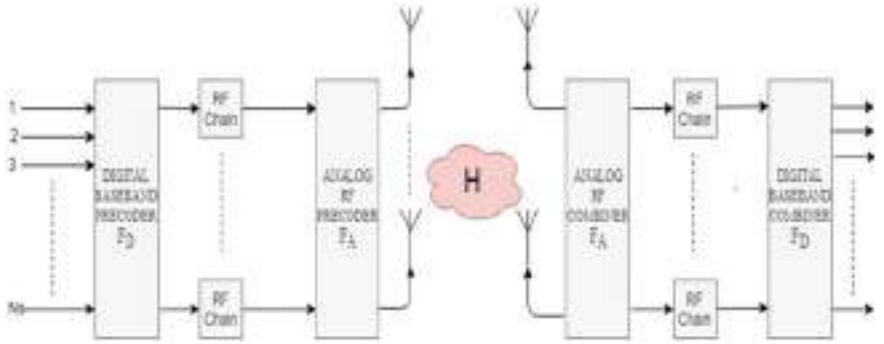

Fig. 2 Hybrid precoder in Mm-wave system

$$r = Hx + n \tag{2}$$

Where r is the estimated signal at mobile station in the form of complex vector as y $\in \mathbb{C}\ N_r \times 1$ and n is white Gaussian noise vector such that n $\sim C\mathcal{N}(0, \sigma^2 I)$ [19].

The channel matrix H of millimeter-wave channel with size $N_r \times N_t$ and L scatterers using geometric channel model is expressed as:

$$H = \sqrt{\frac{N_t N_r}{L}} \sum_{l=1}^{L} \alpha_l a_r\left(\theta_{l,}^r \varnothing_l^r\right) a_t^H\left(\theta_l^t, \varnothing_l^t\right) \tag{3}$$

where, α_l is the notation for complex gain of the lth multi-path, and the vectors $a_r\left(\theta_{l,}^r \varnothing_l^r\right) a_t^H\left(\theta_l^t, \varnothing_l^t\right)$ represent the normalized antenna array with angle of arrival/departure, i.e.$\left(\theta_{l,}^r \varnothing_l^r\right)and\left(\theta_l^t, \varnothing_l^t\right)$ at BS and MS, respectively [20, 21].

H in matrix form is signified as,

$$H = \sqrt{\frac{N_t N_r}{L}}[a_r\left(\theta_1^r\right) a_r\left(\theta_2^r\right) \ldots\ldots\ldots a_r\left(\theta_l^r\right) * \begin{bmatrix} \alpha_1 & \cdots & 0 \\ \vdots & \ddots & \vdots \\ 0 & \cdots & \alpha_l \end{bmatrix} * \begin{bmatrix} a_t\left(\theta_1^t\right) \\ \cdot \\ \cdot \\ a_t\left(\theta_1^t\right) \end{bmatrix} \tag{4}$$

3 Problem Formulation

The objective of this paper is to enhance the achievable rate R (F_A, F_D) by using Kalman-based approach in hybrid precoding matrix for millimeter-wave system [22–24]. Therefore, these matrixes (F_A, F_D) are designed by Gaussian signaling to achieve maximum information rate over the mm-wave channel.

$$\mathrm{R}(\mathrm{F}_A, \mathrm{F}_D) = log_2(|\mathrm{I} + \frac{\rho}{N_S \sigma_n^2} H \mathrm{F}_A \mathrm{F}_D F_D^H F_A^H H^H|) \tag{5}$$

The optimization problem of precoder with the appropriate design of its parameters (F_A, F_D) can be represented by [35]:

$$F_A^{opt} F_D^{opt} = Arg \min_{\mathrm{F}_A, \mathrm{F}_D} ||F^{opt} - \mathrm{F}_A \mathrm{F}_D||$$

$$s.t \mathrm{F}_A \in \{f_1, \ldots\ldots\ldots, f_L\} \tag{6}$$

$$||\mathrm{F}_A \mathrm{F}_D||_F^2 < P = ||F_D^H F_A^H \mathrm{F}_A \mathrm{F}_D||_F \tag{7}$$

$$= \sqrt{Tr(F_D^H F_A^H \mathrm{F}_A \mathrm{F}_D F_D^H F_A^H \mathrm{F}_A \mathrm{F}_D)} \tag{8}$$

where the first condition in Eq. (6) represents the limitation on search within a set of quantized RF vectors $\{f_1, \ldots\ldots\ldots, f_L\}$. The second condition in (7) represents power constraint and P is the transmitted power.

Now, Kalman approach is applied at BS to calculate F_D digital precoder matrix on quantized channels to achieve spectral efficiency comparable to optimal precoder.

In particular, F_D is computed using the calculated value of RF precoder F_A. The conditional mean F_D(n|n), the Kalman gains K(n) and variance R(n|n) at any constant time n is given by the following equations [2]:

$$F_D(n|n) = F_D(n|n-1) + K(n) + \frac{I - H_D F_D(n|n-1)}{||I - H_D F_D(n|n-1)||_F^2} \tag{9}$$

$$K(n) = R(n|n-1)H_D^H[H_D R(n|n-1)H_D^H + Q_n]^{-1} \tag{10}$$

$$R(n|n-1) = [I - K(n)H_D]R(n|n-1) \tag{11}$$

where H_D is equivalent to estimate channel matrix and Q_n represents the covariance matrix of Gaussian noise n. Number of users is proportional to the size of this matrix [22–24].

4 Performance Evaluation

Consider a mm-wave system with a BS using an 8×8 antenna array and MS with a 2×2 antenna array. Simulations are implemented in Matlab 2016b for multi-path channels (5 and 10).

The azimuth arrival/departure angle is uniformly distributed from 0 to π and the elevation from -90^0 to $+90^0$ with the knowledge of perfect channel [9].

Figure 3 compares the proposed Kalman-based precoding scheme with analog precoding and digital precoding schemes for multipath channels = 5 and number of users is 2. Mentioned algorithms discuss the system design in the multipath state

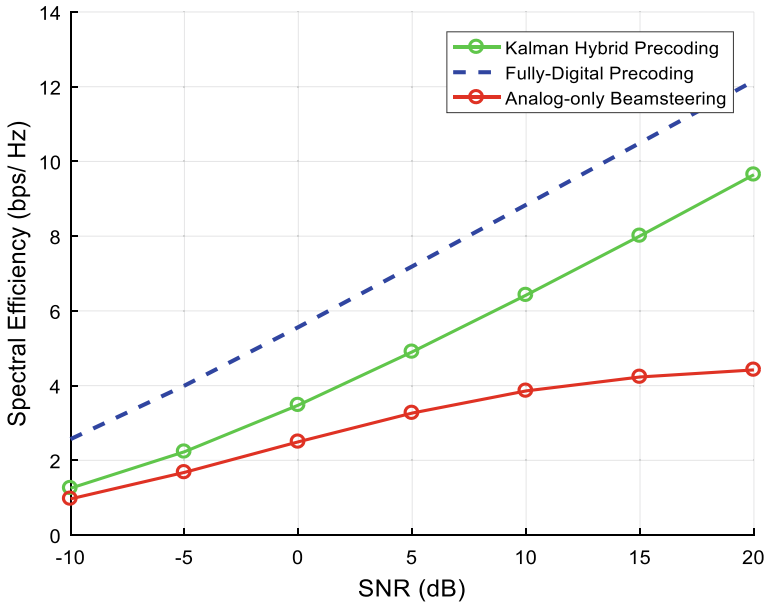

Fig. 3 Achievable rate with number of users = 2 in multipath(L = 10)

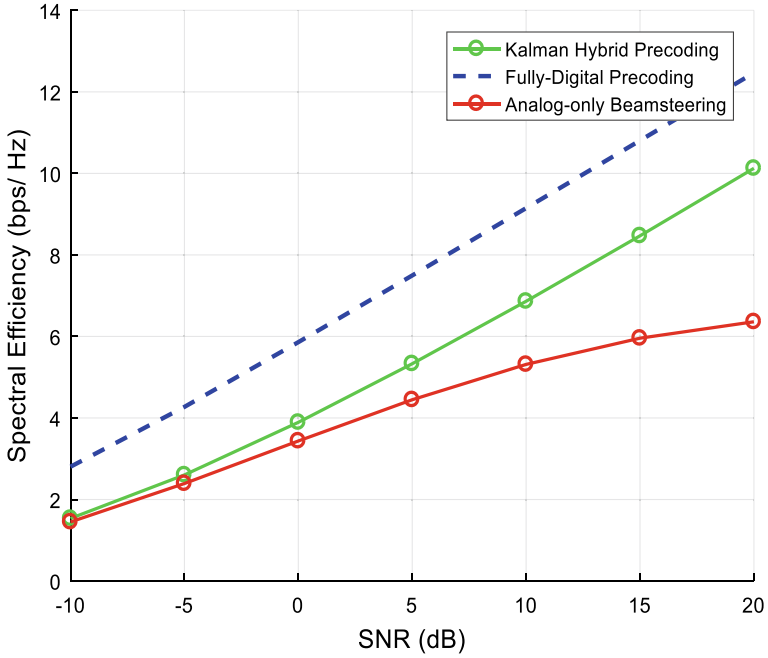

Fig. 4 Achievable rate with number of users = 2 in multipath(L = 5)

equipped with numerous RF chains at the BS and one RF chain per user. The Kalman-based precoding shows the best performance along with analog precoding method that results in the lowest performance.

Figure 4 shows the performance comparison of the proposed hybrid Kalman solution and other two precoding schemes considering the same system model and same channel estimate for multipath channels = 10 and same number of users.

Figures 5 and 6 show the effect of variation in the number of users on the performance in terms of the spectral efficiency in a multipath scenario. While the analog procedure declines its performance for a large number of users and Kalman algorithm illustrates good results nearly close to the fully digital procedure. Anyway, the Kalman approach is used to give better results. This approach uses iterative Kalman solution for the better adjustment of the precoding baseband matrix and the Kalman parameters in a hybrid system. It requires a very less number of iterations that is set to 10. There is no effect of variation in number of users on the distance between the fully digital and Kalman-based hybrid curve.

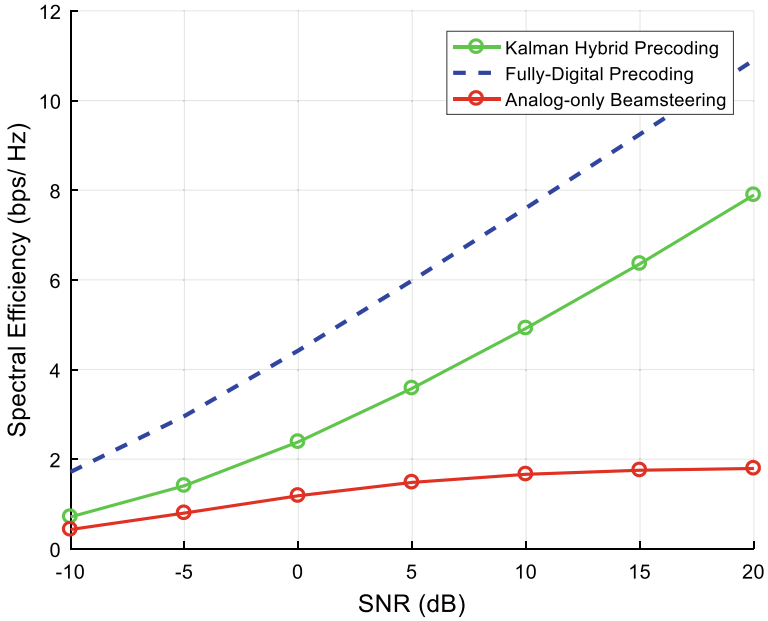

Fig. 5 Achievable rate with number of users = 4 in multipath(L = 10)

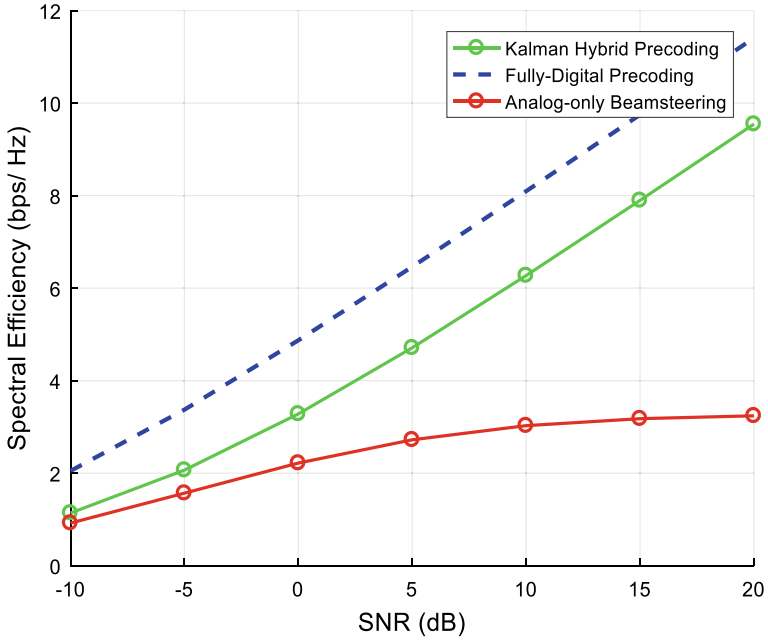

Fig. 6 Achievable rate with number of users = 4 in multipath(L = 5)

5 Conclusion

This paper presents the performance comparison of Kalman-based hybrid precoder for multi-user mm-wave systems, by minimizing the distance between the communicated and estimated data. This method follows this procedure in two steps: first compute the RF precoder matrix and then calculate the baseband precoder with the help of the estimated channel matrix at the BS. Simulation results indicate that this algorithm gives the performance in terms of achievable rate comparable with existing solutions. Kalman approach is able to adjust the baseband precoder matrix.

References

1. V.S.R. Wong, D.W.K. Ng, *Key Technologies for 5GWireless Systems* (Cambridge Univ. Press, Cambridge, U.K., 2017)
2. R.W. Boccardi, Jr. Heath, A. Lozano, T.L. Marzetta, P. Popovski, Five disruptive technology directions for 5G. IEEE Commun. Mag. **52**(2), 74–80 (2014)
3. R.W. Heath, Jr. N. González-Prelcic, S. Rangan, W. Roh, A.M. Sayeed, An overview of signal processing techniques for millimeter wave MIMO systems. IEEE J. Sel. Topics Signal Process. **10**(3), 436–453 (2016). 55720 Volume 6, 2018
4. Vizziello, P, Savazzi, K.R. Chowdhury, A Kalman based hybrid precoding for multi-user millimeter wave MIMO systems. IEEE Access **6**, 55712–55722 (2018). https://doi.org/10.1109/ACCESS.2018.2872738
5. M.E. Özçevik, B. Canberk, T.Q. Duong, 'End to end delay modeling of heterogeneous traffic flows in software defined 5G networks. Ad Hoc Netw. **60**, 26–39 (2017). [Online]. Available: http://www.sciencedirect.com/science/article/pii/S1570870517300422
6. J.G. Andrews et al., What will 5G be? IEEE J. Sel. Areas Commun. **32**(6), 1065–1082 (2014)
7. S.K. Saha, D.G. Malleshappa, A. Palamanda, V.V. Vira, A. Garg, D. Koutsonikolas, 60 GHz indoor WLANs: insights into performance and power consumption. Wirel. Netw. **24**(7), 2427–2450 (2017). https://doi.org/10.1007/s11276-017-1475-4
8. O.E. Ayach, S. Rajagopal, S. Abu-Surra, Z. Pi, R.W. Heath, Spatially sparse precoding in millimeter wave MIMO systems. IEEE Trans. Wirel. Commun. **13**(3), 1499–1513 (2014)
9. R.W Alkhateeb, Jr. Heath, G. Leus, Achievable rates of multiuser millimeter wave systems with hybrid precoding. in *Proceedings IEEE International Conference Communication Workshop (ICCW)*, pp. 1232–1237 (2015)
10. Alkhateeb, G. Leus, R.W. Heath, Limited feedback hybrid precoding for multi-user millimeter wave systems. IEEE Trans. Wirel. Commun. **14**(11), 6481–6494 (2015)
11. W. Roh et al., Millimeter-wave beamforming as an enabling technology for 5G cellular communications: theoretical feasibility and prototype results. IEEE Commun. Mag. **52**(2), 106–113 (2014)
12. V. Petrov, M. Komarov, D. Moltchanov, J.M. Jornet, Y. Koucheryavy, Interference and SINR in millimeter wave and terahertz communication systems with blocking and directional antennas. IEEE Trans. Wirel. Commun. **16**(3), 1791–1808 (2017)
13. T. Yilmaz, G. Gokkoca, O.B. Akan, Millimetre wave communication for 5G IoT applications. in *Internet of Things (IoT) in 5G Mobile Technologies* (Springer, Cham, Switzerland, 2016), pp. 37–53. https://doi.org/10.1007/978-3-319-30913-2_3
14. F. Akyildiz, W-Y. Lee, M.C. Vuran, S. Mohanty, NeXt generation/dynamic spectrum access/cognitive radio wireless networks: a survey. Comput. Netw. **50**, 2127–2159 (2006)
15. R. Méndez-Rial, C. Rusu, N. González-Prelcic, A. Alkhateeb, R.W. Heath, Hybrid MIMO architectures for millimeter wave communications: phase shifters or switches? IEEE Access **4**, 247–267 (2016)

16. H. Li, Z. Wang, Q. Liu, M. Li, Transmit antenna selection and analog beamforming with low-resolution phase shifters inmmWave MISO systems. IEEE Commun. Lett. **22**(9), 1878–1881 (2018)
17. X. Li,Y. Zhu, P. Xia, Enhanced analog beamforming for single carrier millimeterwave MIMO systems. IEEE Trans.Wirel. Commun. **16**(7), 4261–4274 (2017)
18. M. Jasim, J.E. Pezoa, N. Ghani, Simultaneous multi-beam analog beamforming and coded grating lobes for initial access in mmWave systems. in *Proceedings of CHILEAN Conference on Electrical, Electronics Engineering, Information and Communication Technologies (CHILECON)*, pp. 1–6 (2017)
19. M.-C. Lee, W.-H. Chung, Transmitter design for analog beamforming aided spatial modulation in millimeter wave MIMO systems. in *Proceedings of IEEE International Symposium on Personal, Indoor and Mobile Radio Communications (PIMRC)*, Sep. 2016, pp. 1–6.
20. T Hur, T. Kim, D.J. Love, J.V. Krogmeier, T.A. Thomas, A. Ghosh, Millimeter wave beamforming for wireless backhaul and access in small cell networks. IEEE Trans. Commun. **61**(10), 4391–4403 (2013)
21. D.H.N. Nguyen, L.B. Le, T. Le-Ngoc, Jr. R.W. Heath, Hybrid MMSE precoding and combining designs for mmWave multiuser systems. IEEE Access. **5**, 19167–19181 (2017)
22. F. Molisch et al., Hybrid beamforming for massive MIMO: a survey. IEEE Commun. Mag. **55**(9), 134–141 (2017)
23. R. Magueta, D. Castanheira, A. Silva, R. Dinis, A. Gameiro, Nonlinear space-time equalizer for single-user hybrid mmWave massive MIMO systems. in *Proceedings of 8th International Congress on Ultra Modern Telecommunications and Control Systems and Workshops (ICUMT)*, pp. 177–182 (2016)
24. D. Singh, A. Shukla, Sparse channel and antenna array performance of hybrid precoding for millimeter wave systems. in Patnaik S., Yang XS., Sethi I. (eds.) *Advances in Machine Learning and Computational Intelligence.* Algorithms for Intelligent Systems. (Springer, Singapore, 2021)
25. D. Singh, A. Shukla, Analysis of optimum precoding schemes in millimeter wave system. Recent Advan. Comput. Sci. Commun. **13**, 1 (2020)
26. C. Kim, T. Kim, J.-Y. Seol, Multi-beam transmission diversity with hybrid beamforming for MIMO-OFDM systems. in *Proceedings of IEEE GLOBE-COM*, pp. 61–65 (2013)
27. X. Zhang, A.F. Molisch, S.-Y. Kung, Variable-phase-shift-based RF-baseband code design for MIMO antenna selection. IEEE Trans. Signal Process. **53**(11), 4091–4103 (2005)
28. V. Venkateswaran, A.V.D. Veen, Analog beamforming in MIMO communications with phase shift networks and online channel estimation. IEEE Trans. Signal Process. **58**(8), 4131–4143 (2010)
29. L. Zhao, D.W.K. Ng, J. Yuan, Multi-user precoding and channel estimation for hybrid millimeter wave systems. IEEE J. Sel. Areas Commun. **35**(7), 1576–1590 (2017)
30. D.H.N. Nguyen, L.B. Le, T. Le-Ngoc, Hybrid MMSE precoding for mmWave multiuser MIMO systems. in *Proceedings of IEEE International Conference Commun*ication *(ICC)*, pp. 1–6 (2016)
31. Z. Wang, M. Li, X. Tian, Q. Liu, Iterative hybrid precoder and combiner design for mmWave multiuser MIMO systems. IEEE Commun. Lett. **21**(70), 1581–1584 (2017)
32. J. Mao, Z. Gao, Y. Wu, M.-S. Alouini, Over-sampling codebook based hybrid minimum sum-mean-square-error precoding for millimeter wave 3D-MIMO. IEEE Wirel. Commun. Lett. To be published. https://doi.org/10.1109/LWC.2018.2839723
33. J. Li, L. Xiao, X. Xu, S. Zhou, Robust and low complexity hybrid beamforming for uplink multiuser mmWave MIMO systems. IEEE Commun. Lett. **20**(6), 1140–1143 (2016)
34. W. Ni, X. Dong, Hybrid block diagonalization for massive multiuser MIMO systems. IEEE Trans. Commun. **64**(1), 201–211 (2016)
35. C. Hu, J. Liu, X. Liao, Y. Liu, J. Wang, A novel equivalent baseband channel of hybrid beamforming in massive multiuser MIMO systems. IEEE Commun. Lett. **22**(4), 764–767 (2018)

Congestion Estimation and Mitigation Using Fuzzy System in Wireless Sensor Network

Hemanth Kumar, S. M. Dilip Kumar, and E. Nagarjun

Abstract In Wireless Sensor Networks (WSNs), issues including energy management, topology management, bandwidth estimation, packet loss calculation, etc. are dealt. Only a few works have paid attention to mitigating congestion while estimating delay and bandwidth for transmitting data packets in WSNs. Several works on queue management and congestion control have incorporated Soft Computing (SC) techniques to solve some of the problems in WSNs. In this paper, an Active Queue Management (AQM) model to estimate congestion using Random Early Detection (RED) and mitigate congestion is proposed. It is found that the results obtained outperform the existing methods in terms of delay between intermediate nodes, end-to-end delay, packet loss ratio, packet loss probability, queue size and energy consumption.

Keywords Wireless sensor networks · Congestion control · Active queue management · Random early detection · Fuzzy system

1 Introduction

Sensor nodes in WSNs are deployed to gather information from the monitoring area and the same is forwarded to the sink for further processing with the help of forwarding nodes as shown in Fig. 1. Sensor nodes that are deployed in the sensing environment are powered by batteries and are not replaceable. Forwarding the collected data by the deployed sensor nodes may cause congestion at the junction nodes due to high rate of traffic flowing toward the sink. Congestion in the network occurs due to an increase in the traffic load than the allowed traffic load by the network at any instance. Delay in packet arrival, raise in packet loss, re-transmissions leads

H. Kumar (✉)
Department of MCA, J N N College of Engineering, Shivamogga, India

S. M. D. Kumar · E. Nagarjun
Department of Computer Science and Engineering, University Visvesvaraya College of Engineering (UVCE), Bengaluru, India

S. Rawat et al. (eds.), *Proceedings of First International Conference on Computational Electronics for Wireless Communications*, Lecture Notes in Networks and Systems 329,
https://doi.org/10.1007/978-981-16-6246-1_56

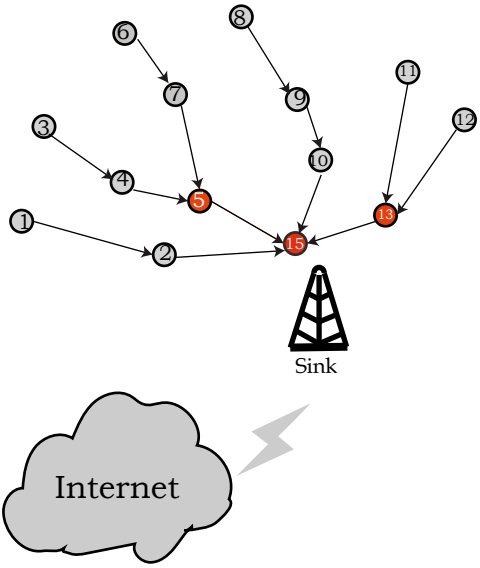

Fig. 1 Network scenario of WSN

to excess consumption of energy, degrade in channel quality are some of the impacts of congestion in the sensor network. Therefore, congestion has to be detected and mitigated for smooth operation of the network. Many protocols have been proposed for dealing with congestion and they are categorized based on traditional congestion control protocols and soft computing-based congestion control protocols.

The current work proposes a fuzzy mechanism for detecting, estimating and mitigating congestion. The contribution to this work is as follows:

Active Queue Management (AQM) is used for detecting and estimating the level of congestion using Fuzzy Logic System (FLS).
Information about the congestion is informed to child nodes using Implicit Congestion Notification (ICN).
Congestion is mitigated using rate adaptation method.

The flow of paper is as follows: Investigation on existing congestion control protocols in WSNs is done in Sect. 2. Section 3 highlights the preliminary of the proposed protocol. The proposed congestion control method is described in Sect. 4. Results are discussed in Sect. 5, and Sect. 6 concludes the work.

2 Related Works

Extensive studies are made on congestion control protocols since recent years. These studies are made on different layers of WSNs. Some of the studies are as follows:

The modified version of priority-based congestion control protocol (PCCP) is Queue-based Congestion Control Protocol with Priority Support (QCCP-PS) [1]. PCCP is enhanced by including queue management function. To measure the degree of congestion, queue length is used as an index. Each source node's traffic rate depending on the congestion degree will either increase or decrease. To minimize the packet drop in WSNs, buffer of each sensor is regulated matching the transmitting rate of the downstream sensor nodes. An algorithm assigns a data forwarding rate to the nodes to avoid packet drops, which is caused by congestion. The algorithm equally allocates the bandwidth to the sources and solves the fairness problem. Detecting congestion and adjusting the transmission rates of the nodes for the purpose of mitigating congestion with minimum loss is presented in ref. [2]. Queue Management-Based Congestion Control (QMCC) [3] reduces the packet loss by efficiently managing the queue. Congestion is detected by assessing length of node's queue and its parent's queue. Based on the buffer occupancy of a node and its parent's, the transmission rate is adjusted. Packets are of various types and are of different importance. Packets having higher priority have to be handled in different ways than the packets having lower priority. Congestion control protocols based on priority mentioned are as follows: In priority-based congestion control protocol (PCCP) [4], computing the degree of congestion is done using the ratio between the arrival of packets and service time of packet. Various levels of priority indices are taken into account considering the requirement of higher bandwidth by a node for generating high traffic. According to the degree of congestion and priority index of a node, rate adjustment is undertaken. Prioritized Heterogeneous Traffic-oriented Congestion Control Protocol (PHTCCP) [5] ensures an efficient rate control for prioritized heterogeneous traffic. When a packet enters a node, it is classified based on the priority and is placed in specific traffic class. A packet generated by a node will be assigned a lower priority than a packet, which is forwarded by neighboring node. Congestion notification is implicit and controlling the congestion is implemented using hop-by-hop manner. Dynamic predictive congestion control protocol DPCC [6] is designed to predict congestion and dynamically distribute the traffic over the network in a fairly manner. DPCC has three parts, viz., dynamic rate adjustment using priority, predictive congestion detection technique and node selection based on backward and forward mechanism. DPCC detects the congestion by integrating the unused buffer of a node along with the traffic rate at MAC layer. Considering the queue length, a congestion control mechanism based on priority is proposed in Wireless Body Area Network [7]. Having two modules, quick start module begins with large number of packets but packet forwarding rate to sink is low. Congestion detection, congestion notification and congestion avoidance are three different phases present in congestion control module. Fuzzy-Based Adaptive Congestion Control (FBACC) [8] detects and manages congestion by providing a fuzzy logic controller

for the purpose of predicting the congestion, and traffic rate is adjusted. Traffic rate, occupancy of buffer and the number of participating nodes are the inputs for fuzzy logic controller by the algorithm, and rate of transmission is used as output. A node upon identifying congestion, it sends congestion notification to its neighboring nodes for adjusting the transmission rate. Zone-based routing protocol in association with balancing the energy in the network approach is proposed in ref. [9]. The work in ref. [10] has proposed an energy efficient-based hierarchical multi-path routing protocol with an intension of clearing the congestion and balancing the energy consumption in the network.

3 Preliminaries of the Proposed AQM Model

3.1 Active Queue Management

The basic idea behind active queue management scheme is to proactively drop all the incoming packets by a node much earlier the node's buffer gets overflow. It provides different Quality-of-Service (QoS) for different traffic and priorities.

AQM scheme has the performance advantage of two thresholds over single threshold. The two threshold values can be adjusted for a lesser delay for the same throughput.

3.1.1 Random Early Detection (RED)

RED is a frequently used technique for AQM in WSNs. Congestion probability is identified by this algorithm and if congestion is detected, the arriving packet will be marked or dropped. Figure 2 depicts the working of RED algorithm.

The decision for marking or dropping a packet is based on average weighted queue length (Q_{lenavg}). Suppose a packet enters a node and the weighted average queue is less than *MinTh*, the minimum threshold, then the incoming packet is kept in queue and if (Q_{lenavg}) is higher than *MaxTh*, a maximum threshold, then the arriving packet is marked or dropped. But if (Q_{lenavg}) is between *MinTh* and *MaxTh*, packets are marked *Pa*, which is the packet drop probability. *Maxp* is default value of maximum packet drop probability. Probability for dropping or marking a packet is expressed as in Eq. (1):

$$P(a) = \begin{cases} 0 & Q_{len_{avg}} < MinTh \\ \frac{Q_{len_{avg}} - MinTh}{MaxTh - MinTh} \times Max_p & MinTh \otimes Q_{len_{avg}} < MaxTh \\ 1 & MaxTh < Q_{len_{avg}} \end{cases} \tag{1}$$

Fig. 2 Operation of RED

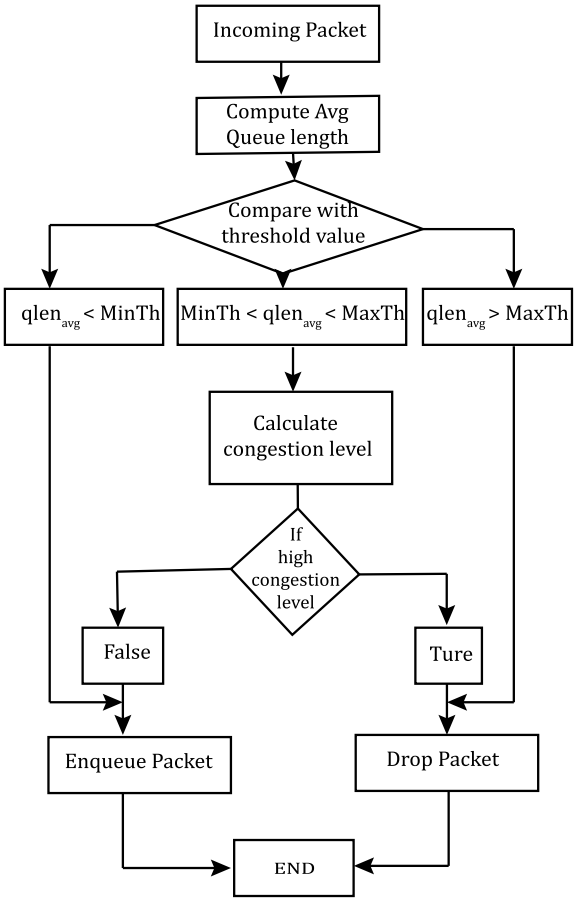

If *Maxp* is at higher probability, than an incoming packet is dropped by RED algorithm and shows the presence of congestion at higher level in the network. If *Maxp* is at lower level, then the packet is allowed to enter the queue and is further processed.

4 System Model

Nodes that are deployed in the network are autonomous and perform computation and dos the communication job with each other by exchanging and forwarding messages.

4.1 Problem Statement and Objectives

The objective of this work lies in identifying congestion level and mitigating it using fuzzy system. Fuzzy system takes two variables as inputs and generates the output using the inference mechanism. Output of the fuzzy system informs the presence of congestion and its level in the network. Based on the level of congestion identified by the fuzzy system, notification for the presence of congestion is sent to the child nodes and congestion is mitigated using the rate adaptation method.

4.2 System Architecture

System architecture consists of three different models, viz. congestion detection module, congestion notification module and congestion mitigation module. System architecture for the proposed work is as shown in Fig. 3.

4.2.1 Congestion Detection Module

Incoming and outgoing ratio of packets, average queue size, number of competitors nodes waiting to send the data packets and the average delay of packets are some of the indicators that can used as metrics by fuzzy logic system to estimate the congestion. Numbers of contending nodes are the neighboring nodes having packets in their buffer and waiting to send them into the MAC layer region instead on transmission path. The count of contender nodes can be calculated with the help of RTS/CTS packets, which are originated by neighboring nodes. If the number of contenders is high, probability of packet collision is also high. Hence, the number of contenders can play a vital role in congestion indicator. The hop count value is inserted into the header of the packet and initialized with the value zero when generated by a source

Fig. 3 System architecture

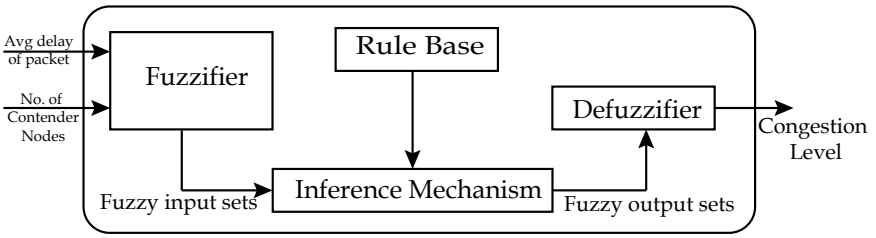

Fig. 4 Congestion Detection Module

node. At each hop, as soon as a packet arrives at a node, it increases the current hop count value by one. This indicates how many hops a packet has traveled to reach a node from the source node. The total delay faced by a packet is also inserted in the header part of packet. Just before transmitting a packet, a sensor node calculates the time duration between the time a packet is received by the node and the time a packet is about to be forwarded by a node. The average delay is computed by dividing the total delay by hop count current value. Average delay is divided into four intervals, viz. d_1, d_2 and d_3 where $d_1 < d_2 < d_3$. The weight of the average delay of packets (Wd) is computed as follows:

$$P(a) = \begin{cases} 0 & \text{if average delay} \otimes d_1 \\ 1 & \text{if } \mathrm{d}_1 < \text{average delay} \otimes d_2 \\ 2 & \text{if } \mathrm{d}_2 < \text{average delay} \otimes d_3 \\ 3 & \text{if } \mathrm{d}_3 < \text{average delay} \end{cases} \tag{2}$$

Fuzzy logic system uses average delay and the number of contender nodes as metrics and hence, fuzzy set has two fuzzy variables as shown in Fig. 4.

$$F = (C, D) \tag{3}$$

where C denotes the number of competitor nodes and D represents the average delay of packet.

Fuzzy Logic System embeds average delay and number of contender nodes into a single value for estimating the congestion level. The membership function for the inputs is denoted using three linguistic variables *Low*(l), *Medium*(m) and *High*(h). Output membership function is having four linguistic variables *Zero*(Ze), *Lower*(Lo), *Medium*(Md) and *High*(Hg). The resources available in sensor networks are not abundant and hence triangular shape membership.

Function is used considering it as an easier one for computation. Membership function for the fuzzy variables $_{\mathrm{C}}$ and $_{\mathrm{D}}$ is as shown in Fig. 5.

Fuzzification and defuzzification steps use the membership functions and there are two membership function set, each has a separate function for l, m and h variables. The three different fuzzy classes for fuzzifier are l, m and h for each fuzzy variable:

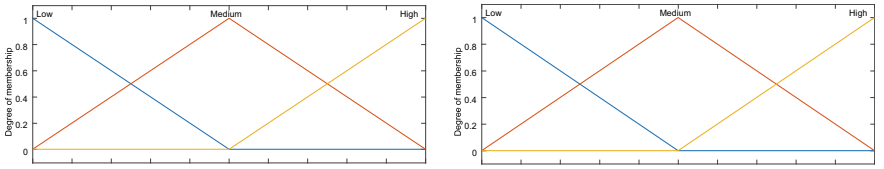

Fig. 5 Membership function for fuzzy variables (a) *C* and (b) D **a** number of competitor nodes **b** average delay of packets

$$F : (\alpha, \beta) \approx \left(\alpha^f, \beta^f\right) \tag{4}$$

$$X^f = \left[\mu_X^l, \mu_X^m, \mu_X^h\right] \tag{5}$$

where X is the representation for the variable α and β membership function is used to calculate the fuzzy values. In the second step inference, combining the fuzzy rules which are taken from the fuzzy rule base is used for generating the output variable. Fuzzy rules are made up of simple *if*−*then* condition with a conclusion. Having two fuzzy variables with three different fuzzy classes for each variable, rule base has ${}_3{}^2 = 9$ rules. The outcome of each rule is computed using rule evaluation method (REM). The weights of the fuzzy classes for α and β are assigned as $l = 1$, $m = 2$ and $h = 3$. The output of a fuzzy rule ${}_{\theta r}$ is calculated by adding the weight of $f\alpha^r$ and $f\beta^r$. Rule base of the proposed fuzzy inference system is shown in Table 1, where ${}_\theta$ corresponds to the output calculated using REM.

Product inference rule is used in the proposed FIS as it allows mathematical simplification in the defuzzification. Therefore,

$$\mu_r = \mu_\alpha^{f_\alpha^r}(\alpha) \times \mu_\beta^{f_\beta^r}(\beta) \times \mu_c^r(\theta_r) \tag{6}$$

Table 1 Fuzzy rules

α	β	θ
l	l	2
l	m	3
l	h	4
m	l	3
m	m	4
m	h	5
h	l	4
h	m	5
h	h	6

where $f\alpha^r$ and ${}_{f\beta}{}^r$ are fuzzy classes l, m or h Defuzzification is the final step and is a process of converting fuzzy output obtained from FIS to a crisp value. The output of the defuzzifier can be calculated as follows:

$$\omega = \frac{\sum_{n=0}^{9} \theta_r \mu_r}{\sum_{n=0}^{9} \mu_r} \tag{7}$$

where ${}_{\theta r}$ is the output of the rule and μr is the output of the product inference system. The output of the FLS, w becomes a crisp value.

4.2.2 Congestion Notification Module

Upon detecting the congestion in the network, intermediate nodes are sent a signal regarding the congestion using Implicit Congestion Notification (ICN) method. It piggybacks the congestion message to intermediate nodes using header part of data packet and thus an extra control message is avoided.

4.2.3 Congestion Mitigation Module

Our proposed model classifies w into three different classes like *No Congestion* (*NC*), *Medium Congestion* (*MC*) and *High Congestion* (*HC*). At *NC* level, congestion mitigation module does not take any action as sensor nodes are able to handle the traffic load. If the congestion level is at (MC) or (HC), congestion mitigation is activated using rate adaptation method. Rate adaptation presented using a generic function is given as follows:

$$r = \begin{cases} r_1 \text{ if CL = NC} \\ r_2 \text{ if CL = MC} \\ r_3 \text{ if CL = HC} \end{cases} \tag{8}$$

CL indicates the congestion level and r is the rate of data packet of the application. The data rates defined by the application are as follows: r_1 r_2 and r_3. Transmission rates of data packets are adjusted by the sensor nodes based on the r value in the congestion mitigation module. Algorithm for mitigating congestion is presented in Algorithm 1.

5 Experimental Results and Discussions

In this work, for simulating the results of the proposed work, Matlab is used. The proposed work is compared with PCCP and PHTCCP protocols. *Matlab* is used to

Algorithm 1: Congestion Mitigation Algorithm

```
Input:Congestion Level (CL)
Output:Drop Packet/ Retain Packet
while true do
    if CL == NC then
        En queue the packet
    end
    else if CL == MC then
        En queue the packet
        Activate rate adaptation method
    end
    else
        De queue the packet
        Activate rate adaptation method
    end
end
```

implement fuzzy systems and simulation. To find the packet loss rate, the following equation is used:

$$\text{Loss Rate} = \text{Packet loss/Time} \tag{9}$$

Figure 6 shows the packet loss ratio. Packet loss ratio is the count of packets lost per unit time normalized between [0.0 and 1.0]. During the early stages of simulation,

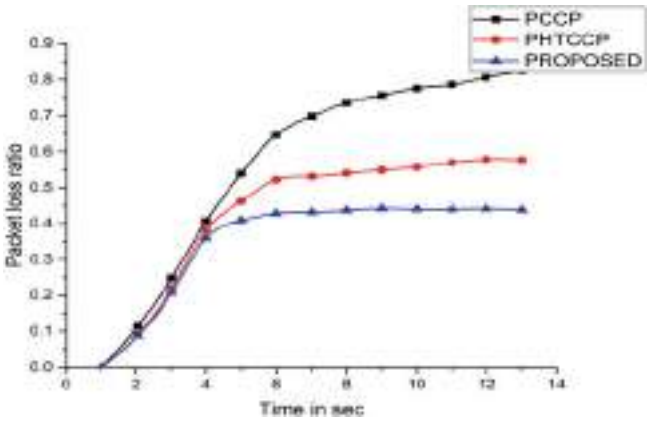

Fig. 6 Packet loss ratio

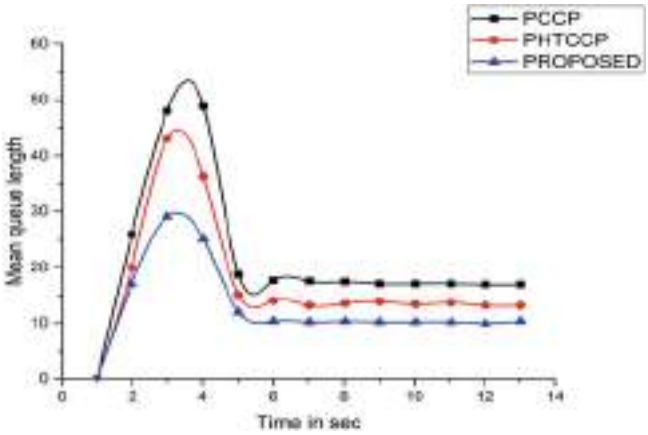

Fig. 7 Average queue length

congestion is not observed, and rate adjustment also does not get initiated, and hence, high packet loss rate is observed. In the next stages, as the rate is adjusted, decreased packet loss can be seen. End-to-End delay is defined as the sum of delays at a source node and delay on a path. The total number of packets stored in a queue is termed as length of the queue. Length of the queue increases during the inter-arrival time of the packet is higher than the servicing time spent for a packet. Shorter queue length is the result of the better congestion control algorithm. If congestion control algorithm fails, it leads to an increase in queue length at intermediate nodes in the network. Fuzzy rate adjustment unit allocates the forwarding rate for each sensor node such that the rate of output will always be equal to or higher than the input rate. Figure 7 depicts the average length of the queue of a node positioned near the sink node. The proposed protocol has resulted in shorter queue length than PCCP and PHTCCP approaches. The Proposed approach well suits for the applications which are not delay tolerant. Packet loss probability tells about the frequency of packet drops by a node in the network. In case of packet drop, source node has to retransmit the dropped packet. Figure 8 shows the increase in packet loss probability at initial stage and after some time, the same is controlled by the proposed methodology.

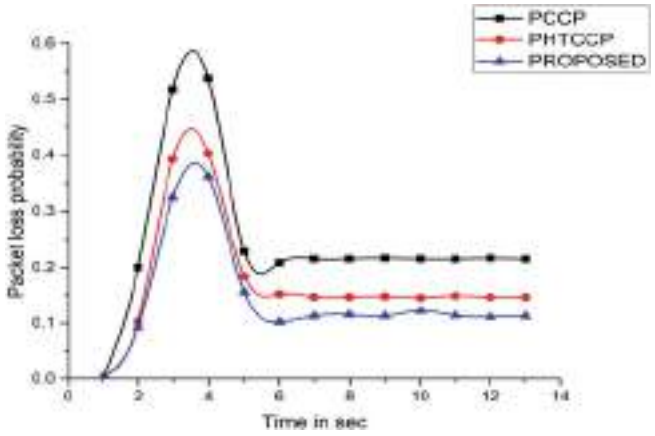

Fig. 8 Packet loss probability

6 Conclusion

A congestion control mechanism based on FLS is proposed in this paper. The number of contender nodes waiting to send packets to their parent nodes and average delay of packets are the two variables considered as input to the FLS. The output of the FLS determines the level of congestion at a node. The rate adjustment scheme is applied to mitigate congestion and avoid packet drops. Results obtained through simulation depict that the parameters like packet loss ratio, End-to-End delay and average queue length perform better than PCCP and PHTCCP schemes.

References

1. H.Y. Mohammad, A. Donald, A new priority-based congestion control protocol for wireless multimedia sensor networks. in *International Symposium on a World of Wireless, Mobile and Multimedia Networks* (2008), pp. 1–8
2. M. Vasilis, G. Lin, P. Iain, A new congestion control mechanism for WSNs. in *10th IEEE International Conference on Computer and Information Technology* (2010), pp. 709–714
3. Md. Samiullah, S.M. Abdullah, A.F.M.H.B Imamul, A. Shahed, Queue management based congestion control in wireless body sensor network. in *International Conference on Informatics, Electronics and Vision (ICIEV)* (2012), pp. 493–496
4. C. Wang, B. Li, K. Sohraby, M. Daneshmand, Upstream congestion control in wireless sensor networks through cross-layer optimization. IEEE J. Sel. Areas Commun. **25**(4), 786–795 (2007)
5. M. Muhammad, R. Obaidur, K.P. Al-Sakib, S.H. Choong, Prioritized heterogeneous traffic-oriented congestion control protocol for WSNs. Int. Arab J. Inf. Technol. **9**(1), (2012)
6. S. H. Rasouli, A. Ghaffari, M.A. Hadian, H. Rasouli, DPCC: Dynamic predictive congestion control in wireless sensor networks. IJCSI Int. J. Comput. Sci. Iss. **8**(1), 472–477 (2011)
7. G. Sapna, T. Vrisha, M. Madhumita, Priority based congestion control in WBAN. in *Eighth International Conference on Contemporary Computing (IC3)* (2015), pp. 428–433

8. J. Saurabh, Y. Anamika, Fuzzy based adaptive congestion control in wireless sensor networks. in *6th International Conference on Contemporary Computing (IC3)* (2013), pp. 433–438
9. G.P. Sunitha, S.M.K. Dilip, B.P.K. Vijaya, Energy balanced zone based routing protocol to mitigate congestion in wireless sensor networks. Wirel. Pers. Commun. (**97**)2, 90–107 (2017)
10. G.P. Sunitha, S.M.K. Dilip, B.P.K. Vijaya, Energy efficient hierarchical multi-path routing protocol to alleviate congestion in WSN. Int. J. Ad Hoc Ubiquitious Comut. **32**(1), 59–73 (2019)

Refractive Index-based Ethanol Sensor using Hollow Core Photonic Crystal Fiber in THz region

Kajal Choudhary, Pankaj Verma, and Amit Kumar

Abstract In this paper, a refractive index-based ethanol sensor is proposed. The hollow core Photonic Crystal Fiber (PCF) with hybrid cladding structure is used. Ethanol is taken as the chemical analytes for sensing at terahertz frequency. TOPAS is used as a fiber material in photonic crystal fiber with asymmetrical rectangular hollow core. The outer layer of the PCF is considered as Perfectly Matched Layer (PML) for boundary conditions. Finite Element Analysis (FEA) is used for mathematical analysis with COMSOL Multiphysics software. As results, the investigated parameters are sensitivity, confinement loss and effective area. The proposed PCF-based refractive index sensor shows the high relative sensitivity of 97.28%, low confinement loss (CL) of 6.27×10^{-13}(dB/m) and high effective area of $14.4 \mu m^2$ at terahertz frequency (0.8–1.6 THz). So, the proposed refractive index-based sensor can be used for various applications like marine industries, healthcare and food industry.

Keywords Hollow core PCF · Effective mode index · Effective area · Confinement loss · Terahertz wave · Relative sensitivity

1 Introduction

In recent years, the right amount of detection of ethanol is very necessary for different areas like industrial applications, medical applications, food preservatives etc. Ethanol is depicted as grain alcohol, spirits or drinking alcohol. Ethanol is utilized in bactericidal hand sanitizer gels, beverages, fuels and industrial applications. There is a need to assure the quantity of ethanol should be in a defined ratio. The meticulous amount of ethanol detection is very crucial to reduce the harmful effect. PCF

K. Choudhary (✉) · P. Verma · A. Kumar
National Institute of Technology, Kurukshetra, Haryana, India
e-mail: kajal_31909114@nitkkr.ac.in

P. Verma
e-mail: pankaj@nitkkr.ac.in

S. Rawat et al. (eds.), *Proceedings of First International Conference on Computational Electronics for Wireless Communications*, Lecture Notes in Networks and Systems 329,
https://doi.org/10.1007/978-981-16-6246-1_57

is named as a microstructured optical fiber with periodically arranged air holes in cladding. PCF-based sensor has shown potential in the sensing field due to its novel guiding properties. In the last decade, PCF-based sensors are used in healthcare [1–3], marine, chemical industry [4, 5] and monitoring of various industrial products [6, 7]. The various types of core structures like hollow core [8], porous core [9] and solid core [10] have been developed and shown light controlling capabilities.

In this manuscript, a Hollow Core (HC) PCF is used for sensing the Refractive Index (RI) of the ethanol at Terahertz (THz) frequency range. The THz (0.1–10 THz) frequency used in electromagnetic radiation has far less energy than electromagnetic radiation at higher frequencies. Due to this, they do not have the potential to ionize the material and it would not damage the living tissue or the properties of the analytes. These properties of THz ray make them very special for chemical, biochemical use as well as security applications.

There are different fiber materials such as TOPAS, ZEONEX, undoped silica and TEFLON that have been used in PCF-based sensor to attain high sensitivity and optical sensing parameters. In the proposed HC-PCF sensor, TOPAS is selected as the fiber material because of its novel optical properties like high heat resistance, negligible material dispersion, excellent transparency and constant RI (1.53) for THz frequency range.

Based on novel guidance properties of the PCF, several PCF-based sensors have been reported like temperature sensor [11], pressure sensor [12], chemical sensors [13]. In latest years, the liquid or gas infiltration within the core and cladding of the PCF is enhanced its sensing application. The PCF-based sensors are used to detect the toxic and flammable gases for the avoidance of various environmental pollution, explosion and fire. Md. S. Hossain et al. [14] have presented a heptagonal PCF with rotated hexacore for chemical sensing application. Authors have investigated the different sensing parameters and attained the highest sensitivity of 69% in THz band. In 2020, a novel liquid-filled PCF-based biosensor has been proposed [15]. The author introduced an elliptical shaped hollow core and filled with the sensing analytes in THz region. Authors obtained the maximum 87% sensitivity with low CL of 10^{-4} dB/cm. E. Podder et al. [16] have reported a sensor with hexagonal structure of the PCF and it is designed to get high performance for ethanol sensing. The purposed study has been shown the improvement in performance like high sensitivity and low confinement loss.

In 2016, a hybrid core PCF-based RI sensor for chemical sensing has been reported for sensing applications in industrial field [17]. The authors used micro elliptical shaped air holes, the birefringence values are 0.001513 for ethanol, 0.001514 for benzene and 0.001474 for water with maximum sensitivity of 49.17%. In 2018, a Terahertz-based sensor with hollow core PCF was introduced. Zeonex is used as a fiber base material [18]. The rectangular shaped air holes are filled with the analytes and obtained very high sensitivity of 96% and very low CL of 6.95×10^{-14} dB/cm at THz frequency, the total diameter of this structure is very large, and it fails to maintain the microstructure size. Another THz sensor was proposed using kagome-structured cladding and rectangular shaped air holes in the core [19]. In 2021, a ring-based solid core PCF was introduced with both cladding, and core region holes were arranged

in ring pattern. Cladding air holes were arranged in a four-layer pattern for detection of blood component with sensitivity of more than 84% and low confinement loss in terahertz range [20]. This research gained the sensitivity of 85.7% for chemical identification using PCF at 1.6 THz but the fabrication feasibility of the kagome structure in PCF is very poor with the currently available fabrication techniques. As going through the literature, it is cleared that the rectangular hollow core structure of the PCF has gained the maximum sensitivity of 96% to the best of our knowledge.

In this paper, a RI-based chemical sensor is represented. The structure of the PCF consists of a rectangular hollow core with hybrid cladding. This form of fabrication friendly PCF building is proposed for the first time for ethanol detection. The detection of ethanol is numerically analyzed by FEA with COMSOL Multiphysics software. The proposed sensor shows the high sensitivity, low CL and high effective area at THz frequency.

2 Design and modeling

The proposed structure of HC-PCF-based RI sensor is shown in Fig. 1. The structure having a hollow rectangular core with width ($w = 390\mu m$) and length ($l = 500\mu m$), it is filled with ethanol (RI = 1.36) [21]. Three rectangular air holes ($l_1 = 1100\mu m$, $l_2 = 2740\mu m$ and $w_1 = w_2 = 390\mu m$) are used in cladding for maintaining the confinement within the core, also the circular air holes with diameter $d = 180\mu m$ provide the polarization to the guided optical wave. A PML is used in the outer part of the structure for absorbing the electromagnetic radiation. The single fiber material of the PCF is TOPAS (RI = 1.53) [22]. The accuracy of liquid sensing depends on the RI difference of the liquid in core hole and fiber background material. Cladding rings of different shapes like rectangular and circular are used in the proposed PCF sensor to create the large difference in RI of the core and cladding, it ensures that the light will be highly restricted into the core region where the liquid analyte is placed.

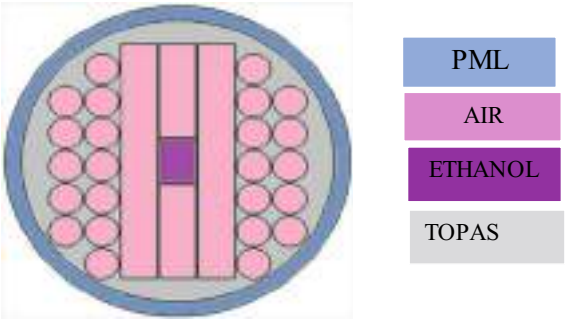

Fig. 1 Internal geometry of proposed HC-PCF

3 Results and Analyses

The numerical analysis has been carried out by the FEA; it is a method for solving Maxwell's equation. In this method, the object is broken into the finite element known as meshing and solves the effects of each element. The COMSOL Multiphysics software is used to simulate the proposed model. The triangular mesh is considered for entire geometry of the model and obtains the sensing parameters like sensitivity, confinement loss and effective area. The field distribution into the core is shown in Fig. 2 (a) x-polarization (b) y-polarization for ethanol.

Relative sensitivity is an important constraint to investigate the sensing performance of the PCF-based sensor in THz band. Sensitivity (r) of the sensor defines the accuracy of sensing. It is directly proportional to the core power fraction (f) and defined by the given equation as [23],

$$r = \frac{n_r}{n_{eff}} \times f \tag{1}$$

In this equation, η_{eff} is the real effective mode index of the PCF and η_r represents the RI of the target liquid. Here, f denotes the fractional core power to the total optical power distributed into the PCF. The fractional power is obtained by the given formula,

$$f = \frac{\sum\left(E_x H_y - E_y H_x\right)\partial x \partial y(sample)}{\sum\left(E_x H_y - E_y H_x\right)\partial x \partial y(total)} \tag{2}$$

where H_x and H_y represent the magnetic domain field in x and y directions and E_x and E_y denote the electric field elements in x and y directions. The sensitivity curve with frequency variation is shown in Fig. 3. The proposed PCF-based RI sensor has been numerically analyzed in THz regime (0.8–1.6 THz). For x-polarization and y-polarization, the sensor attained 97.27% and 97.09% sensitivity, respectively. The plot depicts that confinement of the light or the interaction of optical power with analyte is increased as frequency increases, and it is maximum at 1.5 THz frequency.

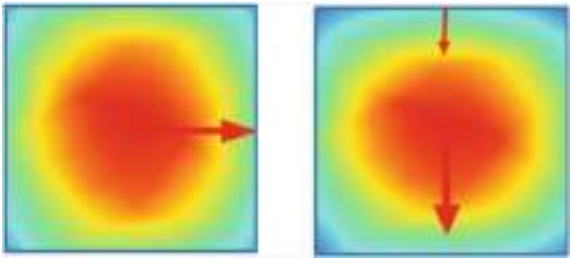

Fig. 2 Field distribution for ethanol for **a** x-polarization mode **b** y-polarization mode

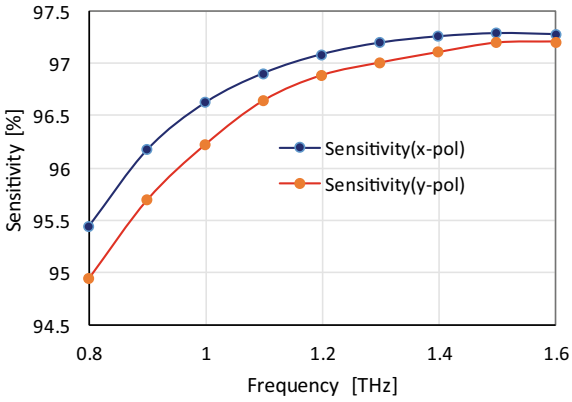

Fig. 3 Sensitivity vs. frequency plot

Confinement loss (CL) is another important parameter to evaluate the sensor's accuracy. It is the loss that occurs because of leakage occurring in the mode and due to positioning or ordering of air holes in an irregular shape. The role of the dielectric medium is played by the air holes. It is proportional to the transmitted frequency and imaginary part of the Effective Mode Index (EMI). Leakage loss or CL (L_c) can be precise by altering the structural parameters. By using the below equation, CL is given as [24],

$$L_c = \frac{\sum 4\pi f}{c}\left(Im\left(n_{eff}\right), m^{-1}\right. \tag{3}$$

Here, f denotes the operating frequency, c is the velocity of light and $Im\left(n_{eff}\right)$ is the imaginary part of EMI. The plot between CL with THz frequency is shown in Fig. 4. It shows that CL's value is decreasing rapidly as frequency in THz increases. The almost constant CL is obtained from 1.2–1.6 THz frequency. The minimum value of the CL is obtained as 6.27×10^{-13} dB/m at 1.5 THz for x-polarization and 2.21×10^{-13}

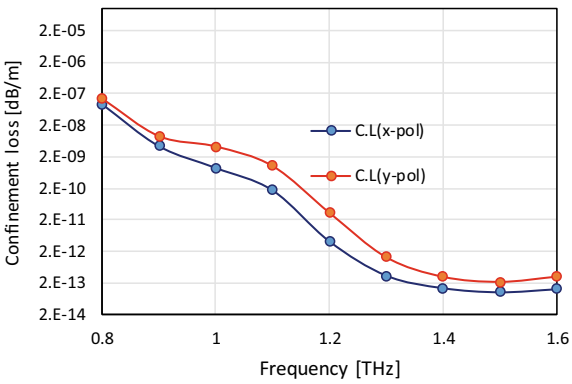

Fig. 4 CL vs. frequency plot

dB/m. Hence, it is cleared that the sensitivity is high when CL is minimum at 1.5 THz.

Effective Mode Area (EMA) is the fiber area that covers transverse dimensions of the fiber. It is represented by where E is represented by guided-mode transverse electric field [25].

$$A_{eff} = \frac{(\iint |E(x, y)|^2 dxdy)^2}{\iint (|E(x, y)|^4 dxdy} \tag{4}$$

The EMA variation with THz frequency is shown in Fig. 5. The area of the effective modes is increasing with the frequency means the confinement of light into the core gets narrower at high frequency, thus, produces a small effective mode area. The maximum value of the EMA is obtained as 1.95×10^{-7} m^2 or 1.95×10^5 μm^2, which is almost equal to the core area. At 1.5 THz frequency, the EMA is approximately 75% of the core area, and it confirms that the proposed sensor has high sensing accuracy. Figure 6 shows for x-polarization and y-polarization, effective mode index n_{eff} is increasing as frequency increases. The n_{eff} begins from 1.2904 for x-pol at

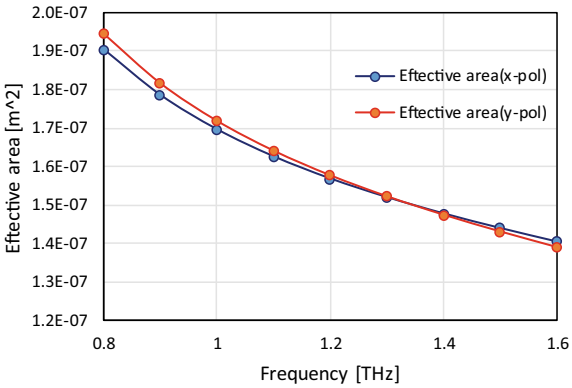

Fig. 5 EMA vs. frequency plot

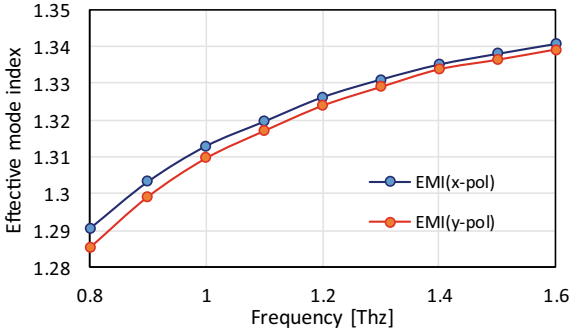

Fig. 6 EMI vs. frequency plot

0.8 THz and reaches up to 1.3407 whereas for y-pol effective mode index begins from 1.2852 and extent up to the 1.3392. The linear variation of n_{eff} and the maximum value of the n_{eff} are close to the RI of sensing analyte.

The optimization of the core width can be achieved by varying the core width and observing the sensing parameters. The variation of sensitivity of the proposed PCF-based sensor with width w = 389 μm, 390 μm, and 391 μm as frequency varied from 0.8–1.6 THz is shown in Fig. 7. Hence, the optimum width is selected as 390 μm. The core width variation and selection of the optimum width is also tabulated in Table 1.

The performance comparison of the proposed PCF-based sensor and previously reported PCF-based sensor is summarized in Table 2. The proposed PCF-based sensor reported the highest sensitivity at THz frequency comparatively with simple and fabrication friendly structure.

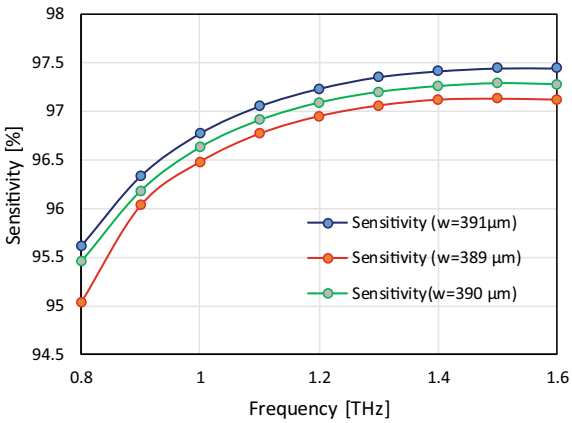

Fig. 7 Sensitivity vs. frequency plot as the width of the core is varied

Table 1 Optimization of the core width by changing the width of the core

Width (W)	Parameters (%)	Relative Sensitivity (%)
391 μm	+2%	97.44
390 μm	Optimum	97.29
389 μm	−2%	97.13

Table 2 Performance comparison between proposed and previous research

References	Frequency (THz)	Sensitivity (%)	CL (dB/m)
PCF [26]	f = 1 THz	77.14	2.26×10^{-03}
PCF [27]	f = 1 THz	68.87	1.89×10^{-09}
PCF [18]	f = 1.4 THz	96	6.95×10^{-12}
PCF [19]	f = 1.6 THz	85.7	1.7×10^{-09}
Proposed PCF	f = 1.5 THz	97.28	6.27×10^{-13}

4 Conclusion

In this paper, a HC-PCF-based RI sensor for ethanol detection is designed and simulated on COMSOL Multiphysics software. The numerical analysis has been obtained by FEA with TOPAS as fiber material. A PML has been employed for absorbing the radiation out of the PCF. The structural parameters are optimized by varying the width of the core. The results show the highest sensitivity of 97.28% at 1.5 THz frequency with minimum confinement loss of 6.27×10^{-13} dB/m. Hence, the proposed sensor will be very useful to detect the ethanol level. This type of PCF-based RI sensor can be used for several industrial applications like in food industry, pharmaceutical industry, chemical industry and security applications.

References

1. Md. Mr. Rahman, F.A. Mou, Md. I.H. Bhuiyan, Md. R. Islam, Photonic crystal fiber based terahertz sensor for cholesterol detection in human blood and liquid foodstuffs. Sens. Bio-Sens. Res. **29**, 1–6 (2000)
2. P. Sharma, P. Sharan, Design of photonic crystal based biosensor for detection of Glucose concentration in urine. IEEE Sens. J. **15**(2), 1035–1042 (2015)
3. V. Kaur, S. Singh, Design approach of solid core photonic crystal fiber sensor with sensing ring for blood detection. J. Nanophoton **13**(2), 1–11 (2019)
4. Md. Mr. Rahman, F.A. Mou, Md. I.H. Bhuiyan, Md. R. Islam, Development of photonic crystal fiber for THz wave guidance environmental pollutants detection. Sens. Bio-Sens. Res. **29**, 1–6
5. J. Qin, B. Zhu, Y. Du, Z. Han, Terahertz detection of toxic gas using a photonic crystal fiber. Opt. Fiber Technol. **52**, 1–4 (2019)
6. S.M. Atiqullah, A. Palit, Md.I. Reja, J. Akhtar, S. Fatema, R. Absar, Detection of harmful food additives using highly sensitive photonic crystal fiber. Sens. Bio-Sens. Res. **23**(100275), 2019 (2019)
7. S.S. Kumar, S. Revathi, Photonic crystal fiber for sensing food additives. Int. J. Innov. Expl. Eng. **9**(8), 545–551 (2021)
8. B. Wan, L. Zhu, X. Ma, T. Li, J. Zhang, Characterstics analysis and structural design of hollow core photonic crystal fibers with band gap cladding structures. Sensors **21**(8), 545–551 (2020)
9. Md.R. Sardar, Md. Faisal, K. Ahmed, Design and characterization of rectangular slotted porous core photonic crystal fiber for sensing CO2 gas. Sens. Bio-Sens. Res. **30**, 1–9 (2020)
10. B.K. Paul, S. Islam, K. Ahmed, S. Asaduzzaman, Alcohol sensing over O+E+S+C+L+U transmission band based on porous cored octagonal photonic crystal fiber. Photon. Sens. **7**(2), 123–130 (2017)
11. N. Ayyanar, R.V. Raja, D. Vigneswaran, B. Lakshmi, M. Sumathi, K. Porsezian, Highly efficient compact temperature sensor using liquid infiltrate asymmetric dual elliptical core photonic crystal fiber. Opt. Mater. **64**, 574–582 (2017)
12. N. Ayyanar, D. Vigneswaran, M. Sharma, M. Sumathi, M. Rajan, S. Konar, Hydrostatic pressure sensor using high birefringence photonic crystal fibers. IEEE Sens. J. **17**(3), 650–656 (2017)
13. M.F.H. Arif, J.H. Biddut, Enhancement of relative sensitivity of photonics crystal fiber with higher birefringence and low confinement loss . Optik-Int. J. Light Electron Opt. **131**, 697–704 (2017)
14. M.S. Hossain, S. Sen, Design and performance improvement of optical chemical sensor based photonic crystal fiber (pcf) in the terahertz (THz) wave propogation. Silicon (2020)

15. N.A.N.B. Suhaimi, I.K. Yakasai, E. Abas, S. Kaijage, F. Begum, Modelling and simulation of novel liquid—infiltrated PCF biosensor in Terahertz frequencies. IET Optoelectronics **14**(6), 411–416 (2020)
16. E. Podder et al., in *Ethanol Detection through Photonic Crystal Fiber* (Springer, 2020), pp.175–181
17. S. Asaduzzaman, K. Ahmed, T. Bhuiyan, T. Farah, Hybrid photonic crystal fiber in chemical sensing. Springer plus **15**(1), 1–11 (2016)
18. Md.S. Islam et al., Terahertz sensing in a hollow core photonic crystal fiber. IEEE Sensor **18**(10), 4073–4079 (2018)
19. Md. S. Islam et al., A novel approach for spectroscopic chemical identification using photonic crystal fiber in the terahertz regime. IEEE Sens. J. **18**(2), 575–582
20. Amit Kumar, Pankaj Verma, Poonam Jindal, Decagonal solid core PCF based refractive index sensor for blood component detection in terahertz regime. Opt. Quant. Electron. **53**(165), 1–13 (2021)
21. H. Ademgil, S. Haxha, PCF based sensor with high relative sensitivity, high birefringence and low confinement losses for liquid analyte sensing applications. Sensors **15**(12), 31833–31842 (2015)
22. Topas Advanced Polymer: https://topas.com/markets/optical/displays
23. H. Ademgil, Highly sensitive octagonal photonic crystal fiber based sensor. Optik-Int. J. Light Electron Opt. **122**(39), 9534–9537 (2000)
24. C.M.B. Cordeiro et al., Microstructured—Core optical fibre for evanescent sensing applications. Opt. Exp. **24**, 6–11 (2016)
25. J. Sultana, S. Islam, J. Atai, M.R. Islam, D. Abbott, Near—Zero dispersion flattened, low-loss porous-core waveguide design for terahertz signal transmission. Opt. Eng. **56**(7), 076114 (2017)
26. Md. Abdullah-Al-Shafi, S. Sen, Design and analysis of a chemical sensing octagonal photonic crystal fiber (O-PCF) based optical sensor with high relative sensitivity for terahertz (THz) regime. Sens. Bio-Sens. Res. **29**, 1–6 (2020)
27. J. Sultana, S. Islam, K. Ahmed, A. Dinovitser, B.W.-H. Ng, D. Abbott, Terahertz detection of alcohol using a photonic crystal fiber sensor. Appl. opt. **57**(10), 2426–2433 (2018)

Improving the Lifetime of Wireless Rechargeable Sensors Using Mobile Charger in On-Demand Charging Environment Based on Energy Consumption Rate Prediction

Anil Kumar Dudyala and Lalan Kumar Ram

Abstract Wireless rechargeable sensor network (WRSN) is gaining a significant place in the current research field due to its wide range of applications including in the field of Internet of Things (IoT). The sensors in WRSN will soon deplete their energy due to their limited battery capacity. The wireless charging (WC) is one of the prominent methods for enhancing the sensors lifetime in wireless rechargeable sensor networks. In WC, with the help of mobile charger (MC), we can steadily provide energy to sensors using electromagnetic signals. However, the promising issue in this area is scheduling MC efficiently for charging the sensors so that the network is up to its maximum time. This article contributes to addressing the above-mentioned problem, by proposing an efficient way of scheduling the MC with the help of sensor's Energy Consumption Rate Prediction. From our experimental results, it can be observed that the proposed method has a given good survival rate of sensors compared with the existing methods like FCFS and NJN without preemption.

Keywords Wireless charging · Wireless rechargeable sensors networks · Mobile charger · Energy consumption rate

1 Introduction

1.1 Background

Wireless sensor network (WSN) is a network that is built up using a collection of sensors, which are deployed in a certain region. These sensors are capable of sensing some information from the environment where they have been deployed. Along with this, the sensors would be communicating with other sensors and base station in wireless mode. The sensors would be having a limited capacity of the batteries as well as limited storage capability. Hence, when the sensors are busy with sensing data, they may soon run out of their energy and may full up their data storage buffer.

A. K. Dudyala (✉) · L. K. Ram
National Institute of Technology Patna, Patna Bihar -800005, India

S. Rawat et al. (eds.), *Proceedings of First International Conference on Computational Electronics for Wireless Communications*, Lecture Notes in Networks and Systems 329,
https://doi.org/10.1007/978-981-16-6246-1_58

So, to keep the sensors running continuously, the data has to be transferred to the base station and the sensors must be charged before they exhaust their capabilities. To address these issues of data gathering and charging, a lot of research has been carried out individually and collectively.

A wireless rechargeable sensor network (WRSN) is one of the variants of the WSN, where the sensors deployed are having the capabilities of energy harvesting, which can be done using different modes like solar energy or with the help of a mobile charger (MC), which moves to the requested sensors and provide charging. The mobile charger is a mobile device that is equipped with a charger and moves to requested sensors and provides the charging wirelessly. The mobile charger can be scheduled in two ways, one is periodic and the second is on-demand charging. In periodic charging, the MC moves toward sensors periodically at a certain interval of times and provides charging to all sensors irrespective of whether they are actually in need of it or not. Whereas in the on-demand charging, the MC goes to only those sensors that have requested for charging and serves them. Scheduling of MC in on-demand charging optimally so that it can serve all the requested sensors with high survival rate is a challenging problem in the current scenario. A lot of research has been done in this area, but using the prediction-based scheduling of the MC has not been explored to its full extent. As the prediction-based scheduling works in line with real-time energy consumption, it gives ample scope for getting the optimal results. Here, in this paper, we tried to explore this gap and have come up with promising results compared with existing methods like FCFS and Nearest Job Next without preemption.

The remaining sections of the paper are organized as follows, Sect. 2 discusses about the related works in the field of on-demand charging in wireless rechargeable sensor networks and WSNs. The system description and problem statement are briefed in Sect. 3. In Sect. 4, the proposed algorithm and its working methodology are discussed followed by results and discussion including the experimental setup in Sect. 5. Conclusion of the proposed work is given in Sect. 6.

2 Related Works

Energy charging is one of the crucial aspects of the sensors in a WRSN for keeping the network live for a maximum possible time, lot of research has been carried out to address this particular problem. The following are some of the related works done in this domain.

Constantinos et al. [1] worked on the energy management in wireless rechargeable sensor networks and proposed a protocol for mobile charging that uses the circular trajectory paths within each sub-region of the WRSN as per the energy dissipation rate in that region. They were successful in achieving high energy balancing compared with Greedy and LEACH protocol. In the quest to minimize the charging delay in WRSN, Lingkun et al. [2] proposed a linear programming-based optimal solution that

was able to achieve around 25% of higher energy efficiency compared with the set-cover-based design. The authors tried to find the optimal set of sojourn locations so that the cost of complete charging time is minimized. The maximization of charging throughput with the help of approximation algorithm and online heuristics is done by Ren et al. [3]. Xie et al. [4] tried to partition the network area into a hexagonal cellular structure and with the help of reformulation linearization technique, they tried to optimize charging time along with flow routing and travel path. Using multiple mobile chargers to optimize the energy usage, Zhang et al. [5] proposed collaborative mobile charging. He tried to prove theoretically the effectiveness of the proposed method by considering the 1-dimensional WSN to two-dimensional WSN. In an attempt to improvise over the existing methods, Fu et al. [6] used the RFID-based WRS nodes that can be charged using the mobile device whose route has been solved using linear programming and heuristic solution. Shu et al. [7] tried to address the problem of charging in WRSNs by optimizing the velocity of mobile charger with the help of a heuristic solution. With the objective of charging all the sensors fully and quickly, a concurrent charging scheduling problem has been proposed by Guo et al. [8] that uses two efficient greedy algorithms. Kaswan et al. [9] tried to formulate scheduling of MC using linear programming and proposed a gravitational search algorithm as solution. Unlike others, Ma et al. [10] had considered an actual charging model where sensors were taken as nonlinear super-position for charging by multiple MCs, and charging scheduling problem has been framed using weight-greedy algorithm. Leveraging the decision-making capabilities of the fuzzy logic, Tomar et al. [11] worked on on-demand charging and proposed an efficient MC scheduling scheme. They [13] also tried to explore the efficiency of the fuzzy logic in the context of multiple chargers. In the context of periodic charging, Huong et al. [15] proposed a Genetic Algorithm-based charging scheme for avoiding the sensors energy depletion. He et al. [12] proposed an FCFS-based scheduling algorithm for on-demand charging in WRSN. To beat the earlier proposed method, they [14] had come up with the NJNP algorithm, which was preemptive and had given good energy efficiency and survival rate. Most of the works tried to optimize the charging efficiency but prediction-based optimization has not been explored yet. So, to address this gap, we have come up with a prediction-based charging scheduling in the context of on-demand charging.

3 System Description

The wireless rechargeable sensor network (WRSN) consists of set or rechargeable sensors with limited battery capacity that has been randomly deployed in a given geographical area. The sensors have a rechargeable battery that can be recharged using different modes like solar charging or using a mobile charger. The disadvantage of solar charging is that it is non-reliable as it cannot provide charging continuously all the time. So, addressing the charging problem using the mobile charger is a viable solution that had gained a lot of prominence in the current research. Charging using mobile charger can be classified into two categories, periodic charging and

on-demand charging. In periodic charging, the mobile charger goes to all sensors at a certain interval of times for providing charging. In the case of on-demand charging, the sensors are provided charging by the MC, when they raise a request on reaching a certain set threshold.

In this scenario, scheduling the MC in such a way that the requested nodes do not die in the process of waiting for getting charged is one of the main challenging issues. So, in order to address the said issue, this paper proposes the following problem statement.

> **Problem Statement**: Given a subset of sensors $S_i \leq \{S\}$ that had raised a request for charging with the following input, $S_i = \{S_i(x,y), BC(S_i), TH(S_i)\}$ where $S_i(x,y)$ is the ith sensor's location, $BC(S_i)$ is battery capacity of ith sensor and $TH(S_i)$ is the threshold value of ith sensor, an optimized scheduling algorithm must be designed so that the survival rate of the requested sensors has to maximized.

$\{S\}$ is a collection of all sensors in the network.

The proposed solution for the given problem statement is described in the next section. Different notations used in this paper have been described in Table 1.

4 Proposed Solution

For the problem stated in the above section, the following solution based on the predicted energy consumption rate of sensors is proposed. The actual working of the proposed solution can be clearly understood with the help of block diagram shown in Fig. 1. All the sensors deployed in the wireless rechargeable sensor networks (WRSN) are initialized with their respective battery capacities ($BC(S_i)$) and threshold ($TH(S_i)$) for raising a request. The remaining energy (RE) of all sensors is first initialized with the full battery capacity of their respective sensors. All the sensors with different battery capacities (i.e., heterogeneous) are taken in this WRSN. The threshold of all the sensors is set to 30% of their battery capacity. The sensors sense the data from the environment where it has been deployed. In the due course, its energy consumption rate (ECR) is collected at an interval of every half an hour and it is reduced from the RE of the respective sensor. When any sensor's RE reaches the set threshold or less, it sends a charging request message to the Base Station (BS). The BS adds that sensor to the request queue (Q_{req}). Now, for all the sensors present in the $Q_{req,}$ we compute their predicted energy consumption rate (PECR) based on their past 8-h ECR using linear regression. Next, we compute the predicted remaining life time (PRLT) of each sensor with the help of PECR and the remaining life time (RLT) as given in the Eq. (1). Then the distance of each requested sensor from the MC is computed and is sorted in non-decreasing order. In order to give due weightage to both the DRN (distance between the sensor and the mobile charger) and PRLT, a weighted average is computed as given in Eq. (3). The results of the weighted average of all the requested sensors are sorted in ascending order. Thus obtained sensors are stored in the charging schedule (CS) queue and based on the storage

Table 1 Notations used

Notation	Description
S_i	Ith sensor node
MCX	Mobile charger X-coordinate
MCY	Mobile charger Y-coordinate
BS	Base station
ECR	Energy consumption Rate
RE	Remaining energy
$BC(S_i)$	Battery capacity of ith sensor node
PECR	Predictable energy consumption rate
RLT	Remaining life time
PRLT	Predictable remaining life time
$DRN(S_i)$	Distance of requested nodes from mobile charger
DF	Distance factor
$XC(S_i)$	X-Coordinate of ith sensor node
$YC(S_i)$	Y-Coordinate of ith sensor node
$C_{Schedule}$	Charging schedule
Q_{req}	Request queue
$TH(S_i)$	Threshold of ith sensor node
DBS_{max}	Maximum possible distance between base stations and mobile chargers
CR	Charging rate
CE	Charging efficiency
V_{mc}	Velocity of mobile chargers
BCMC	Battery capacity of mobile chargers

order of sensors the MC serves the requested sensors. This step of computing the PRLT, DRN and weighted average is repeated at every point when MC completes providing charging to a sensor which is at the beginning of the CS queue and the charging schedule(CS) queue is updated accordingly. The experimental results were compared with the FCFS algorithm proposed by He et al. [12] and non-preemptive version of NJNP proposed by He et al. [14].

The following equations are used for computation of optimal MC charging scheduling.

$$\mathrm{PRLT}(S_i) = (\mathrm{RLT}(S_i)/\mathrm{PECR}(S_i)) \tag{1}$$

$$\mathrm{DF} = \mathrm{DRN}(S_i)/\min(\mathrm{DRN}(S_i)) \tag{2}$$

$$\text{Weighted Average} = (\mathrm{PRLT}(S_i) - \mathrm{DRN}(S_i)/V_{mc}) * \mathrm{DF} \tag{3}$$

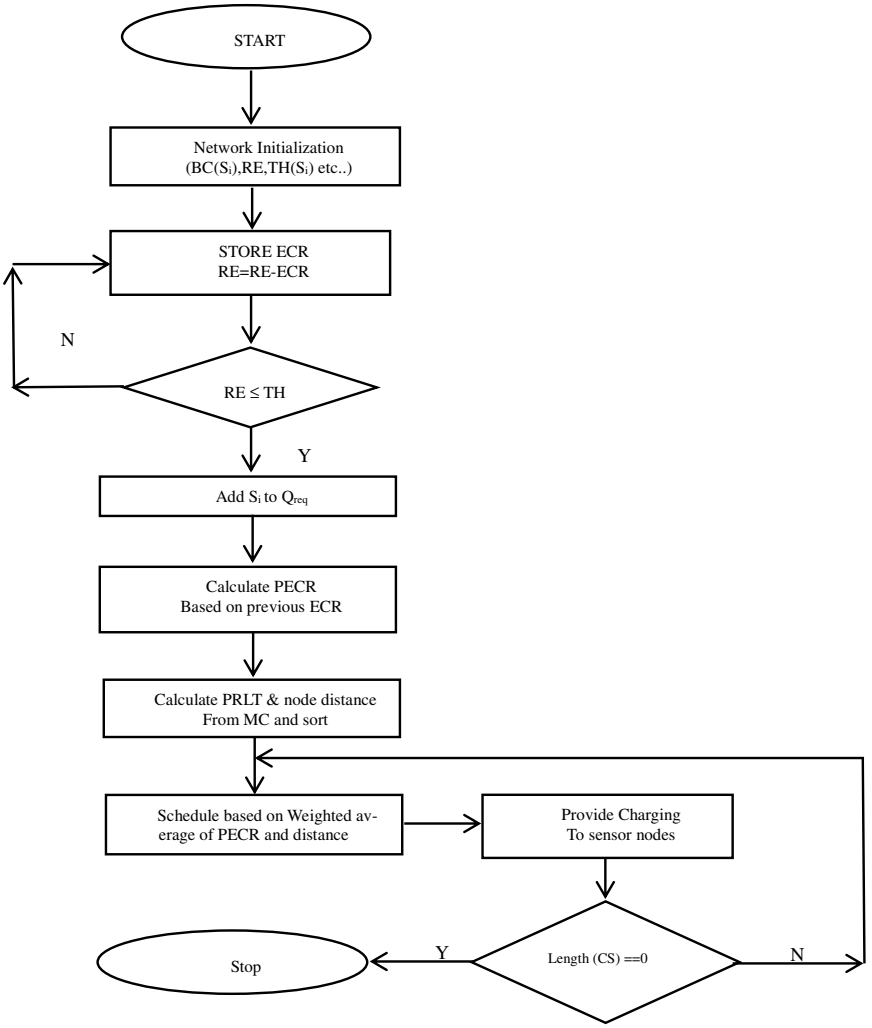

Fig. 1 Block diagram of the proposed model

$$\text{Survival rate} = (\text{number of successfully charged nodes by the MCs})/\text{total number of requesting nodes} \quad (4)$$

$$\text{Energy usage of effciency} = \text{Total energy gained by requesting sensor nodes/over energy consumption of the mobile charger} \quad (5)$$

Table 2 Charging Schedule Algorithm

Input : Q_{req} : queue containing ID of each requesting node; RE_{max}; D_{max}; $BC(S_i)_{max}$; ECR_{max}

Output : $C_{Schedule}$: Charging Scheduling

1. BS gets the request for charging from the sensors S_i, when their battery capacity reaches the set threshold $TH(S_i)$. The BS places these sensors in Q_{req} with the following parameters [RE_{max}; D_{max}; $BC(S_i)_{max}$; ECR_{max}] $\forall$ $S_i \in Q_{req}$
2. for i=1: | Q_{req} |
3. Calculate PECR $\forall$ $S_i \in Q_{req}$ */*Using Linear Regression on the basis of previous ECR*/*
4. end
5. for i=1: | Q_{req} |
   $PRLT(S_i)=RE(S_i)/PECR(S_i)$ $\forall$ $S_i \in Q_{req}$ */*Calculate remaining life time*/*
6. end
7. $CS1=Q_{req}$ /* Charging schedule queue */
8. for i=1: | Q_{req} |
9. for j=1: | CS1 |
   $DRN(S_i)$ = sqrt((MCX-$XC(S_j)$)^2+(MCY-$YC(S_j)$)^2) $\forall$ $S_j \in Q_{req}$ *from current location of MC /* Distance between MC and sensor */*
   end for // end of j loop
   DF=DRN/min(DRN)) / Distance factor */*
   for j=1: | CS1 |
   CS1(j) = (PRLT-$DRN(S_j)/V_{mc}$)*DF */*Temporary scheduling */*
   end for // end of j loop
   Sort(CS1) */* Sorting in ascending order */*
   $C_{Schedule} \leftarrow C_{Schedule} \cup$ CS1(1) */*sending to actual scheduling queue */*
   CS1(1)=empty
   Update the location of MC with selected node.
   end for // end of i loop
10. Schedule MC for Charging */* Scheduling MC to serve sensors in the order defined in $C_{Schedule}$ */*
11. Delete S_i from $C_{Schedule}$
12. If $C_{Schedule}$ == 0 then Stop : goto 10

Determination of charging schedule

The charging schedule of the proposed algorithm can be seen in Table 2. For all the sensors in the Q_{req}, we compute the RLT and PRLT. Next the distance between the mobile charger (MC) and all other sensors in the Q_{req} is computed and stored in DRN. Now, the distance factor (DF) is computed from DRN using Eq. (2). Finally, the weighted average is computed as shown in Eq. (3) with due weightage to both the PRLT and DRN, so that the sensor having lesser PRLT and closer to the MC can be served first. Thus, the sensors are stored in the actual scheduling queue in the increasing order of the weighted average and they are served by MC in the same order.

5 Results and Discussion

Experimental setup

The proposed algorithm and experimental setup were done using Matlab 2018 on an i7 system with 8 GB RAM. The simulation parameters taken for experimental purpose can be seen in Table 3. The network area of 100 by 100 square meters is considered for experiment purposes. All the experiments were conducted exhaustively with a variable number of sensors ranging from 50 to 200 sensors having

Table 3 Simulation parameters

Parameters	Values/Ranges taken
Sensors battery capacity	5–8 k Joules
ECR	0.5–3 J/min
Sensors	50–200
Runtime	10 rounds
Threshold	30% of battery capacity of sensors
Velocity of MC	6 m/sec
Charging rate	5 J/sec
Charging efficiency	68%
Area	100×100 m^2
Mobile charger battery capacity	4000 KJoules

different battery capacities varying in the range of 5–8 k Joules and variable ECR and the results shown are the average of 10 independent runs. The obtained results were compared with the FCFS and non-preemptive NJNP, which have been run using the same parameters.

The following assumptions were made. The mobile charger is assumed to have full charging and its charging time may be considered as negligible. The traveling time of the mobile is considered. The mobile charger's charging efficiency is considered as 68% as taken in [13].

The results of the proposed predicted energy consumption rate-based mobile charger scheduling algorithm can be seen in Figs. 2 and 3. Figure 2 shows the survival rate of sensors computed using the formula as shown in Eq. (4) using three different models. It could be observed from Fig. 2 that the survival rate of the sensors is 100% for all the models when tested using 50 sensors. It is evident that as the number of sensors increases, the survival rate decreases. In our case, the decreasing

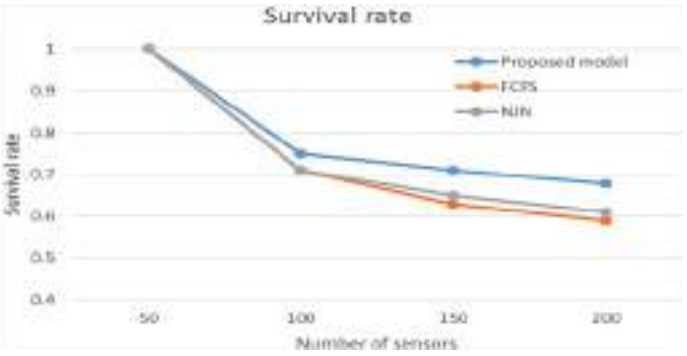

Fig. 2 Survival rate of sensors versus number of sensors

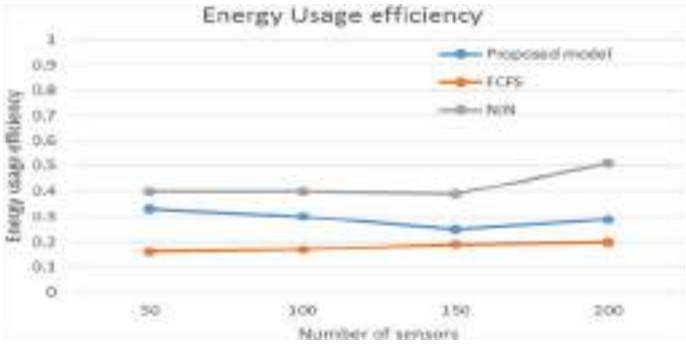

Fig. 3 Energy usage efficiency versus number of sensors

rate of survival rate is slow compared with other used models. We had achieved an average survival rate of 67.8% in the case of 200 sensors data, which is around 10% more compared with other methods used for the experiment purpose.

This was possible due to the optimal scheduling of MC considering the predicted energy consumption rate of requested sensors, which was closely related to real-time scenarios. The other models were considering only the remaining energy of the requested sensors, which was sent to the base station at the time of request.

Figure 3 shows the energy usage efficiency of all three models, which is computed using the formula shown in Eq. (5). It can be seen that our proposed model was able to perform better than the FCFS model but could not outperform the non-preemptive-based NJN model. This is due to the point that the proposed model was trying to maximize the survival rate of the sensors rather than concentrating on increasing the energy usage efficiency. Though there is not much difference in energy consumption rate of our proposed model and the NJN, considering the fact that the network uptime is maximized using our model, our model may be considered as superior to the other two models used in the experiment.

6 Conclusion

The problem of maximizing the lifetime of sensors in wireless rechargeable sensor networks has been addressed in this paper. The sensor's energy consumption-based prediction method for scheduling of mobile charger has been proposed whose time complexity is $O(n^2)$. The exhaustive simulation results show superiority of the proposed method in terms of survival rate as compared with FCFS and NJN without preemption method but at the cost of little higher energy usage efficiency. This is due to the distance traveled and the path taken by mobile charger for the process of charging the sensors so that their survival rate is increased. The proposed method is

more suitable to a small WRSN Network having around 200 sensors. The optimization of energy usage efficiency along with prediction-based high survival rate may be considered as future scope of work.

References

1. Angelopoulos, M. Constantinos et al., Efficient energy management in wireless rechargeable sensor networks.in *Proceedings of the 15th ACM international conference on Modeling, analysis and simulation of wireless and mobile systems* (2012)
2. L. Fu et al., Minimizing charging delay in wireless rechargeable sensor networks.in *2013 Proceedings IEEE INFOCOM*, (IEEE, 2013)
3. X. Ren, Xiaojiang, L. Weifa, X. Wenzheng, Maximizing charging throughput in rechargeable sensor networks. in *2014 23rd International Conference on Computer Communication and Networks (ICCCN)*, (IEEE, 2014)
4. L. Xie et al., Multi-Node wireless energy charging in sensor networks. IEEE/ACM Trans. Netw. **23**(2), 437–450 (2014)
5. S. Zhang, W. Jie, L. Sanglu, Collaborative mobile charging. IEEE Trans. Comput. **64**(3), 654–667 (2014)
6. L. Fu et al., Optimal charging in wireless rechargeable sensor networks. IEEE Trans. Veh. Technol. **65**(1), 278–291 (2015)
7. Y. Shu et al., Near-Optimal velocity control for mobile charging in wireless rechargeable sensor networks. IEEE Trans. Mob. Comput. **15**(7), 1699–1713 (2015)
8. P. Guo et al., Concurrently wireless charging sensor networks with efficient scheduling. IEEE Trans. Mob. Comput. **16**(9) 2450–2463 (2016)
9. A. Kaswan, A. Tomar, P.K. Jana, An efficient scheduling scheme for mobile charger in on-demand wireless rechargeable sensor networks. J. Netw. Comput. Appl. **114**, 123–134 (2018)
10. Z. Ma et al., Prolonging WSN lifetime with an actual charging model. in *2018 IEEE Wireless Communications and Networking Conference (WCNC)*, (IEEE, 2018)
11. A. Tomar, M. Lalatendu, K.J. Prasanta, An efficient scheduling scheme for on-demand mobile charging in wireless rechargeable sensor networks. Pervasive and Mob. Comput. **59**, 101074 (2019)
12. L. He, Z. Yanyan, P. Jianping, X. Jingdong, Evaluating on-demand data collection with mobile elements in wireless sensor networks. in *2010 IEEE 72nd Vehicular Technology Conference-Fall*, (IEEE, 2010), pp. 1–5
13. A. Tomar, M. Lalatendu, K.J. Prasanta, A fuzzy logic-based on-demand charging algorithm for wireless rechargeable sensor networks with multiple chargers. IEEE Trans. Mob Comput. (2020)
14. L. He, K. Linghe, G. Yu, P. Jianping, Z. Ting, Evaluating the on-demand mobile charging in wireless sensor networks. IEEE Trans. Mob. Comput. **14**(9), 1861–1875 (2014)
15. Huong, T. Tran et al., Genetic algorithm-based periodic charging scheme for energy depletion avoidance in WRSNs. in *2020 IEEE Wireless Communications and Networking Conference (WCNC)*, (IEEE, 2020)

Author Index

A
Abhinayaa, P., 215
Adithya, K. S., 303
Agrawal, Alka, 535
Aman, 363
Ansari, Saher Jawaid, 487
Aulakh, Inderdeep Kaur, 451
Aulakh, Navneet Singh, 451

B
Babu, Kore Shivanagendra, 337
Badiganti, Prem Kumar, 205
Bansal, Aarti, 59
Bhavanigari, Venkata Harish Babu, 391
Bhola, Amit, 327
Bhurchandi, Kishor, 553
Boora, Ritu, 403

C
Chakraborty, Sudeshna, 419, 431, 441
Chandrasekhar, Thanneru, 391
Chatterjee, Kakali, 511
Chawla, Priyanka, 337, 567
Chinmay, Ayes, 75
Choraria, Amit, 303
Choudhary, Kajal, 669
Choudhary, Surya Deo, 487

D
Dabas, Annu, 173
Dalvadi, Pravin, 21
Dar, Shahid Shabir, 431
Dhawan, Ruchika, 477
Dhull, Sanjeev Kumar, 97, 403
Dhumal, Dattaji Diliprao, 47
Dudhe, Ravishankar, 139, 319
Dudyala, Anil Kumar, 679
Durga, A. Mounika, 615

E
Ezhilarasie, R., 215

F
Farman, Shaik Afifa, 115
Farooq, Sameer, 567
Fusic, S. Julius, 241

G
Gaur, Abhishek, 627
Ghanekar, Umesh, 477
Gupta, Kartik, 441
Gupta, Maneesha, 173
Gupta, Mansi, 451
Gupta, Shilpi, 583, 593, 603

H
Hussain, Shaik Jakeer, 615

J
Jaiswal, Akriti, 603
Jayaram, Kumarapu, 337
Jha, Nisha, 419

S. Rawat et al. (eds.), *Proceedings of First International Conference on Computational Electronics for Wireless Communications*, Lecture Notes in Networks and Systems 329,
https://doi.org/10.1007/978-981-16-6246-1

Joshna, Aisha, 139

K
Kannaujia, Binod Kumar, 1
Karamalaputti, Pujitha, 155
Kaur, Anterpreet, 545
Kaur, Jasleen, 535
Keskar, Avinash, 47
Khan, Anum, 161
Khanna, Rajesh, 59
Khan, Raees Ahmad, 535
Kittur, Lakshmi Jayant, 635
Kochhar, Aarti, 87
Komal, 127
Krishnama Raju, A., 603
Kulsum, Umme, 319
Kumar, Amit, 669
Kumar, Arvind, 155, 523
Kumar, Balla Pavan, 523
Kumar, Hemanth, 655
Kumari, Jyoti, 327
Kumar, Naresh, 87
Kumar, Prabhat, 327
Kumar, Pramod, 303, 377, 419, 441
Kumar, Ramnish, 127
Kumar, R. Pradheep, 241
Kumar, S. M. Dilip, 655
Kumar, Yada Arun, 337

M
Mathur, Swati, 227
Maurya, Ajay K., 1
Maurya, Rakesh K., 1
Mehdi, Mohd Javeed, 115
Meshineni, Deepchand, 501
Miriyala, Suneel, 351
Mittal, Usha, 337
Muthusamy, Pachiyaannan, 37

N
Nagarjun, E., 655
Neha, 87
Nelaturi, Suman, 13

P
Pais, Alwyn Roshan, 635
Pal, Vipin, 465
Pandey, Rajoo, 523
Pant, Ashreeya, 431
Patel, Amrut, 21
Pati, Hemanta Kumar, 75
Peddirsi, Sumanth, 205
Popli, Rashmi, 419
Prabhu, Srikanth, 377
Prakash, Ravi, 1
Prasad, M. P. R., 281, 291, 391
Prithviraj, P., 377
Priyadarshini, Rashmi, 441
Purushottama, T. L., 259
Pushkar, K. L., 127

R
Rajni, 97
Ramesh, H., 241
Ram, Lalan Kumar, 679
Rana, Pooja, 337
Rathna, G. N., 501
Reddy, Ambavaram Pratap, 37
Reddy, Ravula Bharath Chandra, 337
Rupesh, Alla Tirumala Jagannadha, 205

S
Sai ram, M. Satya, 351
Samson, Mamatha, 115
Sangal, A. L., 363
Saxena, Sobhit, 195
Shahadat, C. M., 431
Sharma, Ananya, 377
Sharma, Rishabh, 431
Sharma, Surbhi, 59
Shirbhate, Ritwik, 47
Shrimali, Vibhakar, 627
Sigatapu, Vikas Venkat, 377
Singh, Aditya, 545
Singh, Ashish, 511
Singh, Divya, 645
Singh, Vivek Kumar, 431
Solanki, Mitesh, 583, 593
Sowmya, Pabba, 115
Sree, G. Naga Jyothi, 13
Srihari, Pathipati, 259
Srivastava, Pragya, 185
Srivastava, Richa, 185
Sunkaria, Ramesh K., 545
Surya, K. Jai, 195

T
Telang, Malhaar, 337
Tendolkar, Atharv, 303
Tripathi, Suman Lata, 205

U
Uma Maheswari, G., 271
Umamakeswari, A., 215

V
Vasudevan, K., 271
Verma, Aishita, 161
Verma, Pankaj, 669
Verma, Priyanka, 487
Verulkar, Anurag, 553
Vijaya Kumar, T. S. V. S., 281
Vijayvargy, Lokesh, 227
Vinay, Ratnala, 281, 291

W
Wairya, Subodh, 161
Wasim, Ahmed, 319

X
Xavier, S. Arockia Edwin, 241

Y
Yadav, Aryamaan, 377
Yadav, Nitin, 441
Yadav, Richa, 173, 185
Yadav, Ruchi, 441
Yogita, 465